frontiers | Research Topics

How can corneal biomechanics help with clinical applications?

Edited by
FangJun Bao, Ahmed Elsheikh, Weiyi Chen and Yan Wang

Published in
Frontiers in Bioengineering and Biotechnology

ISSN 1664-8714
ISBN 978-2-8325-2257-8
DOI 10.3389/978-2-8325-2257-8

About Frontiers

Frontiers is more than just an open access publisher of scholarly articles: it is a pioneering approach to the world of academia, radically improving the way scholarly research is managed. The grand vision of Frontiers is a world where all people have an equal opportunity to seek, share and generate knowledge. Frontiers provides immediate and permanent online open access to all its publications, but this alone is not enough to realize our grand goals.

Frontiers journal series

The Frontiers journal series is a multi-tier and interdisciplinary set of open-access, online journals, promising a paradigm shift from the current review, selection and dissemination processes in academic publishing. All Frontiers journals are driven by researchers for researchers; therefore, they constitute a service to the scholarly community. At the same time, the *Frontiers journal series* operates on a revolutionary invention, the tiered publishing system, initially addressing specific communities of scholars, and gradually climbing up to broader public understanding, thus serving the interests of the lay society, too.

Dedication to quality

Each Frontiers article is a landmark of the highest quality, thanks to genuinely collaborative interactions between authors and review editors, who include some of the world's best academicians. Research must be certified by peers before entering a stream of knowledge that may eventually reach the public - and shape society; therefore, Frontiers only applies the most rigorous and unbiased reviews. Frontiers revolutionizes research publishing by freely delivering the most outstanding research, evaluated with no bias from both the academic and social point of view. By applying the most advanced information technologies, Frontiers is catapulting scholarly publishing into a new generation.

What are Frontiers Research Topics?

Frontiers Research Topics are very popular trademarks of the *Frontiers journals series*: they are collections of at least ten articles, all centered on a particular subject. With their unique mix of varied contributions from Original Research to Review Articles, Frontiers Research Topics unify the most influential researchers, the latest key findings and historical advances in a hot research area.

Find out more on how to host your own Frontiers Research Topic or contribute to one as an author by contacting the Frontiers editorial office: frontiersin.org/about/contact

How can corneal biomechanics help with clinical applications?

Topic editors

FangJun Bao — Affiliated Eye Hospital to Wenzhou Medical University, China
Ahmed Elsheikh — University of Liverpool, United Kingdom
Weiyi Chen — Taiyuan University of Technology, China
Yan Wang — Tianjin Eye Hospital, China

Citation

Bao, F., Elsheikh, A., Chen, W., Wang, Y., eds. (2023). *How can corneal biomechanics help with clinical applications?* Lausanne: Frontiers Media SA. doi: 10.3389/978-2-8325-2257-8

Table of contents

frontiers | Frontiers in Bioengineering and Biotechnology

TYPE Editorial
PUBLISHED 12 April 2023
DOI 10.3389/fbioe.2023.1184840

OPEN ACCESS

EDITED AND REVIEWED BY
Salavat Aglyamov,
University of Houston, United States

*CORRESPONDENCE
Ahmed Elsheikh,
elsheikh@liverpool.ac.uk

RECEIVED 12 March 2023
ACCEPTED 04 April 2023
PUBLISHED 12 April 2023

CITATION
Bao F, Chen W, Wang Y and Elsheikh A (2023), Editorial: How can corneal biomechanics help with clinical applications?
Front. Bioeng. Biotechnol. 11:1184840. doi: 10.3389/fbioe.2023.1184840

Editorial: How can corneal biomechanics help with clinical applications?

FangJun Bao[1], WeiYi Chen[2], Yan Wang[3] and Ahmed Elsheikh[4]*

[1]Eye Hospital, Wenzhou Medical University, Wenzhou, China, [2]College of Biomedical Engineering, Taiyuan University of Technology, Taiyuan, China, [3]Tianjin Eye Hospital, Tianjin, China, [4]School of Engineering, University of Liverpool, Liverpool, United Kingdom

KEYWORDS

cornea, biomechanics, *ex-vivo* measurement, *in-vivo* measurement, clinical application

Editorial on the Research Topic
How can corneal biomechanics help with clinical applications?

For those of us on the corneal biomechanics bandwagon, the 25-year journey to date has been challenging and yet extremely exciting. Although interest in the field goes back to the 1970s and before, serious interest from renowned researchers like Woo, Wollensak, Nash and Bryant started to make significant contributions in the 1990s. At that time, most, if not all, efforts were focused on the *ex-vivo* testing of corneal tissue in an attempt to understand and quantify the material's hyperelasticity, viscoelasticity and hysteresis, and the behaviour changes associated with ageing and diseases such as diabetes and keratoconus. Most of that work used uniaxial extensometry testing, with narrow strips separated from corneal tissue (and surrounding limbus and anterior sclera) and subjected to tension forces. The tests suffered from fundamental drawbacks arising from the specimen's non-uniform thickness, straightening an originally curved tissue and the severing of collagen fibrils along specimen edges. Furthermore, the loading applied (axial tension) was not compatible with the usual loading of the cornea under intraocular pressure.

Efforts to improve the testing protocol led to cornea inflation testing, in which the cornea remained intact and loaded with a posterior pressure simulating closely the effects of intraocular pressure. Still, the test method relied on non-physiologic boundary conditions along the specimen edge, which did not represent the actual stiffness of the limbus. In addition, approximations were also introduced in the analysis of the pressure-deformation results to produce estimates of the stress-strain behaviour; this analysis relied first on a form of shell theory that involved necessary approximations of the cornea as a spherical segment with rotational symmetry and uniform thickness. These features inevitably affected the reliability of the resulting stress-strain behaviour and underscored the need for improvements in the test method.

Improvements came first in the form of the finite element-based inverse analysis of the cornea inflation test results–removing the need for shell theory. A more substantial improvement followed with whole globe inflation testing, where complete intact eye globes were tested under variable intraocular pressure while suspending the eye and monitoring its deformation response to pressure changes. This technique presented the ultimate solution as the tissue remained intact, loaded with physiologic intraocular pressure, and no approximations were made in the analysis method; however, the drawback was in the complexity of the testing protocol and the associated high chance of analysis mistakes. The

protocol was also very time consuming and required the development of highly complex testing apparatus, access to which was limited to a small number of research groups around the world. Despite this, the resulting information on corneal biomechanical behaviour was invaluable in quantifying trends related to stiffness changes with age, disease and rate of loading.

The results also showed that corneas with the same conditions (age, race, medical history) still experienced different behaviours. This outcome meant that, while *ex-vivo* testing helped identify corneal behaviour trends, these trends could not simply be applied to individual corneas. Another Research Topic arose with the realisation–or expectation–that *ex-vivo* tissue may have undergone deterioration post-mortem, and therefore its experimental behaviour cannot be assumed to apply directly to *in vivo* eyes. For these reasons, it became evident that *in vivo* testing and measurement of tissue biomechanics was a necessary next step. The first breakthrough here was in 2005 with the Ocular Response Analyzer (ORA, Reichert, USA), a non-contact air-puff-based instrument that provided two measures of corneal biomechanics; these are Corneal Resistance Factor (CRF), which relates to corneal geometric stiffness–in turn, dominated by changes in corneal thickness–and Corneal Hysteresis (CH), which relates to corneal viscoelasticity. This instrument had a significant impact on the field by showing promise in the *in vivo* measurement of corneal biomechanics, even though the CRF and CH could not be linked directly to standard measures of stiffness such as the tangent modulus.

A subsequent development took place a few years later, in 2012, with the Corvis ST (Oculus, Germany). This device used similar non-contact, air puff technology and used its much-enhanced monitoring technique to derive several dynamic corneal response (DCR) parameters. Some of the DCRs, most notably the Stiffness Parameter (SP), the Integrated Inverse Radius (IIR), and the Deflection Amplitude (DA) could be related statistically to corneal biomechanical stiffness, even though (like the CRF and CH) no direct links between them and the standard stiffness measures could be established. A further development then took place in 2018 with the Stress Strain Index (SSI), which promised to estimate the stress-strain behaviour of the tissue and, hence, its tangent modulus at any stress or strain. This development was taken further 2 years later when it became possible to turn the SSI from a single value to a map covering the corneal surface. This step was made possible by relying on the evident link between corneal stiffness and the density and orientation of the tissue's collagen fibrils, as well as our current knowledge of the tissue's microstructure maps of both healthy and diseased corneas.

Other *in vivo* behaviour testing methods are under development and expected to become commercially available within a few years. Most notably, Brillouin Microscopy and elastography are among the most detailed and most advanced techniques with strong scientific evidence of their ability to map corneal stiffness in 3D.

As we now move into the second quarter of the 21st century, the wealth of knowledge on 'trends' of corneal behaviour identified in *ex-vivo* tests, and 'quantification and mapping' of the behaviour of individual corneas measured *in vivo*, is allowing us to move into treatment optimisation for the first time. This area is the ultimate goal of all our previous efforts as a research community over the last 25 years. And it is exciting because now the target is to benefit patients, rather than to develop methods or understand behaviour. Several applications in which clinicians have had to rely on experience can now be optimised on a scientific basis and with reference to accurate measurements of corneal biomechanics *in vivo*. These applications include the optimisation of the crosslinking treatment used in patients with keratoconus, customisation of the intracorneal ring segment surgeries used to restore the healthy geometry in irregular corneas, and the incisions used in cataract surgeries which may have an effect on corneal astigmatism.

These applications and others are expected to provide bright examples of how corneal biomechanics can really benefit clinical practice over the next few years. So, watch the space!

Author contributions

Study concept and design (FB, WC, YW, AE); writing the manuscript (FB, WC, YW, AE); critical revision of the manuscript (FB, WC, YW, AE).

Conflict of interest

The authors declare that the research was conducted in the absence of any commercial or financial relationships that could be construed as a potential conflict of interest.

Publisher's note

frontiers | Frontiers in Bioengineering and Biotechnology

TYPE Editorial
PUBLISHED 04 May 2023
DOI 10.3389/fbioe.2023.1186938

OPEN ACCESS

EDITED AND REVIEWED BY
Salavat Aglyamov,
University of Houston, United States

*CORRESPONDENCE
Yan Wang,
wangyan7143@vip.sina.com

RECEIVED 15 March 2023
ACCEPTED 27 April 2023
PUBLISHED 04 May 2023

CITATION
Wang Y, Cao H, Chen W, Bao F and Elsheikh A (2023), Editorial: How can corneal biomechanics help with clinical applications?
Front. Bioeng. Biotechnol. 11:1186938.
doi: 10.3389/fbioe.2023.1186938

Editorial: How can corneal biomechanics help with clinical applications?

Yan Wang[1,2]*, HuaZheng Cao[2,3], WeiYi Chen[4], FangJun Bao[5] and Ahmed Elsheikh[6]

[1]Tianjin Key Lab of Ophthalmology and Visual Science, Tianjin Eye Hospital, Tianjin Eye Institute, Nankai University Affiliated Eye Hospital, Tianjin, China, [2]Nankai University Eye Institute, Nankai University, Tianjin, China, [3]School of Medicine, Nankai University, Tianjin, China, [4]College of Biomedical Engineering, Taiyuan University of Technology, Taiyuan, China, [5]Eye Hospital, Wenzhou Medical University, Wenzhou, China, [6]School of Engineering, University of Liverpool, Liverpool, United Kingdom

KEYWORDS

corneal biomechanics, corneal refractive surgery, keratoconus, myopia, finite element analysis, clinical application

Editorial on the Research Topic
How can corneal biomechanics help with clinical applications?

There is growing interest in corneal biomechanics associated with demands for better precision in clinical diagnosis, treatment of corneal disease and corneal refractive surgery. The cornea possesses a complex balance of stiffness, strength, toughness, and extensibility in order to withstand internal and external forces (Esporcatte et al., 2020). These important properties of the cornea, besides optical characteristics, have often been ignored by clinicians until devices for the *in-vivo* corneal biomechanical assessment were developed. For decades, corneal biomechanical description remained an elusive target until nondestructive testing has taken corneal biomechanics to the clinic and placed it in the hands of clinicians. A deep understanding of corneal biomechanical behavior has critical implications for the management of certain ocular diseases and planning of corneal surgeries. A few examples of the various key clinical applications that highly depend on corneal biomechanical assessment are progression of keratoconus, assessment of corneal refractive surgery, and determination of intraocular pressure (IOP). Recent studies have shown an explosive trend and broadened the scope of clinical translation. Here, we present a Research Topic in this booming field. The topic covers a broad range of themes that reflect the latest progress, most culled from unsolicited original studies and reviews. We hope that this will inspire further enthusiasm for the subject and foster further progress in its clinical applications.

The accurate detection of keratoconus has been widely studied. Tian et al. calculated the corneal elastic modulus according to the relationship between the air-puff forces and corneal apical displacement, and demonstrated that it is more precise than other known dynamic corneal response variables in detecting forme fruste keratoconus. Zhang et al. developed a prognostic nomogram for the diagnosis of subclinical keratoconus. Integrated corneal tomographic and biomechanical assessments achieved significantly better predictability when compared with separate tomographic and biomechanical parameters. Tian et al. reported a gradually decreasing trend in the distance between corneal landmarks (thinnest point, coordinate point of maximum curvature, and corneal apex) with the progression of

keratoconus, and the correlation between the three landmark distances and the dynamic corneal response parameters became significant from stage II keratoconus. These results confirmed that the weakening of corneal biomechanical properties from normal to keratoconus might be accompanied by the merging of typical landmark positions.

Based on the current development trend, corneal dynamic deformation in disease diagnosis does not apply to keratoconus only. For example, Ye et al. introduced an air-puff dynamic anterior-segment optical coherence tomography system that was effective in identifying the presence of peripheral anterior synechia in a non-contact approach, avoiding the inconvenience and discomfort caused by traditional indentation gonioscopy. The peripheral cornea is deformed by the air puff jetted from the device, and pressure is transferred to the anterior chamber angle through the aqueous humor. This approach shows great potential for guidance in the diagnosis of angle-closure glaucoma. It is noteworthy that most dynamic corneal response parameters are more significantly correlated with IOP than corneal thickness, as reported by Ye et al., who determined the effect of IOP fluctuation caused by mydriasis on corneal biomechanical metrics. Therefore, changes in corneal thickness and IOP should be considered when evaluating corneal biomechanical changes during disease progression.

Corneal biomechanics is coming of age as an important consideration in surgical procedures designed to change corneal shape and in cross-linking treatments aimed at stiffening the cornea and halting disease progression in keratoconus and iatrogenic ectasia. Xin et al. compared the corneal biomechanical response to transepithelial photorefractive keratectomy (tPRK), femtosecond laser-assisted *in situ* keratomileusis (FS-LASIK), and small-incision lenticule extraction (SMILE), in a population matched for age, sex, corrected refraction, corneal thickness, optical zone, and IOP. The SMILE procedure led to less corneal biomechanical degradation than FS-LASIK, but more than tPRK, in cases with comparable corneal thickness loss. This is in agreement with previous studies reported by our team, indicating that the FS-LASIK procedure induced a greater reduction in corneal tensile strength than SMILE, providing robust evidence for the selection of refractive surgery (Wu et al., 2014; Ma et al., 2018). In a prospective study, Sun et al. reported that topography-guided transepithelial-accelerated corneal collagen crosslinking is effective and safe in correcting low refractive error in keratoconus treatment, as more than 30% of the patients presented an enhanced UCVA by more than three lines, and all topographies showed no sign of disease progression at each examination. On the basis of long-term observations, Tian et al. reported improved CDVA, increased corneal thickness, stable keratometry, and posterior corneal elevation after accelerated transepithelial corneal crosslinking for post-LASIK ectasia during a follow-up period of 2 years.

The current Research Topic covers the corneal biomechanical changes in myopia, which have been viewed as an interesting biomechanical problem. Liu et al. found a lower stress-strain index (SSI), a biomechanical parameter representing corneal material stiffness, in severely elongated eyes (axial length ≥ 26 mm) than in moderately elongated eyes (axial length < 26 mm), and the SSI was negatively correlated with axial length in the former group, but not in the latter group. These results have provided insights into the different eye growth patterns in lower myopia and higher myopia, as axial length carries information about the degree of ocular myopia. Nevertheless, owing to the different refractive powers of the refractive system between individuals, myopic refraction may vary for the same axial length. The ratio of axial length to corneal radius of curvature (AL/CR) is likely to be reliable for the quantitative description of myopic refraction (Scheiman et al., 2016). A retrospective study by Chu et al. showed a negative correlation between SSI and AL/CR regardless of the degree of myopia; however, SSI did not decrease with the worsening of myopia; rather, it exhibited gradual stability at a low level. These findings validate the possibility of assessing dynamic changes in ocular wall stiffness based on corneal biomechanical measurements during the development of myopia.

This Research Topic collects several kinds of plausible, capable technologies in a challenging field and *in vivo* characterization of the corneal constitutive mechanical composition, as the current devices in clinical practice do not yet provide classic biomechanical properties, such as the tangent modulus, with the exception of the SSI. Taking the natural frequency of corneal tissue as a biomarker for corneal biomechanics, Lan et al. confirmed the possibility of micro-forced optical coherence elastography to characterize the global and local features of heterogeneous samples, which can resolve local variations in tissue structure, complementary to current clinical biomechanical assessments. Zhang et al. calculated the corneal strain energy using the viscoelastic strain energy density function and the first-order Prony relaxation function with the first-order Ogden strain energy of the cornea. After completely considering the work done by the air puff as the strain energy of the cornea in attaining whole-corneal displacement, the evaluation of corneal viscoelastic properties *in vivo* was performed by applying an optimized genetic algorithm. Yousefi et al. reported that the experienced load of the cornea during the concave phase of the Corvis test was significantly altered by dynamic changes in the corneal shape, implying a subject-specific loading fluctuation even if the air puff itself was identical. Stiffer corneas showed the least sensitivity to a change in load, whereas more compliant corneas exhibited higher sensitivity. This is important when comparing the same eye after a surgical procedure or topical medication that alters corneal properties. Song et al. linked the elastic modulus of the human corneal stroma measured by tensile testing with optical coherence tomography imaging (*ex vivo*) to corneal deformation measurements using visualization Scheimpflug technology (*in vivo*). They found that a low strain tangent modulus was accompanied by a larger A1 length and A1 deflection area. This indicated the relationship between corneal dynamic response parameters and their intrinsic elasticity, which is helpful in understanding the nature of the measurements produced and the compromises that had to be made to allow nondestructive biomechanical assessment to optimize clinical interpretation.

One of the most useful tools for the simulation of corneal biomechanical response is finite element analysis. In the last two decades, corneal mechanical behavior under different conditions has been discussed using numerical simulation methods, providing theoretical support for clinical practice (Fang et al., 2020a; Fang et al., 2020b). In this Research Topic, Qin et al. propose a method to determine corneal biomechanical parameters based on Ocular Response Analyzer measurements. Redaelli et al.

developed a high-fidelity fluid-structure interaction simulation to virtually apply a defined air pulse to a 3D idealized eye model comprising the cornea, limbus, sclera, lens, and humors, and explained the correct variation of IOP during a non-contact tonometry test. Moreover, in order to evaluate biomechanical differences between LASIK and SMILE procedures, Wang et al. applied the iterative algorithm to retrieve the stress-free state of the intact corneal model, LASIK model, and SMILE model. To improve corneal biomechanical stability, it is recommended to create a corneal cap rather than a corneal flap. Using finite-element modeling during orthokeratology, Wu et al. reported that the target myopia reduction had the greatest effect on the central corneal stress value, followed by corneal curvature, while the opposite results were observed in the peripheral corneal area. The authors suggested considering the orthokeratology lens design and the lens fitting process in clinical practice, especially for patients with high myopia and steep corneas.

Another exciting aspect is the cellular and molecular exploration of corneal biomechanics. As reviewed by Yang et al., different types of corneal cells can perceive and transduce mechanical signals in distinct ways, which modulate the expression of specific genes and influence diverse biological functions. These mechanical cues include substrate stiffness, shear stress, and tensile and compressive forces. The mechanisms by which corneal cells interact with different mechanical microenvironments determine many major biological functions under physiological and pathological conditions, which enable physicians to develop therapeutic strategies for corneal disorders from a mechanobiological perspective.

In summary, corneal biomechanics has blossomed from a predominantly academic discipline to a translational enterprise throughout its two-decade history, and we are on the brink of a new era of biomechanics-based intervention. The study on the early diagnosis of keratoconus has attracted the greatest readership, and this is a good example that motivates our efforts to explore, build, and develop this promising field. Further studies on corneal biomechanics will continue to develop methods and measuring parameters. More profound investigation and daring attempts are necessary to build a bridge to clinical application, as well as more accurate and effective diagnosis. The ultimate goal is to optimize the surgical design and guide for disease treatment, and such a future now appears within reach.

Author contributions

All authors listed have made a substantial, direct and intellectual contribution to the work, and approved it for publication. All authors contributed to the article and approved the submitted version.

Funding

This study was supported by the National Program on Key Research Project of China (2022YFC2404502), the National Natural Science Foundation of China (No. 82271118), and the Tianjin Key Medical Discipline (Specialty) Construction Project (TJYXZDXK-016A).

Conflict of interest

The authors declare that the research was conducted in the absence of any commercial or financial relationships that could be construed as a potential conflict of interest.

Publisher's note

References

Esporcatte, L. P. G., Salomão, M. Q., Lopes, B. T., Vinciguerra, P., Vinciguerra, R., Roberts, C., et al. (2020). Biomechanical diagnostics of the cornea. *Eye Vis. (Lond).* 7, 9. doi:10.1186/s40662-020-0174-x

Fang, L., Ma, W., Wang, Y., Dai, Y., and Fang, Z. (2020a). Theoretical analysis of wave-front aberrations induced from conventional laser refractive surgery in a biomechanical finite element model. *Invest. Ophthalmol. Vis. Sci.* 61, 34. doi:10.1167/iovs.61.5.34

Fang, L., Wang, Y., Yang, R., Deng, S., Deng, J., and Wan, L. (2020b). Effects of the LASIK flap thickness on corneal biomechanical behavior: A finite element analysis. *BMC Ophthalmol.* 20, 67. doi:10.1186/s12886-020-01338-8

Ma, J., Wang, Y., Wei, P., and Jhanji, V. (2018). Biomechanics and structure of the cornea: Implications and association with corneal disorders. *Surv. Ophthalmol.* 63, 851–861. doi:10.1016/j.survophthal.2018.05.004

Scheiman, M., Gwiazda, J., Zhang, Q., Deng, L., Fern, K., Manny, R. E., et al. (2016). Longitudinal changes in corneal curvature and its relationship to axial length in the Correction of Myopia Evaluation Trial (COMET) cohort. *J. Optom.* 9, 13–21. doi:10.1016/j.optom.2015.10.003

Wu, D., Wang, Y., Zhang, L., Wei, S., and Tang, X. (2014). Corneal biomechanical effects: Small-incision lenticule extraction versus femtosecond laser-assisted laser *in situ* keratomileusis. *J. Cataract. Refract. Surg.* 40, 954–962. doi:10.1016/j.jcrs.2013.07.056

frontiers in Bioengineering and Biotechnology

ORIGINAL RESEARCH
published: 11 October 2021
doi: 10.3389/fbioe.2021.743745

The Biomechanical Response of the Cornea in Orthokeratology

Jinfang Wu[1], *Wenxuan Fang*[1], *Huiwen Xu*[2,3], *Xiaode Liu*[1,4], *Dongliang Zhao*[5]* and *Qiguo Rong*[1]*

[1]Department of Mechanics and Engineering Science, College of Engineering, Peking University, Beijing, China, [2]Department of Epidemiology and Biostatistics, School of Public Health, Peking University, Beijing, China, [3]Medical Informatics Center, Peking University, Beijing, China, [4]X Lab, the Second Academy of CASIC, Beijing, China, [5]School of Chemical Biology and Biotechnology, Peking University Shenzhen Graduate School, Shenzhen, China

Orthokeratology has been widely used to control myopia, but the mechanism is still unknown. To further investigate the underlying mechanism of corneal reshaping using orthokeratology lenses *via* the finite element method, numerical models with different corneal curvatures, corneal thicknesses, and myopia reduction degrees had been developed and validated to simulate the corneal response and quantify the changes in maximum stress in the central and peripheral corneal areas during orthokeratology. The influence of the factors on corneal response had been analyzed by using median quantile regression. A partial eta squared value in analysis of variance models was established to compare the effect size of these factors. The results showed central and peripheral corneal stress responses changed significantly with increased myopia reduction, corneal curvature, and corneal thickness. The target myopia reduction had the greatest effect on the central corneal stress value (partial eta square = 0.9382), followed by corneal curvature (partial eta square = 0.5650) and corneal thickness (partial eta square = 0.1975). The corneal curvature had the greatest effect on the peripheral corneal stress value (partial eta square = 0.5220), followed by myopia reduction (partial eta square = 0.2375) and corneal thickness (partial eta square = 0.1972). In summary, the biomechanical response of the cornea varies significantly with the change in corneal conditions and lens designs. Therefore, the orthokeratology lens design and the lens fitting process should be taken into consideration in clinical practice, especially for patients with high myopia and steep corneas.

Keywords: orthokeratology, myopia control, ocular biomechanics, finite element simulation, corneal response

OPEN ACCESS

Edited by:
Weiyi Chen,
Taiyuan University of Technology, China

Reviewed by:
Ashkan Eliasy,
University of Liverpool, United Kingdom
Xingtao Zhou,
Fudan University, China

***Correspondence:**
Qiguo Rong
qrong@pku.edu.cn
Dongliang Zhao
zhaodl@pku.edu.cn

Specialty section:
This article was submitted to Biomechanics, a section of the journal Frontiers in Bioengineering and Biotechnology

Received: *19 July 2021*
Accepted: *06 September 2021*
Published: *11 October 2021*

Citation:
Wu J, Fang W, Xu H, Liu X, Zhao D and Rong Q (2021) The Biomechanical Response of the Cornea in Orthokeratology. Front. Bioeng. Biotechnol. 9:743745. doi: 10.3389/fbioe.2021.743745

INTRODUCTION

As one of the most effective methods of myopia control, orthokeratology (ortho-k) has been widely used around the world in the past two decades (Wolffsohn et al., 2016; Cho and Tan, 2019; Jonas et al., 2021). The ortho-k lens, a specially designed rigid contact lens, is different from ordinary optical contact lenses because it can change the corneal shape to achieve the purpose of clear vision during the daytime when the lens is removed after overnight wear. The strong effect on myopia control of ortho-k lens for children and adolescents has been proved and reported by numerous clinical researchers. The investigations revealed a slight variance in myopia control effect with an unweighted average 43% (Cho and Cheung, 2012; Hiraoka et al., 2012; Cheung and Cho, 2016; Cho and Cheung, 2017).

Currently, the clinician fits the ortho-k lens based on the patient's examination results, which include refractive target degree, corneal curvature, corneal e value, and corneal diameter, under the guidance of the manufacturer and clinical experience. Although the effectiveness in reducing myopia and controlling myopia progression of ortho-k lens has been proven by statistical data, the results vary for the individual subjects (Cho et al., 2005). Furthermore, the mechanism by which it controls the development of myopia, the influences, and the weight of these influencing factors are still unknown, while the clinical application of the ortho-k lens has been reported extensively.

Previous researchers had mentioned that the ortho-k lens plays its role mainly *via* the mechanical interaction between the lens and the cornea or the eyeball (Swarbrick, 2004; Wan et al., 2020). Numerous studies (Kobayashi et al., 2008; Lau et al., 2019; Mohidin et al., 2020; Queiros et al., 2020) had attempted to reveal the mechanical effect of wearing ortho-k lenses on the cornea by comparing the change of refractive states, corneal topographies, and corneal thicknesses before and after ortho-k treatment, but few researchers went into details of the analysis due to the complexity of measurement and calculation.

In the current study, finite element modeling was used to analyze the corneal stress responses produced by changing the ortho-k lens parameters and fitting the lenses on various corneas. The purpose of our research was to establish a deeper understanding of the mechanical response of the cornea during ortho-k treatment. The interaction between the lenses and the cornea had been simulated, and the stress responses of the cornea with different designs of ortho-k lens had been analyzed quantitatively. By investigating the corneal stress response, our research strives to reveal the mechanism of ortho-k and contribute to the evaluation of the lens performance and corneal response during the treatment.

MATERIALS AND METHODS

Study Design

The finite element methods were used to analyze the ortho-k process. First, the corneal models were built based on the common corneal thicknesses and corneal curvatures. Second, the corresponding ortho-k lenses were selected in accordance with the manufacturer's fitting instructions, and the lens parameters were extracted for simulation. Then, the interactions during the wearing process were numerically modeled, and corneal mechanical responses were investigated under these specific conditions. According to the post-fitting changes in the corneal topography, the central area was defined as the central 4 mm area of the corneal apex, outside of which was defined as the peripheral area. The central and peripheral corneal stress under the ortho-k lens was quantified, and the impact of a refractive target, corneal curvature, and corneal thickness on the corneal stress were analyzed.

Corneal Geometry

Based on the common corneal curvatures and corneal thicknesses, cornea models were developed, with the curvature of 40.25 D, 41.25 D, 42.25 D, 43.25 D, and 44.25 D, respectively, and thicknesses of 500 μm, 525 μm, 550 μm, and 575 μm, respectively, as shown in **Table 1**. The corneal radius was calculated by the following formula:

$$r = \frac{1000 \times (n-1)}{D}, \tag{1}$$

where n is the refractive index of the cornea (n=1.337), D is the corneal refractive power, and r is the corneal curvature radius. A total of 20 ideal cornea models were established for the finite element analysis.

TABLE 1 | Corneal curvature, corneal thickness, and myopia.

Variable	Value				
Corneal curvature (D)	40.25	41.25	42.25	43.25	44.25
Corneal thickness (μm)	500	525	550	575	
Myopia (D)[a]	−2.00	−3.00	−4.00	−5.00	

[a]*The degree of myopia used for lens selection.*

Ortho-k Lens Geometry

Four-zone ortho-k lenses (α ortho-k; Alpha Corp., Nagoya, Japan) made of highly oxygen permeable lens material (Boston EM, nominal Dk of 104×10^{-11} (cm^2/sec) (mL O_2/mL × mmHg)) were used in this study. Based on the parameters of the corneal curvatures (40.25 D, 41.25 D, 42.25 D, 43.25 D, and 44.25 D) and the target myopia reduction degrees (−2.00 D, −3.00 D, −4.00 D, and −5.00 D), twenty commonly used ortho-k lens parameters were selected for the investigation, as shown in **Table 2**. The two-dimensional geometry of the ortho-k lenses was measured by a noncontact optical coherence tomography (OCT) metrology system, the Optimec *is*830 (Optimec Systems Limited, United Kingdom), in four meridians (0°, 90°, 180°, and 270°) (Coldrick et al., 2016). The lens' thickness, diameter, sagittal data, and all of the curvatures of each zone were extracted. The geometry model is shown in **Figure1A**. The average coordinates of the four meridians captured by OCT were used to rotate into three-dimensional models of the ortho-k lenses using SolidWorks software (SOLIDWORKS 2017, Dassault Systemes, the United States), as shown in **Figure 1B**.

Finite Element Model

Histologically, the microanatomical structure of the cornea can be divided into five layers from the anterior to the posterior: epithelium, Bowman's membrane, stroma, Descemet's membrane, and endothelium. In our modeling of the cornea, three layers of different elastic modulus were assigned to represent the real corneal structure. The corneal epithelium and Bowman's membrane were regarded as one layer, as was Descemet's membrane and endothelium. The layer thickness of the epithelial and Bowman's membrane was presumed to be 50–57.5 μm, 10 percent of the total corneal thickness, as in routine clinical findings (Ehlers et al., 2010). The cornea was assumed to be a nonhomogeneous elastic material (Pinsky et al., 2005; Elsheikh et al., 2009; Last et al., 2009), and all material properties are shown in **Table 3** (Wollensak et al., 2003; Pinsky et al., 2005;

TABLE 2 | The selected lens parameters.

Item	Flat K (D)	Diameter (mm)	BCR (mm)	BCRP (D)	CF (D)	CT (mm)	Myopia (D)
1	40.25	10.6	9.00	37.50	+0.75	0.22	–2.00
2	40.25	10.6	9.25	36.50	+0.75	0.22	–3.00
3	40.25	10.6	9.51	35.50	+0.75	0.22	–4.00
4	40.25	10.6	9.78	34.50	+0.75	0.22	–5.00
5	41.25	10.6	8.77	38.50	+0.75	0.22	–2.00
6	41.25	10.6	9.00	37.50	+0.75	0.22	–3.00
7	41.25	10.6	9.25	36.50	+0.75	0.22	–4.00
8	41.25	10.6	9.51	35.50	+0.75	0.22	–5.00
9	42.45	10.6	8.50	39.70	+0.75	0.22	–2.00
10	42.45	10.6	8.72	38.70	+0.75	0.22	–3.00
11	42.45	10.6	8.95	37.70	+0.75	0.22	–4.00
12	42.45	10.6	9.20	36.70	+0.75	0.22	–5.00
13	43.25	10.6	8.33	40.50	+0.75	0.22	–2.00
14	43.25	10.6	8.54	39.50	+0.75	0.22	–3.00
15	43.25	10.6	8.77	38.50	+0.75	0.22	–4.00
16	43.25	10.6	9.00	37.50	+0.75	0.22	–5.00
17	44.25	10.6	8.13	41.50	+0.75	0.22	–2.00
18	44.25	10.6	8.33	40.50	+0.75	0.22	–3.00
19	44.25	10.6	8.54	39.50	+0.75	0.22	–4.00
20	44.25	10.6	8.77	38.50	+0.75	0.22	–5.00

Flat K: flat keratometry; D: degree; BCR: base curve radius; BC: base curve refractive power; CF: compression factor; CT: central thickness.

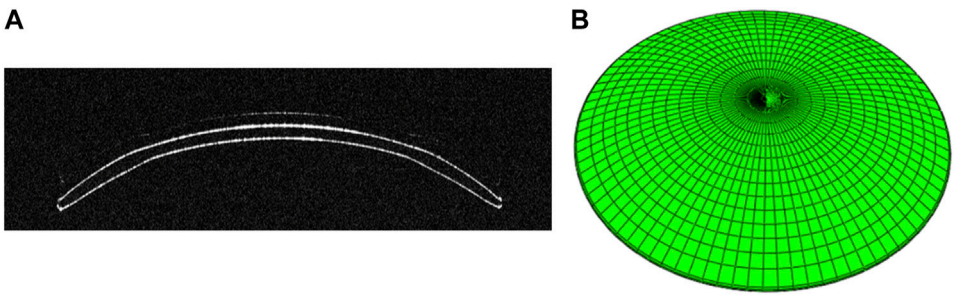

FIGURE 1 | (A) OCT B-Scan image of ortho-k lens from the Optimec is830. **(B)** Three-dimensional model of ortho-k lens.

TABLE 3 | Lens and cornea material properties.

	Young's modules	Poisson ratio
Ortho-k lenses	100 MPa	0.3
Outermost layer*	127 kPa	0.49
Interlayer*	1270 kPa	0.49
Innermost layer*	127 kPa	0.49

Outermost layer: epithelium and Bowman's membrane; interlayer: corneal stroma; innermost layer: Descemet's membrane and endothelium.

Elsheikh et al., 2008; Elsheikh et al., 2009; Last et al., 2009). According to the previous studies (Elsheikh et al., 2008; Elsheikh et al., 2009), the stiffness of both the outermost and innermost layers were assumed to be 10 percent as stiff as the corneal stroma. The finite element mesh of structured elements was generated. A mesh dependency study was conducted such that the relative error in two consecutive mesh refinements was <0.5% for computation. The mesh and boundary conditions are shown in **Figure 2**. Clinical studies have proven that principally only the thickness of the corneal epithelium and the curvature of the anterior cornea are changed when wearing an ortho-k lens, without bending of the entire cornea or affecting the depth of the anterior chamber (Alharbi and Swarbrick, 2003; Kim et al., 2018; Swarbrick et al., 2020). Therefore, in our model, the sclera was constrained from moving in all directions. To best match with the model of the whole eye, the orientation of corneal edge support was set to 23 (Elsheikh and Wang, 2007). The intraocular pressure (IOP) was set to 13 mmHg and homogeneously applied on the inner corneal surface, while the eyelid pressure was set to 9 mmHg and applied on the outer surface of the lens (Shaw et al., 2010). Eighty static finite element simulations were performed using the Abaqus software (version 6.14 Dassault Systemes, Simulia Corp., RI, the United States) for revealing the stress and displacement status of ortho-k lenses' wearing.

Statistical Analysis

The normality of residuals and homogeneity of variance were tested by using the Shapiro–Wilk test and Levene's test,

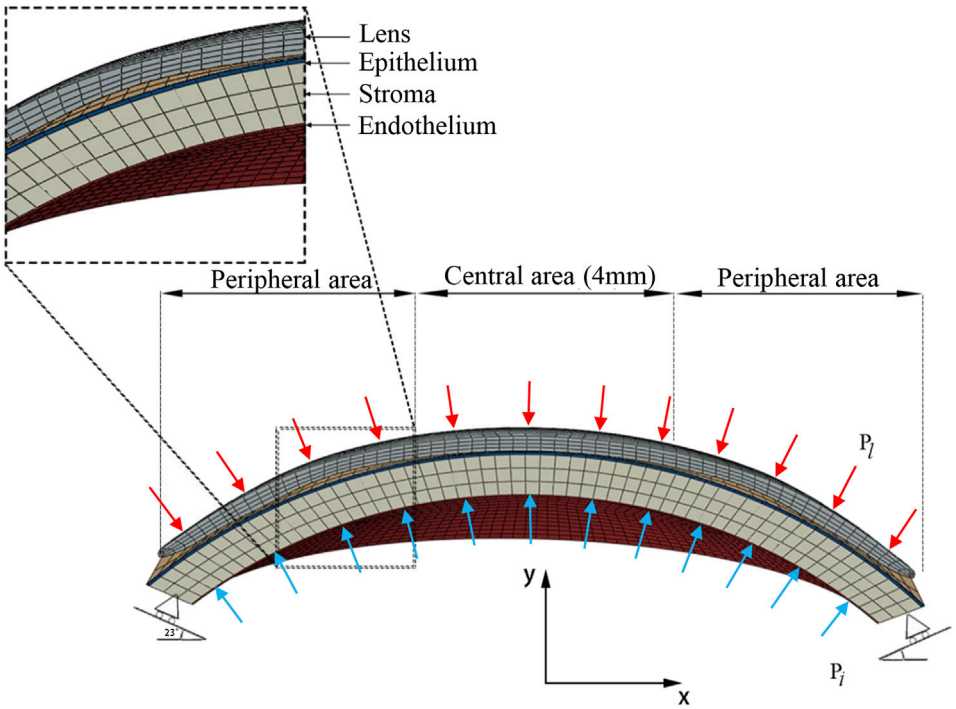

FIGURE 2 | FEA models of ortho-k lens and the cornea.

respectively. Because data were found to violate normality, median quantile regression was conducted to explore factors influencing central corneal stress and peripheral corneal stress. Quantile regression is an approach that models the distribution of the responses and performs better than conventional means of regression when the normality assumption is violated. The central corneal stress value and the peripheral corneal stress value were, respectively, used as dependent variables (continuous variables), and the degree of myopia, corneal curvature, and corneal thickness were included as independent variables (categorical variables) in the models. Furthermore, to estimate the effect size of the independent variables on dependent variables, we used the analysis of variance (ANOVA) method and reported partial eta square as the measure of effect size. Partial eta squared ($partial\ \eta^2$) describes the ratio of variance explained in the dependent variable by an independent variable while controlling other independent variables. It is defined as

$$partial\ \eta^2 = \frac{SS_{effect}}{SS_{effect} + SS_{error}}. \tag{2}$$

Since residuals in the stress value model are non-normally distributed and residuals in the curvature change do not have constant variance, the Box–Cox transformation was performed on the stress value and the curvature change to meet the ANOVA assumptions. The Box–Cox transformation can obtain a normal distribution of the transformed data (after transformation) and a constant variance. The one-parameter Box–Cox transformation is defined as

$$y_i^{(\lambda)} = \begin{cases} \dfrac{y_i^{\lambda} - 1}{\lambda} & if\ \lambda \neq 0 \\ \ln y_i & if\ \lambda = 0 \end{cases}, \tag{3}$$

and the two-parameter Box–Cox transformations as

$$y_i^{(\lambda)} = \begin{cases} \dfrac{(y_i + \lambda_2)^{\lambda_1} - 1}{\lambda_1} & if\ \lambda_1 \neq 0 \\ \ln(y_i + \lambda_2) & if\ \lambda_1 = 0 \end{cases}. \tag{4}$$

Moreover, the first transformation holds for $y_i > 0$ and the second for $y_i > -\lambda_2$. All statistical analyses were performed by SAS 9.4 (SAS Institute, Inc., Cary, NC), and two-sided p-values of less than 0.05 were considered statistically significant.

RESULTS

Corneal Biomechanical Responses Under ortho-k With FEA

In the current study, the central corneal stress and the peripheral corneal stress were regarded as continuous variables, while myopia, corneal curvature, and corneal thickness were regarded as categorical variables. The maximum von Mises stress in the central corneal area and the peripheral area are shown in **Table 4** and **Table 5**. It can be found that the maximum von Mises stress of the corneal central area showed an upward trend with the increase of myopia reduction degree, corneal curvature, and corneal

TABLE 4 | Maximum stress in the central corneal area (MPa).

Myopia degree: 2.00 D				
Corneal curvature (D)/thickness (μm)	**500**	**525**	**550**	**575**
40.25	0.01035	0.01039	0.01050	0.01089
41.25	0.01107	0.01132	0.01154	0.01162
42.25	0.01128	0.01151	0.01183	0.01219
43.25	0.01167	0.01186	0.01200	0.01219
44.25	0.01238	0.01256	0.01270	0.01289
Myopia degree: 3.00 D				
Corneal curvature (D)/thickness (μm)	**500**	**525**	**550**	**575**
40.25	0.01356	0.01379	0.01405	0.01482
41.25	0.01407	0.01432	0.01456	0.01491
42.25	0.01480	0.01510	0.01562	0.01597
43.25	0.01527	0.01586	0.01605	0.01619
44.25	0.01608	0.01636	0.01662	0.16810
Myopia degree: −4.00 D				
Corneal curvature (D)/thickness (μm)	**500**	**525**	**550**	**575**
40.25	0.01663	0.01682	0.01695	0.01707
41.25	0.01719	0.01826	0.01852	0.01881
42.25	0.01853	0.01887	0.01917	0.01951
43.25	0.02036	0.02094	0.02151	0.02206
44.25	0.02166	0.02194	0.02216	0.02237
Myopia degree: −5.00 D				
Corneal curvature (D)/thickness (μm)	**500**	**525**	**550**	**575**
40.25	0.02021	0.02057	0.02146	0.02258
41.25	0.02127	0.02196	0.02260	0.02291
42.25	0.02190	0.02233	0.02297	0.02351
43.25	0.02286	0.02325	0.02354	0.02373
44.25	0.02402	0.02448	0.02477	0.02513

thickness. The average of central cornea stress was 0.019178 MPa (SD = 0.017438). For the central cornea, wearing a −2.00 D ortho-k lens with a curvature of 40.25 D and a corneal thickness of 500 μm had the smallest maximum von Mises stress (0.01035 MPa), while wearing a −5.00 D ortho-k lens with a curvature of 44.25 D and a thickness of 575 μm had the largest maximum von Mises stress (0.02513 MPa). It can be seen that the maximum von Mises stress of different ortho-k lenses with different degrees increased by 2.42 times in the corneal center. **Figure 3** shows the distribution of the maximum von Mises stress in the cornea with different corneal thickness, curvature, and refractive change.

The trend of the maximum von Mises stress in the peripheral cornea was opposite to that in the corneal center. As the cornea thickness increased, the maximum von Mises stress in the peripheral area decreased gradually under the same curvature. The change of the maximum von Mises stress under various degrees was not large, and the maximum von Mises stress ranged from 0.00985 to 0.01733 MPa, with an average stress of the 80 models being 0.014451 MPa (SD = 0.011908). For −3.00 D, −4.00 D, and −5.00 D lens wearing, the maximum von Mises stress occurred in the central cornea, while for −2.00 D, the maximum von Mises stress was at the peripheral cornea. The representative maximum von Mises stress appearing in the central and peripheral areas are shown in **Figure 4** and **Figure 5**.

Quantile Regression Results of Dependent Variables and Independent Variables

The quantile regression results of central corneal stress and independent variables are shown in **Table 6**. Compared with myopia of −2.00 D, the central corneal stress value increased when the myopia was −3.00 D (β = 0.0036, $p < 0.001$), −4.00 D (β = 0.0074, $p < 0.01$), and −5.00 D (β = 0.0111, $p < 0.01$). Compared with corneal curvature of 40.25 D, the central corneal stress value increased when the corneal curvature was 41.25 D (β = 0.0007, $p < 0.01$), 42.25 D (β = 0.0014, $p < 0.01$), 43.25 D (β = 0.0019, $p < 0.01$), and 44.25 D (β = 0.0031, $p < 0.01$). Compared with a corneal thickness of 500 μm, the central corneal stress value increased when the corneal thickness was 525 μm (β = 0.0004, p = 0.0298), 550 μm (β = 0.0007, $p < 0.01$), and 575 μm (β = 0.0011, $p < 0.01$). All models were controlled for the other covariates.

The quantile regression results of corneal peripheral stress and independent variables are shown in **Table 7**. In patients with myopia of −3.00 D (β = 0.0007, $p < 0.01$) and −4.00 D (β = 0.0009, $p < 0.01$), the corneal peripheral stress increased compared with patients with myopia of −2.00 D. In patients with corneal curvature of 42.25 D (β = 0.0007, p = 0.0324), 43.25 D (β = 0.0015, $p < 0.01$), and 44.25 D (β

TABLE 5 | Maximum stress in the peripheral corneal area (MPa).

Myopia degree: –2.00 D				
Corneal curvature (D)/ thickness (μm)	**500**	**525**	**550**	**575**
40.25	0.01146	0.01093	0.01058	0.00985
41.25	0.01234	0.01208	0.01183	0.01063
42.25	0.01345	0.01247	0.01270	0.01158
43.25	0.01374	0.01331	0.01299	0.01250
44.25	0.01733	0.01682	0.01610	0.01552
Myopia degree: –3.00 D				
Corneal curvature (D)/ thickness (μm)	**500**	**525**	**550**	**575**
40.25	0.01236	0.01187	0.01163	0.01121
41.25	0.01317	0.01266	0.01228	0.01190
42.25	0.01381	0.01321	0.01267	0.01238
43.25	0.01472	0.01401	0.01380	0.01335
44.25	0.01706	0.01674	0.01631	0.01582
Myopia degree: –4.00 D				
Corneal curvature (D)/ thickness (μm)	**500**	**525**	**550**	**575**
40.25	0.01335	0.01308	0.01261	0.01187
41.25	0.01301	0.01267	0.01184	0.01119
42.25	0.01392	0.01336	0.01291	0.01260
43.25	0.01519	0.01444	0.01382	0.01358
44.25	0.01699	0.01513	0.01468	0.01425
Myopia degree: –5.00 D				
Corneal curvature (D)/ thickness (μm)	**500**	**525**	**550**	**575**
40.25	0.01273	0.01227	0.01158	0.01175
41.25	0.01304	0.01245	0.01176	0.01189
42.25	0.01309	0.01269	0.01226	0.01190
43.25	0.01324	0.01273	0.01234	0.01215
44.25	0.01358	0.01289	0.01274	0.01253

= 0.0040, $p < 0.01$), the peripheral corneal stress value increased compared with patients with corneal curvature of 40.25 D. In patients with corneal thickness of 525 μm ($\beta = -0.0005$, $p < 0.01$), 550 μm ($\beta = -0.0009$, $p < 0.01$), and 575 μm ($\beta = -0.0013$, $p < 0.01$), the peripheral corneal stress value decreased compared with patients with corneal thickness of 500 μm. All models were controlled for the other covariates.

Comparison of the Effect of Each Independent Variable on the Dependent Variable

The larger the partial eta value, the greater the effect of the independent variable on the dependent variable. The results of the variance (ANOVA) method are as follows: The degree of myopia had the greatest effect on the central corneal stress value (partial eta square = 0.9382), followed by corneal curvature (partial eta square = 0.5650) and corneal thickness (partial eta square = 0.1975). The curvature of the cornea had the greatest effect on the peripheral stress value of the cornea (partial eta square = 0.5220), followed by myopia (partial eta square = 0.2375) and corneal thickness (partial eta square = 0.1972).

DISCUSSION

The rapidly growing myopic prevalence has sparked intense research interest in the methods of myopia control (Cho and Cheung, 2012; Gonzalez-Meijome et al., 2016; Bremond-Gignac, 2020; Bullimore and Johnson, 2020). Ortho-k, a most promising treatment approach to slow down myopia progression, is gaining popularity among myopic patients due to its effectiveness and convenience. By using specially designed gas-permeable contact lenses to reshape the cornea, ortho-k has an effect in temporarily correcting myopia and controlling myopia progression (Cho et al., 2008; Hiraoka et al., 2012). However, the corneal integrity can be compromised if an improperly designed lens is fitted (Li S.-M. et al., 2016; Cheng et al., 2016; Bullimore et al., 2021). Therefore, there is an urgent need to understand the biomechanical change during ortho-k treatment and to identify the population most suitable for this treatment.

Currently all the existing theoretical hypotheses that the ortho-k lens controls myopia progression, such as the retinal peripheral defocus theory (Gardner et al., 2015; Smith et al., 2020), the aberration theory (Hiraoka et al., 2015; Zhang X. et al., 2020; Lau et al., 2020), and the accommodation theory (Batres et al., 2020; Song et al., 2021), are based on the change of the corneal shape or reduction of the refractive error after ortho-k lens wear. The biomechanical interaction between the lens and the cornea or the entire eyeball is vitally important in the course of ortho-k treatment. Different from the regular rigid contact lenses, the ortho-k lens has a special design, which is reversed against the corneal surface to reshape the cornea. The difference in the lens parameters will create different pressure to the cornea. Under the action of this force, the corneal morphology changes. Then, the lens can achieve its effects of reducing refractive error and controlling the myopia progression. However, the force of the interaction between the lens and cornea, or the pressure under the ortho-k lens on the cornea is difficult to measure or calculate. To the best of the authors' knowledge, the research in this field remains very limited. Therefore, mathematical modeling quantifying the pressure and force that the cornea receives can play a key role to reveal the mechanism.

A finite element analysis (FEA), a commonly used numerical method, is an effective way to study and analyze the mechanical behavior and functional mechanism of the cornea, which has been extensively implemented to study corneal mechanical problems (Kling et al., 2014; Li ZD. et al., 2016; Fang et al., 2020; Meng et al., 2020). Not only has the FEA been widely recognized for its potential in simulating and analyzing the effects of corneal surgery, it has also been used in corneal diseases and ocular trauma because of its predictive feature. The focus of our current work was to use the FEA to analyze the biomechanical response of the cornea under the ortho-k lens. Based on the finite element models, this article compared and analyzed the von Mises stress in different areas of the corneas of various thicknesses and curvatures within the wearing course of a variety of ortho-k lens designs.

The whole-eye model with both the cornea and the sclera would provide a better representation of the actual state. However, it was extremely time-consuming. Some studies showed that if the boundary conditions were defined properly

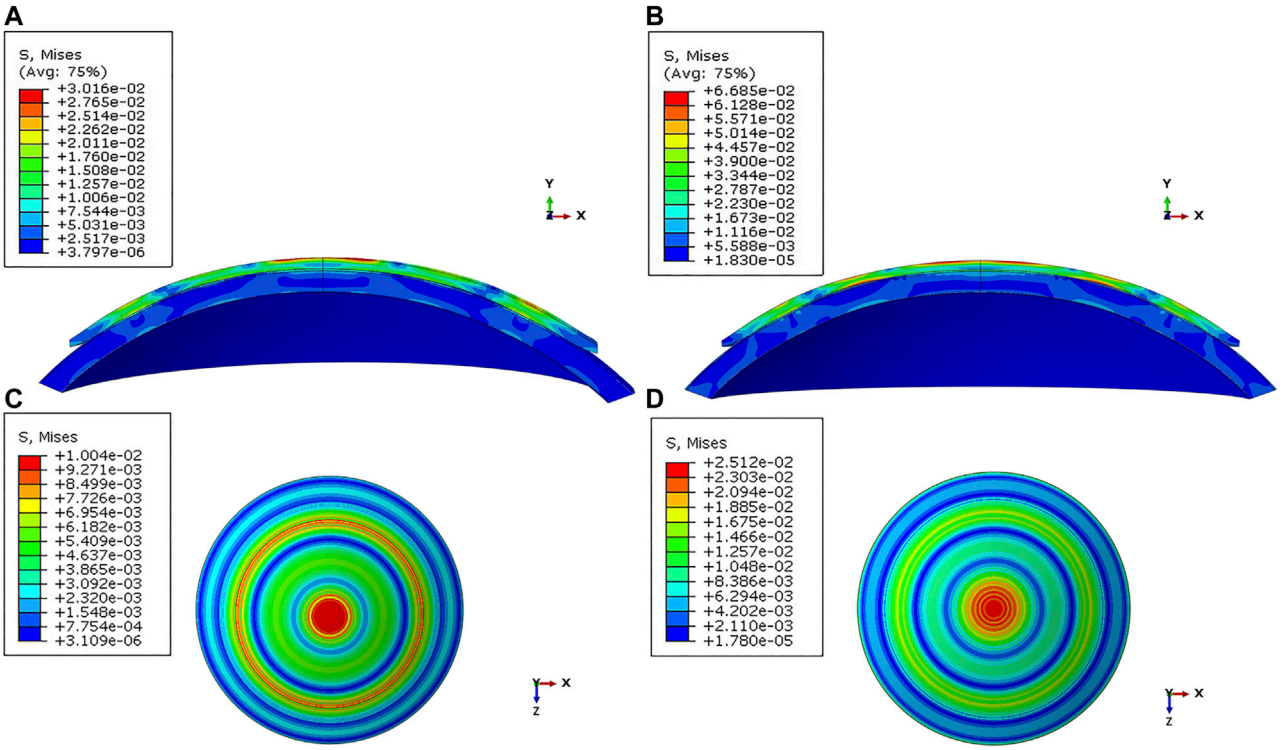

FIGURE 3 | Distribution of the von Mises stress in the cornea under varied conditions. **(A)** Sagittal face: –2.00 D/40.25 D/500 μm; **(B)** Sagittal face: –5.00 D/44.25 D/575 μm; **(C)** En face: –2.00 D/40.25 D/500 μm; **(D)** En face: –5.00 D/44.25 D/575 μm.

TABLE 6 | Quantile regression results of central corneal stress and independent variables.

Variables	Category	β	*p*-value
Myopia (D)	–2.00	Ref	Ref
	–3.00	0.0036	<0.001
	–4.00	0.0074	<0.001
	–5.00	0.0111	<0.001
Corneal curvature (D)	40.25	Ref	Ref
	41.25	0.0007	0.0072
	42.25	0.0014	<0.001
	43.25	0.0019	<0.001
	44.25	0.0031	<0.001
Corneal thickness (μm)	500	Ref	Ref
	525	0.0004	0.0298
	550	0.0007	<0.001
	575	0.0011	<0.001

TABLE 7 | Quantile regression results of corneal peripheral stress and independent variables.

Variables	Category	β	*p*-value
Myopia (D)	–2.00	Ref	Ref
	–3.00	0.0007	<0.001
	–4.00	0.0009	0.0001
	–5.00	0.0002	0.5713
Corneal curvature (D)	40.25	Ref	Ref
	41.25	0.0001	0.7053
	42.25	0.0007	0.0324
	43.25	0.0015	<0.001
	44.25	0.0040	<0.001
Corneal thickness (μm)	500	Ref	Ref
	525	–0.0005	0.0037
	550	–0.0009	<0.001
	575	–0.0013	<0.001

along the corneal edge, the cornea-only models can represent the whole-eye model very well. We set the orientation of corneal edge support to 23 in FEA according to Elsheikh and Wang (2007). The final results of our study were fair and showed consistent trends with clinical studies. In our model, the selection ranges of corneal curvature and corneal thickness were based on common clinical values. Although dividing the cornea into five layers according to the physiological structure can better show its mechanical response, due to the lack of relevant research data, it is impossible to accurately define the material properties of each layer and the interaction between the layers. Many articles showed that the corneal changes after wearing the ortho-k lens were mainly confined to the epithelial layer (Kim et al., 2018; Mohidin et al., 2020). Furthermore, the other layers of the cornea are relatively much thinner than the stromal layer, which may cause little effect on the simulation results. Therefore, the hypothesis of the three-layer corneal model is reasonable. Recently, many studies performed the corneal simulation using

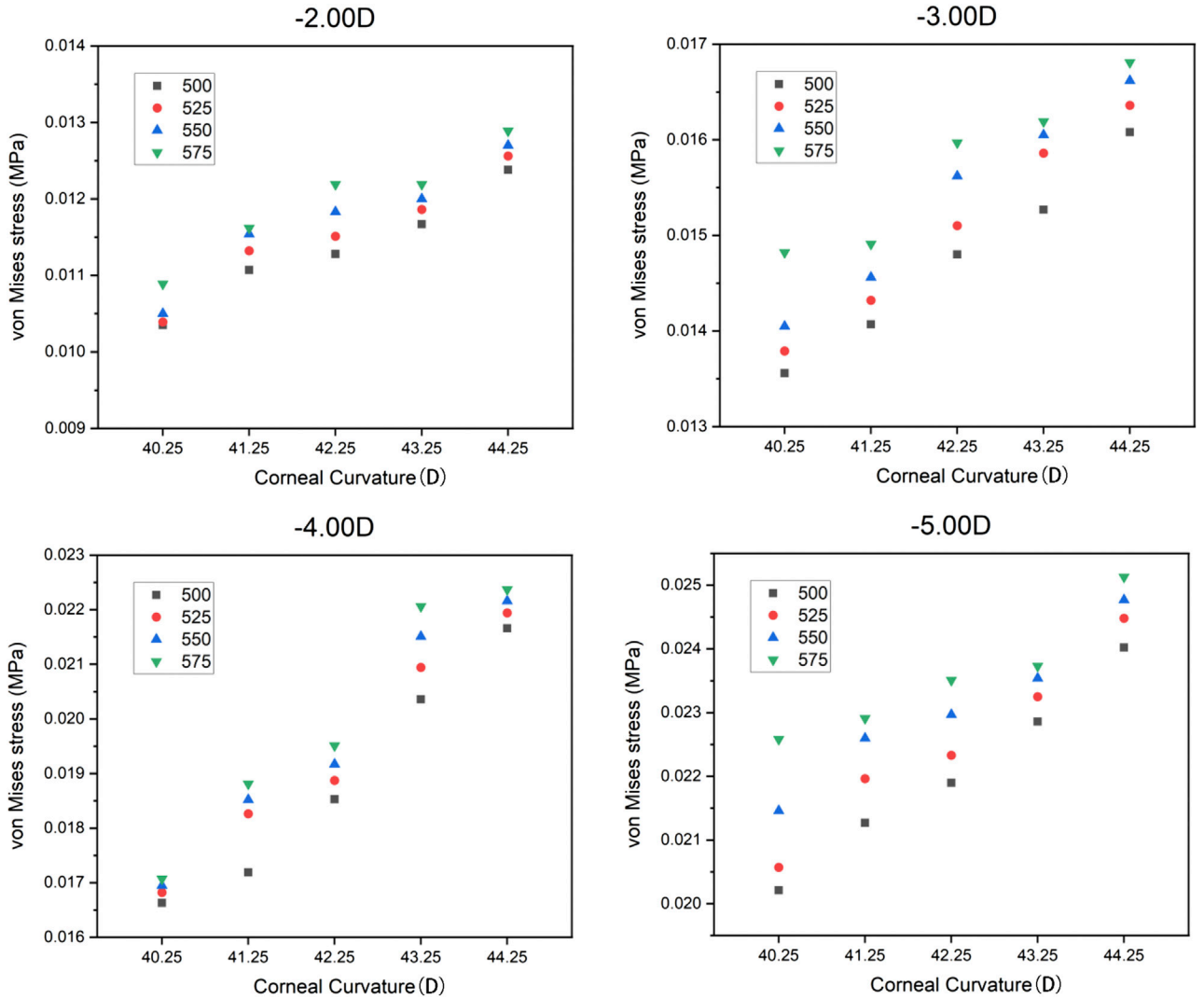

FIGURE 4 | Representative maximum von Mises stress in the central corneal area.

the hyper-elastic material model (Elsheikh and Wang, 2007; Bao et al., 2018). However, the behavior of a nonlinear material model is very similar to that of the elastic material model under 13 mmHg (1.73 KPa) IOP (Elsheikh and Wang, 2007). Nonlinear elastic materials can deform linearly for very small deformation (Wollensak et al., 2003). In order to improve the simulation's efficiency, the corneal material was assumed to be elastic in this study.

According to the above results, the change of the targeted myopia reduction degree had the greatest impact on corneal stress. In the ortho-k lens design, the reduction degree mainly affects the base curve radius (BCR), a means of controlling the refractive change, which makes the cornea flatter if the target reduction is increased and base curve becomes flatter. From a biomechanical point of view, increasing the target degree means applying more compressive pressure on the corneal center. We analyzed the corneal responses with the change of targeted reduction degree. As the refractive target increased, both the central and peripheral corneal stress responses increased significantly, especially in the corneal center. Although the FDA or other health authorities approve the use of ortho-k treatment in myopia up to −6.00 D in some lens designs, the safest and most successful outcome will be achieved for those patients with lower baseline levels of myopia (Mika et al., 2007; Liu and Xie, 2016; Singh et al., 2020; Hu et al., 2021). Therefore, for patients with high myopia or for doctors who used to increase the target degrees, more attention must be paid to the possible side effects of the ortho-k lens wear, such as damage to the integrity of the cornea, since those lenses are designed with increased compressive pressure.

The corneal curvature is a very important parameter in ortho-k lens design. The calculation of BCR and the design of the lens alignment curve are based on the corneal curvature. The range of the corneal curvatures for most patients is between 40 and 46 D, and the most common is between 42 and 43 D. If the cornea is too flat or too steep, it can cause

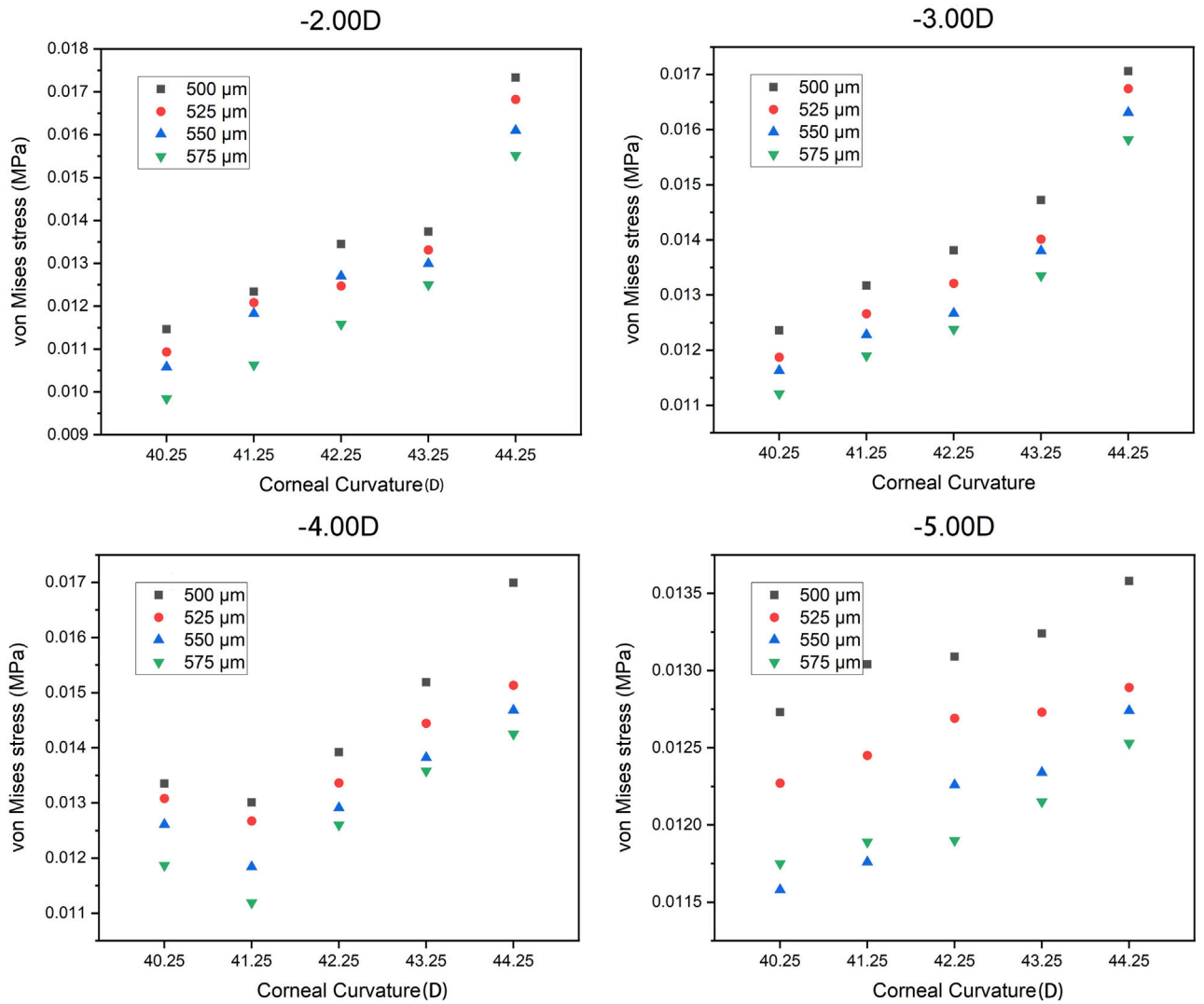

FIGURE 5 | Representative maximum von Mises stress in the peripheral corneal area.

problems during lens fitting. When the cornea is too flat, the range of corneal deformation is limited, and adequate treatment may not be achieved, especially for high myopia. However, if the corneal is too steep, the incident of corneal staining is higher than that of the common corneal curvature (Cheng et al., 2016). In our study, it was found that the cornea had a larger stress response when the corneal curvature became steeper for both the central and peripheral areas. Therefore, practitioners need to be more cautious in treating patients with steep corneas and high myopia for safety concerns.

From our research results, it can be seen that corneal thickness also affects corneal stress in the central and peripheral areas. However, in the normal range, the corneal thickness is the factor that has the least influence on the corneal stress response among all the factors. After wearing ortho-k lenses, the corneal thickness has a certain amount of thinning (Wan et al., 2021). However, a large number of studies have found that the changes of corneal thickness are mainly confined to the corneal epithelium (Kim et al., 2018; Zhang J. et al., 2020; Zhou et al., 2020a; b). Therefore, it is relatively safe to wear an ortho-k lens within the range of normal corneal thickness.

There are some limitations in the current study. First, our model was mainly designed to analyze the positive pressure of the lens on the cornea without analyzing the tear layer force. Factors such as squeeze film force, or tension force, which are related to the tear viscosity and the tear thickness under the lens, are important in helping to alter the corneal shape and ideally centralize the lens position. In the future research, we will establish the tear flow field and analyze the tear layer under the lens. Second, this research assumed the cornea to be an ideal sphere. However, there have been some controversy about the changes of corneal shape during ortho-k, and the initial corneal eccentricity may affect lens selection. Creating the definite model of the eyeball according to the actual shape of the human cornea could be the foundation for the individual

predictive model. Third, in this study, we were trying to reveal the biomechanical response of the cornea in the ortho-k treatment under the condition of various corneal shapes and thicknesses, and a refractive change with the uniform setting criteria of the pressures, including the IOP and eyelid tension. However, the lid tension and IOP may have potential effects on ortho-k. Therefore, we will explore the influence of these factors on the corneal mechanical response during ortho-k treatment in the future.

CONCLUSION

This article investigated the interaction between the cornea and the ortho-k lens through finite element methods to clearly reveal the mechanical response of the cornea under ortho-k. The current work provides ortho-k lens practitioners with an objective, reliable, and noncontact approach for quantitative assessment of risk and effectiveness of ortho-k for specific patients. This research also provides insights into the design of future ortho-k lenses. In ortho-k treatment, both the refractive target and the corneal curvature have a significant impact on corneal stress. Any change in corneal thickness within the normal range has minimal impact on stress. In clinical practice, more attention should be paid to patients with high myopia and high corneal curvature.

DATA AVAILABILITY STATEMENT

The original contributions presented in the study are included in the article/Supplementary Material; further inquiries can be directed to the corresponding authors.

AUTHOR CONTRIBUTIONS

JW, DZ, and QR contributed to the conception of the study. JW performed lens measurement and wrote the manuscript. WF, DZ, JW, and XL contributed to the finite element analysis. JW and HX performed data analyses. QR and DZ reviewed the manuscript, and they contributed equally to this study. All authors approved it for publication.

FUNDING

This work was supported by the National Key Research and Development Program (2016YFB1101503).

ACKNOWLEDGMENTS

We thank all participants of the study at the Peking University.

REFERENCES

Alharbi, A., and Swarbrick, H. A. (2003). The Effects of Overnight Orthokeratology Lens Wear on Corneal Thickness. *Invest. Ophthalmol. Vis. Sci.* 44 (6), 2518–2523. doi:10.1167/iovs.02-0680

Bao, F., Wang, J., Cao, S., Liao, N., Shu, B., Zhao, Y., et al. (2018). Development and Clinical Verification of Numerical Simulation for Laser *In Situ* Keratomileusis. *J. Mech. Behav. Biomed. Mater.* 83, 126–134. doi:10.1016/j.jmbbm.2018.04.016

Batres, L., Peruzzo, S., Serramito, M., and Carracedo, G. (2020). Accommodation Response and Spherical Aberration during Orthokeratology. *Graefes Arch. Clin. Exp. Ophthalmol.* 258 (1), 117–127. doi:10.1007/s00417-019-04504-x

Bremond-Gignac, D. (2020). Myopie de l'enfant. *Med. Sci. (Paris)* 36 (8-9), 763–768. doi:10.1051/medsci/2020131

Bullimore, M. A., and Johnson, L. A. (2020). Overnight Orthokeratology. *Contact Lens and Anterior Eye* 43 (4), 322–332. doi:10.1016/j.clae.2020.03.018

Bullimore, M. A., Mirsayafov, D. S., Khurai, A. R., Kononov, L. B., Asatrian, S. P., Shmakov, A. N., et al. (2021). Pediatric Microbial Keratitis with Overnight Orthokeratology in Russia. *Eye Contact Lens* 47, 420–425. doi:10.1097/ICL.0000000000000801

Cheng, H.-C., Liang, J.-B., Lin, W.-P., and Wu, R. (2016). Effectiveness and Safety of Overnight Orthokeratology with Boston XO2 High-Permeability Lens Material: A 24 Week Follow-Up Study. *Contact Lens and Anterior Eye* 39 (1), 67–71. doi:10.1016/j.clae.2015.07.002

Cheung, S.-W., and Cho, P. (2016). Long-term Effect of Orthokeratology on the Anterior Segment Length. *Contact Lens and Anterior Eye* 39 (4), 262–265. doi:10.1016/j.clae.2016.02.003

Cho, P., and Cheung, S.-W. (2017). Protective Role of Orthokeratology in Reducing Risk of Rapid Axial Elongation: A Reanalysis of Data from the ROMIO and TO-SEE Studies. *Invest. Ophthalmol. Vis. Sci.* 58 (3), 1411–1416. doi:10.1167/iovs.16-20594

Cho, P., and Cheung, S.-W. (2012). Retardation of Myopia in Orthokeratology (ROMIO) Study: a 2-year Randomized Clinical Trial. *Invest. Ophthalmol. Vis. Sci.* 53 (11), 7077–7085. doi:10.1167/iovs.12-10565

Cho, P., Cheung, S. W., and Edwards, M. (2005). The Longitudinal Orthokeratology Research in Children (LORIC) in Hong Kong: a Pilot Study on Refractive Changes and Myopic Control. *Curr. Eye Res.* 30 (1), 71–80. doi:10.1080/02713680590907256

Cho, P., Cheung, S. W., Mountford, J., and White, P. (2008). Good Clinical Practice in Orthokeratology. *Contact Lens and Anterior Eye* 31 (1), 17–28. doi:10.1016/j.clae.2007.07.003

Cho, P., and Tan, Q. (2019). Myopia and Orthokeratology for Myopia Control. *Clin. Exp. Optom.* 102 (4), 364–377. doi:10.1111/cxo.12839

Coldrick, B. J., Richards, C., Sugden, K., Wolffsohn, J. S., and Drew, T. E. (2016). Developments in Contact Lens Measurement: A Comparative Study of Industry Standard Geometric Inspection and Optical Coherence Tomography. *Contact Lens and Anterior Eye* 39 (4), 270–276. doi:10.1016/j.clae.2016.01.002

Ehlers, N., Heegaard, S., Hjortdal, J., Ivarsen, A., Nielsen, K., and Prause, J. U. (2010). Morphological Evaluation of normal Human Corneal Epithelium. *Acta Ophthalmol.* 88 (8), 858–861. doi:10.1111/j.1755-3768.2009.01610.x

Elsheikh, A., Alhasso, D., and Rama, P. (2008). Assessment of the Epithelium's Contribution to Corneal Biomechanics. *Exp. Eye Res.* 86 (2), 445–451. doi:10.1016/j.exer.2007.12.002

Elsheikh, A., Ross, S., Alhasso, D., and Rama, P. (2009). Numerical Study of the Effect of Corneal Layered Structure on Ocular Biomechanics. *Curr. Eye Res.* 34 (1), 26–35. doi:10.1080/02713680802535263

Elsheikh, A., and Wang, D. (2007). Numerical Modelling of Corneal Biomechanical Behaviour. *Comp. Methods Biomech. Biomed. Eng.* 10 (2), 85–95. doi:10.1080/10255840600976013

Fang, L., Wang, Y., Yang, R., Deng, S., Deng, J., and Wan, L. (2020). Effects of the LASIK Flap Thickness on Corneal Biomechanical Behavior: a Finite Element Analysis. *BMC Ophthalmol.* 20 (1), 67. doi:10.1186/s12886-020-01338-8

Gardner, D. J., Walline, J. J., and Mutti, D. O. (2015). Choroidal Thickness and Peripheral Myopic Defocus during Orthokeratology. *Optom. Vis. Sci.* 92 (5), 579–588. doi:10.1097/OPX.0000000000000573

González-Méijome, J. M., Carracedo, G., Lopes-Ferreira, D., Faria-Ribeiro, M. A., Peixoto-de-Matos, S. C., and Queirós, A. (2016). Stabilization in Early Adult-Onset Myopia with Corneal Refractive Therapy. *Contact Lens and Anterior Eye* 39 (1), 72–77. doi:10.1016/j.clae.2015.06.009

Hiraoka, T., Kakita, T., Okamoto, F., and Oshika, T. (2015). Influence of Ocular Wavefront Aberrations on Axial Length Elongation in Myopic Children Treated with Overnight Orthokeratology. *Ophthalmology* 122 (1), 93–100. doi:10.1016/j.ophtha.2014.07.042

Hiraoka, T., Kakita, T., Okamoto, F., Takahashi, H., and Oshika, T. (2012). Long-term Effect of Overnight Orthokeratology on Axial Length Elongation in Childhood Myopia: a 5-year Follow-Up Study. *Invest. Ophthalmol. Vis. Sci.* 53 (7), 3913–3919. doi:10.1167/iovs.11-8453

Hu, P., Zhao, Y., Chen, D., and Ni, H. (2021). The Safety of Orthokeratology in Myopic Children and Analysis of Related Factors. *Contact Lens and Anterior Eye* 44 (1), 89–93. doi:10.1016/j.clae.2020.08.011

Jonas, J. B., Ang, M., Cho, P., Guggenheim, J. A., He, M. G., Jong, M., et al. (2021). IMI Prevention of Myopia and its Progression. *Invest. Ophthalmol. Vis. Sci.* 62 (5), 6. doi:10.1167/iovs.62.5.6

Kim, W. K., Kim, B. J., Ryu, I.-H., Kim, J. K., and Kim, S. W. (2018). Corneal Epithelial and Stromal Thickness Changes in Myopic Orthokeratology and Their Relationship with Refractive Change. *PLoS One* 13 (9), e0203652. doi:10.1371/journal.pone.0203652

Kling, S., Bekesi, N., Dorronsoro, C., Pascual, D., and Marcos, S. (2014). Corneal Viscoelastic Properties from Finite-Element Analysis of *In Vivo* Air-Puff Deformation. *PLoS One* 9 (8), e104904. doi:10.1371/journal.pone.0104904

Kobayashi, Y., Yanai, R., Chikamoto, N., Chikama, T.-i., Ueda, K., and Nishida, T. (2008). Reversibility of Effects of Orthokeratology on Visual Acuity, Refractive Error, Corneal Topography, and Contrast Sensitivity. *Eye Contact Lens* 34 (4), 224–228. doi:10.1097/ICL.0b013e318165d501

Last, J. A., Liliensiek, S. J., Nealey, P. F., and Murphy, C. J. (2009). Determining the Mechanical Properties of Human Corneal Basement Membranes with Atomic Force Microscopy. *J. Struct. Biol.* 167 (1), 19–24. doi:10.1016/j.jsb.2009.03.012

Lau, J. K., Vincent, S. J., Cheung, S.-W., and Cho, P. (2020). Higher-order Aberrations and Axial Elongation in Myopic Children Treated with Orthokeratology. *Invest. Ophthalmol. Vis. Sci.* 61 (2), 22. doi:10.1167/iovs.61.2.22

Lau, J. K., Wan, K., Cheung, S.-W., Vincent, S. J., and Cho, P. (2019). Weekly Changes in Axial Length and Choroidal Thickness in Children during and Following Orthokeratology Treatment with Different Compression Factors. *Trans. Vis. Sci. Tech.* 8 (4), 9. doi:10.1167/tvst.8.4.9

Li, S.-M., Kang, M.-T., Wu, S.-S., Liu, L.-R., Li, H., Chen, Z., et al. (2016a). Efficacy, Safety and Acceptability of Orthokeratology on Slowing Axial Elongation in Myopic Children by Meta-Analysis. *Curr. Eye Res.* 41 (5), 600–608. doi:10.3109/02713683.2015.1050743

Li, Z. D., Bao, F. J., Wang, Q. M., and Huang, J. H. (2016b). [Finite Element Analysis of Astigmatic Keratotomy Based on Corneal Biomechanical Properties]. *Zhonghua Yan Ke Za Zhi* 52 (9), 674–680. doi:10.3760/cma.j.issn.0412-4081.2016.09.008

Liu, Y. M., and Xie, P. (2016). The Safety of Orthokeratology-A Systematic Review. *Eye Contact Lens* 42 (1), 35–42. doi:10.1097/ICL.0000000000000219

Meng, Q., Wang, X., Chen, W., Li, X., and He, R. (2020). [Finite Element Analysis of Determining Corneal Biomechanical Properties *In Vivo* Based on Corvis ST]. *Sheng Wu Yi Xue Gong Cheng Xue Za Zhi* 37 (4), 608–613. doi:10.7507/1001-5515.201911081

Mika, R., Morgan, B., Cron, M., Lotoczky, J., and Pole, J. (2007). Safety and Efficacy of Overnight Orthokeratology in Myopic Children. *Optom. - J. Am. Optometric Assoc.* 78 (5), 225–231. doi:10.1016/j.optm.2006.12.013

Mohidin, N., Mat Yacob, A., and Norazman, F. N. (2020). Corneal Thickness and Morphology after Orthokeratology of Six-Month Lens Wear Among Young Malay Adults. *Med. J. Malaysia* 75 (5), 538–542.

Pinsky, P. M., van der Heide, D., and Chernyak, D. (2005). Computational Modeling of Mechanical Anisotropy in the Cornea and Sclera. *J. Cataract Refract Surg.* 31 (1), 136–145. doi:10.1016/j.jcrs.2004.10.048

Queirós, A., Lopes-ferreira, D., Yeoh, B., Issacs, S., Amorim-de-sousa, A., Villa-collar, C., et al. (2020). Refractive, Biometric and Corneal Topographic Parameter Changes during 12-months of Orthokeratology. *Clin. Exp. Optom.* 103 (4), 454–462. doi:10.1111/cxo.12976

Shaw, A. J., Collins, M. J., Davis, B. A., and Carney, L. G. (2010). Eyelid Pressure and Contact with the Ocular Surface. *Invest. Ophthalmol. Vis. Sci.* 51 (4), 1911–1917. doi:10.1167/iovs.09-4090

Singh, K., Bhattacharyya, M., Goel, A., Arora, R., Gotmare, N., and Aggarwal, H. (2020). Orthokeratology in Moderate Myopia: A Study of Predictability and Safety. *Jovr* 15 (2), 210–217. doi:10.18502/jovr.v15i2.6739

Smith, E. L., III, Arumugam, B., Hung, L.-F., She, Z., Beach, K., and Sankaridurg, P. (2020). Eccentricity-dependent Effects of Simultaneous Competing Defocus on Emmetropization in Infant Rhesus Monkeys. *Vis. Res.* 177, 32–40. doi:10.1016/j.visres.2020.08.003

Song, Y., Zhu, S., Yang, B., Wang, X., Ma, W., Dong, G., et al. (2021). Accommodation and Binocular Vision Changes after Wearing Orthokeratology Lens in 8- to 14-Year-Old Myopic Children. *Graefes Arch. Clin. Exp. Ophthalmol.* 259, 2035–2045. doi:10.1007/s00417-021-05106-2

Swarbrick, H. A., Kang, P., and Peguda, R. (2020). Corneal Total and Epithelial Thickness Measured by Sonogage Ultrasound Pachometry and High-Resolution Optical Coherence Tomography. *Optom. Vis. Sci.* 97 (5), 346–350. doi:10.1097/OPX.0000000000001508

Swarbrick, H. A. (2004). Orthokeratology (Corneal Refractive Therapy). *Eye Contact Lens: Sci. Clin. Pract.* 30 (4), 181–185. discussion 205-186. doi:10.1097/01.icl.0000140221.41806.6e

Wan, K., Lau, J. K.-k., Cheung, S. W., and Cho, P. (2020). Refractive and Corneal Responses of Young Myopic Children to Short-Term Orthokeratology Treatment with Different Compression Factors. *Contact Lens and Anterior Eye* 43 (1), 65–72. doi:10.1016/j.clae.2019.10.134

Wan, K., Yau, H. T., Cheung, S. W., and Cho, P. (2021). Corneal Thickness Changes in Myopic Children during and after Short-term Orthokeratology Lens Wear. *Ophthalmic Physiol. Opt.* 41, 757–767. doi:10.1111/opo.12824

Wolffsohn, J. S., Calossi, A., Cho, P., Gifford, K., Jones, L., Li, M., et al. (2016). Global Trends in Myopia Management Attitudes and Strategies in Clinical Practice. *Contact Lens and Anterior Eye* 39 (2), 106–116. doi:10.1016/j.clae.2016.02.005

Wollensak, G., Spoerl, E., and Seiler, T. (2003). Stress-strain Measurements of Human and Porcine Corneas after Riboflavin-Ultraviolet-A-Induced Cross-Linking. *J. Cataract Refract Surg.* 29 (9), 1780–1785. doi:10.1016/s0886-3350(03)00407-3

Zhang, J., Li, J., Li, X., Li, F., and Wang, T. (2020a). Redistribution of the Corneal Epithelium after Overnight Wear of Orthokeratology Contact Lenses for Myopia Reduction. *Contact Lens and Anterior Eye* 43 (3), 232–237. doi:10.1016/j.clae.2020.02.015

Zhang, X., Ma, J.-H., Xi, X., and Guan, L. (2020b). Characteristics of Corneal High-Order Aberrations in Adolescents with Mild to Moderate Myopia. *BMC Ophthalmol.* 20 (1), 465. doi:10.1186/s12886-020-01727-z

Zhou, J., Xue, F., Zhou, X., Naidu, R. K., and Qian, Y. (2020a). Correction to: Thickness Profiles of the Corneal Epithelium along the Steep and Flat Meridians of Astigmatic Corneas after Orthokeratology. *BMC Ophthalmol.* 20 (1), 338. doi:10.1186/s12886-020-01607-6

Zhou, J., Xue, F., Zhou, X., Naidu, R. K., and Qian, Y. (2020b). Thickness Profiles of the Corneal Epithelium along the Steep and Flat Meridians of Astigmatic Corneas after Orthokeratology. *BMC Ophthalmol.* 20 (1), 240. doi:10.1186/s12886-020-01477-y

Conflict of Interest: XL was employed by the company the Second Academy Of CASIC.

The remaining authors declare that the research was conducted in the absence of any commercial or financial relationships that could be construed as a potential conflict of interest.

Publisher's Note: All claims expressed in this article are solely those of the authors and do not necessarily represent those of their affiliated organizations, or those of the publisher, the editors, and the reviewers. Any product that may be evaluated in this article, or claim that may be made by its manufacturer, is not guaranteed or endorsed by the publisher.

frontiers in Bioengineering and Biotechnology

ORIGINAL RESEARCH
published: 17 November 2021
doi: 10.3389/fbioe.2021.771763

Exploring the Biomechanical Properties of the Human Cornea *In Vivo* Based on Corvis ST

Di Zhang[1,2], *Haixia Zhang*[1,2], *Lei Tian*[3,4], *Yan Zheng*[5], *Caiyun Fu*[5], *Changbin Zhai*[5]* and *Lin Li*[1,2]*

[1]Beijing Key Laboratory of Fundamental Research on Biomechanics in Clinical Application, Capital Medical University, Beijing, China, [2]School of Biomedical Engineering, Capital Medical University, Beijing, China, [3]Beijing Tongren Eye Center, Beijing Tongren Hospital, Beijing Ophthalmology and Visual Sciences Key Laboratory, Beijing Institute of Ophthalmology, Capital Medical University, Beijing, China, [4]Beijing Advanced Innovation Center for Big Data-Based Precision Medicine, Beijing Tongren Hospital, Beihang University and Capital Medical University, Beijing, China, [5]Beijing Tongren Eye Center, Beijing Tongren Hospital, Beijing Ophthalmology and Visual Sciences Key Laboratory, Capital Medical University, Beijing, China

Purpose: The aim of this study was to provide a method to determine corneal nonlinear viscoelastic properties based on the output data of corneal visualization Scheimpflug technology (Corvis ST).

Methods: The Corvis ST data from 18 eyes of 12 healthy humans were collected. Based on the air-puff pressure and the corneal displacement from the Corvis ST test of normal human eyes, the work done by the air-puff attaining the whole corneal displacement was obtained. By applying a visco-hyperelastic strain energy density function of the cornea, in which the first-order Prony relaxation function and the first-order Ogden strain energy were employed, the corneal strain energy during the Corvis ST test was calculated. Then the work done by the air-puff attaining the whole corneal displacement was completely regarded as the strain energy of the cornea. The identification of the nonlinear viscoelastic parameters was carried out by optimizing the sum of difference squares of the work and the strain energy using the genetic algorithm.

Results: The visco-hyperelastic model gave a good fit to the data of corneal strain energy with time during the Corvis ST test ($R^2 > 0.95$). The determined Ogden model parameter μ ranged from 0.42 to 0.74 MPa, and α ranged from 32.76 to 55.63. The parameters A and τ in the first-order Prony function were 0.09–0.36 and 1.21–1.95 ms, respectively.

Conclusion: It is feasible to determine the corneal nonlinear viscoelastic properties based on the corneal contour information and air-puff pressure of the Corvis ST test.

Keywords: cornea, corneal biomechanical properties, *in vivo*, CorVis ST, visco-hyperelastic model

OPEN ACCESS

Edited by:
FangJun Bao,
Affiliated Eye Hospital of Wenzhou Medical College, China

Reviewed by:
Min Shen,
Tianjin University, China
Zhiwei Li,
Shandong Provincial Hospital, China

***Correspondence:**
Lin Li
lil@ccmu.edu.cn
Changbin Zhai
17091006117@163.com

Specialty section:
This article was submitted to Biomechanics, a section of the journal Frontiers in Bioengineering and Biotechnology

Received: *07 September 2021*
Accepted: *21 October 2021*
Published: *17 November 2021*

Citation:
Zhang D, Zhang H, Tian L, Zheng Y, Fu C, Zhai C and Li L (2021) Exploring the Biomechanical Properties of the Human Cornea In Vivo *Based on Corvis ST. Front. Bioeng. Biotechnol. 9:771763. doi: 10.3389/fbioe.2021.771763*

INTRODUCTION

Cornea is a kind of biological soft tissue with nonlinear viscoelasticity. The biomechanical property of cornea has been considered as a helpful index in the diagnosis of keratoconus (Wang et al., 2015), selection of refractive surgery (Dupps and Wilson, 2006; Shen et al., 2014), screening before refractive surgery (Piñero and Alcón, 2014), measurement of intraocular pressure (IOP) (Brown et al., 2018),

and evaluation of the curative effect of corneal cross-linking surgery (Vinciguerra et al., 2017; Sedaghat et al., 2018).

At present, corneal visualization Scheimpflug technology (Corvis ST) has been used in the diagnosis of keratoconus (Chan et al., 2018) and glaucoma (Wang et al., 2015). Corneal viscoelasticity is closely related to the progressive keratoconus (Fraldi et al., 2011; Kling et al., 2014). However, the mechanical meaning of the obtained dynamic corneal response (DCR) parameter output by Corvis ST has not been clear exactly. The relationship between DCR parameters and classical biomechanical properties has not been established either. More importantly, the DCR parameters from Corvis ST could not be directly used by numerical methods, such as finite element methods, to predict corneal deformation after refractive surgery. Therefore, many researchers have paid great attention to attempt to have a comprehensive understanding of corneal biomechanical properties based on the tests of cornea *in vivo*. By applying inverse finite element method and corneal deformation data from Corvis ST, investigators studied the nonlinear mechanical characteristics of the cornea (Lago et al., 2015; Sinha Roy et al., 2015; Bekesi et al., 2016), in which a complicated constitutive equation and a fine geometry model were applied. Our previous study (Qin et al., 2019a) applied a thin spherical shell model to identify corneal elastic modulus based on Corvis ST data. These studies have demonstrated the feasibility of using the output data of Corvis ST to acquire corneal biomechanical parameters, such as elastic modulus. However, a full description of corneal biomechanical properties based on *in vivo* tests has been still an issue of great concern to the researchers.

This study will establish a method to identify corneal nonlinear viscoelastic mechanical properties based on the output data of Corvis ST. We shall apply a visco-hyperelastic model to fit the corneal deformation data extracted from the image information during a Corvis ST test. It is expected that the method of determination of corneal nonlinear viscoelastic parameters can be used in the optimization design of corneal refractive surgery scheme and the prediction of corneal morphology after refractive surgery.

MATERIALS AND METHODS

Subjects

This study included 18 eyes of 12 healthy subjects. The institutional review board of Capital Medical University approved this study, and all participants signed an informed consent form in accordance with the tenets of the Declaration of Helsinki.

Subjects met the following criteria: age 18–45 years. All patients had no history of corneal, ocular surgery, trauma, or systemic diseases that might affect the eye and had abandoned soft contact lenses or rigid contact lenses at least 1 month and no contact lens utilization within 2 weeks before the examination.

Ocular Examination

All subjects underwent a thorough tomographic measurement using Corvis ST (Oculus; Optikgeräte GmbH, Wetzlar, Germany, software version: 1.6b2042) and Pentacam (Oculus; Optikgeräte GmbH, Wetzlar, Germany). The DCR parameters in the analysis mainly included deflection amplitude at the highest concavity (HCDA), central concave curvature at the highest concavity (HCR), peak distance at the highest concavity (PD), deflection amplitude ratio maximal 2 mm (DAR2), stiffness parameter at the first applanation (SPA1), corneal stress–strain index (SSI), corneal biomechanical index (CBI), and biomechanically corrected IOP (bIOP).

Method to Evaluate Corneal Nonlinear Viscoelasticity

Visco-Hyperelastic Model

Considering the time dependence of corneal stress responding to any loads, a visco-hyperelastic model based on strain energy function has been shown to describe corneal nonlinear and viscoelastic properties (Liu et al., 2020a; Su et al., 2015; Whitford et al., 2018). As one of well-known isotropic strain energy functions, the Ogden model can better describe the nonlinear stress–strain relationship of the cornea (Bao et al., 2017; Bao et al., 2018; Joda et al., 2016; Lago et al., 2015; Maklad et al., 2019). Therefore, we adopted the Ogden model in the visco-hyperelastic constitutive model. Also, the widely used Prony series model (Huang et al., 2017; Ramzanpour et al., 2020) as relaxation function was introduced in the visco-hyperelastic model. The cornea was regarded as a nonlinear incompressible viscoelastic material. The visco-hyperelastic model (Snedeker et al., 2005; Taylor et al., 2009) (**Eq. 1**) was applied, in which the strain energy density U was given by the Ogden model (**Eq. 2**), and the stress relaxation function G was given by the first-order Prony model (**Eq. 3**).

$$U\_e = \int_0^t G(t-s)\frac{\partial U}{\partial s}ds \tag{1}$$

$$U = \sum_{i=1}^{N}\frac{2\mu_i}{a_i^2}\left(\lambda_1^{a_i}+\lambda_2^{a_i}+\lambda_3^{a_i}-3\right), \lambda_1\lambda_2\lambda_3 = 1 \tag{2}$$

$$G(t) = 1 - A\left(1-e^{-\frac{t}{\tau}}\right) \tag{3}$$

In **Eq. 2**, N, μ_i, and α_i are material parameters, and λ_j ($j = 1, 2, 3$) is the stretch ratio of materials in three main directions. Taking into consideration that the first-order Ogden model can better describe the mechanical properties of cornea (Bao et al., 2017; Bao et al., 2018), in this study, we let $N = 1$. In **Eq. 3**, A and τ are the stress relaxation parameters, $1 - A$ is the relaxation limit, and τ is the relaxation time.

It is assumed that the three main directions of cornea are circumferential, radial, and perpendicular (or thick) directions. It is further assumed that the circumferential elongation ratio is equal to the elongation ratio of the radial arc length under air-puff. It follows that $\lambda_1 = \lambda_2 = \lambda$, $\lambda_3 = \lambda^{-2}$ due to the assumption of incompressibility of the cornea, i.e., $\lambda_1\lambda_2\lambda_3 = 1$. Then, **Eq. 2** gives

$$U = \frac{2\mu}{\alpha^2}\left(2\lambda^{\alpha}+\lambda^{-2\alpha}-3\right) \tag{2a}$$

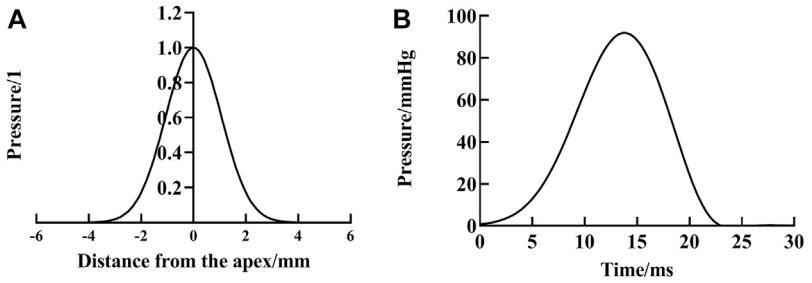

FIGURE 1 | Air-puff applied to cornea by Corvis ST, variation of space **(A)** and time **(B)**.

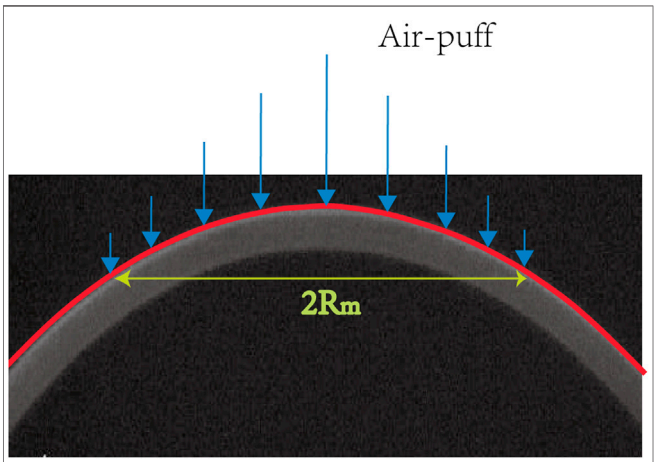

FIGURE 2 | Schematic of air-puff acts on the cornea during the Corvis ST test.

According to the corneal contour imagines obtained from Corvis ST, the overall corneal strain under the air-puff at each time point was calculated. The stretch ratio was set by **Eq. 4**.

$$\lambda = \frac{L_1}{L_0} \tag{4}$$

where L_1 and L_0 are the arc length of the anterior corneal surface during deformation and at the initial state, respectively. L_1 and L_0 can be obtained from the corneal anterior surface contour by image processing.

The Work Done by Air-Puff During the Corvis ST Test

We employed cylindrical coordinates to describe the work done by air-puff attaining the whole corneal displacement during the Corvis ST test. According to literatures (Simonini et al., 2016; Eliasy et al., 2019), the pressure of the air-puff, $P(r, t)$, at the point with polar coordinate r from the corneal apex and time t was obtained (**Figure 1**). We let $S(r, t)$ be the corneal vertical displacement of the point r from the corneal apex on the anterior surface of the cornea at time t. Then for an element $rdrd\theta$ on the corneal anterior surface, the work element was given by $dw = P(r,t)S(r,t)rdrd\theta$. The work done by the air-puff attaining the whole corneal displacement up to time t from the beginning of a Corvis ST test can be obtained according to **Eq. 5**.

$$W_e = \int_0^{2\pi}\int_0^{R_m} P(r,t)S(r,t)rdrd\theta = 2\pi\int_0^{R_m} P(r,t)S(r,t)rdr \tag{5}$$

where R_m is the radius of the maximum deformed area of the corneal anterior surface by the air-puff; R_m can be estimated by the data of the corneal anterior surface contour (**Figure 2**).

The Deformation Data of the Cornea During the Corvis ST Test

In this study, according to the corneal contour images obtained from Corvis ST, we extracted the outer contour of the cornea (**Figure 3**) according to the OTSU threshold method. L_1 and L_0 in **Eq. 4** were obtained from the extracted corneal anterior surface contour, where $L_1 = \sum_{i=-287}^{286}\sqrt{(x_{i+1}-x_i)^2 + (y_{i+1}-y_i)^2}$; (x_i, y_i) is the coordinate of a point on the anterior surface of the cornea, where the Y axis passes through the corneal apex in the Cartesian coordinate system. Moreover, the difference between the initial corneal contour ($t = 0$) and the outer contour of the cornea at time t was recorded as vertical displacement of anterior corneal surface at the time t. Then, the vertical displacement of the anterior corneal surface during the Corvis ST test was obtained after removing the whole eye movement (the displacement of the whole eyeball is shown in **Figure 4**).

In order to complete the calculation of the work done by air-puff attaining the whole corneal displacement based on **Eq. 5**, we need to fit these deformation data sets. We applied

$$S(r,t) = \left(w_0 - w_1 e^{S_1(t-c)-S_2(t-c)^2-S_3(t-c)^3-S_4(t-c)^4}\right)\left(a_1 e^{-\left(\frac{r-b_1}{c_1}\right)^2} + a_2 e^{-\left(\frac{r-b_2}{c_2}\right)^2}\right) \tag{6}$$

to fit the vertical displacement of the anterior surface of the cornea at point (r, t), where $0 \le t \le 30$ (ms), $0 \le r \le R_m$ (mm). According to the extracted corneal anterior surface contour, the radius of the maximum corneal deformation area is 4.29 mm, i.e., R_m is 4.29 mm. Parameter c is the time when the corneal apex in the corneal vertical displacement time curve is at the maximum position which is given from Corvis ST data.

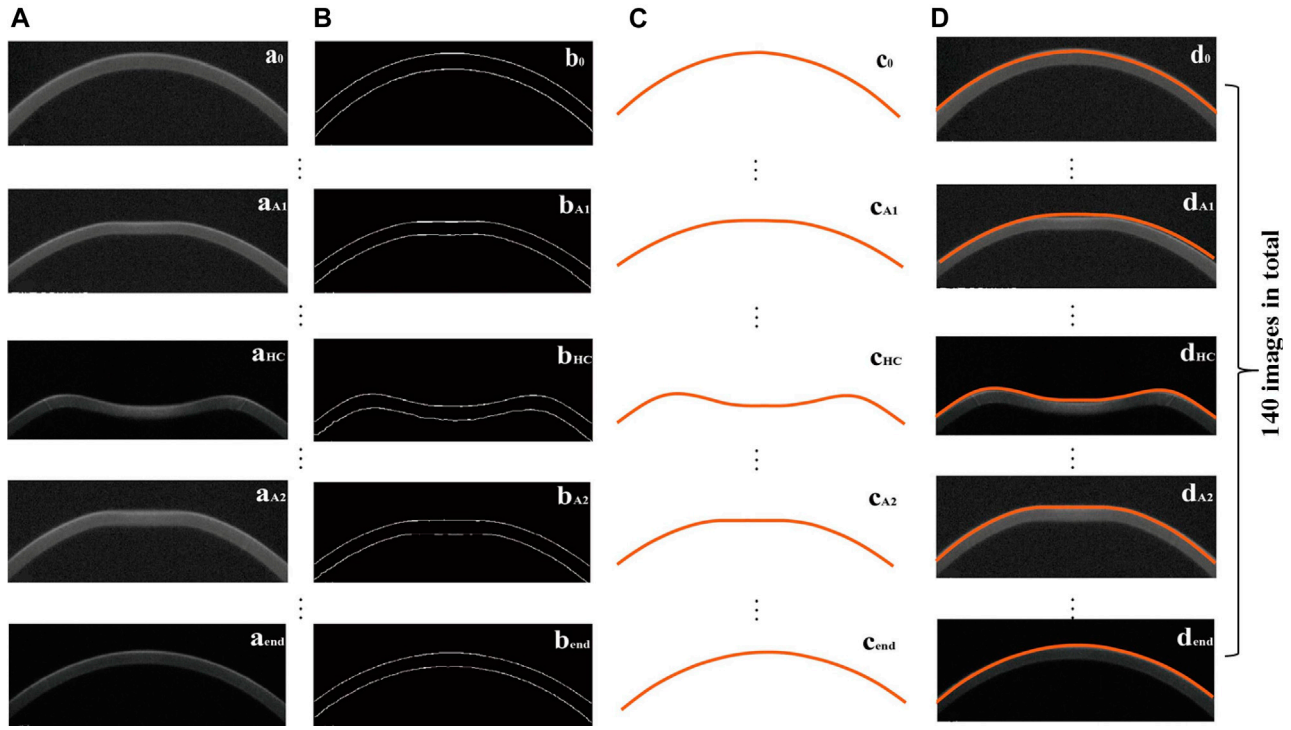

FIGURE 3 | Original corneal image (a_n) **(A)**, the corresponding processed image (b_n) **(B)**, extracted corneal anterior surface contour (c_n) **(C)**, and the position of the extracted corneal anterior surface contour in the original image (d_n) **(D)**, where n = 0 (initial state), A_1 (first applanation), HC (highest concavity), A_2 (second applanation), end.

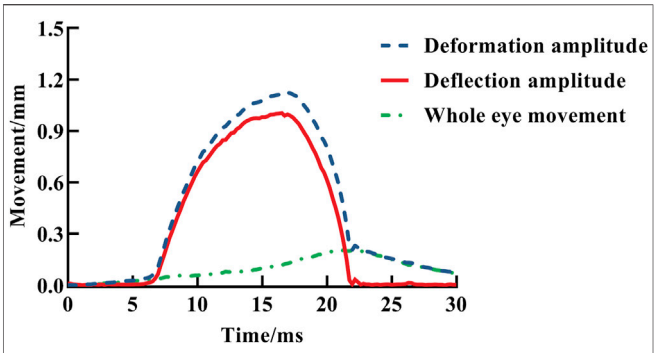

FIGURE 4 | Change of apex total displacement, apex pure displacement, and eye globe movement with time, indicated by blue dotted line, red solid line, and green dotted line, respectively.

The Determination of the Material Parameters

The cornea was regarded as a nonlinear incompressible viscoelastic material, and the Corvis ST test process was assumed to be a loading and unloading process with constant strain rate. The work done by an air-puff attaining the whole corneal displacement was completely regarded as the strain energy. Based on **Eqs. 1**, **2a**, **3–6**, the material parameters could be determined by minimizing the objective function shown in **Eq. 7**.

$$\mathrm{RM} = \sum_{k=1}^{n} (W_{ek} - VU_k)^2 \tag{7}$$

where W_{ek} is the work done by the air-puff attaining the whole corneal displacement during the Corvis ST test which is computed according to **Eq. 5**, and U_k is the strain energy density theoretical value which is calculated by **Eq. 1**. The n in **Eq. 7** is the number of the selected time points within 30 ms (The time of 30 ms was evenly divided into 71 time periods). V is the volume of the cornea in a zone around the anterior corneal apex with an 8.5-mm diameter. In this study, n was set 71, and V was from the Pentacam data.

The material parameters needed to identify were μ, α, A, and τ. The genetic algorithm based on Matlab (R2020b, MathWorks, Natick, MA, USA) was applied to solve the minimization of *RM* in **Eq. 7**. The value ranges of material parameters were set according to the literatures (Lago et al., 2015; Bao et al., 2018; Qin et al., 2019b).

Statistical analysis

All analyses were performed using SPSS (version 23.0, IBM Corporation, Armonk, NY, USA). The data were tested for normality of distribution using the Shapiro–Wilk test and expressed as mean ± SD or median (interquartile range, IQR). Power of the tests was calculated using the data of the determined parameter μ.

TABLE 1 | Baseline information of the human eyes.

Parameters	Age (years)	CCT (μm)	bIOP (mmHg)
Mean ± SD	23.4 ± 2.9	573 ± 24	16.06 ± 2.37

CCT: central corneal thickness.

TABLE 2 | DCR parameters from Corvis ST.

Parameters	Mean ± SD [median (IQR)]	Range
HCDA (mm)	0.89 (0.09)	0.78–1.15
HCR (mm)	7.93 (1.43)	7.17–9.68
PD (mm)	5.05 (0.39)	4.89–5.80
DAR2	4.17 (0.76)	3.50–4.64
SPA1 (mmHg/mm)	107.27 ± 13.08	79.82–135.95
SSI	0.99 ± 0.13	0.73–1.27
CBI	0.01 (0.03)	0.00–0.17

RESULTS

This study included 18 eyes of 12 participants (9 males, 3 females); the baseline information of participants is shown in **Table 1**.

DCR parameters from Corvis ST

The values of DCR parameters in the eyes are shown in **Table 2**. The SPA1 and SSI were normal distribution, but HCDA, HCR, PD, DAR2, and CBI were non-normal distribution.

Anterior corneal surface displacement

For each subject's 140-frame Corvis ST image data set, we extracted the contour data of the anterior corneal surface and then obtained the data set (r_j, t_j, d_{ij}), where $i = -287, -286, \cdots, 286, 287$; $j = 0, 1, \cdots, 139$, with $r_{-287} = r_{287} = 4.29$ mm, $t_0 = 0$, $t_{139} = 30$ ms, and d_{ij} is the displacement of the anterior corneal surface at point (i, j). **Figure 5** is the displacement data of the anterior corneal surface of a typical subject.

In order to verify the effectiveness of the displacement results from image extractions, the data set (t_j, d_{0j}) from image extractions was compared with the deflection amplitude (DA) output from Corvis ST. The root mean square (RMS) of displacement difference of about 140 data points was calculated. The RMS of displacement was 0.0245 ± 0.0092 mm (range: 0.0119–0.0439 mm). The corneal anterior surface vertex displacements from image extractions with time are shown in **Figure 6A**, which shows that the image extraction results gave a good agreement and closed to the DA with time. Moreover, the arc length variation data of the anterior corneal surface within 3.5 mm from the corneal apex with time was obtained from Corvis ST and was calculated as shown in **Eq. 4** based on image extractions, respectively. **Figure 6C** is the comparison of arc length variation between the outputs of Corvis ST and then calculated for one typical eye. It only found slight differences (the RMS of arc length variation was 0.006 mm). Therefore, the accuracy of the data gotten from image extraction was comparable with that from Corvis ST.

$S(r, t)$ (**Eq. 6**) was used to fit the vertical displacement of the anterior corneal surface at different distances from the corneal apex at different times, and the goodness of fit (R^2) was greater than 0.97 (**Table 3**).

Nonlinear Viscoelastic Parameters

Descriptive statistics of the model parameters identified based on the work done by air-puff force attaining the whole corneal displacement from Corvis ST are shown in **Table 4**. μ and α were normal distribution, and A and τ were non-normal distribution. **Table 4** shows the median, mean, standard deviation, IQR, minimum, and maximum of the material parameters for all corneas of the participants, and the median of goodness of fit (R^2) was over 0.96. Furthermore, power of the tests calculated by using the data of μ was about 0.87.

A typical fitting result of the visco-hyperelastic model to the work–time curve for one eye is shown in **Figure 7**. It shows a good agreement and is close to the work done by air-puff force attaining the whole corneal displacement in the Corvis ST test with time.

DISCUSSION

This study established a method to identify the nonlinear viscoelastic properties of human corneas from the output data of Corvis ST. The results showed feasibility of the method.

The morphology of the normal cornea has almost no change under IOP. For abnormal cornea, corneal viscoelasticity plays an important role (Vellara and Patel, 2015) in the maintenance of corneal morphology under long-term IOP. Keratoconus, a common clinical disease characterized by progressive corneal dilation, is highly related to corneal viscoelasticity (Vellara and Patel, 2015; Jin et al., 2020; Rahmati et al., 2021). This study gives a more comprehensive understanding of corneal biomechanical properties from the test of cornea *in vivo*. Compared with other studies, the innovation of this research is the determination of the nonlinear viscoelastic properties of human corneas from the output data of Corvis ST. It is expected that the biomechanical properties of the human cornea will be widely used in the early diagnosis of keratoconus, the screening of cornea before refractive surgery, and the early diagnosis of iatrogenic corneal ectasia after refractive surgery.

IOP is always acting on the inner surface of the cornea. So the cornea has been under the tension generated by IOP, before, during, and after the Corvis ST test. In this study, the cornea under normal IOP has been regarded as an equilibrium state. It is similar in that the pre-stress is taken into account in corneal tests *in vitro*. For example, in the uniaxial tensile test of corneal strips, the stress–strain relationship should be $\sigma - \sigma_0 = f(\varepsilon - \varepsilon_0)$, where σ_0, ε_0 are the initial stress and strain of the specimen, respectively. In many studies, the zero stress state has been taken as the initial state, i.e., σ_0 and ε_0 are zero (Elsheikh et al., 2010; Liu et al., 2020a; Liu et al., 2020b). According to the Laplace formula, the corneal stress under IOP is $\sigma = pr/2t$ (p, r, and t are the IOP, corneal radius, and corneal thickness, respectively); if the IOP is 16 mmHg, corneal radius and corneal thickness are 6 and 0.57 mm, respectively, the tensile stress of

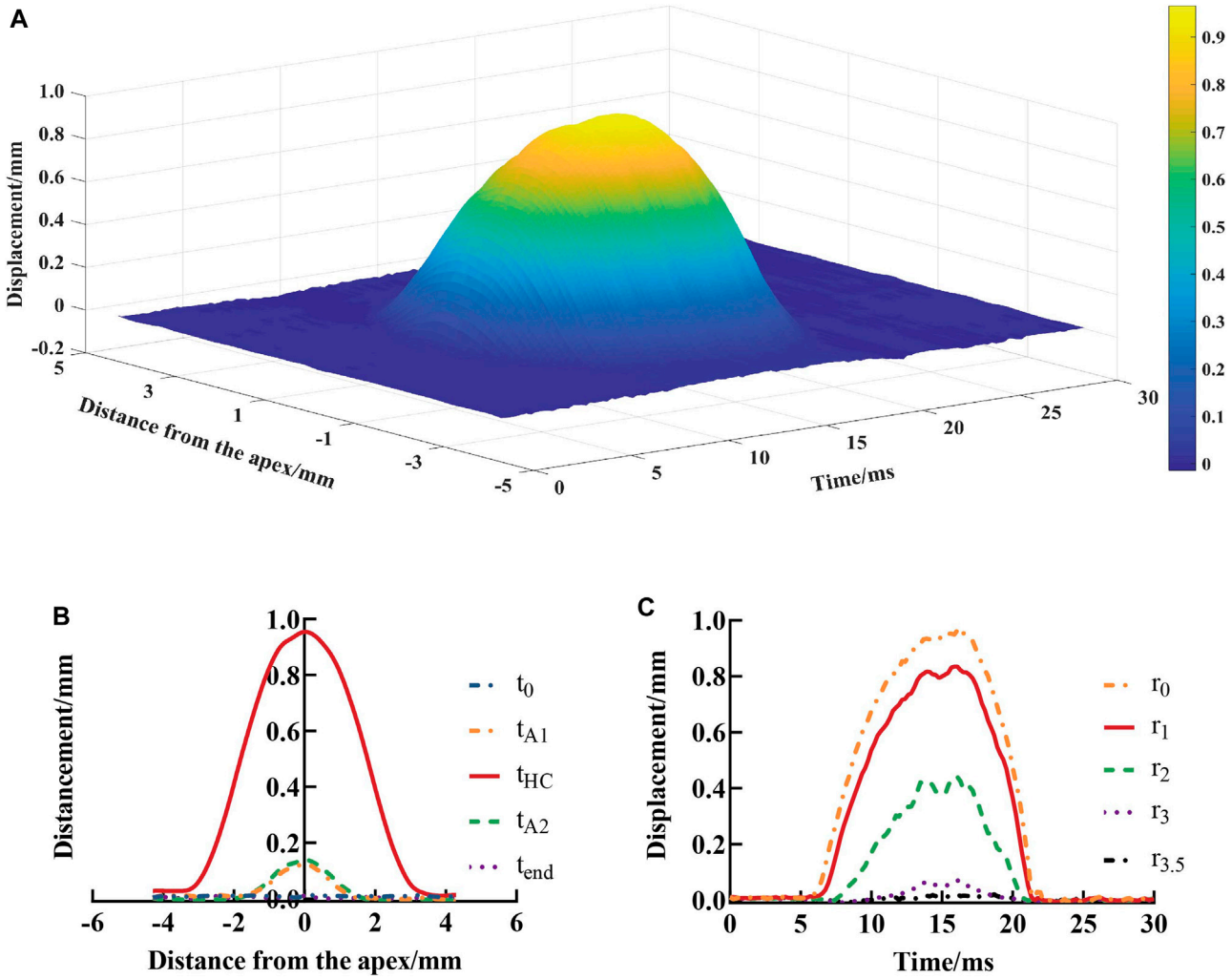

FIGURE 5 | Vertical displacements of the anterior surface of the cornea at each position and test time point **(A)**, spatial distribution **(B)**, and temporal variation **(C)**. t_0, t_{A1}, t_{HC}, t_{A2}, and t_{end} represent the time at initial state, first applanation, highest concavity, second applanation, and end state, respectively; r_l represents the distance from the corneal apex which was l (l = 0, 1, 2, 3, 3.5) mm.

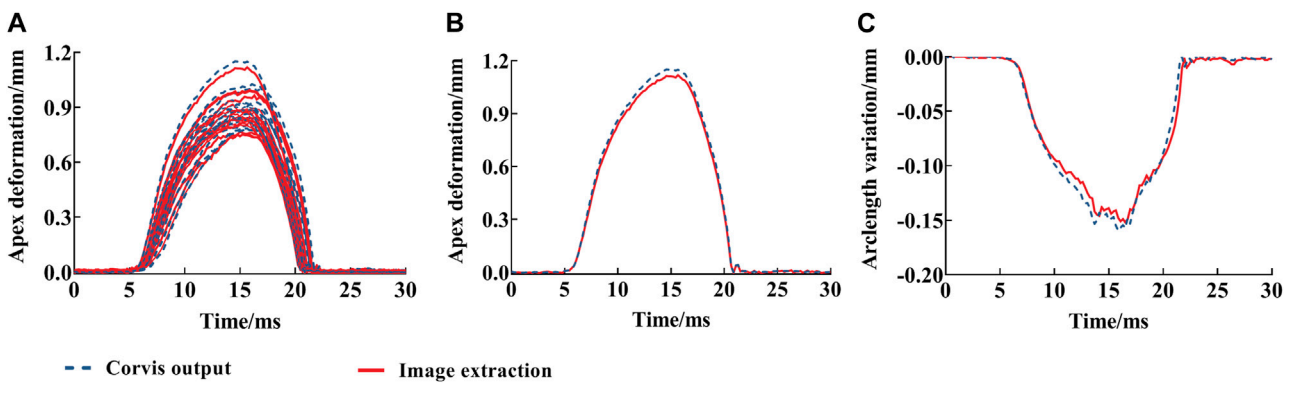

FIGURE 6 | Deflection amplitude and arc length variation of corneal anterior surface vertices from image extractions with time: deflection amplitude of all eyes **(A)**, one eye **(B)**, and arc length variation **(C)**. The red solid line is the image extraction result; blue dotted line is the deflection amplitude from Corvis ST.

TABLE 3 | The fitted parameters of $S(r, t)$.

Parameters	Mean ± SD [median (IQR)]	Range
w_0	−0.0006 (0.0051)	−0.0573 to 0.0033
w_1	−1.1220 (0.1378)	−1.2000 to −0.9283
S_1	0.0109 (0.0092)	0.0000–0.0218
S_2	0.0170 ± 0.0045	0.0100–0.0274
S_3	0.0039 (0.0010)	0.0011–0.0078
S_4	0.0006 (0.0002)	0.0001–0.0009
a_1	0.4547 ± 0.1219	0.2304–0.6774
a_2	0.6521 (0.1784)	0.5146–0.8000
b_1	1.0341 ± 0.1189	0.8422–1.2000
b_2	−0.6471 (0.3408)	−0.7599 to −0.6471
c_1	1.2220 (0.2330)	0.9882–1.3180
c_2	1.4755 ± 0.1323	1.2750–1.6920
R^2	0.9865 ± 0.0064	0.9742–0.9956

the cornea is 0.0112 MPa under IOP. Therefore, this study regarded tensile stress of 0.0112 MPa as the equilibrium state of cornea, based on which the visco-hyperelasticity of the cornea was obtained. The identified material parameters may be called as *in vivo* corneal biomechanical parameters.

Our previous study suggested a method (Qin et al., 2019a), following the studies of Ko et al. (2013) and Reissner (1946), to determine the corneal elastic modulus from corneal apical displacements between 0.1 and 0.2 mm at the first applanation state during the Corvis ST test based on the relationship between force and displacements of the shallow spherical model. It gave a corneal elastic modulus of human which ranged from 0.16 to 0.30 MPa. Shih et al. (2017) took the average pressure of air-puff during the Corvis ST test as the external pressure, did not consider the pressure changes with time, and applied Taber's model to obtain the elastic modulus of human which ranged from 0.053 to 0.363 MPa. These elastic moduli are given at the equilibrium of the first applanation state. The present study was initially motivated by Taber's model (Shih et al., 2017; Taber, 1982) and applied a visco-hyperelastic model to determine corneal nonlinear viscoelastic parameters. According to **Eq. 4** in the present study, the stretch ratio is about 0.995 at the first applanation state. This also demonstrates that our research was carried out under normal IOP as an equilibrium. Furthermore, in the studies of identifying corneal material parameters from Corvis ST data by the inverse finite element method, the zero stress state is also regarded as an initial state (Lago et al., 2015; Rahmati et al., 2021). Therefore, our study is different from most previous studies. We have given the *in vivo* corneal biomechanical parameters.

As we have known, the uniaxial stretch test is usually used to identify the tangential modulus of the cornea (Wollensak et al., 2003; Elsheikh et al., 2010; Zhang et al., 2018). If we let the stretch ratio λ_t be from the tensile direction data and the stretch ratios from transverse and thickness directions be equal to each other, then from the Ogden model follows $U = \frac{2\mu}{\alpha^2}(\lambda_t^{\alpha} + 2\lambda_t^{-\frac{\alpha}{2}} - 3)$. The tangential modulus of the cornea can be regarded as the second derivative of strain energy density function with respect to λ_t, i.e., $E_t = \frac{2\mu}{\alpha}[(\alpha - 1)\lambda_t^{\alpha-2} + (\frac{\alpha}{2} + 1)\lambda_t^{-\alpha/2-2}]$. According to the determined material parameters in the present study, the corneal tangential modulus is 1.61 ± 0.22 MPa when the strain is 0.01. Elsheikh et al. (2010) obtained the tangential modulus of the human cornea which was in the range of 0.32–1.66 MPa by uniaxial tensile test when the strain was about 0.01, and Liu et al. (2020b) obtained the elastic modulus of the corneal lenticule from young people which was about 1.2 MPa from the uniaxial tensile test when the strain is within 0.02. The tangential modulus at a strain of 0.01 obtained in this study may be compared with those at a strain of 0.02 or more provided by uniaxial tests. Since the elastic modulus that we calculated from Corvis ST data is under the normal IOP, this may result in slightly different results from previous studies.

The researchers believe that the strain rate under loading affects the stress–strain relationship of soft tissue (Snedeker et al., 2005; Kim et al., 2012) and that the stiffness of the cornea is directly proportional to its strain rate (Rahmati et al., 2021). It should be noted that this study is based on the test data of Corvis ST to identify the corneal nonlinear viscoelastic parameters. The test time is only about 30 ms, a fast loading and unloading process with the loading rate being about 2.5/s. This may lead to the difference between the parameters of the Ogden model obtained in this study and the results of the uniaxial tensile test of the *in vitro* cornea (strain rate less than 0.005/s). Moreover, the parameter A (0.10–0.39) is close to the values of A_k (k = 1, 2, 3) in Prony relaxation function, according to the studies by Kling et al. (2014) and Qin et al. (2019b). However, τ (1–2 ms) is smaller than τ_k (k = 1, 2, 3) in Prony relaxation function compared with the reported results. Because viscoelasticity is a time-dependent property, and the strain rate (~2.5/s) during the Corvis ST test is larger than during the stress relaxation test (less than 0.1/s), this may lead to the smaller τ in the Prony series obtained in this study.

In addition, a visco-hyperelastic model has been used to describe the stress–strain curve of the kidney capsule obtained by the uniaxial tensile test at high strain rates, and to identify the biomechanical characteristics of the tissue (Snedeker et al., 2005); this indicates that the visco-hyperelastic model has the possibility to be applied to identify the biomechanical properties of soft tissue under rapid deformation. The results of our study also confirm this possibility. The established method provides the evaluation biomechanical properties of the human cornea *via in vivo* test.

In addition, there are some advantages and limitations of using the visco-hyperelastic model to describe the biomechanical behavior of the human cornea. First of all, visco-hyperelastic

TABLE 4 | The determined material parameters.

Parameters	μ (MPa)	α	A	τ (ms)	R^2
Mean (median)	0.62	44.40	(0.23)	(1.35)	(0.969)
SD (IQR)	0.08	6.95	(0.16)	(0.35)	(0.025)
Range	0.42–0.74	32.76–55.63	0.09–0.36	1.21–1.95	0.951–0.988

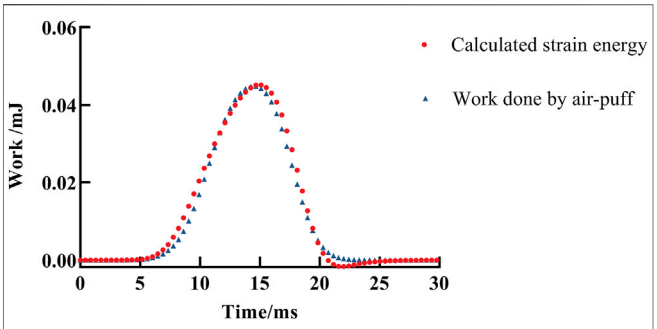

FIGURE 7 | A fitting result of work done by air-puff force attaining the whole corneal displacement during the Corvis ST test by the visco-hyperelastic model. The red solid dot is the fitting result, and the blue triangle represents the calculated work done by air-puff force attaining the whole corneal displacement during the Corvis ST test.

models based on strain energy functions have been shown to reproduce both the time-dependent and large strain aspects of the response (Ahearne et al., 2007; Boyce et al., 2007). A visco-hyperelastic model can give both elastic and viscous characteristics of the cornea. Secondly, this research showed that the calculation to determine model parameters is easy to carry out and saves time compared with inverse finite element methods. Thirdly, the simple model we selected, the convenient and fast computation, and the nonlinear viscoelasticity make the method of this study a potential method adopted by clinic applications, such as corneal screening before refractive surgery and early diagnosis of keratoconus. The limitation includes that researchers have not reached a consensus on how to identify the viscoelastic properties of the cornea based on Corvis ST data. The existing literature on whether the viscoelasticity of cornea can be evaluated from Corvis ST data implemented the study based on a specific constitutive model of cornea. Due to the different methods adopted, therefore, there were some differences in the results. Francis et al. (2019) believed that corneal viscous properties cannot be determined from air-puff applanation. However, majority of studies have shown that the viscoelasticity of the cornea can be obtained according to the output data of Corvis ST; for example, based on the output data of Corvis ST, the viscoelasticity of the cornea of normal people and patients with keratoconus has been compared and analyzed by the inverse finite element method (Rahmati et al., 2021), and Abass et al. (2020) believed that the viscoelasticity of the cornea can be determined by using the output data of Corvis ST. Our research showed that Corvis ST data can be used to explore the viscoelasticity of cornea. Further, Corvis ST records the morphological changes of cornea under the action of air-puff within about 30 ms, which is a rapid loading and unloading process. In the existing studies, the period of corneal stress relaxation tests was not less than 2 min (Hammer et al., 2015; Kling et al., 2015; Zhang et al., 2018). The difference in test time between Corvis ST and classical relaxation or creep tests may result in different orders of magnitude of the model parameters. How to understand the relationship between them and corneal stress relaxation characteristics needs to be further investigated.

There are some limitations in this study. First, the number of participants included was small, considering that the population with different cornea stiffness may have different responses to Corvis ST; its clinical significance needs to be further validated with study on patients with corneal biomechanics disorder, such as keratoconus, or patients that received corneal collagen crosslinking. Second, we studied the cornea with certain tension under IOP as the initial state and failed to obtain the biomechanical parameters of the cornea under zero stress state. However, we also note that the initial state that should be paid attention to in the research of applying corneal biomechanical properties to clinical problems is the state under IOP, so the method we provide to identify corneal biomechanical properties may be more useful. Third, in this study, we did not consider the corneal anisotropic mechanical properties. It should be further studied in the future.

CONCLUSION

In conclusion, it is provided that the corneal nonlinear viscoelastic properties can be determined based on a visco-hyperelastic model from the corneal contour information and air-puff pressure of Corvis ST test. All in all, the present conclusion should be substantiated with more investigation, by which to provide more useful information for clinical practice.

DATA AVAILABILITY STATEMENT

The original contributions presented in the study are included in the article/Supplementary Material, further inquiries can be directed to the corresponding authors.

ETHICS STATEMENT

The studies involving human participants were reviewed and approved by the institutional review board of Capital Medical University which approved this study, and all participants signed an informed consent form in accordance with the tenets of the Declaration of Helsinki. The patients/participants provided their written informed consent to participate in this study.

AUTHOR CONTRIBUTIONS

Manuscript writing and review: DZ, HZ, and LT. Data collection, analysis, and interpretation: DZ, YZ, and CF. Design of this study and revision of the manuscript: CZ and LL. All authors read and approved the final manuscript.

FUNDING

This study was financially supported by the National Natural Science Foundation of China (Nos. 31370952, 31470914, 31600758, 82171101, 32171304); Beijing Nova Program (Z181100006218099); and the Open Research Fund from Beijing Advanced Innovation Center for Big Data-Based Precision Medicine, Beijing Tongren Hospital, Beihang University and Capital Medical University (BHTR-KFJJ-202001).

REFERENCES

Abass, A., Roberts, C. J., Lopes, B., Eliasy, A., Vinciguerra, R., Ambrósio, R., Jr., et al. (2020). Can the Corvis St Estimate Corneal Viscoelasticity. *J. Refract. Surg.* 36, 346–347. doi:10.3928/1081597X-20200212-04

Ahearne, M., Yang, Y., Then, K. Y., and Liu, K.-K. (2007). An Indentation Technique to Characterize the Mechanical and Viscoelastic Properties of Human and Porcine Corneas. *Ann. Biomed. Eng.* 35, 1608–1616. doi:10.1007/s10439-007-9323-9

Bao, F., Deng, M., Zheng, X., Li, L., Zhao, Y., Cao, S., et al. (2017). Effects of Diabetes Mellitus on Biomechanical Properties of the Rabbit Cornea. *Exp. Eye Res.* 161, 82–88. doi:10.1016/j.exer.2017.05.015

Bao, F., Zheng, Y., Liu, C., Zheng, X., Zhao, Y., Wang, Y., et al. (2018). Changes in Corneal Biomechanical Properties with Different Corneal Cross-Linking Irradiances. *J. Refract. Surg.* 34, 51–58. doi:10.3928/1081597X-20171025-01

Bekesi, N., Kochevar, I. E., and Marcos, S. (2016). Corneal Biomechanical Response Following Collagen Cross-Linking with Rose Bengal-green Light and Riboflavin-UVA. *Invest. Ophthalmol. Vis. Sci.* 57, 992–1001. doi:10.1167/iovs.15-18689

Boyce, B. L., Jones, R. E., Nguyen, T. D., and Grazier, J. M. (2007). Stress-Controlled Viscoelastic Tensile Response of Bovine Cornea. *J. Biomech.* 40, 2367–2376. doi:10.1016/j.jbiomech.2006.12.001

Brown, L., Foulsham, W., Pronin, S., and Tatham, A. J. (2018). The Influence of Corneal Biomechanical Properties on Intraocular Pressure Measurements Using a Rebound Self-Tonometer. *J. Glaucoma* 27, 511–518. doi:10.1097/IJG.0000000000000948

Chan, T. C., Wang, Y. M., Yu, M., and Jhanji, V. (2018). Comparison of Corneal Dynamic Parameters and Tomographic Measurements Using Scheimpflug Imaging in Keratoconus. *Br. J. Ophthalmol.* 102, 42–47. doi:10.1136/bjophthalmol-2017-310355

Dupps, W. J., Jr., and Wilson, S. E. (2006). Biomechanics and Wound Healing in the Cornea. *Exp. Eye Res.* 83, 709–720. doi:10.1016/j.exer.2006.03.015

Eliasy, A., Chen, K.-J., Vinciguerra, R., Lopes, B. T., Abass, A., Vinciguerra, P., et al. (2019). Determination of Corneal Biomechanical Behavior *In-Vivo* for Healthy Eyes Using CorVis ST Tonometry: Stress-Strain index. *Front. Bioeng. Biotechnol.* 7, 105. doi:10.3389/fbioe.2019.00105

Elsheikh, A., Geraghty, B., Rama, P., Campanelli, M., and Meek, K. M. (2010). Characterization of Age-Related Variation in Corneal Biomechanical Properties. *J. R. Soc. Interface* 7, 1475–1485. doi:10.1098/rsif.2010.0108

Fraldi, M., Cutolo, A., Esposito, L., and Guarracino, F. (2011). The Role of Viscoelasticity and Stress Gradients on the Outcome of Conductive Keratoplasty. *Biomech. Model. Mechanobiol.* 10, 397–412. doi:10.1007/s10237-010-0242-6

Francis, M., Matalia, H., Nuijts, R. M. M. A., Haex, B., Shetty, R., and Sinha Roy, A. (2019). Corneal Viscous Properties Cannot Be Determined from Air-Puff Applanation. *J. Refract. Surg.* 35, 730–736. doi:10.3928/1081597x-20191010-03

Hammer, A., Kling, S., Boldi, M.-O., Richoz, O., Tabibian, D., Randleman, J. B., et al. (2015). Establishing Corneal Cross-Linking with Riboflavin and UV-A in the Mouse Cornea *In Vivo*: Biomechanical Analysis. *Invest. Ophthalmol. Vis. Sci.* 56, 6581–6590. doi:10.1167/iovs.15-17426

Huang, H., Tang, W., Tan, Q., and Yan, B. (2017). Development and Parameter Identification of a Visco-Hyperelastic Model for the Periodontal Ligament. *J. Mech. Behav. Biomed. Mater* 68, 210–215. doi:10.1016/j.jmbbm.2017.01.035

Jin, Z., Zhou, Y., Shen, M., Wang, Y., Lu, F., and Zhu, D. (2020). Assessment of Corneal Viscoelasticity Using Elastic Wave Optical Coherence Elastography. *J. Biophotonics* 13, e201960074. doi:10.1002/jbio.201960074

Joda, A. A., Shervin, M. M., Kook, D., and Elsheikh, A. (2016). Development and Validation of a Correction Equation for Corvis Tonometry. *Comput. Methods Biomech. Biomed. Engin.* 19, 943–953. doi:10.1080/10255842.2015.1077515

Kim, W., Argento, A., Rozsa, F. W., and Mallett, K. (2012). Constitutive Behavior of Ocular Tissues over a Range of Strain Rates. *J. Biomech. Eng.* 134, 061002. doi:10.1115/1.4006847

Kling, S., Bekesi, N., Dorronsoro, C., Pascual, D., and Marcos, S. (2014). Corneal Viscoelastic Properties from Finite-Element Analysis of *In Vivo* Air-Puff Deformation. *Plos One* 9, e104904. doi:10.1371/journal.pone.0104904

Kling, S., Richoz, O., Hammer, A., Tabibian, D., Jacob, S., Agarwal, A., et al. (2015). Increased Biomechanical Efficacy of Corneal Cross-Linking in Thin Corneas Due to Higher Oxygen Availability. *J. Refract. Surg.* 31, 840–846. doi:10.3928/1081597X-20151111-08

Ko, M. W. L., Leung, L. K. K., Lam, D. C. C., and Leung, C. K. S. (2013). Characterization of Corneal tangent Modulus *in Vivo*. *Acta Ophthalmol.* 91, e263–e269. doi:10.1111/aos.12066

Lago, M. A., Rupérez, M. J., Martínez-Martínez, F., Monserrat, C., Larra, E., Güell, J. L., et al. (2015). A New Methodology for the *In Vivo* Estimation of the Elastic Constants that Characterize the Patient-specific Biomechanical Behavior of the Human Cornea. *J. Biomech.* 48, 38–43. doi:10.1016/j.jbiomech.2014.11.009

Liu, T., Shen, M., Huang, L., Xiang, Y., Li, H., Zhang, Y., et al. (2020a). Characterization of Hyperelastic Mechanical Properties for Youth Corneal Anterior central Stroma Based on Collagen Fibril Crimping Constitutive Model. *J. Mech. Behav. Biomed. Mater.* 103, 103575. doi:10.1016/j.jmbbm.2019.103575

Liu, T., Shen, M., Li, H., Zhang, Y., Mu, B., Zhao, X., et al. (2020b). Changes and Quantitative Characterization of Hyper-Viscoelastic Biomechanical Properties for Young Corneal Stroma after Standard Corneal Cross-Linking Treatment with Different Ultraviolet-A Energies. *Acta Biomater.* 113, 438–451. doi:10.1016/j.actbio.2020.06.005

Maklad, O., Eliasy, A., Chen, K. J., Theofilis, V., and Elsheikh, A. (2019). Simulation of Air Puff Tonometry Test Using Arbitrary Lagrangian-Eulerian (ALE) Deforming Mesh for Corneal Material Characterisation. *Int. J. Environ. Res. Public Health* 17, 54. doi:10.3390/ijerph17010054

Piñero, D. P., and Alcón, N. (2014). *In Vivo* characterization of Corneal Biomechanics. *J. Cataract. Refract. Surg.* 40, 870–887. doi:10.1016/j.jcrs.2014.03.021

Qin, X., Tian, L., Zhang, H., Chen, X., and Li, L. (2019a). Evaluation of Corneal Elastic Modulus Based on Corneal Visualization Scheimpflug Technology. *Biomed. Eng. Online* 18, 42. doi:10.1186/s12938-019-0662-1

Qin, X., Yu, M., Zhang, H., Chen, X., and Li, L. (2019b). The Mechanical Interpretation of Ocular Response Analyzer Parameters. *Biomed. Res. Int.* 2019, 5701236. doi:10.1155/2019/5701236

Rahmati, S. M., Razaghi, R., and Karimi, A. (2021). Biomechanics of the Keratoconic Cornea: Theory, Segmentation, Pressure Distribution, and Coupled FE-Optimization Algorithm. *J. Mech. Behav. Biomed. Mater.* 113, 104155. doi:10.1016/j.jmbbm.2020.104155

Ramzanpour, M., Hosseini-Farid, M., McLean, J., Ziejewski, M., and Karami, G. (2020). Visco-Hyperelastic Characterization of Human Brain White Matter Micro-Level Constituents in Different Strain Rates. *Med. Biol. Eng. Comput.* 58, 2107–2118. doi:10.1007/s11517-020-02228-3

Reissner, E. (1946). Stresses and Small Displacements of Shallow Spherical Shells. *J. Math. Phys.* 25, 80–85. doi:10.1002/sapm194625180

Sedaghat, M.-R., Momeni-Moghaddam, H., Ambrósio, R., Jr., Roberts, C. J., Yekta, A.-A., Danesh, Z., et al. (2018). Long-term Evaluation of Corneal Biomechanical Properties after Corneal Cross-Linking for Keratoconus: A 4-Year Longitudinal Study. *J. Refract. Surg.* 34, 849–856. doi:10.3928/1081597X-20181012-02

Shen, Y., Chen, Z., Knorz, M. C., Li, M., Zhao, J., and Zhou, X. (2014). Comparison of Corneal Deformation Parameters after SMILE, LASEK, and Femtosecond Laser-Assisted LASIK. *J. Refract. Surg.* 30, 310–318. doi:10.3928/1081597x-20140422-01

Shih, P.-J., Huang, C.-J., Huang, T.-H., Lin, H.-C., Yen, J.-Y., Wang, I.-J., et al. (2017). Estimation of the Corneal Young's ModulusIn VivoBased on a Fluid-Filled Spherical-Shell Model with Scheimpflug Imaging. *J. Ophthalmol.* 2017, 5410143. doi:10.1155/2017/5410143

Simonini, I., Angelillo, M., and Pandolfi, A. (2016). Theoretical and Numerical Analysis of the Corneal Air Puff Test. *J. Mech. Phys. Solids* 93, 118–134. doi:10.1016/j.jmps.2016.04.012

Sinha Roy, A., Kurian, M., Matalia, H., and Shetty, R. (2015). Air-puff Associated Quantification of Non-linear Biomechanical Properties of the Human Cornea *In Vivo*. *J. Mech. Behav. Biomed. Mater.* 48, 173–182. doi:10.1016/j.jmbbm.2015.04.010

Snedeker, J. G., Niederer, P., Schmidlin, F. R., Farshad, M., Demetropoulos, C. K., Lee, J. B., et al. (2005). Strain-rate Dependent Material Properties of the Porcine and Human Kidney Capsule. *J. Biomech.* 38, 1011–1021. doi:10.1016/j.jbiomech.2004.05.036

Su, P., Yang, Y., Xiao, J., and Song, Y. (2015). Corneal Hyper-Viscoelastic Model: Derivations, Experiments, and Simulations. *Acta Bioeng. Biomech.* 17, 73–84. doi:10.5277/ABB-00142-2014-03

Taber, L. A. (1982). Large Deflection of a Fluid-Filled Spherical Shell under a point Load. *J. Appl. Mech.* 49, 121–128. doi:10.1115/1.3161953

Taylor, Z. A., Comas, O., Cheng, M., Passenger, J., Hawkes, D. J., Atkinson, D., et al. (2009). On Modelling of Anisotropic Viscoelasticity for Soft Tissue Simulation: Numerical Solution and GPU Execution. *Med. Image Anal.* 13, 234–244. doi:10.1016/j.media.2008.10.001

Vellara, H. R., and Patel, D. V. (2015). Biomechanical Properties of the Keratoconic Cornea: a Review. *Clin. Exp. Optom.* 98, 31–38. doi:10.1111/cxo.12211

Vinciguerra, R., Romano, V., Arbabi, E. M., Brunner, M., Willoughby, C. E., Batterbury, M., et al. (2017). *In Vivo* Early Corneal Biomechanical Changes after Corneal Cross-Linking in Patients with Progressive Keratoconus. *J. Refract. Surg.* 33, 840–846. doi:10.3928/1081597X-20170922-02

Wang, W., Du, S., and Zhang, X. (2015). Corneal Deformation Response in Patients with Primary Open-Angle Glaucoma and in Healthy Subjects Analyzed by Corvis ST. *Invest. Ophthalmol. Vis. Sci.* 56, 5557–5565. doi:10.1167/iovs.15-16926

Whitford, C., Movchan, N. V., Studer, H., and Elsheikh, A. (2018). A Viscoelastic Anisotropic Hyperelastic Constitutive Model of the Human Cornea. *Biomech. Model. Mechanobiol.* 17, 19–29. doi:10.1007/s10237-017-0942-2

Wollensak, G., Spoerl, E., and Seiler, T. (2003). Stress-strain Measurements of Human and Porcine Corneas after Riboflavin-Ultraviolet-A-Induced Cross-Linking. *J. Cataract. Refract. Surg.* 29, 1780–1785. doi:10.1016/s0886-3350(03)00407-3

Zhang, H., Khan, M. A., Zhang, D., Qin, X., Lin, D., and Li, L. (2018). Corneal Biomechanical Properties after FS-LASIK with Residual Bed Thickness Less Than 50% of the Original Corneal Thickness. *J. Ophthalmol.* 2018, 2752945. doi:10.1155/2018/2752945

Conflict of Interest: The authors declare that the research was conducted in the absence of any commercial or financial relationships that could be construed as a potential conflict of interest.

Publisher's Note: All claims expressed in this article are solely those of the authors and do not necessarily represent those of their affiliated organizations, or those of the publisher, the editors, and the reviewers. Any product that may be evaluated in this article, or claim that may be made by its manufacturer, is not guaranteed or endorsed by the publisher.

frontiers in Bioengineering and Biotechnology

ORIGINAL RESEARCH
published: 26 November 2021
doi: 10.3389/fbioe.2021.751628

Effect of Mydriasis-Caused Intraocular Pressure Changes on Corneal Biomechanical Metrics

Yufeng Ye[1†], Yi Li[2†], Zehui Zhu[1], Anas Ziad Masoud Abu Said[1], Kevin Nguelemo Mayopa[1], Stephen Akiti[1], Chengyi Huang[1], Bernardo T. Lopes[3], Ashkan Eliasy[3], Yuanyuan Miao[1], Junjie Wang[1,4], Xiaobo Zheng[1,4], Shihao Chen[1,4], Fangjun Bao[1,4]* and Ahmed Elsheikh[3,5,6]*

[1]Eye Hospital, Wenzhou Medical University, Wenzhou, China, [2]North Huashan Hospital, Fudan University, Shanghai, China, [3]School of Engineering, University of Liverpool, Liverpool, United Kingdom, [4]The Institute of Ocular Biomechanics, Wenzhou Medical University, Wenzhou, China, [5]National Institute for Health Research (NIHR), Biomedical Research Centre for Ophthalmology, Moorfields Eye Hospital NHS Foundation Trust, UCL Institute of Ophthalmology, London, United Kingdom, [6]Beijing Advanced Innovation Center for Biomedical Engineering, Beihang University, Beijing, China

Purpose: To evaluate the dependence of biomechanical metrics on intraocular pressure (IOP).

Methods: 233 refractive surgery patients were included in this study—all were examined 3 times with the Corvis ST before and after dilation, and the differences (Δ) in the main device parameters were assessed. The data collected included the biomechanically corrected IOP (bIOP), the central corneal thickness (CCT), and six dynamic corneal response (DCR) parameters, namely DA, DARatio2mm, IIR, SP-A1, CBI, and SSI. Participants were divided into three groups according to the changes in patients' bIOP after mydriasis.

Results: Intra-operator repeatability was generally high in most of the DCR parameters obtained before and after dilation. The mean changes in bIOP and CCT after dilation were −0.12 ± 1.36 mmHg and 1.95 ± 5.23 μm, respectively. Only ΔDARatio2mm, ΔIIR, and ΔCBI exhibited a statistically significant correlation with ΔCCT ($p < 0.05$). The changes in all DCR parameters, especially ΔDA and ΔSP-A1 were also correlated with ΔbIOP ($p < 0.01$)—a 1-mmHg change in bIOP was associated, on average, with 5.612 and −0.037 units of change in SP-A1 and DA, respectively. In contrast, the weakest correlation with ΔbIOP was exhibited by ΔSSI.

Conclusion: Most corneal DCR parameters, provided by the Corvis ST, were correlated with IOP, and more weakly with CCT. Changes experienced in CCT and IOP should therefore be considered in studies on corneal biomechanics and how it is affected by disease progression and surgical or medical procedures.

Keywords: biomechanical metrics, intraocular pressure, mydriasis, stiffness parameter at first applanation, stress-strain index

OPEN ACCESS

Edited by:
Yang Liu,
Hong Kong Polytechnic University,
Hong Kong SAR, China

Reviewed by:
Uriel Zapata,
EAFIT University, Colombia
Aike Qiao,
Beijing University of Technology, China

***Correspondence:**
Shihao Chen
chenshihao73@126.com
Fangjun Bao
bfjmd@126.com

[†]These authors have contributed equally to this work and share first authorship

Specialty section:
This article was submitted to Biomechanics, a section of the journal Frontiers in Bioengineering and Biotechnology

Received: *01 August 2021*
Accepted: *26 October 2021*
Published: *26 November 2021*

Citation:
Ye Y, Li Y, Zhu Z, Abu Said AZM, Nguelemo Mayopa K, Akiti S, Huang C, Lopes BT, Eliasy A, Miao Y, Wang J, Zheng X, Chen S, Bao F and Elsheikh A (2021) Effect of Mydriasis-Caused Intraocular Pressure Changes on Corneal Biomechanical Metrics. Front. Bioeng. Biotechnol. 9:751628. doi: 10.3389/fbioe.2021.751628

HIGHLIGHTS

Most corneal biomechanical metrics, especially SP-A1 and DA provided by Corvis ST, proved to be correlated with IOP in a study of matched clinical data obtained before and after dilation.

INTRODUCTION

To focus light rays on the retina, the cornea needs to remain transparent and maintain a suitable shape that stays stable with the diurnal changes in intraocular pressure (IOP). This is made possible by the cornea's microstructure, which confers the tissue with complex biomechanical properties (Meek and Knupp, 2015). Corneal biomechanics has been a hot topic in ophthalmology research due to its prospective applications in the diagnosis, management and treatment of several clinical conditions, including keratoconus (Rabinowitz, 1998). Understanding corneal biomechanical properties is also of great importance in the planning of refractive surgery, where these properties can help identify patients at high risk of developing iatrogenic ectasia after laser vision correction (Esporcatte et al., 2020).

The *in vivo* evaluation of corneal biomechanical behavior has recently become possible through the introduction of the Ocular Response Analyzer (ORA) and Corvis ST (CVS). Of the two devices, Corvis ST provides more information on corneal biomechanical response, based on ultra-high-speed Scheimpflug technology which records the entire process of corneal deformation and provides measurements such as the stiffness parameter at first applanation (SP-A1) and the integrated inverse radius (IIR). While these biomechanical metrics have been shown to have strong correlation with the cornea's overall stiffness, they are not independent parameters, but influenced by stiffness-unrelated events such as the diurnal variation in the IOP (Bao et al., 2015).

One of these events is mydriasis; an integral part of the pre-refractive surgery evaluation of patients. Qian et al., reported 35% of patients had a post-dilation variation in IOP of more than 2 mm Hg—31.1% of these patients experienced significant IOP increases after mydriasis, while the other 68.9% showed significant decreases (Qian et al., 2012). These changes may have had an effect on the Corvis ST biomechanical metrics. This study aims to identify the influence of changes in IOP caused by mydriasis on these metrics and evaluate the repeatability of these effects.

METHODS

Study Design

The study followed the tenets of the Declaration of Helsinki and was approved by the Ethics Committee of the Eye Hospital, Wenzhou Medical University, China. The records of patients seeking myopic or astigmatic correction were examined at the corneal refractive surgery center and evaluated for inclusion in this study. The inclusion criteria were: the presence of myopia with astigmatism not exceeding 3.25 D, and with manifest spherical equivalent ≥ −10.00 D; and absence of ocular diseases (other than refractive errors). All 233 patients included underwent complete ophthalmic examination, and those wearing soft contact lenses were asked to suspend their use for 2 weeks prior to the examination. Informed consent was provided by all participants to use their data in research.

Mydriasis Test

As part of the routine posterior segment examination, each participant received Mydrin-P (0.5% tropicamide and 0.5% phenylephrine hydrochloride; Santen Pharmaceuticals, Japan) three times (one drop each time) with 10 min between applications. The 233 participants included were divided into three groups (Group I, Group D, and Group S) according to the patients' biomechanically corrected IOP (bIOP) value (obtained with the Corvis ST) after mydriasis test. If the bIOP value fell after the mydriasis test by more than $(Sw_{pre} + Sw_{pos})/2$ (where Sw_{pre} and Sw_{pos} meant the within-subject standard deviation before and after mydriasis test), the subject was included in Group D (47 subjects). If the bIOP value increased by more than $(Sw_{pre} + Sw_{pos})/2$ after the mydriasis test, the subject was included in Group I (33 subjects), and all remaining subjects were included in Group S (153 subjects).

Biomechanical Evaluation

All Corvis ST (CVS) exams were taken in the sitting position, and all participants underwent measurements in a single session (≤2 h). CVS measurements were taken at two stages: pre- and post-dilation (before and after the mydriasis test, respectively). In each stage, measurements were repeated every 2 min until three satisfactory readings were obtained with the difference between the lowest and highest readings being ≤2 mmHg (i.e., a total of six readings per subject). The same experienced clinician (WC) took all measurements, using the same instruments throughout, to limit potential variability associated with either the instrument or the operator. The Corvis ST was calibrated by the clinic's technician before the study was started.

Central corneal thickness (CCT) and six dynamic corneal response (DCR) parameters that have been consistently linked to corneal stiffness (Vinciguerra et al., 2016; Roberts et al., 2017) were recorded at both pre- and post-dilation stages from Corvis ST. These parameters included the deformation amplitude (DA), the ratio between DA values at the apex and 2 mm from the apex (DARatio2mm), and the integrated inverse radius (IIR, the integrated sum of inverse concave radius values between first and second applanation events). The stiffness parameter at first applanation (SP-A1) was also included, and represented the difference between the adjusted air puff pressure at first applanation (AdjAP1) and bIOP divided by the defection amplitude at the first applanation (A1DeflAmp) (Reinstein et al., 2013).

SP-A1 = (adjAP1—bIOP)/(A1DeflAmp) Equation 1.

Also included were the Corvis biomechanical index (CBI) and the stress-strain index (SSI) which was developed to evaluate the material stiffness of corneal tissue (Eliasy et al., 2019).

TABLE 1 | Repeatability of corvis ST parameters.

Metrics	Stages	Mean + Std	Sw	CoV	ICC
bIOP, mmHg	Pre	15.5 ± 2.2	0.93	5.99	0.835
	Pos	15.4 ± 2.1	0.96	6.29	0.818
CCT, μm	Pre	549.6 ± 33.8	5.15	0.94	0.977
	Pos	551.5 ± 33.5	5.05	0.92	0.978
DA, mm	Pre	1.04 ± 0.1	0.04	3.84	0.851
	Pos	1.04 ± 0.1	0.04	4.10	0.845
DARatio2mm	Pre	4.27 ± 0.4	0.14	3.23	0.879
	Pos	4.24 ± 0.39	0.16	3.75	0.849
IIR, mm^{-1}	Pre	8.85 ± 0.98	0.41	4.68	0.827
	Pos	8.81 ± 0.98	0.38	4.26	0.864
SP-A1, mmHg/mm	Pre	106.60 ± 17.31	6.22	5.83	0.882
	Pos	105.99 ± 17.73	6.84	6.47	0.867
CBI	Pre	0.32 ± 0.23	0.08	-	0.887
	Pos	0.30 ± 0.23	0.08	-	0.899
SSI	Pre	0.90 ± 0.12	0.06	6.12	0.804
	Pos	0.90 ± 0.13	0.05	5.80	0.846

bIOP, biomechanically corrected IOP; CCT, central corneal thickness; DA, deformation amplitude; DARatio2mm, the ratio between DA values at the apex and 2 mm from apex; IIR, integrated inverse radius; SP-A1, the stiffness parameter at first applanation; CBI, corvis biomechanical index; SSI, stress-strain index; Pre, undilated pupil; Pos, after mydriasis test; Sw, within-subject standard deviation; CoV, coefficient of variation (%); ICC, intraclass correlation coefficient.

Statistical Analyses

Repeatability of the three CVS measurements was assessed using the within-subject standard deviation (Sw), within-subject coefficient of variation (CoV) and intraclass correlation coefficient (ICC), and was used to evaluate the reliability of CVS measurements both before and after dilation. The average of the three readings considered in each stage was used for statistical analysis using SPSS (version 20.0, IBM, Inc.). The min sample size was calculated based on paired-sample t-tests with the help of G*Power (version 3.1.2, Franz Faul, University Kiel, Germany), and at least 30 participants were required for each subgroup. Paired-sample T tests analyzed the differences between pre- and post-dilation biometric values, while Groups I, D, and S were compared *via* One-way ANOVA. Δ meant the differences between before and after mydriasis test. The relationship between ΔDA, ΔDARatio2mm, ΔIIR, ΔSP-A1, ΔCBI, ΔSSI, and differences in CCT or bIOP pre-versus post-dilation were assessed using Pearson's or Spearman's correlation factor for normally and non-normally distributed data, respectively. A stepwise approach to multiple linear regression analysis was used to identify associations between ΔCCT and ΔbIOP on one hand, and the changes in ocular biomechanical metrics pre- and post-dilation on the other. p values <0.05 were considered statistically significant.

RESULTS

The mean age of all participants was 26.3 ± 7.1 years and was not significantly different among the three study groups ($p = 0.590$). Corvis ST results before and after mydriasis, along with the repeatability measures, are displayed in **Table 1**. The data indicated that there was generally high intra-operator repeatability in most the DCR parameters recorded. For bIOP, within-subject standard deviation (Sw) was 0.93 mmHg before mydriasis and similar after (0.96 mmHg). The coefficient of variation (CoV) was approximately 6% (5.99% before mydriasis and 6.29% after). 20.2% of subjects showed an increase in bIOP measurement post-dilation (2.01 ± 1.50 mmHg, 1.00–9.37 mmHg, Group I), 14.2% exhibited a decrease post-dilation (−1.85 ± 0.80 mmHg, −0.97 ~ −5.4 mmHg, Group D), and the remaining 65.6% had stable bIOP readings (−0.06 ± 0.50 mmHg, −0.93–0.93 mmHg, Group S).

One of the parameters, CCT, showed excellent repeatability (ICC ≥ 0.90), while all others had good repeatability (ICC ≥ 0.75). Most DCR parameters presented CoV for repeatability below 5%. SP-A1 and SSI had slightly higher CoV (5.83%/6.47% and 6.12%/5.80%, respectively, before and after pupil dilation). As the mean CBI was very low (~0.32), the CoV was not calculated. Repeatability of the biomechanical metrics was similar at the pre- and post-dilation stages.

The CVS metrics collected before and after the mydriasis test are presented in **Tables 1**, **2**; **Figure 1**. CCT, DARatio2mm, and CBI changed statistically significantly after mydriasis, while the other five DCR parameters remained stable. Before dilation, all metrics except bIOP, DA, and SP-A1 were similar across the three patient groups ($p > 0.05$), while statistically significant differences ($p < 0.05$) were observed in bIOP, DA, IIR, SP-A1, and SSI after dilation. bIOP, DA, IIR, and SP-A1 changed significantly after the mydriasis test in Groups D and I while remaining stable in Group S. DARatio2mm and CBI also changed significantly in all three groups after dilation. Further, the corresponding changes in CCT were significant in Groups D and S, while SSI only varied significantly in Group D.

In both pre and post dilation stages, all metrics except SSI were statistically different in male and female populations (all $p < 0.05$), but the differences in most metrics became non-significant ($p > 0.05$) after correction for CCT and bIOP. Changes in all DCR parameters were correlated with ΔbIOP ($p < 0.01$); only ΔDARatio2mm, ΔIIR and ΔCBI exhibited a correlation with ΔCCT (**Table 3**; **Figure 2**). ΔbIOP was most closely correlated with ΔDA and ΔSP-A1 (r = −0.857 and 0.856, respectively), and least correlated with ΔSSI (r = 0.414).

In addition, multiple linear regression analyses were conducted (see **Table 4**). Correlation between ΔbIOP and the six DCR parameters was analyzed based on a second-order polynomial regression. ΔDA and ΔSP-A1 were highly correlated with ΔbIOP (R^2 = 0.677 and 0.737, respectively), while there was minimal correlation between ΔbIOP and each of ΔCBI and ΔSSI (R^2 = 0.173 and 0.033, respectively). Results of the analysis indicated that a 1-mmHg change in bIOP was associated with -0.037, −0.056, −0.198, and 5.612 units of change in DA, DARatio2mm, IIR, and SP-A1, respectively.

DISCUSSION

Corneal biomechanics is a subject of tremendous clinical research interest in modern ophthalmology. Knowledge of corneal

TABLE 2 | CVS metrics collected before and after the mydriasis test in three groups.

Metrics	Groups	Pre-dilation	Post-dilation	Difference	*p*
bIOP, mmHg	Group D	16.7 ± 2.6	14.9 ± 2.2	−1.8 ± 0.8	<0.001
	Group I	14.6 ± 1.4	16.6 ± 2.1	2.0 ± 1.5	<0.001
	Group S	15.3 ± 2.0	15.2 ± 2.0	−0.1 ± 0.5	0.169
	p	<0.001	0.001	<0.001	-
CCT, μm	Group D	554.4 ± 35.9	556.0 ± 35.7	1.7 ± 5.6	0.046
	Group I	553.9 ± 32.1	554.9 ± 31.7	1.0 ± 4.7	0.247
	Group S	547.2 ± 33.4	549.5 ± 33.2	2.2 ± 5.2	<0.001
	p	0.327	0.414	0.412	-
DA, mm	Group D	0.99 ± 0.10	1.06 ± 0.10	0.07 ± 0.03	<0.001
	Group I	1.07 ± 0.10	0.99 ± 0.09	−0.08 ± 0.06	<0.001
	Group S	1.05 ± 0.10	1.04 ± 0.10	−0.01 ± 0.04	0.069
	p	<0.001	0.004	<0.001	-
DARatio2mm	Group D	4.18 ± 0.35	4.27 ± 0.35	0.10 ± 0.19	0.001
	Group I	4.25 ± 0.41	4.13 ± 0.45	−0.12 ± 0.15	<0.001
	Group S	4.31 ± 0.41	4.25 ± 0.39	−0.06 ± 0.23	0.002
	p	0.134	0.223	<0.001	-
IIR, mm^{-1}	Group D	8.69 ± 0.93	8.96 ± 0.86	0.27 ± 0.33	<0.001
	Group I	8.84 ± 1.09	8.38 ± 1.12	−0.46 ± 0.87	0.005
	Group S	8.90 ± 0.97	8.85 ± 0.97	−0.05 ± 0.51	0.267
	p	0.445	0.022	<0.001	-
SP-A1, mmHg/mm	Group D	115.02 ± 17.86	104.13 ± 17.45	−10.89 ± 4.64	<0.001
	Group I	102.97 ± 16.89	116.04 ± 18.08	13.06 ± 7.20	<0.001
	Group S	104.80 ± 16.51	104.39 ± 17.12	−0.41 ± 5.72	0.382
	p	0.001	0.002	<0.001	
CBI	Group D	0.28 ± 0.21	0.31 ± 0.24	0.03 ± 0.09	0.032
	Group I	0.35 ± 0.25	0.29 ± 0.23	−0.06 ± 0.07	<0.01
	Group S	0.32 ± 0.23	0.30 ± 0.23	−0.02 ± 0.08	0.002
	p	0.409	0.944	<0.001	-
SSI	Group D	0.92 ± 0.13	0.87 ± 0.14	−0.05 ± 0.05	<0.01
	Group I	0.93 ± 0.14	0.94 ± 0.16	0.02 ± 0.10	0.306
	Group S	0.89 ± 0.11	0.90 ± 0.11	0.00 ± 0.06	0.420
	p	0.262	0.038	<0.001	-

bIOP, biomechanically corrected IOP; CCT, central corneal thickness; DA, deformation amplitude; DARatio2mm, the ratio between DA values at the apex and 2 mm from apex; IIR, integrated inverse radius; SP-A1, the stiffness parameter at first applanation; CBI, corvis biomechanical index; SSI, stress-strain index.

biomechanics is useful in several clinical applications, including management of glaucoma and ectasia risk profiling (Esporcatte et al., 2020; Zimprich et al., 2020). The integration of tomographic and biomechanical data has demonstrated potential to improve the accuracy of detection of ectatic disease and identify susceptibility to develop this complication after laser vision correction (Ambrósio et al., 2017). Despite substantial developments over the last 2 decades, *in vivo* characterization of dynamic corneal biomechanical response remains influenced by IOP, as observed by Bao et al. (2015) and Roberts (2014). This new study uses the IOP changes observed after pupil dilation to assess the effects of these changes on the corneal biomechanical metrics provided by the Corvis ST.

Previous studies showed that most corneal biomechanical metrics provided by ORA and Corvis ST were related to IOP and CCT (Roberts, 2014; Bao et al., 2015). In the present study, it was observed that DA, DARatio2mm, IIR, and SP-A1 may be correlated with the overall stiffness of the cornea, which is dependent on CCT but also directly influenced by IOP. Meanwhile, we have confirmed that these DCR parameters are influenced by the biomechanically corrected IOP to different extents. Our results showed that a 1-mmHg change in bIOP can induce −0.037, −0.056, −0.198, and 5.612 units of change in DA, DARatio2mm, IIR, and SP-A1, respectively, and that the correlation between each of these metrics and bIOP was significant. Likewise, SSI, which was designed to represent the tissue's material stiffness and was intended to be independent of IOP (Eliasy et al., 2019), was also dependent on IOP, although to a lesser extent than other parameters.

Previous reports of these relationship were mixed, the DA was correlated with CCT and IOP (Hon and Lam, 2013; Ali et al., 2014; Huseynova et al., 2014), the DARatio2mm had high correlation with CCT and IOP (Vinciguerra et al., 2016), and the IIR correlated with CCT (Vinciguerra et al., 2016) while not with IOP. In other studies, DA, DARatio2mm, IIR, and SP-A1 were all correlated with CCT and IOP (Sedaghat et al., 2020), CBI was correlated with IOP and CCT (Yang et al., 2019), and SSI was correlated with IOP but not with CCT (Liu et al., 2020). The studies noted above were cross-sectional, and the variation range in both subjects and biometric parameters was large, which may have influenced the correlation results. In our longitudinal study, the changes in corneal biomechanical metrics caused, in the same patient, by dilation were used to evaluate the relationships between the DCR parameters and both CCT and IOP. The study was designed as self-matched (between a short period

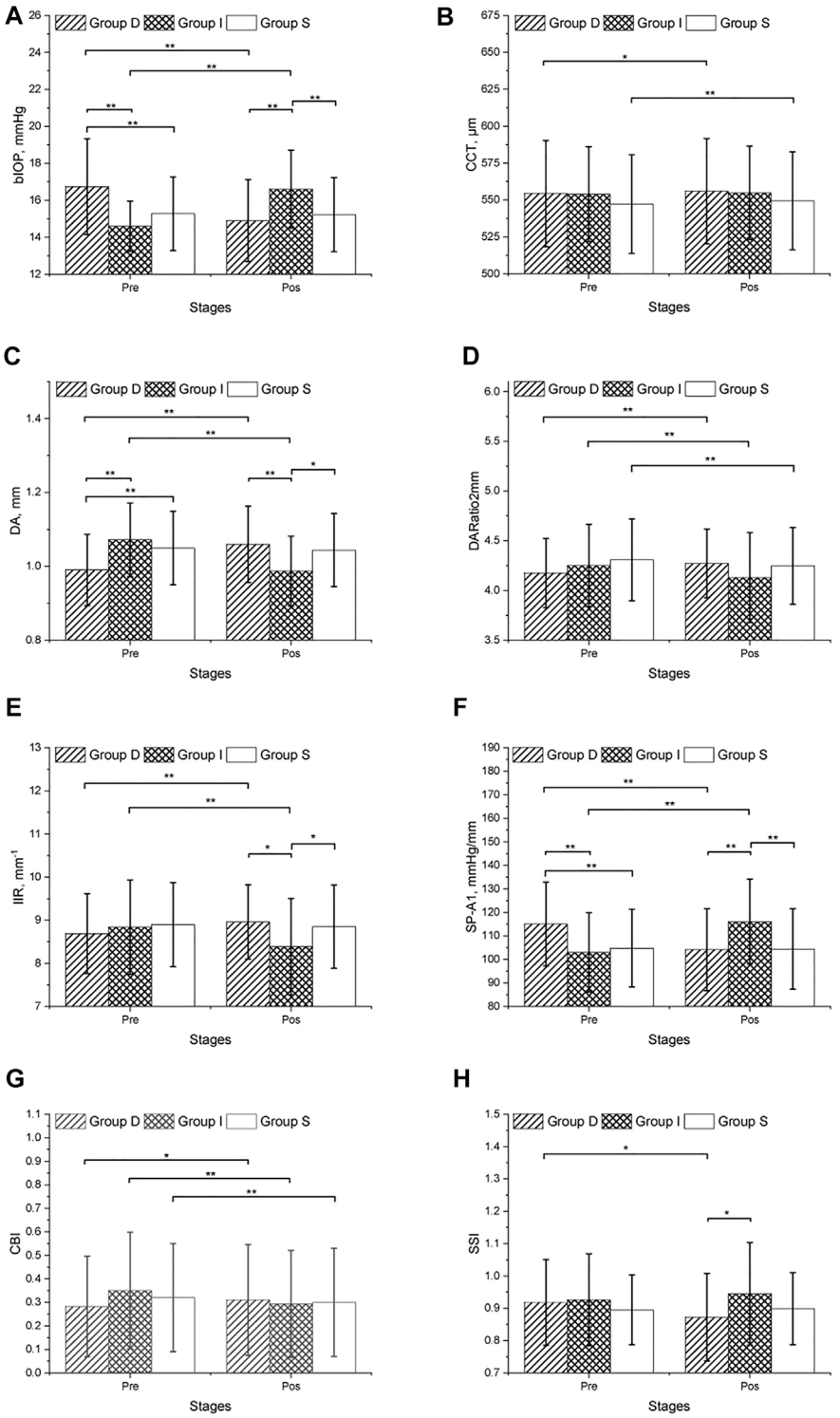

FIGURE 1 | CVS metrics collected before and after the mydriasis test in three groups.

before and after dilation) to exclude the effects of potential confounding factors such as race, gender, age, CCT and IOP.

Recently, SP-A1, was introduced as a clinical metric with strong association with corneal stiffness. Considerable discussion has ensued in the literature around this novel parameter and its application in the diagnosis of corneal diseases like keratoconus (Yang et al., 2019). In this study, a strong positive correlation ($r = 0.856$, $p < 0.001$) was observed between the changes in SP-A1 and

TABLE 3 | Correlation between differences in DCR parameters recorded before and after the mydriasis test and the corresponding differences in bIOP and CCT.

Dependent variables	ΔbIOP, mmHg		ΔCCT, μm	
	r	*p*	*r*	*p*
ΔDA, mm	−0.857	<0.001	−0.080	0.226
ΔDARatio2mm	−0.524	<0.001	−0.154	0.019
ΔIIR, mm^{-1}	−0.479	<0.001	−0.192	0.003
SP-A1, mmHg/mm	0.856	<0.001	0.119	0.070
ΔCBI	−0.423	<0.001	−0.288	<0.001
ΔSSI	0.414	<0.001	0.087	0.186

Δ, the difference before and after mydriasis; bIOP, biomechanically corrected IOP; CCT, central corneal thickness; DA, deformation amplitude; DARatio2mm, the ratio between DA values at the apex and 2 mm from apex; IIR, integrated inverse radius; SP-A1, the stiffness parameter at first applanation; CBI, Corvis biomechanical index; SSI, stress-strain index; Pre, undilated pupil; Pos, after mydriasis test; Sw, within-subject standard deviation; CoV, coefficient of variation (%); ICC, intraclass correlation coefficient.

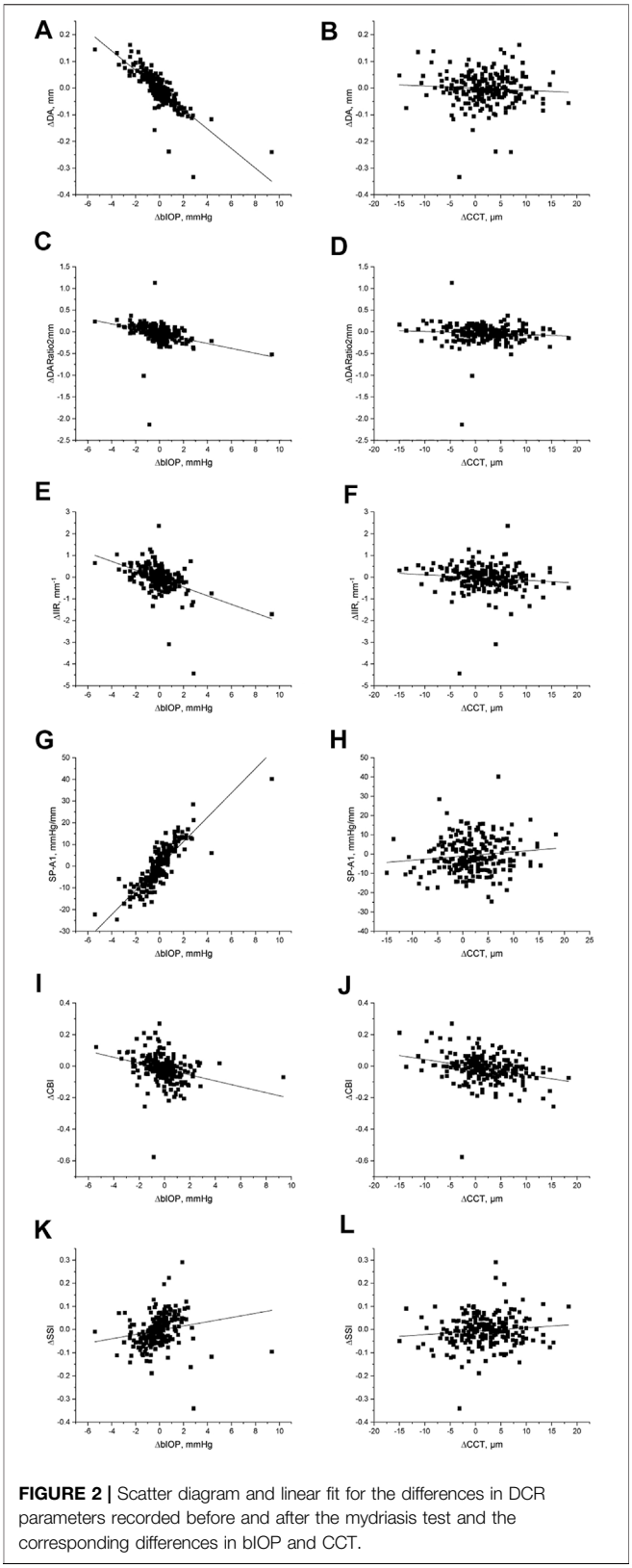

FIGURE 2 | Scatter diagram and linear fit for the differences in DCR parameters recorded before and after the mydriasis test and the corresponding differences in bIOP and CCT.

those in bIOP associated with dilation, suggesting that an increase in IOP would induce higher corneal stiffness. This finding has important clinical applications, for instance in detecting subclinical keratoconus in those due to undergo refractive surgeries. The difference in the Stiffness Parameter, SP-A1, between subclinical keratoconus and healthy eyes is within 15–20 (Koc et al., 2019; Ren et al., 2021), a gap which can be covered by an IOP change of 3–4 mmHg. Therefore, a higher bIOP may influence the effectiveness of SP-A1 in detecting keratoconus.

Although our results showed that all six dynamic corneal response parameters were dependent on bIOP. This is compatible with research done by Herber et al., who found that CBI were minimally influenced by bIOP (Herber et al., 2019). And contradicted with earlier statement in which SSI was reported to be independent on IOP (Eliasy et al., 2019). The limited correlation between CBI and SSI on one hand, and bIOP on the other, suggests the potential of these novel parameters for use in clinical practice.

Some studies have shown that IOP fluctuates during the 24-h cycle. Chun et al. confirmed that while IOP fluctuations can vary, phasing over a 24-h period is relatively consistent (Zhu et al., 2020), and others have reported that IOP fluctuation was between 3 and 5 mmHg in healthy subjects (Luebke et al., 2019). The dependence of DCR parameters on IOP can then lead to changes in these metrics with the IOP diurnal fluctuation affecting their ability to detect corneal diseases such as keratoconus. Precautions were therefore taken to limit the possible influence of IOP diurnal fluctuations in this study, including ensuring that all exams were performed within a 2-h time period. The strong repeatability of the readings and the relatively low CoV for CCT suggested the limited impact of diurnal fluctuations both before and after mydriasis.

The components of Mydrin-P (tropicamide and phenylephrine hydrochloride) have been shown to cause increases in CCT although the underlying mechanism is unclear (Gao et al., 2006; Zeng and Gao, 2017). On the other hand, changes in IOP with pupil dilation may come from different sources. First, Phenylephrine can cause an increase in arterial blood pressure (Stavert et al., 2015), possibly leading to a similar effect in IOP. Second, pupil dilation may induce pigment liberation and the subsequent obstruction of the trabecular meshwork, which may hinder aqueous outflow and increase IOP (Kristensen, 1965). In contrast, uveoscleral outflow facilitation and inflow decrease can also occur after dilation,

TABLE 4 | Multiple linear regression analysis results between of correlation between ΔbIOP, ΔCCT, and six DCR parameters.

Dependent variables	Parameters	B	*p* value	Regression equation	Adjusted R^2	F[b]	*p* value
ΔDA	ΔbIOP	−0.824	<0.001	ΔDA (mm) = −0.037 × ΔbIOP (mmHg) − 0.002 (mm)	0.677	487.409	0.000
ΔDARatio2mm	ΔbIOP	−0.344	<0.001	Δ DA Ratio 2 mm (mm) = −0.056 × ΔbIOP (mmHg) − 0.043 (mm)	0.114	30.919	0.000
ΔIIR	ΔbIOP	−0.462	<0.001	Δ IIR (mm) = −0.198 × ΔbIOP (mmHg) − 0.013 × ΔCCT − 0.040 (mm)	0.220	33.738	0.000
	ΔCCT	−0.115	0.049				
ΔSP-A1	ΔbIOP	0.850	<0.001	Δ SP-A1 (mmHg) = 5.612 × ΔbIOP (mmHg) + 0.126 × ΔCCT −0.341 (mmHg)	0.737	326.045	0.000
	ΔCCT	0.125	<0.001				
ΔCBI	ΔbIOP	−0.298	<0.001	Δ CBI (mmHg) = −0.019 × ΔbIOP (mmHg) − 0.005 × ΔCCT − 0.009 (mmHg)	0.173	25.225	0.000
	ΔCCT	−0.302	<0.001				
ΔSSI	ΔbIOP	0.192	0.003	Δ SSI (mmHg) = 0.009 × ΔbIOP − 0.003 (mmHg)	0.033	8.838	0.003

leading to a decrease in IOP (Valle, 1974; Tan et al., 2009). These conflicting factors can therefore cause an increase or a decrease in IOP as has been observed in our study.

One limitation of the study is the potential, unquantified pharmacologic effect of mydriasis on corneal microstructure and consequently corneal biomechanical properties. However, the small change in CCT after mydriasis (1.95 ± 5.23 μm) indicated that the possible effect of mydriasis may have been limited, and further study is required to consider the role of patient-specific factors in these relationships.

In conclusion, most corneal DCR parameters have been shown to be strongly related to IOP. This study focused on the correlation of biomechanical parameters and IOP and analyzed the repeatability of CVS measurement. The data collected confirmed our group's previous conclusions, that comparing research groups based on Corvis ST with different IOPs and CCTs may lead to possible misinterpretations if both or one of which are not considered in the analysis; the results also validate the stability of several new corneal parameters. Importantly, most parameters provided by Corvis ST, including some stiffness parameters, are influenced by IOP.

DATA AVAILABILITY STATEMENT

The original contributions presented in the study are included in the article/Supplementary Material, further inquiries can be directed to the corresponding authors.

ETHICS STATEMENT

The studies involving human participants were reviewed and approved by the Ethics Committee of the Eye Hospital, Wenzhou Medical University, China. The patients/participants provided their written informed consent to participate in this study.

AUTHOR CONTRIBUTIONS

YY and YL conducted the research. YY, YL, SC, FB, and AE interpreted data and drafted the article. ZZ, AAS, KNM, SA, CH, BL, AE, YM, JW, and XZ performed interpretation of data, collected clinical data and performed statistical analysis. SC, FB, and AE developed the concept, design the project and supervised the entire research and secured funding. All authors reviewed the article and provided final approval.

FUNDING

This study was supported by the National Natural Science Foundation of China (31771020, 82001924), Zhejiang Provincial Natural Science Foundation of China under Grant (LY20H120001, LQ20A020008), the Projects of Medical and Health Technology Development Program in Zhejiang Province (2019RC056, 2018KY541, 2016ZHB012), Science and Technology Plan Project of Wenzhou Science and Technology Bureau (Y2020354, Y20180172, Y20170198, Y20170792), and the General Projects of Department of Education of Zhejiang Province (Y201839651).

ACKNOWLEDGMENTS

The authors thank Wei Chen of Eye Hospital, WenZhou Medical University for Corvis ST measurements provided for this study.

REFERENCES

Ali, N. Q., Patel, D. V., and McGhee, C. N. J. (2014). Biomechanical Responses of Healthy and Keratoconic Corneas Measured Using a Noncontact Scheimpflug-Based Tonometer. *Invest. Ophthalmol. Vis. Sci.* 55, 3651–3659. doi:10.1167/iovs.13-13715

Ambrósio, R., Jr., Lopes, B. T., Faria-Correia, F., Salomão, M. Q., Bühren, J., Roberts, C. J., et al. (2017). Integration of Scheimpflug-Based Corneal Tomography and Biomechanical Assessments for Enhancing Ectasia Detection. *J. Refract Surg.* 33, 434–443. doi:10.3928/1081597x-20170426-02

Bao, F., Deng, M., Wang, Q., Huang, J., Yang, J., Whitford, C., et al. (2015). Evaluation of the Relationship of Corneal Biomechanical Metrics with Physical

Intraocular Pressure and central Corneal Thickness in *Ex Vivo* Rabbit Eye Globes. *Exp. Eye Res.* 137, 11–17. doi:10.1016/j.exer.2015.05.018

Eliasy, A., Chen, K.-J., Vinciguerra, R., Lopes, B. T., Abass, A., Vinciguerra, P., et al. (2019). Determination of Corneal Biomechanical Behavior *In-Vivo* for Healthy Eyes Using CorVis ST Tonometry: Stress-Strain Index. *Front. Bioeng. Biotechnol.* 7, 105. doi:10.3389/fbioe.2019.00105

Esporcatte, L. P. G., Salomão, M. Q., Lopes, B. T., Vinciguerra, P., Vinciguerra, R., Roberts, C., et al. (2020). Biomechanical Diagnostics of the Cornea. *Eye Vis.* 7, 9. doi:10.1186/s40662-020-0174-x

Gao, L., Fan, H., Cheng, A. C. K., Wang, Z., and Lam, D. S. C. (2006). The Effects of Eye Drops on Corneal Thickness in Adult Myopia. *Cornea* 25, 404–407. doi:10.1097/01.ico.0000214205.29823.f6

Herber, R., Ramm, L., Spoerl, E., Raiskup, F., Pillunat, L. E., and Terai, N. (2019). Assessment of Corneal Biomechanical Parameters in Healthy and Keratoconic Eyes Using Dynamic Bidirectional Applanation Device and Dynamic Scheimpflug Analyzer. *J. Cataract Refract Surg.* 45, 778–788. doi:10.1016/j.jcrs.2018.12.015

Hon, Y., and Lam, A. K. (2013). Corneal Deformation Measurement Using Scheimpflug Noncontact Tonometry. *Optom. Vis. Sci.* 90, E1–E8. doi:10.1097/OPX.0b013e318279eb87

Huseynova, T., Waring, G. O., Roberts, C., Krueger, R. R., and Tomita, M. (2014). Corneal Biomechanics as a Function of Intraocular Pressure and Pachymetry by Dynamic Infrared Signal and Scheimpflug Imaging Analysis in normal Eyes. *Am. J. Ophthalmol.* 157, 885–00813. doi:10.1016/j.ajo.2013.12.024

Koc, M., Aydemir, E., Tekin, K., Inanc, M., Kosekahya, P., and Kiziltoprak, H. (2019). Biomechanical Analysis of Subclinical Keratoconus with Normal Topographic, Topometric, and Tomographic Findings. *J. Refract Surg.* 35, 247–252. doi:10.3928/1081597x-20190226-01

Kristensen, P. (1965). Mydriasis-induced Pigment Liberation in the Anterior Chamber Associated with Acute Rise in Intraocular Pressure in Open-Angle Glaucoma. *Acta Ophthalmol. (Copenh)* 43, 714–724. doi:10.1111/j.1755-3768.1965.tb00343.x

Liu, G., Rong, H., Pei, R., Du, B., Jin, N., Wang, D., et al. (2020). Age Distribution and Associated Factors of Cornea Biomechanical Parameter Stress-Strain index in Chinese Healthy Population. *BMC Ophthalmol.* 20, 436. doi:10.1186/s12886-020-01704-6

Luebke, J., Bryniok, L., Neuburger, M., Jordan, J. F., Boehringer, D., Reinhard, T., et al. (2019). Intraocular Pressure Measurement with Corvis ST in Comparison with Applanation Tonometry and Tomey Non-contact Tonometry. *Int. Ophthalmol.* 39, 2517–2521. doi:10.1007/s10792-019-01098-5

Meek, K. M., and Knupp, C. (2015). Corneal Structure and Transparency. *Prog. Retin. Eye Res.* 49, 1–16. doi:10.1016/j.preteyeres.2015.07.001

Qian, C. X.-y., Duperré, J., Hassanaly, S., and Harissi-Dagher, M. (2012). Pre- versus post-dilation Changes in Intraocular Pressure: Their Clinical Significance. *Can. J. Ophthalmol.* 47, 448–452. doi:10.1016/j.jcjo.2012.07.005

Rabinowitz, Y. S. (1998). Keratoconus. *Surv. Ophthalmol.* 42, 297–319. doi:10.1016/s0039-6257(97)00119-7

Reinstein, D. Z., Archer, T. J., and Randleman, J. B. (2013). Mathematical Model to Compare the Relative Tensile Strength of the Cornea after PRK, LASIK, and Small Incision Lenticule Extraction. *J. Refract Surg.* 29, 454–460. doi:10.3928/1081597x-20130617-03

Ren, S., Xu, L., Fan, Q., Gu, Y., and Yang, K. (2021). Accuracy of New Corvis ST Parameters for Detecting Subclinical and Clinical Keratoconus Eyes in a Chinese Population. *Sci. Rep.* 11, 4962. doi:10.1038/s41598-021-84370-y

Roberts, C. J. (2014). Concepts and Misconceptions in Corneal Biomechanics. *J. Cataract Refract Surg.* 40, 862–869. doi:10.1016/j.jcrs.2014.04.019

Roberts, C. J., Mahmoud, A. M., Bons, J. P., Hossain, A., Elsheikh, A., Vinciguerra, R., et al. (2017). Introduction of Two Novel Stiffness Parameters and Interpretation of Air Puff-Induced Biomechanical Deformation Parameters with a Dynamic Scheimpflug Analyzer. *J. Refract Surg.* 33, 266–273. doi:10.3928/1081597x-20161221-03

Sedaghat, M. R., Momeni-Moghaddam, H., Azimi, A., Fakhimi, Z., Ziaei, M., Danesh, Z., et al. (2020). Corneal Biomechanical Properties in Varying Severities of Myopia. *Front. Bioeng. Biotechnol.* 8, 595330. doi:10.3389/fbioe.2020.595330

Stavert, B., McGuinness, M. B., Harper, C. A., Guymer, R. H., and Finger, R. P. (2015). Cardiovascular Adverse Effects of Phenylephrine Eyedrops. *JAMA Ophthalmol.* 133, 647–652. doi:10.1001/jamaophthalmol.2015.0325

Tan, G. S., Wong, C.-Y., Wong, T. Y., Govindasamy, C. V., Wong, E. Y., Yeo, I. Y., et al. (2009). Is Routine Pupil Dilation Safe Among Asian Patients with Diabetes? *Invest. Ophthalmol. Vis. Sci.* 50, 4110–4113. doi:10.1167/iovs.08-2745

Valle, O. (1974). Effect of Cyclopentolate on the Aqueous Dynamics in Incipient or Suspected Open-Angle Glaucoma. *Acta Ophthalmol. Suppl.* 123, 52–60.

Vinciguerra, R., Elsheikh, A., Roberts, C. J., Ambrósio, R., Kang, D. S. Y., Lopes, B. T., et al. (2016). Influence of Pachymetry and Intraocular Pressure on Dynamic Corneal Response Parameters in Healthy Patients. *J. Refract Surg.* 32, 550–561. doi:10.3928/1081597x-20160524-01

Yang, K., Xu, L., Fan, Q., Zhao*, D., and Ren*, S. (2019). Repeatability and Comparison of New Corvis ST Parameters in normal and Keratoconus Eyes. *Sci. Rep.* 9, 15379. doi:10.1038/s41598-019-51502-4

Zeng, Y., and Gao, J. h. (2017). Effects of Mydrin Eye-drops on central Corneal Thickness Values in Adult Patients with Myopia. *Clin. Exp. Optom.* 100, 151–154. doi:10.1111/cxo.12465

Zhu, R., Zheng, X., Guo, L., Zhao, Y., Wang, Y., Wu, J., et al. (2020). Biomechanical Effects of Two Forms of PGF2α on *Ex-Vivo* Rabbit Cornea. *Curr. Eye Res.*, 1–9. doi:10.1080/02713683.2020.1805771

Zimprich, L., Diedrich, J., Bleeker, A., and Schweitzer, J. A. (2020). Corneal Hysteresis as a Biomarker of Glaucoma: Current Insights. *Opth* Vol. 14, 2255–2264. doi:10.2147/opth.s236114

Conflict of Interest: AE is a consultant to Oculus Optikgeräte GmbH.

The remaining authors declare that the research was conducted in the absence of any commercial or financial relationships that could be construed as a potential conflict of interest.

Publisher's Note: All claims expressed in this article are solely those of the authors and do not necessarily represent those of their affiliated organizations, or those of the publisher, the editors and the reviewers. Any product that may be evaluated in this article, or claim that may be made by its manufacturer, is not guaranteed or endorsed by the publisher.

frontiers in Bioengineering and Biotechnology

ORIGINAL RESEARCH
published: 02 December 2021
doi: 10.3389/fbioe.2021.777239

The Effect of Axial Length Elongation on Corneal Biomechanical Property

Guihua Liu[1†], Hua Rong[1†], Ping Zhang[1], Yu Xue[2,3], Bei Du[1], Biying Wang[1], Jiamei Hu[1], Zhi Chen[2,3] and Ruihua Wei[1]**

[1]Tianjin Key Laboratory of Retinal Functions and Diseases, Tianjin Branch of National Clinical Research Center for Ocular Disease, Eye Institute and School of Optometry, Tianjin Medical University Eye Hospital, Tianjin, China, [2]NHC Key Laboratory of Myopia, Eye Institute and Department of Ophthalmology, Eye and ENT Hospital, Fudan University, Shanghai, China, [3]Key Laboratory of Myopia, Shanghai Research Center of Ophthalmology and Optometry, Chinese Academy of Medical Sciences, Shanghai, China

Background: To investigate the correlation between the corneal biomechanical parameter stress-strain index (SSI) and axial length (AL) in moderately elongated eye (MEE) and severely elongated eye (SEE).

Methods: This study included 117 eyes from 117 participants. Among them, 59 (50.4%) had MEE (AL<26 mm) and 58 (49.6%) had SEE (AL≥26 mm). AL was measured using Lenstar LS-900, and central corneal thickness (CCT) and anterior chamber volume (ACV) were measured using Pentacam. SSI was measured *via* corneal visualisation Scheimpflug technology (Corvis ST). Kolmogorov-Smirnov test, Student's *t*-test, and Pearson and partial correlation analyses were used for statistical analyses.

Results: The mean (±SD) SSI was 1.08 ± 0.15 in the MEE group and 0.92 ± 0.13 in the SEE group ($p < 0.01$). SSI was positively correlated with age (MEE: $r = 0.326$, $p < 0.05$; SEE: $r = 0.298$, $p < 0.05$) in both groups; it was negatively correlated with AL ($r = -0.476$, $p < 0.001$) in the MEE group but not in the SEE group ($p > 0.05$). CCT was negatively correlated with AL ($r = -0.289$, $p < 0.05$) and ACV positively correlated with AL ($r = 0.444$, $p < 0.001$) in the MEE group. Neither CCT nor ACV was correlated with AL ($p > 0.05$) in the SEE group.

Conclusion: Corneal biomechanical parameter SSI, which represents the stiffness of corneal tissue, was lower in the SEE group than in the MEE group. When analyzed separately, SSI was negatively correlated with AL in the MEE group, but not in the SEE group, which may provide insight into different ocular growth patterns between lower myopia and higher myopia.

Keywords: CorVis ST, corneal biomechanics, anterior segment, axial length, myopia

OPEN ACCESS

Edited by:
FangJun Bao, Affiliated Eye Hospital of Wenzhou Medical College, China

Reviewed by:
Xiaofei Wang, Beihang University, China
Kai-Jung Chen, National Chin-Yi University of Technology, Taiwan

****Correspondence:***
Zhi Chen
peter459@aliyun.com
Ruihua Wei
rwei@tmu.edu.cn

[†]These authors have contributed equally to this work and share first authorship

Specialty section:
This article was submitted to Biomechanics, a section of the journal Frontiers in Bioengineering and Biotechnology

Received: *15 September 2021*
Accepted: *15 November 2021*
Published: *02 December 2021*

Citation:
Liu G, Rong H, Zhang P, Xue Y, Du B, Wang B, Hu J, Chen Z and Wei R (2021) The Effect of Axial Length Elongation on Corneal Biomechanical Property. Front. Bioeng. Biotechnol. 9:777239. doi: 10.3389/fbioe.2021.777239

BACKGROUND

Myopia is a common ocular disorder worldwide, and its incidence is increasing with an alarming rate. A total of 49.8% of the world population, i.e., approximately 4,758 million, will be affected by myopia by the year 2050 (Holden et al., 2016). High myopia, defined by a myopic refractive error worse than -5.00D or -6.00D (Flitcroft et al., 2019), is accompanied by a severely elongated eye along with other ocular component changes, which potentially leads to a higher chance of complications,

such as retinal detachment, glaucoma (Haarman et al., 2020), scleral thinning, and localized ectasia of the posterior sclera (Rada et al., 2006).

Axial elongation is an important indicator of the development of myopia and a major factor leading to visual impairment. Previous studies have shown that eyes with axial length (AL) of 26 mm or greater had significantly higher risk for visual impairment than eyes with AL shorter than 26 mm in Europeans under 60 years of age (Tideman et al., 2016). In severely elongated eyes, scleral thickness and rigidity are significantly reduced (Sergienko and Shargorogska, 2012; Jonas et al., 2019). Some researchers believe that the eyeball is an integral organ, and the anterior segment parameters, including corneal biomechanics, are related to those of the posterior sclera (Chansangpetch et al., 2017; Bataille et al., 2021). Previous studies found that high myopia can cause corneal biomechanical changes (Moshirfar et al., 2019). Some studies found a negative correlation between corneal biomechanics and AL (Long et al., 2019; Tubtimthong et al., 2020; Yu et al., 2020) and suggested that measuring corneal biomechanics can predict axial elongation (Haseltine et al., 2012; Zadnik et al., 2015; Long et al., 2019; Wu et al., 2019). In contrast, other studies suggested that corneal biomechanics is independent of the severity of refractive error (Lim et al., 2008; Inceoglu et al., 2018). Therefore, exploring the relationship between corneal biomechanical parameters and axial elongation, especially in different refractive groups, can help develop suitable clinical interventions for myopia.

Regarding corneal biomechanical measurement technology, the new parameter stress-strain index (SSI) provided by corneal visualization Scheimpflug technology (Corvis ST) can reflect corneal stiffness without being affected by central corneal thickness (CCT) or intraocular pressure (IOP) (Eliasy et al., 2019). One of our previous studies found that the SSI was negatively correlated with AL, but high myopia was not included for that study (Liu et al., 2020). However, the extent of myopia may influence corneal biomechanics (Yu et al., 2020). For example, at the outset, corneal stiffness are weakened as the eye elongates in physiological processes (Khokhar et al., 2018; Han et al., 2020; Liu et al., 2020). When the elongation enters the pathological stage, corneal stiffness may tend to stabilize (Larsen, 1971; Khokhar et al., 2018).

In the current study, we first expanded the AL range of the study participants and divided them into the moderately elongated eye (MEE) and severely elongated eye (SEE) groups according to their AL (<26 mm and ≥26 mm, respectively). Corneal stiffness parameter SSI and its influencing factors were then compared between the two groups. The purpose of this study was to investigate the relationship between AL and corneal stiffness and to provide an explanation for the controversies raised in previous studies.

METHODS

Subjects

This prospective study included 117 participants who were consecutively recruited from May to October 2020 at Tianjin Medical University Eye Hospital. Only participants without ocular diseases such as corneal pathology, refractive surgery history, keratoconus, allergic eye disease, uveitis, glaucoma, history of intraocular surgery, or any significant systemic illness were included. Written informed consent was obtained from all enrolled participants or their parents or guardians if the participants were under 16 years old. All study procedures adhered to the tenets of the Declaration of Helsinki and were approved by the ethics committee of Tianjin Medical University Eye Hospital.

The subjects were divided into two groups based on their ALs, with AL greater than or equal to 26 mm defined as SEE, and AL less than 26 mm defined as MEE. All subjects underwent a complete ophthalmic examination, including slit-lamp ophthalmic examination, visual acuity measurement, subjective refraction, fundus examination, and IOP measurement.

AL Measurement

AL was measured using a non-contact biometer (Lenstar LS-900; Haag-Streit AG, Berne, Switzerland). During the examination, the subjects were instructed to keep both eyes open and fixate on the target. The subjects were allowed to blink their eyes between the measurements to ensure an intact tear film and to avoid potential measurement errors. The results for data analysis were obtained by averaging three repeated measurements in which intrasession differences were no greater than 0.02 mm.

CCT and Anterior Chamber Volume (ACV)

Pentacam (Oculus, Wetzlar, Germany) was used to measure CCT, corneal curvature, and ACV. All measurements were performed in a dark room. Before examination, the participants blinked their eyes briskly several times and were then asked to fixate on the target and keep their eyes wide open for the scan. Only measurements with an "OK" quality index were saved.

Corneal Biomechanical Parameters

Corneal biomechanical parameters were measured using Corvis ST (Oculus, Wetzlar, Germany). It is a dynamic and non-contact tonometer equipped with an optical pachymetry function that allows imaging in response to an air puff. The cornea was recorded at 4,330 images per second by using a built-in high-speed camera. The SSI was also recorded using this device. The SSI is a new parameter, which was established to eliminate the interference of IOP and corneal geometry and to estimate the stiffness of a material that differs from the stiffness parameter (SP). The SSI algorithm was based on the prediction of corneal behavior by using finite element numerical modeling simulation of the influence of IOP and Corvis ST air puff on corneal behavior. All measurements were performed by certified technicians. Only measurements with an "OK" quality index were included in the analysis.

Statistical Analysis

Data were summarized into Microsoft Excel sheets, and statistical analyses were performed using SPSS statistical package 25 (SPSS, IBM, Chicago, IL, United States). The differences in ocular

TABLE 1 | Kolmogorov-Smirnov test of parameters.

	MEE		SEE		All patients	
	K-S Z	*p*	K-S Z	*p*	K-S Z	*p*
SSI	0.83	>0.2[a]	0.115	0.056[a]	0.057	>0.2[a]
Age, years	0.79	>0.2[a]	0.107	0.097[a]	0.067	>0.2[a]
AL, mm	0.83	>0.2[a]	0.116	0.051[a]	0.067	>0.2[a]
CCT, μm	0.62	>0.2[a]	0.084	>0.2[a]	0.550	>0.2[a]
ACV, mm^3	0.72	>0.2[a]	0.095	>0.2[a]	0.070	>0.2[a]

[a]*Normal distribution. SSI, Stress-Strain index; AL, Axial length; CCT, Central corneal thickness; ACV, Anterior chamber volume; K-S Z, Kolmogorov-Smirnov Z value; MEE, moderately elongated eye; SEE, severely elongated eye.*

TABLE 2 | Paired *t*-test comparison of left eye and right eye.

	OD		OS		*p* value
	Mean	SD	Mean	SD	
SSI	0.99	0.19	1.00	0.16	0.405
AL, mm	26.06	2.34	26.09	2.35	0.225
CCT, μm	537.22	32.60	536.92	31.46	0.586
ACV, mm^3	197.32	34.16	197.66	34.32	0.642

SSI, Stress-Strain index; AL, Axial length; CCT, Central corneal thickness; ACV, Anterior chamber volume; SD, Standard deviation.

TABLE 3 | Comparison of parameters between two groups.

	MEE		SEE		*p* value
	Mean	SD	Mean	SD	
SSI	1.08	0.15	0.92	0.13	<0.001[a]
Age, years	24.88	9.77	24.47	8.06	0.802
AL, mm	24.14	1.15	28.07	1.42	<0.001[a]
CCT, μm	539.49	28.76	534.31	34.03	0.375
ACV, mm^3	182.97	34.91	212.60	26.59	<0.001[a]

[a]*Statistically significant. SSI, Stress-Strain index; AL, Axial length; CCT, Central corneal thickness; ACV, Anterior chamber volume; SD, Standard deviation; MEE, moderately elongated eye; SEE, severely elongated eye.*

parameters were determined using a paired *t*-test. The Kolmogorov-Smirnov test was used to assess the normal distribution of data. Student's *t*-test was used to compare the corneal parameters between the two groups. Pearson correlation analysis was used to test the correlation between the SSI and age, while the partial correlation coefficient adjusted for age was used to analyze the correlation between the SSI, CCT, ACV, and AL. A *p* value less than 0.05 was considered statistically significant.

RESULTS

In total, 117 left eyes of 117 patients who met the study inclusion criteria were analyzed. Among them, 59 (50.4%) were included in the MEE group and 58 (49.6%) in the SEE group. The SSI and age showed a normal distribution ($p > 0.05$) in both groups. The normal distribution of each parameter was summarized in **Table 1**. The comparison of the parameters of the left and right eyes was summarized in **Table 2**. Because the SSI showed no significant difference between the contralateral eyes ($p > 0.05$), only the left eyes were included in the subsequent analysis.

The mean age of the subjects was 24.7 ± 8.9 years old and not different between the MEE and SEE groups ($p = 0.802$). The overall AL was 26.09 ± 2.35 mm, being significantly longer in the SEE group (28.07 ± 1.42 mm) than in the MEE group (24.14 ± 1.15 mm) ($p < 0.001$). The overall SSI was 1.00 ± 0.16, being significantly lower in the SEE group (0.92 ± 0.13) than in the MEE group (1.08 ± 0.15) ($p < 0.001$). Data were presented in **Table 3**.

SSI was positively correlated with age in both groups [MEE: $r = 0.326$, $p < 0.05$ (**Figure 1A**); SEE: $r = 0.298$, $p < 0.05$ (**Figure 1B**)].

Age was used as a control variable in the following analyses. SSI was negatively correlated with AL in the MEE group ($r = -0.476$, $p < 0.001$) (**Figure 2A**) but not in the SEE group ($r = 0.033$, $p = 0.809$) (**Figure 2B**).

In the MEE group, CCT was negatively correlated with AL ($r = -0.289$, $p < 0.05$) (**Figure 3A**) and ACV positively correlated with AL ($r = 0.444$, $p < 0.001$) (**Figure 3C**). In the SEE group, neither CCT (**Figure 3B**) nor ACV (**Figure 3D**) was correlated with AL ($p > 0.05$). Partial correlation coefficients adjusted for age between the clinical characteristics of the two groups were summarized in **Table 4**.

DISCUSSION

In this study, we investigated the relationship between the corneal stiffness parameter SSI and AL in a Chinese population. Overall we found that the eyes with longer AL had lower SSI. In the MEE group, AL was negatively correlated to the SSI. While in the SEE group, SSI was no longer correlated to AL.

Age is an important factor that affects corneal biomechanics (Blackburn et al., 2019). Previous studies have shown that CH, CRF, and deformation amplitude at highest concavity are related to age (Elsheikh et al., 2008a; Wang et al., 2017; Momeni-Moghaddam et al., 2019). In addition, the stiffness of the cornea increases with age (Elsheikh et al., 2010). Compared to CH (an indicator of the viscous properties of the cornea) and CRF (an indicator of the overall resistance or elastic properties of the cornea) (Nongpiur et al., 2015), SSI in this study reflects corneal stiffness (Eliasy et al., 2019). To verify the reliability of this conclusion, we analyzed the relationship between the SSI and age. Our results showed that although the SSI was more significantly reduced in the SEE group than in the MEE group, it was still positively correlated with age in both groups. This suggested that the cornea progressively stiffened with age, regardless of their AL. The fibrous stroma was the main layer that dominated the corneal biomechanical behavior (Boyce et al., 2008). With the presence of proteoglycan in the interfibrillar matrix, stromal microstructural components, including both collagen fibrils and fibrillar molecules, increase with age (Daxer et al., 1998; Elsheikh et al., 2008a).

Excessive axial elongation can lead to a higher myopic refractive error. This may cause excessive stretching of the retina, choroid, and sclera, which in turn result in a series of eye complications such as macular degeneration, retinal

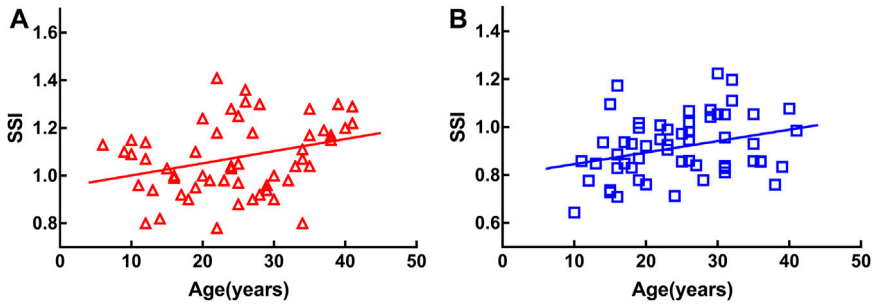

FIGURE 1 | Stress-strain index (SSI) was positively correlated with age in both groups [moderately elongated eye: $r = 0.326$, $p < 0.05$ **(A)**, severely elongated eye: $r = 0.298$, $p < 0.05$ **(B)**].

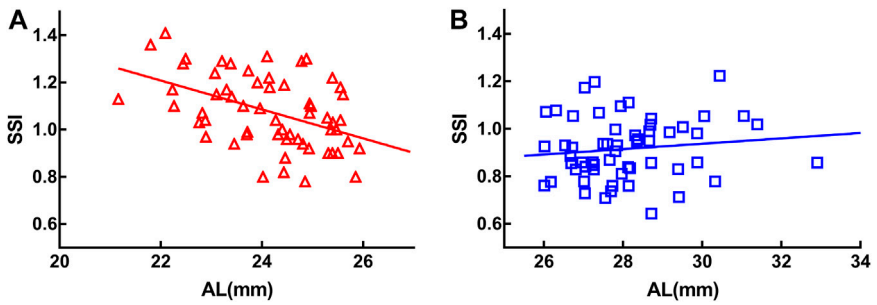

FIGURE 2 | Stress-strain index (SSI) was negatively correlated with axial length (AL) in the moderately elongated eye group ($r = -0.476$, $p < 0.001$) **(A)**. There was no significant correlation between SSI and axial length in the severely elongated eye group ($p > 0.05$) **(B)**.

detachment, and posterior staphyloma (Ohno-Matsui and Jonas, 2019). In recent years, researchers have investigated the relationship between corneal biomechanics and axial elongation, and have arrived at various conclusions (Hon et al., 2017; Matalia et al., 2017; Long et al., 2019; Tubtimthong et al., 2020; Yu et al., 2020). Long et al. believed that spherical equivalent refraction was significantly positively correlated with the stiffness parameter at the first applanation (SP-A1) (Long et al., 2019). Bueno-Gimeno et al. found that lower CH and CRF were significantly associated with longer AL (Bueno-Gimeno et al., 2014). However, some studies have also shown that corneal biomechanics do not correlate with AL or refractive error (Inceoglu et al., 2018; Lim et al., 2008). Nevertheless, it is noteworthy that the biomechanical parameters provided by different instruments reflect different biomechanical properties of the cornea (Hon et al., 2017). In addition, it is believed that the range of selected myopic eyes might affect the correlation analysis between corneal biomechanics and AL (Del Buey et al., 2014). Therefore, in this study, we divided the subjects into groups according to the distribution of AL ranges to further investigate the relationship between SSI and AL.

In concordance with our previous findings, the SSI of the SEE group was significantly lower than that of the MEE group (Liu et al., 2020). In the MEE group, the SSI was significantly negatively correlated with AL. In contrast, no significant correlation was observed between the SSI and AL in the SEE group. This suggested that the effect of AL on corneal stiffness was not linear. We propose this could be due to the uneven growth of the eyeball. In the process of physiological myopia progression, axial elongation is relatively uniform and corresponds to the other components within the ocular structures. For instance, the crystalline lens thickness and corneal refractive power decrease in proportion to AL elongation (Meng et al., 2011). However, when the eye is elongated further, pathological changes start to appear (Backhouse and Phillips, 2010; Kang et al., 2018). When the eye progresses to a pathological state, the traction resulting from the AL elongation is mainly from the posterior pole with minimal or no collaboration with the other parts of the globe; hence, the changes in the anterior structures tend to be relatively stable and irrelevant to the excessive AL elongation (Larsen, 1971; Khokhar et al., 2018). Khokhar et al. suggested that the anterior and posterior segments of the eye with low myopia or ametropia were proportional to eye growth but disproportionate in high myopia (Khokhar et al., 2018). Research using 3D MRI of myopia morphology also found that the longitudinal and transverse diameter ratio of the eyeball was larger in high myopia than in non-high myopia (Wen et al., 2017). This suggested that the expansion of the eyeball was uneven in SEE as compared to MEE.

It has been revealed that scleral biomechanics may influence the axial elongation rate, with poor scleral biomechanics

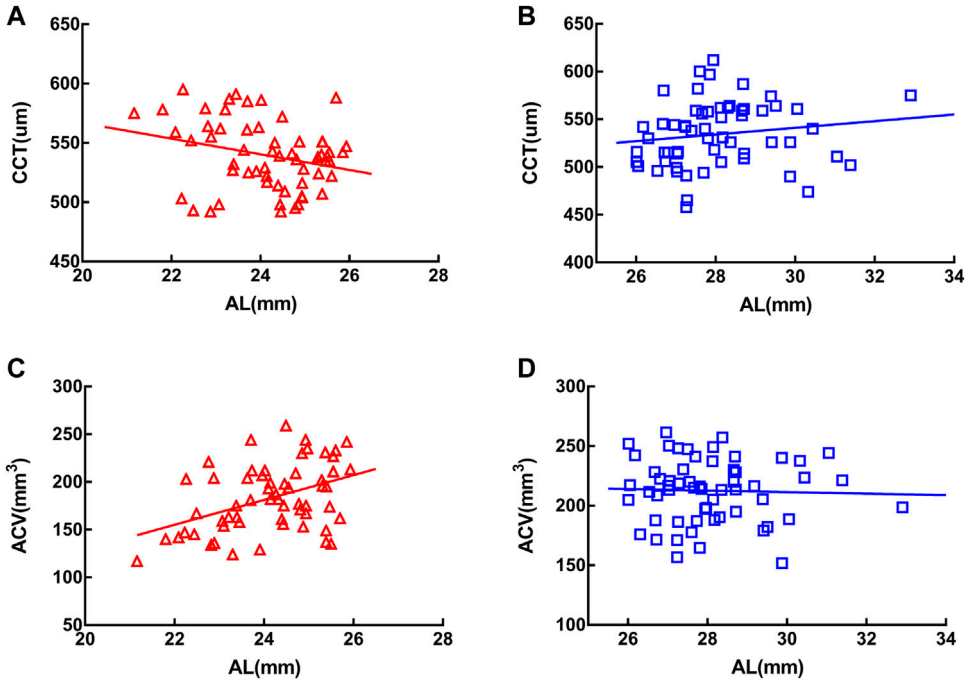

FIGURE 3 | Central corneal thickness (CCT) was negatively correlated with axial length in the moderately elongated eye group ($r = -0.289$, $p < 0.05$) **(A)** and anterior chamber volume (ACV) was positively correlated with axial length ($r = 0.444$, $p < 0.001$) **(C)**. In the severely elongated eye group, neither CCT **(B)** nor ACV **(D)** was associated with axial length ($p > 0.05$).

TABLE 4 | Partial correlation coefficient adjusted for age between ocular parameters of the two groups.

Parameters	MEE		SEE	
	r	p	r	p
SSI vs. AGE	0.326[b]	<0.05[a]	0.298[b]	<0.05[a]
SSI vs. AL	−0.476[c]	<0.001[a]	-[c]	0.809
AL vs. CCT	−0.289[c]	<0.05[a]	-[c]	0.304
AL vs. ACV	0.444[c]	<0.001[a]	-[c]	0.900

[a]*Statistically significant.*
[b]*Pearson correlation.*
[c]*Coefficient of partial correlation after adjusting for age, SSI, Stress-Strain index; AL, Axial length; CCT, Central corneal thickness; ACV, Anterior chamber volume; MEE, moderately elongated eye; SEE, severely elongated eye.*

corresponding to a faster axial elongation rate (Haseltine et al., 2012; Hon et al., 2017). However, owing to the difficulty in measuring posterior scleral biomechanics *in vivo*, some researchers suggested measuring the anterior segment parameters instead of posterior scleral biomechanics to predict the development of myopia (Hayashi et al., 2010; Long et al., 2019; Wu et al., 2019). Bataille et al. investigated the relationship between AL and various anterior segment parameters and developed a model to predict AL; however, the author pointed out that a larger sample size was needed for validation (Bataille et al., 2021).

In the current study, we also found that CCT was negatively correlated with AL and ACV positively correlated with AL in MEE, whereas neither CCT nor ACV was correlated with AL in SEE. Similar findings have been reported in previous studies. Hashemi et al. found that anterior chamber depth plus crystalline lens thickness was associated with AL only in eyes with a shorter AL, but not in eyes with a longer AL (Hashemi et al., 2015). Cheng et al. found that when AL was less than 27 mm, the crystalline lens power was negatively correlated with AL, whereas in eyes with an AL greater than 27 mm, the crystalline lens power was no longer correlated with AL (Cheng et al., 2020). This also proved that in SEE, the correlation between the anterior segment and posterior pole of the eye are weakened. This may explain why the corneal SSI was no longer correlated with AL in SEE.

Previous studies suggested that corneal biomechanics could be used to evaluate the structural and functional glaucomatous damage, because the biomechanics of the sclera and lamina cribrosa could be represented by that of the cornea to some extent (Chansangpetch et al., 2017; Aoki et al., 2020; Miki et al., 2020). Hocaoglu et al. found that in patients with glaucoma whose ALs ranged from 21.10 to 25.51 mm, CH was negatively correlated with global retinal nerve fiber layer thickness. Aoki et al. showed that in glaucomatous eyes with 21.10–27.00 mm ALs, the optic nerve head (ONH) morphology was associated with the biomechanical properties measured using Corvis ST. Glaucomatous ONH superior-inferior asymmetries were associated with small deformations and slow recovery of the cornea (Aoki et al., 2020). Pillunat et al. believed that lower adjusted CH and CRF was negatively correlated with the severity of open-angle glaucoma in patients with ALs from 21.80 to 25.10 mm (Pillunat et al., 2016). Although these studies

explored the relationship between corneal biomechanics and glaucoma, most of the selected participants had MEE. In this study, we found a lower correlation between corneal stiffness and posterior polar region morphology in SEE. Considering the correlation between corneal stiffness and glaucomatous changes in MEE, further studies are warranted on these parameters in patients with SEE.

LIMITATIONS

A limitation of this research was that scleral biomechanics could not be directly measured to analyze the biomechanical correlation between the cornea and sclera in different AL groups. Whether the parameters of scleral mechanics can be reflected indirectly through the measurement of corneal biomechanical parameters has not been supported by this research, and warrants further investigation.

CONCLUSION

To conclude, SSI, the corneal stiffness parameter was lower in the SEE group than in the MEE group. This study analyzed for the first time the correlation between SSI and AL in subjects with MEE and SEE. The SSI was negatively correlated with AL in the MEE group, but not in the SEE group. This may explain the controversial correlation between corneal stiffness and AL in previous studies and provide insights into the different eye growth pattern in lower myopia and higher myopia.

DATA AVAILABILITY STATEMENT

The raw data supporting the conclusion of this article will be made available by the authors, without undue reservation.

ETHICS STATEMENT

The studies involving human participants were reviewed and approved by The Ethics Committee of Tianjin Medical University Eye Hospital. Written informed consent to participate in this study was provided by the participants' legal guardian/next of kin.

AUTHOR CONTRIBUTIONS

GL and HR: Data analysis and interpretation and manuscript drafting. PZ and BD: Data analysis. ZC: Manuscript revision. YZ, BW and JH: Data acquisition. ZC and RW: Study design.

REFERENCES

Aoki, S., Kiuchi, Y., Tokumo, K., Fujino, Y., Matsuura, M., Murata, H., et al. (2020). Association between Optic Nerve Head Morphology in Open-Angle Glaucoma and Corneal Biomechanical Parameters Measured with Corvis ST. *Graefes Arch. Clin. Exp. Ophthalmol.* 258, 629–637. doi:10.1007/s00417-019-04572-z

Backhouse, S., and Phillips, J. R. (2010). Effect of Induced Myopia on Scleral Myofibroblasts and *In Vivo* Ocular Biomechanical Compliance in the guinea Pig. *Invest. Ophthalmol. Vis. Sci.* 51, 6162–6171. doi:10.1167/iovs.10-5387

Bataille, L., Molina-Martín, A., and Piñero, D. P. (2021). Relationship between Axial Length and Corneo-Scleral Topography: A Preliminary Study. *Diagnostics* 11, 542. doi:10.3390/diagnostics11030542

Blackburn, B. J., Jenkins, M. W., Rollins, A. M., and Dupps, W. J. (2019). A Review of Structural and Biomechanical Changes in the Cornea in Aging, Disease, and Photochemical Crosslinking. *Front. Bioeng. Biotechnol.* 7, 66. doi:10.3389/fbioe.2019.00066

Boyce, B. L., Grazier, J. M., Jones, R. E., and Nguyen, T. D. (2008). Full-field Deformation of Bovine Cornea under Constrained Inflation Conditions. *Biomaterials* 29, 3896–3904. doi:10.1016/j.biomaterials.2008.06.011

Bueno-Gimeno, I., España-Gregori, E., Gene-Sampedro, A., Lanzagorta-Aresti, A., and Piñero-Llorens, D. P. (2014). Relationship Among Corneal Biomechanics, Refractive Error, and Axial Length. *Optom. Vis. Sci.* 91, 507–513. doi:10.1097/OPX.0000000000000231

Chansangpetch, S., Panpruk, R., Manassakorn, A., Tantisevi, V., Rojanapongpun, P., Hurst, C. P., et al. (2017). Impact of Myopia on Corneal Biomechanics in Glaucoma and Nonglaucoma Patients. *Invest. Ophthalmol. Vis. Sci.* 58, 4990–4996. doi:10.1167/iovs.17-22219

Cheng, T., Deng, J., Xiong, S., Yu, S., Zhang, B., Wang, J., et al. (2021). Crystalline Lens Power and Associated Factors in Highly Myopic Children and Adolescents Aged 4 to 19 Years. *Am. J. Ophthalmol.* 223, 169–177. doi:10.1016/j.ajo.2020.07.007

Daxer, A., Misof, K., Grabner, B., Ettl, A., and Fratzl, P. (1998). Collagen Fibrils in the Human Corneal Stroma: Structure and Aging. *Invest. Ophthalmol. Vis. Sci.* 39, 644–648.

Del Buey, M. A., Lavilla, L., Ascaso, F. J., Lanchares, E., Huerva, V., and Cristóbal, J. A. (2014). Assessment of Corneal Biomechanical Properties and Intraocular Pressure in Myopic Spanish Healthy Population. *J. Ophthalmol.* 2014, 1–6. doi:10.1155/2014/905129

Eliasy, A., Chen, K.-J., Vinciguerra, R., Lopes, B. T., Abass, A., Vinciguerra, P., et al. (2019). Determination of Corneal Biomechanical Behavior Iin-Vvivo for Healthy Eyes Using CorVis ST Tonometry: Stress-Strain Index. *Front. Bioeng. Biotechnol.* 7, 105. doi:10.3389/fbioe.2019.00105

Elsheikh, A., Alhasso, D., and Rama, P. (2008a). Assessment of the Epithelium's Contribution to Corneal Biomechanics. *Exp. Eye Res.* 86, 445–451. doi:10.1016/j.exer.2007.12.002

Elsheikh, A., Geraghty, B., Rama, P., Campanelli, M., and Meek, K. M. (2010). Characterization of Age-Related Variation in Corneal Biomechanical Properties. *J. R. Soc. Interf.* 7, 1475–1485. doi:10.1098/rsif.2010.0108

Elsheikh, A., Wang, D., Rama, P., Campanelli, M., and Garway-Heath, D. (2008b). Experimental Assessment of Human Corneal Hysteresis. *Curr. Eye Res.* 33, 205–213. doi:10.1080/02713680701882519

Flitcroft, D. I., He, M., Jonas, J. B., Jong, M., Naidoo, K., Ohno-Matsui, K., et al. (2019). IMI - Defining and Classifying Myopia: A Proposed Set of Standards for Clinical and Epidemiologic Studies. *Invest. Ophthalmol. Vis. Sci.* 60, M20–M30. doi:10.1167/iovs.18-25957

Fotouhi, A., Hashemi, H., Khabazkhoob, M., Emamian, M., Shariati, M., Miraftab, M., et al. (2015). Association between Refractive Errors and Ocular Biometry in Iranian Adults. *J. Ophthalmic Vis. Res.* 10, 214–220. doi:10.4103/2008-322X.170340

Haarman, A. E. G., Enthoven, C. A., Tideman, J. W. L., Tedja, M. S., Verhoeven, V. J. M., and Klaver, C. C. W. (2020). The Complications of Myopia: A Review and Meta-Analysis. *Invest. Ophthalmol. Vis. Sci.* 61, 49. doi:10.1167/iovs.61.4.49

Han, F., Li, M., Wei, P., Ma, J., Jhanji, V., and Wang, Y. (2020). Effect of Biomechanical Properties on Myopia: a Study of New Corneal Biomechanical Parameters. *BMC Ophthalmol.* 20, 459. doi:10.1186/s12886-020-01729-x

Haseltine, S. J., Pae, J., Ehrlich, J. R., Shammas, M., and Radcliffe, N. M. (2012). Variation in Corneal Hysteresis and central Corneal Thickness Among Black,

Hispanic and white Subjects. *Acta Ophthalmol.* 90, e626–e631. doi:10.1111/j.1755-3768.2012.02509.x

Hayashi, K., Ohno-Matsui, K., Shimada, N., Moriyama, M., Kojima, A., Hayashi, W., et al. (2010). Long-term Pattern of Progression of Myopic Maculopathy. *Ophthalmology* 117, 1595–1611. doi:10.1016/j.ophtha.2009.11.003

Hoang, Q. V., Rohrbach, D., McFadden, S. A., and Mamou, J. (2019). Regional Changes in the Elastic Properties of Myopic Guinea Pig Sclera. *Exp. Eye Res.* 186, 107739. doi:10.1016/j.exer.2019.107739

Holden, B. A., Fricke, T. R., Wilson, D. A., Jong, M., Naidoo, K. S., Sankaridurg, P., et al. (2016). Global Prevalence of Myopia and High Myopia and Temporal Trends from 2000 through 2050. *Ophthalmology* 123, 1036–1042. doi:10.1016/j.ophtha.2016.01.006

Hon, Y., Chen, G.-Z., Lu, S.-H., Lam, D. C. C., and Lam, A. K. C. (2017). High Myopes Have Lower Normalised Corneal tangent Moduli (Less 'stiff' Corneas) Than Low Myopes. *Ophthalmic Physiol. Opt.* 37, 42–50. doi:10.1111/opo.12335

İnceoğlu, N., Emre, S., and Ulusoy, M. O. (2018). Investigation of Corneal Biomechanics at Moderate to High Refractive Errors. *Int. Ophthalmol.* 38, 1061–1067. doi:10.1007/s10792-017-0560-0

Jonas, J. B., Ohno-Matsui, K., and Panda-Jonas, S. (2019). Myopia: Anatomic Changes and Consequences for its Etiology. *Asia Pac. J. Ophthalmol. (Phila).* 8, 355–359. doi:10.1097/01.APO.0000578944.25956.8b

Kang, B. S., Wang, L.-K., Zheng, Y.-P., Guggenheim, J. A., Stell, W. K., and Kee, C.-s. (2018). High Myopia Induced by Form Deprivation Is Associated with Altered Corneal Biomechanical Properties in Chicks. *PLoS One* 13, e0207189. doi:10.1371/journal.pone.0207189

Khokhar, S., Takkar, B., Agarwal, E., Gaur, N., Ravani, R., and Venkatesh, P. (2018). Biometric Evaluation of Myopic Eyes without Posterior Staphyloma: Disproportionate Ocular Growth. *Int. Ophthalmol.* 38, 2427–2434. doi:10.1007/s10792-017-0745-6

Larsen, J. S. (1971). The Sagittal Growth of the Eye. 1. Ultrasonic Measurement of the Depth of the Anterior Chamber from Birth to Puberty. *Acta Ophthalmol. (Copenh).* 49, 239–262. doi:10.1111/j.1755-3768.1971.tb00949.x

Lim, L., Gazzard, G., Chan, Y.-H., Fong, A., Kotecha, A., Sim, E.-L., et al. (2008). Cornea Biomechanical Characteristics and Their Correlates with Refractive Error in Singaporean Children. *Invest. Ophthalmol. Vis. Sci.* 49, 3852–3857. doi:10.1167/iovs.07-1670

Liu, G., Rong, H., Pei, R., Du, B., Jin, N., Wang, D., et al. (2020). Age Distribution and Associated Factors of Cornea Biomechanical Parameter Stress-Strain index in Chinese Healthy Population. *BMC Ophthalmol.* 20, 436. doi:10.1186/s12886-020-01704-6

Long, W., Zhao, Y., Hu, Y., Li, Z., Zhang, X., Zhao, W., et al. (2019). Characteristics of Corneal Biomechanics in Chinese Preschool Children with Different Refractive Status. *Cornea* 38, 1395–1399. doi:10.1097/ICO.0000000000001971

Matalia, J., Francis, M., Gogri, P., Panmand, P., Matalia, H., and Roy, A. S. (2017). Correlation of Corneal Biomechanical Stiffness with Refractive Error and Ocular Biometry in a Pediatric Population. *Cornea* 36, 1221–1226. doi:10.1097/ICO.0000000000001290

Meng, W., Butterworth, J., Malecaze, F., and Calvas, P. (2011). Axial Length of Myopia: a Review of Current Research. *Ophthalmologica* 225, 127–134. doi:10.1159/000317072

Miki, A., Yasukura, Y., Weinreb, R. N., Maeda, N., Yamada, T., Koh, S., et al. (2020). Dynamic Scheimpflug Ocular Biomechanical Parameters in Untreated Primary Open Angle Glaucoma Eyes. *Invest. Ophthalmol. Vis. Sci.* 61, 19. doi:10.1167/iovs.61.4.19

Momeni-moghaddam, H., Hashemi, H., Zarei-ghanavati, S., Ostadimoghaddam, H., Yekta, A., Aghamirsalim, M., et al. (2019). Four-year Changes in Corneal Biomechanical Properties in Children. *Clin. Exp. Optom.* 102, 489–495. doi:10.1111/cxo.12890

Moshirfar, M., Motlagh, M. N., Murri, M. S., Momeni-Moghaddam, H., Ronquillo, Y. C., and Hoopes, P. C. (2019). Advances in Biomechanical Parameters for Screening of Refractive Surgery Candidates: A Review of the Literature, Part III. *Med. Hypothesis Discov. Innov. Ophthalmol.* 8, 219–240. doi:10.1007/s40123-019-0199-1

Nongpiur, M. E., Png, O., Chiew, J. W., Fan, K. R., Girard, M. J. A., Wong, T., et al. (2015). Lack of Association between Corneal Hysteresis and Corneal Resistance Factor with Glaucoma Severity in Primary Angle Closure Glaucoma. *Invest. Ophthalmol. Vis. Sci.* 56, 6879–6885. doi:10.1167/iovs.15-17930

Ohno-Matsui, K., and Jonas, J. B. (2019). Posterior Staphyloma in Pathologic Myopia. *Prog. Retin. Eye Res.* 70, 99–109. doi:10.1016/j.preteyeres.2018.12.001

Pillunat, K. R., Hermann, C., Spoerl, E., and Pillunat, L. E. (2016). Analyzing Biomechanical Parameters of the Cornea with Glaucoma Severity in Open-Angle Glaucoma. *Graefes Arch. Clin. Exp. Ophthalmol.* 254, 1345–1351. doi:10.1007/s00417-016-3365-3

Sergienko, N. M., and Shargorogska, I. (2012). The Scleral Rigidity of Eyes with Different Refractions. *Graefes Arch. Clin. Exp. Ophthalmol.* 250, 1009–1012. doi:10.1007/s00417-012-1973-0

Summers Rada, J. A., Shelton, S., and Norton, T. T. (2006). The Sclera and Myopia. *Exp. Eye Res.* 82, 185–200. doi:10.1016/j.exer.2005.08.009

Tideman, J. W. L., Snabel, M. C. C., Tedja, M. S., van Rijn, G. A., Wong, K. T., Kuijpers, R. W. A. M., et al. (2016). Association of Axial Length with Risk of Uncorrectable Visual Impairment for Europeans with Myopia. *JAMA Ophthalmol.* 134, 1355–1363. doi:10.1001/jamaophthalmol.2016.4009

Tubtimthong, A., Chansangpetch, S., Ratprasatporn, N., Manassakorn, A., Tantisevi, V., Rojanapongpun, P., et al. (2020). Comparison of Corneal Biomechanical Properties Among Axial Myopic, Nonaxial Myopic, and Nonmyopic Eyes. *Biomed. Res. Int.* 2020, 1–7. doi:10.1155/2020/8618615

Wang, W., He, M., He, H., Zhang, C., Jin, H., and Zhong, X. (2017). Corneal Biomechanical Metrics of Healthy Chinese Adults Using Corvis ST. *Contact Lens and Anterior Eye* 40, 97–103. doi:10.1016/j.clae.2016.12.003

Wen, B., Yang, G., Cheng, J., Jin, X., Zhang, H., Wang, F., et al. (2017). Using High-Resolution 3D Magnetic Resonance Imaging to Quantitatively Analyze the Shape of Eyeballs with High Myopia and Provide Assistance for Posterior Scleral Reinforcement. *Ophthalmologica* 238, 154–162. doi:10.1159/000477466

Wu, W., Dou, R., and Wang, Y. (2019). Comparison of Corneal Biomechanics between Low and High Myopic Eyes-A Meta-Analysis. *Am. J. Ophthalmol.* 207, 419–425. doi:10.1016/j.ajo.2019.07.007

Yu, A.-Y., Shao, H., Pan, A., Wang, Q., Huang, Z., Song, B., et al. (2020). Corneal Biomechanical Properties in Myopic Eyes Evaluated via Scheimpflug Imaging. *BMC Ophthalmol.* 20, 279. doi:10.1186/s12886-020-01530-w

Zadnik, K., Sinnott, L. T., Cotter, S. A., Jones-Jordan, L. A., Kleinstein, R. N., Manny, R. E., et al. (2015). Prediction of Juvenile-Onset Myopia. *JAMA Ophthalmol.* 133, 683–689. doi:10.1001/jamaophthalmol.2015.0471

Conflict of Interest: The authors declare that the research was conducted in the absence of any commercial or financial relationships that could be construed as a potential conflict of interest.

Publisher's Note: All claims expressed in this article are solely those of the authors and do not necessarily represent those of their affiliated organizations, or those of the publisher, the editors and the reviewers. Any product that may be evaluated in this article, or claim that may be made by its manufacturer, is not guaranteed or endorsed by the publisher.

frontiers in Bioengineering and Biotechnology

ORIGINAL RESEARCH
published: 22 December 2021
doi: 10.3389/fbioe.2021.809262

Long-Term Follow-Up of Accelerated Transepithelial Corneal Crosslinking for Post-LASIK Ectasia: A Pilot Prospective Observational Study

Mi Tian[1,2,3,4,5†], *Xiaoyu Zhang*[1,2,3,4,5†], *Weijun Jian*[1,2,3,4,5], *Ling Sun*[1,2,3,4,5], *Yang Shen*[1,2,3,4,5] *and Xingtao Zhou*[1,2,3,4,5*]

[1]Eye Institute and Department of Ophthalmology, Eye and ENT Hospital, Fudan University, Shanghai, China, [2]NHC Key Laboratory of Myopia, Fudan University, Shanghai, China, [3]Key Laboratory of Myopia, Chinese Academy of Medical Sciences, Shanghai, China, [4]Shanghai Research Center of Ophthalmology and Optometry, Shanghai, China, [5]Shanghai Engineering Research Center of Laser and Autostereoscopic 3D for Vision Care (20DZ2255000), Shanghai, China

OPEN ACCESS

Edited by:
FangJun Bao,
Affiliated Eye Hospital of Wenzhou Medical College, China

Reviewed by:
Kai-Jung Chen,
National Chin-Yi University of Technology, Taiwan
Zhipeng Yan,
Third Hospital of Hebei Medical University, China

***Correspondence:**
Xingtao Zhou
doctzhouxingtao@163.com

[†]These authors have contributed equally to this work and share first authorship

Specialty section:
This article was submitted to Biomechanics, a section of the journal Frontiers in Bioengineering and Biotechnology

Received: 04 November 2021
Accepted: 06 December 2021
Published: 22 December 2021

Citation:
Tian M, Zhang X, Jian W, Sun L, Shen Y and Zhou X (2021) Long-Term Follow-Up of Accelerated Transepithelial Corneal Crosslinking for Post-LASIK Ectasia: A Pilot Prospective Observational Study. Front. Bioeng. Biotechnol. 9:809262. doi: 10.3389/fbioe.2021.809262

Background: Keratectasia after corneal refractive surgery is a rare but serious postoperative complication, and reports on accelerated transepithelial corneal crosslinking (ATE-CXL)-based treatment of patients with post-laser-assisted *in situ* keratomileusis (LASIK) ectasia are limited. Therefore, this study evaluated the long-term efficacy and safety of ATE-CXL for progressive post-LASIK ectasia.

Methods: This prospective observational study was conducted at the Eye and ENT Hospital, Fudan University, Shanghai, China, and 25 eyes from 25 patients with post-LASIK ectasia undergoing ATE-CXL were examined. Clinical examinations were conducted preoperatively and postoperatively to assess parameters such as manifest refraction, corrected distance visual acuity (CDVA), endothelial cell density; keratometry, corneal thickness, posterior elevation and topometric indices were measured using Pentacam; sectoral pachymetry and epithelial thickness were evaluated using optical coherence tomography. A paired t-test, Wilcoxon rank-sum test, Kruskal-Wallis test, and repeated measures analysis of variance were used for statistical analysis.

Results: Participants were examined for an average of 46 months. No severe complications occurred during or after ATE-CXL. CDVA improved from 0.25 ± 0.31 preoperatively to 0.15 ± 0.17 postoperatively ($p = 0.011$). Maximum keratometry decreased from 55.20 ± 8.33 D to 54.40 ± 7.98 D, with no statistical significance ($p = 0.074$), and the central corneal thickness increased from 414.92 ± 40.96 µm to 420.28 ± 44.78 µm ($p = 0.047$) at the final follow-up. Posterior elevation, pachymetry, and epithelial thickness remained stable ($p > 0.05$) throughout the follow-up. No significant differences were noted in topometric indices, except the central keratoconus index, which decreased significantly ($p < 0.001$) at the final follow-up.

Conclusion: Improvements in CDVA and stabilization in corneal keratometry and posterior elevation after ATE-CXL were noted at the 46-months follow-up, demonstrating that ATE-CXL is a safe and effective treatment for progressive post-LASIK ectasia.

Keywords: corneal crosslinking, keratectasia, laser-assisted *in situ* keratomileusis (LASIK), safety, efficacy

Clinical Trial Registration: http://www.chictr.org.cn/showproj.aspx?proj=13701, identifier ChiCTR-OIC-16008181

INTRODUCTION

Keratectasia after corneal refractive surgery is a rare but serious postoperative complication. Since the first reported case of post-laser-assisted *in situ* keratomileusis (LASIK) ectasia by Seiler et al. (1998) in 1998, an increasing number of such cases has been reported. Although the precise incidence of post-LASIK ectasia remains unclear, it has been estimated to be between 0.04 and 0.6% (Binder, 2007; Chen et al., 2008). Post-LASIK ectasia can cause severe and irreversible visual impairment in patients, with progressive thinning of the cornea, progressive steepening of corneal curvature, and significant increases in myopia and astigmatism. The most common risk factors related to post-LASIK ectasia are low residual stromal bed thickness, abnormal preoperative corneal topography, thin preoperative corneal thickness, and high refractive correction (Randleman et al., 2008; Spadea et al., 2012).

There has been an increase in the number of studies exploring the application of corneal crosslinking (CXL) for patients with post-LASIK ectasia (Kymionis et al., 2009a; Salgado et al., 2011; Sueke et al., 2011; Alhayek and Lu, 2015). CXL can increase the strength and biomechanical stability of the cornea through the interaction of riboflavin and ultraviolet (UV) radiation. Previous studies (Salgado et al., 2011; Alhayek and Lu, 2015) have reported that conventional CXL (C-CXL) is an effective technique for halting keratectasia progression and has a good safety profile. Accelerated transepithelial CXL (ATE-CXL) (Shen et al., 2016; Zhang et al., 2016; Tian et al., 2018; Tian et al., 2020; Zhang et al., 2020) is an advanced CXL technique that helps maintain the integrity of the corneal epithelial layer, with a higher UV irradiation intensity (45 mW/cm^2) and shorter irradiation duration (5 min and 20 s) than C-CXL (3 mW/cm^2, 30 min).

To the best of our knowledge, our research team (Shen et al., 2016; Zhang et al., 2016; Tian et al., 2018; Tian et al., 2020; Zhang et al., 2020) was the first to report that ATE-CXL is safe and effective for treating adult and pediatric keratoconus. However, ATE-CXL-based treatment of patients with post-LASIK ectasia has rarely been reported in the literature. Our ophthalmology department received a referral for a larger number of patients diagnosed with post-LASIK ectasia on Chinese mainland. Therefore, this study aimed to evaluate the long-term outcomes of ATE-CXL in the treatment of patients with post-LASIK ectasia.

MATERIALS AND METHODS

Subjects

This study adhered to the tenets of the Declaration of Helsinki and was approved by the Ethics Committee of the Eye and ENT Hospital of Fudan University (Project ID: ky 2012-017). Written informed consent was obtained from all the subjects after they were informed of the nature and possible consequences of the procedure.

The study prospectively included referral patients with progressive post-LASIK ectasia treated with ATE-CXL at the Eye and ENT Hospital of Fudan University in Shanghai, China. Evidence of progressive ectasia included an increase in maximum keratometry (K_{max}) or astigmatism >1 D in the last year, excessive posterior elevation on topography mapping, or thinning in corneal thickness (Gomes et al., 2015). The exclusion criteria were: 1) history of ocular disease, 2) previous ocular surgeries (except LASIK), or 3) pregnancy or lactation during the study. Patients were instructed to discontinue wearing soft contact lenses and rigid gas-permeable lenses for at least 2 and 4 weeks, respectively, before commencing the study.

Ophthalmologic Examinations

Preoperative and postoperative examinations were performed in all the patients as follows: slit-lamp biomicroscope examination, manifest refraction, test for corrected distance visual acuity (CDVA), and endothelial cell density (ECD). K_{max}, flattest meridian keratometry (K1), steepest meridian keratometry (K2), corneal astigmatism, central corneal thickness (CCT), apex thickness (AT), and thinnest corneal thickness (TCT) were measured using Pentacam (Oculus Optikgeräte, Wetzlar, Germany). At each follow-up, the same best-fit values were used to calculate corneal posterior elevation data, including posterior central elevation (PCE) and posterior mean elevation (PME) across pre- and postoperative examinations. Pentacam was also used to evaluate topography indices, including the index of surface variance (ISV), index of vertical asymmetry (IVA), index of height asymmetry (IHA), index of height decentration (IHD), keratoconus index (KI), central KI (CKI), and minimum radius of curvature (R_{min}).

Sectoral pachymetry and epithelial thickness were measured using spectral-domain optical coherence tomography (RTVue-100; Optovue, Fremont, CA, United States). The measurement area included the central cornea (central area of 2 mm diameter) and paracentral cornea (central annuli with a diameter ranging from 2 to 5 mm). Patients were followed up at 1, 6, 12 months, and four-years postoperatively. All examinations were performed by the same technician.

Surgical Procedures

All surgeries were performed by the same experienced surgeon (Zhou). The ATE-CXL treatment was performed in an outpatient clinic using a previously described procedure (Shen et al., 2016; Zhang et al., 2016; Tian et al., 2018; Tian et al., 2020; Zhang et al., 2020). The corneal epithelium was left intact, and corneal soaking with riboflavin was performed using Paracel (containing 0.25% riboflavin-5-phosphate, hydroxypropyl methylcellulose, sodium edetate, trometamol, benzalkonium chloride, and NaCl) for 4 min, and VibeX Xtra (containing 0.25% riboflavin-5-

TABLE 1 | Refraction outcomes and endothelial cell density.

—	Preoperative		Last visit		*p* Value
	Mean ± SD	Range	Mean ± SD	Range	—
Sphere (D)	–5.92 ± 5.24	(–16.00, 1.00)	–6.38 ± 5.33	(–17.25, 0.75)	0.893
Cylinder (D)	–2.74 ± 2.12	(–8.75, –0.75)	–2.68 ± 1.97	(–5.75, 0)	0.666
Spherical Equivalent (D)	–7.29 ± 5.40	(–16.88, –1.25)	–7.72 ± 5.52	(–18.88, –0.75)	0.954
CDVA (logMAR)	0.25 ± 0.31	(0, 0.70)	0.15 ± 0.17	(0, 0.40)	0.011*
ECD (cell/mm^2)	3,096.22 ± 288.61	(2,761, 3,561)	2,930.11 ± 249.06	(2,598, 3,254)	0.089

*D, diopters; CDVA, corrected distance visual acuity; logMAR, logarithm of the minimal angle of resolution; ECD, endothelial cell density; *, a significant difference compared with preoperative.*

phosphate and NaCl) for 6 min, successively. A UV-A light system (Avedro's KXL System, MA, United States) was used to apply UV radiation (intensity of 45 mW/cm^2) with 1-s pulsed illumination for a total duration of 5 min and 20 s, delivering a surface dose of 7.2 J/cm^2. A bandage contact lens was applied at the end of the procedure. Postoperative medications included levofloxacin (four times daily for 3 days), 0.1% fluorometholone (seven times daily initially, gradually reduced over 2 weeks), and artificial tears (four times daily for 1 month).

Statistical Analysis

Normality was verified using the Kolmogorov-Smirnov Z test. Comparisons between preoperative and postoperative outcomes were made using a paired t-test, Wilcoxon rank-sum test, Kruskal-Wallis test, and repeated measures analysis of variance. Statistical analysis was performed using SPSS version 23.0 (IBM Corp., Armonk, NY, United States); statistical significance was set at $p < 0.05$.

RESULTS

In this study, we enrolled 25 eyes from 25 patients (19 males and 6 females) who underwent ATE-CXL, with a mean age of 28.16 ± 4.84 (range, 21–38) years. Participants were followed up for an average of 46 (range, 40–54) months. All surgeries were completed successfully, and no serious complications were reported during or after ATE-CXL. The operated corneas exhibited mild edema on the first postoperative day. The bandage contact lens was removed on postoperative days 1–5 after evaluating the degree of epithelialization.

Visual Acuity

The visual acuity outcomes are presented in **Table 1**. CDVA (logarithm of the minimum angle of resolution) improved from 0.25 ± 0.31 preoperatively to 0.15 ± 0.17 at 46-months postoperatively ($p = 0.011$). By the last visit, 11 eyes (44%) showed improvement in one or more Snellen lines, with a maximum increase of three lines; 11 eyes (44%) remained stable; two eyes lost one line; and one eye lost two lines.

Manifest Refraction and ECD

The spherical equivalent was −7.29 ± 5.40 D preoperatively and −7.72 ± 5.52 D at the last follow-up ($p = 0.954$). Differences between the spherical and cylindrical degrees before and after ATE-CXL were not significant ($p > 0.05$; **Table 1**). No significant difference was observed in ECD at the last visit than that at the baseline ($p = 0.089$; **Table 1**).

Keratometry Value and Corneal Astigmatism

Changes in K1, K2, and K_{max} during the 46-months follow-up are shown in **Figure 1A**. The K_{max} value was 55.20 ± 8.33 D before ATE-CXL, and 55.40 ± 8.44, 54.98 ± 7.87, 54.19 ± 8.03, and 54.40 ± 7.98 D at 1, 6, 12, and 46 months postoperatively, respectively. There were no significant differences in K_{max}, K1, K2, and corneal astigmatism before or after ATE-CXL during the 46-months follow-up period ($p > 0.05$). The topographic map changes in a typical case are shown in **Figure 2**.

Epithelial and Pachymetry Thickness

Corneal thickness, including the CCT, AT, and TCT changes at different time points, is shown in **Figure 1B**. The CCT value was 414.92 ± 40.96 μm before ATE-CXL, and 414.32 ± 36.85, 416.00 ± 42.03, 415.50 ± 41.89, and 420.28 ± 44.78 μm at 1, 6, 12, and 46 months postoperatively, respectively. The CCT significantly increased between the preoperative and last follow-up values ($p = 0.047$). Preoperative AT and TCT were 407.52 ± 42.43 μm and 404.56 ± 42.58 μm, respectively, and postoperative 46-months follow-up thicknesses were 409.52 ± 48.20 μm and 406.16 ± 47.51 μm, respectively, with no significant change ($p > 0.05$).

The mean thicknesses of the epithelial and pachymetry sectors before and after treatment are listed in **Table 2**. The pachymetry thickness of the central 2-mm sector increased from 413.48 ± 37.44 μm preoperatively, to 416.26 ± 38.33 μm postoperatively ($p = 0.094$), and the average epithelial and pachymetry thickness of neither sector showed a significant change at the last visit when compared with those at the baseline.

Posterior Elevation and Topography Indices

The mean PCE and PME values were 55.04 ± 42.22 μm and -18.72 ± 14.57 μm before ATE-CXL, and 57.76 ± 43.62 μm and −18.85 ± 13.37 μm at the last visit. There was no significant change in posterior elevation at each follow-up point ($p > 0.05$).

The preoperative and postoperative 46-months outcomes of the topography indices are shown in **Table 3**. The CKI value was significantly decreased from 1.08 ± 0.07 at the baseline to 1.07 ± 0.07 at the last follow-up ($p < 0.001$). The R_{min} value increased from 6.24 ± 0.91 to 6.32 ± 0.97; however, the difference was not

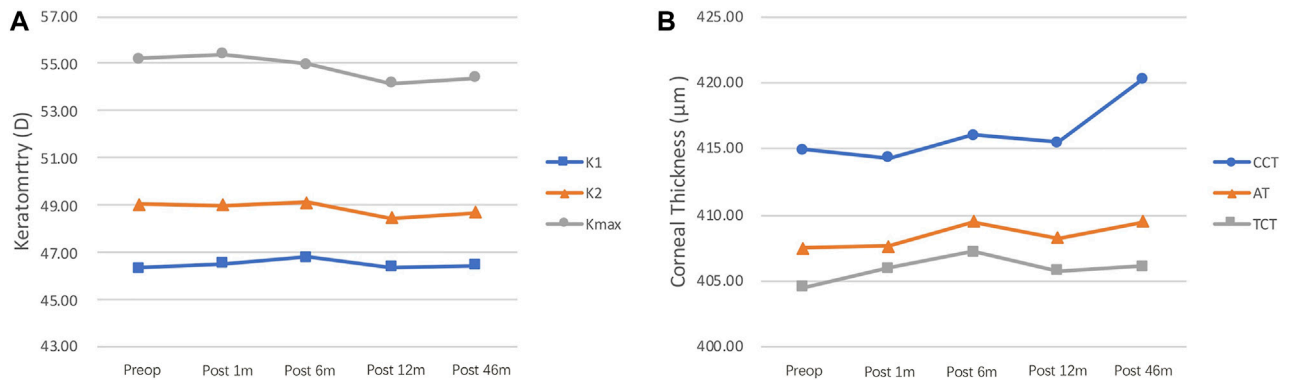

FIGURE 1 | (A) K_{max}, K1, and K2 values at different follow-up time points. No significant changes were observed in K_{max}, K1, and K2 during the 46-months follow-up ($p > 0.05$). K_{max}, maximum keratometry; K1, steepest meridian keratometry; K2, flattest meridian keratometry. **(B)** CCT, AT, and TCT values at different follow-up time points. The CCT value improved from 414.92 ± 40.96 µm preoperatively to 420.28 ± 44.78 µm at 46-months postoperatively ($p = 0.047$). No significant changes were observed in AT and TCT during the 46-months follow-up period ($p > 0.05$). CCT, central corneal thickness; AT, apex thickness; TCT, thinnest corneal thickness.

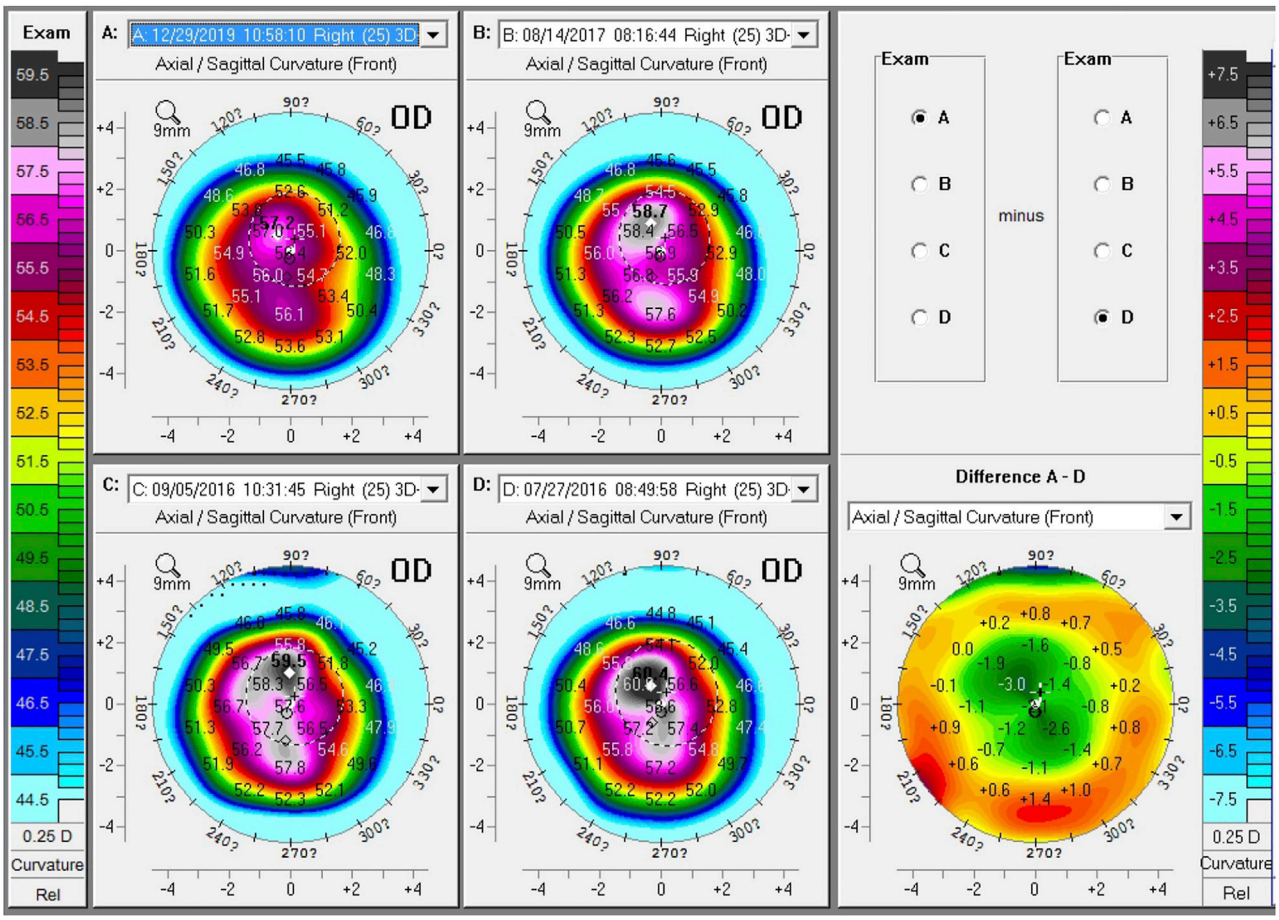

FIGURE 2 | Topographic map changes of a typical case during follow-up. Comparison of preoperative and 41-months postoperative topographic maps, showing a 3.2 D decrease in K_{max}, a 0.8 D decrease in K1, a 2.4 D decrease in K2, and a 1.5 D decrease in astigmatism. **(A)** postoperative 46-months; **(B)** postoperative 12-months; **(C)** postoperative 1-month; **(D)** preoperative; Difference **(A–D)**, comparison of the preoperative and 41-months postoperative front curvature.

TABLE 2 | Sectoral epithelial and pachymetry thicknesses (μm) (Mean ± SD).

—	Sectoral epithelial thicknesses			Sectoral pachymetry thicknesses		
	Preoperative	Last visit	*p* Value	Preoperative	Last visit	*p* Value
Min	40.91 ± 7.67	41.35 ± 7.57	0.660	393.26 ± 42.39	395.91 ± 42.80	0.134
Central 2 mm	50.39 ± 6.79	51.70 ± 7.00	0.328	413.48 ± 37.44	416.26 ± 38.33	0.094
S (2–5 mm)	58.91 ± 5.65	57.09 ± 6.51	0.090	493.91 ± 27.92	495.61 ± 30.77	0.482
SN (2–5 mm)	58.74 ± 6.22	57.65 ± 6.09	0.252	489.39 ± 25.00	490.04 ± 27.43	0.810
N (2–5 mm)	56.35 ± 7.57	55.96 ± 5.46	0.756	477.57 ± 26.24	477.83 ± 27.98	0.933
IN (2–5 mm)	53.35 ± 7.27	53.13 ± 5.51	0.857	473.87 ± 29.43	473.57 ± 31.88	0.934
I (2–5 mm)	51.35 ± 7.04	51.30 ± 5.15	0.958	474.39 ± 27.21	476.17 ± 30.36	0.646
IT (2–5 mm)	52.17 ± 6.73	50.48 ± 6.33	0.100	472.09 ± 29.59	474.74 ± 31.35	0.417
T (2–5 mm)	55.13 ± 6.18	53.04 ± 5.97	0.055	476.57 ± 32.82	478.52 ± 30.24	0.567
ST (2–5 mm)	56.78 ± 8.45	54.22 ± 6.97	0.419	487.09 ± 31.85	490.30 ± 29.18	0.225

S, superior; N, nasal; I, inferior; T, temporal.

TABLE 3 | Topography indices outcomes.

—	Preoperative		Last visit		*p* Value
	Mean ± SD	Range	Mean ± SD	Range	—
ISV	88.16 ± 41.92	(28, 171)	84.32 ± 41.55	(23, 167)	0.103
IVA	24.88 ± 19.78	(3.0, 81.3)	26.85 ± 20.45	(2.4, 70.5)	0.647
IHA	0.85 ± 0.51	(0.27, 1.94)	0.84 ± 0.48	(0.25, 1.67)	0.657
IHD	0.12 ± 0.08	(0.03, 0.26)	0.11 ± 0.07	(0.03, 0.27)	0.389
KI	1.21 ± 0.16	(0.97, 1.52)	1.21 ± 0.16	(0.97, 1.56)	0.873
CKI	1.08 ± 0.07	(0.97, 1.24)	1.07 ± 0.07	(0.96, 1.21)	<0.001*
R_{min}	6.24 ± 0.91	(4.59, 7.81)	6.32 ± 0.87	(4.77, 7.69)	0.068

*ISV, index of surface variance; IVA, index of vertical asymmetry; IHA, index of height asymmetry; IHD, index of height decentration; KI, keratoconus index; CKI, central keratoconus index; R_{min}, minimum radius of curvature; *, a significant difference compared with preoperative.*

significant ($p = 0.068$). There were no significant changes in the other evaluated topographic indices at 46 months postoperatively compared with the preoperative values ($p > 0.05$).

DISCUSSION

As a surgical treatment used to increase corneal strength and stabilize the ectatic cornea, CXL has been widely adopted for the clinical treatment of keratoconus and post-LASIK ectasia. Kohlhaas et al. (2005) were the first to report the use of C-CXL in the treatment of post-LASIK ectasia. To the best of our knowledge, this study is the first to evaluate the long-term benefits of ATE-CXL in treating post-LASIK ectasia.

The patients included in the study exhibited progressive keratectasia after LASIK, with an increase of at least 1D in maximal keratometry or central corneal astigmatism within one year of the procedure. During the 46-months follow-up period after ATE-CXL, the K_{max} value decreased from 55.20 ± 8.33 D to 54.40 ± 7.98 D. No significant changes in K1, K2, corneal astigmatism, and K_{max} were observed before and after ATE-CXL during the 46-months follow-up, suggesting that ATE-CXL was effective in these cases and could halt the progression of keratectasia. Among the previous studies regarding the use of C-CXL for the treatment of progressive post-LASIK ectasia, Yildirim et al. (2014) observed that in 20 eyes, K_{max} decreased from 46.0 ± 4.4 D to 45.6 ± 3.8 D in the 42-months follow-up period, and Hafezi et al. (2007) found that in 10 eyes, K_{max} decreased from 57.4 D to 56.3 D in the two-year follow-up. Our study findings are similar to the results of these two studies, suggesting that ATE-CXL has the same effectiveness as C-CXL in the treatment of post-LASIK ectasia at long-term follow-up.

Several published studies (Kobashi et al., 2018; Stulting et al., 2018) have reported that transepithelial CXL (T-CXL) provided more rapid visual recovery in ectatic eyes than C-CXL and was superior to C-CXL by exhibiting a better CDVA at the 1-year follow-up. In our study, 46-months postoperative results showed a significantly favorable outcome in CDVA, with a mean improvement of 0.1 logMAR and a maximum increase of three Snellen lines, which indicated that ATE-CXL improved the visual acuity of ectatic patients in the long term. This might be due to the absence of corneal haze after ATE-CXL, confirmed by the lesser extent of keratocyte apoptosis and inflammation. In contrast, only a few studies have reported significant improvement in CDVA after performing C-CXL for post-LASIK ectasia (Richoz et al., 2013; Yildirim et al., 2014).

Changes in corneal thickness after CXL should be documented well since patients with post-LASIK ectasia already have a relatively thin cornea. Thinning of the cornea owing to C-CXL has been observed at the commencement of treatment and may continue up to 3 months postoperatively (Hafezi et al., 2007; Kymionis et al., 2009b); continued reduction of CCT has even been reported to occur for a duration of 3–6 years postoperatively (Kanellopoulos and Asimellis, 2014; Poli et al., 2015). The corneal thickness after ATE-CXL for keratoconus has been reported to recover and reach the baseline by 1 month (Zhang et al., 2016). In the present study, the CCT, AT and TCT values remained stable at 1, 6, 12, and 46 months postoperatively, and at the same time, the epithelial and pachymetry sector thicknesses did not show a significant change at the last visit than those at baseline, suggesting that corneal thickness remained stable after ATE-CXL throughout the 46-months follow-up period.

Regarding corneal tomographic parameters, our study found that corneal posterior elevation values showed statistically insignificant differences from preoperative values at each postoperative follow-up, suggesting that ATE-CXL prevents

the corneal expansion process, thereby ensuring structural stability of the ectatic cornea. Corneal posterior elevation was reliably used to evaluate the stability of the corneal structure (Zhao et al., 2016; Zhao et al., 2017). Zhang et al. (2020) reported stable PCE values throughout the 48-months follow-up period after ATE-CXL in progressive adult keratoconus; however, PCE values were significantly increased at the three-years follow-up compared with the baseline in our previous study of ATE-CXL for progressive pediatric keratoconus (Tian et al., 2020). Therefore, the differences in pathophysiologic features between keratoconic and ectatic corneas should be investigated further.

As for corneal asymmetry parameters, CKI increases with the severity of central keratoconus (Kanellopoulos and Asimellis, 2013; Hashemi et al., 2016). The CKI value was significantly decreased at the 46-months follow-up in this study, indicating an improvement in corneal irregularities. Richoz et al. (2013) found that CKI reduced significantly at a mean follow-up of 25 months after C-CXL for ectasia after LASIK and photorefractive keratectomy and reported a significant decrease in KI, ISV, and IVA during follow-up; however, no significant differences were found in the other topographic indices in this study. Additionally, Lang et al. (2019) compared the 12-months outcomes of C-CXL with accelerated CXL and concluded that C-CXL led to greater improvements in topographic indices compared with A-CXL in patients with progressive keratoconus.

Although the efficacy of CXL has been proven, evaluating its safety is also important due to the associated cytotoxic effect of UV radiation, as well as the nonregenerative nature of endothelial cells (Thorsrud et al., 2012). Therefore, an appropriate CXL therapeutic procedure must be selected to ensure efficacy and safety. ATE-CXL treatment preserves the epithelial layer and shortens the time of infiltration and irradiation, making the patients more comfortable, accelerating postoperative recovery, conserving corneal morphology, and reducing complications. Furthermore, this approach is more suitable for patients with a relatively thin cornea. Satisfactory clinical results of T-CXL have been reported in several published articles (Yuksel et al., 2015; Chen et al., 2016; Aixinjueluo et al., 2017). Mannschreck et al. (2019) reported a case of diffuse lamellar keratitis in a post-LASIK ectatic eye that underwent C-CXL, which was unsuccessful in stopping the disease progression; however, T-CXL successfully treated the ectasia with no reported reoccurrence. In our study, no intraoperative or postoperative complications occurred, and ECD remained stable during the four-years follow-up, indicating the long-term safety of ATE-CXL treatment in patients with post-LASIK ectasia.

In our previous study (Li et al., 2018), lenticule addition followed by ATE-CXL was performed on a patient with post-LASIK ectasia. Improved CDVA and stable corneal keratometry and elevation was observed at 30 months postoperatively; thus, lenticule addition prior to ATE-CXL was proven to be a potential treatment option for patients with keratectasia associated with a thin cornea. Wallerstein et al. (2017) and El-Khoury et al. (2018) used under-flap stromal bed T-CXL for treating early post-LASIK ectasia, which facilitated early postoperative corneal stability with rapid recovery. The above methods provide promising treatment modalities for halting and stabilizing the progression of post-LASIK ectasia.

This pilot observational study had some limitations, such as the relatively small sample size and lack of a control group undergoing standard CXL. However, our results were strengthened by a long duration of postoperative follow-up. In the future, we intend to conduct a study with a larger sample size and investigate corneal biomechanical changes involved in ATE-CXL.

In summary, treatment with ATE-CXL was both effective and safe in halting the progression of keratectasia in patients with post-LASIK ectasia. Overall, the patients benefit from improvements in CDVA and stabilization in corneal keratometry and posterior elevation after a mean follow-up of 46 months, proving that ATE-CXL is safe and suitable for patients with post-LASIK ectasia.

DATA AVAILABILITY STATEMENT

The original contributions presented in the study are included in the article/Supplementary Material, further inquiries can be directed to the corresponding author.

ETHICS STATEMENT

The studies involving human participants were reviewed and approved by the Eye and ENT Hospital, Fudan University, Shanghai, China. The patients/participants provided their written informed consent to participate in this study. Written informed consent was obtained from the individual(s) for the publication of any potentially identifiable images or data included in this article.

AUTHOR CONTRIBUTIONS

All authors read and approved the final manuscript. MT and XZha: Conceptualization, data collection, manuscript drafting, critical revision, and statistical analysis. WJ, MT, and LS: Data collection and manuscript drafting. YS and XZha: Data collection and analyzing. XZho: Conceptualization, critical revision of manuscript, funding, and supervision. All authors approved the final submission of this manuscript.

FUNDING

This study was supported by the National Natural Science Foundation of China (Grant No. 81770955), a joint research project of new Frontier technology in municipal hospitals (Grant No. SHDC12018103), Project of Shanghai Science and Technology (Grant No. 20410710100), Clinical Research Plan of SHDC (Grant No. SHDC2020CR1043B), Project of Shanghai Xuhui District Science and Technology (Grant No. 2020-015).

REFERENCES

Aixinjueluo, W., Usui, T., Miyai, T., Toyono, T., Sakisaka, T., and Yamagami, S. (2017). Accelerated Transepithelial Corneal Cross-Linking for Progressive Keratoconus: a Prospective Study of 12 Months. *Br. J. Ophthalmol.* 101 (9), 1244–1249. doi:10.1136/bjophthalmol-2016-309775

Alhayek, A., and Lu, P. R. (2015). Corneal Collagen Crosslinking in Keratoconus and Other Eye Disease. *Int. J. Ophthalmol.* 8 (2), 407–418. doi:10.3980/j.issn.2222-3959.2015.02.35

Binder, P. S. (2007). Analysis of Ectasia after Laser *In Situ* Keratomileusis: Risk Factors. *J. Cataract Refract Surg.* 33 (9), 1530–1538. doi:10.1016/j.jcrs.2007.04.043

Chen, M. C., Lee, N., Bourla, N., and Hamilton, R. D. (2008). Corneal Biomechanical Measurements before and after Laser *In Situ* Keratomileusis. *J. Cataract Refract Surg.* 34 (11), 1886–1891. doi:10.1016/j.jcrs.2008.06.035

Chen, S., Chan, T. C. Y., Zhang, J., Ding, P., Chan, J. C. K., Yu, M. C. Y., et al. (2016). Epithelium-on Corneal Collagen Crosslinking for Management of Advanced Keratoconus. *J. Cataract Refract Surg.* 42 (5), 738–749. doi:10.1016/j.jcrs.2016.02.041

El-Khoury, S., Abdelmassih, Y., Amro, M., Chelala, E., and Jarade, E. (2018). Under-the-Flap Crosslinking and LASIK in Early Ectasia with Hyperopic Refractive Error. *J. Ophthalmol.* 2018, 4342984. doi:10.1155/2018/4342984

Gomes, J. A. P., Tan, D., Rapuano, C. J., Belin, M. W., Ambrósio, R., Jr., Guell, J. L., et al. (2015). Global Consensus on Keratoconus and Ectatic Diseases. *Cornea* 34 (4), 359–369. doi:10.1097/ico.0000000000000408

Hafezi, F., Kanellopoulos, J., Wiltfang, R., and Seiler, T. (2007). Corneal Collagen Crosslinking with Riboflavin and Ultraviolet A to Treat Induced Keratectasia after Laser *In Situ* Keratomileusis. *J. Cataract Refract Surg.* 33 (12), 2035–2040. doi:10.1016/j.jcrs.2007.07.028

Hashemi, H., Beiranvand, A., Yekta, A., Maleki, A., Yazdani, N., and Khabazkhoob, M. (2016). Pentacam Top Indices for Diagnosing Subclinical and Definite Keratoconus. *J. Curr. Ophthalmol.* 28 (1), 21–26. doi:10.1016/j.joco.2016.01.009

Kanellopoulos, J., and Asimellis, G. (2013). Revisiting Keratoconus Diagnosis and Progression Classification Based on Evaluation of Corneal Asymmetry Indices, Derived from Scheimpflug Imaging in Keratoconic and Suspect Cases. *Clin. Ophthalmol.* 7, 1539–1548. doi:10.2147/opth.s44741

Kanellopoulos, A. J., and Asimellis, G. (2014). Keratoconus Management: Long-Term Stability of Topography-Guided Normalization Combined with High-Fluence CXL Stabilization (The Athens Protocol). *J. Refract Surg.* 30 (2), 88–93. doi:10.3928/1081597x-20140120-03

Kobashi, H., Rong, S. S., and Ciolino, J. B. (2018). Transepithelial versus Epithelium-Off Corneal Crosslinking for Corneal Ectasia. *J. Cataract Refract Surg.* 44 (12), 1507–1516. doi:10.1016/j.jcrs.2018.08.021

Kohlhaas, M., Spoerl, E., Speck, A., Schilde, T., Sandner, D., and Pillunat, L. E. (2005). A New Treatment of Keratectasia after LASIK by Using Collagen with Riboflavin/UVA Light Cross-Linking. *Klin Monbl Augenheilkd* 222 (5), 430–436. doi:10.1055/s-2005-857950

Kymionis, G. D., Diakonis, V. F., Kalyvianaki, M., Portaliou, D., Siganos, C., Kozobolis, V. P., et al. (2009). One-Year Follow-Up of Corneal Confocal Microscopy after Corneal Cross-Linking in Patients with post Laser *In Situ* Keratosmileusis Ectasia and Keratoconus. *Am. J. Ophthalmol.* 147 (5), 774–778. doi:10.1016/j.ajo.2008.11.017

Kymionis, G. D., Kounis, G. A., Portaliou, D. M., Grentzelos, M. A., Karavitaki, A. E., Coskunseven, E., et al. (2009). Intraoperative Pachymetric Measurements during Corneal Collagen Cross-Linking with Riboflavin and Ultraviolet A Irradiation. *Ophthalmology* 116 (12), 2336–2339. doi:10.1016/j.ophtha.2009.09.018

Lang, P. Z., Hafezi, N. L., Khandelwal, S. S., Torres-Netto, E. A., Hafezi, F., and Randleman, J. B. (2019). Comparative Functional Outcomes after Corneal Crosslinking Using Standard, Accelerated, and Accelerated with Higher Total Fluence Protocols. *Cornea* 38 (4), 433–441. doi:10.1097/ico.0000000000001878

Li, M., Yang, D., Zhao, F., Han, T., Li, M., Zhou, X., et al. (2018). Thirty-Month Results after the Treatment of post-LASIK Ectasia with Allogenic Lenticule Addition and Corneal Cross-Linking: A Case Report. *BMC Ophthalmol.* 18 (1), 294. doi:10.1186/s12886-018-0967-z

Mannschreck, D. B., Rubinfeld, R. S., Soiberman, U. S., and Jun, A. S. (2019). Diffuse Lamellar Keratitis after Epi-Off Corneal Crosslinking: An Under-Recognized Complication? *Am. J. Ophthalmol. Case Rep.* 13, 140–142. doi:10.1016/j.ajoc.2019.01.004

Poli, M., Lefevre, A., Auxenfans, C., and Burillon, C. (2015). Corneal Collagen Cross-Linking for the Treatment of Progressive Corneal Ectasia: 6-Year Prospective Outcome in a French Population. *Am. J. Ophthalmol.* 160 (4), 654–662. doi:10.1016/j.ajo.2015.06.027

Randleman, J. B., Woodward, M., Lynn, M. J., and Stulting, R. D. (2008). Risk Assessment for Ectasia after Corneal Refractive Surgery. *Ophthalmology* 115 (1), 37–50. doi:10.1016/j.ophtha.2007.03.073

Richoz, O., Mavrakanas, N., Pajic, B., and Hafezi, F. (2013). Corneal Collagen Cross-Linking for Ectasia after LASIK and Photorefractive Keratectomy. *Ophthalmology* 120 (7), 1354–1359. doi:10.1016/j.ophtha.2012.12.027

Salgado, J. P., Khoramnia, R., Lohmann, C. P., and Winkler von Mohrenfels, C. (2011). Corneal Collagen Crosslinking in Post-LASIK Keratectasia. *Br. J. Ophthalmol.* 95 (4), 493–497. doi:10.1136/bjo.2010.179424

Seiler, T., Koufala, K., and Richter, G. (1998). Iatrogenic Keratectasia after Laser *In Situ* Keratomileusis. *J. Refract Surg.* 14 (3), 312–317. doi:10.3928/1081-597x-19980501-15

Shen, Y., Jian, W., Sun, L., Li, M., Han, T., Son, J., et al. (2016). One-Year Follow-Up of Changes in Corneal Densitometry after Accelerated (45 mW/cm2) Transepithelial Corneal Collagen Cross-Linking for Keratoconus. *Cornea* 35 (11), 1434–1440. doi:10.1097/ico.0000000000000934

Spadea, L., Cantera, E., Cortes, M., Evangelista Conocchia, N. E., and Stewart, C. W. (2012). Corneal Ectasia after Myopic Laser *In Situ* Keratomileusis: A Long-Term Study. *Clin. Ophthalmol.* 6, 1801–1813. doi:10.2147/opth.s37249

Stulting, D. R., Trattler, W. B., Woolfson, J. M., and Rubinfeld, R. S. (2018). Corneal Crosslinking without Epithelial Removal. *J. Cataract Refract Surg.* 44 (11), 1363–1370. doi:10.1016/j.jcrs.2018.07.029

Sueke, H., Ramasamy, B., Tey, A., and Kaye, S. (2011). Methodological Issues in Corneal Collagen Crosslinking in post-LASIK Keratectasia. *Br. J. Ophthalmol.* 95 (12), 1759–1760. doi:10.1136/bjophthalmol-2011-300680

Thorsrud, A., Nicolaissen, B., and Drolsum, L. (2012). Corneal Collagen Crosslinking *In Vitro*: Inhibited Regeneration of Human Limbal Epithelial Cells after Riboflavin-Ultraviolet-A Exposure. *J. Cataract Refract Surg.* 38 (6), 1072–1076. doi:10.1016/j.jcrs.2011.12.038

Tian, M., Jian, W., Sun, L., Shen, Y., Zhang, X., and Zhou, X. (2018). One-year Follow-Up of Accelerated Transepithelial Corneal Collagen Cross-Linking for Progressive Pediatric Keratoconus. *BMC Ophthalmol.* 18 (1), 75. doi:10.1186/s12886-018-0739-9

Tian, M., Jian, W., Zhang, X., Sun, L., and Zhou, X. (2020). Three-Year Follow-Up of Accelerated Transepithelial Corneal Cross-Linking for Progressive Paediatric Keratoconus. *Br. J. Ophthalmol.* 104 (11), 1608–1612. doi:10.1136/bjophthalmol-2019-315260

Wallerstein, A., Adiguzel, E., Gauvin, M., Mohammad-Shahi, N., and Cohen, M. (2017). Under-Flap Stromal Bed CXL for Early Post-LASIK Ectasia: A Novel Treatment Technique. *Clin. Ophthalmol.* 11, 1–8. doi:10.2147/OPTH.S118831

Yildirim, A., Cakir, H., Kara, N., Uslu, H., Gurler, B., Ozgurhan, E. B., et al. (2014). Corneal Collagen Crosslinking for Ectasia after Laser *In Situ* Keratomileusis: Long-Term Results. *J. Cataract Refract Surg.* 40 (10), 1591–1596. doi:10.1016/j.jcrs.2014.01.042

Yuksel, E., Bektas, C., and Bilgihan, K. (2015). Transepithelial Versus Epithelium-Off Corneal Cross-Linking for the Treatment of Progressive Keratoconus: A Randomized Controlled Trial. *Am. J. Ophthalmol.* 160 (2), 399–400. doi:10.1016/j.ajo.2015.05.022

Zhang, X., Sun, L., Chen, Y., Li, M., Tian, M., and Zhou, X. (2016). One-Year Outcomes of Pachymetry and Epithelium Thicknesses after Accelerated (45 mW/cm2) Transepithelial Corneal Collagen Cross-Linking for Keratoconus Patients. *Sci. Rep.* 6, 32692. doi:10.1038/srep32692

Zhang, X., Sun, L., Tian, M., Shen, Y., Li, M., Zhao, J., et al. (2020). Accelerated (45 mW/cm2) Transepithelial Corneal Cross-Linking for Progressive Keratoconus Patients: Long-Term Topographical and Clinical Outcomes. *Front. Med.* 7, 283. doi:10.3389/fmed.2020.00283

Zhao, Y., Li, M., Zhao, J., Knorz, M. C., Sun, L., Tian, M., et al. (2016). Posterior Corneal Elevation after Small Incision Lenticule Extraction for Moderate and High Myopia. *PLoS One* 11 (2), e0148370. doi:10.1371/journal.pone.0148370

Zhao, Y., Jian, W., Chen, Y., Knorz, M. C., and Zhou, X. (2017). Three-Year Stability of Posterior Corneal Elevation after Small Incision Lenticule

Extraction (SMILE) for Moderate and High Myopia. *J. Refract Surg.* 33 (2), 84–88. doi:10.3928/1081597x-20161117-01

Conflict of Interest: The authors declare that the research was conducted in the absence of any commercial or financial relationships that could be construed as a potential conflict of interest.

Publisher's Note: All claims expressed in this article are solely those of the authors and do not necessarily represent those of their affiliated organizations, or those of the publisher, the editors and the reviewers. Any product that may be evaluated in this article, or claim that may be made by its manufacturer, is not guaranteed or endorsed by the publisher.

frontiers in Bioengineering and Biotechnology

ORIGINAL RESEARCH
published: 22 December 2021
doi: 10.3389/fbioe.2021.766163

Distribution of Corneal Geometric Landmarks and Relationship Between Their Distances and Biomechanical Parameters in the Development of Keratoconus

Lei Tian[1,2†], Hui Zhang[3,4†], Li-Li Guo[5], Xiao Qin[3], Di Zhang[3,6], Lin Li[3,6], Ying Wu[7], Ying Jie[1] and Haixia Zhang[3,6]**

[1]Beijing Institute of Ophthalmology, Beijing Tongren Eye Center, Beijing Tongren Hospital, Capital Medical University and Beijing Ophthalmology and Visual Sciences Key Laboratory, Beijing, China, [2]Beijing Advanced Innovation Center for Big Data-Based Precision Medicine, Beihang University & Capital Medical University, Beijing, China, [3]School of Biomedical Engineering, Capital Medical University, Beijing, China, [4]Department of Medical Engineering, Peking Union Medical College Hospital, Chinese Academy of Medical Sciences, Beijing, China, [5]The First People's Hospital of Xuzhou, Jiangsu, China, [6]Beijing Key Laboratory of Fundamental Research on Biomechanics in Clinical Application, Capital Medical University, Beijing, China, [7]Department of Ophthalmology, Chinese People's Liberation Army General Hospital, Beijing, China

OPEN ACCESS

Edited by:
Yan Wang,
Tianjin Eye Hospital, China

Reviewed by:
Hongli Yang,
Devers Eye Institute, United States
Aike Qiao,
Beijing University of Technology, China

***Correspondence:**
Haixia Zhang
Zhanghx@ccmu.edu.cn
Ying Jie
jie_yingcn@aliyun.com

†These authors have contributed equally to this work and share first authorship.

Specialty section:
This article was submitted to Biomechanics, a section of the journal Frontiers in Bioengineering and Biotechnology

Received: 28 August 2021
Accepted: 21 October 2021
Published: 22 December 2021

Citation:
Tian L, Zhang H, Guo L-L, Qin X, Zhang D, Li L, Wu Y, Jie Y and Zhang H (2021) Distribution of Corneal Geometric Landmarks and Relationship Between Their Distances and Biomechanical Parameters in the Development of Keratoconus. Front. Bioeng. Biotechnol. 9:766163. doi: 10.3389/fbioe.2021.766163

Purpose: To analyze the changes in coordinates and distances among three typical geometric landmarks of the cornea, namely, the thinnest point (TP), maximum curvature (Kmax), and corneal apex (AP) during the development of keratoconus, and explore the potential relationship between these changes and the abnormalities of corneal biomechanics.

Methods: Normal eyes (n = 127), clinical keratoconic eyes (CKC, n = 290), and the eyes of forme fruste keratoconus (FFKC, n = 85) were included; among them, the CKC group was classified into four grades based on the Topographic Keratoconus Classification (TKC) provided by Pentacam. A total of 38 Corvis ST output parameters and three distance parameters of three typical landmarks ($D_{Kmax\text{-}AP}$, $D_{TP\text{-}AP}$, and $D_{Kmax\text{-}TP}$) based on Pentacam were included. The differences of parameters among the abovementioned six groups (Normal, FFKC, and CKC stage I to CKC stage IV) were analyzed. Spearman's rank correlation test was performed to choose several dynamic corneal response (DCR) parameters that could best reflect the changes of corneal biomechanical characteristics during the progression of the disease, and the Pearson's or Spearman's correlation test was conducted to determine the association between the three distances and the selected DCR parameters in each grade. In addition, by flipping the X coordinate of the left eye on the vertical axis to reflect the direction of the right eye, the coordinates of TP and Kmax in different developmental grades were highlighted.

Results: From CKC stage II, the three geometric landmark distances commenced to correlate with the corneal DCR parameters (CBI, SPA1, IR, DA Ratio 2, ARTh, MIR, Radius, Pachy, and DA Ratio 1), which could better represent the changes of biomechanical properties from normal cornea to keratoconus. From normal cornea to CKC stage IV, the

coordinates of Kmax were gradually tended to the inferior temporal region from dispersion, while TP was always concentrated in the inferior temporal region. Although $D_{Kmax-AP}$, $D_{Kmax-TP}$, and D_{TP-AP} all showed a gradual decreasing trend with the progress of the disease, the first two did not change significantly, and only D_{TP-AP} significantly approached AP in the later stage of disease development. In addition, from the FFKC group, the corresponding values of $D_{Kmax-TP}$ in each disease development group were smaller than $D_{Kmax-AP}$.

Conclusions: In the later stage of keratoconus, the relationship between the three typical landmark distance parameters and DCR parameters is stronger, and even the weakening of corneal biomechanical properties may be accompanied by the merger of typical landmark positions.

Keywords: keratoconus, forme fruste keratoconus, morphology, biomechanics, geometric landmark

INTRODUCTION

With respect to in-depth understanding of the biomechanical mechanism of corneal diseases, evaluation of the biomechanical properties of cornea has greatly attracted scholars' attention in terms of prevention and treatment of corneal dilatation diseases, especially keratoconus (Herber et al., 2019). It has been gradually found that the biomechanical properties of the cornea depend on the collagen fiber, collagen fiber bundle, and their spatial structure composition (Oxlund and Simonsen, 1985), and studies (Meek et al., 2005; Catalán-López et al., 2018) have shown that the mechanical strength of keratoconus is often remarkably weaker than that of normal cornea. In addition, a number of scholars have pointed out that the morphological changes of keratoconus may be secondary to the changes in corneal biomechanics (Roberts et al., 2017; Sedaghat et al., 2018).

At present, the Ocular Response Analyzer (ORA) and Corneal Visualization Scheimpflug Technology (Corvis ST) are the two most recognized devices for the measurement of cornea biomechanics *in vivo*. Among them, ORA cannot display the process of corneal deformation dynamically in real time, and its main biomechanical parameters, corneal hysteresis (CH) and corneal resistance factor (CRF), are derived by analyzing the measured waveforms (McMonnies, 2012), while Corvis ST can dynamically record the whole process under impulse pressure and generate DCR parameters to reflect the biomechanical characteristics of cornea (Elham et al., 2017). For now, the combined diagnosis of keratoconus with Corvis ST and three-dimensional anterior segment analysis and diagnosis system Pentacam, which characterizes the morphological features of cornea, has been clinically recognized.

That is to say, although morphological changes are not the primary cause of keratoconus, its diagnostic value cannot be easily ignored. As we all know, the most typical morphological change of keratoconus is the thinning and protruding of cornea (Hashemi et al., 2019). To date, numerous studies (Galletti et al., 2015; Chan et al., 2018) have concentrated on the analysis of the numerical changes of the thinnest thickness and the maximum curvature caused by the gradual corneal protrusion, while few people have analyzed the coordinates of these two typical geometric landmarks and the distance between them and the central apex of the cornea. Only several studies simply compared the distance between the cornea apex and the thinnest point of cornea in different groups, and found that there were remarkable differences among normal cornea, subclinical keratoconus (Muftuoglu et al., 2013), and clinical keratoconus (Muftuoglu et al., 2015).

As mentioned above, DCR parameters and distance parameters of typical geometric landmarks representing morphological characteristics are both significantly different between normal cornea and keratoconus. Thus, we speculated that there may be a certain correlation between the DCR parameters and distance parameters with the development of keratoconus disease.

The main purpose of the present study was to evaluate the relationship between the distances among the typical geometric landmarks of cornea and the DCR parameters output by Corvis ST in the assumed different grades of keratoconus development, and explore more potential patterns of disease development.

PATIENTS AND METHODS

Study Subjects

This prospective comparative study included patients with clinical keratoconus (CKC group), forme fruste keratoconus (FFKC group), and candidates undergoing refractive surgery with normal corneas (Normal group).

A diagnosis of keratoconus was made if the eye met the following conditions (Tian et al., 2014; Cui et al., 2016): (1) an irregular cornea determined by distorted keratometry mires, distortion of the retinoscopic or ophthalmoscopic red reflex (or a combination of the two); (2) with at least one of the following biomicroscopic signs: Vogt's striae, Fleischer's ring of >2 mm arc, or corneal scarring consistent with keratoconus. In the CKC group, the seven classes of topographic keratoconus classification (TKC) provided by Pentacam (Oculus, Wetzlar, Germany) were included (i.e., 1, 1-2, 2, 2-3, 3, 3-4, and 4). Those classes could be divided into four four subgroups based on their TKC number: TKC 1 was classified as

CKC stage I, TKC 1-2 and 2 were classified as CKC stage II, TKC 2-3 and 3 were classified as CKC stage III, and TKC 3-4 and 4 were classified as CKC stage IV.

An eye was diagnosed with FFKC if it was the fellow eye of a patient with keratoconus and showed the following features (Peña-García et al., 2016): (1) a normal-appearing cornea on slit-lamp examination, retinoscopy, and ophthalmoscopy; (2) topography was normal with no asymmetric bowtie and no focal or inferior steepening pattern; (3) the level of TKC was normal, namely, it was "-"; and (4) the patient had no history of contact lens use, ocular surgery, or trauma. For participants undergoing refractive surgery, only one eye from each individual was chosen using a random numbers table. In addition, the TKC level of eyes in the Normal group and FFKC group was normal.

Exclusion criteria were a history of undergoing ocular surgery and cases with eye diseases that may potentially affect the outcomes. For contact lens-wearing patients, they were asked to remove soft contact lenses at least 2 weeks and rigid contact lenses at least 1 month before assessment. Data were collected from May 2013 to January 2020 at the Beijing Tongren Hospital affiliated to Capital Medical University (Beijing, China). All participants signed the written informed consent form prior to commencing the study. The study was carried out in accordance with the Declaration of Helsinki, and it was approved by the Ethics Committee of the Beijing Tongren Hospital affiliated to Capital Medical University.

Ocular Examination

A comprehensive ocular examination was performed on all eyes, including uncorrected visual acuity, slit-lamp and fundoscopic examinations, Pentacam tomographic examination, and Corvis ST (Oculus; Wetzlar, Germany) measurements. All measurements were undertaken between 9:00 a.m. and 5:00 p.m. by the same trained ophthalmologists during the same visit.

Pentacam Measurement

The Pentacam software (ver. 1.20r134) reconstructs a three-dimensional (3D) image of the entire anterior segment from the anterior surface of the cornea to the posterior surface of the lens by utilizing the high-speed rotating Scheimpflug system. Details and principles of the Pentacam are described elsewhere (Cui et al., 2016). Only scans that the Pentacam's "quality specification" (QS) function determined as "OK" were included for analysis.

In the study, we focused on three points on the cornea: corneal apex (AP), thinnest point (TP), and maximum curvature (Kmax). Extracted parameters from Pentacam data for analysis included the coordinates of TP (TP X, TP Y) and Kmax (Kmax X, Kmax Y); then, we calculated the absolute distances from the cornea apex (geometric center of the examination [x = 0; y = 0]): $D_{TP\text{-}AP}$ and $D_{Kmax\text{-}AP}$, and the distance between Kmax and TP ($D_{Kmax\text{-}TP}$). The formula of distance was as follows:

$$d = \sqrt{(x_1 - x_2)^2 + (y_1 - y_2)^2}$$

Corvis ST Measurement

The Corvis ST software (ver. 1.5r1902) measures dynamic corneal deformation response to an air-puff pulse. Details and principles of the Corvis ST are described elsewhere (Elham et al., 2017). The measurements were checked under the QS window; only correct measurements were accepted (comment box reading "OK"). If the comment box was marked yellow or red, the examination was repeated. The following parameters were detected by Corvis ST: intraocular pressure (IOP), Pachymetry (Pachy), time from the initiation of air puff until the first applanation (A1T), second applanation (A2T) and maximum deformation (HCT), corneal velocity at the first (A1V) and second applanation (A2V), peak distance (PD) and radius of curvature (Radius), deformation amplitude at the first applanation (A1DA), second applanation (A2DA) and highest concavity (HCDA), deflection length at the first applanation (A1DLL), second applanation (A2DLL) and highest concavity (HCDLL), deflection amplitude at the first applanation (A1DLA), second applanation (A2DLA) and highest concavity (HCDLA), deflection area at the first applanation (A1DLAr), second applanation (A2DLAr) and highest concavity (HCDLAr), delta arc length at the first applanation (A1dArcL), second applanation (A2dArcL) and highest concavity (HCdArcL), max time and length at deflection amplitude (DLAMT, DLAML), max time and amplitude of whole eye movement (WEMT, WEMA), delta arc length max (dArcLM) and PachySlope, the maximal value of the ratio between deformation amplitude at the apex and that at 1 (DA Ratio 1) and 2 mm (DA Ratio 2) from the corneal apex, max inverse radius (MIR) and integrated radius (IR), Ambrósio relational thickness to the horizontal profile (ARTh), Biomechanical-corrected intraocular pressure (bIOP), stiffness parameter at first applanation (SPA1), and Corvis biomechanical index (CBI).

Statistical Analysis

Statistical analysis was performed using SPSS 20.0 (IBM, Armonk, NY, USA). Drawing was completed by R Core Team (version 3.6.1; R Foundation for Statistical Computing, Vienna, Austria; https://www.R-project.org/) software and GraphPad Prism software version 8.0, respectively.

The Shapiro–Wilk test was used to assess normal distribution of quantitative data. The normally distributed data were expressed as the mean ± standard deviation (SD), while abnormally distributed data were presented as median and range of variation.

One-way analysis of variance (ANOVA) test or non-parametric Kruskal–Wallis test was used to analyze the differences among the four subgroups of CKC group, Normal group, and FFKC group. Spearman's rank correlation test was performed to assess correlation among all parameters measured by Corvis ST and the developmental grades of keratoconus (Rank-group). Then, the Pearson's or Spearman's correlation test was applied to determine the association between the distance of three geometric landmarks and the above selected DCR parameters in each grade, and Bonferroni correction was performed ($p < 0.0056$). Moreover, we plotted the variation trend of three typical landmark distance parameters and the selected

TABLE 1 | Comparison of distance of three geometric landmarks and DCR parameters by groups.

	Normal group (*n* = 142)	FFKC group (*n* = 93)	CKC group (*n* = 290)				*p*-value
			Stage I (*n* = 54)	Stage II (*n* = 123)	Stage III (*n* = 82)	Stage IV (*n* = 31)	
Geometric landmarks distances							
$D_{Kmax\text{-}AP}$ [mm]	1.02 (0.06–4.78)	1.13 (0.06–5.13)	1.12 (0.13–3.03)	1.17 ± 0.66	0.89 (0.13–2.84)	0.85 ± 0.59	0.058[a]
$D_{TP\text{-}AP}$ [mm]	0.72 ± 0.19	0.76 (0.29–1.92)	0.77 ± 0.30	0.74 (0.06–2.96)	0.58 (0.13–2.25)	0.41 (0.18–1.26)	<0.001[a]
$D_{Kmax\text{-}TP}$ [mm]	1.04 (0.01–5.17)	1.16 (0.14–5.00)	0.98 (0.21–2.52)	0.93 (0.08–2.45)	0.83 ± 0.40	0.43 (0.13–1.91)	<0.001[a]
DCR parameters (Corvis ST's output parameters)							
IOP [mmHg]	14.5 (9.0–30.5)	13.6 ± 2.1	13.5 (8.0–30.0)	11.5 (5.0–19.0)	10.5 ± 2.3	10.4 ± 3.0	<0.001[a]
Pachy [μm]	543 ± 34	518 ± 33	502 ± 26	479 (402–591)	461 ± 32	449 ± 37	<0.001[a]
A1T [ms]	7.319 (6.782–8.990)	7.172 ± 0.225	7.156 (6.590–8.934)	6.992 ± 0.240	6.857 ± 0.222	6.873 ± 0.287	<0.001[a]
A1V [m/s]	0.146 ± 0.021	0.158 (0.095–0.196)	0.160 ± 0.021	0.170 ± 0.020	0.181 ± 0.023	0.185 ± 0.020	<0.001[a]
A2T [ms]	21.892 ± 0.400	21.961 ± 0.378	21.902 ± 0.378	22.132 ± 0.350	22.249 ± 0.338	22.260 ± 0.396	<0.001[b]
A2V [m/s]	−0.277 (−0.363 to −0.118)	−0.288 (−0.356 to −0.166)	−0.297 ± 0.044	−0.322 ± 0.046	−0.345 (−0.562 to −0.149)	−0.348 ± 0.049	<0.001[a]
HCT [ms]	16.863 (15.477–18.108)	16.863 (15.246–18.249)	17.094 (15.708–17.787)	16.863 (15,477–18.018)	17.094 (14.784–17.787)	16.772 ± 0.409	0.098[a]
PD [mm]	5.194 (4.228–5.768)	5.209 ± 0.268	5.142 ± 0.289	5.268 ± 0.286	5.311 ± 0.278	5.283 (4.569–5.559)	0.009[a]
Radius [mm]	7.387 ± 0.766	6.833 ± 0.768	6.316 ± 0.678	5.850 (4.152–9.040)	5.391 ± 0.670	5.090 ± 0.867	<0.001[a]
A1DA [mm]	0.131 ± 0.011	0.132 (0.098–0.150)	0.136 ± 0.010	0.137 (0.105–0.191)	0.141 ± 0.015	0.154 ± 0.017	<0.001[a]
HCDA [mm]	1.074 ± 0.110	1.116 ± 0.110	1.138 ± 0.116	1.192 (0.943–1.676)	1.281 (1.037–1.877)	1.298 (1.125–1.756)	<0.001[a]
A2DA [mm]	0.373 (0.244–0.617)	0.373 ± 0.068	0.381 ± 0.064	0.367 (0.226–0.567)	0.398 ± 0.074	0.394 (0.268–0.702)	0.246[a]
A1DLL [mm]	2.313 (1.835–2.895)	2.300 (1.891–2.684)	2.319 ± 0.129	2.339 ± 0.143	2.362 ± 0.184	2.394 ± 0.173	0.008[a]
HCDLL [mm]	6.832 (5.614–7.788)	6.708 ± 0.498	6.575 ± 0.518	6.674 ± 0.460	6.610 ± 0.472	6.380 ± 0.496	0.003[a]
A2DLL [mm]	2.716 (1.660–4.234)	2.652 (1.630–4.510)	2.608 (1.582–6.441)	2.866 ± 0.642	2.910 ± 0.680	2.877 ± 0.510	0.910[a]
A1DLA [mm]	0.094 ± 0.008	0.095 ± 0.007	0.099 ± 0.008	0.103 (0.079–0.166)	0.110 ± 0.014	0.120 ± 0.016	<0.001[a]
HCDLA [mm]	0.923 ± 0.104	0.965 ± 0.105	0.967 ± 0.116	1.061 ± 0.134	1.122 (0.870–1.734)	1.158 ± 0.122	<0.001[a]
A2DLA [mm]	0.103 (0.080–0.142)	0.107 (0.080–0.142)	0.104 (0.078–0.162)	0.115 (0.090–0.250)	0.124 (0.083–0.209)	0.138 ± 0.017	<0.001[a]
DLAML [mm]	0.938 ± 0.105	0.979 ± 0.111	0.972 ± 0.131	1.063 (0.825–1.558)	1.140 (0.905–1.936)	1.169 ± 0.120	<0.001[a]
DLAMT [ms]	16.388 (14.637–17.455)	16.334 (13.677–17.684)	16.436 (14.350–17.396)	16.438 (14.535–17.605)	16.297 (8.419–17.397)	16.219 ± 0.609	0.978[a]
WEMA [mm]	0.270 (0.156–0.504)	0.271 ± 0.066	0.276 ± 0.062	0.260 (0.143–0.445)	0.278 (0.155–0.482)	0.255 (0.181–0.562)	0.943[a]
WEMT [ms]	21.742 (20.585–23.230)	21.862 (20.536–23.701)	21.454 ± 1.760	21.823 (20.070–23.544)	21.997 ± 0.467	21.879 ± 0.460	<0.001[a]
A1DLAr [mm^2]	0.180 ± 0.027	0.176 ± 0.023	0.185 ± 0.023	0.190 ± 0.030	0.206 ± 0.038	0.221 ± 0.045	<0.001[b]
HCDLAr [mm^2]	3.457 ± 0.549	3.577 ± 0.555	3.470 ± 0.590	3.878 (2.433–6.218)	3.981 (2.846–7.195)	4.067 ± 0.520	<0.001[a]
A2DLAr [mm^2]	0.233 ± 0.041	0.234 (0.171–0.369)	0.232 (0.167–0.373)	0.260 (0.152–0.736)	0.280 (0.152–0.534)	0.307 ± 0.056	<0.001[a]
A1dArcL [mm]	−0.019 (−0.029 to −0.008)	−0.019 (−0.022 to −0.005)	−0.019 ± 0.003	−0.020 ± 0.004	−0.021 (−0.040 to −0.012)	−0.025 ± 0.007	<0.001[a]
HCdArcL [mm]	−0.135 ± 0.028	−0.127 ± 0.024	−0.115 ± 0.020	−0.119 (-0.230 to −0.014)	−0.115 (−0.231 to −0.019)	−0.115 ± 0.032	<0.001[a]
A2dArcL [mm]	−0.022 (−0.036 to −0.004)	−0.023 (−0.040 to −0.016)	−0.023 (-0.036 to -0.016)	−0.025 (−0.057 to 0.006)	−0.029 ± 0.008	-0.031 (-0.051 to 0.002)	<0.001[a]
dArcLM [mm]	−0.153 ± 0.035	−0.148 ± 0.030	−0.146 ± 0.064	−0.142 (−0.452 to −0.034)	−0.135 (−0.399 to −0.041)	−0.137 (−0.270 to -0.050)	0.023[a]
MIR [mm^{-1}]	0.167 ± 0.016	0.178 (0.140–0.259)	0.199 ± 0.024	0.209 ± 0.026	0.223 (0.170–0.336)	0.251 ± 0.040	<0.001[a]
DA Ratio 2	4.188 (3.081–5.946)	4.646 ± 0.440	4.880 ± 0.596	5.409 ± 0.786	6.208 ± 0.861	6.615 ± 1.013	<0.001[a]
PachySlope [μm]	50.435 (29.036–98.805)	50.480 ± 10.247	55.290 ± 13.335	65.865 (−24.281–145.630)	76.817 (38.351–154.705)	98.906 ± 24.373	<0.001[a]
DA Ratio 1	1.558 (1.407–1.729)	1.593 ± 0.044	1.613 ± 0.052	1.650 (1.509–1.918)	1.710 (1.560–1.971)	1.744 ± 0.074	<0.001[a]
ARTh	415.883 ± 86.639	392.170 ± 92.140	322.116 (195.308–603.057)	226.520 (28.989–630.625)	174.476 (71.233–417.461)	133.123 ± 56.762	<0.001[a]
	14.7 (10.8–26.5)	14.3 ± 1.9	14.6 (10.4–29.2)	13.3 ± 2.3	12.4 ± 2.2	12.6 ± 2.9	<0.001[a]

(Continued on following page)

TABLE 1 | (*Continued*) Comparison of distance of three geometric landmarks and DCR parameters by groups.

	Normal group (*n* = 142)	FFKC group (*n* = 93)	CKC group (*n* = 290)				*p*-value
			Stage I (*n* = 54)	Stage II (*n* = 123)	Stage III (*n* = 82)	Stage IV (*n* = 31)	
bIOP [mmHg]							
IR [mm^{-1}]	7.918 (5.300–12.555)	8.898 ± 1.025	9.698 ± 1.192	10.858 ± 1.716	11.967 (8.085–17.603)	13.401 ± 2.298	<0.001[a]
SPA1	102.040 ± 19.505	85.088 ± 16.692	77.961 ± 18.804	59.822 ± 15.639	47.491 ± 12.512	41.476 ± 14.298	<0.001[b]
CBI	0.065 (0.000–1.000)	0.404 (0.001–1.000)	0.957 (0.000–1.000)	1.000 (0.001–1.000)	1.000 (0.943–1.000)	1.000 (0.970–1.000)	<0.001[a]

[a]*Non-parametric Kruskal–Wallis test.*
[b]*One-way ANOVA test.*

DCR parameters with the progress of disease stage. The differences of parameters in any disease stage and its adjacent previous disease stage were compared by independent sample *t*-test or nonparametric Mann–Whitney test, and Bonferroni correction was performed ($p < 0.01$).

In addition, with flipping the X coordinate of the left eye on the vertical axis to reflect the direction of the right eye, the coordinates of Kmax and TP in different developmental grades of keratoconus were drawn. $p < 0.05$ was considered statistically significant, except for the Bonferroni correction.

RESULTS

Herein, 290 eyes of 223 patients (mean age, 23.19 ± 7.39 years old; range of age, 9–53 years old) were assigned to the CKC group, of whom both eyes of 59 patients were included, one eye of 85 patients was involved because of unilateral keratoconus, and one eye of 79 patients was included because the fellow eye had undergone eye surgery or the quality of the examination did not meet the predefined criteria. The normal contralateral eye of the unilateral keratoconus constituted the FFKC group (mean age, 23.61 ± 7.73 years old; range of age, 10–49 years old). The Normal group consisted of 127 normal individuals (mean age, 24.39 ± 4.38 years old; range of age, 15–37 years old), and only one eye per person was randomly evaluated. There were no statistically significant differences between the groups in age distribution ($p = 0.065$, the Kruskal–Wallis test).

With the exception of $D_{Kmax\text{-}AP}$, HCT, A2DA, A2DLL, DLAMT, and WEMA, statistically significant differences in other parameters were found among four subgroups of the CKC group, Normal group, and FFKC group ($p < 0.05$) (**Table 1**).

Figure 1 shows the correlation among 38 parameters measured by Corvis ST and developmental grades of keratoconus. The results unveiled that there were nine DCR parameters that were strongly correlated with Rank-group ($|r| > 0.6$), and they were CBI, SPA1, IR, DA Ratio 2, ARTh, MIR, Radius, and Pachy in the order of correlation from high to low. **Figure 2** shows the change trend of the nine DCR parameters screened above with the increase of disease stage. Obviously, these nine parameters would change significantly in the process of disease progression (normal to CKC stage IV), that is, gradually increased or decreased.

Figure 3 illustrates the coordinates of Kmax and TP in different developmental grades of keratoconus, and **Figure 4** depicts the variation trend of three typical landmark distance parameters of geometric landmarks with the progress of disease stage. As shown in **Figure 3**, from normal to CKC stage IV, the coordinates of Kmax were gradually concentrated from dispersion, and finally tended to the inferior temporal region, while the coordinates of TP were always concentrated in the inferior temporal region. However, it can be seen from **Figure 4** that although $D_{Kmax\text{-}AP}$, $D_{Kmax\text{-}TP}$, and $D_{TP\text{-}AP}$ all showed a gradual decreasing trend with the progress of the disease, the first two ($D_{Kmax\text{-}AP}$ and $D_{Kmax\text{-}TP}$) did not change significantly, and only $D_{TP\text{-}AP}$ significantly approached AP in the later stage of disease development.

Figure 5 represents the correlation between the three geometric landmark distance parameters and the abovementioned nine DCR parameters in each grade from normal to CKC stage IV. From the results, it could be seen that starting from CKC stage II, the distance parameters of the three geometric landmarks were correlated with the DCR parameters ($p < 0.0056$), and with the aggravation of disease, the correlation between the two parameters of $D_{Kmax\text{-}AP}$ and $D_{Kmax\text{-}TP}$ with the DCR parameters was basically strengthened.

DISCUSSION

The purpose of the present study was to analyze the changes in coordinates and distances between the three typical geometric landmarks, namely, the thinnest point (TP), the maximum curvature (Kmax), and corneal apex (AP) during the development of keratoconus (Normal, FFKC, and CKC stage I to CKC stage IV), as well as to explore the potential relationship among these changes and the abnormalities of corneal biomechanics.

Our results showed that from normal cornea to CKC stage IV, the coordinates of Kmax gradually tended to focus from the scattered distribution, and finally concentrated on the region under the temporal cornea. However, although the coordinates of Kmax were converging gradually, in fact, its variation range was basically stable within the range of 2 mm in diameter. For TP, as mentioned in other studies (Muftuoglu et al., 2013; Huseynli et al., 2018), it is always concentrated in the inferior temporal

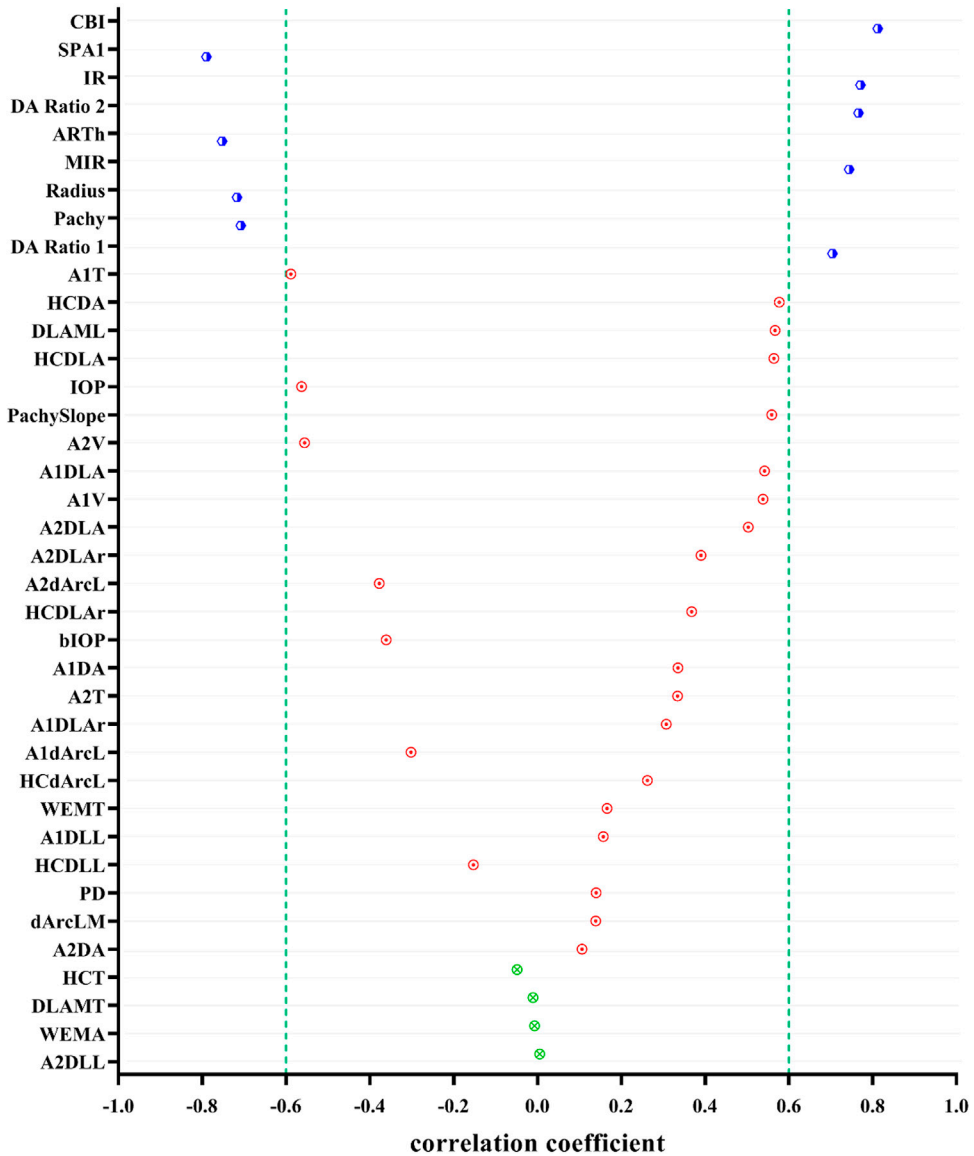

FIGURE 1 | Spearman correlations of DCR parameters and the developmental grades of keratoconus (strong correlation: $0.6 \leq |r| < 1$ and $p < 0.05$, weak correlation: $|r| < 0.6$ and $p < 0.05$, irrelevant: $p \geq 0.05$).

region of the cornea, indicating inferior decentration of the thinnest point of the cornea in eyes with early keratoconus. In addition, although there was no significant change in $D_{Kmax\text{-}AP}$ and $D_{Kmax\text{-}TP}$ in the process of disease progression, it should be pointed out that $D_{Kmax\text{-}TP}$ values of each disease grade from FFKC were basically smaller than $D_{Kmax\text{-}AP}$, which also illustrated that Kmax might be more inclined to corresponding TP than AP with the development of keratoconus to a certain extent.

Previous studies (Kaya et al., 2007; Ashwin et al., 2009) found that the average distance between the TP and AP in normal eyes was 0.52–1.01 mm, and that in keratoconus eyes was 0.78 mm, which was basically consistent with the results of the current study: normal group (0.72 mm), FFKC group (0.79 mm), and CKC group (0.70 mm). It can be seen from the results of this study that from CKC stage II, the value of $D_{TP\text{-}AP}$ would gradually decrease with significant changes, that is, TP would be relatively close to AP in the late stage of disease development. Combined with the discussion in the previous paragraph, it seems that in the late development of keratoconus disease, there will be a trend of proximity or merging between the typical landmark positions of the cornea.

In the present study, there were nine DCR parameters (CBI, SPA1, IR, DA Ratio 2, ARTh, MIR, Radius, Pachy, and DA Ratio 1) that had strong correlation with Rank-group; that is to say, they

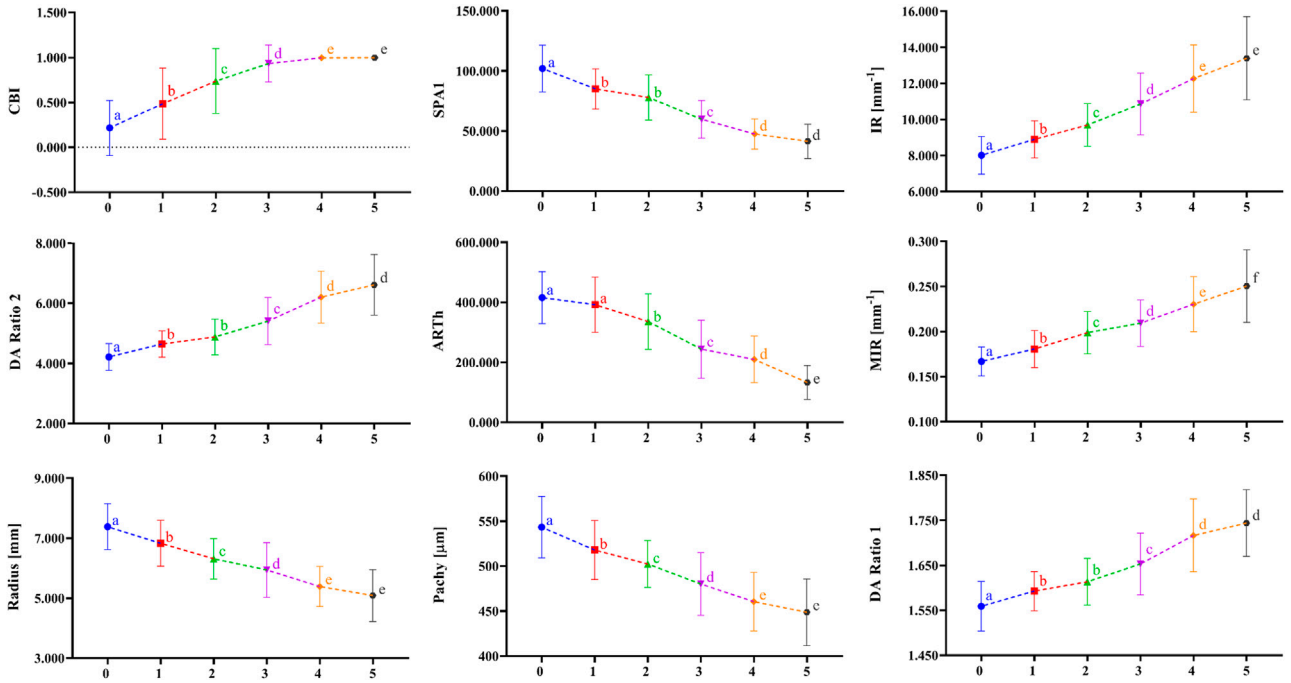

FIGURE 2 | The change tendency of DCR parameters, which are highly correlated as disease progression with the disease stage increasing. a, b, c, d, and e indicate that the parameters in a certain stage are statistically different from the corresponding parameters in the previous adjacent stage ($p < 0.01$); 0 = Normal group, 1 = FFKC group, 2 = CKC Stage I group, 3 = CKC Stage II group, 4 = CKC Stage III group, 5 = CKC Stage IV group.

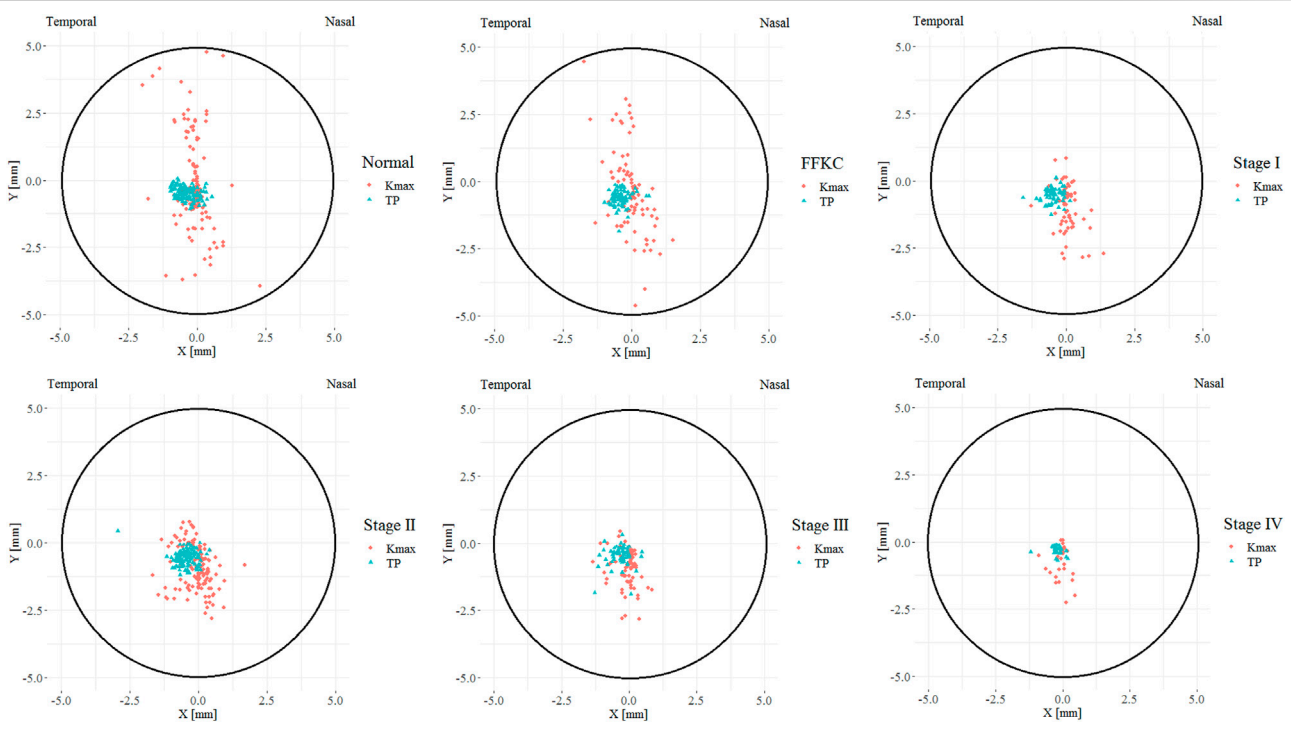

FIGURE 3 | The coordinate distribution of TP and Kmax in different developmental grades of keratoconus, where the X coordinate of the left eye was flipped on the vertical axis to reflect the direction of the right eye (TP = Thinnest point; Kmax = Maximum keratometry of the front surface).

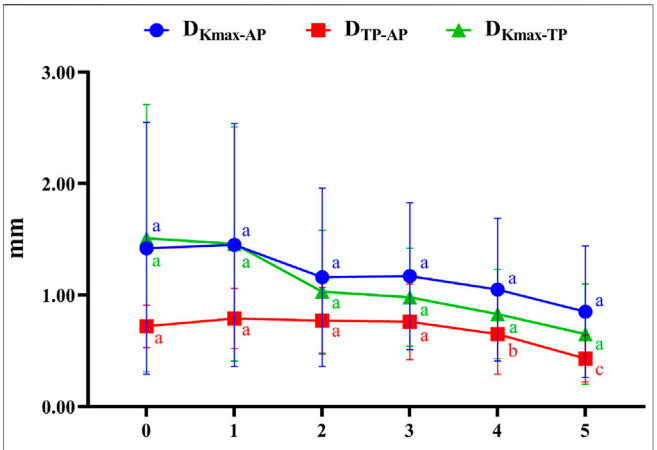

FIGURE 4 | The variation trend of three typical landmark distance parameters with the progress of disease stage (0 = Normal group, 1 = FFKC group, 2 = CKC Stage I group, 3 = CKC Stage II group, 4 = CKC Stage III group, 5 = CKC Stage IV group; $D_{Kmax\text{-}AP}$: the absolute distances from the maximum curvature of the anterior surface to the apex of the cornea; $D_{Kmax\text{-}TP}$: the absolute distances from the maximum curvature of the anterior surface to the thinnest point; $D_{TP\text{-}AP}$: the absolute distances from the cornea apex (geometric center of the examination [x = 0; y = 0]) to the thinnest point).

could well represent the changes in morphological characteristics and biomechanical behavior of cornea during the progress of keratoconus. Studies (Kataria et al., 2019; Yang et al., 2019) pointed out the significant role of these parameters in the diagnosis of keratoconus, which was confirmed by the area under the receiver operating characteristic (ROC) curve. Among the above parameters, in addition to Pachy, ARTh is another DCR parameter that more characterizes the changes of corneal geometric characteristics, which is calculated by the division between corneal thickness at the thinnest point and pachymetric progression index, and a lower value means a faster increase of thickness toward the periphery or a thinner cornea (Vinciguerra et al., 2016). The DA Ratio 1 and DA Ratio 2 are measured at 1 or 2 mm from the center (Wang et al., 2017), and a greater value indicates less resistance to the cornea or a softer cornea. For SPA1, it is developed by using displacement of the apex from the undeformed state to first applanation in the deformation process, and it more characterizes the stiffness behavior of cornea to resist deformation (Vinciguerra et al., 2016). That is, the smaller the SPA1, the smaller the overall stiffness of the cornea. The MIR is the maximum value of radius of curvature during concave phase of the deformation (Yang

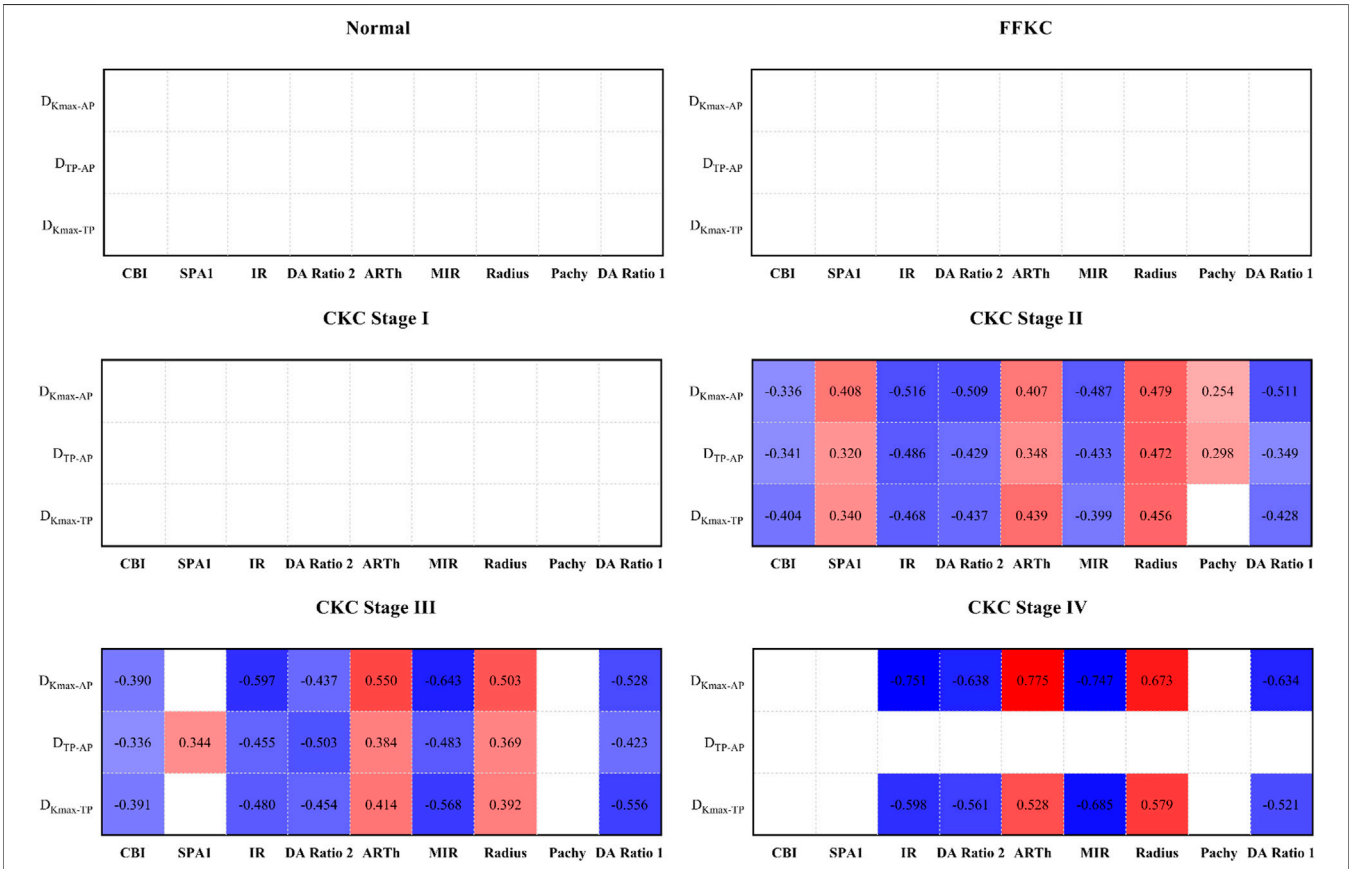

FIGURE 5 | Correlation between the three geometric landmark distance parameters and the nine DCR parameters in each grade from normal to CKC Stage IV (the small lattice filled with color indicates that the correlation is statistically significant, in which red indicates that the correlation coefficient is positive, blue indicates that the correlation coefficient is negative, and the depth of color indicates the absolute value of the correlation coefficient).

et al., 2019), while IR is defined as the area under the inverse radius curve with respect to time, and with the progress of keratoconus, both gradually increases, that is, the cornea gradually softens. Of course, the significant trend of the above parameters that can characterize the biomechanical properties of cornea with the increase of disease developmental grades further shows that the cornea will gradually soften during the process of disease progression, that is, the biomechanical properties will gradually weaken (Scarcelli et al., 2014).

According to the results, we found that starting from CKC stage II, the three geometric landmark distance parameters, namely, $D_{Kmax\text{-}TP}$, $D_{Kmax\text{-}AP}$, and $D_{TP\text{-}AP}$, began to be correlated with the selected biomechanical parameters, and with the aggravation of disease, the correlation between the two parameters ($D_{Kmax\text{-}TP}$ and $D_{Kmax\text{-}AP}$) and the corneal biomechanical parameters was basically strengthened. On this basis, if we synthesize the above discussion, that is, there will be certain proximity or merger between the typical landmark positions of cornea in the later stage of disease development, it is not difficult to believe that the weakening of corneal biomechanical properties may be accompanied by the merger between the typical landmark positions of cornea, especially in the later stage of disease progression.

Of course, our study also had certain limitations. First of all, we did not consider the cone center and the distances in this study because the cone centers of keratoconus were not available in the Pentacam data. Thus, if we can obtain the cone centers of anterior and posterior corneal surfaces by using the Pentacam data, further relevant analysis on the coordinate of the cone center should be carried out in the future research. In addition, this study was not a longitudinal study in the strict sense. The reason why the cross-sectional data were used to study some changes in the development of keratoconus was that the course of keratoconus disease itself was irreversible and would continue to deteriorate over time.

In conclusion, in the later stage of keratoconus, the relationship between the three typical landmark distance parameters and DCR parameters is stronger, and even the weakening of corneal biomechanical properties may be accompanied by the merger of typical landmark positions. It is believed that these findings have certain value for us to further understand the significance of corneal response parameters under external force. Moreover, the coordinate of Kmax may also be used as a reference parameter to judge the disease stage in the future; that is, it will gradually tend to focus from dispersion with the progress of the disease.

DATA AVAILABILITY STATEMENT

The original contributions presented in the study are included in the article/supplementary material. Further inquiries can be directed to the corresponding authors.

ETHICS STATEMENT

The studies involving human participants were reviewed and approved by the Ethics Committee of the Beijing Tongren Hospital. Written informed consent to participate in this study was provided by the participants' legal guardian/next of kin.

AUTHOR CONTRIBUTIONS

LT and HZ contributed equally to this work. HZ, L-LG, XQ, and DZ collected data that met the inclusion criteria. LT conceived the original idea, provided guidance for clinical knowledge, and revised the article. HZ completed the statistical analysis and produced the first draft of the manuscript. LL and YW helped analyze the data and revised the article. YJ and HX-Z helped supervise the project and gave critical revision of article. All authors contributed to manuscript revision, read, and approved the submitted version.

FUNDING

This work was financially supported by grants from the National Natural Science Foundation of China (32171304 and 82171101); Beijing Nova Program (Z181100006218099); and The Open Research Fund from Beijing Advanced Innovation Center for Big Data-Based Precision Medicine, Beijing Tongren Hospital, Beihang University & Capital Medical University (BHTR-KFJJ-202001).

REFERENCES

Ashwin, P. T., Shah, S., Pushpoth, S., Wehbeh, L., and Ilango, B. (2009). The Relationship of Central Corneal Thickness (CCT) to Thinnest Central Cornea (TCC) in Healthy Adults. *Contact Lens and Anterior Eye* 32 (2), 64–67. doi:10.1016/j.clae.2008.07.006

Catalán-López, S., Cadarso-Suárez, L., López-Ratón, M., and Cadarso-Suárez, C. (2018). Corneal Biomechanics in Unilateral Keratoconus and Fellow Eyes with a Scheimpflug-Based Tonometer. *Optom. Vis. Sci.* 95 (7), 608–615. doi:10.1097/OPX.0000000000001241

Chan, T. C. Y., Wang, Y. M., Yu, M., and Jhanji, V. (2018). Comparison of Corneal Tomography and a New Combined Tomographic Biomechanical Index in Subclinical Keratoconus. *J. Refract Surg.* 34 (9), 616–621. doi:10.3928/1081597X-20180705-02

Cui, J., Zhang, X., Hu, Q., Zhou, W.-Y., and Yang, F. (2016). Evaluation of Corneal Thickness and Volume Parameters of Subclinical Keratoconus Using a Pentacam Scheimflug System. *Curr. Eye Res.* 41 (7), 923–926. doi:10.3109/02713683.2015.1082188

Elham, R., Jafarzadehpur, E., Hashemi, H., Amanzadeh, K., Shokrollahzadeh, F., Yekta, A., et al. (2017). Keratoconus Diagnosis Using Corvis ST Measured Biomechanical Parameters. *J. Curr. Ophthalmol.* 29 (3), 175–181. doi:10.1016/j.joco.2017.05.002

Galletti, J. D., Ruiseñor Vázquez, P. R., Minguez, N., Delrivo, M., Bonthoux, F. F., Pförtner, T., et al. (2015). Corneal Asymmetry Analysis by Pentacam Scheimpflug Tomography for Keratoconus Diagnosis. *J. Refract Surg.* 31 (2), 116–123. doi:10.3928/1081597X-20150122-07

Hashemi, H., Khabazkhoob, M., Pakzad, R., Bakhshi, S., Ostadimoghaddam, H., Asaharlous, A., et al. (2019). Pentacam Accuracy in Discriminating

Keratoconus from Normal Corneas: A Diagnostic Evaluation Study. *Eye Contact Lens* 45 (1), 46–50. doi:10.1097/ICL.0000000000000531

Herber, R., Ramm, L., Spoerl, E., Raiskup, F., Pillunat, L. E., and Terai, N. (2019). Assessment of Corneal Biomechanical Parameters in Healthy and Keratoconic Eyes Using Dynamic Bidirectional Applanation Device and Dynamic Scheimpflug Analyzer. *J. Cataract Refract Surg.* 45 (6), 778–788. doi:10.1016/j.jcrs.2018.12.015

Huseynli, S., Salgado-Borges, J., and Alio, J. L. (2018). Comparative Evaluation of Scheimpflug Tomography Parameters between Thin Non-keratoconic, Subclinical Keratoconic, and Mild Keratoconic Corneas. *Eur. J. Ophthalmol.* 28 (5), 521–534. doi:10.1177/1120672118760146

Kataria, P., Padmanabhan, P., Gopalakrishnan, A., Padmanaban, V., Mahadik, S., and Ambrósio, R., Jr (2019). Accuracy of Scheimpflug-Derived Corneal Biomechanical and Tomographic Indices for Detecting Subclinical and Mild Keratectasia in a South Asian Population. *J. Cataract Refract Surg.* 45 (3), 328–336. doi:10.1016/j.jcrs.2018.10.030

Kaya, V., Karakaya, M., Utine, C. A., Albayrak, S., Oge, O. F., and Yilmaz, O. F. (2007). Evaluation of the Corneal Topographic Characteristics of Keratoconus with Orbscan II in Patients with and without Atopy. *Cornea* 26 (8), 945–948. doi:10.1097/ICO.0b013e3180de1e04

McMonnies, C. W. (2012). Assessing Corneal Hysteresis Using the Ocular Response Analyzer. *Optom. Vis. Sci.* 89 (3), E343–E349. doi:10.1097/OPX.0b013e3182417223

Meek, K. M., Tuft, S. J., Huang, Y., Gill, P. S., Hayes, S., Newton, R. H., et al. (2005). Changes in Collagen Orientation and Distribution in Keratoconus Corneas. *Invest. Ophthalmol. Vis. Sci.* 46 (6), 1948–1956. doi:10.1167/iovs.04-1253

Muftuoglu, O., Ayar, O., Hurmeric, V., Orucoglu, F., and Kılıc, I. (2015). Comparison of Multimetric D index with Keratometric, Pachymetric, and Posterior Elevation Parameters in Diagnosing Subclinical Keratoconus in Fellow Eyes of Asymmetric Keratoconus Patients. *J. Cataract Refract Surg.* 41 (3), 557–565. doi:10.1016/j.jcrs.2014.05.052

Muftuoglu, O., Ayar, O., Ozulken, K., Ozyol, E., and Akıncı, A. (2013). Posterior Corneal Elevation and Back Difference Corneal Elevation in Diagnosing Forme Fruste Keratoconus in the Fellow Eyes of Unilateral Keratoconus Patients. *J. Cataract Refract Surg.* 39 (9), 1348–1357. doi:10.1016/j.jcrs.2013.03.023

Oxlund, H., and Simonsen, A. H. (1985). Biochemical Studies of normal and Keratoconus Corneas. *Acta Ophthalmol. (Copenh)* 63 (6), 666–669. doi:10.1111/j.1755-3768.1985.tb01578.x

Peña-García, P., Peris-Martínez, C., Abbouda, A., and Ruiz-Moreno, J. M. (2016). Detection of Subclinical Keratoconus Through Non-Contact Tonometry and the Use of Discriminant Biomechanical Functions. *J. Biomech.* 49 (3), 353–363. doi:10.1016/j.jbiomech.2015.12.031

Roberts, C. J., Mahmoud, A. M., Bons, J. P., Hossain, A., Elsheikh, A., Vinciguerra, R., et al. (2017). Introduction of Two Novel Stiffness Parameters and Interpretation of Air Puff-Induced Biomechanical Deformation Parameters with a Dynamic Scheimpflug Analyzer. *J. Refract Surg.* 33 (4), 266–273. doi:10.3928/1081597X-20161221-03

Scarcelli, G., Besner, S., Pineda, R., and Yun, S. H. (2014). Biomechanical Characterization of Keratoconus Corneas *Ex Vivo* with Brillouin Microscopy. *Invest. Ophthalmol. Vis. Sci.* 55 (7), 4490–4495. doi:10.1167/iovs.14-14450

Sedaghat, M.-R., Momeni-Moghaddam, H., Ambrósio, R., Jr, Heidari, H.-R., Maddah, N., Danesh, Z., et al. (2018). Diagnostic Ability of Corneal Shape and Biomechanical Parameters for Detecting Frank Keratoconus. *Cornea* 37 (8), 1025–1034. doi:10.1097/ICO.0000000000001639

Tian, L., Ko, M. W. L., Wang, L.-k., Zhang, J.-y., Li, T.-j., Huang, Y.-f., et al. (2014). Assessment of Ocular Biomechanics Using Dynamic Ultra High-Speed Scheimpflug Imaging in Keratoconic and normal Eyes. *J. Refract Surg.* 30 (11), 785–791. doi:10.3928/1081597X-20140930-01

Vinciguerra, R., Ambrósio, R., Jr, Elsheikh, A., Roberts, C. J., Lopes, B., Morenghi, E., et al. (2016). Detection of Keratoconus with a New Biomechanical Index. *J. Refract Surg.* 32 (12), 803–810. doi:10.3928/1081597X-20160629-01

Wang, Y. M., Chan, T. C. Y., Yu, M., and Jhanji, V. (2017). Comparison of Corneal Dynamic and Tomographic Analysis in Normal, Forme Fruste Keratoconic, and Keratoconic Eyes. *J. Refract Surg.* 33 (9), 632–638. doi:10.3928/1081597X-20170621-09

Yang, K., Xu, L., Fan, Q., Zhao*, D., and Ren*, S. (2019). Repeatability and Comparison of New Corvis ST Parameters in normal and Keratoconus Eyes. *Sci. Rep.* 9 (1), 15379. doi:10.1038/s41598-019-51502-4

Conflict of Interest: The authors declare that the research was conducted in the absence of any commercial or financial relationships that could be construed as a potential conflict of interest.

Publisher's Note: All claims expressed in this article are solely those of the authors and do not necessarily represent those of their affiliated organizations, or those of the publisher, the editors, and the reviewers. Any product that may be evaluated in this article, or claim that may be made by its manufacturer, is not guaranteed or endorsed by the publisher.

GLOSSARY

A1DA Deformation amplitude at the first applanation

A1dArcL Chang in arc length (length along the curved line) at first applanation

A1DLA Deflection amplitude at the first applanation

A1DLAr Deflection area at the first applanation

A1DLL Deflection length at the first applanation

A1T Time from the initiation of air puff until the first applanation

A1V The first velocity of applanation

A2DA Deformation amplitude at the second applanation

A2dArcL Chang in arc length (length along the curved line) at second applanation

A2DLA Deflection amplitude at the second applanation

A2DLAr Deflection area at the second applanation

A2DLL Deflection length at the second applanation

A2T Time from the initiation of air puff until the second applanation

A2V The second velocity of applanation

ANOVA One-way analysis of variance

AP Corneal thickness at the apex

ARTh Ambrósio relational thickness to the horizontal profile

bIOP Biomechanical-corrected intraocular pressure

CBI Corvis Biomechanical Index

CH Corneal hysteresis

CKC Clinical keratoconus

Corvis ST Corneal Visualization Scheimpflug Technology

CRF Corneal resistance factor

DA Ratio 1 The maximal value of the ratio between deformation amplitude at the apex and that at 1 mm from the corneal apex

DA Ratio 2 The maximal value of the ratio between deformation amplitude at the apex and that at 2 mm from the corneal apex

dArcLM Delta arc length max

DCR Dynamic corneal response

$D_{Kmax\text{-}AP}$ The absolute distances from the maximum curvature of the anterior surface to the apex of the cornea

$D_{Kmax\text{-}TP}$ The absolute distances from the maximum curvature of the anterior surface to the thinnest point

DLAML Max length at deflection amplitude

DLAMT Max time at deflection amplitude

$D_{TP\text{-}AP}$ The absolute distances from the cornea apex to the thinnest point

FFKC Forme fruste keratoconus

HCDA Deformation amplitude at the highest concavity

HCdArcL Chang in arc length (length along the curved line) at the highest concavity

HCDLAr Deflection area at the highest concavity

HCDLL Deflection length at the highest concavity

HCT Time from the start until the highest concavity

IOP Intraocular pressure

IR Integrated radius

Kmax Maximum keratometry from the anterior corneal surface

Kmax X The position of maximum keratometry in X direction relative to apex

Kmax Y The position of maximum keratometry in Y direction relative to apex

MIR Max inverse radius

ORA Ocular Response Analyzer

Pachy Pachymetry

PD Peak distance

QS Quality specification

Radius Radius of curvature

SD Standard deviation

SPA1 Stiffness parameter at first applanation

TKC Topographic keratoconus classification

TP Corneal thickness at the thinnest point

TP X The X position of thinnest corneal thickness related to apex

TP Y The Y position of thinnest corneal thickness related to apex

WEMA Max amplitude of whole eye movement

WEMT Max time of whole eye movement

frontiers in Bioengineering and Biotechnology

ORIGINAL RESEARCH
published: 23 December 2021
doi: 10.3389/fbioe.2021.766605

A Potential Screening Index of Corneal Biomechanics in Healthy Subjects, Forme Fruste Keratoconus Patients and Clinical Keratoconus Patients

Lei Tian[1,2†], *Xiao Qin*[3,4,5†], *Hui Zhang*[3,4], *Di Zhang*[3,4], *Li-Li Guo*[6], *Hai-Xia Zhang*[3,4], *Ying Wu*[7], *Ying Jie*[1*] and *Lin Li*[3,4*]

[1]Beijing Institute of Ophthalmology, Beijing Tongren Eye Center, Beijing Tongren Hospital, Capital Medical University and Beijing Ophthalmology and Visual Sciences Key Laboratory, Beijing, China, [2]Beijing Advanced Innovation Center for Big Data-Based Precision Medicine, Beijing Tongren Hospital, Beihang University & Capital Medical University, Beijing, China, [3]Beijing Key Laboratory of Fundamental Research on Biomechanics in Clinical Application, Capital Medical University, Beijing, China, [4]School of Biomedical Engineering, Capital Medical University, Beijing, China, [5]Department of Otolaryngology, Peking Union Medical College Hospital, Beijing, China, [6]The First People's Hospital of Xuzhou, Xuzhou, China, [7]Department of Ophthalmology, Chinese People's Liberation Army General Hospital, Beijing, China

Purpose: This study aims to evaluate the validity of corneal elastic modulus (E) calculated from corneal visualization Scheimpflug technology (Corvis ST) in diagnosing keratoconus (KC) and forme fruste keratoconus (FFKC).

Methods: Fifty KC patients (50 eyes), 36 FFKC patients (36 eyes, the eyes were without morphological abnormality, while the contralateral eye was diagnosed as clinical keratoconus), and 50 healthy patients (50 eyes) were enrolled and underwent Corvis measurements. We calculated E according to the relation between airpuff force and corneal apical displacement. One-way analysis of variance (ANOVA) and receiver operating characteristic (ROC) curve analysis were used to identify the predictive accuracy of the E and other dynamic corneal response (DCR) parameters. Besides, we used backpropagation (BP) neural network to establish the keratoconus diagnosis model.

Results: 1) There was significant difference between KC and healthy subjects in the following DCR parameters: the first/second applanation time (A1T/A2T), velocity at first/second applanation (A1V/A2V), the highest concavity time (HCT), peak distance (PD), deformation amplitude (DA), Ambrosio relational thickness to the horizontal profile (ARTh). 2) A1T and E were smaller in FFKC and KC compared with healthy subjects. 3) ROC analysis showed that E (AUC = 0.746) was more accurate than other DCR parameters in detecting FFKC (AUC of these DCR parameters was not more than 0.719). 4) Keratoconus diagnosis model by BP neural network showed a more accurate diagnostic efficiency of 92.5%. The ROC analysis showed that the predicted value (AUC = 0.877) of BP neural network model was more sensitive in the detection FFKC than the Corvis built-in parameters CBI (AUC = 0.610, p = 0.041) and TBI (AUC = 0.659, p = 0.034).

OPEN ACCESS

Edited by:
FangJun Bao,
Affiliated Eye Hospital of Wenzhou Medical College, China

Reviewed by:
Hongli Yang,
Devers Eye Institute, United States
Joshua Thomas Morgan,
University of California, Riverside, United States

***Correspondence:**
Ying Jie
jie_yingcn@aliyun.com
Lin Li
lil@ccmu.edu.cn

[†]These authors have contributed equally to this work and share first authorship

Specialty section:
This article was submitted to Biomechanics, a section of the journal Frontiers in Bioengineering and Biotechnology

Received: 29 August 2021
Accepted: 08 November 2021
Published: 23 December 2021

Citation:
Tian L, Qin X, Zhang H, Zhang D, Guo L-L, Zhang H-X, Wu Y, Jie Y and Li L (2021) A Potential Screening Index of Corneal Biomechanics in Healthy Subjects, Forme Fruste Keratoconus Patients and Clinical Keratoconus Patients. Front. Bioeng. Biotechnol. 9:766605. doi: 10.3389/fbioe.2021.766605

Conclusion: Corneal elastic modulus was found to have improved predictability in detecting FFKC patients from healthy subjects and may be used as an additional parameter for the diagnosis of keratoconus.

Keywords: forme fruste keratoconus, clinical keratoconus, corneal visualization Scheimpflug technology, corneal elastic modulus, dynamic corneal response parameters

INTRODUCTION

Keratoconus (KC) presents as a progressive, non-inflammatory disease with a strong genetic component in which the cornea thins locally and forms into a conical shape. KC results in irregular astigmatism, loss of visual acuity and corneal bulge (Krachmer et al., 1984). Although KC is a bilateral disease, it may be a very asymmetric ectasia with a complete absence of, or very subtle variations commonly referred to as, "unilateral keratoconus" (McMahon et al., 2006; Randleman et al., 2008). When observed for a sufficient follow-up time, the disease will likely occur in their fellow eyes, at which point the eyes are referred to as "forme fruste keratoconus" or "subclinical keratoconus" (Rabinowitz et al., 1993; Holland et al., 1997; Li et al., 2004; Klyce 2009; Fontes et al., 2010). The etiology of keratoconus is poorly understood.

The diagnosis of keratoconus is mainly based on the abnormal corneal topography in keratoconus patients at present. Pentacam was one of the most widely used device for detection of abnormal corneas, while it has been hypothesized that corneal biomechanical destabilization in keratoconus patients may emerge prior to the corneal abnormal topography (Elham et al., 2017). As corneal topographical variations might be detectable before the tomographic and clinical signs of KC, corneal biomechanical properties might also be able to detect forme fruste keratoconus (Meek et al., 2005; Dupps and Wilson 2006; Morishige et al., 2007; Sinha Roy et al., 2013; Vellara and Patel 2015). Therefore, an increasing number of ophthalmologists and researchers in the field expect to determine corneal biomechanical properties through clinical measurements alone.

As a transparent biological soft tissue with complex material properties, the cornea is a nonlinear elastic, viscoelastic and anisotropic material. At present, corneal biomechanical experiments *in vitro*, such as corneal strip uniaxial tensile tests (Elsheikh and Anderson, 2005; Hatami-Marbini and Rahimi 2015a; Hatami-Marbini and Rahimi 2015b), corneal swelling tests (Elsheikh et al., 2007; Elsheikh et al., 2008; Kling et al., 2010) and corneal indentation tests (Ahearne et al., 2007; Wang et al., 2016) have been used to measure corneal biomechanical properties directly. Corneal elastic modulus can be extracted from these experiments effectively and found to be a function of strain. However, these experiments cannot be carried out in clinical settings directly.

Two devices have been widely used in measuring corneal biomechanics *in vivo*, corneal visualization Scheimpflug technology (Corvis ST) and ocular response analyzer (ORA). Both devices evaluate corneal biomechanical properties based on corneal response under rapid airpuff. Parameters provided by these devices have shown their values in diagnosing preliminarily keratoconus (Ayar et al., 2015; Elham et al., 2017; Koc et al., 2019; Atalay et al., 2020). Although parameters of these two devices are not only related to corneal biomechanics, they are highly confounded by corneal geometrical parameters and intraocular pressure (IOP) (Vinciguerra et al., 2016; Wang et al., 2016; Wu et al., 2016; Nemeth et al., 2017; Herber et al., 2019). Compared with ORA, Corvis measurements provided corneal deformations under airpuff, which make them evaluate the corneal biomechanical properties more intuitively.

The Corvis will be better applied in the clinic if the corneal typical biomechanical parameters (such as corneal elastic), which were not influenced by corneal geometrical parameters or IOP can be obtained directly by Corvis test. More and more studies have placed great concerns on extracting corneal biomechanical parameters from Corvis parameters directly (Wang et al., 2016; Shih et al., 2017). In the latest version of the Corvis software, a new parameter, the Stiffness Parameter (SP-A1), has been provided to reflect corneal stiffness. Shih et al. proposed a method to determine corneal elastic modulus according to the energy conversion during Corvis measurement (Shih et al., 2017). These new parameters may provide more accurate biomechanical information for diagnosing keratoconus. While the early diagnosis of keratoconus remains challenging and represents a significant area of interest, the technique of corneal tomography remains the diagnostic mode of choice (Shen et al., 2019). The combination of corneal mechanical and topographic parameters is expected to improve the efficiency of the early diagnosis of keratoconus. At present, more and more researchers and ophthalmologists are committed to relevant research.

Studies have found that the cornea can be regarded as a linear elastic material under physiological state (Zhang et al., 2018), so the mechanical properties of cornea under physiological state may be described by elastic modulus, or Young's modulus, according to most of the concerned researchers. In our previous study, we proposed an effective method to evaluate the corneal elastic modulus (E) based on Corvis ST and in accordance with Reissner's theory (Reissner, 1946). tThe calculated E was found less influenced by IOP and corneal geometrical parameters (Qin et al., 2019). In this current study, the sensitivity of the calculated corneal elastic modulus to distinguish forme fruste keratoconus patients and clinical keratoconus patients from healthy subjects are reported.

METHODS

Subjects and measurements

Fifty clinical keratoconus patients (50 eyes), 36 forme fruste keratoconus patients (36 eyes), and 50 healthy subjects (50

TABLE 1 | Abbreviations of Corvis and Pentacam output parameters.

Parameters short name	Description
IOP	Intraocular pressure (mmHg)
BIOP	Biomechanically corrected intraocular pressure
A1T	First applanation time (ms)
A1V	Velocity at first applanation (m/s)
A2T	Second applanation time (ms)
A2V	Velocity at second applanation (m/s)
HCT	Highest concavity time (ms)
DA	The maximum deformation amplitude (mm)
DARatio1	Ratio between deformation amplitude at apex and at 1 mm nasal and temporal
DARatio2	Ratio between deformation amplitude at apex and at 2 mm nasal and temporal
PD	Peak distance (mm)
SPA1	Adjusted pressure at (A1-bIOP)/A1 deflection amplitude
ARTh	Ambrosio relational thickness to the horizontal profile
TBI	The tomographic and biomechanical index
CBI	The corvis biomechanical index
B.Ele.Th	The elevation of the back surface at the thinnest location
Kmax	Maximum keratometry from the anterior corneal surface
Pachymin	Pachymetry at the thinnest point

eyes) were enrolled in the study. Subjects who had ocular diseases other than keratoconus, had corneal or ocular surgery history, or had systemic diseases that may affect the ocular function were excluded from this study. All participants had removed their soft contact lenses or rigid contact lenses at least 1 month before examination. A comprehensive ophthalmologic examination and a standardized interview were performed for all participants. All ophthalmologic examinations were performed at the same time to exclude the possible influence of diurnal fluctuation. The ophthalmic examinations included visual quality examination, slit-lamp microscopy examination, and fundus examination. All of keratoconus diagnosis was made by experienced ophthalmologists from Beijing Tongren Hospital.

For all subjects, Pentacam (Oculus Optikgeräte GmbH, Wetzlar, Germany) measurement was carried out to obtain corneal topography and tomography. Corvis ST measurements were carried out to obtain corneal biomechanical parameters. The Pentacam reconstructs a three-dimensional image of the entire anterior segment of the eye from the anterior surface of the cornea to the posterior surface of the lens by utilizing the high-speed rotating Scheimpflug system. Details and principles of the Pentacam are described by Fontes et al. (2010). Only scans that the Pentacam "quality specification" (QS) function determined as "OK" were included for analysis. According to our previous studies, B. Ele.Th, K_{max}, $Pachy_{min}$ et al. were sensitive to keratoconus (Zhang et al., 2021) and used as corneal topographic parameters in this study. The Corvis evaluates the dynamic corneal deformation response to an airpuff. Details and principles of the Corvis ST are described by Catalan-Lopez et al. (2018). In Corvis, the Corvis biomechanical index (CBI) and the tomographic and biomechanical index (TBI) were two comprehensive parameters reported to be sensitive to keratoconus. Only measurements where the "quality specification" read OK were accepted. If the comment was marked as yellow or red, the examination was repeated. The meaning of the partial parameters provided by Corvis and Pentacam are in **Table 1**. The bIOP reading from Corvis was used for the relevant data analysis.

The clinical keratoconus was diagnosed as follows: a) There was a scissoring reflex on retinoscopic or red reflex on ophthalmoscopic; b) The corneal topography results showed central or paracentral steepening. c) One or more of the following was found in slit-lamp examination: Vogt's striae, Fleischer's ring with an arc >2 mm, and corneal scarring consistent with keratoconus. In patients wherein only one eye was diagnosed as keratoconus, the keratoconus eye was included in the clinical keratoconus group, and the other eye was included in the forme fruste keratoconus (FFKC) group. There was no abnormal or suspect tomography characteristic in FFKC. For participants who were diagnosed with keratoconus in both eyes, one eye was selected randomly included in the clinical keratoconus group. For healthy subjects, one eye was selected randomly and included in the healthy group.

Data were collected from August to November 2019 at the Beijing Tongren Hospital, Beijing, China. All subjects were informed about the consent and had signed the informed consent form before the examination. The informed consent form was in compliance with the tenets of the Declaration of Helsinki. This study was approved by the institutional review board of the Beijing Tongren Hospital, Beijing Institute of Ophthalmology, Beijing, China.

Determination of corneal elastic modulus

The method to evaluate the corneal elastic modulus has been proposed in our previous study (Qin et al., 2019). Corvis measurements were regarded as indentation experiments, in which the rapid airpuff was taken as a surface pressure acted on the corneal apex, and corneal deformation was recorded by the Scheimpflug camera. The airpuff amplitude with time was reported by Wang et al.,(2016), and the first applanation radius was regarded as the radius of the airpuff (r_p). The corneal apical displacements were detected based on the edge detection of corneal anterior surface, which excluded the movement of the whole eyeball. When we take the cornea as a shallow spherical shell, we can determine the corneal elastic

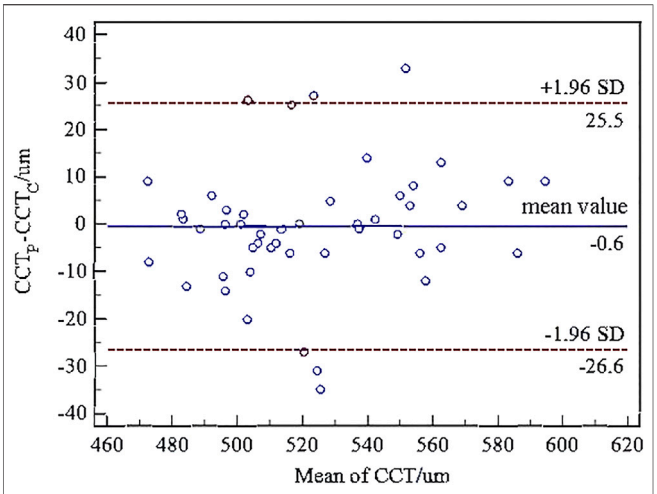

FIGURE 1 | Bland–Altman plots of central corneal thickness (CCT) from Corvis ST and Pentacam. The *x*-axis was the mean value of the CCT from Corvis ST and Pentacam, and the *y*-axis was the difference of the CCT from Corvis ST and Pentacam. The horizontal dotted lines in the figure represent the 95% limits of agreement. The horizontal solid line represents the average value of the difference. Most of the differences are in this interval, which can be considered that the CCT from Corvis ST and Pentacam have good consistency.

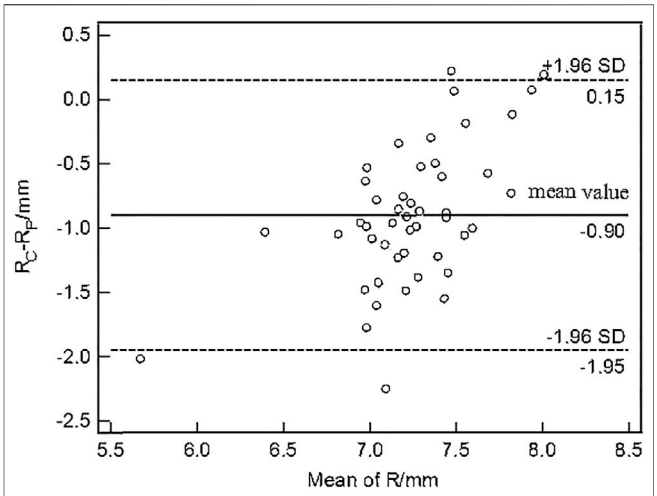

FIGURE 2 | Bland–Altman plots of corneal curvature radius (R) from Corvis ST and Pentacam. The *x*-axis was the mean value of the R from Corvis ST and Pentacam, and the *y*-axis was the difference of the R from Corvis ST and Pentacam. The horizontal dotted lines in the figure represent the 95% limits of agreement. The horizontal solid line represents the average value of the difference. Most of the differences are in this interval, which can be considered that the R from Corvis ST and Pentacam have good consistency.

modulus according to the relation between the airpuff forces and corneal apical displacement presented in **Eq. 1**.

$$E = \frac{\Delta f}{\Delta \delta} \frac{(R - t/2)\sqrt{12(1-\nu^2)}}{\pi t} \frac{1 - c_1}{\mu^2} \tag{1}$$

$$\mu = r_p \left[\frac{12(1-\upsilon^2)}{\left(R - \frac{t}{2}\right)^2 t^2} \right]^{1/4} \tag{2}$$

In **Eq. 1** above, f is the airpuff force acted on the corneal apex, δ is the corneal apical displacement, R is the central corneal curvature radius, t is the corneal central thickness, and R and t were extracted and calculated from the corneal anterior surface edge. As the airpuff force–corneal apical displacement curve was approximately linear when the corneal apical displacement was between 0.2 and 0.4 mm during loading process (Wang et al., 2016), $\Delta f/\Delta\delta$ (mN/mm) is the slope of this curve when displacement is between 0.2 and 0.4 mm, ν is the corneal Poisson's ratio and was set to 0.49 in this study, μ is defined by **Eq. 2**, and c_1 is determined by ν, R, t, and the radius of the airpuff (r_p) according to the equations reported in our previous study (Qin et al., 2019).

Backpropagation neural network Establishment

Based on the one-way ANOVA results, we combined some sensitive topometric and tomographic parameters in Pentacam of keratoconus (B.Ele.Th, K_{max}, $Pachy_{min}$ et al.) and DCR parameters to establish the keratoconus diagnosis model with BP (backpropagation) neural network. The implementation software is Matlab 2018a (MathWorks, United States). Of the data, 70% was used as the training set, and 30% of the data was used as the verification set. Several neural network models were tested with different hidden layer numbers and hidden layer neurons, and the one with high accuracy was selected. After testing, a three-layer neural network was selected. The number of neurons in the input layer depends on the number of parameters with statistical differences among the three groups, and the number of neurons in the output layer is set as 1; trainlm is selected as the activation function because it is suitable for medium-sized networks and have the fastest convergence speed. The learning rate is set to 0.01, the target error is set to 0.005, and the maximum number of iterations is set to 1,000 times.

Statistical analyses

Statistical software SPSS (SPSS Inc., Chicago, IL, USA) version 21.0 was used for the statistical analysis in this study. The Kolmogorov–Smirnov (K-S) test was used to examine the normal distribution of quantitative data, and the results were presented as the mean and standard deviation (SD). Paired *t*-test and Bland–Altman plots were used to compare the agreement of CCT and R provided by Pentacam and Corvis ST. Besides, intraclass correlation coefficient (ICC) and concordance correlation coefficient (CCC) were calculated to more deeply analyze the agreement. One-way analysis of variance (ANOVA) and the least significant difference (LSD) test was used to evaluate the differences among different groups. Receiver operating characteristic (ROC) curve analysis was used with the aim of identifying the predictive accuracy of the calculated corneal

TABLE 2 | Comparison of ocular morphology in different groups.

Parameters	Healthy group	KC group	FFKC group	Difference between healthy and KC group	Difference between healthy and FFKC group	Difference between KC and FFKC group	*p*
Age/years	25.9 ± 5.2	23.3 ± 7.7	23.6 ± 8.7	0.079	0.152	0.858	0.166
bIOP/mmHg	15.3 ± 2.0	14.3 ± 2.5	14.6 ± 1.8	0.120	0.119	0.456	0.059
CCT/μm	534.5 ± 34.6	462.8 ± 51.8	522.8 ± 39.5	<0.001	0.215	<0.001	<0.001*
R/mm	7.75 ± 0.92	5.36 ± 1.01	6.94 ± 0.95	<0.001	0.276	<0.001	<0.001*

Note. BIOP, biomechanical corrected IOP; R, corneal curvature radius; CCT, central corneal thickness; FFKC, forme fruste keratoconus; KC, keratoconus.
**There was statistical difference among different groups.*

TABLE 3 | Corneal biomechanical parameters in different groups.

Parameters	Healthy group	KC group	FFKC group	Difference between healthy and KC group	Difference between healthy and FFKC group	Difference between KC and FFKC group	*p*
A1T/ms	7.33 ± 0.23	6.82 ± 0.26	7.16 ± 0.20	<0.001	0.001	<0.001	<0.001
A1V/ m s^{-1}	0.15 ± 0.02	0.19 ± 0.02	0.16 ± 0.02	<0.001	0.505	<0.001	<0.001
A2T/ms	21.84 ± 0.29	22.22 ± 0.97	21.90 ± 0.67	0.009	0.703	0.042	0.021
A2V/ m s^{-1}	−0.28 ± 0.03	−0.35 ± 0.10	−0.28 ± 0.06	<0.001	0.653	<0.001	<0.001
HCT/ms	17.08 ± 0.40	16.85 ± 0.54	16.90 ± 0.44	0.016	0.078	0.651	0.042
PD/mm	5.21 ± 0.23	5.37 ± 0.23	5.25 ± 0.24	0.001	0.440	0.022	0.003
DA/mm	1.09 ± 0.08	1.35 ± 0.18	1.12 ± 0.09	<0.001	0.081	<0.001	<0.001
SP-A1	93.301 ± 14.487	41.581 ± 13.542	79.574 ± 14.127	<0.001	<0.001	<0.001	<0.001
ARTh	451.27 ± 112.74	193.17 ± 109.83	400.41 ± 97.93	<0.001	0.083	<0.001	<0.001
CBI	0.19 ± 0.27	0.97 ± 0.14	0.42 ± 0.41	<0.001	<0.001	<0.001	<0.001
STSC/ mN mm^{-1}	25.64 ± 1.79	15.88 ± 2.53	24.59 ± 3.85	<0.001	0.081	<0.001	<0.001
E/MPa	0.35 ± 0.04	0.16 ± 0.04	0.30 ± 0.08	<0.001	<0.001	<0.001	<0.001

elastic modulus and other DCR parameters provided by Corvis to analyze the sensitivity and specificity of these parameters. CBI and TBI were reported as keratoconus-sensitive parameters provided by Corvis. The ROC curve analysis was also applied to compare the predicted value and TBI, CBI in screening FFKC patients. Besides, the ROC curve comparison was used to analyze the value of E in the further identification of keratoconus. It was considered statistically significant when the alpha value of p was less than 0.05.

RESULTS

The paired t-test showed there was no significant difference between the central corneal thickness (CCT) provided Corvis and Pentacam ($p = 0.293$) in healthy subjects. Corneal curvature radius (R) provided by Corvis was about 0.9 mm smaller than that provided by Pentacam ($p < 0.001$). **Figures 1**, **2** showed the Bland–Altman plots of CCT and R provided by Pentacam and Corvis ST. The ICC of CCT and R between Corvis and Pentacam was 0.909 and 0.785, respectively, and the CCC was 0.909 and 0.832, respectively. These results remind us that the CCT and R calculated from Corvis ST were reliable. The mean value, SD of age range, bIOP, CCT, and R, obtained from Corvis measurements are shown in **Table 2**. The correlation between corneal elastic modulus (E) and bIOP, CCT, and R showed that E was significantly positively correlated with IOP in all of the three groups ($r = 0.310, 0.384, 0.561$ for healthy, KC, and FFKC groups, respectively; $p < 0.05$). E was positively correlated with R and negatively correlated with CCT, while the correlation was not statically significant ($p > 0.05$). These correlations were in agreement with the results of healthy subjects reported in our previous literature roughly (Qin et al., 2019). One-way ANOVA showed a significant difference in CCT and R among different groups. LSD tests results showed that there was no significant difference between the healthy and forme fruste keratoconus group for these parameters ($p = 0.215, 0.276$).

The DCR parameters that were significantly different among groups and the corneal elastic modulus are shown in **Table 3**. The LSD tests results showed that the A1T and E were smaller in the forme fruste keratoconus group than those in the healthy group ($p < 0.001$), while there was no significant difference seen between the healthy and forme fruste keratoconus group for the other DCR parameters ($p > 0.05$).

The ROC curve analysis was used to detect forme fruste keratoconus/clinic keratoconus from healthy subjects. The cutoff point, specificity, sensitivity, and AUC are shown in **Table 4**. **Figures 3**, **4** and show the ROC curves. Most of the parameters in **Table 4** can diagnose clinical keratoconus with high specificity and sensitivity (AUC > 0.9), while E (AUC =

TABLE 4 | Receiver operating characteristic (ROC) curve analysis results for the detection of KC and FFKC.

Parameters	FFKC				KC			
	Cutoff point	Specificity	Sensitivity	AUC	Cutoff point	Specificity	Sensitivity	AUC
A1T/ms	7.22	0.667	0.700	0.719	7.049	0.980	0.820	0.941
A1V/ m s^{-1}	0.144	0.300	0.833	0.517	0.171	0.920	0.860	0.954
A2T/ms	22.236	0.960	0.278	0.599	22.128	0.900	0.780	0.856
A2V/ m s^{-1}	0.303	0.880	0.417	0.599	0.317	0.940	0.900	0.926
PD/mm	5.517	0.920	0.222	0.543	5.32	0.720	0.580	0.678
DA/mm	1.195	0.980	0.278	0.603	1.179	0.960	0.920	0.984
SP-A1	88.191	0.620	0.778	0.710	57.526	1.000	0.940	0.997
ARTh	330.34	0.880	0.333	0.611	272.60	1.000	0.840	0.950
CBI	0.039	0.500	0.778	0.684	0.764	0.960	0.960	0.986
STSC/mN mm^{-1}	25.27	0.583	0.640	0.556	22.21	1.000	1.000	1.000
E/MPa	0.31	0.649	0.860	0.746	0.245	1.000	1.000	1.000

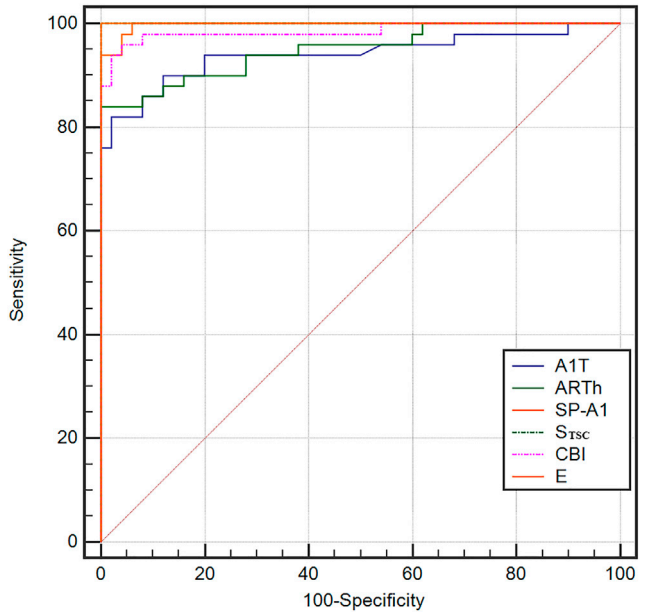

FIGURE 3 | Receiver operating characteristic (ROC) curves for the dynamic corneal response (DCR) parameters provided by Corvis ST in the detection of clinical keratoconus. All of these parameters in the figure can diagnose clinical keratoconus with high specificity and sensitivity (AUC > 0.9).

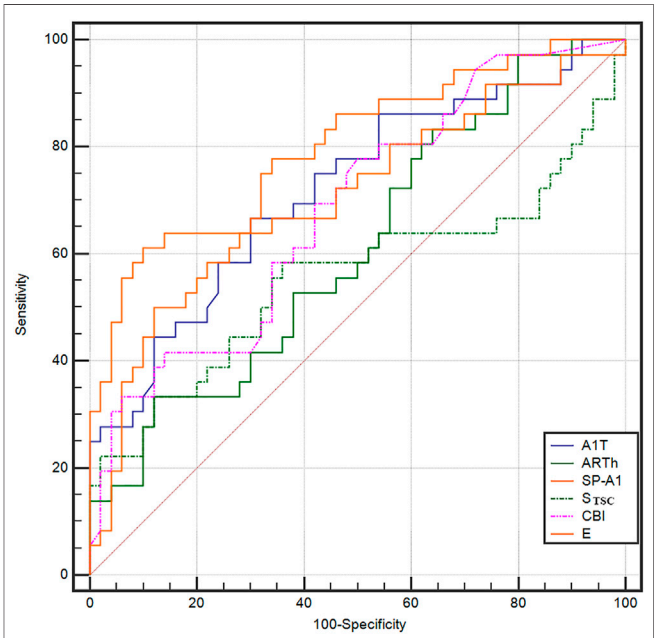

FIGURE 4 | ROC curves for the DCR parameters provided by Corvis ST in the detection of forme fruste keratoconus. The AUC of E was 0.746, which was more accurate than the other parameters, such as the Stiffness Parameter (SP-A1; AUC = 0.710) and Corvis biomechanical index (CBI) (AUC = 0.684), in the diagnosis of forme fruste keratoconus (FFKC). The E can be a potential index in screening FFKC.

0.746) was more accurate than the other parameters, such as SP-A1 (AUC = 0.710, $p = 0.084$) and CBI (AUC = 0.684, $p = 0.041$) in the diagnosis of FFKC.

According to one-way ANOVA, eight parameters provided by Corvis in **Table 3** (A1T, A1V, A2T, A2V, SP-A1, PD, DA, ARTh) and three sensitive Pentacam parameters of keratoconus (B.Ele.Th, K_{max}, $Pachy_{min}$) and E were used to establish the keratoconus diagnosis model. According to the preliminary test, we selected a three-layer neural network, and the number of neuron nodes are 12, 5, and 1, respectively. **Figure 5** and **Table 5** show the results of the diagnosis. The diagnosis model has an accuracy of 92.5% in distinguishing healthy cornea, keratoconus in the frustration stage, and keratoconus in the clinical stage. **Figure 6** shows the ROC curves of the predicted value provided by the keratoconus diagnosis model and TBI, CBI provided by Corvis in screening FFKC patients. **Table 5** shows that our predicted value (AUC = 0.877) is more sensitive to FFKC than CBI (AUC = 0.610, $p = 0.041$) and TBI (AUC = 0.659, $p = 0.034$).

DISCUSSION

Keratoconus (KC) is a progressive, non-inflammatory ectatic corneal disorder in which the normal cornea thins locally and

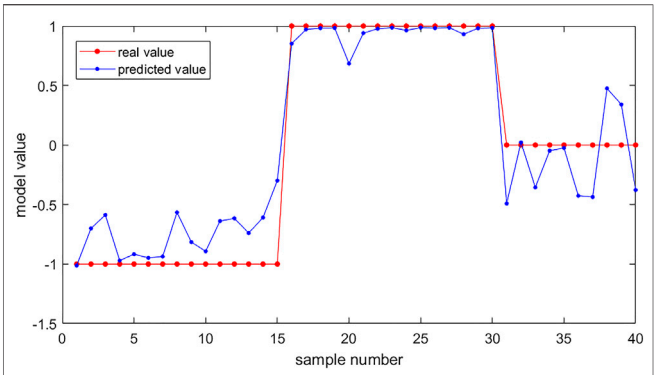

FIGURE 5 | The results of keratoconus diagnosis with the keratoconus diagnosis model. Subjects (40) were used as the verification set. The red dots are the real value of the subjects according to their group (the healthy group was set to be 1, the FFKC group was set to be 0, and the KC group was set to be −1). The blue dots are the predicted value of the subjects calculated by the backpropagation (BP) neural network. We can predict the group of the subjects according to the predicted value (<−0.5: healthy group; −0.5~0.5: FFKC group; >0.5: KC group).

forms into a conical shape. Abnormal corneal tomography is one of the most commonly used indexes for the diagnosis of keratoconus (Meek et al., 2005; Morishige et al., 2007). Histopathological studies have found the losses of the collagen fibrils and interfibrillary substance during the development of keratoconus. Besides, corneal collagen fibrils were found to slip in the stroma. These structural changes may result in the instability of corneal biomechanical properties. The instability of corneal biomechanics can consequently lead to changes in corneal tomography. Therefore, comprehending corneal biomechanics is important to describe and diagnose KC (Vinciguerra et al., 2017; Shao et al., 2019). In this study, the corneal elastic modulus was calculated from the Corvis measurements to characterize corneal biomechanical properties in patients with forme fruste keratoconus patients, clinical keratoconus patients, and healthy subjects. The results showed that corneas with keratoconus exhibited less elastic modulus than did IOP matched healthy control corneas. Besides, the results also showed that corneal biomechanical properties were altered in forme fruste keratoconus eyes. The results of the ROC curve analysis showed that the corneal elastic modulus has a good level of predictive accuracy in detecting forme fruste keratoconus from healthy corneas.

Several prior research studies have described corneal biomechanical properties in healthy and keratoconus subjects *in vivo* (Goebels et al., 2017; Hashemi et al., 2017; Herber et al., 2019). Hashemi et al. examined the diagnostic validity of the different corneal biomechanical parameters provided by ORA in detecting early keratoconus. This study demonstrated that the novel waveform-derived indices provided by ORA have important role in the detection of early keratoconus. Furthermore, the results showed that the p1area, p2area, h1, h2, dive1, mslew1, aspect1, aplhf, dslope1, and CRF had a high degree of sensitivity and specificity in detecting early keratoconus (Goebels et al., 2017; Hashemi et al., 2017), while the mechanical significance of these parameters derived from ORA was not clear, and there is a large cross in the range of these parameters between healthy subjects and FFKC patients. Elham et al. also assessed the capacity of Corvis in diagnosing keratoconus (Kozobolis et al., 2012; Elham et al., 2017). They found that some parameters, such as CCT, the highest concavity radius, and DA, were significantly different between healthy corneas and keratoconus. Studies on the corneal biomechanical properties of keratoconic eyes with different severity grades showed that both ORA and Corvis ST allowed for good differentiation between healthy eyes and keratoconic eyes with different severity grades (Koh et al., 2020).

Since forme fruste keratoconus eyes lacked any, or presented with very subtle changes in geometrical parameters, many built-in parameters of these devices cannot be utilized for diagnosing forme fruste keratoconus patients because of their strong correlation with corneal geometrical parameters (Shen et al., 2019). Thus, parameters directly describing the mechanical meaning could help in understanding the corneal biomechanical changes in early keratoconus patients better.

In this study, both the corneal elastic modulus and S_{TSC} were smaller in clinical keratoconus patients, which was an observation that agreed with our previous study (Wang et al., 2016). However, there was no significant difference between healthy subjects and forme fruste keratoconus patients for S_{TSC}. In our last study, the corneal elastic modulus was calculated, and this value was found to be less correlated with IOP than S_{TSC} and corneal geometrical parameters (Qin et al., 2019).

According to the results of the ROC curve analysis, several parameters showed good predictability in distinguishing clinical keratoconus patients from healthy corneas (AUC > 0.9), which was agreed with the reported results (Kozobolis et al., 2012; Kozobolis et al., 2012; Elham et al., 2017; Elham et al., 2017). Corneal elastic modulus showed better predictability (AUC was 0.746) in distinguishing forme fruste keratoconus patients from healthy corneas. The LSD test and ROC curve analysis showed that the corneal elastic modulus was significantly smaller in the forme fruste keratoconus patients than in healthy patients. The results of the present study confirmed that the changes in corneal biomechanical properties arose in early keratoconus before the

TABLE 5 | ROC curve comparison for the detection of FFKC among the backpropagation (BP) neural network model model predicted value and TBI, CBI.

Parameters	Specificity	Sensitivity	AUC	ROC comparison with predicted value (*p*)
Predicted value of BP neural network model	0.800	0.909	0.877	—
CBI	0.500	0.771	0.610	0.041
TBI	0.428	0.829	0.659	0.034

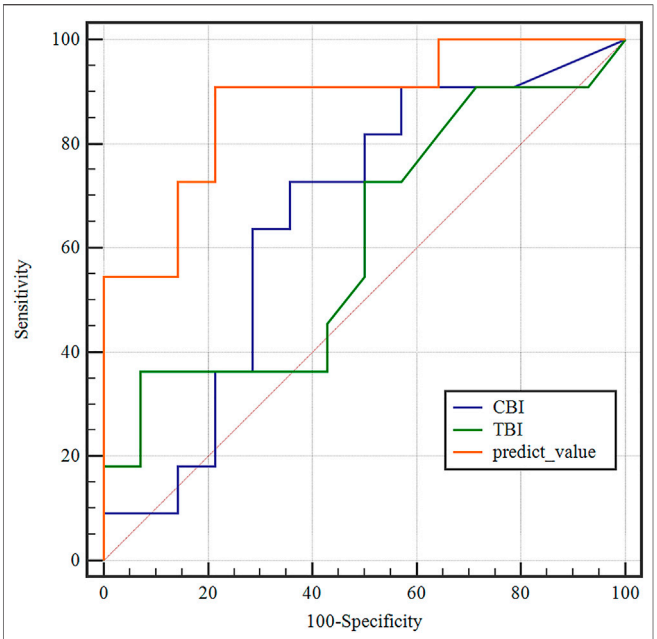

FIGURE 6 | Receiver operating characteristic (ROC) curves of the predicted values of the BP neural network model and tomographic and biomechanical index (TBI), CBI in the detection of forme fruste keratoconus. The predicted value of the BP neural network model (AUC = 0.877) was more accurate than TBI (AUC = 0.659), CBI (AUC = 0.610) in the detection of FFKC.

evident corneal geometry changes (Kozobolis et al., 2012). Several literature have reported the diagnostic validity of CBI in the detection of FFKC (Steinberg et al., 2018; Herber et al., 2019; Koh et al., 2020). In this study, the built-in parameters provided by Corvis ST Software were also compared between forme fruste keratoconus patients and healthy subjects, and the results showed that A1T was the best predictive parameter with an AUC of 0.719. A1T has been found to be an important parameter to reflect corneal biomechanical properties, while it was strongly correlated with IOP (Wang et al., 2017). In this study, there was no significant difference in IOP among the three groups, and the sensitivity and specificity of the A1T were similar to those of the corneal elastic modulus, which may demonstrate that A1T can reflect corneal elastic properties under normal IOP. The corneal elastic modulus showed better predictability in diagnosing keratoconus compared with the Corvis built-in parameters. The keratoconus diagnosis model combining E, DCR parameters, and corneal Pentacam parameters by the BP neural network showed a more accurate diagnostic efficiency of 92.5%. Besides, the ROC curve analysis results showed that the predicted value provided by BP neural network is more sensitive to FFKC than to TBI and CBI, while additional work based on more clinical data should be done in the future for clinical applications because of the limited amount of sample in this study.

One of the limitations was that the sample number in this study is small. More subjects may be necessary to verify the results of this study. Another limitation was that the parameters related to corneal viscoelasticity were not applied to detect forme fruste keratoconus patients from healthy subjects. Although the corneal elastic modulus showed better identifiability of forme fruste keratoconus, a great number of researchers have believed that corneal viscoelasticity is also important to diagnose KC. Thus, further study should be carried out to determine corneal viscoelastic parameters from Corvis measurements and to apply the outcome to detect KC by combining the results of this study in the future.

In conclusion, the corneal elastic modulus was calculated and compared in healthy subjects, forme fruste keratoconus patients, and clinical keratoconus patients. The corneal elastic modulus showed improved predictability in detecting forme fruste keratoconus patients compared with normal apparently healthy subjects, which might be used as an additional parameter for keratoconus diagnosis. Further study is needed to generate more accurate methods to diagnose forme fruste keratoconus patients when also combined with corneal biomechanical and corneal topography parameters.

DATA AVAILABILITY STATEMENT

The raw data supporting the conclusion of this article will be made available by the authors, without undue reservation.

ETHICS STATEMENT

The studies involving human participants were reviewed and approved by the Ethics Committee of the Beijing Tongren Hospital. The patients/participants provided their written informed consent to participate in this study.

AUTHOR CONTRIBUTIONS

LT and XQ contributed equally to this work. YJ, LL: Corresponding author; conception and design of the study; LT, XQ: acquisition of the data, drafting the article; HZ, DZ: analysis and interpretation of the data; L-LG and YW: acquisition of the data; H-XZ: analysis of the data, revise the article. All authors read and approved the final manuscript.

FUNDING

This research was supported by grants from the National Natural Science Foundation of China (Nos. 82171101, 31370952, and 32171304), Beijing Nova Program (Z181100006218099), and The Open Research Fund from Beijing Advanced Innovation Center for Big Data-Based Precision Medicine, Beijing Tongren Hospital, Beihang University, and Capital Medical University (BHTR-KFJJ-202001).

REFERENCES

Ahearne, M., Yang, Y., Then, K. Y., and Liu, K.-K. (2007). An Indentation Technique to Characterize the Mechanical and Viscoelastic Properties of Human and Porcine Corneas. *Ann. Biomed. Eng.* 35, 1608–1616. doi:10.1007/s10439-007-9323-9

Atalay, E., Özalp, O., Erol, M. A., Bilgin, M., and Yıldırım, N. (2020). A Combined Biomechanical and Tomographic Model for Identifying Cases of Subclinical Keratoconus. *Cornea* 39, 461–467. doi:10.1097/ico.0000000000002205

Ayar, O., Ozmen, M. C., Muftuoglu, O., Akdemir, M. O., Koc, M., and Ozulken, K. (2015). *In-vivo* Corneal Biomechanical Analysis of Unilateral Keratoconus. *Int. J. Ophthalmol.* 8, 1141–1145. doi:10.3980/j.issn.2222-3959.2015.06.11

Catalán-López, S., Cadarso-Suárez, L., López-Ratón, M., and Cadarso-Suárez, C. (2018). Corneal Biomechanics in Unilateral Keratoconus and Fellow Eyes with a Scheimpflug-Based Tonometer. *Optom. Vis. Sci.* 95, 608–615. doi:10.1097/opx.0000000000001241

Dupps, W. J., Jr., and Wilson, S. E. (2006). Biomechanics and Wound Healing in the Cornea. *Exp. Eye Res.* 83, 709–720. doi:10.1016/j.exer.2006.03.015

Elham, R., Jafarzadehpur, E., Hashemi, H., Amanzadeh, K., Shokrollahzadeh, F., Yekta, A., et al. (2017). Keratoconus Diagnosis Using Corvis ST Measured Biomechanical Parameters. *J. Curr. Ophthalmol.* 29, 175–181. doi:10.1016/j.joco.2017.05.002

Elsheikh, A., Alhasso, D., and Rama, P. (2008). Biomechanical Properties of Human and Porcine Corneas. *Exp. Eye Res.* 86, 783–790. doi:10.1016/j.exer.2008.02.006

Elsheikh, A., and Anderson, K. (2005). Comparative Study of Corneal Strip Extensometry and Inflation Tests. *J. R. Soc. Interf.* 2, 177–185. doi:10.1098/rsif.2005.0034

Elsheikh, A., Wang, D., and Pye, D. (2007). Determination of the Modulus of Elasticity of the Human Cornea. *J. Refract Surg.* 23, 808–818. doi:10.3928/1081-597x-20071001-11

Fontes, B. M., Ambrósio, R., Jr., Salomão, M., Velarde, G. C., and Nosé, W. (2010). Biomechanical and Tomographic Analysis of Unilateral Keratoconus. *J. Refract Surg.* 26, 677–681. doi:10.3928/1081597x-20091105-04

Goebels, S., Eppig, T., Wagenpfeil, S., Cayless, A., Seitz, B., and Langenbucher, A. (20172017). Complementary Keratoconus Indices Based on Topographical Interpretation of Biomechanical Waveform Parameters: a Supplement to Established Keratoconus Indices. *Comput. Math. Methods Med.* 2017, 5293573. doi:10.1155/2017/5293573

Hashemi, H., Beiranvand, A., Yekta, A., Asharlous, A., and Khabazkhoob, M. (2017). Biomechanical Properties of Early Keratoconus: Suppressed Deformation Signal Wave. *Contact Lens and Anterior Eye* 40, 104–108. doi:10.1016/j.clae.2016.12.004

Hatami-Marbini, H., and Rahimi, A. (2015a). Collagen Cross-Linking Treatment Effects on Corneal Dynamic Biomechanical Properties. *Exp. Eye Res.* 135, 88–92. doi:10.1016/j.exer.2015.04.005

Hatami-Marbini, H., and Rahimi, A. (2015b). Evaluation of Hydration Effects on Tensile Properties of Bovine Corneas. *J. Cataract Refract Surg.* 41, 644–651. doi:10.1016/j.jcrs.2014.07.029

Herber, R., Ramm, L., Spoerl, E., Raiskup, F., Pillunat, L. E., and Terai, N. (2019). Assessment of Corneal Biomechanical Parameters in Healthy and Keratoconic Eyes Using Dynamic Bidirectional Applanation Device and Dynamic Scheimpflug Analyzer. *J. Cataract Refractive Surg.* 45, 778–788. doi:10.1016/j.jcrs.2018.12.015

Holland, D. R., Maeda, N., Hannush, S. B., Riveroll, L. H., Green, M. T., Klyce, S. D., et al. (1997). Unilateral Keratoconus. *Ophthalmology* 104, 1409–1413. doi:10.1016/s0161-6420(97)30123-7

Kling, S., Remon, L., Pérez-Escudero, A., Merayo-Lloves, J., and Marcos, S. (2010). Corneal Biomechanical Changes after Collagen Cross-Linking from Porcine Eye Inflation Experiments. *Invest. Ophthalmol. Vis. Sci.* 51, 3961–3968. doi:10.1167/iovs.09-4536

Klyce, S. D. (2009). Chasing the Suspect: Keratoconus. *Br. J. Ophthalmol.* 93, 845–847. doi:10.1136/bjo.2008.147371

Koc, M., Aydemir, E., Tekin, K., Inanc, M., Kosekahya, P., and Kiziltoprak, H. (2019). Biomechanical Analysis of Subclinical Keratoconus with Normal Topographic, Topometric, and Tomographic Findings. *J. Refract Surg.* 35, 247–252. doi:10.3928/1081597x-20190226-01

Koh, S., Inoue, R., Ambrósio, R., Maeda, N., Miki, A., and Nishida, K. (2020). Correlation between Corneal Biomechanical Indices and the Severity of Keratoconus. *Cornea* 39, 215–221. doi:10.1097/ico.0000000000002129

Kozobolis, V., Sideroudi, H., Giarmoukakis, A., Gkika, M., and Labiris, G. (2012). Corneal Biomechanical Properties and Anterior Segment Parameters in Forme Fruste Keratoconus. *Eur. J. Ophthalmol.* 22, 920–930. doi:10.5301/ejo.5000184

Krachmer, J. H., Feder, R. S., and Belin, M. W. (1984). Keratoconus and Related Noninflammatory Corneal Thinning Disorders. *Surv. Ophthalmol.* 28, 293–322. doi:10.1016/0039-6257(84)90094-8

Li, X., Rabinowitz, Y. S., Rasheed, K., and Yang, H. (2004). Longitudinal Study of the normal Eyes in Unilateral Keratoconus Patients. *Ophthalmology* 111, 440–446. doi:10.1016/j.ophtha.2003.06.020

McMahon, T. T., Szczotka-Flynn, L., Barr, J. T., Anderson, R. J., Slaughter, M. E., Lass, J. H., et al. (2006). A New Method for Grading the Severity of Keratoconus. *Cornea* 25, 794–800. doi:10.1097/01.ico.0000226359.26678.d1

Meek, K. M., Tuft, S. J., Huang, Y., Gill, P. S., Hayes, S., Newton, R. H., et al. (2005). Changes in Collagen Orientation and Distribution in Keratoconus Corneas. *Invest. Ophthalmol. Vis. Sci.* 46, 1948–1956. doi:10.1167/iovs.04-1253

Morishige, N., Wahlert, A. J., Kenney, M. C., Brown, D. J., Kawamoto, K., Chikama, T.-i., et al. (2007). Second-harmonic Imaging Microscopy of normal Human and Keratoconus Cornea. *Invest. Ophthalmol. Vis. Sci.* 48, 1087–1094. doi:10.1167/iovs.06-1177

Nemeth, G., Szalai, E., Hassan, Z., Lipecz, A., Flasko, Z., and Modis, L. (2017). Corneal Biomechanical Data and Biometric Parameters Measured with Scheimpflug-Based Devices on normal Corneas. *Int. J. Ophthalmol.* 10, 217–222. doi:10.18240/ijo.2017.02.06

Qin, X., Tian, L., Zhang, H., Chen, X., and Li, L. (2019). Evaluation of Corneal Elastic Modulus Based on Corneal Visualization Scheimpflug Technology. *Biomed. Eng. Online* 18, 42. doi:10.1186/s12938-019-0662-1

Rabinowitz, Y. S., Nesburn, A. B., and McDonnell, P. J. (1993). Videokeratography of the Fellow Eye in Unilateral Keratoconus. *Ophthalmology* 100, 181–186. doi:10.1016/s0161-6420(93)31673-8

Randleman, J. B., Woodward, M., Lynn, M. J., and Stulting, R. D. (2008). Risk Assessment for Ectasia after Corneal Refractive Surgery. *Ophthalmology* 115, 37–50. doi:10.1016/j.ophtha.2007.03.073

Reissner, E. (1946). Stresses and Small Displacements of Shallow Spherical Shells. *J. Math. Phys.* 25 (1-4), 80–85. doi:10.1002/sapm194625180

Roy, A., Shetty, R., and Kummelil, M. (2013). Keratoconus: a Biomechanical Perspective on Loss of Corneal Stiffness. *Indian J. Ophthalmol.* 61, 392–393. doi:10.4103/0301-4738.116057

Shao, P., Eltony, A. M., Seiler, T. G., Tavakol, B., Pineda, R., Koller, T., et al. (2019). Spatially-resolved Brillouin Spectroscopy Reveals Biomechanical Abnormalities in Mild to Advanced Keratoconus *In Vivo*. *Sci. Rep.* 9, 7467. doi:10.1038/s41598-019-43811-5

Shen, Y., Han, T., Jhanji, V., Shang, J., Zhao, J., Li, M., et al. (2019). Correlation between Corneal Topographic, Densitometry, and Biomechanical Parameters in Keratoconus Eyes. *Trans. Vis. Sci. Tech.* 8, 12. doi:10.1167/tvst.8.3.12

Shih, P. J., Huang, C. J., Huang, T. H., Lin, H. C., Yen, J. Y., Wang, I. J., et al. (20172017). Estimation of the Corneal Young's Modulus *In Vivo* Based on a Fluid-Filled Spherical-Shell Model with Scheimpflug Imaging. *J. Ophthalmol.* 2017, 5410143. doi:10.1155/2017/5410143

Steinberg, J., Siebert, M., Katz, T., Frings, A., Mehlan, J., Druchkiv, V., et al. (2018). Tomographic and Biomechanical Scheimpflug Imaging for Keratoconus Characterization: a Validation of Current Indices. *J. Refract Surg.* 34, 840–847. doi:10.3928/1081597x-20181012-01

Vellara, H. R., and Patel, D. V. (2015). Biomechanical Properties of the Keratoconic Cornea: a Review. *Clin. Exp. Optom.* 98, 31–38. doi:10.1111/cxo.12211

Vinciguerra, R., Ambrósio, R., Jr., Roberts, C. J., Azzolini, C., and Vinciguerra, P. (2017). Biomechanical Characterization of Subclinical Keratoconus without Topographic or Tomographic Abnormalities. *J. Refract Surg.* 33, 399–407. doi:10.3928/1081597x-20170213-01

Vinciguerra, R., Elsheikh, A., Roberts, C. J., Ambrósio, R., Jr., Kang, D. S. Y., Lopes, B. T., et al. (2016). Influence of Pachymetry and Intraocular Pressure on Dynamic Corneal Response Parameters in Healthy Patients. *J. Refract Surg.* 32, 550–561. doi:10.3928/1081597x-20160524-01

Wang, L.-K., Tian, L., and Zheng, Y.-P. (2016). Determiningin Vivoelasticity and Viscosity with Dynamic Scheimpflug Imaging Analysis in Keratoconic and Healthy Eyes. *J. Biophoton* 9, 454–463. doi:10.1002/jbio.201500245

Wang, W., He, M., He, H., Zhang, C., Jin, H., and Zhong, X. (2017). Corneal Biomechanical Metrics of Healthy Chinese Adults Using Corvis ST. *Contact Lens and Anterior Eye* 40, 97–103. doi:10.1016/j.clae.2016.12.003

Wu, Y., Tian, L., and Huang, Y. F. (2016). *In Vivo* corneal Biomechanical Properties with Corneal Visualization Scheimpflug Technology in Chinese Population. *Biomed. Res. Int.* 2016, 7840284. doi:10.1155/2016/7840284

Zhang, H., Khan, M. A., Zhang, D., Qin, X., Lin, D., and Li, L. (2018). Corneal Biomechanical Properties after Fs-Lasik with Residual Bed Thickness Less Than 50% of the Original Corneal Thickness. *J. Ophthalmol.* 2018 (5), 2752945. doi:10.1155/2018/2752945

Zhang, H., Tian, L., Guo, L., Qin, X., Zhang, D., Li, L., et al. (2021). Comprehensive Evaluation of Corneas from normal, Forme Fruste Keratoconus and Clinical Keratoconus Patients Using Morphological and Biomechanical Properties. *Int. Ophthalmol.* 2021, 1–13. doi:10.1007/s10792-020-01679-9

Conflict of Interest: The authors declare that the research was conducted in the absence of any commercial or financial relationships that could be construed as a potential conflict of interest.

frontiers in Bioengineering and Biotechnology

ORIGINAL RESEARCH
published: 17 February 2022
doi: 10.3389/fbioe.2022.839545

Prognostic Nomograms Predicting Risk of Keratoconus in Very Asymmetric Ectasia: Combined Corneal Tomographic and Biomechanical Assessments

Xiaoyu Zhang[1,2,3,4†], *Lan Ding*[1,2,3,4†], *Ling Sun*[1,2,3,4], *Yangyi Huang*[1,2,3,4], *Tian Han*[1,2,3,4], *Yishan Qian*[1,2,3,4*] *and Xingtao Zhou*[1,2,3,4*]

[1]Eye Institute and Department of Ophthalmology, Eye & ENT Hospital, Fudan University, Shanghai, China, [2]NHC Key Laboratory of Myopia (Fudan University), Shanghai, China, [3]Key Laboratory of Myopia, Chinese Academy of Medical Sciences, Shanghai, China, [4]Shanghai Research Center of Ophthalmology and Optometry, Shanghai, China

OPEN ACCESS

Edited by:
FangJun Bao,
Affiliated Eye Hospital of Wenzhou Medical College, China

Reviewed by:
Shiming Li,
Capital Medical University, China
Gilbert Yong San Lim,
SingHealth, Singapore
Jin Yuan,
Sun Yat-sen University, China

***Correspondence:**
Yishan Qian
thronebird31@hotmail.com
Xingtao Zhou
doctzhouxingtao@163.com

[†]These authors have contributed equally to this work

Specialty section:
This article was submitted to Biomechanics, a section of the journal Frontiers in Bioengineering and Biotechnology

Received: 20 December 2021
Accepted: 25 January 2022
Published: 17 February 2022

Citation:
Zhang X, Ding L, Sun L, Huang Y, Han T, Qian Y and Zhou X (2022) Prognostic Nomograms Predicting Risk of Keratoconus in Very Asymmetric Ectasia: Combined Corneal Tomographic and Biomechanical Assessments. Front. Bioeng. Biotechnol. 10:839545. doi: 10.3389/fbioe.2022.839545

Purpose: The aim of the study was to develop and validate a prognostic nomogram for subclinical keratoconus diagnosis using corneal tomographic and biomechanical integration assessments.

Design: This is a retrospective case–control study.

Methods: *Setting:* The study was carried out in a hospital setting. *Patients:* The study included patients with very asymmetric ectasia (VAE) and normal controls. Patients with VAE had defined clinical ectasia in one eye and normal topography (VAE-NT) in the fellow eye, and VAE-NT eyes were selected for analysis. VAE-NT was defined as stratified stage 0 using the ABCD keratoconus grading system. The normal control group was selected from corneal refractive surgery candidates at our clinic, and the right eye was enrolled. *Observation Procedures:* Scheimpflug-based corneal tomography (Pentacam) and corneal biomechanical assessment (Corvis ST) were performed. *Main Outcome Measures:* We performed multiple logistic regression analysis and constructed a simple nomogram via the stepwise method. The receiver operating characteristic (ROC) curve and discrimination and calibration of prognostic nomogram were performed by 500 bootstrap resamplings to assess the determination and clinical value, respectively.

Results: A total of 59 VAE-NT and 142 normal eyes were enrolled. For differentiating normal and VAE-NT eyes, the values of specificity, sensitivity, and area under the ROC (AUROC) were 0.725, 0.610, and 0.713 for tomographic parameters, 0.886, 0.632, and 0.811 for biomechanical parameters, and 0.871, 0.754, and 0.849 for combined parameters, respectively. Combined parameters showed better predictability than separated tomographic or biomechanical parameters.

Conclusion: Our nomogram developed with combined tomographic and biomechanical parameters demonstrated a plausible, capable, and widely implementable tool to predict risk of

keratoconus. The identification of at-risk patients can provide advanced strategies to epitomize ectasia susceptibility.

Keywords: asymmetric ectasia, keratoconus, prognostic nomogram, diagnosis, cornea, biomechanical

INTRODUCTION

Early detection of keratoconus is mandatory in candidates for corneal refractive surgery in order to avoid postoperative ectasia and for increased safety in corneal refractive surgery (Binder et al., 2005; Ambrosio and Randleman 2013). The gold standards for screening keratoconus are topographic and tomographic analyses, which are used to detect alterations in corneal morphology, such as thinning, increased curvature, or elevated corneal elevation (de Sanctis et al., 2008; Mihaltz et al., 2009).

Previous studies, which sparked interest in corneal biomechanical assessment, found that biomechanical changes may occur even before tomographic changes (Kozobolis et al., 2012; Tian et al., 2014; Vinciguerra et al., 2016) may appear, and that early diagnosis of biomechanical disorders may provide a new way of detecting *forme fruste* keratoconus and other ectatic corneal diseases. Recently, substantial progress made in the field of *in vivo* corneal biomechanical characteristics has enabled a more robust and accurate biomechanical *in vivo* keratoconus screening and better compensation of the parameters. Corvis ST (OCULUS Optikgeräte GmbH, Wetzlar, Germany) monitors corneal dynamic deformation due to a constant-pressure air pulse using an ultrahigh-speed Scheimpflug camera, and the latest improvement has been the combination of tomographic and biomechanical data derived from Scheimpflug analyses (Pentacam and Corvis ST; OCULUS Optikgeräte GmbH) (Nemeth et al., 2013; Ali et al., 2014). The tomography biomechanical index (TBI) calculated by Pentacam and Corvis ST parameters has provided the possibility of discriminating the tomographical normal eyes from subclinical keratoconus eyes (Vinciguerra et al., 2016; Ambrósio et al., 2017; Ferreira-Mendes et al., 2019).

The purpose of this study was to determine the diagnostic ability of tomographic and biomechanical parameters for keratoconus. We included patients with subclinical keratoconus who demonstrated neither clinical nor tomographic signs of ectasia in one eye and were diagnosed with very asymmetric ectasia (VAE) in the contralateral eye. We developed and validated a prognostic nomogram for diagnosing subclinical keratoconus using corneal tomographic and biomechanical integration assessments.

PATIENTS AND METHODS

This retrospective comparative case–control study was approved by the Ethics Committee of the Eye and ENT Hospital of Fudan University (approval number 2021118-1) and adhered to the tenets of the Declaration of Helsinki. All participants were assessed to fulfill informed consent requirements.

Study Patients

The patients diagnosed with VAE at the Eye and ENT Hospital of Fudan University were enrolled in the study. These patients had defined clinical ectasia in one eye and normal tomography (VAE-NT) in the contralateral eye. Objective tomography for confirming VAE-NT cases included comprehensive ophthalmic examination, normal cornea on slit-lamp examination, the best corrected distance acuity of 20/20 or better, no risk of keratoconus by Pentacam topometric/keratoconus (KC) staging, and stage A0B0C0 by the ABCD keratoconus grading system (Belin and Duncan 2016). The patients with a history of corneal surgery, pregnancy, ophthalmic disease, eye rubbing, or systemic diseases with ocular manifestations were excluded.

A control group with no ocular disorders except refractive errors and no ectasia throughout the 2-year follow-up period was selected from the corneal refractive surgery candidates at our clinic. The right eyes from normal controls were included in this study.

Corneal Imaging Measurement and Parameters

Scheimpflug-based corneal tomography and corneal biomechanical assessment were performed using Pentacam and Corvis ST (OCULUS Optikgeräte GmbH), respectively. The principles and procedures of these devices have been described in previous articles (Ambrósio et al., 2017; Chan et al., 2018). Both measurements were performed by experienced examiners under the same lighting conditions. The parameters from the Pentacam and Corvis ST were obtained for each eye.

Statistical Analyses

The characteristics of all included VAE-NT and normal eyes are presented as means (with standard deviations) for continuous variables. One-way analysis of variance and Kruskal–Wallis tests were used to show differences between groups. Multivariate linear regression analysis was used to test the association between the VAE-NT and normal groups.

The receiver operating characteristic (ROC) curves were plotted, and their areas under the ROC curve were calculated. Sensitivity, specificity, positive predictive value, negative predictive value (NPV), diagnostic odds ratio, positive likelihood ratio, and negative likelihood ratio of the applied models were also calculated. The selected tomographic and biomechanical variables were used to construct the predictive models, including multiple fractional polynomial model (MFP model, which allows software to determine whether an explanatory variable was important for the model as well as its functional form), full model, and stepwise selected model (a

TABLE 1 | Corneal tomographic and biomechanical parameters and clinical characteristics for normal and VAE-NT eyes.

	Normal	VAE-NT	*p*-value	Univariate		Multivariate	
				OR (95%CI)	*p*-value	OR (95%CI)	*p*-value
Number	142	59		—	—	—	—
Female (N)	91 (64.08%)	12 (20.34%)		—	—	—	—
Male (N)	51 (35.92%)	47 (79.66%)		—	—	—	—
Age (Y)	27.75 ± 6.96	21.22 ± 6.14	<0.001	—	—	—	—
Corneal tomographic parameters							
Kflat (D)	42.64 ± 1.41	42.30 ± 1.40	0.179	0.84 (0.68, 1.05)	0.125	1.12 (0.85, 1.48)	0.422
Ksteep (D)	43.83 ± 1.54	43.62 ± 1.57	0.543	0.91 (0.75, 1.11)	0.373	1.06 (0.83, 1.35)	0.643
Kmax (D)	44.35 ± 1.62	44.27 ± 1.59	0.995	0.97 (0.80, 1.17)	0.735	1.12 (0.89, 1.41)	0.351
BFS anterior	7.91 ± 0.26	7.95 ± 0.27	0.327	2.04 (0.64, 6.50)	0.230	0.66 (0.16, 2.75)	0.569
BFS posterior	6.46 ± 0.24	6.50 ± 0.23	0.269	2.18 (0.60, 7.97)	0.238	0.69 (0.14, 3.34)	0.648
F.Ele. TP (μm)	2.65 ± 1.32	2.73 ± 1.54	0.892	1.04 (0.84, 1.30)	0.706	1.12 (0.86, 1.45)	0.417
B.Ele. TP (μm)	5.44 ± 3.09	6.92 ± 4.37	0.019	1.12 (1.03, 1.22)	0.010	1.11 (1.00, 1.23)	0.055
PPI-min	0.71 ± 0.12	0.77 ± 0.14	0.003	43.82 (3.46, 555.22)	0.004	17.71 (0.98, 321.47)	0.052
PPI-max	1.27 ± 0.16	1.43 ± 0.26	<0.001	56.12 (9.54, 330.23)	<0.001	54.03 (7.15, 408.23)	<0.001
PPI-avg	1.01 ± 0.11	1.08 ± 0.14	<0.001	101.12 (7.64, 1338.44)	0.001	57.03 (3.00, 1083.63)	0.007
ARTmax	429.33 ± 65.88	382.36 ± 76.84	<0.001	0.99 (0.98, 0.99)	<0.001	0.99 (0.98, 1.00)	0.001
Df	0.47 ± 0.96	0.32 ± 1.09	0.264	0.86 (0.63, 1.17)	0.337	1.00 (0.68, 1.45)	0.982
Db	0.08 ± 0.78	0.03 ± 0.92	0.529	0.93 (0.64, 1.35)	0.700	0.96 (0.63, 1.46)	0.845
Dp	0.71 ± 0.76	1.19 ± 0.97	<0.001	1.98 (1.35, 2.91)	0.001	1.83 (1.18, 2.83)	0.007
Dt	0.14 ± 0.75	0.35 ± 0.66	0.056	1.49 (0.96, 2.30)	0.072	1.33 (0.81, 2.17)	0.263
Da	0.54 ± 0.60	0.97 ± 0.70	<0.001	3.23 (1.81, 5.76)	<0.001	2.94 (1.54, 5.59)	0.001
BAD-D	1.11 ± 0.54	1.38 ± 0.72	0.011	2.11 (1.25, 3.58)	0.005	2.32 (1.22, 4.39)	0.010
ARC (3 mm zone) (mm)	7.80 ± 0.26	7.84 ± 0.26	0.431	1.86 (0.58, 5.97)	0.295	0.57 (0.13, 2.47)	0.457
PRC (3 mm zone) (mm)	6.38 ± 0.25	6.33 ± 0.26	0.119	0.45 (0.13, 1.58)	0.213	0.15 (0.03, 0.72)	0.018
Thinnest pachymetry (μm)	533.99 ± 25.90	526.95 ± 22.29	0.058	0.99 (0.98, 1.00)	0.071	0.99 (0.98, 1.01)	0.250
ISV (8 mm Zone)	17.23 ± 4.79	18.05 ± 4.80	0.314	1.04 (0.97, 1.10)	0.267	1.00 (0.93, 1.08)	0.935
IVA (8 mm Zone)	0.12 ± 0.05	0.12 ± 0.06	0.826	2.51 (0.01, 736.22)	0.751	9.11 (0.01, 7263.70)	0.517
KI (8 mm Zone)	1.03 ± 0.02	1.03 ± 0.02	0.342	0.00 (0.00, 6073.86)	0.451	0.81 (0.00, inf.)	0.981
CKI (8 mm Zone)	1.01 ± 0.01	1.01 ± 0.01	0.474	0.00 (0.00, inf.)	0.636	118.12 (0.00, inf.)	0.874
IHA (8 mm Zone)	5.67 ± 4.60	5.42 ± 4.14	0.920	0.99 (0.92, 1.06)	0.721	0.98 (0.91, 1.07)	0.683
IHD (8 mm Zone)	0.01 ± 0.01	0.01 ± 0.01	0.449	11.11 (0.00, inf.)	0.929	1867514.45 (0.00, inf.)	0.640
RMin (8 mm Zone)	7.62 ± 0.28	7.62 ± 0.31	0.909	0.99 (0.34, 2.87)	0.988	0.52 (0.15, 1.89)	0.322
Corneal biomechanical parameters							
A1L	2.30 ± 0.33	2.21 ± 0.36	0.069	0.46 (0.18, 1.15)	0.098	0.49 (0.17, 1.39)	0.180
A2V	0.14 ± 0.02	0.14 ± 0.02	0.868	0.09 (0.00, 98016.29)	0.732	195.81 (0.00, inf.)	0.538
A2L	1.93 ± 0.30	1.83 ± 0.31	0.124	0.33 (0.11, 0.96)	0.042	0.37 (0.11, 1.30)	0.122
A2V	-0.26 ± 0.03	-0.26 ± 0.03	0.671	0.27 (0.00, 10671.37)	0.809	0.30 (0.00, 43403.07)	0.841
Peak distance	4.85 ± 0.27	4.95 ± 0.26	0.024	4.26 (1.26, 14.44)	0.020	4.13 (1.00, 17.09)	0.050
Radius	7.14 ± 0.84	6.79 ± 0.84	0.016	0.60 (0.41, 0.88)	0.009	0.76 (0.48, 1.18)	0.219
Deformation amplitude	1.00 ± 0.08	1.03 ± 0.09	0.022	81.98 (1.83, 3677.67)	0.023	147.64 (1.91, 11421.91)	0.024
IOPnct	17.17 ± 2.85	15.95 ± 2.97	<0.001	0.84 (0.74, 0.96)	0.009	0.86 (0.75, 0.99)	0.042
bIOP	17.33 ± 2.55	16.33 ± 2.76	0.002	0.85 (0.74, 0.97)	0.016	0.84 (0.71, 0.98)	0.024
SSI	0.96 ± 0.15	0.91 ± 0.16	0.014	0.09 (0.01, 0.75)	0.026	0.15 (0.01, 1.62)	0.119
DA ratio (2 mm)	4.30 ± 0.38	4.53 ± 0.51	<0.001	3.55 (1.66, 7.58)	0.001	4.28 (1.75, 10.47)	0.002
Integr. radius	8.38 ± 0.97	8.99 ± 1.09	<0.001	1.87 (1.34, 2.62)	<0.001	1.78 (1.21, 2.61)	0.003
ARTh	469.74 ± 80.21	490.21 ± 112.88	0.316	1.00 (1.00, 1.01)	0.150	1.00 (1.00, 1.01)	0.291
SP-A1	104.68 ± 16.80	107.54 ± 19.32	0.709	1.01 (0.99, 1.03)	0.296	1.01 (0.99, 1.03)	0.513
CBI	0.12 ± 0.20	0.17 ± 0.25	0.688	2.67 (0.69, 10.31)	0.154	2.02 (0.41, 10.02)	0.390
TBI	0.24 ± 0.18	0.40 ± 0.31	0.001	17.67 (4.43, 70.44)	<0.001	14.27 (2.98, 68.34)	0.001

K, keratometry; D, diopters; BFS, best-fit sphere; F.Ele. Th, front elevation at thinnest pachymetry; B.Ele. Th, back elevation at thinnest pachymetry; PPI, pachymetric progression index; min, minimum; avg, average; ARTmax, maximum Ambrósio's relational thickness; Df, deviation of front elevation difference map; Db, derivation of back elevation difference map; Dp, deviation of average pachymetric progression; Dt, deviation of minimum thickness; Da, deviation of ARTmax; BAD-D, Belin/Ambrósio enhanced ectasia deviation; ARC, anterior radius of curvature; PRC, posterior radius of curvature; ISV, index of surface variance; IVA, index of vertical asymmetry; KI, keratoconus index; CKI, center keratoconus index; IHA, index of height asymmetry; IHD, index of height decentration; RMin, minimum axial/sagittal curvature. A1 L, applanation length at first applanation; A1V, corneal apex velocity at first applanation; A2L, applanation length at second applanation; A2V, corneal apex velocity at second applanation; bIOP, biomechanically corrected IOP; SSI, stress–strain index; ARTh, Ambrósio's relational thickness in the horizontal profile; DA, deformation amplitude; Integr. radius, integrated radius; SP-A1, stiffness parameter at first applanation; CBI, Corvis biomechanical index; TBI, tomography and biomechanical index.

method of fitting regression models, in which the choice of predictive variables is carried out by an automatic procedure). We also adopted bootstrapping for internal validation (by using 500 bootstrap (BS) resamplings) to verify the models as the relatively small sample size of our study. In the model-development phase, according to the Akaike information criterion, we performed a backward step-down selection process using a threshold of $p < 0.05$, to establish a parsimonious model (stepwise model), and formulated a nomogram.

The model was validated for discrimination and calibration abilities by calculating the probability of each patient in the entire dataset according to the model and comparing it with the actual risk of developing keratoconus. Discrimination was defined as the ability of a model to correctly distinguish between nonevents and events.

The statistical analyses were 2-tailed, and a p value < 0.05 was considered statistically significant. All statistical analyses were performed using the statistical packages R (http://www.R-project.org; R Foundation for Statistical Computing, Vienna, Austria) and EmpowerStats (www.empowerstats.com, X&Y Solutions, Inc., Boston, MA, United States).

RESULTS

Patient Characteristics and Logistic Regression Analysis of Risk Factors of Keratoconus

A total of 59 eyes with VAE-NT and 142 normal eyes were enrolled in this study. The mean ages were 21.22 ± 6.14 and 27.75 ± 6.96 in the VAE-NT and normal eyes groups, respectively ($p < 0.001$). The percentage of male participants was 79.66% and 35.92% in the VAE-NT and normal eyes groups, respectively.

The baseline corneal tomographic and biomechanical characteristics of the patients are summarized in **Table 1**. Univariate and multivariate linear regression analyses were performed to determine the association between VAE-NT and normal groups. A total of 27 corneal tomographic variables and 16 biomechanical variables were analyzed to detect subclinical corneal ectasia.

In the univariate analysis, eight tomographic variables involved with back elevation in the thinnest location, minimum pachymetric progression index (PPI-min), maximum PPI (PPI-max), average PPI (PPI-avg), maximum Ambrósio's relational thickness (ARTmax), deviation of average pachymetric progression (Dp), deviation of ARTmax (Da), Belin/Ambrósio enhanced ectasia deviation (BAD-D) values, and 10 biomechanical variables involving applanation length at second applanation, peak distance, radius, and deformation amplitude (Def. Amp.), intraocular pressure (IOP) measurements using an automated noncontact tonometer (NCT), biomechanically corrected IOP (bIOP), stress–strain index, deflection amplitude ratio (DA Ratio), and TBI showed significant differences between the two groups. In the multivariate logistic analysis, after adjusting for age and sex, based on the odds ratios (95% CI) and p values, PPI-max, PPI-avg, ARTm, Dp, Da, BAD-D, posterior radius of curvature (PRC), peak distance, Def. Amp., IOP using NCT, bIOP, DA ratio, integrated radius, and TBI were significantly different between the two groups.

Discrimination of the Prognostic Nomogram

The prediction accuracy of tomographic and biomechanical parameters, including ROC curve analysis and optimal threshold analysis, is presented in **Table 2**, and the ROC curves are shown in **Figure 1**. The area under the receiver operating characteristic (AUROC) values for the corneal tomographic and biomechanical parameters were 0.713 and 0.811, respectively, for the BS stepwise model. The AUROC for combined tomographic and biomechanical parameters was higher than that of separated tomographic or biomechanical parameters and showed better predictability, reaching 0.900, 0.865, 0.849, 0.865, and 0.849 for the applied MFP model, full model, stepwise model, BS full model, and BS stepwise model, respectively. The optimal cutoff values of the nomogram for the combined tomographic and biomechanical parameters were 0.257, 0.361, 0.337, -1.088, and -0.821 for the applied models, and the specificity rates were 0.814, 0.850, 0.857, 0.829, and 0.871, respectively. The sensitivity percentages were 0.825, 0.772, 0.754, 0.807, and 0.754, respectively (**Table 2**).

The nomograms for the applied models are shown in **Supplementary Material**. The nomogram of the stepwise model was drawn to provide a convenient and quantitative tool for predicting the risk of developing keratoconus using PPI-min, PPI-max, derivation of back elevation difference map (Db), DA ratio, Ambrósio's relational thickness in the horizontal profile, stiffness parameter at first applanation, and TBI, as it was easy to use and generally accepted in clinical practice (**Figure 2**). To estimate the risk of keratoconus, the values of the different parameters are located on each variable axis. A vertical line is drawn from that value to the top point scale for determining how many points are assigned by that variable value. The points from each variable value are then summed. The sum is located at the total points scale and is vertically projected onto the bottom axis, thus obtaining a personalized risk of keratoconus.

Calibration of the Prognostic Nomogram

The calibration curves showing the risk of developing keratoconus in the VAE-NT cornea according to tomographic indices, biomechanical indices, and combined tomographic and biomechanical indices are shown in **Figure 3**, which showed good overall discrimination using the combined tomographic and biomechanical indices nomogram. However, among patients with an actual probability for developing keratoconus of >50%, the model underestimated the risk of keratoconus by ≥ 10%. For an observed keratoconus probability of <50%, the model-predicted probability might be overestimated.

TABLE 2 | ROC curve analysis and optimal threshold analysis for the predictive model between normal and VAE-NT groups for tomographic parameters, biomechanical parameters, and combined tomographic and biomechanical parameters.

	AUROC	95% CI	Cutoff value	Specificity	Sensitivity	PLR	NLR	DOR	PPV	NPV
Tomographic parameters										
MFP	0.791	0.724 to 0.858	0.396	0.845	0.593	3.829	0.481	7.955	0.614	0.833
Full	0.751	0.672 to 0.829	0.387	0.852	0.610	4.126	0.458	9.019	0.632	0.840
Stepwise	0.714	0.632 to 0.796	0.291	0.704	0.644	2.178	0.505	4.308	0.475	0.826
BS full	0.750	0.6713 to 0.829	-0.454	0.866	0.593	4.434	0.470	9.441	0.648	0.837
BS stepwise	0.713	0.631 to 0.795	-0.855	0.725	0.610	2.222	0.537	4.134	0.480	0.818
Biomechanical parameters										
MFP	0.812	0.745 to 0.880	0.366	0.871	0.632	4.912	0.423	11.619	0.667	0.853
Full	0.825	0.754 to 0.895	0.351	0.850	0.754	5.029	0.289	17.405	0.672	0.895
Stepwise	0.814	0.742 to 0.885	0.403	0.900	0.649	6.491	0.390	16.650	0.726	0.863
BS full	0.821	0.752 to 0.891	−0.642	0.871	0.702	5.458	0.342	15.948	0.690	0.878
BS stepwise	0.811	0.741 to 0.881	−0.302	0.886	0.632	5.526	0.416	13.286	0.692	0.855
Combined tomographic and biomechanical parameters										
MFP	0.900	0.853 to 0.947	0.257	0.814	0.825	4.440	0.216	20.608	0.644	0.919
Full	0.865	0.803 to 0.928	0.361	0.850	0.772	5.146	0.268	19.180	0.677	0.902
Stepwise	0.849	0.782 to 0.917	0.337	0.857	0.754	5.281	0.287	18.429	0.683	0.896
BS full	0.865	0.803 to 0.928	−1.088	0.829	0.807	4.708	0.233	20.212	0.657	0.913
BS stepwise	0.849	0.781 to 0.917	−0.821	0.871	0.754	5.867	0.282	20.818	0.705	0.897

VAE-NT, fellow eye from patients with very asymmetric ectasia with normal tomography; AUROC, area under the receiver operating characteristic curve; PLR, positive likelihood ratio; NLR, negative likelihood ratio; DOR, diagnostic odds ratio; PPV, positive predictive value; NPV, negative predictive value.

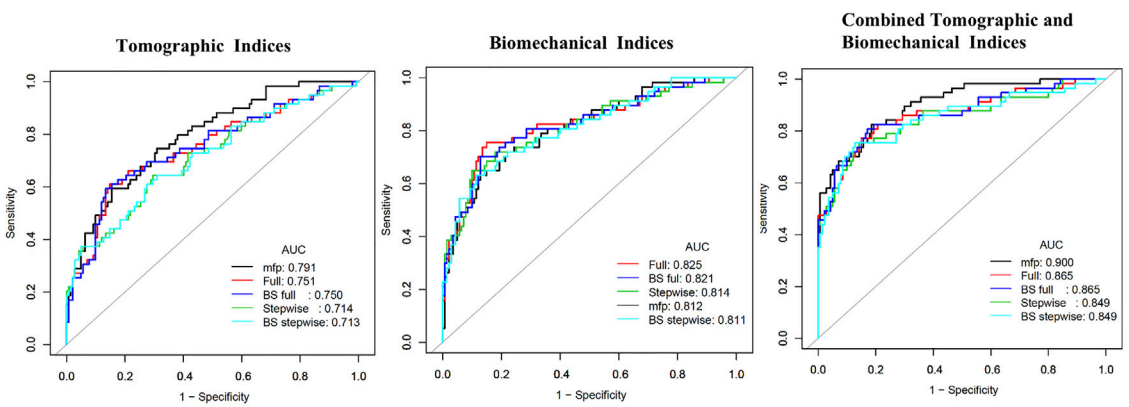

FIGURE 1 | Receiving operating characteristic curve and area under the curve (AUC) in tomographic indices, biomechanical indices, and combined tomographic and biomechanical indices.

DISCUSSION

The current study demonstrated the early detection of subclinical keratoconus using Scheimpflug tomography and biomechanical assessments in a specific group of patients diagnosed with VAE to detect valuable diagnostic indexes. We constructed a nomogram-based prognostic model, performed an internal validation, and found that model discrimination effectively evaluated the risk of keratoconus and had a good ability to categorize patients into separate risk strata. To our knowledge, only a few previous studies have applied a prognostic nomogram for the early detection of subclinical keratoconus with combined tomography and biomechanical parameters.

The incidence of keratoconus varies greatly, from 0.5% to 1% (Kennedy et al., 1986; Chan et al., 2021). Increasing morbidity contributes to improved detection methods. With the increasing prevalence of keratoconus, its pathophysiology has been widely discussed. Biomechanical disorders are often considered the main pathogenesis of keratoconus (Ambekar et al., 2011; Wolffsohn et al., 2012; Salomao et al., 2021). Therefore, after ruling out asymmetric external factors causing unilateral keratoconus (Gomes et al., 2015), it is vital to analyze the corneal tomography and biomechanical features of VAE-NT to help

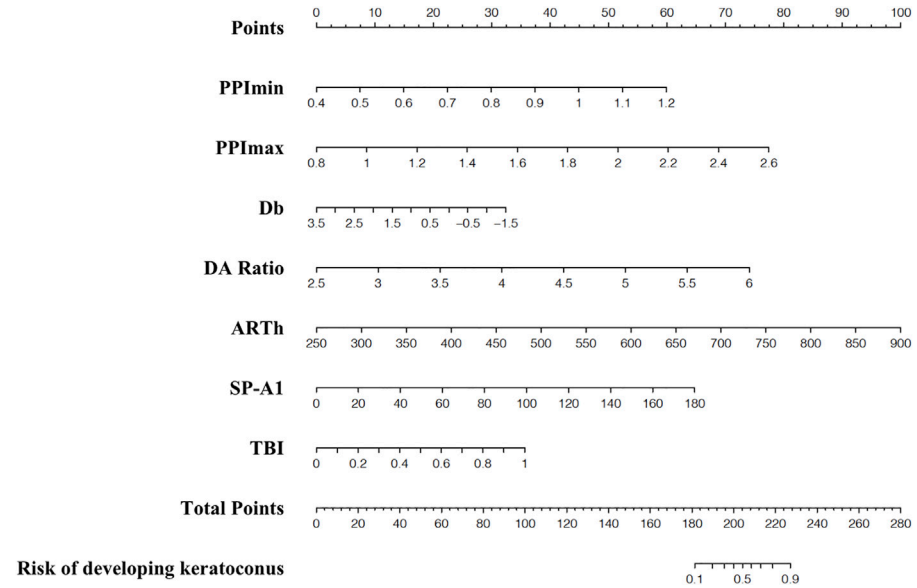

FIGURE 2 | Nomogram for predicting developed-into-keratoconus in VAE-NT patients. VAE-NT, defined clinical ectasia in one eye and normal tomography.

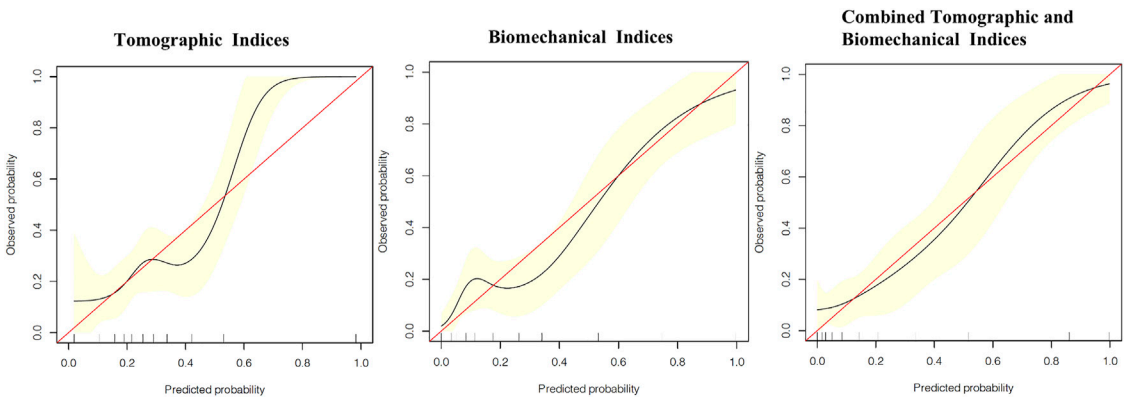

FIGURE 3 | Calibration curves showing the risk of developed-into-keratoconus in VAE-NT cornea according to tomographic indices, biomechanical indices, and combined tomographic and biomechanical indices.

clinicians in the early diagnosis of keratoconus and provide a basis for accurate diagnosis.

The shape, ROC, and AUROC were used to estimate the discriminative power of the test. Previous studies have reported good discrimination of AUROC values in individual tomographic and biomechanical parameters. TBI, BAD-D, and CBI have been reported in several published studies that reported the discriminating capability of VAE-NT from normal controls (Ambrósio et al., 2017; Ferreira-Mendes et al., 2019; Kataria et al., 2019; Koh et al., 2019). Some studies reported high AUROC in variables from anterior elevation, including KI, IHD, and IVA (Donoso et al., 2021); however, our study reported other tomographic parameters, including the PPI and Db. This difference can be attributed to the inclusion criteria and racial differences in the anterior segments. Our study enrolled patients who reported no risk of keratoconus by Pentacam topometric/KC staging, which is based primarily on morphological parameters of anterior corneal elevation. A possible confounding factor of asymmetric anterior corneal morphology was excluded and therefore has stronger diagnostic implications for occult keratoconus with normal anterior corneal morphology.

The criterion of "VAE-NT" varies among studies. A comparison of the VAE-NT classification criteria and AUROC of the main outcome measures with previous studies is shown in **Table 3**. According to the Global Consensus on Keratoconus and Ectatic Disease, posterior corneal elevation is indispensable for the diagnosis of early or subclinical keratoconus (Gomes et al., 2015). Therefore, we referred to the ABCD keratoconus grading system based on the anterior radius of curvature and PRC,

TABLE 3 | Comparison of VAE-NT classify criteria and AUROC of the main outcome measures with previous studies.

Study	VAE-NT classification criteria	Comparison	AUROC of main outcomes	Sensitivity	Specificity
Ambrósio et al. (2017)	Objective front surface curvature metrics derived from Pentacam, such as a keratoconus percentage index (KISA %) score lower than 60 and a paracentral inferior–superior (I-S value) asymmetry value at 6 mm (3 mm radii) less than 1.45	480 normal vs. 94 VAE-NT	TBI: 0.985 BAD-D: 0.839 CBI: 0.822	TBI: 90.4	TBI: 96.0
Chan et al. (2018)	With an average corneal power of 49.00 D or less or HOAs of 1.50 μm or less in either eye or normal topography but obvious keratoconus in the contralateral eye	37 normal vs. 23 VAE-NT	TBI: 0.925 BAD-D: 0.786	TBI: 84.4	TBI: 82.4
Ferreira-Mendes et al. (2019)	Objective front surface curvature metrics derived from Pentacam HR, such as a keratoconus percentage index (KISA%) score lower than 60 and a paracentral inferior–superior (I-S value) asymmetry value at 6 mm (3 mm radii) less than 1.45	312 normal vs. 57 VAE-NT	TBI: 0.960	TBI: 89.5	TBI: 91.0
Kataria et al. (2019)	Objective front surface curvature metrics derived from Pentacam, such as a keratoconus percentage index (KISA %) score lower than 60 and a paracentral inferior–superior (I-S value) asymmetry value at 6 mm (3 mm radii) less than 1.45	100 normal vs. 100 VAE-NT	TBI: 0.901 BAD-D: 0.812 CBI: 0.775 SPAI: 0.762	TBI: 84.0 BAD-D: 87.0 CBI: 68.0 SPA1: 66.0	TBI: 85.0 BAD-D: 76.5 CBI: 72.5 SPA1: 74.5
Steinberg et al. (2018)	KISA% index of less than 60%, I-S difference of less than 1.45 D, and Kmax of 47.00 D or less	105 normal vs. 32 VAE-NT	TBI: 0.825 BAD-D: 0.748 CBI: 0.787	TBI: 72.0 BAD-D: 69.0 CBI: 69.0	TBI: 71.0 BAD-D: 69.0 CBI: 69.0
Koh et al. (2019)	Distance-corrected visual acuity of 20/20 or better and a normal Placido-disk topographic map (Klyce/Maeda keratoconus index and Smolek/Klyce keratoconus severity index), based on the definition of *forme fruste* keratoconus	70 normal vs. 23 VAE-NT	TBI: 0.751 BAD-D: 0.668 CBI: 0.660	TBI: 52.17 BAD-D: 60.87 CBI: 30.43	TBI: 88.57 BAD-D: 85.70 CBI: 98.57
Koh et al. (2019)	Central mean keratometry value of less than 47.20 diopters (D), an inferior–superior asymmetry for the average keratometry value of less than 1.40 D, a keratoconus percentage index (KISA%) of less than 60%, and no clinical evidence	35 normal vs. 21 VAE-NT	TBI: 0.790	TBI: 67	TBI: 86
Current study	Best corrected distance acuity of 20/20 or better, reporting no risk of keratoconus by Pentacam topometric/KC staging and stage 0 by the ABCD keratoconus grading system	142 normal vs. 59 VAE-NT	BS stepwise model for combined parameters: 0.849	0.754	0.871

thinnest pachymetry, best corrected visual acuity, and a modifier for the presence of corneal scarring and only enrolled VAE-NT patients who were diagnosed with stage A0B0C0D0 (Belin and Duncan 2016). Owing to the restricted inclusion criteria, the ratio of the VAE-NT eyes to normal BAD-D, CBI, TBI, and other parameters might be higher than in other published studies, which led to the diagnostic yield of individual parameter underscores in comparison with a more complex multivariate approach for each parameter. To address this issue, our study combined variables taken from both tomography and biomechanical parameters and demonstrated a high diagnostic capability. The nomogram using combined parameters demonstrated good predictive accuracy, with an AUROC above 0.84 in the applied five models.

Accurate prognostic information for keratoconus is vitally important, not only for determining suitability for corneal refractive surgery, but also for assessing the risk of developing keratoconus in the future. As for the calibration curves, good overall discrimination was achieved using the combined tomographic and biomechanical indices nomogram. For patients with an actual keratoconus probability of greater than 50%, the model underestimated the risk of keratoconus and may result in a reduction of the frequency of follow-up. Our model, with adequate calibration by predicted risk strata, will provide abundant information for clinical decision-making.

It is worth noting that we applied a restricted inclusion criterion, which pooled extensive corneal tomographic and biomechanical data. We also applied discrimination and calibration for the prognostic nomogram, obtaining a robust metric for early diagnosis of keratoconus, which can be applied to a broad range of eyes.

Our study had some limitations, mainly that there were racial differences in the anterior segments, and validation of these tomographic parameters should be noted. Second, combining epithelial thickness mapping with the assistance of anterior segment optical coherence tomography can be useful in future studies. Third, the relatively short postoperative follow-up in the normal control group may not cover the possible development of keratoconus, which may also lead to overestimation of the performance of the ROC analysis. Finally, since the

construction and verification of the model were conducted through the single-center database, which may decline the prediction value. A larger sample of clinical data will be needed in the future to externally validate our model in order to improve diagnostic efficacy.

CONCLUSION

Several parameters of corneal tomographic and biomechanical examinations can be useful for the early diagnosis of subclinical keratoconus. The prognostic nomogram demonstrated better results when both devices were combined. These results indicate that careful assessment combining different techniques or devices is needed for the detection of subclinical ectasia.

DATA AVAILABILITY STATEMENT

The raw data supporting the conclusion of this article will be made available by the authors, without undue reservation.

ETHICS STATEMENT

The studies involving human participants were reviewed and approved by the Ethics Committee of the Eye and ENT Hospital of Fudan University. Written informed consent to participate in this study was provided by the participants' legal guardian/next of kin.

AUTHOR CONTRIBUTIONS

All authors read and approved the final manuscript. XZha: conceptualization, methodology, and software; LD: data curation and writing—original draft preparation; LS: data curation; YH: visualization and investigation; TH: software and validation; YQ: writing—reviewing and editing; XZho: supervision, project administration, and funding acquisition.

FUNDING

The study was supported by the National Natural Science Foundation of China (Grant No. 81770955), Project of Shanghai Science and Technology (Grant No.20410710100), Clinical Research Plan of SHDC (SHDC2020CR1043B), Project of Shanghai Xuhui District Science and Technology (2020-015), and Project of Shanghai Xuhui District Science and Technology (XHLHGG202104).

SUPPLEMENTARY MATERIAL

The Supplementary Material for this article can be found online at: https://www.frontiersin.org/articles/10.3389/fbioe.2022.839545/full#supplementary-material

REFERENCES

Ali, N. Q., Patel, D. V., and McGhee, C. N. J. (2014). Biomechanical Responses of Healthy and Keratoconic Corneas Measured Using a Noncontact Scheimpflug-Based Tonometer. *Invest. Ophthalmol. Vis. Sci.* 55 (6), 3651–3659. doi:10.1167/iovs.13-13715

Ambekar, R., Toussaint Jr., K. C., Jr., and Wagoner Johnson, A. (2011). The Effect of Keratoconus on the Structural, Mechanical, and Optical Properties of the Cornea. *J. Mech. Behav. Biomed. Mater.* 4 (3), 223–236. doi:10.1016/j.jmbbm.2010.09.014

Ambrósio, R., Jr., Lopes, B. T., Faria-Correia, F., Salomão, M. Q., Bühren, J., Roberts, C. J., et al. (2017). Integration of Scheimpflug-Based Corneal Tomography and Biomechanical Assessments for Enhancing Ectasia Detection. *J. Refract Surg.* 33 (7), 434–443. doi:10.3928/1081597X-20170426-02

Ambrósio, R., Jr., and Randleman, J. B. (2013). Screening for Ectasia Risk: What Are We Screening for and How Should We Screen for it? *J. Refract Surg.* 29 (4), 230–232. doi:10.3928/1081597X-20130318-01

Belin, M., and Duncan, J. (2016). Keratoconus: The ABCD Grading System. *Klin Monatsbl Augenheilkd* 233 (6), 701–707. doi:10.1055/s-0042-100626

Binder, P. S., Lindstrom, R. L., Stulting, R. D., Donnenfeld, E., Wu, H., McDonnell, P., et al. (2005). Keratoconus and Corneal Ectasia after LASIK. *J. Refract Surg.* 21 (6), 749–752. doi:10.3928/1081-597x-20051101-15

Chan, E., Chong, E. W., Lingham, G., Stevenson, L. J., Sanfilippo, P. G., Hewitt, A. W., et al. (2021). Prevalence of Keratoconus Based on Scheimpflug Imaging. *Ophthalmology* 128 (4), 515–521. doi:10.1016/j.ophtha.2020.08.020

Chan, T. C., Wang, Y. M., Yu, M., and Jhanji, V. (2018). Comparison of Corneal Dynamic Parameters and Tomographic Measurements Using Scheimpflug Imaging in Keratoconus. *Br. J. Ophthalmol.* 102 (1), 42–47. doi:10.1136/bjophthalmol-2017-310355

de Sanctis, U., Loiacono, C., Richiardi, L., Turco, D., Mutani, B., and Grignolo, F. M. (2008). Sensitivity and Specificity of Posterior Corneal Elevation Measured by Pentacam in Discriminating Keratoconus/subclinical Keratoconus. *Ophthalmology* 115 (9), 1534–1539. doi:10.1016/j.ophtha.2008.02.020

Donoso, R., Rodríguez, Á., Esteffan, K., Lagos, C., Aránguiz, D., and Hernández, N. (2021). Analysis of OPD-Scan and Pentacam Parameters for Early Keratoconus Detection. *Am. J. Ophthalmol.* 226, 235–242. doi:10.1016/j.ajo.2021.01.012

Ferreira-Mendes, J., Lopes, B. T., Faria-Correia, F., Salomão, M. Q., Rodrigues-Barros, S., and Ambrósio, R., Jr (2019). Enhanced Ectasia Detection Using Corneal Tomography and Biomechanics. *Am. J. Ophthalmol.* 197, 7–16. doi:10.1016/j.ajo.2018.08.054

Gomes, J. A. P., Tan, D., Rapuano, C. J., Belin, M. W., Ambrósio, R., Jr., Guell, J. L., et al. (2015). Global Consensus on Keratoconus and Ectatic Diseases. *Cornea* 34 (4), 359–369. doi:10.1097/ICO.0000000000000408

Kataria, P., Padmanabhan, P., Gopalakrishnan, A., Padmanaban, V., Mahadik, S., and Ambrósio, R., Jr (2019). Accuracy of Scheimpflug-Derived Corneal Biomechanical and Tomographic Indices for Detecting Subclinical and Mild Keratectasia in a South Asian Population. *J. Cataract Refract Surg.* 45 (3), 328–336. doi:10.1016/j.jcrs.2018.10.030

Kennedy, R. H., Bourne, W. M., and Dyer, J. A. (1986). A 48-year Clinical and Epidemiologic Study of Keratoconus. *Am. J. Ophthalmol.* 101 (3), 267–273. doi:10.1016/0002-9394(86)90817-2

Koh, S., Ambrósio, R., Jr., Inoue, R., Maeda, N., Miki, A., and Nishida, K. (2019). Detection of Subclinical Corneal Ectasia Using Corneal Tomographic and Biomechanical Assessments in a Japanese Population. *J. Refract Surg.* 35 (6), 383–390. doi:10.3928/1081597X-20190417-01

Kozobolis, V., Sideroudi, H., Giarmoukakis, A., Gkika, M., and Labiris, G. (2012). Corneal Biomechanical Properties and Anterior Segment Parameters in Forme

Fruste Keratoconus. *Eur. J. Ophthalmol.* 22 (6), 920–930. doi:10.5301/ejo.5000184

Mihéltz, K., Kovács, I., Takács, Á., and Nagy, Z. Z. (2009). Evaluation of Keratometric, Pachymetric, and Elevation Parameters of Keratoconic Corneas with Pentacam. *Cornea* 28 (9), 976–980. doi:10.1097/ICO.0b013e31819e34de

Nemeth, G., Hassan, Z., Csutak, A., Szalai, E., Berta, A., and Modis, L., Jr (2013). Repeatability of Ocular Biomechanical Data Measurements with a Scheimpflug-Based Noncontact Device on normal Corneas. *J. Refract Surg.* 29 (8), 558–563. doi:10.3928/1081597X-20130719-06

Salomão, M. Q., Hofling- Lima, A. L., Gomes Esporcatte, L. P., Correa, F. F., Lopes, B., Sena, N., Jr., et al. (2021). Ectatic Diseases. *Exp. Eye Res.* 202, 108347. doi:10.1016/j.exer.2020.108347

Steinberg, J., Siebert, M., Katz, T., Frings, A., Mehlan, J., Druchkiv, V., et al. (2018). Tomographic and Biomechanical Scheimpflug Imaging for Keratoconus Characterization: A Validation of Current Indices. *J. Refract Surg.* 34 (12), 840–847. doi:10.3928/1081597X-20181012-01

Tian, L., Ko, M. W. L., Wang, L.-k., Zhang, J.-y., Li, T.-j., Huang, Y.-f., et al. (2014). Assessment of Ocular Biomechanics Using Dynamic Ultra High-Speed Scheimpflug Imaging in Keratoconic and normal Eyes. *J. Refract Surg.* 30 (11), 785–791. doi:10.3928/1081597X-20140930-01

Vinciguerra, R., Ambrósio, R., Jr., Elsheikh, A., Roberts, C. J., Lopes, B., Morenghi, E., et al. (2016). Detection of Keratoconus With a New Biomechanical Index. *J. Refract Surg.* 32 (12), 803–810. doi:10.3928/1081597X-20160629-01

Wolffsohn, J. S., Safeen, S., Shah, S., and Laiquzzaman, M. (2012). Changes of Corneal Biomechanics with Keratoconus. *Cornea* 31 (8), 849–854. doi:10.1097/ICO.0b013e318243e42d

Conflict of Interest: The authors declare that the research was conducted in the absence of any commercial or financial relationships that could be construed as a potential conflict of interest.

Publisher's Note: All claims expressed in this article are solely those of the authors and do not necessarily represent those of their affiliated organizations, or those of the publisher, the editors and the reviewers. Any product that may be evaluated in this article, or claim that may be made by its manufacturer, is not guaranteed or endorsed by the publisher.

frontiers in Bioengineering and Biotechnology

ORIGINAL RESEARCH
published: 23 February 2022
doi: 10.3389/fbioe.2022.830776

Topography-Guided Transepithelial Accelerated Corneal Collagen Cross-Linking for Low Refractive Error Correction in Keratoconus Treatment: A Pilot Study

Ling Sun[1,2†], Xiaoyu Zhang[1,2†], Mi Tian[1,2], Yang Shen[1,2], Jing Zhao[1,2] and Xingtao Zhou[1,2]*

[1]Department of Ophthalmology, Eye and ENT Hospital, Fudan University, NHC Key Laboratory of Myopia (Fudan University), Laboratory of Myopia, Chinese Academy of Medical Sciences, Shanghai, China, [2]Shanghai Research Center of Ophthalmology and Optometry, Shanghai, China

Purpose: To investigate the safety and efficacy of topography-guided transepithelial accelerated corneal collagen cross-linking for low refractive error correction in patients with keratoconus.

Methods: This was a prospective self-controlled study. Eighteen patients (18 eyes) were enrolled and assessed at 6 visits (pre-operation, 1 w, 1 month, 3 months, 6 months, and 1 year postoperatively). The examination at every visit included analysis of uncorrected visual acuity (UCVA), best-corrected visual acuity (BCVA), corneal topography, and corneal endothelial cell counts. Data are expressed as mean ± standard deviation (SD). The *p*-value was determined using repeated-measures analysis of variance.

Results: No complications occurred in any eye during 1 year follow-up period. At each visit after the operation, the corneal K values and spherical equivalent (SE) were reduced, while the visual acuity values were increased compared with those preoperatively, although these results were not statistically significant ($p > 0.05$). UCVA of nearly 1/3 of the patients was enhanced by at least 3 lines at each follow-up visit. During the whole follow-up, corneal endothelial cell counts were stable ($p > 0.05$). Regarding topography, part of the corneal cone was flattened after the operation.

Conclusion: Topography-guided transepithelial-accelerated corneal collagen cross-linking is safe and may correct low refractive error in keratoconus treatment. Further studies and improvements are required in this regard.

Keywords: transepithelial accelerated corneal collagen cross-linking, refractive error, keratoconus, pilot study, topography guided

OPEN ACCESS

Edited by:
FangJun Bao,
Affiliated Eye Hospital of Wenzhou Medical College, China

Reviewed by:
Zhipeng Yan,
Third Hospital of Hebei Medical University, China
Mengmeng Wang,
Hebei Provincial Eye Hospital, China
Shiming Li,
Capital Medical University, China
Fengju Zhang,
Capital Medical University, China

***Correspondence:**
Xingtao Zhou
doctzhouxingtao@163.com

[†]These authors have contributed equally to this work

Specialty section:
This article was submitted to Biomechanics, a section of the journal Frontiers in Bioengineering and Biotechnology

Received: *07 December 2021*
Accepted: *04 February 2022*
Published: *23 February 2022*

Citation:
Sun L, Zhang X, Tian M, Shen Y, Zhao J and Zhou X (2022) Topography-Guided Transepithelial Accelerated Corneal Collagen Cross-Linking for Low Refractive Error Correction in Keratoconus Treatment: A Pilot Study. Front. Bioeng. Biotechnol. 10:830776. doi: 10.3389/fbioe.2022.830776

INTRODUCTION

Keratoconus is a chronic ectatic corneal disease that leads to progressive corneal thinning and irregular astigmatism. A substantial number of keratoconus patients suffer severe visual impairment, which may severely disrupt their lives. These individuals usually use spectacles and rigid gas-permeable contact lenses to improve their visual acuity; however, these instruments are inconvenient and can damage the cornea when keratoconus progresses.

Currently, corneal collagen crosslinking (CXL) is accepted by ophthalmologists as a technique that changes the biomechanics of the cornea and delays or prevents the development of corneal ectasia (Wollensak et al., 2003; Vinciguerra et al., 2013). Meanwhile, many studies have shown that patient visual acuity improves, while corneal curvature flattens after the operation (Kanellopoulos, 2012; Wittig-Silva et al., 2014; Chow et al., 2015). Therefore, some scientists have hypothesized that corneal collagen cross-linking may be used in the treatment of low refractive error correction if this technique can be modified to obtain more obvious corneal flattening. This new technique could benefit patients who are unsuitable for corneal ablation. Roy et al. (Sinha Roy and Dupps, 2011a) found that corneal cone irradiation resulted in greater reduction in curvature than full corneal collagen cross-linking patterns. Based on this theory, the concept of topography-guided corneal collagen cross-linking was proposed, and a related system was developed (KXL II device, Avedro Inc., Waltham, MA, United States).

To date, several case reports of topography-guided transepithelial corneal collagen cross-linking have been published, and the results have shown that patients demonstrated improved vision and decreased corneal curvature (Kanellopoulos, 2014; Kanellopoulos et al., 2014). In this prospective study, we investigated the feasibility of topography-guided transepithelial-accelerated corneal collagen cross-linking (TG-CXL) for low refractive error correction in patients with keratoconus.

MATERIALS AND METHODS

Subjects

This was a prospective self-controlled study. Eighteen patients (18 eyes) were recruited from the Department of Ophthalmology of the Fudan University EENT Hospital. The enrolled eyes were diagnosed with keratoconus and were kept stable for 12 months. The stability of keratoconus was defined as less than 0.5 diopter(D) increase in maximum keratometry, manifest cylinder, manifest refraction spherical equivalent, or no loss or loss of one line of corrected distance visual acuity over the previous 12 months (Kamiya et al., 2015; Doroodgar et al., 2017). The diagnosis of keratoconus was based on corneal topographic data and stromal thinning.

Inclusion criteria were the following: patients aged at least 18 years;

CDVA of 20/80 or better; SE 0 to −3.00 D; minimal corneal thickness 475 micron or better; clear cornea without visible scar on slit-lamp examination.

Exclusion criteria were previous ocular trauma or surgery, other ocular disease or systemic disease that may affect the cornea, and vitamin C (ascorbic acid) supplementation within 1 week of the cross-linking treatment.

The Amsler–Krumeich (AK) classification of keratoconus was used in this study (Rabinowitz, 1998-; Kamiya et al., 2014). According to this classification, 10 eyes were stage I, 5 eyes were stage II, and 3 eyes were stage III. Routine preoperative examinations were performed in order to exclude patients with contraindications. All the patients fully understood the procedure and provided signed informed consent. This study was approved by the Ethics Committee of the Fudan University EENT Hospital Review Board and followed the tenets of the Declaration of Helsinki.

At each visit, the following parameters were assessed: corrected distance visual acuity (CDVA), slit-lamp biomicroscopy, corneal topography, optical tomography, pachymetry with the Pentacam (Oculus, Germany), and endothelial biomicroscopy (NIDEK, Japan). All the postoperative complications were recorded.

Surgical Techniques

All surgeries were performed by the same surgeon (ZXT). After topical anesthesia with 4% oxybuprocaine, 0.1% riboflavin (ParaCel, Avedro Inc.) was applied to the cornea for 4 min, followed by 0.25% riboflavin (VibeX Xtra, Avedro Inc.) for 6 min. The cornea was irradiated with UVA light at 45 mW/cm^2 and pulsed illumination. Treatment profiles included three concentric circular zones centered on maximum posterior elevation to mimic a graded treatment pattern based on the theoretical model proposed by Sinha Roy and Dupps, which suggests that spatial variation of UVA intensity results in the greatest flattening effect (Sinha Roy and Dupps, 2011b). The total UVA dose was 5.4 J when the corneal curvature was no more than 48D, 10 J when it was 48D-51D, and 15 J when it was larger than 51D. The irradiation time and shape were calculated using the KXL II system (Avedro Inc., United States) and corneal topography data (**Figure 1**). At the end of the surgery, a bandage contact lens (ACUVE OASYS, Johnson & Johnson Inc.,) was placed over the cornea.

Post-Operative Medication

The postoperative topical medication regimens were identical for each eye: 0.3% levofloxacin four times per day for 3 days, a 0.1% fluorometholone eye drops was underwent 6 times a day and decrease 1 times every 3 days, and a preservative-free tear supplement four times per day for 1 month. The contact lens was removed on postoperative day one.

Follow-Up

The patients were followed-up at 1 week, 1 month, 3 months, 6 months, and 1 year postoperatively. The examinations included UDVA, CDVA, endothelial cell density, and Pentacam corneal topography to obtain flat K (K1), steep K (K2), mean K (Km), and maximum K (Kmax) values.

Statistical Analysis

Data are expressed as mean ± standard deviation (SD). The *p*-value was determined using single-factor repeated-measures

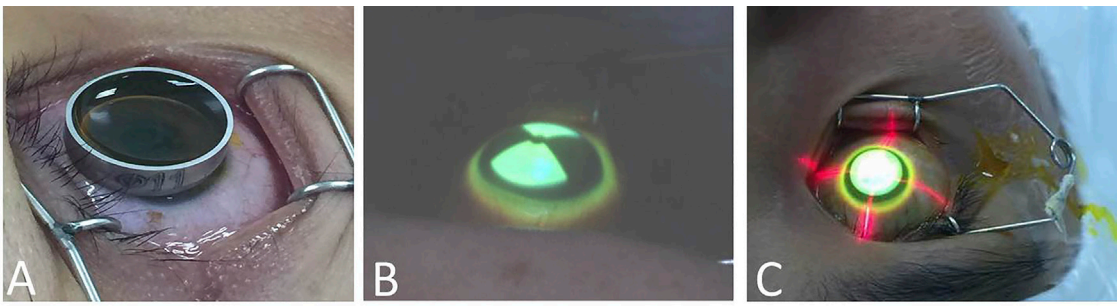

FIGURE 1 | The operation process. **(A)** Application of riboflavin. **(B)** According to the corneal topography, UVA was applied in a sector shape. **(C)** According to the corneal topography, UVA was applied in a circular shape.

TABLE 1 | Ocular examination results at each follow-up point.

	pre	1w po	1 m po	3 m po	6 m po	1 year po
UDVA (logMAR) (mean ± SD)	0.67 ± 0.09	0.48 ± 0.07	0.48 ± 0.07	0.49 ± 0.07	0.60 ± 0.07	0.52 ± 0.08
CDVA (logMAR) (mean ± SD)	0.09 ± 0.04	0.04 ± 0.03	0.03 ± 0.02	0.02 ± 0.03	0.05 ± 0.04	0.05 ± 0.04
SE(D) (mean ± SD)	–3.62 ± 0.39	–3.30 ± 0.35	–3.23 ± 0.32	–3.07 ± 0.32	–3.01 ± 0.34	–2.90 ± 0.34
Steep K(D) (mean ± SD)	46.44 ± 40.70	46.13 ± 0.65	46.29 ± 0.66	46.19 ± 0.65	46.17 ± 0.64	46.15 ± 0.60
Flat K(D) (mean ± SD)	44.40 ± 0.44	44.14 ± 0.41	44.28 ± 0.44	44.24 ± 0.42	44.19 ± 0.41	44.28 ± 0.44
K max(D) (mean ± SD)	49.13 ± 1.22	48.98 ± 1.22	49.11 ± 1.31	48.76 ± 1.09	48.77 ± 1.14	48.82 ± 1.16
TCT (μm) (mean ± SD)	497.25 ± 5.69	485.69 ± 6.62	489.38 ± 6.29	493.94 ± 6.67	492.25 ± 7.07	492.00 ± 6.86
ECD (mean ± SD)	3,095.01 ± 98.85	3,016.15 ± 122.88	3,047.27 ± 104.38	3,255.69 ± 109.20	3,307.11 ± 116.27	3,269.93 ± 126.46

UDVA uncorrected distant visual acuity; CDVA corrected distance visual acuity; SE spherical equivalent; TCT thinnest corneal thick; ECD endothelial cell density.

ANOVA. Statistical significance was set at $p < 0.05$. All statistical analyses were performed using SPSS software (version 16.0, SPSS Inc., Chicago, IL, United States).

RESULTS

No complications occurred in any of the 18 patients (18 eyes) . After the operation, one patient withdrew for personal reasons. Seventeen patients (17 eyes) were included in the data analysis. The patients' mean age was 24.88 ± 4.64 years, and the male to female ratio was 9:8. One patient was lost after 6 months follow-up.

The spherical equivalent (SE), uncorrected distance visual acuity (UDVA), and corrected distance visual acuity (CDVA) at each follow-up visit are shown in **Table 1**. After the operation, the mean SE at each follow-up point decreased compared to that before the operation. At the 1 year postoperative visit, the average SE decreased by 0.73 ± 0.36 D compared to the preoperative SE. This finding was not statistically significant ($p > 0.05$) . The postoperative UDVA and CDVA both increased, although the differences were not significant ($p > 0.05$) . The UCVA changes of patients were showed in **Figure 2**, and the UCVA of nearly 1/3 of the patients was enhanced by at least three lines at each follow-up visit (**Figure 2**). At the last visit, the mean postoperative CDVA and the mean postoperative UCVA were 0.05 ± 0.04 and 0.52 ± 0.08. The safety index (postoperative CDVA/preoperative CDVA) and efficacy index (postoperative UCVA/preoperative CDVA) were 0.56 ± 1.0 and 5.78 ± 2.0.

The results of corneal topography examination at each follow-up visit are shown in **Table 1**. The average postoperative flat K value (K1), steep K value (K2), mean K value (Km), and maximum K value (Kmax) were lower than those determined preoperatively; however, this difference was not statistically significant ($p > 0.05$). The corneal curvatures changed by approximately 0.5D, while the Kmax of the two eyes decreased by 1.5D. Some corneal cones demonstrated flattening in the topographic image during the entire follow-up period (**Figure 3**).

During the follow-up, corneal endothelial cell counts kept stable (**Table 1**).

DISCUSSION

Topography-guided corneal collagen cross-linking is a new technique that has been developed for refractive error correction, the efficacy of which may still be limited; however, for keratoconus patients, the technique is meaningful because it can not only correct refractive error to some extent, but also strengthen the cornea and delay or prevent disease progression. Our study was a prospective self-controlled study and investigated the safety and efficacy of topography-guided transepithelial-accelerated corneal collagen cross-linking for low refractive error correction in keratoconus treatment.

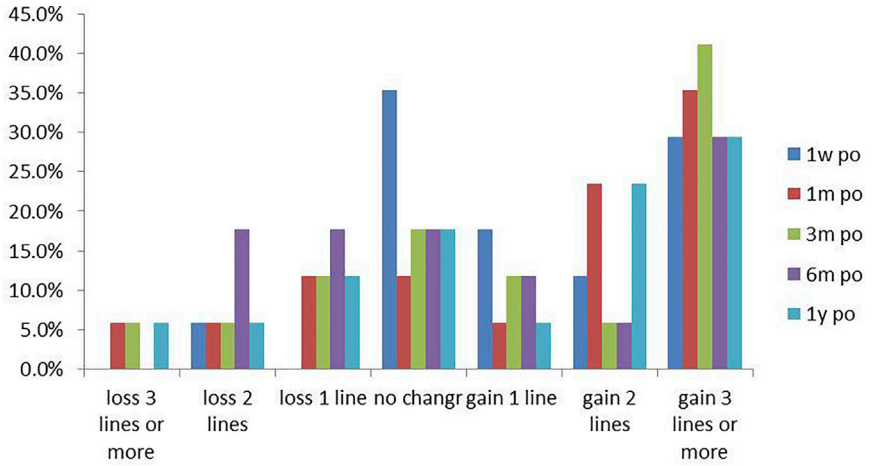

FIGURE 2 | The UCVA of most patients was higher than the pre-operative value, and the UCVA of nearly 1/3 of the patients was enhanced by at least 3 lines at each follow-up visit.

All surgeries were uneventful, and no corneal infection, haze, or other complications occurred at the 1 year follow-up. Moderate corneal epithelial edema was observed on the first postoperative day. At the 1 month postoperative visit, all corneal epithelia had recovered completely. The corneal endothelial cell count did not change significantly at each follow-up visit. These results indicated that topography-guided transepithelial accelerated corneal collagen cross-linking may have good safety comparable to that of general transepithelial-accelerated corneal cross-linking which was showed in author's previous study (Sun et al., 2018).

At the 1 year postoperative visit, the average SE was decreased by 0.73D, while it declined by more than 1D in 6 eyes (35.3%). The maximum reduction is 1.75D. In 9 patients, UDVA was enhanced by two or more lines. Since an improvement of more than 1D in refraction and 2 lines of vision can be considered clinically significant, these results suggest that topography-guided transepithelial accelerated corneal collagen cross-linking may correct a low degree of refractive error correction in some patients. Although UDVA was lost by 2 lines in 1 eye and 3 lines in 2 eyes compared to preoperative results, We found these eyes were classified to stage II or stage III keratoconus, Kmax was larger than 54D and UDVA was larger than 0.4 before operation. We knew patients' visual acuity was blurred in severe keratoconus, so UDVA result may fluctuate. Since CDVA was unchanged and K readings were stable, we thought these eyes didn't get worse after operation.

The Kmax in 2 eyes decreased by 1.5D at the 3 months postoperative visit, while the Kmax value of the other eyes changed by approximately 0.5D throughout the entire follow-up period . The values of K1, K2, and Km decreased slightly after the operation. Although we did not find significantly decreased K values, our results showed that corneal keratometry was stable one 1 year after the operation, which is valuable for keratoconus treatment.

We also found that the decrease in corneal curvature was inconsistent with the decrease in corneal refractive power. For example, the average SE decreased by 0.73D compared to the pre-operation SE at 1 year postoperative follow-up, while the corneal curvatures decreased approximately 0.5D, which was less than changes of SE. Thus, the mechanism of this technology for refractive error correction may include not only corneal flattening, but also other factors, such as remodeling of the corneal epithelium. Further studies are required to confirm this hypothesis.

In our study, the shape of most corneal cones changed after the surgery, where keratometry of part of the corneal cone decreased, while some cone ranges even decreased. Keratometry of most parts was stable outside of the corneal cone. This result was different from that of traditional or accelerated corneal cross-linking without a topography guide, which usually causes a decrease in keratometry both inside and outside the corneal cone. Additionally, the shape and range of the cones did not change. Regarding the mechanism of the technique, topography-guided corneal collagen cross-linking can select different irradiation energies applied to different parts of the cornea according to corneal topography. A greater curvature of the cornea receives more UVA energy; thus, more energy can be provided to the cone area than to the peripheral parts so that the cone can be further flattened. Our results confirm this theory to some extent, and we believe that topography guidance plays a certain role in this operation. Thus, this technique may provide patients with more personalized treatment, selectively reduce the steep portion of the corneal curvature and smooth irregular corneas, and improve visual acuity.

Our results were slightly different from those of published case reports, which demonstrated a more obvious improvement in vision and decreased corneal curvature. For example, in the case report of Kanellopoulos et al. (Kanellopoulos, 2014), the K value of four eyes decreased by 2.3D and 1.44D at 1 week and 6 months postoperatively, respectively. We should note that our study was prospective and enrolled more patients, and thus, the scientificity and reliability should be better compared to the case report.

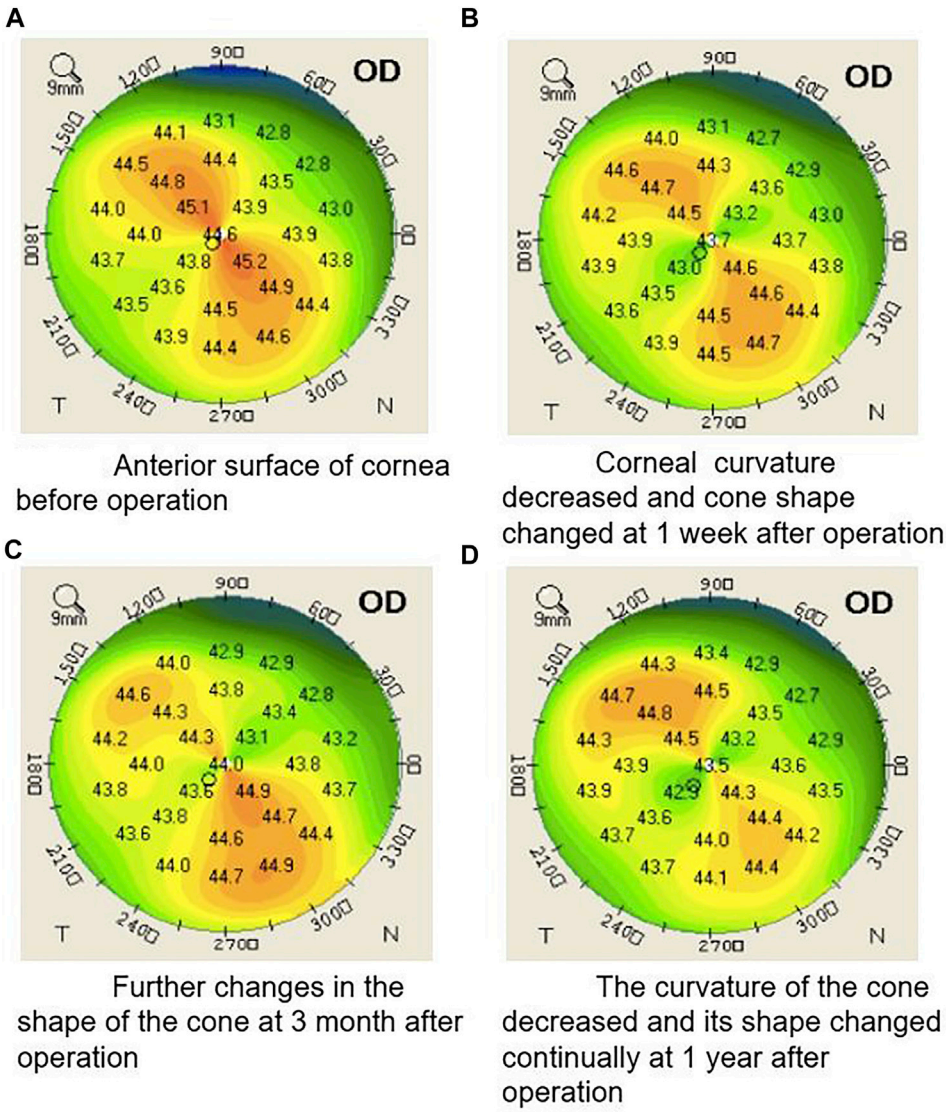

FIGURE 3 | Illustration of a typical case showing the shape of corneal cone changed during the whole follow-up period after the operation **(A)** Anterior surface of cornea before operation. **(B)** Corneal curvature decreased and cone shape changed at 1 week after operation. **(C)** Further changes in the shape of the cone 3 months after operation. **(D)** The curvature of the cone decreased and its shape changed continually at 1 year after operation.

However, we also found that the Kanellopoulos study used a UVA of 12 J, while the average corneal curvature was 44.5D. In the present study, we used much less UVA energy, which might have affected the cross-linking. In Cassagne et al.'s study, CDVA and Kmax improved significantly in the TG-CXL ($p < .05$) (Cassagne et al., 2017). We noted Kmax of patients enrolled in TG-CXL group was 59.23 ± 7.54D, which was much larger than 49.13 ± 1.22D in our study.As Chen et al.'s study showed a higher preoperative maximum K value correlated with greater corneal flattening after epithelium-on CXL (Chen et al., 2016). We hypothesis TG-CXL might be more effective in severe keratoconus treatment. Better results may be obtained using a modified design in future studies.

This study has some limitations. First, the sample size was small, which might have affected the statistical efficacy; therefore, we will continue to enroll more patients for further analysis. Second, the follow-up time may not have been sufficient to evaluate the long-term efficacy. Third, general K values of 9 mm corneal topography were analyzed in this study, which warrants analysis of different regions in future studies with a large sample size as this would yield more detailed information.

In conclusion, we present a new technique that may be applied in keratoconus treatment for low refractive error correction. However, further studies and improvements are needed in topography-guided transepithelial-accelerated corneal collagen cross-linking.

DATA AVAILABILITY STATEMENT

The original contributions presented in the study are included in the article/Supplementary Material, further inquiries can be directed to the corresponding author.

ETHICS STATEMENT

The studies involving human participants were reviewed and approved by Ethical Committee of Fudan University EENT Hospital Review Board. The patients/participants provided their written informed consent to participate in this study.

AUTHOR CONTRIBUTIONS

LS: Conceptualization, data collection, manuscript drafting, critical revision. XYZ: Data collection and manuscript drafting and statistical analysis. MT, YS, JZ: Data collection and analyzing. XTZ: Conceptualization, critical revision of manuscript, funding and supervision. All authors approved the final submission of this manuscript.

FUNDING

Supported by National Natural Science Foundation of China (Grant No. 81770955)

REFERENCES

Cassagne, M., Pierné, K., Galiacy, S. D., Asfaux-Marfaing, M.-P., Fournié, P., and Malecaze, F. (2017). Customized Topography-Guided Corneal Collagen Cross-Linking for Keratoconus. *J. Refract Surg.* 33 (5), 290–297. doi:10.3928/1081597x-20170201-02

Chen, S., Chan, T. C. Y., Zhang, J., Ding, P., Chan, J. C. K., Yu, M. C. Y., et al. (2016). Epithelium-on Corneal Collagen Crosslinking for Management of Advanced Keratoconus. *J. cataract refractive Surg.* 42 (5), 738–749. doi:10.1016/j.jcrs.2016.02.041

Chow, V. W. S., Chan, T. C. Y., Yu, M., Wong, V. W. Y., and Jhanji, V. (2015). One-year Outcomes of Conventional and Accelerated Collagen Crosslinking in Progressive Keratoconus. *Sci. Rep.* 5, 14425. doi:10.1038/srep14425

Doroodgar, F., Niazi, F., Sanginabadi, A., Niazi, S., Baradaran-Rafii, A., Alinia, C., et al. (2017). Comparative Analysis of the Visual Performance after Implantation of the Toric Implantable Collamer Lens in Stable Keratoconus: a 4-year Follow-Up after Sequential Procedure (CXL+TICL Implantation). *BMJ Open Ophthalmol.* 2, e000090. doi:10.1136/bmjophth-2017-000090

Kamiya, K., Ishii, R., Shimizu, K., and Igarashi, A. (2014). Evaluation of Corneal Elevation, Pachymetry and Keratometry in Keratoconic Eyes with Respect to the Stage of Amsler-Krumeich Classification. *Br. J. Ophthalmol.* 98 (4), 459–463. doi:10.1136/bjophthalmol-2013-304132

Kamiya, K., Shimizu, K., Kobashi, H., Igarashi, A., Komatsu, M., Nakamura, A., et al. (2015). Three-year Follow-Up of Posterior Chamber Toric Phakic Intraocular Lens Implantation for the Correction of High Myopic Astigmatism in Eyes with Keratoconus. *Br. J. Ophthalmol.* 99 (2), 177–183. doi:10.1136/bjophthalmol-2014-305612

Kanellopoulos, A. J., Dupps, W. J., Seven, I., and Asimellis, G. (2014). Toric Topographically Customized Transepithelial, Pulsed, Very High-Fluence, Higher Energy and Higher Riboflavin Concentration Collagen Cross-Linking in Keratoconus. *Case Rep. Ophthalmol.* 5 (2), 172–180. doi:10.1159/000363371

Kanellopoulos, J. (2012). Long Term Results of a Prospective Randomized Bilateral Eye Comparison Trial of Higher Fluence, Shorter Duration Ultraviolet A Radiation, and Riboflavin Collagen Cross Linking for Progressive Keratoconus. *Opth* 6, 97–101. doi:10.2147/opth.s27170

Kanellopoulos, J. (2014). Novel Myopic Refractive Correction with Transepithelial Very High-Fluence Collagen Cross-Linking Applied in a Customized Pattern: Early Clinical Results of a Feasibility Study. *Opth* 8, 697–702. doi:10.2147/opth.s59934

Rabinowitz, Y. S. (1998). Keratoconus. *Surv. Ophthalmol.* 42 (4), 297–319. doi:10.1016/s0039-6257(97)00119-7

Sinha Roy, A., and Dupps, W. J., Jr (2011a). Patient-specific Computational Modeling of Keratoconus Progression and Differential Responses to Collagen Cross-Linking. *Invest. Ophthalmol. Vis. Sci.* 52 (12), 9174–9187. doi:10.1167/iovs.11-7395

Sinha Roy, A., and Dupps, W. J., Jr (2011b). Patient-specific Computational Modeling of Keratoconus Progression and Differential Responses to Collagen Cross-Linking. *Invest. Ophthalmol. Vis. Sci.* 52 (12), 9174–9187. doi:10.1167/iovs.11-7395

Sun, L., Li, M., Zhang, X., Tian, M., Han, T., Zhao, J., et al. (2018). Transepithelial Accelerated Corneal Collagen Cross-Linking with Higher Oxygen Availability for Keratoconus: 1-year Results. *Int. Ophthalmol.* 38 (6), 2509–2517. doi:10.1007/s10792-017-0762-5

Vinciguerra, R., Romano, M. R., Camesasca, F. I., Azzolini, C., Trazza, S., Morenghi, E., et al. (2013). Corneal Cross-Linking as a Treatment for Keratoconus. *Ophthalmology* 120 (5), 908–916. doi:10.1016/j.ophtha.2012.10.023

Wittig-Silva, C., Chan, E., Islam, F. M. A., Wu, T., Whiting, M., and Snibson, G. R. (2014). A Randomized, Controlled Trial of Corneal Collagen Cross-Linking in Progressive Keratoconus. *Ophthalmology* 121 (4), 812–821. doi:10.1016/j.ophtha.2013.10.028

Wollensak, G., Spoerl, E., and Seiler, T. (2003). Riboflavin/ultraviolet-a-induced Collagen Crosslinking for the Treatment of Keratoconus. *Am. J. Ophthalmol.* 135 (5), 620–627. doi:10.1016/s0002-9394(02)02220-1

Conflict of Interest: The authors declare that the research was conducted in the absence of any commercial or financial relationships that could be construed as a potential conflict of interest.

Publisher's Note: All claims expressed in this article are solely those of the authors and do not necessarily represent those of their affiliated organizations, or those of the publisher, the editors, and the reviewers. Any product that may be evaluated in this article, or claim that may be made by its manufacturer, is not guaranteed or endorsed by the publisher.

frontiers in Bioengineering and Biotechnology

ORIGINAL RESEARCH
published: 11 March 2022
doi: 10.3389/fbioe.2022.851094

Spatial Assessment of Heterogeneous Tissue Natural Frequency Using Micro-Force Optical Coherence Elastography

Gongpu Lan[1,2,3], Qun Shi[4], Yicheng Wang[4], Guoqin Ma[4], Jing Cai[1,3], Jinping Feng[5], Yanping Huang[1,2,3], Boyu Gu[6], Lin An[2], Jingjiang Xu[1,2,3], Jia Qin[2] and Michael D. Twa[7]**

[1]School of Physics and Optoelectronic Engineering, Foshan University, Foshan, China, [2]Innovation and Entrepreneurship Teams of Guangdong Pearl River Talents Program, Weiren Meditech Co., Ltd., Foshan, China, [3]Guangdong-Hong Kong-Macao Intelligent Micro-Nano Optoelectronic Technology Joint Laboratory, Foshan University, Foshan, China, [4]School of Mechatronic Engineering and Automation, Foshan University, Foshan, China, [5]Institute of Engineering and Technology, Hubei University of Science and Technology, Xianning, China, [6]School of Computer and Information Engineering, Tianjin Chengjian University, Tianjin, China, [7]College of Optometry, University of Houston, Houston, TX, United States

OPEN ACCESS

Edited by:
FangJun Bao,
Affiliated Eye Hospital of Wenzhou Medical College, China

Reviewed by:
Dexi Zhu,
Wenzhou Medical University, China
Pavel Shilyagin,
Institute of Applied Physics (RAS), Russia

***Correspondence:**
Gongpu Lan
langongpu@fosu.edu.cn
Michael D. Twa
mdtwa@uh.edu

Specialty section:
This article was submitted to Biomechanics, a section of the journal Frontiers in Bioengineering and Biotechnology

Received: 09 January 2022
Accepted: 28 February 2022
Published: 11 March 2022

Citation:
Lan G, Shi Q, Wang Y, Ma G, Cai J, Feng J, Huang Y, Gu B, An L, Xu J, Qin J and Twa MD (2022) Spatial Assessment of Heterogeneous Tissue Natural Frequency Using Micro-Force Optical Coherence Elastography. Front. Bioeng. Biotechnol. 10:851094. doi: 10.3389/fbioe.2022.851094

Analysis of corneal tissue natural frequency was recently proposed as a biomarker for corneal biomechanics and has been performed using high-resolution optical coherence tomography (OCT)-based elastography (OCE). However, it remains unknown whether natural frequency analysis can resolve local variations in tissue structure. We measured heterogeneous samples to evaluate the correspondence between natural frequency distributions and regional structural variations. Sub-micrometer sample oscillations were induced point-wise by microliter air pulses (60–85 Pa, 3 ms) and detected correspondingly at each point using a 1,300 nm spectral domain common path OCT system with 0.44 nm phase detection sensitivity. The resulting oscillation frequency features were analyzed via fast Fourier transform and natural frequency was characterized using a single degree of freedom (SDOF) model. Oscillation features at each measurement point showed a complex frequency response with multiple frequency components that corresponded with global structural features; while the variation of frequency magnitude at each location reflected the local sample features. Silicone blocks (255.1 ± 11.0 Hz and 249.0 ± 4.6 Hz) embedded in an agar base (355.6 ± 0.8 Hz and 361.3 ± 5.5 Hz) were clearly distinguishable by natural frequency. In a beef shank sample, central fat and connective tissues had lower natural frequencies (91.7 ± 58.2 Hz) than muscle tissue (left side: 252.6 ± 52.3 Hz; right side: 161.5 ± 35.8 Hz). As a first step, we have shown the possibility of natural frequency OCE methods to characterize global and local features of heterogeneous samples. This method can provide additional information on corneal properties, complementary to current clinical biomechanical assessments, and could become a useful tool for clinical detection of ocular disease and evaluation of medical or surgical treatment outcomes.

Keywords: optical coherence tomography, optical coherence elastography, natural frequency, soft-tissue biomechanics, ophthalmology

INTRODUCTION

Soft tissue biomechanics (e.g., stiffness, elasticity, and viscosity) are highly dependent upon tissue structure, materials, and composition, and they often change alongside pathological changes, such as swelling, inflammation, and tumor growth (Dupps and Wilson, 2006; Sigrist et al., 2017; Chong and Dupps, 2021). Elastic imaging methods, such as ultrasound elastography (Ophir et al., 1991) and magnetic resonance imaging (MRI) elastography (Muthupillai et al., 1995), have been developed to identify lesion areas based on mechanical contrast (e.g., strain map or wave propagations). These methods have been widely used in the diagnosis of diseases such as liver cirrhosis, breast fibrosis, and cancer (Sigrist et al., 2017).

In ophthalmology, corneal elasticity assessment is essential in ocular disease detection and management, such as diagnosing and classifying keratoconus progression (Shah et al., 2007; Roberts and Dupps, 2014; Scarcelli et al., 2014; Bao et al., 2016; Alvani et al., 2020; Tian et al., 2021), preoperatively screening refractive-surgery candidates who are at higher risk of postoperative ectasia (Kanellopoulos, 2007; Shetty et al., 2017; Dackowski et al., 2020; Salomão et al., 2020; Song et al., 2021), and evaluating medical or surgical treatment outcomes (Seven et al., 2016; Bao et al., 2018; Ferguson et al., 2021). Ocular Response Analyzer (ORA, Reichert Inc. Buffalo, NY) (Luce, 2005) and CorVis ST (OCULUS, Inc. Arlington, WA) (Hon and Lam, 2013) are two clinically available devices for assessing intraocular pressure and corneal biomechanics. These two clinical devices are based on an inward corneal applanation event generated by air-puff and an outward applanation event as the cornea recovers to its original shape. Both have been proven reliable in intraocular pressure measurement, but they are still limited in corneal biomechanics evaluation because the estimated corneal biomechanical properties are generally global properties rather than local properties, which would reflect subtle changes in the cornea. Large-amplitude (e.g., 70–300 kPa) stimulation force can result in global corneal deformation, ocular motion, aqueous fluid displacement, as well as globe retraction and rotation (Boszczyk et al., 2017; Jiménez-villar et al., 2019). These factors confound the measurements of these ocular biomechanics measurement methods and limit the capability for detecting regional variations in corneal stiffness (Singh et al., 2017). Previous clinical studies have shown conflicting results: although corneal biomechanics could be differentiated between normal and keratoconus eyes by ORA (Gkika et al., 2012) and CorVis ST (Bak-Nielsen et al., 2014), no significant differences have been found in keratoconus eyes before and after cross-linking treatments (Gkika et al., 2012; Greenstein et al., 2012; Bak-Nielsen et al., 2014). To date, measuring corneal biomechanical properties *in vivo* remains challenging, and there is no gold standard for assessing corneal biomechanics spatially and locally.

Optical coherence elastography (OCE) was developed by combining a loading system to exert a sample stimulation force and an optical coherence tomography (OCT) system to observe the resulting tissue displacements (strains) or mechanical waves (Schmitt, 1998). OCT/OCE provides micrometer-scale axial and lateral resolutions, and the use of phase-sensitive OCT detection (Zhao et al., 2000; Kirkpatrick et al., 2006) can further enhance the dynamic elastography detection sensitivity to a sub-nanometer scale (Lan et al., 2017), making it possible to detect minute-magnitude dynamics for *in vivo* human corneas (Lan et al., 2020a; Ramier et al., 2020; Lan et al., 2021b). The measurement of tissue biomechanics typically centers on Young's modulus, a representation of elasticity expressed as the slope between the force (stress) and the resulting fractional deformation (strain). By analogy with ultrasound elastography, the most commonly used OCE method is based on the measurement of shear (or surface) elastic-wave propagation velocities for Young's modulus estimation (Doyle, 1997; Song et al., 2013a; Wang and Larin, 2014; Zvietcovich and Larin, 2021). However, it has been frequently reported that the shear wave model is useful in bulk tissues/organs, such as the liver and kidney (using ultrasound- or MRI-based elastography detection), but would likely fail in tissues with thin layers and complex boundary conditions, such as the cornea and skin, hence the interest in developing alternative methods (Pelivanov et al., 2019). In the cornea, propagating mechanical waves are not ideal simple Rayleigh waves. Instead, they may contain many highly dispersive Rayleigh-Lamb components requiring a more complex analytic model for accurate interpretation (Han et al., 2015a; Pitre Jr et al., 2019). Thus, the use of a simple shear wave model could have large errors for Young's modulus estimation (Pelivanov et al., 2019). Although a modified Rayleigh-Lamb wave model was presented for corneal viscoelasticity assessment (Han et al., 2015a; Han et al., 2017), this method is based on a first-order assumption that the cornea is isotropic, homogenous, and has a flat curvature. Developing more robust computational methods and tissue modeling techniques is important for enhancing tissue elasticity estimation accuracy in OCE applications (Larin and Sampson, 2017).

In addition to strain- and wave-based OCE strategies, resonant OCE approaches have been developed to quantify sample natural frequencies (the frequencies at which sample tends to oscillate when disturbed) based on the vibrational or resonant response of samples under harmonic or chirp stimulation forces. A variety of modulating forces have been used in resonant OCE approaches, such as acoustic radiation force from ultrasound transducers (Qi et al., 2013), piezoelectric actuators (Adie et al., 2010) or mechanical wave drivers (Liang et al., 2008), magnetic force from embedded nanoparticle transducers (Crecea et al., 2009; Oldenburg and Boppart, 2010; Fischer, 2011), and audio sound waves from a speaker (Akca et al., 2015). Previous studies have shown frequency-enhanced mechanical contrast in cross-sectional or volumetric imaging for *ex vivo* samples (Liang et al., 2008; Adie et al., 2010; Fischer, 2011; Qi et al., 2013), high-resolution measurement of resonant natural frequencies in a stimulation frequency range (Crecea et al., 2009; Adie et al., 2010; Oldenburg and Boppart, 2010; Fischer, 2011; Qi et al., 2013), and the linear relation between the natural frequency and the square root of Young's modulus in a simple elastic model (Crecea et al., 2009; Qi et al., 2013).

These stimulation methods are not suitable for *in vivo* corneal measurements. The labelling agent methods (Crecea et al., 2009; Oldenburg and Boppart, 2010; Fischer, 2011) are not safe, and the

mechanical contact (Liang et al., 2008; Adie et al., 2010) methods may be unsuitable for *in vivo* ocular measurements. Although audio frequency-based OCE was implemented to observe response frequencies from bovine eyes *ex vivo* (Akca et al., 2015); the induced large-scale tissue vibrations (in millimeter scale) require large stimulation forces that are potentially hazardous for ocular tissues *in vivo* as well. In addition, the frequency sweeping method (i.e., using swept harmonic signals over a defined frequency range, or chip signals) usually takes longer time, and could cause discomfort or harm during *in vivo* measurements for the human eye. Transient tissue stimulation methods (e.g., impulse stimulation functions (Wang et al., 2013) and square-wave modulation (Crecea et al., 2009)) can provide broadband stimulation frequencies simultaneously, thereby reducing acquisition time, safety, and comfort for patients. Conversely, wider temporal stimulus duration results in narrower frequency bandwidth responses (Ramier et al., 2019; Zvietcovich and Larin, 2021).

In our previous work, we proposed an OCE method for natural frequency quantification using a microliter air-pulse stimulator to provide transient (~1–4 ms) and broadband frequency excitation (e.g., ~0–1 kHz for a 1-ms duration pulse) with induced tissue damping oscillation magnitudes in sub-micrometer- to sub-nanometer range. Subsequently, we used the method for *in vivo* corneal biomechanics assessment. The dominant tissue oscillation features, such as the dominant natural frequency, decay coefficient, and damping ratio, can be analyzed by utilizing a single degree of freedom (SDOF) quantification method (Lan et al., 2020b). Compared to the *in vivo* OCE measurements of corneal displacements (average coefficient of variation: 17.0%, magnitude: 0.2–0.8 μm (Lan et al., 2020a)) or corneal surface wave speeds (average coefficient of variation: 19.3%, 2.4–4.2 m/s for 18 eyes (Lan et al., 2021b)), the *in vivo* OCE measurements of corneal natural frequency have much better repeatability and reproducibility (average coefficient of variation: 3.2%, 234–277 Hz for 20 eyes (Lan et al., 2021a)). This natural frequency OCE approach could be complementary to the current OCE methods used to estimate Young's modulus from strain- or shear-wave-based measurements for the quantitative determination of corneal biomechanics.

However, there are questions remaining to be solved before we can apply this natural frequency OCE method in eye clinics. Previous studies have focused on characterizing global tissue properties of phantoms and shown the dependency of natural frequencies on the mass, thickness, and stiffness of whole phantoms (Lan et al., 2020b). However, previous studies have not provided any proof as to whether the measurement of natural frequency can be used to distinguish local variations in heterogeneous tissues or samples, such as variations in tissue sub-organizations, interfaces between adjacent tissue components or materials, or stiffness due to injury or pathological progression. Although we have noticed spatial variations of natural frequency in the *in vivo* measurement of the cornea (Lan et al., 2021a), we do not know what parameters caused the natural frequency variations, how they caused the variations, and to what degree each parameter contributed to the variations. Therefore, the goal of this study was to discover the possibility and application scope of the natural frequency OCE method for global and local characterization of corneal biomechanics in a clinical setting. Interpretation of the corneal natural frequency response is not straightforward because the cornea has a very complex microstructure, is spatially inhomogeneous in the lateral and depth directions, and is directionally anisotropic in its response to load according to its structural subcomponents and organizations and its hydration state (Dupps and Wilson, 2006; Meek, 2009; Chong and Dupps, 2021). In this study, as a first step, we focused on the spatial characterization of the oscillation frequency features and the natural frequencies in heterogeneous samples much simpler than the cornea—specifically, agar-silicone phantoms and beef tissue samples. Development of these analytical methods may enable future applications for the use of natural frequency to characterize local tissue properties including corneal elastography and biomechanics estimation *ex vivo* and *in vivo*.

MATERIALS AND METHODS

Samples

Agar and silicone phantoms are commonly used as corneal-mimicking phantoms (Li et al., 2013; Han et al., 2015b; Wang et al., 2018). In this study, we used agar/silicone tissue-mimicking phantoms and beef tissue samples to assess the spatial distributions of natural frequencies. Four types of phantoms were made: a pure silicone phantom (Shore hardness: 25, hereafter referred to as the silicone phantom), a pure 2% agar phantom (hereafter referred to as the agar phantom), and two agar phantoms containing silicone blocks of different shapes (hereafter referred to as silicone-agar mixture phantoms). Each phantom filled a Petri dish with an inner diameter of 57 mm and depth of 14 mm. The use of the Petri dish was to mimic a similar and simplified boundary condition of the cornea by providing an extra constraint in the sample's circumferential direction. The agar phantom (Biowest agarose 111,860) was made following the procedures described previously (Li et al., 2013; Han et al., 2015b; Lan et al., 2020b). The silicone phantom was prepared by mixing silicone components A and B (Shenzhen Ketai Technology Co., Ltd., Shenzhen, China) in a ratio of 1:1 and pouring the mixture into a Petri dish. After 24 h at room temperature, the phantoms were completely dry and ready to be used for measurement. The densities of silicone and 2% agar were 936 kg/m^3 and 933 kg/m^3, respectively. The Young's moduli of the silicone (757.99 kPa) and agar phantoms (1,061.40 kPa) were measured under a 10 N force using a TH-8203A mechanical test frame (Wane Testing Equipment Co., Ltd, Suzhou, Jiangsu, China). Two silicone-agar mixture phantoms were made from two silicone blocks—a rectangular one (length: 5 mm, width: 3 mm, height: 12 mm) and a triangular one (sides: 4–5.5 mm, height: 12.5 mm)—and then each block was embedded in 2% agar. The top of each silicone block was also sealed with agar to achieve a total height of 14 mm. The phantoms roughly mimic tissue lesions or inclusions surrounded by normal tissues. Beef shank samples were bought from a local market, cut into small pieces, and sealed inside 2% agar in a Petri dish with an inner

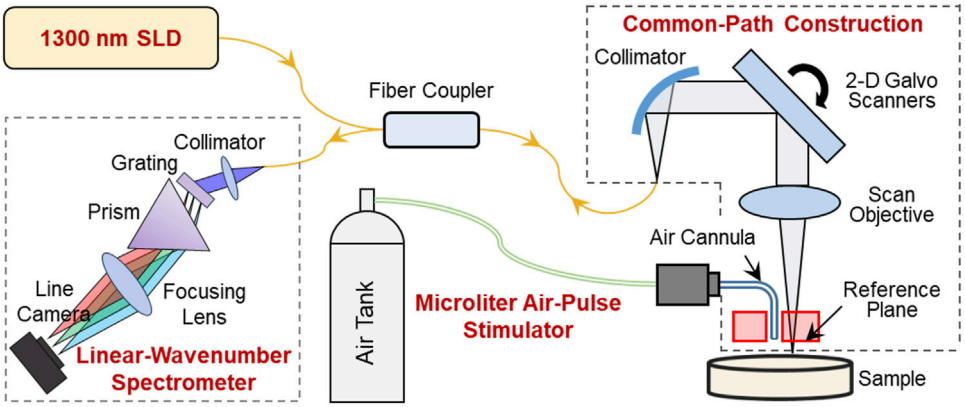

FIGURE 1 | Schematic of the optical coherence elastography (OCE) system. A microliter air pulse stimulator was used to evoke submicron-scale mechanical waves in the sample, and a high-resolution phase-sensitive OCT imaging system was used to track and record the tissue response dynamics. In the OCE imaging subsystem, SLD is a superluminescent laser diode with a waveband of 1,290 ± 40 nm; the sample and reference arms share a common optical path to enhance the phase detection stability; and a linear-wavenumber spectrometer was used to disperse the interference spectrum optically in the wavenumber domain to enhance imaging detection sensitivity.

diameter of 38 mm and inner height of 13 mm. Samples were selected to contain muscle, fat, and connective tissues for natural frequency OCE measurements.

OCE Setup

A home-made OCE system was constructed from a microliter air-pulse mechanical stimulation system and combined with a linear-wavenumber common-path spectral domain OCT platform, as shown in **Figure 1**. The microliter air-pulse stimulation system was controlled with a high-speed solenoid valve that delivered micro-mechanical stimulation perpendicular to the sample surface through a microbore cannula. The cannula provided a spatially-focused (150 μm in diameter), low-pressure (60–85 Pa), and short duration (approximately 3 ms) stimulation force to the samples. The cannula tip was inserted through a hole created in the common-path OCT system reference plate and mounted flush with the surface. The OCT imaging system was synchronized to the stimulation system to record the dynamic response of the sample. The minimum lateral distance measurable by the OCT system was 0.15 mm from the stimulation point.

The OCT/OCE techniques are described in detail in our previous work (Lan et al., 2017; Lan et al., 2021c). In summary, the OCT system was built upon a 1,300 nm linear-wavenumber spectral domain OCT platform (Lan et al., 2021c). The light emitted from a superluminescent diode (SLD, IPSDS1307C-1311, Inphenix Inc., Livermore, CA, United States) with a 3 dB bandwidth of 1,290 ± 40 nm was split equally into sample and reference arms. The reference arm was blocked, whereas a 4 mm thick acrylic reference plate was used in the sample arm to provide a reference plane (the optical surface proximal to the sample). Hence, the sample and reference arms shared a common optical path (**Figure 1**). The common-path construction effectively reduced the amplitude of the background phase disturbance caused by environmental vibrations and improved the phase detection sensitivity (Lan et al., 2017). In the common path, the maximum output power was 1.8 mW, and the output light was collimated by a reflective collimator (RC04APC-P01, Thorlabs, Inc., Newton, NJ, United States) with 4 mm beam diameter, scanned by 2D galvo mirrors (GVS102, Thorlabs Inc., Newton, NJ, United States), and focused by a telecentric scan objective (LSM54-1,310, Thorlabs Inc., Newton, NJ, United States) with a focal length of 54 mm and a maximum field of view of 18.8 × 18.8 mm^2. The interference spectrum generated from the sample and the reference plane was recorded by a linear-wavenumber spectrometer (PSLKS1300-001-GL, Pharostek, Rochester, Minnesota, United States) equipped with an InGaAs line scan camera (GL2048L-10A-ENC-STD-210, Sensors Unlimited, Inc., Princeton, NJ, United States) at a line rate of 76 kHz. The linear-wavenumber spectrometer dispersed the spectrum optically in the wavenumber domain instead of the wavelength domain so that no additional digital interpolation was acquired prior to Fourier transform (Hu and Rollins, 2007; Lan and Li, 2017). Finally, the interference signals were transported through a frame grabber (PCIE-1433, National Instruments Corp., Austin, Texas, United States) into a computer and were then processed directly via Fourier transform to acquire depth profiles (A-scans) using code written in the LabVIEW language. In air, the maximum imaging depth was 6.94 mm for 1,024 pixels (each pixel corresponded to 6.78 μm), the maximum sensitivity was 99.3 dB, the −6 dB fall-off range is ~0–3 mm deep, the maximum sensitivity fall-off is −28.6 dB, and the axial resolution was ~15 μm (2 pixels).

In the transformed OCT interferogram signal, the real component (intensity) illustrates the structural imaging, and the phase signal can be generated by analyzing the complex component. Structural imaging is limited to micron-scale axial resolution, while phase-sensitive detection techniques enhance the dynamic elastography detection sensitivity to a sub-nanometer scale. During micro-force OCE measurements, the tissue displacements were much smaller than the axial resolution

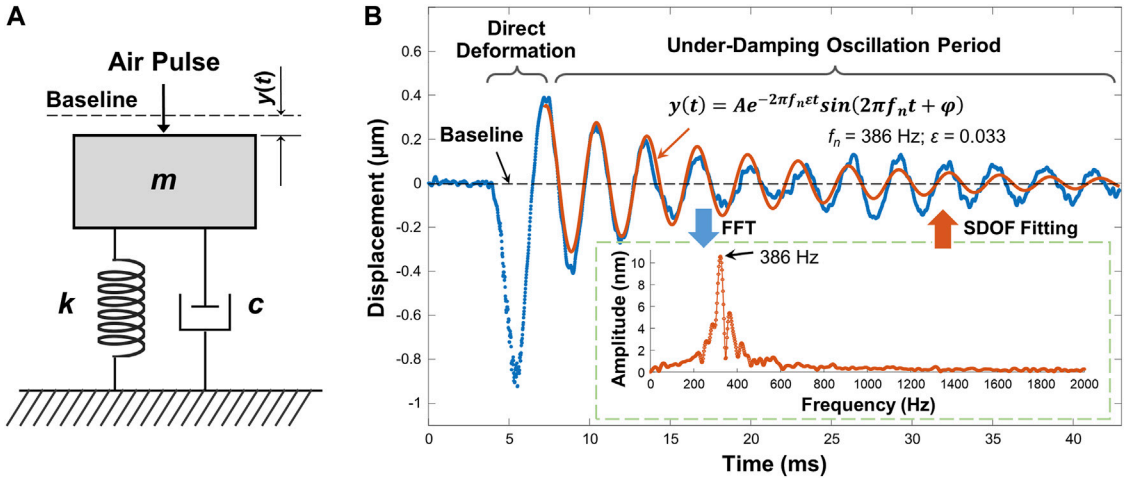

FIGURE 2 | Natural frequency characterization using single degree of freedom (SDOF) model. **(A)** Typical spring-mass-damper system. *m*: mass; *k*: spring stiffness coefficient; *c*: viscous damping coefficient; *y*(*t*): displacement dynamics. **(B)** Typical sample displacement profile and the SDOF fitting for its damping oscillation period (~7.2–42.9 ms). In this example, the sample was the agar phantom. The embedded figure shows the FFT results for the damping oscillation period. The dominant oscillation frequency was substituted into **Eq. 3** to fit the oscillation period.

(~15 μm in this system) or one pixel (6.78 μm). The tissue surface was tracked using structural imaging, and the sub-pixel tissue surface displacements $y(t)$ for each measurement point in the time (t) domain was calculated from the phase change among successive A-scan signals (Song et al., 2013b):

$$y(t) = \frac{\lambda_0}{4\pi n}\phi(t) \quad (1)$$

where $\Phi(t)$ represents the phase change value after phase-unwrapping processing, λ_0 is the center wavelength, and n is the refractive index ($n = 1$ in air). In the absence of applied forces, the average phase variation was measured using a mirror as 4.3 ± 1.4 milliradians over 60 ms (10 repetitive measurements) in the common-path OCT setup, which corresponded to displacements of 0.44 ± 0.14 nm according to **Eq. 1**.

Oscillation Frequency Spectrum and the Dominant Natural Frequency

Tissue natural frequency is an intrinsic property, defined as the frequency at which samples tend to oscillate when disturbed. Natural frequency is determined by factors such as spring stiffness, mass, thickness, size, shape, and boundary conditions, but is not determined by the stimulation force or stimulation frequency. In our previous work (Lan et al., 2020b), the natural frequency concept using OCE measurements was verified on pure agar phantoms: the measured natural frequency was constant for different stimulation pressures and measured distances, and decreased as the sample thickness increased. A single degree of freedom (SDOF) model was used to analyze the dominant natural frequency component with the maximum oscillation magnitude. The SDOF model was built in a simple spring-mass-damper system (**Figure 2A**) to quantify the sample natural frequency. In the SDOF model, the sample natural frequency f_n can be represented as $f_n = \sqrt{k/m}/2\pi$, where m is the mass, and k is the spring stiffness coefficient; and the damping ratio ε is defined as $\varepsilon = c/(4\pi m f_n)$, where c is the viscous damping coefficient. The response oscillation can be described as three different oscillation regimes: critical-damping (damping ration $\varepsilon = 1$), under-damping ($0 \leq \varepsilon < 1$), and over-damping ($\varepsilon > 1$).

Figure 2B demonstrates a typical air-pulse generated surface displacement profile from OCE measurements. The air-pulse duration was ~3 ms, and it can evoke ~0–800 Hz bandwidth frequency response. The observed temporal surface displacement dynamics include a baseline period before sample excitation representing the noise level, a primary deformation period driven by the air-pulse excitation force, and a subsequent period of damped oscillatory motion. The damping oscillation period in **Figure 2B** was obviously an under-damped conditional oscillation. The displacement dynamics $y(t)$ in the damping oscillation period can be represented by Lan et al. (2020b)

$$y(t) = Ae^{-2\pi f_n \varepsilon t} sin\left[2\pi f_n \sqrt{1-\varepsilon^2}\, t + \varphi\right] \quad (2)$$

where A is the amplitude, and φ is a phase value. **Eq. 2** consists of the product of an exponential function and a sinusoidal function, which respectively represent the amplitude decay trend and the oscillation frequency. In the sinusoidal function, the damping natural frequency $f_d = f_n\sqrt{1-\varepsilon^2}$ represents the dominant oscillation frequency, and it can be directly acquired by fast Fourier transform (FFT) (see the inset figure in **Figure 2B**). When the damping ratio ε is small (e.g., <0.3), the natural frequency f_n is in the range of 50–1,000 Hz, and the damped natural frequency f_d is nearly equal to the undamped natural

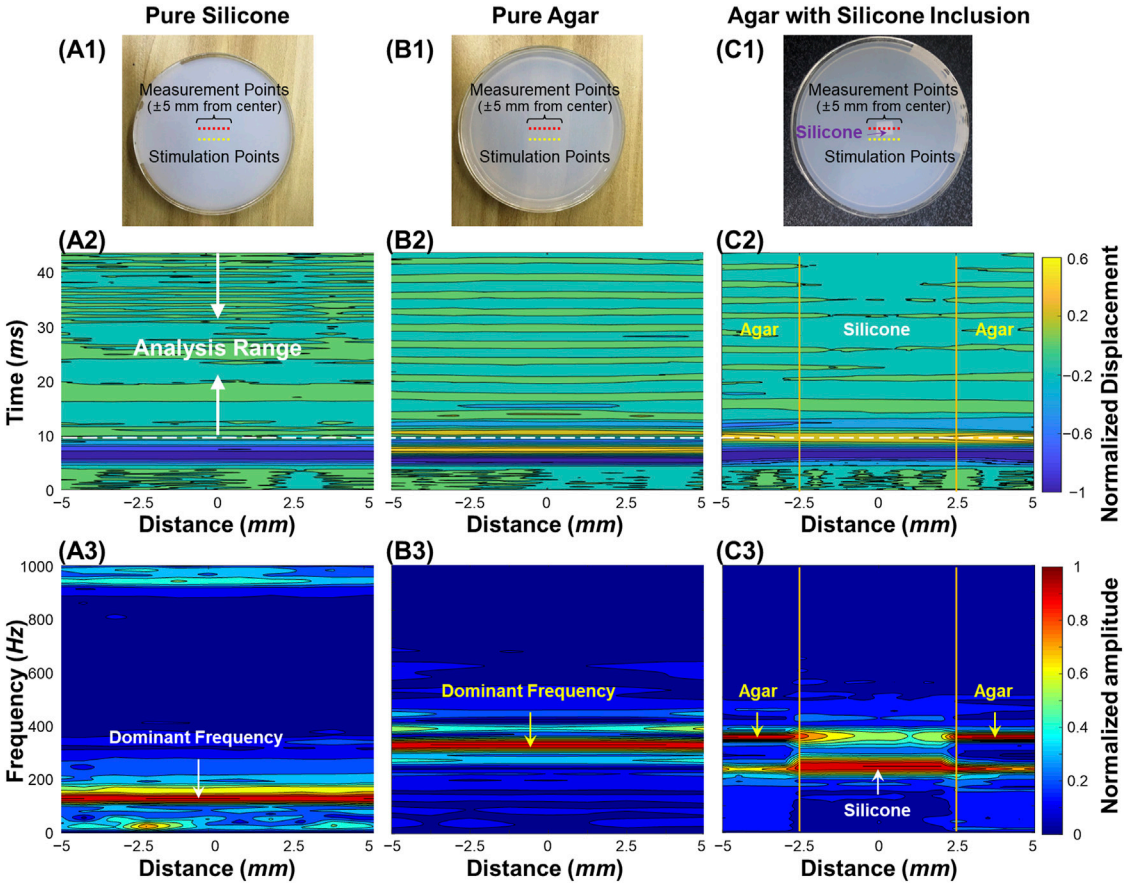

FIGURE 3 | Oscillation feature analysis for the homogeneous and heterogeneous phantom samples. **(A1–C1)**: Top views of the silicone, agar, and silicone-agar mixture phantoms. The measurements were performed at 21 points to cover a 10 mm scan length. The distance between each stimulation and measurement point was 3 mm. **(A2–C2)**: Normalized surface displacement profiles in time domain. Fast-Fourier transformation was performed in the analysis range of 10–43 ms for oscillation frequency feature analysis. **(A3–C3)**: Normalized frequency spectrum in response to the measurement locations for different phantoms. The dominant oscillation frequencies were 128.7 ± 1.0 Hz for the silicone phantom (A3) and 329.7 ± 16.5 Hz for the agar phantom (B3). In (C3), the silicone block can be distinguished in the silicone-agar mixture phantom due to distinct frequency features, which were 247.9 ± 0.7 Hz for the silicone block and 357.6 ± 0.8 Hz for the agar basis.

frequency f_n (i.e., <3 Hz) (Lan et al., 2020b). Here, we assumed $f_d = f_n$. Therefore, **Eq. 2** can be simplified to

$$y(t) = Ae^{-2\pi f_n \epsilon t} \sin[2\pi f_n t + \varphi] \quad (3)$$

In the inset figure of **Figure 2B**, multiple frequency components were observed in the range of approximately 200–600 Hz, and the dominant oscillation frequency was 386 Hz, which was then substituted into **Eq. 3** as f_n to fit the oscillation dynamics. In the fitting results, A = 0.358 μm, ε = 0.033. The R^2 of the fitting was 0.845, and the root mean squared error (RMSE) was 0.045 μm. The residual mismatch between the original displacement data and the fitting data occurred because SDOF was a simplified model that only considered the dominant frequency and discarded other frequency components. The variation of phase (φ) in time could also contributed to the residual error. The residual error could be further reduced if additional frequency components were used to describe the damping oscillation data using a multi degree of freedom (MDOF) method. It was noted that environmental vibrations can lead to low-frequency phase noise (e.g., ~10–40 Hz) (Lan et al., 2017). Therefore, a high-pass filter was applied to the temporal displacement curves to reduce vibrational phase noise prior to SDOF modeling.

Point-to-Point M-Mode Measurement

OCE measurements were performed using a point-to-point M-mode measurement method with a fixed distance (3 mm) between the stimulation and measurement points at sample surface. For each measurement point, a repeated A-scan (M-mode) was performed to acquire the phase variation over time and convert the phase change into the induced displacement profiles using **Eq. 1**. The samples were moved using a translation stage to spatially measure the resulting tissue dynamics. Because the dominant natural frequency was not dependent upon the stimulation force magnitude, as demonstrated in our previous work with agar phantoms (Lan et al., 2020b) and *in vivo* corneas (Lan et al., 2021a). We would expect this holds for other samples,

e.g., silicone, silicone-agar mixture phantoms, or the beef shank samples. The choice of air-pulse pressure can be more flexible on tissues with different stiffness. We adjusted the stimulation pressure over the range of 60–85 Pa to achieve obvious oscillation features (similar to **Figure 2B**), where the induced maximum negative displacements were generally in the range of 0.5–1.5 μm, and the maximum oscillation magnitude (A in **Eq. 3**) was in the range of 0.1–0.4 μm.

RESULTS

Figure 3 demonstrates the air-pulse induced oscillation features in the time and frequency domains for the silicone phantom, the agar phantom, and the silicone-agar mixture phantom with a rectangular silicone block embedded in the center of the agar basis. Measurements were performed at a distance of 3 mm from each stimulation point (as shown in **Figures 3A1–C1**). OCE measurements were performed at 21 points to cover a 10 mm scan length. **Figures 3A2–C2** demonstrate the normalized displacement profiles in the time domain for these phantoms. Across the measurement positions (±5 mm), the coefficients of variation (CVs, standard deviation/mean) of the measured displacements were 7.14% (silicone), 5.30% (agar), and 22.43% (silicone-agar mixture phantom). In **Figure 3C2**, the silicone region had relatively large negative displacements (−1.81 ± 0.04 μm) compared to the agar region (−1.53 ± 0.15 μm), indicating that the silicone was softer than the agar. This was consistent with the Young's modulus measurements (silicone: 757.99 kPa; agar: 1,061.4 kPa). The oscillation periods (10–43 ms) of the displacement dynamics were analyzed using FFT, and the resulting frequency spectrums are shown in **Figures 3A3–C3**. The dominant oscillation frequencies were 128.7 ± 1.0 Hz for the silicone phantom (**Figure 3A3**) and 329.7 ± 16.5 Hz for the agar phantom (**Figure 3B3**). The differences in dominant oscillation frequencies indicated obvious differences in stiffness and elasticity (Young's modulus) for these two phantoms as well. In the silicone-agar mixture phantom, the frequency components were more complex (**Figure 3C3**). There were two main oscillation frequency components across the measurement positions, and the magnitudes of these two frequencies varied in measurement positions and had similar but distinguishable values in the adjunction area. In the agar area, the dominant oscillation frequency was 357.6 ± 0.8 Hz; in the silicone block area, the dominant oscillation frequency was 247.9 ± 0.7 Hz. Notably, measurements of the embedded silicone block were affected by the surrounding 2% agar phantom, so that the silicone block in the silicone-agar mixture phantom had much higher (2 times) oscillation frequencies than the pure silicone phantom. When **Eq. 2** (instead of **Eq. 3**) was used for natural frequency (f_n) estimation, the damping ratios (ε) were small for the silicone (0.010 ± 0.004), agar (0.018 ± 0.006), and silicone-agar mixture phantoms (0.018 ± 0.009). The differences between f_n and f_d were less than 0.1 Hz, so f_n can be assumed to be equal to f_d. The oscillation features reflected both the global and local properties for the silicone-agar mixture phantom. In each measurement position either in the silicone or the agar area, the sample oscillation dynamics included the oscillation frequency components for both the agar and silicone, indicating the global properties; the variation of the frequency magnitude over different areas indicated the local properties.

Figure 4 shows the spatial distributions of the dominant natural frequency (f_n) in the heterogeneous silicone-agar mixture phantoms, where a rectangular or triangular silicone block was embedded in 2% agar (**Figures 4A1, 4B1**). The air cannula and OCT beam were fixed with a distance of 3 mm in the Y direction, and the samples were moved using a translation stage to cover a 10 mm × 10 mm^2 field of view using 21 × 21 sampling points. The sampling length was 0.5 mm in the X and Y directions. In **Figure 4A3**, the dominant natural frequencies (mean ± SD) were 255.1 ± 11.0 Hz for the silicone block and 355.5 ± 1.4 Hz for the agar basis. Similarly, in **Figure 4B3**, the dominant natural frequencies (mean ± SD) were 249.0 ± 4.6 Hz for the silicone block and 361.3 ± 5.5 Hz for the agar basis. The silicone blocks were clearly distinguishable from the agar basis using the natural frequency features. The OCE dominant natural frequency measurement can match the OCT imaging (**Figures 4A2, B2**).

Figure 5 compares the structural imaging and OCE measurement of the dominant natural frequency (f_n) for the beef shank sample. The OCT/OCE measurement region (marked by ink points) was 5 × 3 mm, which included a mixture of connective tissues (e.g., fat, fascia) centered between muscle fibers on both sides (see top view in **Figure 5A**). **Figure 5B** and **Figure 5D** respectively show the OCT volume scan and the *en face* image for the beef sample. **Figure 5E** shows the depth-dependent contour maps of the tissue structure at the depths of 0.8, 1.2, 1.7, and 2.2 mm. The contour maps were acquired using the MATLAB language (R2019b, MathWorks, Inc.). We used the median filter (neighborhood size: 5 pixels × 5 pixels) to smooth the 8-bit *en face* imaging at each depth, and binarized the image with an intensity threshold of 120, and then detected the image edges using the Sobel operator. The OCE sampling was 26 points × 16 points (X × Y) with the spatial sampling of 0.2 mm in both directions. **Figure 5C** shows the normalized oscillation frequency spectrum in both the X and Y directions for the beef tissue sample. Notably, each position had similar low frequency components (e.g., <70 Hz) but different high frequency components (e.g., 70–450 Hz). We set a window of 70–450 Hz to estimate the dominant natural frequency (f_n) using the SDOF method (**Eq. 3**). **Figure 5F** shows the spatial distribution of the dominant natural frequency (f_n) in the X and Y directions. Comparing the *en face* image, depth-dependent contour maps, and the natural frequency distributions in **Figures 5D–F**, we noticed that the natural frequency values correlated with tissue structure and compositions in both the lateral (X and Y) and axial/depth (Z) directions. **Figures 5G–J** compare f_n and the corresponding OCT cross-sections. The central connective tissue had obvious lower natural frequencies (91.7 ± 58.2 Hz) than the muscle regions. The muscle region on the left side had higher frequency (252.6 ± 52.3 Hz) than the muscle region on the right side (161.5 ± 35.8 Hz) due to the sample thickness difference. Using the SDOF method, we can produce a general depiction of the material difference (connective tissue and muscle) and structural difference (e.g., shape and thickness) based on the spatial OCE measurements of the

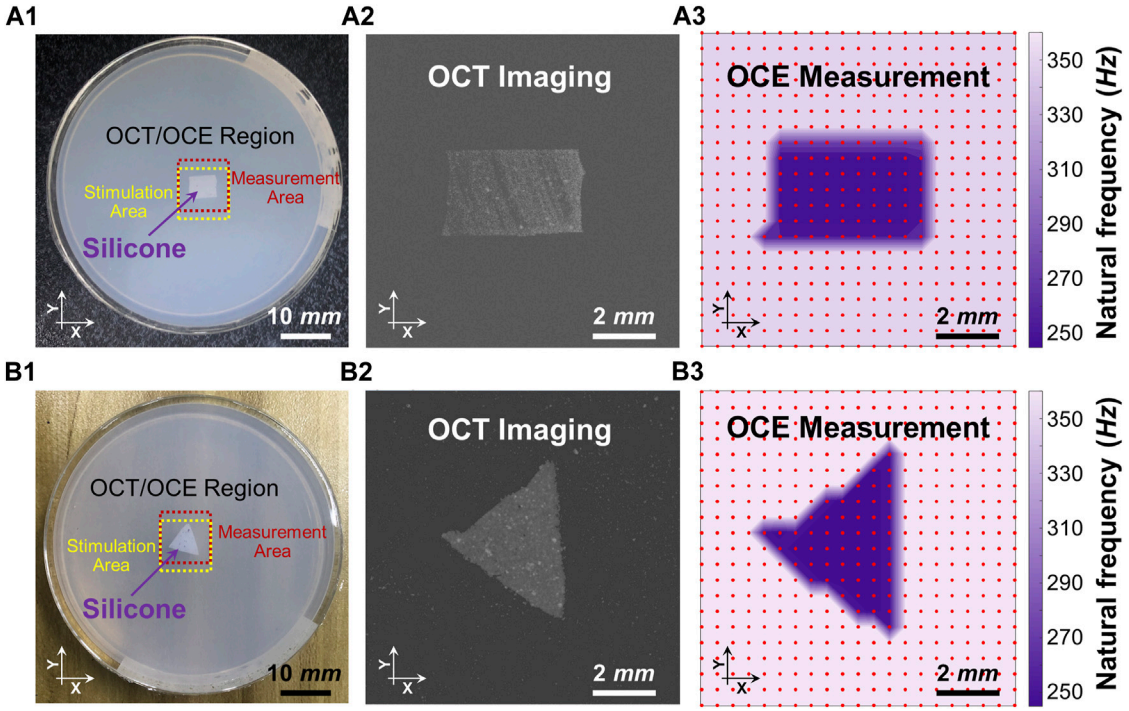

FIGURE 4 | Distinguishing the embedded silicone blocks from the 2% agar using the spatialized dominant natural frequency measurement (f_n). Panels **(A1)** and **(B1)** show the top views of the silicone-agar mixture phantoms and the positions of the stimulation and measurement. Panels **(A2)** and **(B2)** are the *en face* OCT images of the rectangular and triangular silicone blocks, respectively. Panels (A3) and (B3) shows spatial distribution of the dominant natural frequencies (f_n) using the single degree of freedom method. In Panel **(A3)**, the dominant natural frequencies (mean ± SD) were 255.1 ± 11.0 Hz for the silicone block and 355.5 ± 1.4 Hz for the agar basis. In Panel **(B3)**, the dominant natural frequencies (mean ± SD) were 249.0 ± 4.6 Hz for the silicone block and 361.3 ± 5.5 Hz for the agar basis. Optical coherence tomography (OCT); optical coherence elastography (OCE).

dominant natural frequencies. However, the method does not have sufficient spatial resolution to precisely distinguish the boundaries between fat and muscle or to discern muscle fibers and their orientations.

DISCUSSION

In this study, we spatially characterized the dominant natural frequency distributions for heterogeneous tissues and samples using the low-force OCE method, and we demonstrated that the natural frequency property is not only a global factor determined by mass, stiffness, and thickness (Crecea et al., 2009; Qi et al., 2013; Lan et al., 2020b; Lan et al., 2021a), but it is also affected by local features, such as regional variations in shape, stiffness, and material. In the frequency spectrum after the FFT process of the oscillation period, multiple frequency components were usually observed, and these components reflected the global properties. As the magnitude of each frequency component varied across the sample, the dominant natural frequency f_n for a specific measurement position could represent the dominant feature in that region. Since the resonant frequency features are a product of the material properties (e.g., Young's moduli) as well as many other factors, the measured natural frequency of the same material can be very different as the mass, morphology or boundary conditions are different. In this study, we measured the distribution of natural frequencies to spatially distinguish the relative differences in tissue stiffness, structure and composition within heterogeneous tissues and tissue mimicking phantoms. This natural frequency OCE approach could provide a clinically viable, quantitative method to detect local tissue stiffness variations in ocular tissues induced by injuries, pathological degenerations, surgical, or medical treatments.

In a well-controlled phantom with a silicone block embedded in agar to mimic tissue lesions surrounded by normal tissue (**Figure 3C1**), the two materials had measurably different Young's moduli (silicone: 757.99 kPa; agar: 1,061.40 kPa) and clear boundaries. We observed different oscillation patterns in the silicone and agar regions (**Figure 3C2**) as well as distinct frequency features in the oscillation frequency spectrum (**Figure 3C3**). An ideal two-peak frequency spectrum appeared at each of the measurement positions across the agar/silicone/agar regions, indicating that the oscillation frequency components can reflect the global properties of the phantom. We also observed that the magnitude of each peak frequency changed as the measurement location changed. The frequency with the maximum magnitude was 357.6 ± 0.8 Hz in the agar region and 247.9 ± 0.7 Hz in the silicone region. When measurement positions were nearer to the silicone inclusion, we observed lower oscillation frequencies. Thus, the local sample properties are detectable from the oscillation frequency spectrum (as shown in **Figure 3C3**). Thereby, we can conclude that the

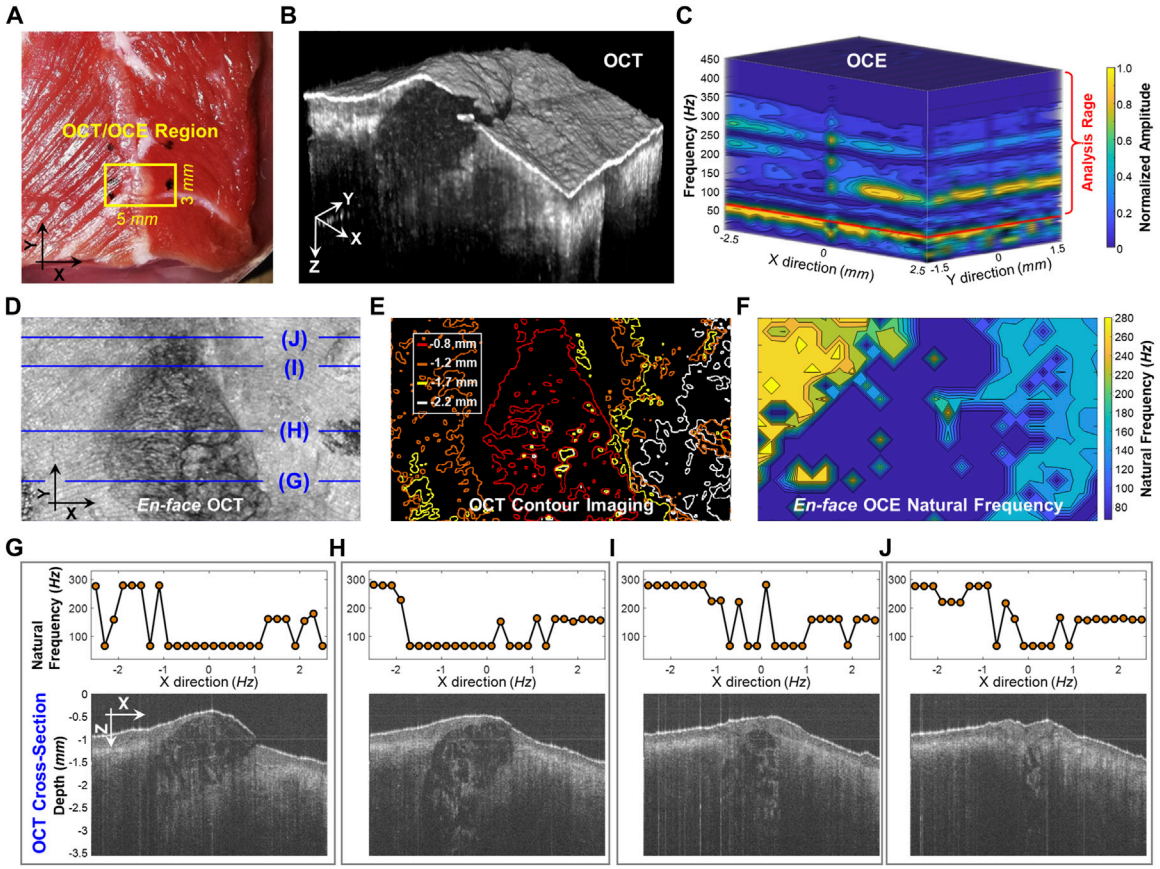

FIGURE 5 | Spatial assessment of the dominant natural frequency (f_n) distribution in a beef shank sample. **(A)** Top view photo of the beef shank sample. The boundary of the beef shank sample was sealed using 2% agar in a Petri dish with an inner diameter of 38 mm and a height of 13 mm. The small window shows the regions (5 × 3 mm) for both the optical coherence tomography (OCT) structural imaging and the optical coherence elastography (OCE) natural frequency measurement. **(B)** OCT volume scan for the beef tissue sample. **(C)** Normalized oscillation frequency spectrum in the *X* and *Y* directions. The f_n for each measurement position was then estimated in the range of 70–450 Hz. **(D)** and **(E)** show the *en face* OCT imaging and the corresponding contour maps at different depths (0.8, 1.2, 1.7, and 2.2 mm). **(F)** Spatial distribution of natural frequency (f_n). **(G–J)** Comparison between the f_n values and the OCT cross-sectional structures at the X-Z planes registered in **(D)**.

measurement of the oscillation frequency components can reflect both the global and local features of the sample. In the resonant frequency spectrum, the numbers of the frequencies may relate to the global properties, whereas the variation of the magnitude of each frequency component at each measurement position may relate to the local properties. To further test our hypothesis, we used the SDOF method to calculate the dominant natural frequency (f_n) for each measurement position and access the spatial distribution of the dominant f_n in the heterogeneous phantoms (**Figure 4**). Both the rectangular and triangular silicone blocks were clearly distinguishable from the agar basis using natural frequency features, and the OCE dominant natural frequency plot matched the OCT imaging well. In the ideal tissue-mimicking phantoms, we can clearly distinguish tissue boundaries using the dominant natural frequencies via the SDOF method (**Figure 4A3** and **Figure 4B3**). It should be noted that tissue natural frequency is not dependent upon elastic modulus alone, but is also determined by other factors, such as mass, thickness, shape, and boundary conditions. That is consistent with our observation that the embedded silicone block in the silicone-agar phantom had twice the natural frequency (247.9 ± 0.7 Hz; **Figure 3C3**) compared to the pure silicone phantom (128.7 ± 1.0 Hz; **Figure 3A3**).

In the spatial measurement of the beef shank sample (**Figure 5**), the frequency spectrum and the dominant natural frequency distribution became more complex than those in the ideal tissue-mimicking phantoms. Although we were able to roughly characterize the material difference (connective tissue and muscle) and the structural difference (e.g., shape and thickness) using the dominant natural frequency values, our method did not offer enough spatial resolution to totally distinguish the boundaries between connective tissue and muscle or to discern muscle fibers and their orientations. There are several possible reasons for the low spatial resolution in the natural frequency measurement. First, the measurement of natural frequency reflects both the local factor near the measurement point and the global factor in lateral and depth directions, while the beef sample was obviously heterogeneous in each direction. Therefore, tissue boundary may not be distinguished clearly based on the resonant features because of the effect of the structure and

material adjacently and globally. Second, The SDOF method is only an approximation and simplification method that used the dominant frequency in the frequency spectrum (**Figure 5C**) while disregarding other frequency features which may reflect subtle structural or material variations. A better analytical model that considers multiple resonant frequency features may better interpret the resonant features and obtain the spatial variations in material and structure. The multi degree of freedom (MDOF) method can be used to describe a more complex system and the general vibration of the system consists of a sum of all the vibration modes, and each vibration mode vibrates at its own frequency. Developing a reliable MDOF method will be the direction of our future work for better characterization of tissue biomechanics. Third, the spatial sampling was only 0.2 mm, which may be insufficient to capture the local changes in tissue stiffness or structure, such as muscle fibers shown in **Figure 5B** and **Figure 5D**. Denser OCE sampling may provide better spatial resolution for natural frequency characterization but require more data acquisition time.

We are enthusiastic about the possibility of using natural frequency observations for clinical characterization of tissue stiffness. Nevertheless, the multi-modal combination of OCT imaging and natural frequency measurements is a complex and unsolved problem. While it is intriguing to consider the collapsed projection of an OCT image, the structural complexity of the underlying tissue cannot be fully represented using *en face* or B-mode projections. Similarly, the natural frequency projections shown in **Figure 5** are an incomplete picture of the underlying mechanical complexity of the samples. Despite these shortcomings, these results are encouraging steps towards a strategy to link structural and mechanical tissue properties.

Additional work is required to adapt this natural frequency OCE method to clinically map corneal biomechanics. A major challenge is that the cornea has a complex tissue organization with a spatially inhomogeneous structure that is directionally anisotropic in its response to loading. Corneal collagen fibrils are preferentially oriented along the superior-inferior and nasal-temporal meridians in the central region and have circumferential orientation in the periphery (Meek, 2009; Chong and Dupps, 2021). The regional and directional uniformity of the collagen fibril organization causes stiffness differences of the cornea in the lateral dimension. Second, collagen fibrils exhibit greater interconnectivity in the anterior third of the corneal stroma than in the posterior stroma, resulting in a nonuniform strength through the depth dimension of the cornea (Komai and Ushiki, 1991). Third, the cornea is composed of many extracellular materials and components with variable charge and chemical interactivity that are distributed inhomogeneously throughout the cornea. For example, the more hydrophilic glycosaminoglycans are found in the deep stroma and promote nonuniform swelling and viscous behaviors (Chong and Dupps, 2021). In addition, ocular disease progression (e.g., keratoconus, ectasia, and glaucoma) and treatments (e.g., corneal cross-linking, refractive surgery) can also add complexity to the regional and directional variations in corneal structure and biomechanical behaviors. How to interpret the pathological or treatment outcomes in corneal biomechanical behaviors from subtle spatial changes in corneal oscillation frequency spectrum, or dominant frequency components, or the variation of magnitude for each main frequency component is challenging but will be an essential part of our research moving forward.

We will further investigate the correlation between corneal natural frequencies and other ocular structural parameters (such as corneal thickness, intraocular pressure, and corneal topography) to better understand the limitations and potential clinical use of the spatial natural frequency measurement method using the low-force OCE system. More advanced analytical methods and finite element eye models must be developed to consider the interactivities among parameters such as corneal biomechanics, intraocular pressure, corneal shape and micro- and macro-compositions, and boundary conditions. Developing such analytical models and investigating the relationships between corneal natural frequency and the above factors could help develop methods to better characterize corneal biomechanical properties. Future studies on patients with ocular disease (e.g., keratoconus or glaucoma) or myopic degeneration, or those who have undergone medical treatments or surgical interventions, are needed to understand the clinical utility of this method for the detection and classification of corneal abnormalities, and for the evaluation of treatment outcomes. Comparison between this OCE method and the clinical biomechanical parameters derived from the Ocular Response Analyzer and the CorVis ST on normal patients and patients with ocular disease or after treatments will also be useful.

DATA AVAILABILITY STATEMENT

The original contributions presented in the study are included in the article/Supplementary Material, further inquiries can be directed to the corresponding authors.

AUTHOR CONTRIBUTIONS

Conceptualization: GL and MT; Methodology: GL, JF, and BG; Experiment: QS, YW, GM and JC; Data Analysis: GL and QS; Visualization: GL and QS; Funding Acquisition: GL, MT, YH, LA, JX and JQ; Writing–Original Draft: GL; Writing–Review and Editing: All authors.

FUNDING

National Natural Science Foundation of China (61975030, 61871130, 81771883, 81801746 and 62005045); Innovation and Entrepreneurship Teams Project of Guangdong Pearl River Talents Program (2019ZT08Y105); Guangdong Basic and Applied Basic Research Foundation (2021A1515011981); Department of Education of Guangdong Province (2020KTSCX130); National Institutes of Health/National Eye Institute (NIH/NEI) R01-EY022362, P30EY07551, and P30EY003039; Guangdong-Hong Kong-Macao Intelligent Micro-Nano Optoelectronic Technology Joint Laboratory (2020B1212030010); University Characteristics Innovation Research Project (2019XJZZ01); Hubei University of Science and Technology (BK202019).

REFERENCES

Adie, S. G., Liang, X., Kennedy, B. F., John, R., Sampson, D. D., and Boppart, S. A. (2010). Spectroscopic Optical Coherence Elastography. *Opt. Express* 18 (25), 25519–25534. doi:10.1364/OE.18.025519

Akca, B. I., Chang, E. W., Kling, S., Ramier, A., Scarcelli, G., Marcos, S., et al. (2015). Observation of Sound-Induced Corneal Vibrational Modes by Optical Coherence Tomography. *Biomed. Opt. Express* 6 (9), 3313–3319. doi:10.1364/BOE.6.003313

Alvani, A., Hashemi, H., Pakravan, M., Mahbod, M., Amanzadeh, K., Seyedian, M. A., et al. (2020). Dynamic Corneal Biomechanics in Different Cell Layers: in Keratoconus and normal Eyes. *Ophthalmic Physiol. Opt.* 41, 414–423. doi:10.1111/opo.12768

Bak-Nielsen, S., Pedersen, I. B., Ivarsen, A., and Hjortdal, J. (2014). Dynamic Scheimpflug-Based Assessment of Keratoconus and the Effects of Corneal Cross-Linking. *J. Refract. Surg.* 30 (6), 408–414. doi:10.3928/1081597X-20140513-02

Bao, F., Geraghty, B., Wang, Q., and Elsheikh, A. (2016). Consideration of Corneal Biomechanics in the Diagnosis and Management of Keratoconus: Is it Important? *Eye Vis.* 3 (1), 18. doi:10.1186/s40662-016-0048-4

Bao, F., Zheng, Y., Liu, C., Zheng, X., Zhao, Y., Wang, Y., et al. (2018). Changes in Corneal Biomechanical Properties with Different Corneal Cross-Linking Irradiances. *J. Refract. Surg.* 34 (1), 51–58. doi:10.3928/1081597X-20171025-01

Boszczyk, A., Kasprzak, H., Jóźwik, A., and Optics, P. (2017). Eye Retraction and Rotation during Corvis ST 'air Puff' Intraocular Pressure Measurement and its Quantitative Analysis. *Ophthalmic Physiol. Opt.* 37 (3), 253–262. doi:10.1111/opo.12383

Chong, J., and Dupps, W. J. (2021). Corneal Biomechanics: Measurement and Structural Correlations. *Exp. Eye Res.* 205, 108508. doi:10.1016/j.exer.2021.108508

Crecea, V., Oldenburg, A. L., Liang, X., Ralston, T. S., and Boppart, S. A. (2009). Magnetomotive Nanoparticle Transducers for Optical Rheology of Viscoelastic Materials. *Opt. Express* 17 (25), 23114–23122. doi:10.1364/OE.17.023114

Dackowski, E. K., Lopath, P. D., and Chuck, R. S. (2020). Preoperative, Intraoperative, and Postoperative Assessment of Corneal Biomechanics in Refractive Surgery. *Curr. Opin. Ophthalmol.* 31 (4), 234–240. doi:10.1097/icu.0000000000000663

Doyle, J. F. (1997). *Wave Propagation in Structure: Spectral Analysis Using Fast Discrete Fourier Transforms*. New York, NY: Springer.

Dupps, W. J., Jr., and Wilson, S. E. (2006). Biomechanics and Wound Healing in the Cornea. *Exp. Eye Res.* 83 (4), 709–720. doi:10.1016/j.exer.2006.03.015

Ferguson, T. J., Singuri, S., Jalaj, S., Ford, M. R., De Stefano, V. S., Seven, I., et al. (2021). Depth-resolved Corneal Biomechanical Changes Measured via Optical Coherence Elastography Following Corneal Crosslinking. *Trans. Vis. Sci. Tech.* 10 (5), 7. doi:10.1167/tvst.10.5.7

Oldenburg, A. L., Wu, G., Spivak, D., Tsui, F., Wolberg, A. S., and Fischer, T. H. (2012). Imaging and Elastometry of Blood Clots Using Magnetomotive Optical Coherence Tomography and Labeled Platelets. *IEEE J. Select. Top. Quan. Electron.* 18 (3), 1100–1109. doi:10.1109/JSTQE.2011.2162580

Gkika, M., Labiris, G., Giarmoukakis, A., Koutsogianni, A., and Kozobolis, V. (2012). Evaluation of Corneal Hysteresis and Corneal Resistance Factor after Corneal Cross-Linking for Keratoconus. *Graefes. Arch. Clin. Exp. Ophthalmol.* 250 (4), 565–573. doi:10.1007/s00417-011-1897-0

Greenstein, S. A., Fry, K. L., and Hersh, P. S. (2012). *In Vivo* biomechanical Changes after Corneal Collagen Cross-Linking for Keratoconus and Corneal Ectasia: 1-year Analysis of a Randomized, Controlled, Clinical Trial. *Cornea* 31 (1), 21–25. doi:10.1097/ICO.0b013e31821eea66

Han, Z., Aglyamov, S. R., Li, J., Singh, M., Wang, S., Vantipalli, S., et al. (2015a). Quantitative Assessment of Corneal Viscoelasticity Using Optical Coherence Elastography and a Modified Rayleigh-Lamb Equation. *J. Biomed. Opt.* 20 (2), 020501. doi:10.1117/1.JBO.20.2.020501

Han, Z., Li, J., Singh, M., Wu, C., Liu, C.-h., Wang, S., et al. (2015b). Quantitative Methods for Reconstructing Tissue Biomechanical Properties in Optical Coherence Elastography: a Comparison Study. *Phys. Med. Biol.* 60 (9), 3531–3547. doi:10.1088/0031-9155/60/9/3531

Han, Z., Li, J., Singh, M., Wu, C., Liu, C.-h., Raghunathan, R., et al. (2017). Optical Coherence Elastography Assessment of Corneal Viscoelasticity with a Modified Rayleigh-Lamb Wave Model. *J. Mech. Behav. Biomed. Mater.* 66, 87–94. doi:10.1016/j.jmbbm.2016.11.004

Hon, Y., and Lam, A. K. C. (2013). Corneal Deformation Measurement Using Scheimpflug Noncontact Tonometry. *Optom. Vis. Sci.* 90 (1), E1–E8. doi:10.1097/Opx.0b013e318279eb87

Hu, Z., and Rollins, A. M. (2007). Fourier Domain Optical Coherence Tomography with a Linear-In-Wavenumber Spectrometer. *Opt. Lett.* 32 (24), 3525–3527. doi:10.1364/ol.32.003525

Jiménez-villar, A., Mączyńska, E., Cichański, A., Wojtkowski, M., Kałużny, B. J., and Grulkowski, I. (2019). High-speed OCT-Based Ocular Biometer Combined with an Air-Puff System for Determination of Induced Retraction-free Eye Dynamics. *Biomed. Opt. Express* 10 (7), 3663–3680. doi:10.1364/BOE.10.003663

Kanellopoulos, A. J. (2007). Post-LASIK Ectasia. *Ophthalmology* 114 (6), 1230–1230. doi:10.1016/j.ophtha.2007.03.041

Kirkpatrick, S. J., Wang, R. K., and Duncan, D. D. (2006). OCT-based Elastography for Large and Small Deformations. *Opt. Express* 14 (24), 11585–11597. doi:10.1364/oe.14.011585

Komai, Y., and Ushiki, T. (1991). The Three-Dimensional Organization of Collagen Fibrils in the Human Cornea and Sclera. *Invest. Ophthalmol. Vis. Sci.* 32 (8), 2244–2258.

Lan, G., and Li, G. (2017). Design of a K-Space Spectrometer for Ultra-broad Waveband Spectral Domain Optical Coherence Tomography. *Sci. Rep.* 7, 42353. doi:10.1038/srep42353

Lan, G., Singh, M., Larin, K. V., and Twa, M. D. (2017). Common-path Phase-Sensitive Optical Coherence Tomography Provides Enhanced Phase Stability and Detection Sensitivity for Dynamic Elastography. *Biomed. Opt. Express* 8 (11), 5253–5266. doi:10.1364/BOE.8.005253

Lan, G., Gu, B., Larin, K. V., and Twa, M. D. (2020a). Clinical Corneal Optical Coherence Elastography Measurement Precision: Effect of Heartbeat and Respiration. *Trans. Vis. Sci. Tech.* 9 (5), 3. doi:10.1167/tvst.9.5.3

Lan, G., Larin, K. V., Aglyamov, S., and Twa, M. D. (2020b). Characterization of Natural Frequencies from Nanoscale Tissue Oscillations Using Dynamic Optical Coherence Elastography. *Biomed. Opt. Express* 11 (6), 3301–3318. doi:10.1364/BOE.391324

Lan, G., Aglyamov, S., Larin, K. V., and Twa, M. D. (2021a). *In Vivo* human Corneal Natural Frequency Quantification Using Dynamic Optical Coherence Elastography: Repeatability and Reproducibility. *J. Biomech.* 121, 110427. doi:10.1016/j.jbiomech.2021.110427

Lan, G., Aglyamov, S. R., Larin, K. V., and Twa, M. D. (2021b). *In Vivo* Human Corneal Shear-Wave Optical Coherence Elastography. *Optom. Vis. Sci.* 98 (1), 58–63. doi:10.1097/OPX.0000000000001633

Lan, G., Xu, J., Hu, Z., Huang, Y., Wei, Y., Yuan, X., et al. (2021c). Design of 1300 Nm Spectral Domain Optical Coherence Tomography Angiography System for Iris Microvascular Imaging. *J. Phys. D: Appl. Phys.* 54, 264002. doi:10.1088/1361-6463/abf577

Larin, K. V., and Sampson, D. D. (2017). Optical Coherence Elastography - OCT at Work in Tissue Biomechanics [Invited]. *Biomed. Opt. Express* 8 (2), 1172–1202. doi:10.1364/Boe.8.001172

Li, J., Wang, S., Manapuram, R. K., Singh, M., Menodiado, F. M., Aglyamov, S., et al. (2013). Dynamic Optical Coherence Tomography Measurements of Elastic Wave Propagation in Tissue-Mimicking Phantoms and Mouse Corneain Vivo. *J. Biomed. Opt.* 18 (12), 121503. doi:10.1117/1.JBO.18.12.121503

Liang, X., Oldenburg, A. L., Crecea, V., Chaney, E. J., and Boppart, S. A. (2008). Optical Micro-scale Mapping of Dynamic Biomechanical Tissue Properties. *Opt. Express* 16 (15), 11052–11065. doi:10.1364/OE.16.011052

Luce, D. A. (2005). Determining *In Vivo* Biomechanical Properties of the Cornea with an Ocular Response Analyzer. *J. Cataract. Refract. Surg.* 31 (1), 156–162. doi:10.1016/j.jcrs.2004.10.044

Meek, K. M. (2009). Corneal Collagen-Its Role in Maintaining Corneal Shape and Transparency. *Biophys. Rev.* 1 (2), 83–93. doi:10.1007/s12551-009-0011-x

Muthupillai, R., Lomas, D. J., Rossman, P. J., Greenleaf, J. F., Manduca, A., and Ehman, R. L. (1995). Magnetic Resonance Elastography by Direct Visualization of Propagating Acoustic Strain Waves. *Science* 269 (5232), 1854–1857. doi:10.1126/science.7569924

Oldenburg, A. L., and Boppart, S. A. (2010). Resonant Acoustic Spectroscopy of Soft Tissues Using Embedded Magnetomotive Nanotransducers and Optical

Coherence Tomography. *Phys. Med. Biol.* 55 (4), 1189–1201. doi:10.1088/0031-9155/55/4/019

Ophir, J., Céspedes, I., Ponnekanti, H., Yazdi, Y., and Li, X. (1991). Elastography: a Quantitative Method for Imaging the Elasticity of Biological Tissues. *Ultrason. Imaging* 13 (2), 111–134. doi:10.1177/016173469101300201

Pelivanov, I., Gao, L., Pitre, J., Kirby, M. A., Song, S., Li, D., et al. (2019). Does Group Velocity Always Reflect Elastic Modulus in Shear Wave Elastography? *J. Biomed. Opt.* 24 (7), 1. doi:10.1117/1.JBO.24.7.076003

Pitre, J. J., Jr, Kirby, M. A., Gao, L., Li, D. S., Shen, T., Wang, R. K., et al. (2019). Super-shear Evanescent Waves for Non-contact Elastography of Soft Tissues. *Appl. Phys. Lett.* 115 (8), 083701. doi:10.1063/1.5111952

Qi, W., Li, R., Ma, T., Li, J., Kirk Shung, K., Zhou, Q., et al. (2013). Resonant Acoustic Radiation Force Optical Coherence Elastography. *Appl. Phys. Lett.* 103 (10), 103704–103796. doi:10.1063/1.4820252

Ramier, A., Tavakol, B., and Yun, S.-H. (2019). Measuring Mechanical Wave Speed, Dispersion, and Viscoelastic Modulus of the Cornea Using Optical Coherence Elastography. *Opt. Express* 27 (12), 16635–16649. doi:10.1364/OE.27.016635

Ramier, A., Eltony, A. M., Chen, Y., Clouser, F., Birkenfeld, J. S., Watts, A., et al. (2020). *In Vivo* measurement of Shear Modulus of the Human Cornea Using Optical Coherence Elastography. *Sci. Rep.* 10 (1), 1–10. doi:10.1038/s41598-020-74383-4

Roberts, C. J., and Dupps, W. J., Jr. (2014). Biomechanics of Corneal Ectasia and Biomechanical Treatments. *J. Cataract Refract. Surg.* 40 (6), 991–998. doi:10.1016/j.jcrs.2014.04.013

Salomão, M. Q., Hofling-Lima, A. L., Gomes Esporcatte, L. P., Lopes, B., Vinciguerra, R., Vinciguerra, P., et al. (2020). The Role of Corneal Biomechanics for the Evaluation of Ectasia Patients. *Int. J. Environ. Res. Public Health* 17 (6), 2113. doi:10.3390/ijerph17062113

Scarcelli, G., Besner, S., Pineda, R., Yun, S. H., and science, v. (2014). Biomechanical Characterization of Keratoconus Corneas *Ex Vivo* with Brillouin Microscopy. *Invest. Ophthalmol. Vis. Sci.* 55 (7), 4490–4495. doi:10.1167/iovs.14-14450

Schmitt, J. M. (1998). OCT Elastography: Imaging Microscopic Deformation and Strain of Tissue. *Opt. Express* 3 (6), 199–211. doi:10.1364/oe.3.000199

Seven, I., Vahdati, A., De Stefano, V. S., Krueger, R. R., and Dupps, W. J., Jr. (2016). Comparison of Patient-specific Computational Modeling Predictions and Clinical Outcomes of LASIK for Myopia. *Invest. Ophthalmol. Vis. Sci.* 57 (14), 6287–6297. doi:10.1167/iovs.16-19948

Shah, S., Laiquzzaman, M., Bhojwani, R., Mantry, S., and Cunliffe, I. (2007). Assessment of the Biomechanical Properties of the Cornea with the Ocular Response Analyzer in normal and Keratoconic Eyes. *Invest. Ophthalmol. Vis. Sci.* 48 (7), 3026–3031. doi:10.1167/iovs.04-0694

Shetty, R., Francis, M., Shroff, R., Pahuja, N., Khamar, P., Girrish, M., et al. (2017). Corneal Biomechanical Changes and Tissue Remodeling after SMILE and LASIK. *Invest. Ophthalmol. Vis. Sci.* 58 (13), 5703. doi:10.1167/iovs.17-22864

Sigrist, R. M. S., Liau, J., Kaffas, A. E., Chammas, M. C., and Willmann, J. K. (2017). Ultrasound Elastography: Review of Techniques and Clinical Applications. *Theranostics* 7 (5), 1303–1329. doi:10.7150/thno.18650

Singh, M., Li, J., Vantipalli, S., Han, Z., Larin, K. V., and Twa, M. D. (2017). Optical Coherence Elastography for Evaluating Customized Riboflavin/UV-A Corneal Collagen Crosslinking. *J. Biomed. Opt.* 22 (9), 091504. doi:10.1117/1.JBO.22.9.091504

Song, S., Huang, Z., Nguyen, T.-M., Wong, E. Y., Arnal, B., O'Donnell, M., et al. (2013a). Shear Modulus Imaging by Direct Visualization of Propagating Shear Waves with Phase-Sensitive Optical Coherence Tomography. *J. Biomed. Opt.* 18 (12), 1. doi:10.1117/1.JBO.18.12.121509

Song, S., Huang, Z., and Wang, R. K. (2013b). Tracking Mechanical Wave Propagation within Tissue Using Phase-Sensitive Optical Coherence Tomography: Motion Artifact and its Compensation. *J. Biomed. Opt.* 18 (12), 121505. doi:10.1117/1.JBO.18.12.121505

Song, Y., Fang, L., Fang, L., Zhu, Q., Du, R., Guo, B., et al. (2021). Biomechanical Responses of the Cornea after Small Incision Lenticule Extraction (SMILE) Refractive Surgery Based on a Finite Element Model of the Human Eye. *Math. Biosci. Eng.* 18 (4), 4212–4225. doi:10.3934/mbe.2021211

Tian, L., Zhang, D., Guo, L., Qin, X., Zhang, H., Zhang, H., et al. (2021). Comparisons of Corneal Biomechanical and Tomographic Parameters Among Thin normal Cornea, Forme Fruste Keratoconus, and Mild Keratoconus. *Eye Vis.* 8 (1), 44. doi:10.1186/s40662-021-00266-y

Wang, S., and Larin, K. V. (2014). Shear Wave Imaging Optical Coherence Tomography (SWI-OCT) for Ocular Tissue Biomechanics. *Opt. Lett.* 39 (1), 41–44. doi:10.1364/OL.39.000041

Wang, S., Larin, K. V., Li, J., Vantipalli, S., Manapuram, R. K., Aglyamov, S., et al. (2013). A Focused Air-Pulse System for Optical-Coherence-Tomography-Based Measurements of Tissue Elasticity. *Laser Phys. Lett.* 10 (7), 075605. doi:10.1088/1612-2011/10/7/075605

Wang, L., Tian, L., Huang, Y., Huang, Y., and Zheng, Y. (2018). Assessment of Corneal Biomechanical Properties with Inflation Test Using Optical Coherence Tomography. *Ann. Biomed. Eng.* 46 (2), 247–256. doi:10.1007/s10439-017-1973-7

Zhao, Y., Chen, Z., Saxer, C., Xiang, S., de Boer, J. F., and Nelson, J. S. (2000). Phase-resolved Optical Coherence Tomography and Optical Doppler Tomography for Imaging Blood Flow in Human Skin with Fast Scanning Speed and High Velocity Sensitivity. *Opt. Lett.* 25 (2), 114–116. doi:10.1364/ol.25.000114

Zvietcovich, F., and Larin, K. V. (2022). Wave-based Optical Coherence Elastography: the 10-year Perspective. *Prog. Biomed. Eng.* 4, 012007. doi:10.1088/2516-1091/ac4512

Conflict of Interest: Authors GL, YH, LA, JX, and JQ were employed by Weiren Meditech Co., Ltd.

The remaining authors declare that the research was conducted in the absence of any commercial or financial relationships that could be construed as a potential conflict of interest.

frontiers in Bioengineering and Biotechnology

ORIGINAL RESEARCH
published: 30 March 2022
doi: 10.3389/fbioe.2022.848060

The Shape of Corneal Deformation Alters Air Puff–Induced Loading

Atieh Yousefi[1,2], *Cynthia J. Roberts*[1,2]* *and Matthew A. Reilly*[1,2]

[1]Department of Ophthalmology and Visual Sciences, The Ohio State University, Columbus, OH, United States, [2]Department of Biomedical Engineering, The Ohio State University, Columbus, OH, United States

Purpose: To determine the dynamic modification of the load exerted on the eye during air-puff testing by accounting for the deformation of the cornea.

Methods: The effect of corneal load alteration with surface shape (*CLASS*) was characterized as an additional component of the load produced during the concave phase where the fluid outflow tangential to the corneal surface creates backward pressure. Concave phase duration (t_{CD}), maximum *CLASS* value ($CLASS_{max}$), and the area under *CLASS*-time curve ($CLASS_{int}$) are calculated for 26 keratoconic (KCN), 102 normal (NRL), and 29 ocular hypertensive (OHT) subjects. Tukey's HSD tests were performed to compare the three subject groups. A p-value less than 0.05 was considered statistically significant.

Results: Accounting for *CLASS* increased the load by 34.6% ± 7.7% at maximum concavity; these differences were greater in KCN subjects ($p < 0.0001$) and lower in OHT subjects ($p = 0.0028$) than in NRL subjects. t_{CD} and $CLASS_{int}$ were significantly longer and larger, respectively, for KCN subjects than those in the NRL and OHT groups ($p < 0.0001$).

Conclusion: Load characterization is an essential step in assessing the cornea's biomechanical response to air-puff–induced deformation. The dynamic changes in the corneal surface shape significantly alter the load experienced by the corneal apex. This implies a subject-specific loading dynamic even if the air puff itself is identical. This is important when comparing the same eye after a surgical procedure or topical medication that alters corneal properties. Stiffer corneas are least sensitive to a change in load, while more compliant corneas show higher sensitivity.

Keywords: biomechanics, cornea, air puff load, deformation, noncontact tonometry

OPEN ACCESS

Edited by:
FangJun Bao,
Affiliated Eye Hospital of Wenzhou Medical College, China

Reviewed by:
Sabine Kling,
ETH Zürich, Switzerland
Johannes Weickenmeier,
Stevens Institute of Technology, United States

***Correspondence:**
Cynthia J. Roberts
roberts.8@osu.edu

Specialty section:
This article was submitted to Biomechanics, a section of the journal Frontiers in Bioengineering and Biotechnology

Received: *03 January 2022*
Accepted: *03 March 2022*
Published: *30 March 2022*

Citation:
Yousefi A, Roberts CJ and Reilly MA (2022) The Shape of Corneal Deformation Alters Air Puff–Induced Loading. Front. Bioeng. Biotechnol. 10:848060. doi: 10.3389/fbioe.2022.848060

INTRODUCTION

Corneal biomechanics is an essential tool in corneal disease diagnosis and in providing timely disease management and treatment (Piñero et al., 2010; Terai et al., 2012; Vinciguerra et al., 2016; Kling and Hafezi, 2017). Biomechanical measurements are used in modifying intraocular pressure (IOP) estimation (Liu and Roberts, 2005; Luce, 2006; Elsheikh et al., 2015), assessing the risk of procedures, such as refractive surgery (Liu and Roberts, 2005; Ambrósio et al., 2010; Santhiago et al., 2016), and diagnosing, monitoring, and treating diseases such as keratoconus and glaucoma (Kotecha, 2007; Gorgun et al., 2011).

Characterizing tissue deformation in response to known loading is a common biomechanical diagnostic approach. These techniques can be divided into the two major categories of contact and

noncontact loads. For example, atomic force microscopy is a well-established technique for micro-indentation and characterization of living cell stiffness *ex vivo* (Thomas et al., 2013). In other studies, noncontact methods are introduced by oscillating acoustic force by ultrasound transducers (Vappou et al., 2015). An alternative approach more commonly used clinically in ocular applications is deformation using an air puff. This method is also utilized in other areas of study, such as skin stiffness characterization (Boyer et al., 2012).

Specifically for ocular applications, two devices are clinically used to assess corneal biomechanics, both of which do so by using an air puff to deform the cornea and characterize the resulting response. The first device detects bidirectional applanation during deformation and produces parameters such as corneal hysteresis to describe viscoelastic biomechanical response (Luce, 2005). The second device characterizes corneal biomechanical response through Scheimpflug imaging *via* a high-speed camera during the application of a consistent air puff and captures the corneal deformation shape, depth, and timing throughout the imaging period. While both devices provide clinically useful parameters to characterize corneal biomechanics, there still are several confounding parameters that may influence interpretation. Many of these confounding factors, such as IOP and corneal thickness, have been assessed previously (Whitacre et al., 1993; Roberts, 2014). However, the dynamic, nonlinear interaction between the deforming surface shape and the noncontact fluid load has not been assessed previously. Corneal biomechanical parameters are currently interpreted under the assumption of similar load application on different subjects. Detailed knowledge of the applied load is, therefore, essential in interpreting the biomechanical response.

As explained by the Coanda effect, (Benner, 1964) the fluid jet tends to stay attached to the deforming surface, altering the angle of fluid outflow. This back flow, therefore, introduces an additional component of the load on the material surface which may vary between patients or even between tests on the same patient. In this study, we aimed to investigate the underlying interaction between dynamic corneal curvature changes in response to the applied air puff on the load experienced by the cornea. We hypothesized that the load experienced by the corneal apex is altered by the changes in corneal surface shape during the deformation process. In order to investigate this hypothesis, we analytically characterized the effect of changing the geometry on the load amplitude in corneal deformation under an air puff.

METHODS

The effect of changing the geometry on the loading is characterized in CorVis ST (OCULUS Optikgeräte GmbH, Wetzlar, Germany), in a similar method introduced by Tanaka et al. (2011), where they have utilized conservation of mass and conservation of momentum to calibrate the load based on the change in surface curvature and surface deformation on the skin.

Characterization of Load Under Deformation

Tanaka et al. (2011) derived an analytical approximation for load amplification due to the two-dimensional, axisymmetric loading of the skin by an air puff. They found that the load experienced on a concave surface can far exceed that experienced on a flat surface, in this case corresponding to the corneal apex. Specifically, the load in the direction of the air puff z is as follows:

$$F_z(t) = \rho v^2 A(1 - \cos(\theta)), \tag{1}$$

where F_z is the load exerted by the air puff and experienced at the corneal apex, ρ is the air density, A is the cross-sectional area of the device nozzle, and θ is the angle between the air puff impacting the cornea normal to the surface and the airflow exiting from the corneal deformation area after interacting with the deformed shape (**Figure 1**).

Corneal Load Alteration With Surface Shape Effect Characterization

The impact of the deforming surface on the load experienced by the corneal apex is represented in **Figure 1**. The values of concave radius and peak-to-peak distance are exported from the CorVis ST research software and used to compute the angle θ for each of the 140 video frames captured during the approximately 30-ms duration immediately following the air puff. As shown in **Figure 1B**, the vector representing the radius is perpendicular to V_2 and the line representing half the peak-to-peak distance is perpendicular to the dashed line, implying that the two angles marked with α are congruent. We can, therefore, conclude that

$$\cos\alpha = \frac{PD}{2R} = -\cos\theta, \tag{2}$$

where *PD/2* is half the peak-to-peak distance and R is the radius of curvature, where the concave values are positive and are exported from CorVis ST and the convex values are negative and are calculated with respect to corneal geometry. All are exported as time-series parameters by CorVis ST Research Software version 1.6r2036 (Research).

Given the coordinate system shown, the positive direction is that of the air puff exiting the device nozzle; therefore, the previously mentioned equation can be rewritten as follows:

$$F_z(\mathrm{t}) = \rho v^2 A\left(1 + \frac{PD}{2R}\right). \tag{3}$$

Based on the abovementioned equation, we can characterize corneal load alteration with surface shape (CLASS), which measures the change in the load experienced by the corneal apex due to the dynamic changes in geometry:

$$F_z(t) = \rho v^2 A(1 + CLASS), \tag{4}$$

where *CLASS* is as follows:

$$CLASS = -\cos\theta = \frac{PD}{2R}. \tag{5}$$

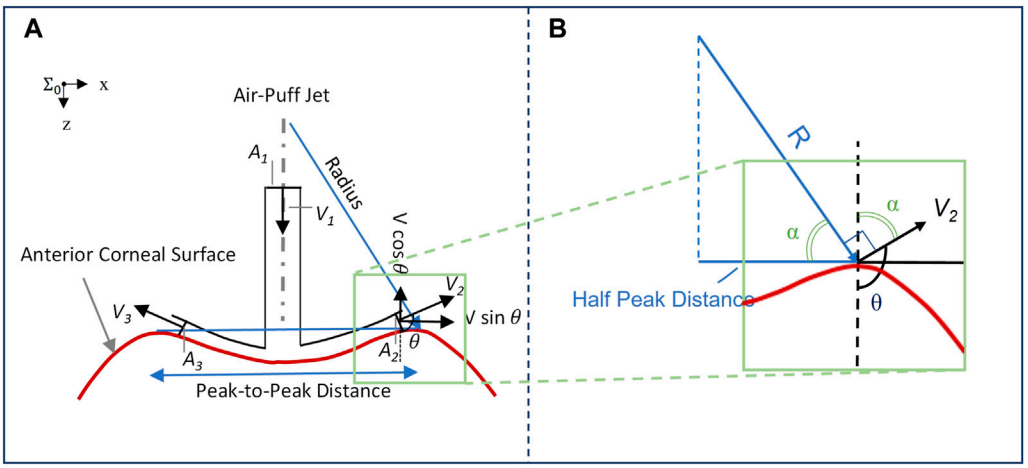

FIGURE 1 | (A) Impact of corneal surface shape on the load experienced post applanation, illustrated with a concave cornea. The inlet airflow velocity and cross-sectional area are denoted by V_1 and A_1, respectively, while the two-dimensional representation of outlet airflow areas and velocities is denoted by A_2 and A_3, and V_2 and V_3, respectively; **(B)** Plotting vectors of interest from the same origin to characterize the response angle θ.

TABLE 1 | Definitions of CLASS-related parameters.

CLASS%	**Time series of % change in corneal load alteration with surface shape (CLASS)**
θ	Angle between airflow impacting the cornea and airflow exiting the area of deformation
CLASSmax	Maximum CLASS% value in time-series
CLASSmin	Minimum CLASS% value in time-series
CLASSint	Integrated Area under the CLASS% curve in the time-series between A1[a] and A2[b]
t_{CD}	Confinement Duration during the concave phase between A1[a] and A2[b]

[a]*First applanation.*
[b]*Second applanation.*

It is to be noted that the CLASS value can, therefore, be bounded between −1 and 1, with zero corresponding to applanation. Thus, *CLASS* indicates a fractional change in the overall air puff loading due to corneal shape: it is negative while the anterior cornea remains convex (i.e., $R > 0$, so the true load is lower than the uncorrected value), and then it becomes positive while the cornea is concave (i.e., $R < 0$, so the true load is higher than the uncorrected value). Time varying parameters include angle θ which is a function of PD and R from the Corvis ST and % CLASS. Other CLASS-related parameters, such as CLASSmax, can be extracted from %CLASS time-series and are described in **Table 1**.

Patient Data

An analysis was performed on a subset of data acquired from two ongoing studies on corneal biomechanics, each under an approved protocol by The Ohio State University Institutional Review Board (IRB). Informed consent was obtained from all subjects after explanation of the nature and possible consequences of the study. The subset included 157 eyes of 157 subjects, with 26 eyes of 26 subjects diagnosed with keratoconus (KCN), 102 eyes of 102 subjects with normal (NRL) eyes without ocular disease, and 29 eyes of 29 subjects diagnosed with ocular hypertension (OHT). To be eligible, subjects had to be older than 18 years, with a clear cornea in at least one eye. Further group-specific inclusion criteria for the KCN group included a diagnosis of keratoconus having clinical signs such as reduced corneal thickness, steepening, Fleischer's ring, Vogt's striae, or scissoring. For the NRL group, subjects with previous or current diagnosis of diabetes mellitus or a history of ocular disease, trauma, or surgery were excluded. For the OHT group, subjects with Goldmann measured IOP greater than 21 mmHg with at least one eye having IOP greater than 24 mmHg were included. The patients were excluded from the study if 1) the subject eye had a nonintact epithelium, 2) the subject was pregnant, less than 12 weeks since post-partum or less than 12 weeks since the completion of breast feeding, 3) the subject eye had nystagmus or any other condition which would prevent a steady gaze at the time of study enrollment, 4) subject had a previous intraocular surgery, except cataracts, 5) subjects with comorbidities that would allow them to be included into more than one of the study cohorts, 6) subjects with systemic conditions that cause defects in collagen (e.g., Marfan's syndrome, Ehlers-–Danlos syndrome, autoimmune diseases or disorders, etc.), and 7) subjects taking a concomitant medication that could affect result interpretation. All subjects had received a

CorVis ST examination along with IOP measurements using dynamic contour tonometry (DCT) (Ziemer Ophthalmic Systems AG; Port, Switzerland).

CorVis ST Measurements

The previously recorded CorVis ST images are analyzed using research software version 1.6r2036 (Research), and the DCRs are exported. The DCRs utilized in our study include the deformation response at different events of interest, including initial position, first applanation, highest concavity, and second applanation. DCRs describing the changing geometry of the cornea have been shown to be relatively independent of IOP and to correlate with measures of stiffness (Vinciguerra et al., 2016).

IOP, biometry, stiffness, and geometry were also considered. These were, namely, bIOP (biomechanically corrected IOP), central corneal thickness (CCT), stiffness parameters (SPs) at inward applanation (SP-A1), and highest concavity (SP-HC), as well as shape parameters of deformation amplitude (DA) ratio 2 mm and integrated inverse radius. These parameters are calculated as a response to the dynamic load experienced by the cornea over the duration of the examination, as has been shown previously (Joda et al., 2016; Roberts et al., 2017; Roberts and Liu, 2016).

Statistical Analysis

To evaluate the difference between stiffness metrics in our three subject groups, ANCOVA (analysis of covariates) was performed on stiffness metrics of SP-A1 and SP-HC, while controlling for the effect of age, CCT, and DCT IOP. Furthermore, Tukey's HSD (honestly significant difference) tests were performed to compare the three subject groups on the maximum *CLASS* value ($CLASS_{max}$) and concave phase duration (t_{CD}), which is defined as the time between the inward and outward applanation times. To assess the impact of $CLASS_{max}$ and the area under *CLASS*–time curve, $CLASS_{int}$, linear regression analyses were performed including these two parameters along with all aforementioned DCRs. Furthermore, regression analyses were performed on $CLASS_{max}$ and $CLASS_{int}$ with respect to CCT and bIOP. Next, in order to investigate the influence of stiffness on *CLASS*, a series of regression analyses were performed with $CLASS_{max}$ and $CLASS_{int}$ as the independent variable and SP-A1, SP-HC, integrated inverse radius, and DA ratio 2 mm as the dependent variables in all groups. Statistical significance was calculated considering a significance level of 0.05. Statistical analyses were performed in JMP Pro 14.0.0 (SAS Institute Inc, Cary, NC).

RESULTS

We assessed how this additional component of load, CLASS, impacts the three subject groups and further evaluated *CLASS*-related parameters for the same subject groups; additional analysis was performed to assess the correlation between *CLASS*-related parameters with respect to bIOP, CCT, and current stiffness metrics and shape parameters exported from CorVis ST research software, which are included in the Supplemental Materials.

TABLE 2 | Subject characteristics for age and IOP, along with stiffness metrics represented by mean ± standard deviation[a].

	KCN[b] (*n* = 26)	NRL[c] (*n* = 102)	OHT[d] (*n* = 29)
Age	36.73 ± 14.13[†]	45.43 ± 13.74[*]	60.83 ± 15.12[*,†]
DCT IOP[e]	15.49 ± 3.47[†]	16.95 ± 2.79[*]	21.29 ± 3.38[*,†]
CCT[f]	496.92 ± 52.85[†]	559.54 ± 31.44[*]	586.10 ± 41.69[*,†]
SP-A1[g]	73.85 ± 27.25[†]	120.66 ± 18.68	150.42 ± 20.37[*]
SP-HC[h]	3.77 ± 2.53	7.72 ± 3.72	15.48 ± 5.27[*,†]

[a]*Significant difference between KCN and NRL (p-value < 0.05) are shown with *and †,respectively. Stiffness metrics were compared between subject groups while accounting for the effect of age, bIOP, and CCT.*
[b]*Keratoconus.*
[c]*Normal.*
[d]*Ocular hypertensive.*
[e]*Dynamic contour tonometry intraocular pressure.*
[f]*Central corneal thickness.*
[g]*Stiffness parameter at first applanation.*
[h]*Stiffness applanation at highest concavity.*

Stiffness in Patient Demographics

Mean and standard deviation of each group for age, CCT, and IOP along with the stiffness metrics are shown in **Table 2**. These parameters were all significantly different between the three groups ($p < 0.05$). ANCOVA results for SP-A1 indicated that when controlling for age, IOP, and CCT, a significant difference exists between all three subject groups (p-value < 0.05). On the other hand, ANCOVA for SP-HC when controlling for the effect of age, IOP, and CCT showed significant difference between OHT subjects and the two other groups (p-value < 0.0001), while showing no difference between KCN and NRL groups (p-value = 0.718).

Changes in CLASS-Related Parameters Between Different Disease States

CLASS-related parameters were compared between KCN, NRL, and OHT subjects. Time-series data on CLASS are shown in **Figure 2A** for all three subject groups. As shown in this figure, the CLASS-adjusted load for KCN subjects indicates that the maximum load experienced by the corneal apex, $CLASS_{max}$, was on average 45.4% ± 9.98% higher than the flow impinging on a flat rigid surface (*p-value < 0.0001*). $CLASS_{max}$ is on average 33.3% ± 4.28% and 29.2% ± 5.33% higher than the load on a flat rigid surface for NRL and OHT subject groups, respectively (*p-value < 0.0001*).

Furthermore, $CLASS_{max}$ is shown in **Figure 2B** for all subjects. A pairwise comparison of all groups using Tukey's HSD for $CLASS_{max}$ indicates significantly different values for each pair, with KCN having significantly higher values than NRL and OHT subjects (*p-value < 0.0001*). OHT subjects had significantly lower $CLASS_{max}$ than NRL subjects (*p-value = 0.00012*). **Figure 2C** shows the minimum value, $CLASS_{min}$, is dependent primarily on the shape of the unloaded cornea, which was significantly lower in KCN than normal controls.

The concave phase duration, represented with t_{CD} shown in **Figure 2D**, was calculated to be 14.92 ± 0.90 ms for KCN subjects, 14.20 ± 0.91 ms for NRL subjects, and 12.54 ± 1.01 ms for the OHT group. Tukey's HSD tests performed on t_{CD} showed

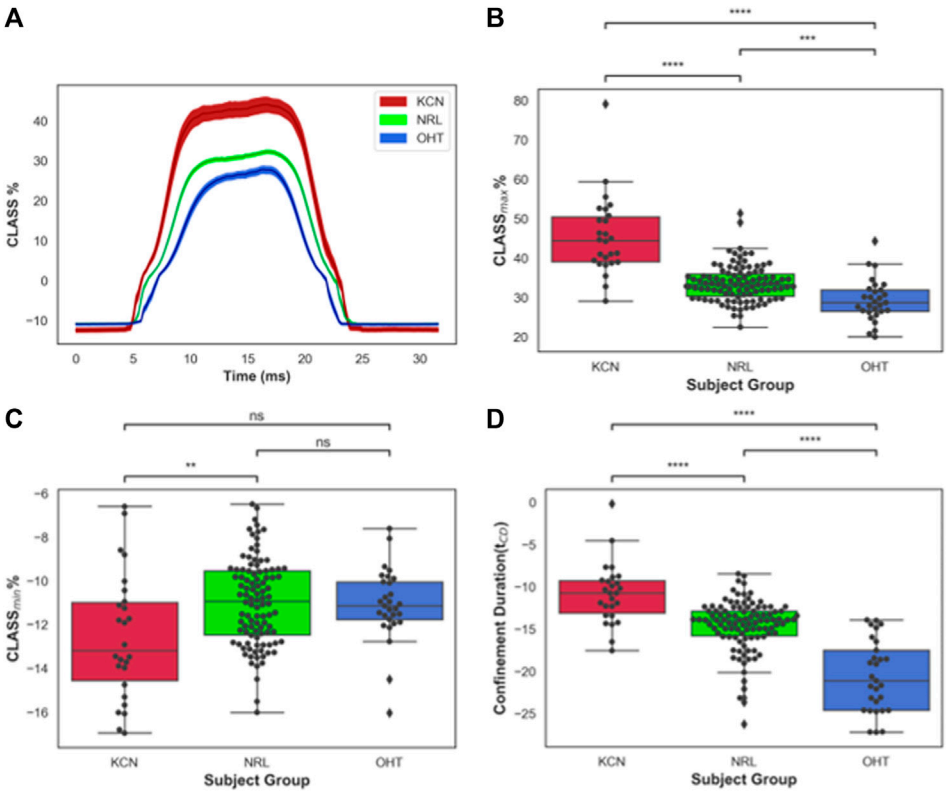

FIGURE 2 | (A) *CLASS%* time-series plot shown in mean ± standard error (shaded area) for keratoconus (KCN), normal (NRL), and ocular hypertension (OHT) subjects; **(B)** Distribution of maximum *CLASS* for KCN, NRL, and OHT subjects; **(C)** Distribution of minimum *CLASS* for KCN, NRL, and OHT subjects; **(D)** Distribution of concave phase duration (t_{CD}) for KCN, NRL, and OHT subjects. *P*-value annotation legend: ns: $0.05 < p$, *: $0.01 < p \leq 0.05$; **: $0.001 < p \leq 0.01$; ***: $0.0001 < p \leq 0.001$; ****: $p \leq 0.0001$.

significantly shorter duration for OHT subjects than that of KCN and NRL subjects (*p-value* < *0.0001*), with the KCN subjects having significantly higher t_{CD} than NRL subjects (*p-value* = *0.0015*).

The area under the *CLASS*-time curve was calculated and integrated *CLASS* ($CLASS_{int}$) was plotted for all subjects (**Figure 3A**). $CLASS_{int}$ was on average 5.48 ± 1.66 for the KCN group, 3.67 ± 0.7 for NRL subjects, and 2.69 ± 0.68 for OHT subjects. Tukey's HSD test comparing the difference in $CLASS_{int}$ for each ocular condition shows significant difference in $CLASS_{int}$ between all three groups (*p-value* < *0.0001*), with KCN having the highest values and OHT having the lowest values, on average.

To better account for the negative *CLASS* values prior to A1 and after A2, $CLASS_{int}$ was divided into three sections: before A1 (**Figure 3B**), between A1 and A2 (**Figure 3C**), and after A2 (**Figure 3D**). OHT and NRL groups were significantly different from each other in terms of $CLASS_{int}$ before A1 and after A2, with *p*-values of 0.0036 and 0.026, respectively. $CLASS_{int}$ for these two regions was not significantly different between KCN and the other two groups. On the other hand, the three groups were significantly different from each other when comparing $CLASS_{int}$ for the concave duration between A1 and A2 (*p-value* < 0.0001).

The Effect of IOP on CLASS

Regression analysis of $CLASS_{max}$ with bIOP is represented by a negative linear relationship for KCN and NRL groups, while showing no significant correlation for OHT (KCN: $R^2 = 0.2029$, $p < 0.0001$, NRL: $R^2 = 0.2415$, $p = 0.209$, OHT: $R^2 = 0.0255$, $p = 0.4081$). Regression analysis of $CLASS_{max}$ with DCT IOP was represented by a negative linear relationship for all NRL subjects and no correlation for the other two groups (KCN: $R^2 = 0.3866$, $p < 0.0001$, NRL: $R^2 = 0.2270$, $p = 0.0007$, OHT: $R^2 = 0.4342$, $p < 0.0001$). Regression analysis of $CLASS_{int}$ vs. bIOP showed significant negative relationship for the KCN subject group, while resulting in no correlation for NRL and OHT groups (KCN: $R^2 = 0.3877$, $p = 0.0007$, NRL: $R^2 = 0.0000$, $p = 0.9616$, OHT: $R^2 = 0.0204$, $p = 0.4587$). For DCT IOP, regression analysis showed no correlation for the three groups (KCN: $R^2 = 0.3192$, $p = 0.0026$, NRL: $R^2 = 0.0386$, $p = 0.0488$, OHT: $R^2 = 0.1252$, $p = 0.0597$). The detailed results of each regression analysis are provided in **Table 3** and **Figure 4**.

How is CLASS Correlated With Other DCRs?

To assess the relationship between the newly introduced *CLASS* parameters and stiffness metrics, regression analyses are

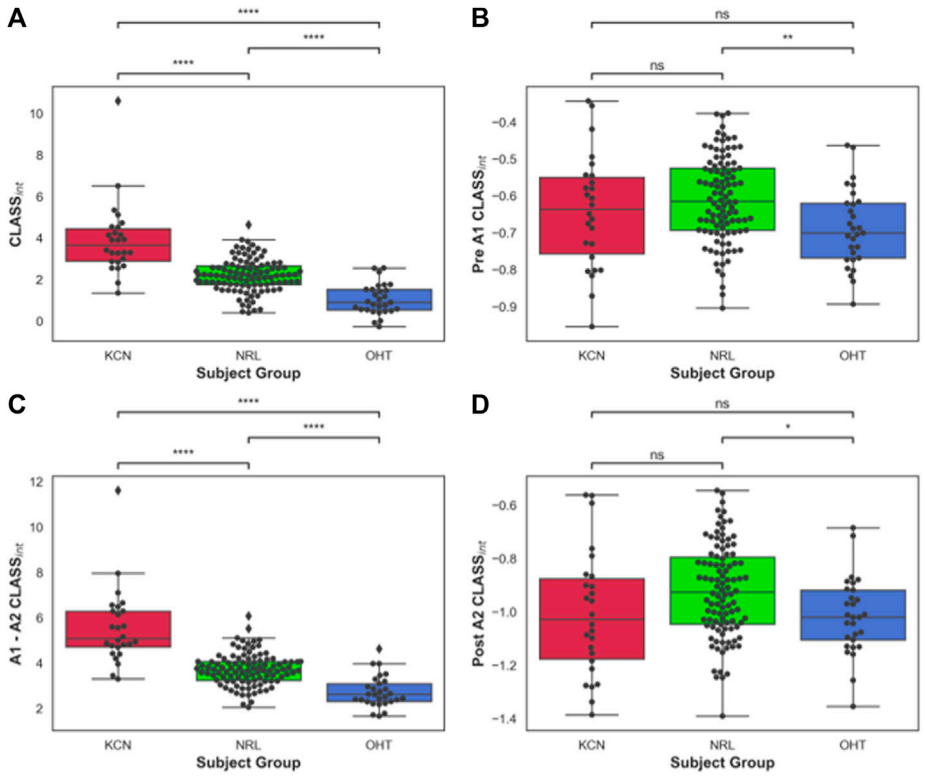

FIGURE 3 | (A) Area under *CLASS* curve ($CLASS_{nt}$) prior to first applanation for keratoconus (KCN), normal (NRL), and ocular hypertension (OHT) subjects; **(B)** $CLASS_{int}$ between the two applanation points for KCN, NRL, and OHT subjects; **(C)** $CLASS_{int}$ after second applanation for KCN, NRL, and OHT subjects. **(D)** Total $CLASS_{int}$ for KCN, NRL, and OHT subjects. *P*-value annotation legend: ns: $0.05 < p$, *: $0.01 < p \leq 0.05$; **: $0.001 < p \leq 0.01$; ***: $0.0001 < p \leq 0.001$; ****: $p \leq 0.0001$.

performed for $CLASS_{max}$ in **Figure 5** and $CLASS_{int}$ in **Figure 6**, with respect to SP-A1, SP-HC, CCT, DA ratio 2 mm, and integrated inverse radius. The details are summarized in **Table 4.** Regression analysis of $CLASS_{max}$ with respect to CCT showed significant negative relationships for KCN and NRL groups, as well, while indicating no correlation for the OHT group (KCN: $R^2 = 0.3866$, $p = 0.0026$, NRL: $R^2 = 0.2270$, $p = 0.0488$, OHT: $R^2 = 0.4342$, $p = 0.0597$). For the SP-A1, regression analysis shows a significant negative linear relationship between the two parameters for KCN and NRL subject groups, while the relationship is not significant for the OHT group (KCN: $R^2 = 0.5211$, $p < 0.0001$, NRL: $R^2 = 0.4611$, $p < 0.0001$, OHT: $R^2 = 0.1330$, $p = 0.0518$). Regression analysis for *CLASS* and SP-HC showed a negative linear relationship this time for NRL and OHT subjects and not for KCN (KCN: $R^2 = 0.1212$, $p = 0.1219$, NRL: $R^2 = 0.5426$, $p < 0.0001$, and OHT: $R^2 = 0.5000$, $p < 0.0001$). As shown in **Figures 5D,E**, linear regression analysis for $CLASS_{max}$ vs. DA ratio 2 mm (KCN: $R^2 = 0.7812$, $p < 0.0001$, NRL: $R^2 = 0.5754$, $p < 0.0001$, and OHT: $R^2 = 0.5493$, $p < 0.0001$) and integrated inverse radius (KCN: $R^2 = 0.8982$, $p < 0.0001$, NRL: $R^2 = 0.5079$, $p < 0.0001$, and OHT: $R^2 = 0.8407$, $p < 0.0001$) showed a positive linear relationship for all subject groups.

Similar statistical analyses were repeated to assess the correlation between $CLASS_{int}$ with the stiffness and shape metrics, shown in **Figure 6**. Regression analysis between integrated *CLASS* and CCT showed significant negative correlation for KCN and NRL groups, while indicating no correlation for OHT subjects (KCN: $R^2 = 0.3192$, $p = 0.0026$, NRL: $R^2 = 0.03865$, $p = 0.0488$, and OHT: $R^2 = 0.1252$, $p = 0.0597$). Similar analysis on the stiffness metrics of SP-A1 and SP-HC showed significant negative correlation for the KCN subject group ($R^2 = 0.5424$ *and* $R^2 = 0.3389$, and $p < 0.0001$ and $p = 0.0056$, respectively), while showing no significant correlation for NRL and OHT groups. Regression analysis between DA ratio 2 mm and $CLASS_{int}$ showed significant correlation between the two parameters for all three subject groups (KCN: $R^2 = 0.7451$, $p < 0.0001$, NRL: $R^2 = 0.0416$, $p = 0.0409$, and OHT: $R^2 = 0.1403$, $p = 0.0453$). Furthermore, regression analysis between $CLASS_{int}$ and integrated inverse radius showed significant correlation for KCN and OHT subject groups, while showing no correlation for NRL subjects (KCN: $R^2 = 0.7453$, $p < 0.0001$, NRL: $R^2 = 0.0013$, $p = 0.7254$, and OHT: $R^2 = 0.1508$, p 0.0374).

DISCUSSION

Noncontact deformation analysis is an effective clinical approach used to characterize corneal biomechanics in different settings. This study sheds light on an important yet previously unknown confounding effect with noncontact air puff–induced

TABLE 3 | Regression results for $CLASS_{max}$ and $CLASS_{int}$ vs. IOP.

	KCN[a] (*n* = 26)	NRL[b] (*n* = 102)	OHT[c] (*n* = 29)
$CLASS_{max}$[d]			
bIOP[e]	R^2 = 0.2029, P < .0001	R^2 = 0.2415, P = 0.0209	R^2 = 0.0255, P = 0.4081
DCT[f]	R^2 = 0.3866, P < .0001	R^2 = 0.2270, P = 0.0007	R^2 = 0.4342, P = 0.0001
$CLASS_{int}$[g]			
bIOP	R^2 = 0.3877, P = 0.0007	R^2 = 0.0000, P = 0.9616	R^2 = 0.0204, P = 0.4587
DCT	R^2 = 0.3192, P = 0.0026	R^2 = 0.03865, P = 0.0488	R^2 = 0.1252, P = 0.0597

[a]*Keratoconus.*
[b]*Normal.*
[c]*Ocular hypertensive.*
[d]*Maximum CLASS, index.*
[e]*Biomechanically corrected IOP.*
[f]*Dynamic contour tonometry intraocular pressure.*
[g]*Integrated CLASS, index.*

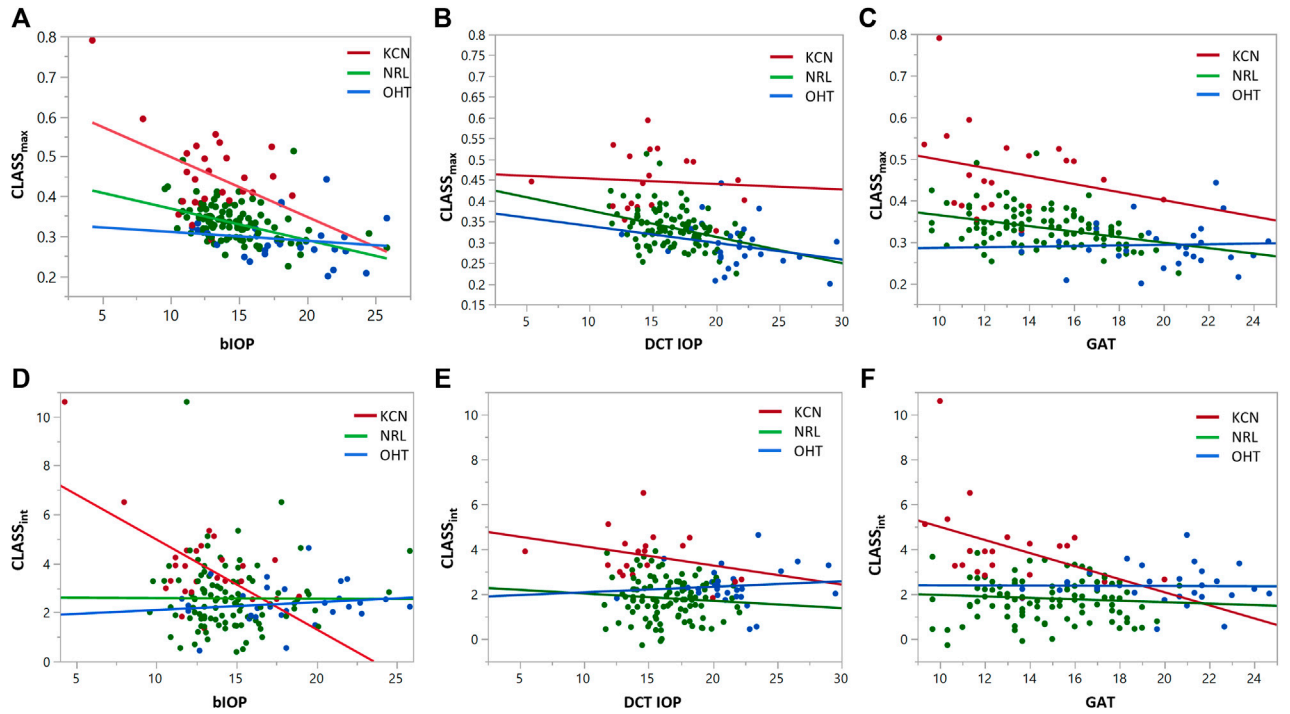

FIGURE 4 | Regression analysis for $CLASS_{max}$ and $CLASS_{int}$ with respect to bIOP **(A,D)**, DCT IOP **(B,E)** and GAT **(C and F)**, for keratoconic (KCN), normal (NRL), and ocular hypertensive (OHT) subjects.

deformation between the fluid-based load magnitude and corneal surface shape. The results presented in this work exhibit significant changes in the load as a response to the corneal surface shape that may alter not only the clinical interpretations but also results from computer simulations of the response to the applied load. To derive the interlinked relationship between corneal surface shape and fluid-based load, we introduced a new nondimensional factor calculated *via* an analytical approach, previously proposed for characterization of skin tissue stiffness with an indentation test using noncontact air puff impingement (Tanaka et al., 2011). The additional component of the load introduced here, *CLASS*, characterizes the %change in the load experienced at the corneal apex based on corneal dynamic shape changes.

Overall, for the 157 subjects in this study, adjusting for the load due to the surface shape resulted in a 34.57% ± 7.7% increase in the maximum load experienced by the corneal apex. The reason behind the modified load is the change in the air puff outflow angle due to the convex corneal shape before and after the two applanation events and the concave corneal shape between the

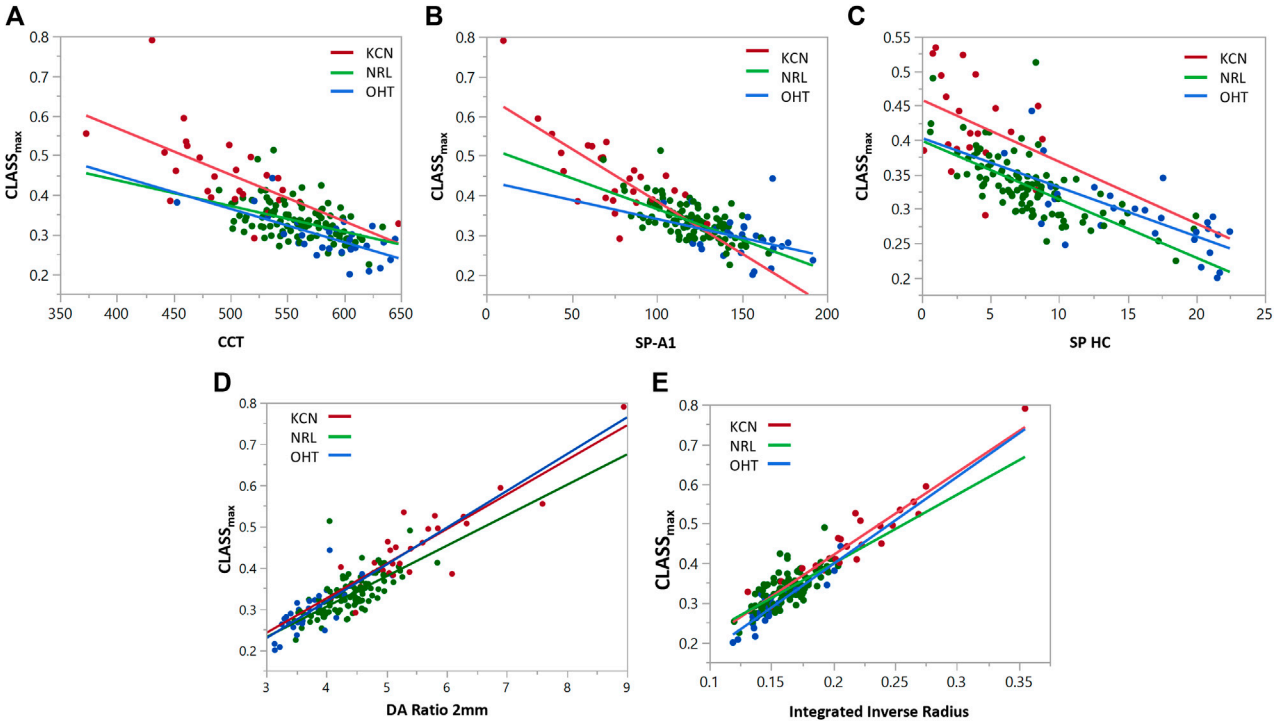

FIGURE 5 | Regression analyses for *CLASS$_{max}$* vs. **(A)** CCT, **(B)** SP-A1, **(C)** SP-HC, **(D)** DA ratio 2 mm, and **(E)** integrated inverse radius for keratoconic (KCN), normal (NRL), and ocular hypertensive (OHT) subjects.

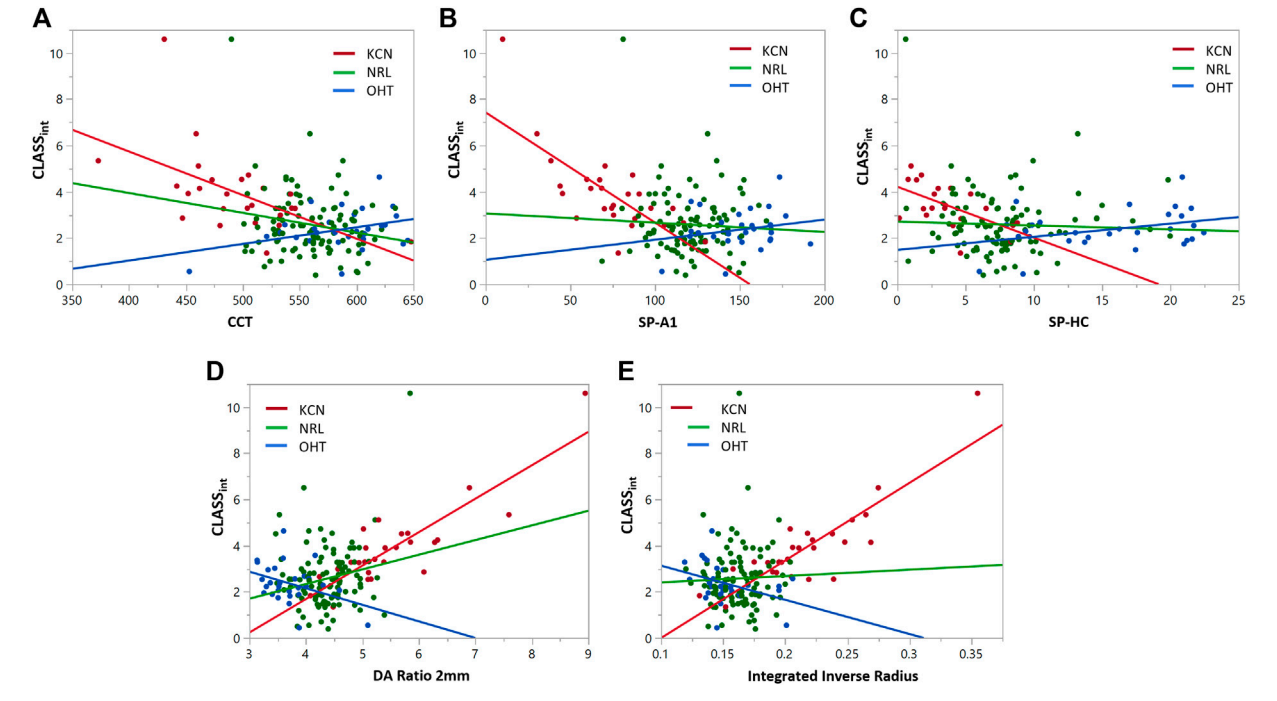

FIGURE 6 | Regression analyses for *CLASS$_{int}$* vs. **(A)** CCT, **(B)** SP-A1, **(C)** SP-HC, **(D)** DA ratio 2 mm, and **(E)** integrated inverse radius for keratoconic (KCN), normal (NRL), and ocular hypertensive (OHT) subjects.

TABLE 4 | Regression analysis results for $CLASS_{max}$ and $CLASS_{int}$ vs. stiffness parameters.

	KCN[a] (*n* = 26)	NRL[b] (*n* = 102)	OHT[c] (*n* = 29)
$CLASS_{max}$[d]			
CCT[e]	$R^2 = 0.3866, P < .0001$	$R^2 = 0.2270, P = 0.0007$	$R^2 = 0.4342, P = 0.0001$
SP-A1[f]	$R^2 = 0.5211, P < .0001$	$R^2 = 0.4611, P < .0001$	$R^2 = 0.1330, P < .0518$
SP-HC[g]	$R^2 = 0.1212, P = 0.1219$	$R^2 = 0.5426, P < .0001$	$R^2 = 0.50, P < .0001$
DA ratio 2 mm[h]	$R^2 = 0.7812, P < .0001$	$R^2 = 0.5754, P < .0001$	$R^2 = 0.5493, P < .0001$
Integrated inverse radius	$R^2 = 0.8982, P < .0001$	$R^2 = 0.5080, P < .0001$	$R^2 = 0.8407, P < .0001$
$CLASS_{int}$[i]			
CCT	$R^2 = 0.3192, P = 0.0026$	$R^2 = 0.03865, P = 0.0488$	$R^2 = 0.1252, P = 0.0597$
SP-A1	$R^2 = 0.5424, P < .0001$	$R^2 = 0.0030, P = 0.5878$	$R^2 = 0.0436, P = 0.2772$
SP-HC	$R^2 = 0.3389, P = 0.0056$	$R^2 = 0.0020, P = 0.6550$	$R^2 = 0.1251, P = 0.0598$
DA ratio 2 mm	$R^2 = 0.7451, P < .0001$	$R^2 = 0.0416, P = 0.0409$	$R^2 = 0.1403, P = 0.0453$
Integrated inverse radius	$R^2 = 0.7453, P < .0001$	$R^2 = 0.0013, P = 0.7254$	$R^2 = 0.1508, P = 0.0374$

[a]*Keratoconus.*
[b]*Normal.*
[c]*Ocular hypertensive.*
[d]*Maximum CLASS, index.*
[e]*Central corneal thickness.*
[f]*Stiffness parameter at first applanation.*
[g]*Stiffness applanation at highest concavity.*
[h]*Deformation amplitude ratio at 2 mm.*
[i]*Integrated CLASS, index.*

two applanation events, which in turn alters the impact experienced on the apex. This considerable change in the load indicates the significant effect of the nonlinear and dynamic changes in corneal geometry on the load itself. These findings are in agreement with Tanaka et al.'s analytical approximation to this dynamic relationship between the load and deformation in a noncontact stiffness sensor used to characterize skin stiffness through air puff indentation (Tanaka et al., 2011). Their findings further explained that the significant impact of recalibrating an air puff load based on the dynamic concave deformation of soft tissue can increase up to two-fold in response to tissue deformation.

The relationship between $CLASS_{max}$ and bIOP for KCN subjects showed that lower bIOP values will experience a larger load with the concave surface shape as explained by CLASS (**Figure 4A**). This association was less profound with NRL subjects and further showed no correlation for OHT subjects. Such behavior may indicate that bIOP measurement could be influenced by the dynamic changes in the corneal surface shape and the extent of this influence can be captured through $CLASS_{max}$ and $CLASS_{int}$. Furthermore, regression analyses exhibited a negative correlation for $CLASS_{max}$ with the stiffness metrics, indicating that stiffer corneas are associated with lower changes in load, while $CLASS_{max}$ exhibited a positive correlation with shape DCRs, which attests to the accuracy of *CLASS* by showing larger changes in the load with larger shape changes.

On the contrary, when assessing the correlation of $CLASS_{int}$ with these parameters, NRL and OHT subjects reflected a different pattern in comparison with using $CLASS_{max}$. The reason behind this behavior is likely that $CLASS_{int}$ is more comprehensive in considering the effect of concavity duration, corneal surface shape before first applanation, after second applanation, and the overall dynamic changes in the surface shape with the load application. Consequently, the shorter t_{CD}, smaller DA ratio and smaller integrated inverse radius in stiffer OHT subjects led to lower $CLASS_{int}$ (shown in **Figures 6C,D**). In short, $CLASS_{int}$ in KCN subjects is driven by the corneal behavior between the two applanation points, while for OHT and NRL subjects, this value is driven by areas outside the two applanation points.

Besides the overall impact of *CLASS* in changing the load experienced by the corneal apex, our study revealed that the confounding effect of corneal surface shape on the load may result in misinterpretation of corneal response in disease states. It is known that keratoconic corneas have reduced the number of collagen lamellae and altered the orientation of these lamellae (Daxer and Fratzl, 1997), which leads to focal weakening and a more compliant response. These characteristics were shown to impact *CLASS*-related parameters by increasing $CLASS_{max}$ due to the more compliant response and increased corneal deflection between the two applanation events. This indicates the critical effect of altered load in disease states since a higher load applied to advanced keratoconic eyes can be misinterpreted as a larger corneal response. Furthermore, this behavior elucidates the importance of *CLASS* in clinical studies considering that the load applied to the corneal apex changes between subjects with different corneal conditions and within subjects before and after a corneal procedure, such as refractive surgery, or the development of corneal disease. While many clinical studies have focused on assessing corneal biomechanics using a dynamic Scheimpflug analyzer, our findings suggest that these analyses may require further evaluations to correct for the effect of *CLASS* and eliminate the confounding role of dynamic surface shape and load in interpreting corneal biomechanical response.

Findings of our work may impact the results of various clinical studies that have utilized uncorrected air puff load values to monitor KCN (Tian et al., 2014; Elham et al., 2017), evaluate corneal crosslinking (Bak-Nielsen et al., 2014; Tian et al., 2014), assess the risk of refractive surgery (Kataria et al., 2019), assess corneal response pre/post refractive surgery (Pedersen et al., 2014; Frings et al., 2015; Sefat et al., 2016; Xu et al., 2017), or compare different methods of refractive surgery (Pedersen et al., 2014; Sefat et al., 2016). Furthermore, the significant change in the air puff load as a response to the deformed corneal surface is neglected in many modeling studies of noncontact corneal deformation (Francis et al., 2019; Jannesari et al., 2019). Although a previous modeling study reported changes in the fluid dynamics characteristics as the cornea deformed, the specifics of these changes were not quantified (Kling et al., 2014). Ignoring this effect may result in misinterpreting the higher load applied to the cornea as a larger corneal response and may in turn generate misleading corneal characterization.

There are limitations to the present study. The current study was limited by a small sample size for OHT and KCN subjects. In addition, the accuracy of CLASS is limited by several factors. First, we utilized the Bernoulli equation in the sub-sonic flow regime (Mach number ~0.3), slightly beyond the incompressible flow regime, where it more rigorously holds. Second, we availed ourselves of the existing geometric parameters already characterized by the CorVis ST software; deviation from the spherical cap geometry will introduce minor errors into the CLASS correction. Third, the presence of localized heterogeneities in the corneal deformation (e.g., keratoconus) could cause the cornea to deviate from the assumed spherical cap geometry. Furthermore, the deformation information is based on one corneal meridian and does not take into account the asymmetric corneal shape specifically for KCN subjects. Nevertheless, the analysis presented here clearly demonstrates that despite delivering a consistent air puff, the resulting dynamic load experienced by the eye can differ significantly.

This study identifies an additional component of the air puff load, *CLASS*, to indicate how the dynamic change in corneal surface shape can alter the load experienced by the cornea. A major impact of *CLASS* is that while the dynamic Scheimpflug analyzer applies a consistent air puff with each examination, the load experienced by the cornea can be different for each subject, depending on the shape of the corneal deformation, which may ultimately affect the characterization of corneal biomechanics. Stiffer corneas of OHT subjects are associated with a lower change in the load, while more compliant corneas of KCN subjects are associated with larger load alterations. Hence, correcting the load to account for corneal surface geometry is an essential initial step to interpret corneal biomechanical behavior. How to specifically include CLASS in this interpretation remains an area of future study, as well as determining the three-dimensional nature of air puff backflow.

DATA AVAILABILITY STATEMENT

The raw data supporting the conclusion of this article will be made available by the authors, without undue reservation.

ETHICS STATEMENT

The studies involving human participants were reviewed and approved by The Ohio State University Institutional Review Board. The patients/participants provided their written informed consent to participate in this study.

AUTHOR CONTRIBUTIONS

AY, CR, and MR contributed to the study. AY conceived the concept, and all authors contributed to the study design, implementation, analysis, and interpretation. All authors contributed to manuscript revision and read and approved the submitted version.

FUNDING

NIH/NEI R01 EY027399 and Ann Ellis Fund of the Columbus Foundation.

REFERENCES

Ambrósio, R., Dawson, D. G., Salomão, M., Guerra, F. P., Caiado, A. L. C., and Belin, M. W. (2010). Corneal Ectasia after LASIK Despite Low Preoperative Risk: Tomographic and Biomechanical Findings in the Unoperated, Stable, Fellow Eye. *J. Refract Surg.* 26 (11), 906–911. doi:10.3928/1081597x-20100428-02

Bak-Nielsen, S., Pedersen, I. B., Ivarsen, A., and Hjortdal, J. (2014). Dynamic Scheimpflug-Based Assessment of Keratoconus and the Effects of Corneal Cross-Linking. *J. Refract Surg.* 30 (6), 408–414. doi:10.3928/1081597x-20140513-02

Benner, S. (1964). *The Coanda Effect at Deflection Surfaces Widely Separated from the Jet Nozzle*.

Boyer, G., Pailler Mattei, C., Molimard, J., Pericoi, M., Laquieze, S., and Zahouani, H. (2012). Non Contact Method for *In Vivo* Assessment of Skin Mechanical Properties for Assessing Effect of Ageing. *Med. Eng. Phys.* 34 (2), 172–178. doi:10.1016/j.medengphy.2011.07.007

Daxer, A., and Fratzl, P. (1997). Collagen Fibril Orientation in the Human Corneal Stroma and its Implication in Keratoconus. *Invest. Ophthalmol. Vis. Sci.* 38 (1), 121–129.

Elham, R., Jafarzadehpur, E., Hashemi, H., Amanzadeh, K., Shokrollahzadeh, F., Yekta, A., et al. (2017). Keratoconus Diagnosis Using Corvis ST Measured Biomechanical Parameters. *J. Curr. Ophthalmol.* 29 (3), 175–181. doi:10.1016/j.joco.2017.05.002

Elsheikh, A., Joda, A., Vinciguerra, R., Eliasy, A., Mir Mohi Sefat, S., Bao, F., et al. (2015). Clinical Evaluation of Correction Algorithm for Corvis ST Tonometry. *Invest. Ophthalmol. Vis. Sci.* 56 (7), 101.

Francis, M., Matalia, H., Nuijts, R. M. M. A., Haex, B., Shetty, R., and Sinha Roy, A. (2019). Corneal Viscous Properties Cannot Be Determined from Air-Puff Applanation. *J. Refract Surg.* 35 (11), 730–736. doi:10.3928/1081597x-20191010-03

Frings, A., Linke, S., Bauer, E., Druchkiv, V., Katz, T., and Steinberg, J. (2015). Effects of Laser *In Situ* Keratomileusis (LASIK) on Corneal Biomechanical Measurements with the Corvis ST Tonometer. *Opth* 9, 305. doi:10.2147/opth.s76491

Gorgun, E., Kucumen, R. B., and Yenerel, N. M. (2011). Influence of Intrastromal Corneal Ring Segment Implantation on Corneal Biomechanical Parameters in Keratoconic Eyes. *Jpn. J. Ophthalmol.* 55 (5), 467–471. doi:10.1007/s10384-011-0057-8

Jannesari, M., Mosaddegh, P., Kadkhodaei, M., Kasprzak, H., and Jabbarvand Behrouz, M. (2019). Numerical and Clinical Investigation on the Material Model of the Cornea in Corvis Tonometry Tests: Differentiation between Hyperelasticity and Viscoelasticity. *Mech. Time-depend Mater.* 23 (3), 373–384. doi:10.1007/s11043-018-9390-3

Joda, A. A., Shervin, M. M. S., Kook, D., and Elsheikh, A. (2016). Development and Validation of a Correction Equation for Corvis Tonometry. *Comp. Methods Biomech. Biomed. Eng.* 19 (9), 943–953. doi:10.1080/10255842.2015.1077515

Kataria, P., Padmanabhan, P., Gopalakrishnan, A., Padmanaban, V., Mahadik, S., and Ambrósio, R., Jr (2019). Accuracy of Scheimpflug-Derived Corneal Biomechanical and Tomographic Indices for Detecting Subclinical and Mild Keratectasia in a South Asian Population. *J. Cataract Refract Surg.* 45 (3), 328–336. doi:10.1016/j.jcrs.2018.10.030

Kling, S., Bekesi, N., Dorronsoro, C., Pascual, D., and Marcos, S. (2014). Corneal Viscoelastic Properties from Finite-Element Analysis of *In Vivo* Air-Puff Deformation. *PloS one* 9 (8), e104904. doi:10.1371/journal.pone.0104904

Kling, S., and Hafezi, F. (2017). Corneal Biomechanics - a Review. *Ophthalmic Physiol. Opt.* 37 (3), 240–252. doi:10.1111/opo.12345

Kotecha, A. (2007). What Biomechanical Properties of the Cornea Are Relevant for the Clinician? *Surv. Ophthalmol.* 52 (6), S109–S114. doi:10.1016/j.survophthal.2007.08.004

Liu, J., and Roberts, C. J. (2005). Influence of Corneal Biomechanical Properties on Intraocular Pressure Measurement. *J. Cataract Refract Surg.* 31 (1), 146–155. doi:10.1016/j.jcrs.2004.09.031

Luce, D. (2006). Methodology for Cornea Compensated IOP and Corneal Resistance Factor for the Reichert Ocular Response Analyzer. *Invest. Ophthalmol. Vis. Sci.* 47 (13), 2266.

Luce, D. A. (2005). Determining *In Vivo* Biomechanical Properties of the Cornea with an Ocular Response Analyzer. *J. Cataract Refract Surg.* 31 (1), 156–162. doi:10.1016/j.jcrs.2004.10.044

Pedersen, I. B., Bak-Nielsen, S., Vestergaard, A. H., Ivarsen, A., and Hjortdal, J. (2014). Corneal Biomechanical Properties after LASIK, ReLEx Flex, and ReLEx Smile by Scheimpflug-Based Dynamic Tonometry. *Graefes Arch. Clin. Exp. Ophthalmol.* 252 (8), 1329–1335. doi:10.1007/s00417-014-2667-6

Piñero, D. P., Alio, J. L., Barraquer, R. I., Michael, R., and Jiménez, R. (2010). Corneal Biomechanics, Refraction, and Corneal Aberrometry in Keratoconus: an Integrated Study. *Invest. Ophthalmol. Vis. Sci.* 51 (4), 1948–1955. doi:10.1167/iovs.09-4177

Roberts, C. J., and Liu, J. (2016). *Corneal Biomechanics: From Theory to Practice*. Amsterdam, Netherlands: Kugler Publications.

Roberts, C. J. (2014). Concepts and Misconceptions in Corneal Biomechanics. *J. Cataract Refract Surg.* 40 (6), 862–869. doi:10.1016/j.jcrs.2014.04.019

Roberts, C. J., Mahmoud, A. M., Bons, J. P., Hossain, A., Elsheikh, A., Vinciguerra, R., et al. (2017). Introduction of Two Novel Stiffness Parameters and Interpretation of Air Puff-Induced Biomechanical Deformation Parameters with a Dynamic Scheimpflug Analyzer. *J. Refract Surg.* 33 (4), 266–273. doi:10.3928/1081597x-20161221-03

Santhiago, M., Giacomin, N., Smadja, D., and Bechara, S. (2016). Ectasia Risk Factors in Refractive Surgery. *Opth* 10, 713. doi:10.2147/opth.s51313

Sefat, S. M. M., Wiltfang, R., Bechmann, M., Mayer, W. J., Kampik, A., and Kook, D. (2016). Evaluation of Changes in Human Corneas after Femtosecond Laser-Assisted LASIK and Small-Incision Lenticule Extraction (SMILE) Using Non-contact Tonometry and Ultra-high-speed Camera (Corvis ST). *Curr. Eye Res.* 41 (7), 917–922. doi:10.3109/02713683.2015.1082185

Tanaka, N., Higashimori, M., and Kaneko, M. (2011). *Non-contact Stiffness Sensing with Deformation Dependent Force Calibration*. IEEE, 248–253.

Terai, N., Raiskup, F., Haustein, M., Pillunat, L. E., and Spoerl, E. (2012). Identification of Biomechanical Properties of the Cornea: the Ocular Response Analyzer. *Curr. Eye Res.* 37 (7), 553–562. doi:10.3109/02713683.2012.669007

Thomas, G., Burnham, N. A., Camesano, T. A., and Wen, Q. (2013). Measuring the Mechanical Properties of Living Cells Using Atomic Force Microscopy. *J. Vis. Exp.* (76), e50497. doi:10.3791/50497

Tian, L., Ko, M. W., ke Wang, L., Zhang, J-Y., Li, T-J., Huang, Y-F., et al. (2014). Assessment of Ocular Biomechanics Using Dynamic Ultra High-Speed Scheimpflug Imaging in Keratoconic and normal Eyes. *J. Refract Surg.* doi:10.3928/1081597x-20140930-01

Vappou, J., Hou, G. Y., Marquet, F., Shahmirzadi, D., Grondin, J., and Konofagou, E. E. (2015). Non-contact, Ultrasound-Based Indentation Method for Measuring Elastic Properties of Biological Tissues Using Harmonic Motion Imaging (HMI). *Phys. Med. Biol.* 60 (7), 2853–2868. doi:10.1088/0031-9155/60/7/2853

Vinciguerra, R., Elsheikh, A., Roberts, C. J., Ambrósio, R., Kang, D. S. Y., Lopes, B. T., et al. (2016). Influence of Pachymetry and Intraocular Pressure on Dynamic Corneal Response Parameters in Healthy Patients. *J. Refract Surg.* 32 (8), 550–561. doi:10.3928/1081597x-20160524-01

Whitacre, M. M., Stein, R. A., and Hassanein, K. (1993). The Effect of Corneal Thickness on Applanation Tonometry. *Am. J. Ophthalmol.* 115 (5), 592–596. doi:10.1016/s0002-9394(14)71455-2

Xu, W., Tao, Y., Wang, L., and Huang, Y. (2017). Evaluation of Biomechanical Changes in Myopia Patients with Unsatisfactory Corneas after Femto Second-Laser *In Situ* Keratomileusis (Fs-lasik) Concurrent with Accelerated Corneal Collagen Cross-Linking Using Corvis-St: Two-Year Follow-Up Results. *Med. Sci. Monit.* 23, 3649–3656. doi:10.12659/msm.905493

Conflict of Interest: CR is a consultant to Oculus Optikgeräte GmbH and Ziemer Ophthalmic Systems AG.

The remaining authors declare that the research was conducted in the absence of any commercial or financial relationships that could be construed as a potential conflict of interest.

Publisher's Note: All claims expressed in this article are solely those of the authors and do not necessarily represent those of their affiliated organizations, or those of the publisher, the editors, and the reviewers. Any product that may be evaluated in this article, or claim that may be made by its manufacturer, is not guaranteed or endorsed by the publisher.

frontiers in Bioengineering and Biotechnology

ORIGINAL RESEARCH
published: 31 March 2022
doi: 10.3389/fbioe.2022.834270

Biomechanical Effects of tPRK, FS-LASIK, and SMILE on the Cornea

Yue Xin[1], Bernardo T. Lopes[2], JunJie Wang[1,3], Jie Wu[1], ManMan Zhu[1], MuChen Jiang[1], YuanYuan Miao[1], HuiNi Lin[4], Si Cao[5], XiaoBo Zheng[1,3], Ashkan Eliasy[2], ShiHao Chen[1,3], QinMei Wang[1,3], YuFeng Ye[1]*, FangJun Bao[1,3]* and Ahmed Elsheikh[2,6,7]*

[1]Eye Hospital, Wenzhou Medical University, Wenzhou, China, [2]School of Engineering, University of Liverpool, Liverpool, United Kingdom, [3]The Institute of Ocular Biomechanics, Wenzhou Medical University, Wenzhou, China, [4]STU-CUHK Joint Shantou International Eye Center, Shantou, China, [5]Wuhan Puren Hospital, Wuhan, China, [6]National Institute for Health Research (NIHR) Biomedical Research Centre for Ophthalmology, Moorfields Eye Hospital NHS Foundation Trust and UCL Institute of Ophthalmology, London, United Kingdom, [7]Beijing Advanced Innovation Center for Biomedical Engineering, Beihang University, Beijing, China

OPEN ACCESS

Edited by:
Yang Liu,
Hong Kong Polytechnic University,
Hong Kong SAR, China

Reviewed by:
Jianmin Shang,
Fudan University, China
Weiwei Yan,
China Jiliang University, China
Jorge L. Alio,
Miguel Hernández University, Spain

***Correspondence:**
ShiHao Chen
chenshihao73@126.com
YuFeng Ye
yeyufeng2000@126.com
FangJun Bao
bfjmd@126.com

Specialty section:
This article was submitted to Biomechanics, a section of the journal Frontiers in Bioengineering and Biotechnology

Received: 13 December 2021
Accepted: 15 February 2022
Published: 31 March 2022

Citation:
Xin Y, Lopes BT, Wang J, Wu J, Zhu M, Jiang M, Miao Y, Lin H, Cao S, Zheng X, Eliasy A, Chen S, Wang Q, Ye Y, Bao F and Elsheikh A (2022) Biomechanical Effects of tPRK, FS-LASIK, and SMILE on the Cornea. Front. Bioeng. Biotechnol. 10:834270. doi: 10.3389/fbioe.2022.834270

Purpose: The objective of this study is to evaluate the *in vivo* corneal biomechanical response to three laser refractive surgeries.

Methods: Two hundred and twenty-seven patients who submitted to transepithelial photorefractive keratectomy (tPRK), femtosecond laser-assisted *in-situ* keratomileusis (FS-LASIK), or small-incision lenticule extraction (SMILE) were included in this study. All cases were examined with the Corvis ST preoperatively (up to 3 months) and postoperatively at 1, 3, and 6 months, and the differences in the main device parameters were assessed. The three groups were matched in age, gender ratio, corneal thickness, refractive error corrections, optical zone diameter, and intraocular pressure. They were also matched in the preoperative biomechanical metrics provided by the Corvis ST including stiffness parameter at first applanation (SP-A1), integrated inverse radius (IIR), deformation amplitude (DA), and deformation amplitude 2 mm away from apex and the apical deformation (DARatio2mm).

Results: The results demonstrated a significant decrease post-operation in SP-A1 and significant increases in IIR, DA, and DARatio2mm ($p < 0.05$), all of which indicated reductions in overall corneal stiffness. Inter-procedure comparisons provided evidence that the smallest overall stiffness reduction was in the tPRK group, followed by the SMILE, and then the FS-LASIK group ($p < 0.05$). These results remained valid after correction for the change in CCT between pre and 6 months post-operation and for the percentage tissue altered. In all three surgery groups, higher degrees of refractive correction resulted in larger overall stiffness losses based on most of the biomechanical metrics.

Conclusion: The corneal biomechanical response to the three surgery procedures varied significantly. With similar corneal thickness loss, the reductions in overall corneal stiffness were the highest in FS-LASIK and the lowest in tPRK.

Keywords: biomechanical response, *in-vivo*, tPRK, FS-LASIK, SMILE

INTRODUCTION

The current growth in interest in the evaluation of corneal biomechanics and the changes caused by laser vision correction (LVC) surgeries is driven mainly by the emergence of cases that developed iatrogenic ectasia (Randleman, 2016). This complication is multifactorial, and some of its risk factors are still to be elucidated (Binder, 2007; Bohac et al., 2018). The corneal instability leading to irregular astigmatism and vision impairment in this complication can be triggered in susceptible corneas by the tissue alterations and the subsequent stiffness reductions associated with the surgical procedures (Ambrósio et al., 2010). Bohac et al. (2018) found that corneal thickness (a major contributing factor to cornea's overall stiffness) below 500 μm was present in 50% of the ectatic cases. Other researchers further noted that corneal instability can develop in previously stiff and stable corneas when the tissue alteration caused by the procedure was large (Santhiago et al., 2014; Santhiago et al., 2015). In connection with this observation, Bohac et al. (2018) identified risk factors related to the tissue alteration induced by procedures such as a low residual stromal bed (≤300 μm) in 30% of the cases and high percentage tissue thickness alteration (≥40%) in 20% (Bohac et al., 2018). Interestingly, these studies have shown that the majority of LASIK cases with these risk factors remained stable for a period between 2 and 8 years before developing ectasia, suggesting that still unknown factors affecting the corneal biomechanical behavior were involved in this complication.

Over the years, and with more cases of iatrogenic ectasia reported (Ambrósio, 2019), there was a search for procedures that would have a low impact on corneal biomechanics—this search led to an increased use of surface ablation surgeries including transepithelial photorefractive keratectomy (tPRK) and the introduction of the small-incision lenticule extraction (SMILE) surgery. However, recent case reports of iatrogenic ectasia post-SMILE have highlighted the need to carefully evaluate the biomechanical advantage of this procedure over laser-assisted *in-situ* keratomileusis (LASIK) (El-Naggar, 2015; Wang et al., 2015; Mattila and Holopainen, 2016; Voulgari et al., 2018; Pazo et al., 2019; Shetty et al., 2019). Even though there is experimental and numerical evidence of the reduced biomechanical effect of SMILE compared to LASIK (Seven et al., 2017; Spiru et al., 2018), this expected reduced effect was not evident in clinical studies (Guo et al., 2019; Raevdal et al., 2019). The same is true for comparisons between LASIK and SMILE on one hand and PRK on the other. Although PRK did not involve tissue separation, or the formation of a cap or a flap, its expected reduced biomechanical effect compared to both LASIK and SMILE was not consistently seen in earlier clinical studies (Chen et al., 2016; Yildirim et al., 2016; Spiru et al., 2018; Yu et al., 2019).

With the fast growth in popularity of laser vision correction surgeries worldwide (Kim et al., 2019), the increased recognition of the effect of corneal biomechanics on surgery outcomes (Roberts, 2016; Esporcatte et al., 2020), and the continued concern about post-surgery ectasia, it is important to reach a definitive answer concerning the mechanical effect of different LVCs. This study is part of our efforts to evaluate clinically the *in vivo* biomechanical impact of the three most common forms of LVCs, namely, femtosecond LASIK (FS-LASIK), SMILE, and tPRK, while controlling for potential confounding factors.

MATERIALS AND METHODS

Patient Inclusion

This prospective comparative case series was approved by the Ethics Committee of the Eye Hospital, Wenzhou Medical University (WMU). Two hundred and twenty-seven Chinese patients, who had undergone corneal refractive surgery for myopia and astigmatism at the Eye Hospital of WMU, were included in this study. All the patients belong to east Asian race and the Han nationality. The patients had myopia between −1.00 and −9.75 D (mean −4.82 ± 1.57 D) and astigmatism between 0 and −3.00 D (mean −0.76 ± 0.59 D). Among these patients, 74 underwent tPRK, 81 accepted FS-LASIK, and 72 underwent SMILE. Informed consent was provided by all participants to use their data in research. Only one eye, randomly selected per patient, was included in the analysis. All the LVC was operated by the same operator, and only patients with no systemic or ocular condition apart from the refractive error and with complete records of the surgical procedure, clinical examination, and Corvis ST (CVS, software version 1.6r2031, OCULUS Optikgeräte, Wetzlar, Germany) results up to 3 months on preoperative (pre), 1 month (pos1m), 3 months (pos3m) and 6 months postoperative (pos6m) were included. Those who did not complete the 6 months postoperative follow-up were excluded from the study.

Surgical Technique

In the tPRK procedure, the epithelium and stroma were ablated with a central ablated epithelium thickness of 55 μm in a single step using the aberration-free mode of the Schwind Amaris 750 Hz excimer laser (Schwind eye-tech-solutions, Kleinostheim, Germany). In the FS-LASIK procedure, the lamellar flap was created with a femtosecond laser (Ziemer Ophthalmic Systems AG, Port, Switzerland). The flaps had a superior hinge, and their thickness ranged from 95 to 110 μm and diameter from 8.5 to 9.0 mm. The FS-LASIK ablation was then performed using the Schwind Amaris 750 Hz excimer laser. The SMILE procedure was performed using the VisuMax femtosecond laser (Carl Zeiss Meditec, Jena, Germany). A stromal lenticule was removed, leaving a cap whose thickness ranged from 115 to 140 μm.

The postoperative care was similar for the three procedures starting with one drop of tobramycin/dexamethasone (Tobradex; Alcon, TX, United States) instilled at the surgical site. This was followed by placing a bandage contact lens (Acuvue Oasys; Johnson & Johnson, FL, United States) on the cornea and keeping it for 1 day in FS-LASIK and for 3–7 days in the tPRK group until complete corneal re-epithelialization. Fluorometholone 0.1% (Flumetholon; Santen, Osaka, Japan) and topical levofloxacin 0.5% (Cravit; Santen, Osaka, Japan) were then applied four times a day in all three groups. In the tPRK group, the fluorometholone dosage was tapered each

subsequent 2–3 weeks and stopped 2–3 months after surgery, while for FS-LASIK and SMILE, the fluorometholone dosage was tapered each subsequent week until 1 month after surgery.

Surgical parameters including optical zone diameter (OZD) and manifest refractive error correction (MRx) were recorded from surgery planning/treatment printouts. The MRx was recorded with spherical (MRxSph) and cylindrical parts (MRxCyl) and was converted into spherical equivalent (SE). Central corneal thickness (CCT) and mean corneal curvature (Km) were measured with a Pentacam (software version: 1.21r65, OCULUS Optikgerate GmbH, Wetzlar, Germany) and used to calculate the difference in CCT (CCT_{dif}) between the values obtained before and 6 months after surgery. The CCT measurements also allowed calculation of the tissue altered (TA) as TA = CCT_{dif} in the tPRK group, TA = flap thickness + CCT_{dif} in the FS-LASIK group, and TA = cap thickness + CCT_{dif} in the SMILE group. PTA was defined as percentage tissue altered (PTA) as PTA = TA/CCT_{pre}. According to SE measured pre surgery, participants were divided into two groups with low-to-moderate myopia (−0.50 D > SE ≥ −5.00 D, LM group) and high myopia (−5.00 D > SE, HM group) as we did in a previous study (Bao et al., 2020). No patients experienced complications related to the surgical procedures.

Biomechanical Evaluation

All Corvis ST exams were taken in the sitting position with undilated pupils by two experienced examiners. They were taken in the same half-day session to minimize diurnal effects. Five Corvis ST biomechanical metrics that had been linked to corneal stiffness (Vinciguerra et al., 2016; Roberts et al., 2017) were recorded pre- and post-surgery. The parameters included the stiffness parameter at first applanation (SP-A1) (Roberts et al., 2017), calculated as the difference between the adjusted air puff pressure at first applanation (AdjAP1) and biomechanically corrected intraocular pressure (bIOP) divided by the defection amplitude at the first applanation (A1DeflAmp).

$$SP - A1 = (adjAP1 - bIOP)/(A1DeflAmp) \quad (1)$$

The metrics also included the integrated inverse radius (IIR)—the integrated sum of the inverse concave radii between the first and second applanation events; the deformation amplitude (DA), which measures the corneal apex maximum displacement under air-puff; and the ratio between the deformation amplitude 2 mm away from apex and the apical deformation (DARatio2mm). These parameters have been described as suitable parameters to evaluate corneal biomechanics *in vivo* (Vinciguerra et al., 2016).

Statistical Analysis

All statistical analyses were performed using PASW Statistics 20.0 (SPSS Inc., Chicago, United States). Baseline characteristics among the three surgery groups were paired using propensity density scores in order to reduce the influence of confounding factor. Comparisons among the three surgery groups were made using the MANOVA of repeated measurements. One-way ANOVA and ANCOVA (analysis of covariates) with a general linear model were used to compare the changes in biomechanical metrics in the three surgery groups, where CCT_{dif} or PTA was considered a covariate. The frequencies of the categorical variable gender were arranged in a 3 × 2 contingency table, and the chi-square test of independence was used to compare them. A p-value of less than 0.05 was considered statistically significant.

RESULTS

The three groups (tPRK, FS-LASIK, and SMILE) were matched in age (27.2 ± 5.2 years vs. 26.1 ± 4.8 years and 26.3 ± 6.0 years, F = 0.876, p = 0.418), gender ratio (male/female: 22/52 vs. 37/44 and 33/39, χ^2 = 5.312, p = 0.070), CCT (540.1 ± 29.3 μm vs. 545.0 ± 27.2 μm and 546.6 ± 21.5 μm, F = 1.838, p = 0.162), MRxSph (−4.69 ± 1.57 D vs. −5.04 ± 1.58 D and −4.72 ± 1.57 D, F = 1.151, p = 0.318), MRxCyl (−0.81 ± 0.57 D vs. −0.66 ± 0.57 D and −0.83 ± 0.63 D, F = 1.776, p = 0.172), OZD (6.59 ± 0.37 mm vs. 6.61 ± 0.34 mm and 6.61 ± 0.18 mm, F = 0.133, p = 0.876), and bIOP (13.90 ± 1.83 mmHg vs. 14.17 ± 1.91 mmHg and 13.67 ± 1.68 mmHg, F = 1.456, p = 0.235). Record matching was also applied for the LM group and HM group individually except for CCT_{dif} (**Table 1**).

Km decreased at pos1m compared with the pre-surgery stage in all surgery groups (all p < 0.01). During follow-up, Km values at pos3m and pos6m were significantly different in the tPRK group (p = 0.007), although there was little change from pos1m to pos3m (p > 0.05). In contrast, in the FS-LASIK group, Km experienced significant fluctuations during follow-up (pos1m vs pos3m: p < 0.01; pos1m vs. pos6m: p < 0.01; pos3m vs. pos6m: p = 0.019). Km values at pos1m and pos6m were also significantly different in the SMILE group (p = 0.020), but the changes were not significant within shorter follow-up stages (p > 0.05).

Figures 1–4 and **Table 2** show the corneal biomechanical metrics measured by Corvis ST for the three groups both pre- and post-operation, which represent the effect of the surgical procedure in each patient group. While there were no significant differences (all p > 0.05) in SP-A1, IIR, DA, and DARatio2mm among the three surgery groups before surgery, uneven shifts towards overall softening were observed after all three surgery procedures (at pos1m) with small, inconsistent, and insignificant stiffness changes taking place between pos1m and pos6m in most situations.

SP-A1 decreased at pos1m compared with the pre-surgery stage in all surgery groups (all p < 0.01), indicating overall stiffness reduction, then experienced non-significant (p > 0.05) fluctuations during follow-up except for the LM-tPRK subgroup (p = 0.039, pos3m vs. pos6m). Comparing pos6m and pre, the change in SP-A1 was larger in FS-LASIK (−34.15 ± 13.17 mmHg/mm, significant when compared with tPRK, p = 0.008), smaller in SMILE (−32.40 ± 10.42 mmHg/mm, non-significant when compared with tPRK, p = 0.090), and smallest in tPRK (−27.40 ± 16.91 mmHg/mm), **Figure 1**. After correction for CCT_{dif}, the changes in SP-A1 between pre and pos6m in tPRK were statistically lower than in FS-LASIK (p = 0.001) and SMILE (p = 0.022). Furthermore, the decrease in SP-A1 from pre to

TABLE 1 | Basic information for the three surgery groups.

Biometric parameter	Groups	tPRK	FS-LASIK	SMILE	F/χ (Binder, 2007)	*p*
Age	LM group	27.0 ± 5.0	26.4 ± 4.6	25.7 ± 6.3	0.558	0.574
	HM group	27.3 ± 5.4	25.8 ± 5.1	26.9 ± 5.7	0.850	0.430
Gender ratio	LM group	12/25	17/17	20/14	5.183	0.075
	HM group	10/27	20/27	13/25	2.213	0.331
CCT, μm	LM group	539.1 ± 33.4	541.6 ± 24.5	546.0 ± 20.3	1.687	0.191
	HM group	541.0 ± 25.5	547.6 ± 29.1	547.0 ± 22.7	0.381	0.684
MRxSph, D	LM group	−3.47 ± 0.84	−3.62 ± 0.87	−3.38 ± 0.72	0.757	0.472
	HM group	−5.91 ± 1.09	−6.06 ± 1.10	−5.93 ± 1.05	0.246	0.783
MRxCyl, D	LM group	−0.68 ± 0.49	−0.62 ± 0.64	−0.81 ± 0.77	0.802	0.451
	HM group	−0.94 ± 0.61	−0.70 ± 0.52	−0.84 ± 0.49	2.143	0.122
OZD, mm	LM group	6.77 ± 0.29	6.79 ± 0.25	6.68 ± 0.11	2.021	0.138
	HM group	6.42 ± 0.36	6.49 ± 0.34	6.56 ± 0.20	1.882	0.157
bIOP, mmHg	LM group	13.78 ± 1.93	13.68 ± 1.69	13.46 ± 1.93	0.273	0.762
	HM group	14.02 ± 1.75	14.52 ± 2.00	13.85 ± 1.42	0.148	0.863
CCT_{dif}, μm	LM group	−75.0 ± 19.8	−71.0 ± 20.3	−74.2 ± 12.2	0.447	0.641
	HM group	−116.1 ± 25.6	−97.9 ± 22.8	−94.7 ± 18.7	9.787	<0.01**
Flap/cap* thickness, μm	LM group	—	102.5 ± 4.7	120.6 ± 3.4	333.5	<0.01**
	HM group	—	100.9 ± 2.8	119.7 ± 1.1	1504.9	<0.01**

CCT, central corneal thickness; MRxSph and MRxCyl, spherical and cylindrical manifest refractive error correction, respectively; OZD, optical zone diameter; CCT_{dif}, the difference in CCT between the values obtained before and 6 months after surgery.

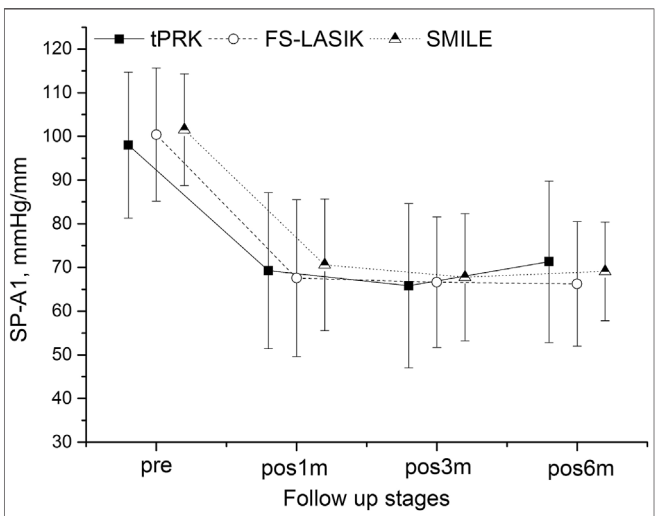

FIGURE 1 | Changes in the stiffness parameter at first applanation (SP-A1) throughout all follow up stages in the transepithelial photorefractive keratectomy (tPRK), femtosecond laser-assisted *in-situ* keratomileusis (FS-LASIK), and small-incision lenticule extraction (SMILE) patient groups (mean and standard deviation).

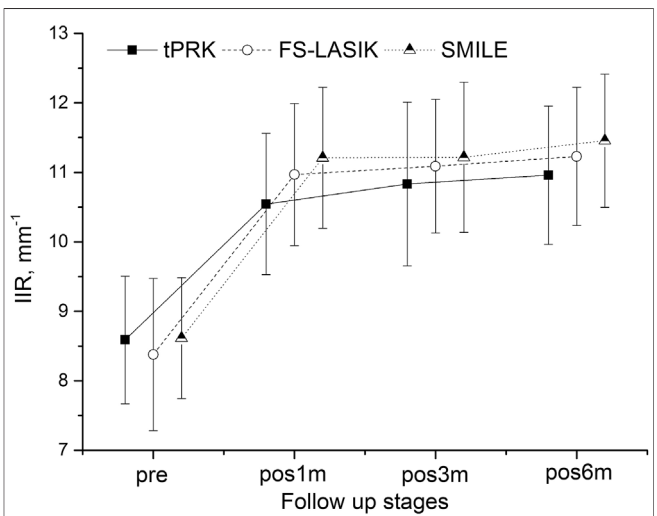

FIGURE 2 | Changes in the integrated inverse radius (IIR) throughout all follow-up stages in the tPRK, FS-LASIK, and SMILE patient groups (mean and standard deviation).

pos6m in FS-LASIK was statistically higher than in SMILE (p = 0.022) after correction for TA. However, after correction for PTA, the changes in SP-A1 between pre and pos6m became non-significant among the three groups ($p > 0.05$). The SP-A1 changes from pre to pos6m were also significantly higher in the HM group than in the LM group after tPRK ($t = 2.715$, $p = 0.008$), FS-LASIK ($t = 3.876$, $p < 0.001$), and SMILE ($t = 2.626$, $p = 0.011$).

IIR exhibited a significant increase from pre to pos1m ($p <$ 0.01), demonstrating overall stiffness reduction, and continued to undergo increases, albeit at a much-reduced rate, from pos1m to pos6m in the three groups, **Figure 2**. The differences between pre and pos6m were statistically significant, being the smallest in tPRK (2.40 ± 0.94 mm^{-1}) and relatively higher in SMILE (2.84 ± 1.03 mm^{-1}) when compared with tPRK (p = 0.020). The IIR changes were also higher in FS-LASIK (2.85 ± 0.96 mm^{-1}) compared with tPRK (p = 0.014). After correction for CCT_{dif}, the changes in IIR between pre and pos6m in tPRK remained lower than in FS-LASIK (p = 0.004) and SMILE (p = 0.002). Also, after correction for TA, the growth in IIR from pre to pos6m was similar in FS-LASIK and SMILE (p = 0.248). However, after correction for PTA, the changes in IIR between pre and pos6m became non-significant among the three groups ($p > 0.05$). The

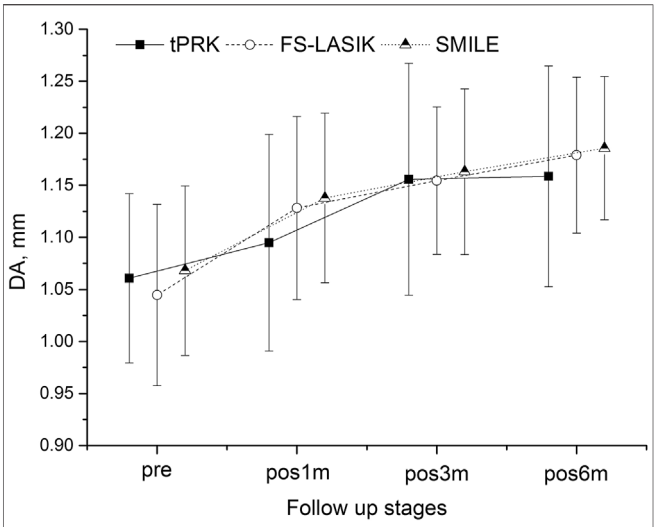

FIGURE 3 | Changes in the deformation amplitude (DA) throughout all follow-up stages in the tPRK, FS-LASIK, and SMILE patient groups (mean and standard deviation).

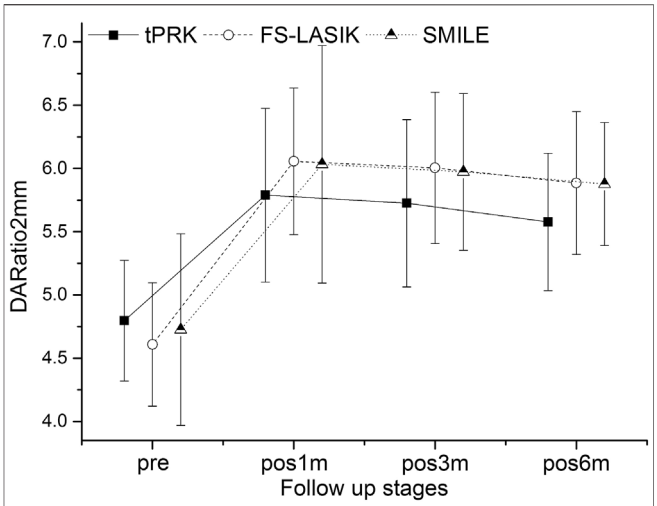

FIGURE 4 | Changes in the deformation amplitude 2 mm away from apex and the apical deformation (DARatio2mm) throughout all follow-up stages in the tPRK, FS-LASIK, and SMILE patient groups (mean and standard deviation).

IIR increases from pre to pos6m were further significantly higher in the HM subgroup than in the LM subgroup (tPRK: $t = -4.678$, $p < 0.001$, FS-LASIK: $t = -4.438$, $p < 0.001$, SMILE: $t = -3.417$, $p = 0.001$).

Another evidence of overall stiffness reduction was seen in the significant increases observed in DA at pos1m compared with the pre-surgery stage in all groups ($p > 0.05$ except in the HM subgroup of tPRK). DA then continued to increase in most follow-up stages from pos1m to pos6m. With tPRK, this trend was more obvious from pos1m to pos3m, **Figure 3**. The change in DA from pre to pos6m in FS-LASIK was significantly higher than that in tPRK (0.134 ± 0.057 mm vs. 0.101 ± 0.086 mm, $p = 0.009$) but was not significantly different from the change in SMILE (0.118 ± 0.063 mm, $p = 0.409$). Meanwhile, the changes in tPRK and SMILE were similar ($p = 0.448$). After correction for CCT_{dif}, the changes in DA between pre and pos6m in tPRK remained statistically lower than in FS-LASIK ($p = 0.024$), but not different from SMILE ($p = 0.750$). Meanwhile, the increase in DA from pre to pos6m after FS-LASIK and SMILE was similar ($p = 0.277$) after correction for TA. However, after correction for PTA, the changes in DA between pre and pos6m were larger in FS-LASIK compared with tPRK ($p = 0.038$) but remained similar in SMILE and tPRK ($p = 1.000$). In contrast, the corresponding changes in DA from pre to pos6m were similar in the LM and HM subgroups of tPRK ($t = -0.855$, $p = 0.396$) and SMILE ($t = 0.084$, $p = 0.934$), but not FS-LASIK ($t = -2.470$, $p = 0.016$).

DARatio2mm also significantly increased, denoting overall stiffness reduction, in all three groups from pre to pos1m (all $p < 0.01$). DARatio2mm then experienced a gradual, slight decrease through the rest of the follow-up period in the three groups, **Figure 4**. The increases in DARatio2mm between pre and pos6m were statistically significant, being the smallest in tPRK (0.79 ± 0.55), higher in SMILE (1.15 ± 0.83) compared with tPRK ($p < 0.01$), and also higher in FS-LASIK (1.28 ± 0.53) when compared with tPRK ($p < 0.01$). After correction for CCT_{dif}, the changes in DARatio2mm between pre and pos6m in tPRK were statistically lower than in those in FS-LASIK ($p = 0.000$) and in SMILE ($p = 0.001$). Furthermore, the increase of DARatio2mm from pre to pos6m in FS-LASIK was statistically higher than that in SMILE ($p = 0.020$) after correction for TA. However, after correction for PTA, the changes in DARatio2mm between pre and pos6m were larger in FS-LASIK compared with tPRK ($p < 0.01$) and remained similar in SMILE and tPRK ($p = 0.416$). The DARatio2mm increases from pre to pos6m were further significantly higher in the HM subgroup than in the LM subgroup (tPRK: $t = -3.309$, $p = 0.001$, FS-LASIK: $t = -2.104$, $p = 0.039$; SMILE: $t = -2.087$, $p = 0.040$).

DISCUSSION

In this study, the biomechanical impact of the three most common LVC procedures was evaluated by monitoring the changes in the *in vivo* biomechanical parameters obtained by the Corvis ST over a 6-month follow-up period. A significant shift in parameter values towards softening was observed following all three surgery forms. After correction for corneal thickness loss (CCT_{Diff}) or percentage tissue altered (PTA), the changes in the four biomechanical metrics (SP-A1, IIR, DA, and DARatio2mm), with strong correlation to the cornea's overall stiffness, showed significant stiffness reductions in all three surgery groups. The metrics' values also indicated that FS-LASIK was associated with the largest stiffness reduction, followed by SMILE and then tPRK. The results also illustrated continued biomechanical changes during the postoperative period, but these changes were small, inconsistent, and insignificant.

The *in vivo* measurement of corneal biomechanics with air-puff systems like the Corvis ST used in this study was assessed in

TABLE 2 | Biomechanical metrics provided by Corvis ST before and after three forms of corneal refractive surgery.

Biometric parameter	Surgery procedure	Subgroups	Pre	Pos1M	Pos3M	Pos6M	*p* (pre vs pos1m)	*p* (pos1m vs pos6m)
SP-A1, mmHg/mm	tPRK	LM group	96.8 ± 16.6	71.0 ± 16.2	68.5 ± 17.6	74.5 ± 19.4	<0.001	1.000
		HM group	99.2 ± 17.0	67.6 ± 19.4	63.1 ± 19.8	68.0 ± 17.1	<0.001	1.000
		p (LM vs HM)	0.545	0.429	0.218	0.139	—	—
	FS-LASIK	LM group	96.3 ± 12.6	70.2 ± 19.5	70.9 ± 17.0	68.3 ± 13.5	<0.001	1.000
		HM group	103.4 ± 16.4	65.8 ± 16.9	63.9 ± 12.9	64.8 ± 14.8	<0.001	1.000
		p (LM vs HM)	0.031	0.301	0.045	0.274	—	—
	SMILE	LM group	99.1 ± 13.9	69.4 ± 13.9	68.2 ± 14.5	70.0 ± 12.4	<0.001	1.000
		HM group	103.7 ± 11.5	71.7 ± 16.2	67.4 ± 14.9	68.4 ± 10.2	<0.001	0.996
		p (LM vs HM)	0.131	0.522	0.816	0.543	—	—
IIR, mm^{-1}	tPRK	LM group	8.69 ± 1.04	10.22 ± 0.98	10.49 ± 1.04	10.64 ± 0.95	<0.001	0.001
		HM group	8.49 ± 0.78	10.86 ± 0.96	11.17 ± 1.22	11.29 ± 0.94	<0.001	0.001
		p (LM vs HM)	0.37	0.006	0.012	0.005	—	—
	FS-LASIK	LM group	8.68 ± 1.08	10.84 ± 1.10	10.97 ± 1.17	11.03 ± 1.00	<0.001	1.000
		HM group	8.16 ± 1.07	11.06 ± 0.97	11.17 ± 0.81	11.38 ± 0.97	<0.001	0.012
		p (LM vs HM)	0.037	0.367	0.389	0.115	—	—
	SMILE	LM group	8.72 ± 0.90	10.87 ± 1.07	10.79 ± 1.00	11.16 ± 1.01	<0.001	0.132
		HM group	8.52 ± 0.85	11.52 ± 0.87	11.6 ± 1.01	11.72 ± 0.83	<0.001	1.000
		p (LM vs HM)	0.313	0.007	0.001	0.012	—	—
DA, mm	tPRK	LM group	1.06 ± 0.09	1.10 ± 0.10	1.15 ± 0.09	1.15 ± 0.11	0.004	0.017
		HM group	1.06 ± 0.07	1.09 ± 0.10	1.17 ± 0.13	1.17 ± 0.10	1.000	<0.001
		p (LM vs HM)	0.765	0.447	0.465	0.491	—	—
	FS-LASIK	LM group	1.04 ± 0.08	1.12 ± 0.09	1.15 ± 0.08	1.16 ± 0.08	<0.001	0.058
		HM group	1.04 ± 0.09	1.13 ± 0.08	1.16 ± 0.06	1.19 ± 0.07	<0.001	<0.001
		p (LM vs HM)	0.979	0.587	0.402	0.074	—	—
	SMILE	LM group	1.06 ± 0.09	1.14 ± 0.09	1.15 ± 0.08	1.18 ± 0.07	<0.001	0.061
		HM group	1.08 ± 0.08	1.14 ± 0.08	1.18 ± 0.07	1.19 ± 0.06	0.001	<0.001
		p (LM vs HM)	0.369	0.797	0.095	0.324	—	—
DARatio2mm	tPRK	LM group	4.85 ± 0.54	5.65 ± 0.51	5.62 ± 0.59	5.44 ± 0.58	<0.001	0.270
		HM group	4.75 ± 0.41	5.93 ± 0.8	5.83 ± 0.72	5.72 ± 0.46	<0.001	0.692
		p (LM vs HM)	0.379	0.087	0.167	0.03	—	—
	FS-LASIK	LM group	4.79 ± 0.45	5.96 ± 0.61	5.89 ± 0.62	5.92 ± 0.64	<0.001	1.000
		HM group	4.48 ± 0.47	6.12 ± 0.56	6.08 ± 0.58	5.86 ± 0.51	<0.001	0.014
		p (LM vs HM)	0.004	0.235	0.191	0.624	—	—
	SMILE	LM group	4.83 ± 1.03	5.95 ± 1.17	5.93 ± 0.55	5.77 ± 0.49	<0.001	0.245
		HM group	4.63 ± 0.37	6.10 ± 0.64	6.01 ± 0.69	5.97 ± 0.46	<0.001	1.000
		p (LM vs HM)	0.276	0.551	0.628	0.075	—	—

SP-A1, stiffness parameter at first applanation; IIR, integrated inverse radius; DA, deformation amplitude, DARatio2mm, deformation amplitude ratio at 2 mm; LM group, low-to-moderate myopia group; HM group, high-myopia group; pre, pos1m, pos3m, and pos6m are the different periods pre- and postoperatively.

earlier publications (Miki et al., 2017). Among the several parameters that Corvis ST offers, four were selected for being closely associated with corneal overall stiffness, namely, SP-A1, IIR, DA, and DARatio2mm. In earlier studies, SP-A1 was correlated with removed corneal tissue in refractive surgery procedures (Fernández et al., 2017), DA was influenced by changes in bIOP (Ye et al., 2021), and IIR and DARatio2mm had the highest correlation with CCT (Vinciguerra et al., 2016). All four parameters were also able to detect corneal softening in keratoconus (Roberts et al., 2017; Sedaghat et al., 2018).

In order to minimize the effect of confounding factors that may have an effect on the four biomechanical parameters selected, the groups were paired for age; gender; and baseline CCT, IOP, and biomechanical parameter readings. The additional pairing for surgical parameters was more challenging since different ablation profiles and depths were obtained with different techniques, even with no statistically significant differences being observed in the corrected manifest equivalent and treated optical zones. Moreover, the difference in the planned tissue removal and achieved stromal reduction could be up to 12 μm in SMILE, while in LASIK, it is as small as less than 1 μm (Reinstein et al., 2014; Ryu et al., 2017).

When SMILE was introduced, it was theorized to be the procedure with the least impact on corneal stiffness (Reinstein et al., 2013). Seven et al. (2017) observed less impact on anterior stromal collagen mechanics in SMILE compared to flap-based procedures in numerical modeling. Several clinical studies were conducted to evaluate the difference between the procedures. Guo et al. (2019) carried out a meta-analysis of *in vivo* evaluation of corneal biomechanical properties after the procedures. They observed using the corneal hysteresis (CH) and corneal resistance factor (CRF), from the Ocular Response Analyzer (ORA), that SMILE was superior to FS-LASIK and comparable to PRK. Raevdal et al. (2019), in a systematic review comparing SMILE with flap-based procedures, did not find significant differences between the procedures using CH or CRF. Both systematic reviews included only a limited number of randomized clinical trials and detected a serious risk of bias due to the presence of confounding factors.

Parameters of the relatively new Corvis ST were evaluated in recent studies on refractive surgeries. Cao et al. (2020) studied the

effect of FS-LASIK and SMILE using two of the parameters evaluated in this study, DARatio2mm and integrated inverse radius. Although FS-LASIK showed higher post-surgery values of both parameters, indicating higher reductions in stiffness, no significant differences were observed between FS-LASIK and SMILE. The bIOP was also significantly reduced by a similar amount postoperatively at both procedures. Khamar et al. (2019) also reported no significant differences between the procedures in DARatio2mm and integrated inverse radius in a contralateral study with up to 1-month follow-up. They also found no significant differences in SP-A1 or bIOP postoperatively, even though the median value of bIOP was 1.1 mmHg lower in SMILE than in FS-LASIK at the postoperative stage. In another study, Lee et al. (2017a) observed significantly higher increases in DARatio2mm and IIR after FS-LASIK compared to tPRK up to 6 months of follow-up. Meanwhile, there were no significant differences between FS-LASIK and tPRK in the reduction of SP-A1 or bIOP readings.

In this study, with a view to uniformize the data analysis and reduce the confounding factors, the three procedures were evaluated together using data from a single center and a single surgeon. All exams were taken at the same period of the day in order to avoid diurnal variance (Ariza-Gracia et al., 2015). Baseline age, CCT, bIOP, and biomechanical parameters were paired along with surgical parameters including optical zone dimeter and refractive corrections. The main trends reported in the literature that tPRK and FS-LASIK were the procedures with the least and highest effects on corneal biomechanics, respectively, were observed in this study. The SMILE procedure, on the other hand, presented intermediate effects.

Considering the pairwise analysis, the three procedures showed significant shifts towards softening at pos1m in all biomechanical metrics considered (SP-A1, IIR, DA, and DARatio2mm). The increases in DARatio2mm were not significantly different between FS-LASIK and SMILE, but were larger than those recorded after tPRK. This was also observed by Cao et al. (2020) in which the SE and the baseline bIOP values were the closest to the ones in this study, but not by Khamar et al. (2019) or by Lee et al. (2017a), in which the SE was lower and the baseline bIOP values higher than corresponding values in this study.

As a further observation, biomechanical changes induced by the surgical operations were generally larger in the high-myopia group compared to the low-to-moderate myopia group. This was evident in the postoperative changes in SPA1, IIR, DA, and DARatio2mm observed after all three procedures. This outcome is expected as higher degrees of myopic correction typically require more tissue removal and hence can introduce larger reductions in corneal biomechanics. This particular observation was also found in several previous studies (Reinstein et al., 2013; Wang et al., 2014; Fernández et al., 2016; Lee et al., 2017a; Lee et al., 2017b).

By conducting a continuous follow-up, the study also revealed an overall softening trend (although the changes were small and insignificant) in the postoperative stages (pos1m to pos6m) in addition to the immediate effects caused by the surgery (pre to pos1m), similar with the results of an animal test using rabbit done by Raghunathan et al. (2017). The results demonstrated that this trend did not show signs of stopping by the time of pos6m, which was most evident in IIR (**Figure 2**) and DA (**Figure 3**). The DARatio2mm however appeared to show an opposite trend with a further decrease from pos1m to pos6m following the immediate increase after surgery at pos1m. At first glance, this finding contradicted the further softening trend suggested by IIR and DA; however, because DARatio2mm is defined as the ratio of deformation amplitude between the corneal apex and the location 2 mm away from it, the results in fact indicated that the corneal deformation amplitude 2 mm away from the apex increased more than that at the apex (DA), which in turn showed non-uniform biomechanical changes (softening) across the cornea. The continuous changes in biomechanical parameters over time and asynchronization of these changes in different regions are believed to be related to the wound healing process after surgery, and they may be the cause of the continuous shape changes after surgery reported above and observed by Bao et al. (2019). The corneal curvature changed statistically significant during the follow-up consisted with that, especially in the FS-LASIK group.

Combined with the correction for corneal thickness loss and percentage tissue altered, which considered the thickness of separated tissue in the FS-LASIK flap and the SMILE cap, the four biomechanical metrics (SP-A1, IIR, DA, and DARatio2mm) showed the largest overall stiffness reductions in FS-LASIK, followed by SMILE, and the lowest stiffness losses in tPRK. These results indicate the negative biomechanical effects of the tissue separation in FS-LASIK flap and SMILE cap, in addition to the tissue ablation in all three procedures. Nevertheless, the decreases in SP-A1 and increases in DARatio2mm from pre to pos6m in FS-LASIK were statistically higher than in SMILE (p = 0.022 and 0.020, respectively). These trends illustrate that the SMILE cap was able to contribute to post-surgery corneal stiffness more than an FS-LASIK flap with equal thickness. Separating the tissue flap in LASIK effectively means losing completely this part of the cornea, and along with the tissue ablation, the tissue loss in LASIK is therefore much more than that in tPRK. In SMILE, an attempt is made to maintain some connection between the cap and the rest of the cornea, but this connection is not perfect, as it is affected by the incision and the loss of support on the posterior side. For these reasons, it is expected that tPRK would have a smaller (or much smaller) biomechanical effect on the cornea than both LASIK and SMILE.

The Stress–Strain Index (SSI) was recently introduced as a measure of the material stiffness of corneal tissues (Eliasy et al., 2019). Material stiffness is part of overall stiffness, alongside geometric stiffness, which is not only dominated by corneal thickness but is also influenced by corneal curvature and diameter. With refractive surgery, it is expected that the large thickness loss (due to both tissue ablation and separation) would lead to substantial geometric stiffness loss and significant reductions in corneal overall stiffness. On the other hand, the material stiffness would not be expected to undergo notable changes, as these would be limited to the small effects of wound healing following surgery (Dupps and Wilson, 2006). For these reasons, the SSI (measure of material stiffness) would not be expected to demonstrate significant changes, unlike those taking place in the overall stiffness parameters like the SP and IIR. Presenting these small changes in SSI alongside the large changes in the overall stiffness metrics could therefore be

confusing—and in any case not relevant to the subject of this study—and for this reason, SSI was not included in the present comparisons.

The study included a number of limitations, one of which was the diurnal fluctuations of the IOP that were reported to influence the values of the four Corvis ST metrics considered (Ye et al., 2021). The variations observed between the pre- and post-surgery stages could have been affected by this change. Furthermore, the use of different femtosecond lasers in FS-LASIK and SMILE, which was necessary due to the Wenzhou Eye Hospital surgical routine, may have led to different flap and cap architectures, although the differences were not significant (Riau et al., 2014).

In conclusion, the biomechanical impact of tPRK, FS-LASIK, and SMILE varied significantly in this study where the data was paired for the main confounding factors. The SMILE procedure induced less corneal biomechanical degradation than FS-LASIK but more than tPRK in cases with comparable corrected refractive errors and optical zone diameter.

DATA AVAILABILITY STATEMENT

The raw data supporting the conclusion of this article will be made available by the authors, without undue reservation.

ETHICS STATEMENT

The studies involving human participants were reviewed and approved by the Eye Hospital, Wenzhou Medical University (WMU). Written informed consent to participate in this study was provided by the participants' legal guardian/next of kin. Written informed consent was obtained from the individual(s) for the publication of any potentially identifiable images or data included in this article.

AUTHOR CONTRIBUTIONS

YY and FB proposed the idea and designed the experiment. YY, FB, and AE built initial constructs and supervised the project. YX, BL, JJW, JiW, MZ, MJ, YM, HL, SiC, XZ, AE, SHC, QW, and FB collected and analyzed data. YX, BL, JJW, JiW, MZ, MJ, YM, HL, SiC, XZ, AE, SHC, QW, and FB drafted the manuscript. YY, SHC, FB, and AE revised the draft. All authors contributed to the article and approved the submitted version.

FUNDING

This study was supported by the National Natural Science Foundation of China (82001924 and 31771020), the Zhejiang Provincial Natural Science Foundation of China under Grant (LY20H120001 and LQ20A020008), the Projects of Medical and Health Technology Development Program in Zhejiang Province (2019RC056 and 2018KY541), the Science and Technology Plan Project of Wenzhou Science and Technology Bureau (Y2020354, Y20180172, Y20170198, and Y20170792), and the General Projects of Department of Education of Zhejiang Province (Y201839651).

REFERENCES

Ambrósio, R., Jr (2019). Post-LASIK Ectasia: Twenty Years of a Conundrum. *Semin. Ophthalmol.* 34, 66–68. doi:10.1080/08820538.2019.1569075

Ambrósio, R., Jr., Dawson, D. G., Salomão, M., Guerra, F. P., Caiado, A. L. C., and Belin, M. W. (2010). Corneal Ectasia after LASIK Despite Low Preoperative Risk: Tomographic and Biomechanical Findings in the Unoperated, Stable, Fellow Eye. *J. Refract Surg.* 26, 906–911. doi:10.3928/1081597x-20100428-02

Ariza-Gracia, M. A., Piñero, D. P., Rodriguez, J. F., Pérez-Cambrodí, R. J., and Calvo, B. (2015). Interaction between Diurnal Variations of Intraocular Pressure, Pachymetry, and Corneal Response to an Air Puff: Preliminary Evidence. *JCRS Online Case Rep.* 3, 12–15. doi:10.1016/j.jcro.2015.01.002

Bao, F., Cao, S., Wang, J., Wang, Y., Huang, W., Zhu, R., et al. (2019). Regional Changes in Corneal Shape over a 6-month Follow-Up after Femtosecond-Assisted LASIK. *J. Cataract Refract Surg.* 45, 766–777. doi:10.1016/j.jcrs.2018.12.017

Bao, F., Huang, W., Zhu, R., Lu, N., Wang, Y., Li, H., et al. (2020). Effectiveness of the Goldmann Applanation Tonometer, the Dynamic Contour Tonometer, the Ocular Response Analyzer and the Corvis ST in Measuring Intraocular Pressure Following FS-LASIK. *Curr. Eye Res.* 45, 144–152. doi:10.1080/02713683.2019.1660794

Binder, P. S. (2007). Analysis of Ectasia after Laser *In Situ* Keratomileusis: Risk Factors. *J. Cataract Refract Surg.* 33, 1530–1538. doi:10.1016/j.jcrs.2007.04.043

Bohac, M., Koncarevic, M., Pasalic, A., Biscevic, A., Merlak, M., Gabric, N., et al. (2018). Incidence and Clinical Characteristics of Post LASIK Ectasia: A Review of over 30,000 LASIK Cases. *Semin. Ophthalmol.* 33, 869–877. doi:10.1080/08820538.2018.1539183

Cao, K., Liu, L., Yu, T., Chen, F., Bai, J., and Liu, T. (2020). Changes in Corneal Biomechanics during Small-Incision Lenticule Extraction (SMILE) and Femtosecond-Assisted Laser *In Situ* Keratomileusis (FS-LASIK). *Lasers Med. Sci.* 35, 599–609. doi:10.1007/s10103-019-02854-w

Chen, M., Yu, M., and Dai, J. (2016). Comparison of Biomechanical Effects of Small Incision Lenticule Extraction and Laser-Assisted Subepithelial Keratomileusis. *Acta Ophthalmol.* 94, e586–e591. doi:10.1111/aos.13035

Dupps, W. J., Jr., and Wilson, S. E. (2006). Biomechanics and Wound Healing in the Cornea. *Exp. Eye Res.* 83, 709–720. doi:10.1016/j.exer.2006.03.015

El-Naggar, M. T. (2015). Bilateral Ectasia after Femtosecond Laser-Assisted Small-Incision Lenticule Extraction. *J. Cataract Refract Surg.* 41, 884–888. doi:10.1016/j.jcrs.2015.02.008

Eliasy, A., Chen, K.-J., Vinciguerra, R., Lopes, B. T., Abass, A., Vinciguerra, P., et al. (2019). Determination of Corneal Biomechanical Behavior *In-Vivo* for Healthy Eyes Using CorVis ST Tonometry: Stress-Strain Index. *Front. Bioeng. Biotechnol.* 7, 105. doi:10.3389/fbioe.2019.00105

Esporcatte, L. P. G., Salomão, M. Q., Lopes, B. T., Vinciguerra, P., Vinciguerra, R., Roberts, C., et al. (2020). Biomechanical Diagnostics of the Cornea. *Eye Vis.* 7, 9. doi:10.1186/s40662-020-0174-x

Fernández, J., Rodríguez-Vallejo, M., Martínez, J., Tauste, A., and Piñero, D. P. (2016). Corneal Thickness after SMILE Affects Scheimpflug-Based Dynamic Tonometry. *J. Refract Surg.* 32, 821–828. doi:10.3928/1081597x-20160816-02

Fernández, J., Rodríguez-Vallejo, M., Martínez, J., Tauste, A., Salvestrini, P., and Piñero, D. P. (2017). New Parameters for Evaluating Corneal Biomechanics and Intraocular Pressure after Small-Incision Lenticule Extraction by Scheimpflug-Based Dynamic Tonometry. *J. Cataract Refract Surg.* 43, 803–811. doi:10.1016/j.jcrs.2017.03.035

Guo, H., Hosseini-Moghaddam, S. M., and Hodge, W. (2019). Corneal Biomechanical Properties after SMILE versus FLEX, LASIK, LASEK, or PRK: a Systematic Review and Meta-Analysis. *BMC Ophthalmol.* 19, 167. doi:10.1186/s12886-019-1165-3

Khamar, P., Shetty, R., Vaishnav, R., Francis, M., Nuijts, R. M. M. A., and Sinha Roy, A. (2019). Biomechanics of LASIK Flap and SMILE Cap: A Prospective, Clinical Study. *J. Refract Surg.* 35, 324–332. doi:10.3928/1081597x-20190319-01

Kim, T.-i., Alió del Barrio, J. L., Wilkins, M., Cochener, B., and Ang, M. (2019). Refractive Surgery. *The Lancet* 393, 2085–2098. doi:10.1016/s0140-6736(18)33209-4

Lee, H., Roberts, C. J., Ambrósio, R., Jr., Elsheikh, A., Kang, D. S. Y., and Kim, T.-i. (2017). Effect of Accelerated Corneal Crosslinking Combined with Transepithelial Photorefractive Keratectomy on Dynamic Corneal Response Parameters and Biomechanically Corrected Intraocular Pressure Measured with a Dynamic Scheimpflug Analyzer in Healthy Myopic Patients. *J. Cataract Refract Surg.* 43, 937–945. doi:10.1016/j.jcrs.2017.04.036

Lee, H., Roberts, C. J., Kim, T.-i., Ambrósio, R., Jr., Elsheikh, A., and Kang, D. S. Y. (2017). Changes in Biomechanically Corrected Intraocular Pressure and Dynamic Corneal Response Parameters before and after Transepithelial Photorefractive Keratectomy and Femtosecond Laser-Assisted Laser *In Situ* Keratomileusis. *J. Cataract Refract Surg.* 43, 1495–1503. doi:10.1016/j.jcrs.2017.08.019

Mattila, J. S., and Holopainen, J. M. (2016). Bilateral Ectasia after Femtosecond Laser-Assisted Small Incision Lenticule Extraction (SMILE). *J. Refract Surg.* 32, 497–500. doi:10.3928/1081597x-20160502-03

Miki, A., Maeda, N., Ikuno, Y., Asai, T., Hara, C., and Nishida, K. (2017). Factors Associated with Corneal Deformation Responses Measured with a Dynamic Scheimpflug Analyzer. *Invest. Ophthalmol. Vis. Sci.* 58, 538–544. doi:10.1167/iovs.16-21045

Pazo, E. E., McNeely, R. N., Arba-Mosquera, S., Palme, C., and Moore, J. E. (2019). Unilateral Ectasia after Small-Incision Lenticule Extraction. *J. Cataract Refract Surg.* 45, 236–241. doi:10.1016/j.jcrs.2018.10.018

Raevdal, P., Grauslund, J., and Vestergaard, A. H. (2019). Comparison of Corneal Biomechanical Changes after Refractive Surgery by Noncontact Tonometry: Small-Incision Lenticule Extraction versus Flap-Based Refractive Surgery - a Systematic Review. *Acta Ophthalmol.* 97, 127–136. doi:10.1111/aos.13906

Raghunathan, V. K., Thomasy, S. M., Strøm, P., Yañez-Soto, B., Garland, S. P., Sermeno, J., et al. (2017). Tissue and Cellular Biomechanics during Corneal Wound Injury and Repair. *Acta Biomater.* 58, 291–301. doi:10.1016/j.actbio.2017.05.051

Randleman, J. B. (2016). Ectasia after Corneal Refractive Surgery: Nothing to SMILE about. *J. Refract Surg.* 32, 434–435. doi:10.3928/1081597x-20160613-01

Reinstein, D. Z., Archer, T. J., and Gobbe, M. (2014). Lenticule Thickness Readout for Small Incision Lenticule Extraction Compared to Artemis Three-Dimensional Very High-Frequency Digital Ultrasound Stromal Measurements. *J. Refract Surg.* 30, 304–309. doi:10.3928/1081597x-20140416-01

Reinstein, D. Z., Archer, T. J., and Randleman, J. B. (2013). Mathematical Model to Compare the Relative Tensile Strength of the Cornea after PRK, LASIK, and Small Incision Lenticule Extraction. *J. Refract Surg.* 29, 454–460. doi:10.3928/1081597x-20130617-03

Riau, A. K., Liu, Y.-C., Lwin, N. C., Ang, H. P., Tan, N. Y. S., Yam, G. H. F., et al. (2014). Comparative Study of nJ- and μJ-Energy Level Femtosecond Lasers: Evaluation of Flap Adhesion Strength, Stromal Bed Quality, and Tissue Responses. *Invest. Ophthalmol. Vis. Sci.* 55, 3186–3194. doi:10.1167/iovs.14-14434

Roberts, C. J. (2016). Importance of Accurately Assessing Biomechanics of the Cornea. *Curr. Opin. Ophthalmol.* 27, 285–291. doi:10.1097/icu.0000000000000282

Roberts, C. J., Mahmoud, A. M., Bons, J. P., Hossain, A., Elsheikh, A., Vinciguerra, R., et al. (2017). Introduction of Two Novel Stiffness Parameters and Interpretation of Air Puff-Induced Biomechanical Deformation Parameters with a Dynamic Scheimpflug Analyzer. *J. Refract Surg.* 33, 266–273. doi:10.3928/1081597x-20161221-03

Ryu, I.-H., Kim, B. J., Lee, J.-H., and Kim, S. W. (2017). Comparison of Corneal Epithelial Remodeling after Femtosecond Laser-Assisted LASIK and Small Incision Lenticule Extraction (SMILE). *J. Refract Surg.* 33, 250–256. doi:10.3928/1081597x-20170111-01

Santhiago, M. R., Smadja, D., Gomes, B. F., Mello, G. R., Monteiro, M. L. R., Wilson, S. E., et al. (2014). Association between the Percent Tissue Altered and post-laser *In Situ* Keratomileusis Ectasia in Eyes with normal Preoperative Topography. *Am. J. Ophthalmol.* 158, 87–95. doi:10.1016/j.ajo.2014.04.002

Santhiago, M. R., Smadja, D., Wilson, S. E., Krueger, R. R., Monteiro, M. L. R., and Randleman, J. B. (2015). Role of Percent Tissue Altered on Ectasia after LASIK in Eyes with Suspicious Topography. *J. Refract Surg.* 31, 258–265. doi:10.3928/1081597x-20150319-05

Sedaghat, M.-R., Momeni-Moghaddam, H., Ambrósio, R., Jr., Heidari, H.-R., Maddah, N., Danesh, Z., et al. (2018). Diagnostic Ability of Corneal Shape and Biomechanical Parameters for Detecting Frank Keratoconus. *Cornea* 37, 1025–1034. doi:10.1097/ico.0000000000001639

Seven, I., Vahdati, A., Pedersen, I. B., Vestergaard, A., Hjortdal, J., Roberts, C. J., et al. (2017). Contralateral Eye Comparison of SMILE and Flap-Based Corneal Refractive Surgery: Computational Analysis of Biomechanical Impact. *J. Refract Surg.* 33, 444–453. doi:10.3928/1081597x-20170504-01

Shetty, R., Kumar, N. R., Khamar, P., Francis, M., Sethu, S., Randleman, J. B., et al. (2019). Bilaterally Asymmetric Corneal Ectasia Following SMILE with Asymmetrically Reduced Stromal Molecular Markers. *J. Refract Surg.* 35, 6–14. doi:10.3928/1081597x-20181128-01

Spiru, B., Kling, S., Hafezi, F., and Sekundo, W. (2018). Biomechanical Properties of Human Cornea Tested by Two-Dimensional Extensiometry *Ex Vivo* in Fellow Eyes: Femtosecond Laser-Assisted LASIK versus SMILE. *J. Refract Surg.* 34, 419–423. doi:10.3928/1081597x-20180402-05

Vinciguerra, R., Elsheikh, A., Roberts, C. J., Ambrósio, R., Kang, D. S. Y., Lopes, B. T., et al. (2016). Influence of Pachymetry and Intraocular Pressure on Dynamic Corneal Response Parameters in Healthy Patients. *J. Refract Surg.* 32, 550–561. doi:10.3928/1081597x-20160524-01

Voulgari, N., Mikropoulos, D., Kontadakis, G. A., Safi, A., Tabibian, D., KymionisCorneal Scarring, G. D., et al. (2018). Corneal Scarring and Hyperopic Shift after Corneal Cross-Linking for Corneal Ectasia after SMILE. *J. Refract Surg.* 34, 779–782. doi:10.3928/1081597x-20180921-01

Wang, D., Liu, M., Chen, Y., Zhang, X., Xu, Y., Wang, J., et al. (2014). Differences in the Corneal Biomechanical Changes after SMILE and LASIK. *J. Refract Surg.* 30, 702–707. doi:10.3928/1081597x-20140903-09

Wang, Y., Cui, C., Li, Z., Tao, X., Zhang, C., Zhang, X., et al. (2015). Corneal Ectasia 6.5 Months after Small-Incision Lenticule Extraction. *J. Cataract Refract Surg.* 41, 1100–1106. doi:10.1016/j.jcrs.2015.04.001

Ye, Y., Li, Y., Zhu, Z., Abu Said, A. Z. M., Nguelemo Mayopa, K., Akiti, S., et al. (2021). Effect of Mydriasis-Caused Intraocular Pressure Changes on Corneal Biomechanical Metrics. *Front. Bioeng. Biotechnol.* 9, 751628. doi:10.3389/fbioe.2021.751628

Yildirim, Y., Olcucu, O., Basci, A., Ağca, A., Özgürhan, E. B., Alagöz, C., et al. (2016). Comparison of Changes in Corneal Biomechanical Properties after Photorefractive Keratectomy and Small Incision Lenticule Extraction. *Turkish J. Ophthalmol.* 46, 47–51. doi:10.4274/tjo.49260

Yu, M., Chen, M., and Dai, J. (2019). Comparison of the Posterior Corneal Elevation and Biomechanics after SMILE and LASEK for Myopia: a Short- and Long-Term Observation. *Graefes Arch. Clin. Exp. Ophthalmol.* 257, 601–606. doi:10.1007/s00417-018-04227-5

Conflict of Interest: Author AE is a consultant to Oculus Optikgeräte GmbH. The authors declare that the research was conducted in the absence of any commercial or financial relationships that could be construed as a potential conflict of interest.

frontiers | Frontiers in Bioengineering and Biotechnology

ORIGINAL RESEARCH
published: 01 April 2022
doi: 10.3389/fbioe.2022.856531

Identification of Peripheral Anterior Synechia by Corneal Deformation Using Air-Puff Dynamic Anterior Segment Optical Coherence Tomography

Shuling Ye[1], Chenhong Bao[2], Yulei Chen[1], Meixiao Shen[1], Fan Lu[1], Shaodan Zhang[1] and Dexi Zhu[1]**

[1]School of Ophthalmology and Optometry, Wenzhou Medical University, Wenzhou, China, [2]Linhai First People's Hospital, Taizhou, China

OPEN ACCESS

Edited by:
Yan Wang,
Tianjin Eye Hospital, China

Reviewed by:
Gilbert Yong San Lim,
SingHealth, Singapore
Xiaofei Wang,
Beihang University, China

***Correspondence:**
Shaodan Zhang
shaodan_zhang_wmu@126.com
Dexi Zhu
zhudexioo@hotmail.com

Specialty section:
This article was submitted to Biomechanics, a section of the journal Frontiers in Bioengineering and Biotechnology

Received: 17 January 2022
Accepted: 07 March 2022
Published: 01 April 2022

Citation:
Ye S, Bao C, Chen Y, Shen M, Lu F, Zhang S and Zhu D (2022) Identification of Peripheral Anterior Synechia by Corneal Deformation Using Air-Puff Dynamic Anterior Segment Optical Coherence Tomography. Front. Bioeng. Biotechnol. 10:856531. doi: 10.3389/fbioe.2022.856531

Indentation gonioscopy is commonly used in the clinic to evaluate peripheral anterior synechia (PAS) of angle closure glaucoma (ACG). The examination requires contacting with the cornea, resulting in an uncomfortable feeling for patients, and it only provides qualitative outcomes which may be affected by subjective judgment of the clinicians. Previous studies had reported to identify the presence of PAS by measuring the changes of morphological parameters of the anterior chamber angle (ACA) under the pupillary light reflex, by anterior segment optical coherence tomography (AS-OCT). However, this method was invalid for some subjects who had low sensitiveness to light. This article describes an air-puff dynamic anterior segment optical coherence tomography (DAS-OCT) system that can evaluate the presence of PAS in a non-contact approach. The peripheral cornea is deformed by an air puff jetted from the DAS-OCT, causing a transfer of force to the ACA, just as how indentation gonioscopy works. The dynamic changes of the ACA before and after the air puff are recorded by OCT. Ten eyes of normal subjects were enrolled in this study to validate the repeatability and availability of the measurements. Then, ten samples of the ACA from five subjects with ACG were recruited and were assigned into two groups, the non PAS group (NPAS) and PAS group, according to the results of gonioscopy. The ACA structural parameters including the angle opening distance at 750 μm to the scleral spur (AOD750) and the trabecular-iris space area at 750 μm anterior to the scleral spur (TISA750) were then calculated automatically by a custom-written algorithm. The intraclass correlation coefficient (ICC) of measured parameters was all above 0.85 for normal subjects, exhibiting good repeatability. For patients, both parameters showed significant differences between the two groups after the air puff, while no differences were observed before the air puff. AOD750dif and TISA750dif between two groups showed more significant differences, indicating that they could be

Abbreviations: PACG, primary angle closure glaucoma; PAS, peripheral anterior synechia; NPAS, non-PAS; ACA, anterior chamber angle; AS-OCT, anterior segment optical coherence tomography; DAS-OCT, dynamic anterior segment optical coherence tomography; ACG, angle closure glaucoma; AOD750, angle opening distance at 750 μm to the scleral spur; TISA750, trabecular-iris space area at 750 μm anterior to the scleral spur.

used as indicators to identify the presence of PAS. In conclusion, the DAS-OCT system proposed in this study is demonstrated effective to identify the presence of PAS by measuring the changes of the ACA *via* a noncontact approach. It shows great potential for applications in guidance for diagnosis of angle closure glaucoma.

Keywords: optical coherence tomography, air puff, peripheral anterior synechia, angle closure glaucoma, imaging

INTRODUCTION

Primary angle closure glaucoma (PACG) is responsible for the vast majority of glaucoma blindness in China and has become a significant burden on health care systems and the society (Foster and Johnson, 2001; Tham et al., 2014; Song et al., 2017). The peripheral anterior synechia (PAS), which blocks the aqueous humor outflow pathway, was thought as one of the primary causes for PACG (Aung et al., 2005; Lee et al., 2006; Sun et al., 2017). Nowadays, indentation gonioscopy is commonly used in the clinic to evaluate the presence and extent of PAS in angle closure glaucoma (ACG). During the examination of indentation gonioscopy, the anterior chamber angle (ACA) open, and more structures in the ACA can be observed caused by cornea deformation for non-PAS (NPAS) patients. On the contrary, no more information will be observed by clinicians for the PAS

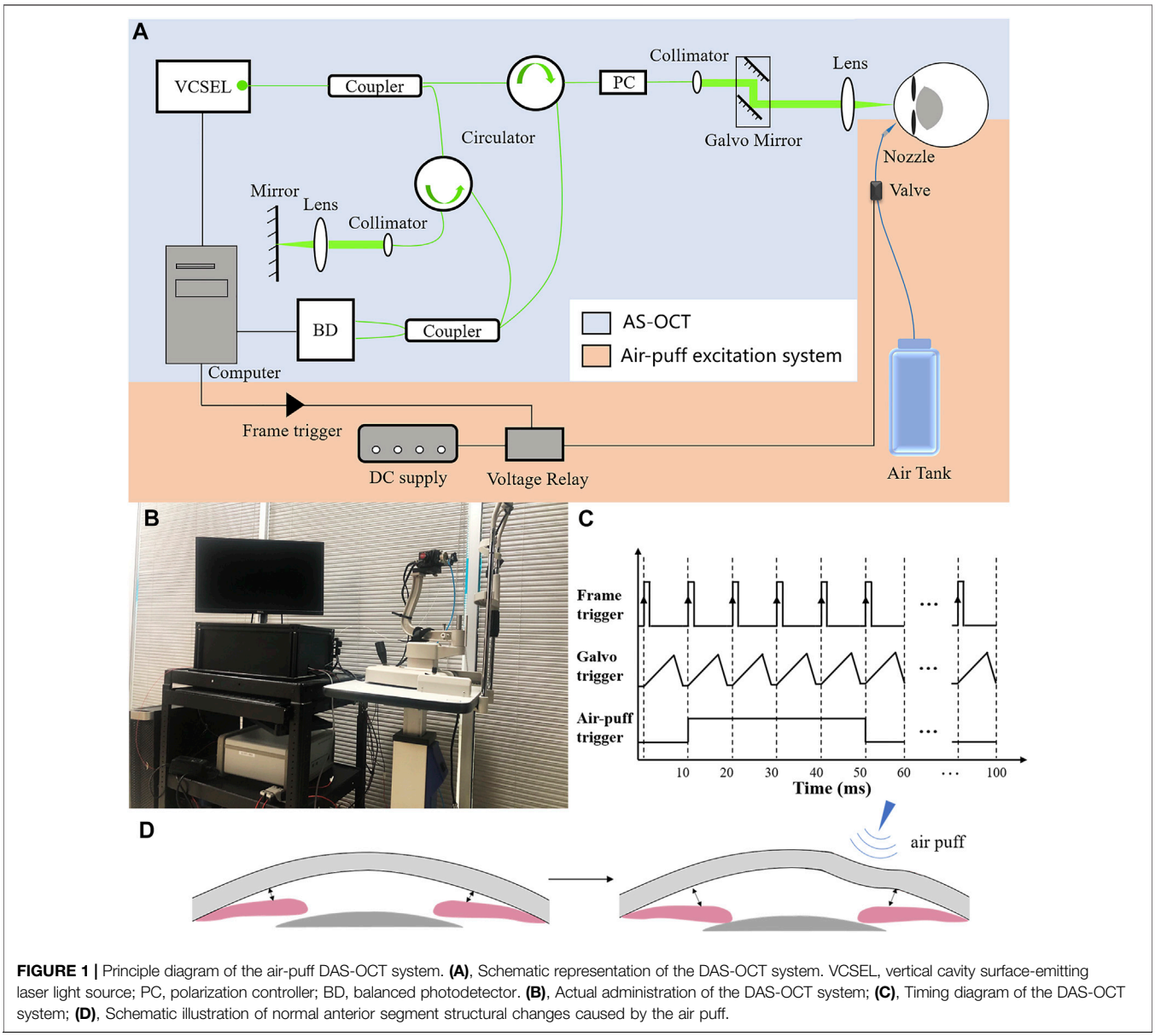

FIGURE 1 | Principle diagram of the air-puff DAS-OCT system. **(A)**, Schematic representation of the DAS-OCT system. VCSEL, vertical cavity surface-emitting laser light source; PC, polarization controller; BD, balanced photodetector. **(B)**, Actual administration of the DAS-OCT system; **(C)**, Timing diagram of the DAS-OCT system; **(D)**, Schematic illustration of normal anterior segment structural changes caused by the air puff.

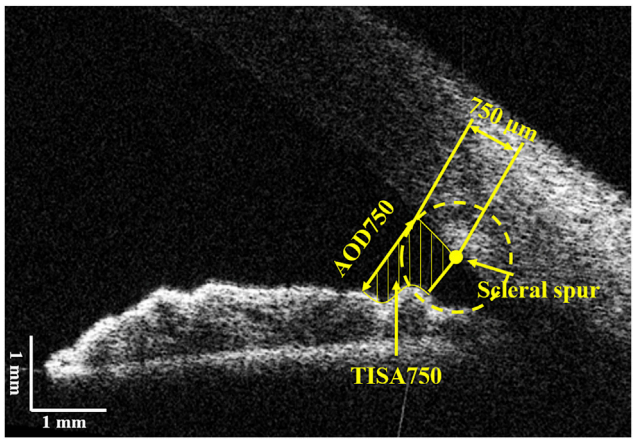

FIGURE 2 | Illustration of the anterior chamber parameters. AOD750, angle opening distance at 750 μm from the scleral spur; TISA750, trabecular-iris space area at 750 μm from the scleral spur.

patients. However, indentation gonioscopy is a contact examination on the cornea, resulting in an uncomfortable feeling for most patients. Besides, it only provides qualitative outcomes which may be affected by the experience and proficiency level of the clinicians (Foster et al., 2000; Phu et al., 2019).

Anterior segment optical coherence tomography (AS-OCT) has been reported to evaluate PAS by measuring the changes of morphological parameters of the ACA under the pupillary light reflex in previous studies (Leung et al., 2007; Lai et al., 2013; Lee et al., 2016). It has great potential for practical use due to its much higher resolution and acquisition speed, as well as being a noncontact and noninvasive measurement. The limitation of this method is that it cannot be carried out for some subjects who have low sensitiveness to light. In addition, a sudden decrease in the luminance may induce the onset of acute angle closure, which is dangerous for PACG.

According to the operating principle of indentation gonioscopy, we assumed that having the peripheral cornea deformed by an air puff, as how an ocular response analyzer and Corvis ST work, may also lead to morphological changes of the ACA, which can be detected by AS-OCT. Inspired by these, an air puff-based dynamic anterior segment optical coherence tomography (DAS-OCT) system was built and validated for evaluating the presence of PAS. The air-puff jet is directed on the cornea and deforms it; meanwhile, the dynamic changes of the morphology of the ACA are recorded by DAS-OCT, and certain structural parameters are calculated as quantitative indicators of PAS. With its high resolution, wide scanning range, and non-contact approach, it may have a great potential for clinical application.

METHODS

Experimental Setup

The custom-made air-puff DAS-OCT consisted of an AS-OCT and an air-puff excitation system (**Figures 1A,B**). The swept source OCT has been described in our previous studies (Dai et al., 2020; Dai et al., 2021), with an A-line scan rate of 200 kHz, a lateral scan range of 17.00 mm, an axial scan depth of 5.86 mm, and an axial resolution of 5.7 μm.

The air-puff excitation system included a DC power supply, a voltage relay, an air-dispensing valve, a nozzle, and an air tank. The high-speed solenoid valve with a response time in the millisecond level (35A-ACA-DDFA-1BA, Wixom, MI, United States) was controlled by the voltage relay and synchronized with the scanning of OCT through a frame trigger from a data acquisition card in the computer (**Figure 1**). In order to simulate the operating principle of indentation gonioscopy, a short duration (40 ms) medical grade air was delivered through a 0.85-mm inner diameter nozzle, which was aligned to normally point to the peripheral area of the cornea with a distance of 15 mm. The nozzle tip was inserted into a hole in a plate and positioned behind the front surface of the plate to prevent contacting with the cornea. The force of the air puff on the surface of the cornea was measured by a custom-built pressure tester based on a strain-sensitive film (Omega Engineering Inc., Norwalk, CT, United States). After calibration, the diameter of the application area of the force on the cornea is 8 mm, and the pressure is 23 kpa, which is less than the force in Corvis ST and ORA. The deformed peripheral cornea caused by the air puff transferred the pressure to the ACA through the aqueous humor, leading to a larger ACA width in case of normal subjects (**Figures 1C,D**).

Data Acquisition and Processing

In this study, the structural images of the anterior chamber were acquired through a B-M scanning protocol. Each B-scan included 2048 A-lines forming a horizontal cross section of the anterior segment. A total of 10 B-scans were captured consecutively at the same scanning position, while the air-puff jet at the beginning of the 2nd imaging with a duration of 40 ms, in order to record the dynamic deformation of the anterior segment during each measurement.

Structural ACA parameters were extracted from each OCT image using a custom-written algorithm described in our previous studies (Zhu et al., 2014; Dai et al., 2020; Dai et al., 2021). The scleral spur on both sides were manually marked after the image was corrected. The anterior and posterior surfaces of the cornea and the anterior surfaces of the iris and lens were automatically segmented by the algorithm. As shown in **Figure 2**, two ACA structural parameters were calculated, that are the angle opening distance at 750 μm to the scleral spur (AOD750) and the trabecular-iris space area at 750 μm anterior to the scleral spur (TISA750) (Dai et al., 2020; Dai et al., 2021). The parameter extracts from the image, in which the deformation of the cornea reach the maximum during the 10 consecutive OCT images, were selected as the values after the air puff, while the first image was considered as the base line. Then, the differences of each parameter between OCT images before and after the air puff were defined as the following, respectively:

$$AOD750_{dif} = AOD750_{after} - AOD750_{before},$$
$$TISA750_{dif} = TISA750_{after} - TISA750_{before}.$$

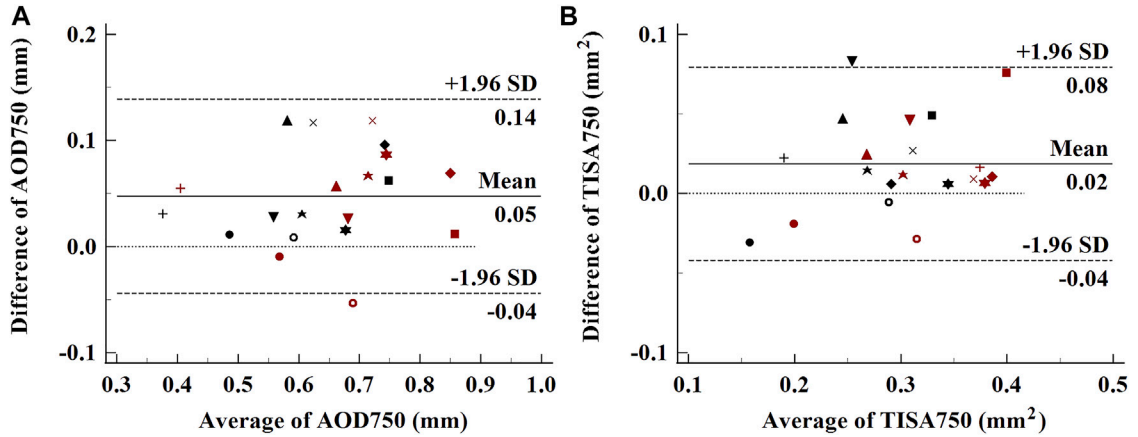

FIGURE 3 | Bland–Altman plots of the repeatability of ACA parameters. **(A)**, AOD750; **(B)**, TISA750. Each subject was labeled by different shapes of spots. Black spots, parameters before the air puff; red spots, parameters after the air puff.

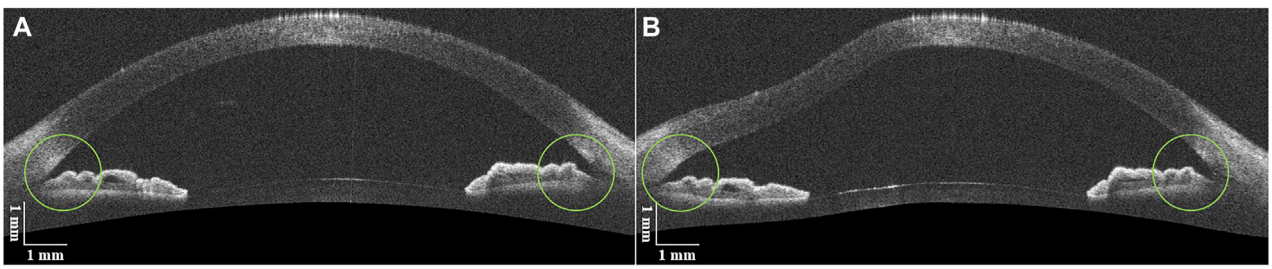

FIGURE 4 | DAS-OCT images of a normal subject eye. **(A)**, image before the air puff; **(B)**, image after the air puff.

Subjects and Grouping

Ten eyes from ten normal subjects (two females and eight males, aged 25.2 ± 0.78 years) and five eyes from five patients with ACG were selected from the Optometry School of Wenzhou Medical University. The right eyes of the volunteers were enrolled. Normal subjects, with best corrected visual acuity ≥1.0 and intraocular pressure (IOP) between 10 and 21 mmHg, were included and assigned into the normal group. Those with remarkable general or ocular diseases, history of eye surgery, poor fixation, and blepharophimosis were excluded. For the patients, gonioscopy was performed by a single experienced ophthalmologist. The eyes with static gonioscopy findings of a grade IV circumferential Scheie gonioscopy classification system in the horizontal direction and without ocular diseases that blocked the OCT scan beam were included. The ACA from patients were further assigned into the NPAS group and PAS group, according to their indentation gonioscopy results.

All volunteers underwent standard ophthalmic examinations including an examination of visual acuity, non-contact tonometer, and slit-lamp biomicroscopy. Then, they were asked to take the DAS-OCT examination. The ACA structural parameters on the same side and on the opposite side of the air-puff position were taken into analysis. All procedures were followed according to the World Medical Association's Declaration of Helsinki.

Statistical Analysis

The intraclass correlation coefficient (ICC) and Bland–Altman plots were used to characterize the repeatability of the measurements. For normal subjects, a paired *t* test was performed to compare the significant differences of ACA structural parameters before and after the air puff. For patients with ACG, independent-sample *t* test analysis was performed to compare the significant differences of ACA structural parameters between the NPAS group and PAS group.

RESULTS

Measurement Repeatability

Each normal subject was measured twice under the same condition, and the obtained OCT images were processed by using one experienced operator. The same side of air puff excitation of ACA was analyzed, and the difference of structural parameters between before and after the air puff was calculated to verify the repeatability of the system. The Bland–Altman plots of AOD750 and TISA750 from the same side ACA (9'o clock) of each normal eye, including the data before and after the excitation, are shown in **Figure 3**. The ICCs of AOD750 and TISA750 are 0.881 and 0.877, respectively, exhibiting great repeatability.

TABLE 1 | Structural parameters on both sides of the ACA in normal subjects.

	The same side (n = 10) mean ± SD	p Value	The opposite side (n = 10) mean ± SD	p Value
$AOD750_{before}$/mm	0.599 ± 0.113	0.000*	0.575 ± 0.086	0.000*
$AOD750_{after}$/mm	0.689 ± 0.131		0.686 ± 0.080	
$TISA750_{before}$/mm^2	0.268 ± 0.059	0.003*	0.264 ± 0.042	0.000*
$TISA750_{after}$/mm^2	0.330 ± 0.063		0.327 ± 0.050	

*p < *0.05, paired* t *test.*

TABLE 2 | Clinical characteristics of patients with angle closure glaucoma.

Subject	Gender	Age/year	Eye	IOP/mmHg	Indentation gonioscopy results	
					3'o clock position	9'o clock position
1	Male	52	OD	13.7	NPAS	NPAS
2	Female	67	OD	26.1	NPAS	PAS
3	Male	46	OD	17.2	NPAS	NPAS
4	Female	62	OD	22.4	PAS	NPAS
5	Male	35	OD	27.9	NPAS	PAS

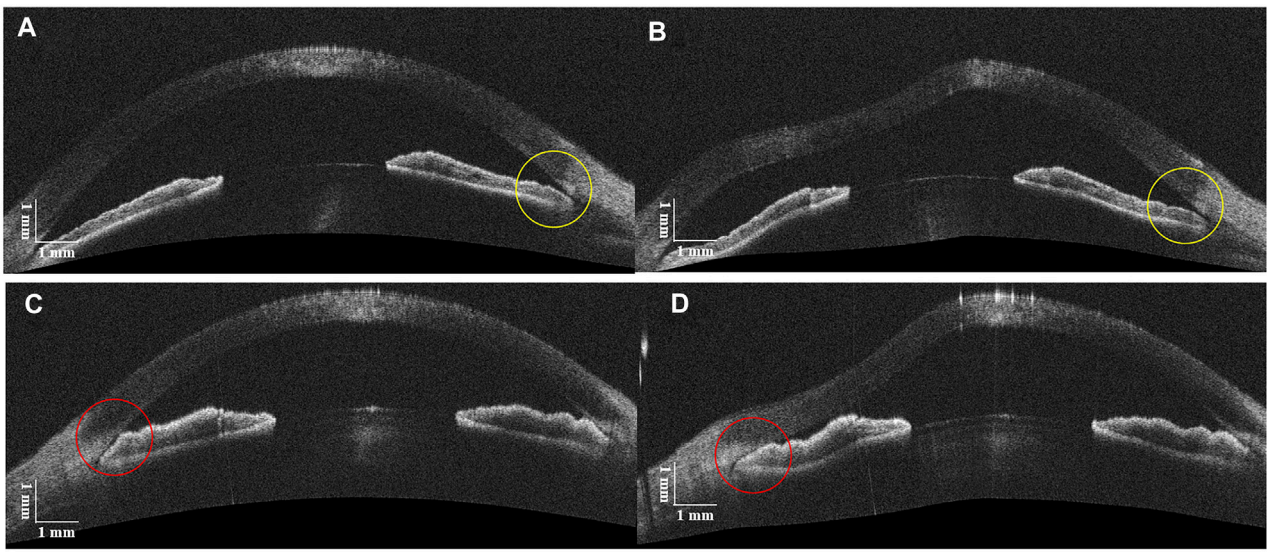

FIGURE 5 | DAS-OCT images before and after the air puff. **(A)**, ACA with NPAS before the air puff; **(B)**, ACA with NPAS after the air puff (yellow circles). **(C)**, ACA with PAS before the air puff; **(D)**, ACA with PAS after the air puff (red circles).

Availability of ACA Data

In order to verify the availability of the ACA on the same side of the air puff compared to the opposite side in one OCT image, ten normal subject eyes before and after the air puff were analyzed. As shown in **Figure 4**, the ACA on both sides opened wider after the air puff. For each side of the ACA, the average of the two measurements of AOD750 and TISA750 was used as an independent sample for analysis. The detailed AOD750 and TISA750 values for both sides of the ACA in all normal subject eyes are listed in **Table 1**. The two parameters both significantly increased after the air puff, indicating both sides of the ACA detected simultaneously by DAS-OCT can be used for the identification of PAS. Therefore, the data from both sides of the ACA in one OCT image will be equally included in this study.

Identification of PAS in Eyes With Angle Closure

The clinical characteristics of five patients with ACG are listed in **Table 2**, from which there are seven ACAs with NPAS and three

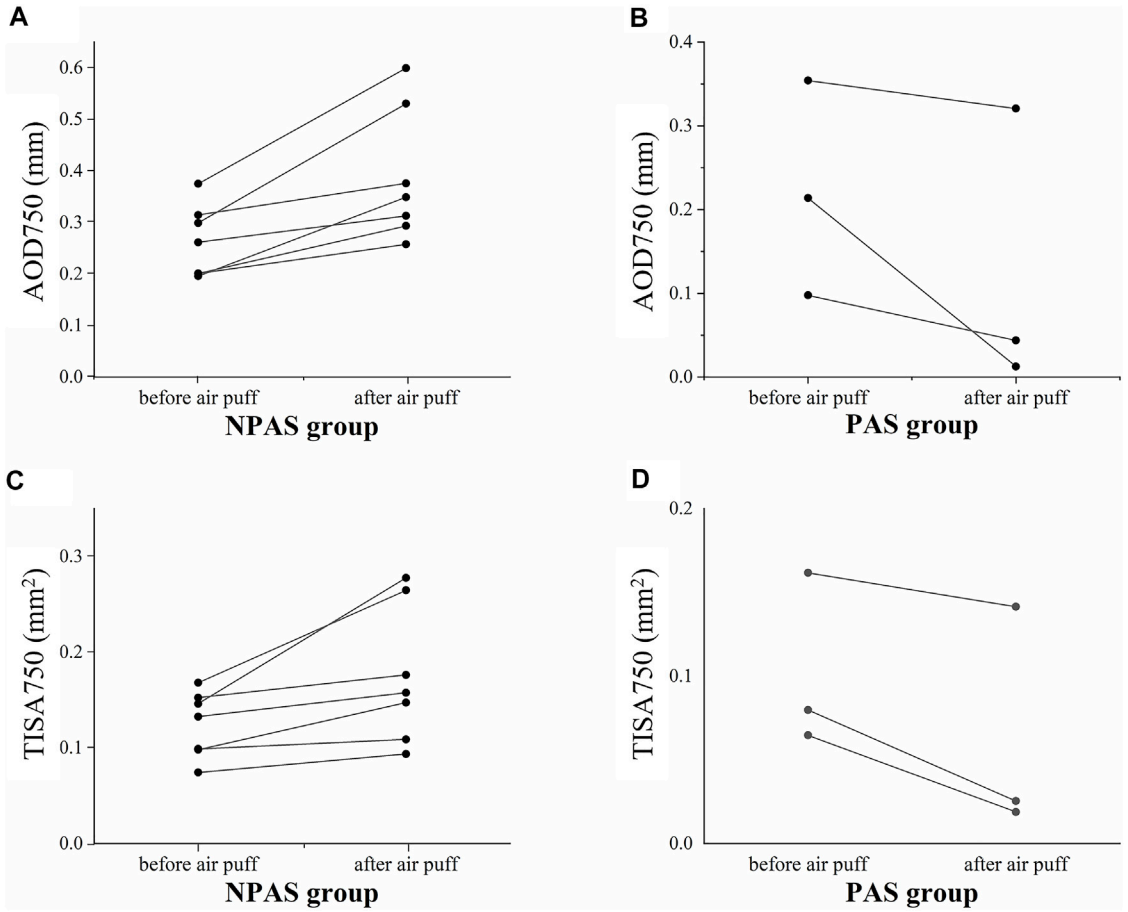

FIGURE 6 | Variations of structural parameters of 10 closed ACAs (five eyes) before and after the air puff. **(A)**, AOD750 in the NPAS group; **(B)**, AOD750 in the PAS group; **(C)**, TISA750 in the NPAS group; **(D)**, TISA750 in the PAS group.

TABLE 3 | Comparisons of structural parameters between the NPAS and PAS groups before and after the air puff.

	NPAS (n = 7)	PAS (n = 3)	p Value
	Mean ± SD	Mean ± SD	
$AOD750_{before}$/mm	0.264 ± 0.692	0.222 ± 0.128	0.507
$AOD750_{after}$/mm	0.388 ± 0.128	0.126 ± 0.170	0.026*
$AOD750_{dif}$/mm	0.124 ± 0.079	−0.096 ± 0.091	0.005*
$TISA750_{before}$/mm^2	0.124 ± 0.034	0.102 ± 0.052	0.437
$TISA750_{after}$/mm^2	0.175 ± 0.071	0.062 ± 0.067	0.049*
$TISA750_{dif}$/mm^2	0.051 ± 0.050	−0.040 ± 0.018	0.012*

*p < *0.05, independent-sample* t *test.*

ACAs with PAS. **Figure 5** shows examples of DAS-OCT images of ACG patients. It is difficult to distinguish the chamber angle without PAS from that with PAS in an OCT image before the air puff, as shown in **Figures 5A,C**. Conversely, after the air puff, the NPAS ACA showed a very modest opening (**Figure 5B**), while the PAS ACA remained close (**Figure 5D**).

For patients with ACG, the variations of the two parameters before and after the air puff for individual ACA are shown in **Figure 6**. Increasing trends could be found in the NPAS group; on the contrary, the values were decreased in the PAS group. The detailed data were analyzed and are listed in **Table 3**. The independent-sample t test showed there were no significant differences of AOD750 and TISA750 before the air puff between the NPAS group and PAS group ($P_{AOD750before}$ = 0.507 and $P_{TISA750before}$ = 0.437). After the air puff, both AOD750 and TISA750 showed significant differences between the two groups ($P_{AOD750after}$ = 0.026 and $P_{TISA750after}$ = 0.049). Compared with the NPAS group, the calculated $AOD750_{dif}$ and $TISA750_{dif}$ were both smaller in the PAS group ($P_{AOD750dif}$ = 0.005 and $P_{TISA750dif}$ = 0.012).

DISCUSSION

In this study, we described a DAS-OCT system to identify the presence of PAS in ACG patients by recording the dynamic process of morphological changes of the ACA excited by the air puff. It has been confirmed that AS-OCT is more sensitive and convenient in detecting angle closure than gonioscopy (Nolan et al., 2007; Sakata et al., 2008). But traditional AS-OCT cannot be an alternative to

indentation gonioscopy, which requires a force applied to promote the ACA opening. In previous studies of our group, a multiple ACA-grade model based on AS-OCT images was demonstrated (Dai et al., 2020). Furthermore, we have reported an AS-OCT–based method for identifying the presence of PAS and evaluating the extent of PAS in a single eye based on the pupillary light reflex (Dai et al., 2021). Changes of ACA structural parameters such as the angle opening distance (AOD), trabecular-iris space area (TISA), and angle opening distance at the scleral spur (AODSS) have been analyzed. Nevertheless, the mechanism of ACA morphological changes caused by the brightness change was different from how gonioscopy works, so the application is limited because of the individual different reaction to light, which resulted in the inconsistent force from the iris contraction. The examination technology by the air puff is widely used in ophthalmology (Terai et al., 2012; Qin et al., 2019; Salouti et al., 2020), non-contact tonometer, and corneal biomechanical measuring instrument for instance and has been proved to be safe enough for eyes. The operating principle of the method proposed in this study was consistent with that of indentation gonioscopy, and more importantly, it provided objective and quantitative ACA parameters without much requirement for clinicians' experience. This technology will reduce the training processing time; thus, it was more valuable in clinical application than gonioscopy.

The repeatability and feasibility of the technique were investigated in this article, showing the well reliability of our method. The fact that the ACA parameters on the same side of the air-puff position were also increased in normal subjects, as same changes as the opposite side, demonstrated that both sides of the ACA imaged during a single B-scan can be used. Hence, the measurement efficiency is improved compared with gonioscopy, which only evaluates the opposite side of the mirror. As shown in **Figures 6B,D**, the structural parameters decreased rather than increasing after the air puff for PAS, no matter on which side relative to the air-puff position. It may be caused by the backward deformation of the entire cornea under the force from the air puff, resulting in more adhesion between the cornea and iris. As shown in **Table 3**, there were no significant differences in $AOD750_{before}$ and $TISA750_{before}$ between the NPAS group and PAS group ($P_{AOD750before}$ = 0.507 and $P_{TISA750before}$ = 0.437), indicating it was difficult to distinguish PAS from appositional angle closure by static OCT images. The calculated $AOD750_{dif}$ and $TISA750_{dif}$ showed greater significances between two groups than $AOD750_{after}$ and $TISA750_{after}$ ($P_{AOD750dif}$ = 0.005, $P_{TISA750dif}$ = 0.012, $P_{AOD750after}$ = 0.026, and $P_{TISA750after}$ = 0.049). In addition, $AOD750_{dif}$ showed a greater difference than $TISA750_{dif}$. Based on the definition of TISA750, the value of that was strongly dependent on the accuracy of surface segmentation of the iris and corneosclera. On the contrary, AOD750 is simply defined as a distance between two points, which may have small detecting deviations compared with TISA750. Therefore, $AOD750_{dif}$ was found to be more sensitive for distinguishing PAS from NPAS.

For the current system, the imaging position was limited only in the horizontal direction of the anterior segment, that is, only 3'o clock and 9'o clock of the ACA can be assessed rather than of the whole 360°. Future studies will update the system to reach a faster acquisition speed and to acquire radial OCT images when the air puff can be applied on the corneal center. Thus, a map of the ACA structure can be formed, and the PAS in all positions can be identified, which would be more valuable in the clinic. Also, we are planning to expand the sample size in following studies so that a binary classification model could be established to evaluate the extent of PAS in patients with ACG.

In summary, we proposed an air-puff–based DAS-OCT system to identify the presence of PAS in a non-contact way. By the corneal deformation under the force of air puff, the ACA without PAS would open, while that with PAS remained close. The structural parameters including AOD750, TISA750, the difference of AOD750, and difference of TISA750 have been demonstrated as effective indicators. An objective parameter, the difference of AOD750, was found to be sensitive enough to distinguish non-PAS from PAS. The system described in this study was demonstrated to be effective for the diagnosis of PAS with good reliability and feasibility and will have potential application in the clinic.

DATA AVAILABILITY STATEMENT

The raw data supporting the conclusions of this article will be made available by the authors, without undue reservation.

ETHICS STATEMENT

The studies involving human participants were reviewed and approved by the ethics committee board of Wenzhou Medical University. The patients/participants provided their written informed consent to participate in this study.

AUTHOR CONTRIBUTIONS

DZ: conceptualization and methodology; SZ: conceptualization; SY: data analysis and writing-original draft preparation; CB: experiment and software; YC: visualization; MS: supervision. All authors reviewed the manuscript.

FUNDING

This work was supported by the National Key R&D Program of China No. 2020YFC2008200 and the National Key Project of Research and Development Program of China, No. 2018YFE0115700.

REFERENCES

Aung, T., Lim, M., Chan, Y., Rojanapongpun, P., Chew, P., and Grp, E. S. (2005). Configuration of the Drainage Angle, Intraocular Pressure, and Optic Disc Cupping in Subjects with Chronic Angle-Closure Glaucoma. *Ophthalmology* 112 (1), 28–32. doi:10.1016/j.ophtha.2004.06.033

Dai, Y., Zhang, S., Shen, M., Jin, Z., Zhou, Y., Ye, S., et al. (2021). Identification of Peripheral Anterior Synechia with Anterior Segment Optical Coherence Tomography. *Graefes Arch. Clin. Exp. Ophthalmol.* 259 (9), 2753–2759. doi:10.1007/s00417-021-05220-1

Dai, Y., Zhang, S., Shen, M., Zhou, Y., Wang, M., Ye, J., et al. (2020). Modeling of Gonioscopic Anterior Chamber Angle Grades Based on Anterior Segment Optical Coherence Tomography. *Eye Vis.* 7 (1), 30. doi:10.1186/s40662-020-00196-1

Foster, P. J., Devereux, J. G., Alsbirk, P. H., Lee, P. S., Uranchimeg, D., Machin, D., et al. (2000). Detection of Gonioscopically Occludable Angles and Primary Angle Closure Glaucoma by Estimation of Limbal Chamber Depth in Asians: Modified Grading Scheme. *Br. J. Ophthalmol.* 84 (2), 186–192. doi:10.1136/bjo.84.2.186

Foster, P. J., and Johnson, G. J. (2001). Glaucoma in China: How Big Is the Problem? *Br. J. Ophthalmol.* 85 (11), 1277–1282. doi:10.1136/bjo.85.11.1277

Lai, I., Mak, H., Lai, G., Yu, M., Lam, D. S. C., and Leung, C. K. S. (2013). Anterior Chamber Angle Imaging with Swept-Source Optical Coherence Tomography: Measuring Peripheral Anterior Synechia in Glaucoma. *Ophthalmology* 120 (6), 1144–1149. doi:10.1016/j.ophtha.2012.12.006

Lee, J. Y., Kim, Y. Y., and Jung, H. R. (2006). Distribution and Characteristics of Peripheral Anterior Synechiae in Primary Angle-Closure Glaucoma. *Korean J. Ophthalmol.* 20 (2), 104–108. doi:10.3341/kjo.2006.20.2.104

Lee, R. Y., Lin, S.-C., Chen, R. I., Barbosa, D. T., and Lin, S. C. (2016). Association between Light-To-Dark Changes in Angle Width and Iris Parameters in Light, Dark and Changes from Light-To-Dark Conditions. *Br. J. Ophthalmol.* 100 (9), 1274–1279. doi:10.1136/bjophthalmol-2015-307393

Leung, C. K.-s., Cheung, C. Y. L., Li, H., Dorairaj, S., Yiu, C. K. F., Wong, A. L., et al. (2007). Dynamic Analysis of Dark-Light Changes of the Anterior Chamber Angle with Anterior Segment OCT. *Invest. Ophthalmol. Vis. Sci.* 48 (9), 4116–4122. doi:10.1167/iovs.07-0010

Nolan, W. P., See, J. L., Chew, P. T. K., Friedman, D. S., Smith, S. D., Radhakrishnan, S., et al. (2007). Detection of Primary Angle Closure Using Anterior Segment Optical Coherence Tomography in Asian Eyes. *Ophthalmology* 114 (1), 33–39. doi:10.1016/j.ophtha.2006.05.073

Phu, J., Wang, H., Khuu, S. K., Zangerl, B., Hennessy, M. P., Masselos, K., et al. (2019). Anterior Chamber Angle Evaluation Using Gonioscopy: Consistency and Agreement between Optometrists and Ophthalmologists. *Optom. Vis. Sci.* 96 (10), 751–760. doi:10.1097/opx.0000000000001432

Qin, X., Yu, M., Zhang, H., Chen, X., and Li, L. (20192019). The Mechanical Interpretation of Ocular Response Analyzer Parameters. *Biomed. Res. Int.* 2019, 1–11. doi:10.1155/2019/5701236

Sakata, L. M., Lavanya, R., Friedman, D. S., Aung, H. T., Gao, H., Kumar, R. S., et al. (2008). Comparison of Gonioscopy and Anterior Segment Ocular Coherence Tomography in Detecting Angle Closure in Different Quadrants of the Anterior Chamber Angle. *Ophthalmology* 115 (5), 769–774. doi:10.1016/j.ophtha.2007.06.030

Salouti, R., Bagheri, M., Shamsi, A., Zamani, M., Ghoreyshi, M., and Nowroozzadeh, M. H. (2020). Corneal Parameters in Healthy Subjects Assessed by Corvis ST. *Jovr* 15 (1), 24–31. doi:10.18502/jovr.v15i1.5936

Song, P., Wang, J., Bucan, K., Theodoratou, E., Rudan, I., and Chan, K. Y. (2017). National and Subnational Prevalence and burden of Glaucoma in China: A Systematic Analysis. *J. Glob. Health* 7 (2), 705. doi:10.7189/jogh.07.020705

Sun, X., Dai, Y., Chen, Y., Yu, D.-Y., Cringle, S. J., Chen, J., et al. (2017). Primary Angle Closure Glaucoma: What We Know and what We Don't Know. *Prog. Retin. Eye Res.* 57, 26–45. doi:10.1016/j.preteyeres.2016.12.003

Terai, N., Raiskup, F., Haustein, M., Pillunat, L. E., and Spoerl, E. (2012). Identification of Biomechanical Properties of the Cornea: The Ocular Response Analyzer. *Curr. Eye Res.* 37 (7), 553–562. doi:10.3109/02713683.2012.669007

Tham, Y.-C., Li, X., Wong, T. Y., Quigley, H. A., Aung, T., and Cheng, C.-Y. (2014). Global Prevalence of Glaucoma and Projections of Glaucoma Burden through 2040. *Ophthalmology* 121 (11), 2081–2090. doi:10.1016/j.ophtha.2014.05.013

Zhu, D., Shao, Y., Leng, L., Xu, Z., Wang, J., Lu, F., et al. (2014). Automatic Biometry of the Anterior Segment during Accommodation Imaged by Optical Coherence Tomography. *Eye Contact Lens-Science Clin. Pract.* 40 (4), 232–238. doi:10.1097/icl.0000000000000043

Conflict of Interest: The authors declare that the research was conducted in the absence of any commercial or financial relationships that could be construed as a potential conflict of interest.

frontiers | Frontiers in Bioengineering and Biotechnology

ORIGINAL RESEARCH
published: 11 April 2022
doi: 10.3389/fbioe.2022.855367

Effects of Laser *In Situ* Keratomileusis and Small-Incision Lenticule Extraction on Corneal Biomechanical Behavior: A Finite Element Analysis

Chenyan Wang[1], *Xiaona Li*[1]*, *Yuan Guo*[1], *Rui He*[2], *Hongmei Guo*[1] *and Weiyi Chen*[1]*

[1]College of Biomedical Engineering, Taiyuan University of Technology, Taiyuan, China, [2]Department of Excimer Laser, Shanxi Eye Hospital, Taiyuan, China

OPEN ACCESS

Edited by:
Salavat Aglyamov,
University of Houston, United States

Reviewed by:
Junjie Wang,
Wenzhou Medical University, China
Gilbert Yong San Lim,
SingHealth, Singapore

***Correspondence:**
Xiaona Li
lixiaona@tyut.edu.cn
Weiyi Chen
chenweiyi211@163.com

Specialty section:
This article was submitted to Biomechanics, a section of the journal Frontiers in Bioengineering and Biotechnology

Received: 15 January 2022
Accepted: 21 February 2022
Published: 11 April 2022

Citation:
Wang C, Li X, Guo Y, He R, Guo H and Chen W (2022) Effects of Laser In Situ Keratomileusis and Small-Incision Lenticule Extraction on Corneal Biomechanical Behavior: A Finite Element Analysis. Front. Bioeng. Biotechnol. 10:855367. doi: 10.3389/fbioe.2022.855367

Myopia, which is the result of the uncoordinated development of the eyeball, has become a major public health focus worldwide. Laser *in situ* keratomileusis (LASIK) and small-incision lenticule extraction (SMILE) have been successfully used in modern corneal refractive surgery. However, there are still controversies about postoperative results of LASIK and SMILE. In this study, a three-dimensional finite element model of the cornea was constructed based on the elevation and pachymetry data of a female volunteer. Surgical parameters, magnitudes of myopic correction, and intraocular pressure (IOP) were varied. Furthermore, an iterative algorithm was applied to retrieve the free-stress state of the intact corneal model, LASIK model, and SMILE model. To better evaluate the differences between LASIK and SMILE procedures, the displacement and Von Mises stress on the anterior and posterior corneal surface along the *x*- and *y*-axes were analyzed. Results for the zero-pressure model showed larger displacement compared to the image-based corneal model, suggesting that the initial corneal pre-stress stiffens the response of the cornea, both in the intact cornea and under refractive surgery. In addition, the displacement on the corneal surface in LASIK (both zero-pressure and image-based model) was obviously higher than that of the SMILE model. In contrast, SMILE increased Von Mises stress in the corneal cap and reduced Von Mises stress in the residual stromal bed compared with the LASIK model. However, the maximum Von Mises stress in the SMILE model was still smaller than that of the LASIK model. Moreover, the displacement and Von Mises stress on the residual stromal bed increased linearly with IOP. Overall, LASIK and SMILE refractive surgery could change biomechanical behaviors of the cornea. Compared to LASIK refractive surgery, SMILE may present a lower risk of ectasia. Creating a corneal cap rather than a corneal flap may have an advantage in improving corneal biomechanical stability.

Keywords: finite element analysis, biomechanics, laser *in situ* keratomileusis, small-incision lenticule extraction, cornea

INTRODUCTION

Myopia has become a major global public health focus (Li et al., 2021). The proportion of people with myopia is gradually increasing, especially in East Asian regions where the incidence of young adults is approximately 80%–90% (Morgan et al., 2018). Furthermore, it has been reported that the myopia prevalence rate can be as high as 49.8% of the world population (about 4.8 billion people) by the year 2050 (Holden et al., 2016). In order to improve the quality of life, there are growing demands for restoring normal visual function. Corneal refractive surgery was introduced to achieve permanent refractive correction and reduce dependence on glasses and contact lenses (Simonini and Pandolfi, 2015; Bao et al., 2018).

Laser *in situ* keratomileusis (LASIK) and small-incision lenticule extraction (SMILE) have been successfully used in modern corneal refractive surgery with good postoperative results. Since 2003, the femtosecond laser had been introduced to replace the mechanical microkeratome in the creation of corneal flap during the LASIK surgery (Nordan et al., 2003). The combination of femtosecond lasers and high-resolution laser instruments makes LASIK an effective method for achieving better control of the flap depth and ablation profile (Roberts, 2000; Farjo et al., 2013). LASIK has been performed to correct myopia with a satisfaction rate of over 95% (Roy et al., 2014). SMILE surgery is a newly developed technique that removes the refractive lenticule through a small incision with less damage to the corneal microstructure (Sekundo et al., 2011; Zhang et al., 2015). Some researchers (Ang et al., 2013; Ivarsen et al., 2014; Shen et al., 2016) suggested that the SMILE approach could provide excellent clinical outcomes in regard to efficacy, predictability, and safety.

In general, the biomechanical behavior of the cornea is related to geometry shapes (Ariza-Gracia et al., 2015), such as corneal central thickness, curvature, and tomography. It is inevitable that lenticule removal and corneal flap/cap creation will directly lead to corneal geometry changes. Theoretically, the absence of a corneal flap creation was believed to allow SMILE procedure benefits beyond those of LASIK because of greater corneal biomechanical strength. Wu et al. investigated the corneal higher-order aberrations after SMILE and FS-LASIK through a comparative experiment (Wu and Wang, 2016). They found that SMILE could decrease corneal spherical aberration compared with FS-LASIK surgery. However, there was little difference in postoperative clinical results between LASIK and SMILE (Vestergaard et al., 2013; Lin et al., 2014; Moshirfar et al., 2015). Agca et al. (2014) conducted a prospective comparative case series and found no difference between SMILE and FS-LASIK in postoperative corneal hysteresis and corneal resistance factor (Agca et al., 2014). Therefore, there is a clear need for additional research to investigate whether the SMILE procedure has advantages over LASIK on postoperative outcomes.

The finite element method is not only a useful tool for simulating the biomechanical properties of the cornea, but also plays an important role in the design of clinical refractive surgery and the prediction of postoperative complications such as keratoconus. In the last 2 decades, the mechanical behavior of the human cornea under normal conditions or refractive surgery has been discussed by methods of numerical simulation (Pandolfi and Manganiello, 2006; Roy and Dupps, 2009; Nguyen and Boyce, 2011; Ariza-Gracia et al., 2015; Katzengold et al., 2021). Katzengold et al. simulated the LASIK surgery and investigated its biomechanical consequences through the finite element method (Katzengold et al., 2021). Roy et al. constructed a human whole-eye finite element model to investigate the impact of corneal properties on biomechanical responses before and after the LASIK surgery (Roy and Dupps, 2009). However, only a few studies had compared the displacement distributions and stress between the LASIK and SMILE procedures using a three-dimensional finite element model.

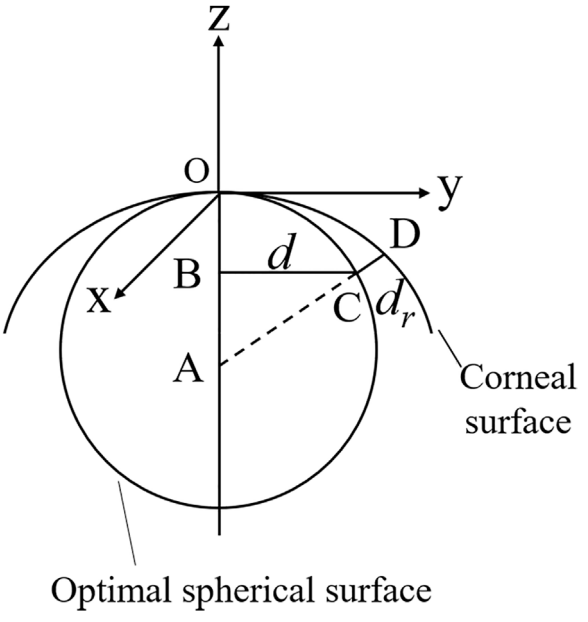

FIGURE 1 | Diagram for the coordinates of the anterior corneal surface.

The purpose of this study was to evaluate differences in displacement and stress on the treated residual stromal bed and corneal flap/cap of the postoperative state resulting from the LASIK and SMILE model, and taking into account the free-stress configuration of the corneal. Furthermore, this study also analyzed biomechanical behaviors of the cornea under different ablation depths and loading conditions. These simulation results could help to clarify whether SMILE is superior to LASIK from a biomechanical view, and provide a valuable reference for the ophthalmologist.

MATERIALS AND METHODS

Geometrical Model of the Cornea

Clinical data from a healthy female volunteer was collected by the Oculus Pentacam. The Pentacam provides the coordinates (x, y) of points belonging to the anterior corneal surface, the pachymetry data for each point, the optimal spherical surface, and the distance from the point on the anterior corneal surface to the optimal spherical surface. Therefore, the value of each point in the z-axis direction can be calculated as (**Figure 1**)

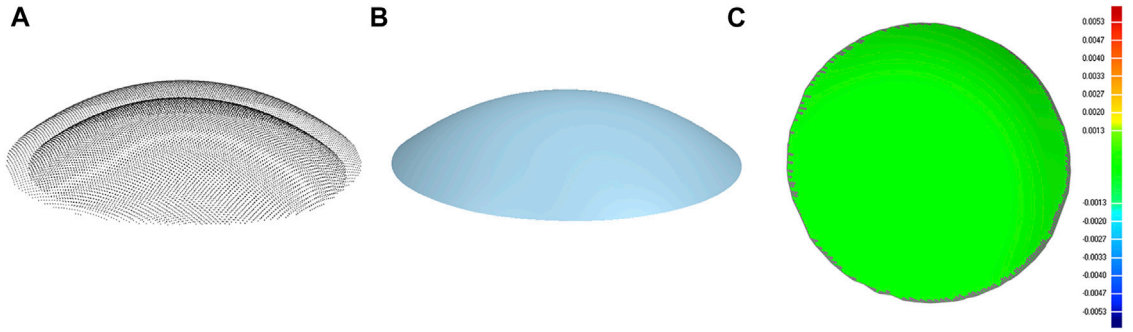

FIGURE 2 | Corneal surface reconstruction. **(A)** Cloud of points of the anterior and posterior corneal surface. **(B)** Geometrical model of the cornea. **(C)** Contour map of the error between the point cloud data and corneal geometrical model (both anterior and posterior corneal surface).

$$d = \left(x^2 + y^2\right)^{1/2} \tag{1}$$

$$z = -\left(r - \left((r + d_r)^2 - d^2\right)^{1/2}\right) \tag{2}$$

Where the optimal sphere is a circle centered at A (0, 0, -r). d is the distance from the corneal surface to the z-axis. d_r is the distance from the corneal surface to the optimal sphere surface.

The points on the posterior corneal surface are obtained by point-to-point subtraction of the anterior surface and the pachymetry data. There were 9,101 and 7,319 coordinate points on the anterior and posterior corneal surface, respectively, and were stored in.csv files. The coordinate points were then imported into the Geomagic studio 2015 (Raindrop, America), and a three-dimensional model of the cornea was reconstructed (**Figure 2**). The subject had given consent for the scientific use of the corneal morphology data. Moreover, ethical approval was obtained from the Ethics Committee of Taiyuan University of Technology (TYUT202107001).

Refractive Procedure Simulation

To treat myopia, refractive surgery ablates a small lenticule from the corneal tissue. After surgery, the change of diopter can be expressed as (Munnerlyn et al., 1988)

$$S = (n-1)\left(\frac{1}{R_2} - \frac{1}{R_1}\right) \tag{3}$$

Where S is the surgical correction of myopia diopter. R_1 and R_2 are the initial and final radius of the corneal anterior surface. n = 1.377 is the refractive index of the cornea.

The shape of the lenticule is thick in the middle and thin around the edge. The thickness of the removed corneal tissue can be described according to the Munnerlyn equation, which is defined as

$$f(\mathrm{r}) = \sqrt{R_1^2 - r^2} - \sqrt{R_1^2 - \frac{t^2}{4}} - \sqrt{\left(\frac{R_1(n-1)}{n-1+R_1S}\right)^2 - r^2} + \sqrt{\left(\frac{R_1(n-1)}{n-1+R_1S}\right)^2 - \frac{t^2}{4}} \tag{4}$$

Where r is the distance from a point to the optical axis, t is the diameter of the optical zone.

The maximum removal of corneal tissue is given by

$$f_{\max} = R_1 - \sqrt{R_1^2 - \frac{t^2}{4}} - \sqrt{\left(\frac{R_1(n-1)}{n-1+R_1S}\right)^2} + \sqrt{\left(\frac{R_1(n-1)}{n-1+R_1S}\right)^2 - \frac{t^2}{4}} \tag{5}$$

In this study, the anterior and posterior corneal surfaces were reconstructed in Geomagic studio. The corneal surfaces were then imported into the Unigraphics NX (Siemens PLM, America) to create the LASIK and SMILE models. Furthermore, each model was assumed to have a single side-cut incision. For the LASIK model, the diameter of the corneal flap was 7.5 mm, and the thickness of the flap was set to be 120 μm. In order to shorten the differences between the two refractive approaches, the cap diameter of the SMILE model was 7.5 mm, and the thickness was also 120 μm (Jin et al., 2018). In addition, for the SMILE surgery, it also considered the actual ablation profile, i.e., an additional 15 μm of the lenticule for easy extraction (**Figure 3**). Moreover, the lenticule diameter (optical zone) was 6.5 mm for both two models. There were two scenarios for myopic corrections of -3D and -6D. The ablation depths are listed in **Table 1**.

Zero-Pressure Configuration of the Cornea

The geometry of the eye, measured *in vivo*, is in a state of deformation due to the presence of intraocular pressure (IOP). Thus, an accurate finite element analysis should recover the zero-pressure configuration of the cornea, i.e., the initial state in which the tissue is free from the IOP. Therefore, an iterative procedure is applied to find the zero-pressure geometry of the cornea (**Figure 4**).

In this study, the algorithm works iteratively by updating the nodal coordinates and comparing the values obtained from the clinical measurements with those provided by the finite element analysis.

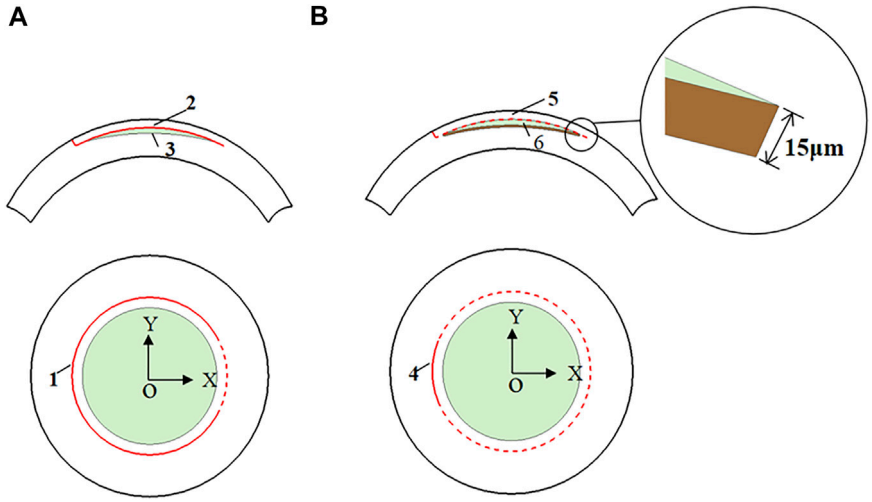

FIGURE 3 | The model features of the LASIK and SMILE procedure. **(A)** LASIK procedure (1 flap opening incision; 2 corneal flap; 3 lenticule); **(B)** SMILE procedure (4 cap opening incision; 5 corneal cap; 6 lenticule).

TABLE 1 | Ablation depths in the LASIK and SMILE model.

Myopic correction	LASIK ablation depth (mm)	SMILE ablation depth (mm)
-3D	42.25	57.25
-6D	84.5	99.5

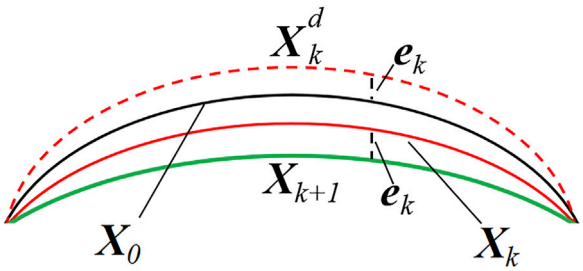

FIGURE 4 | Zero-pressure iterative algorithm.

$$\boldsymbol{X}_{k+1} = \boldsymbol{X}_k + \boldsymbol{X}_0 - \boldsymbol{X}_k^d \tag{6}$$

Where $\boldsymbol{X}$ denotes an N×3 matrix storing the nodal coordinates of the corneal model, and N is the number of nodes in the finite element mesh. $\boldsymbol{X}_0$ represents the geometrical coordinates of the corneal from the clinical data. $\boldsymbol{X}_k$ is the nodal coordinates at the kth iteration. Then, a static finite element analysis was performed by applying physiological IOP to the posterior corneal surface. $\boldsymbol{X}_k^d$ stands for an N×3 matrix that stores the deformation coordinate of each finite element mesh node under the IOP pressure. In the iterative algorithm, the nodal coordinates were set by the inp file in ABAQUS (Simulia, America).

$$e_k = \left\| \boldsymbol{X}_k^d - \boldsymbol{X}_0 \right\|_\infty \tag{7}$$

$$\frac{e_k}{\mathrm{CCT}} < \varepsilon \tag{8}$$

Where e_k is the infinite norm of the difference in nodal coordinates between $\boldsymbol{X}_k^d$ and $\boldsymbol{X}_0$. ε represents the relative tolerance error. CCT is the central corneal thickness, which in the present study was 515 μm. The iterative procedure continues until ε is less than a preset value. In this study, the allowable relative tolerance error is smaller than 0.25 μm (less than 0.05% of the CCT).

Material Properties and Boundary Condition

The anisotropic hyperelastic material property was incorporated into the model to provide a more realistic representation of the cornea (Holzapfel et al., 2000). This property was modeled using Gasser–Holzapfel–Ogden's (G-H-O) constitutive equation. For this study, the same mechanical properties and dispersion parameters were considered for the LASIK and SMILE models. The parameters of C_{10}, D, k_1, k_2, and κ were 0.05 MPa, 0 MPa^{-1}, 130.9 MPa, 2,490, and 0.33329, respectively (Ariza-Gracia et al., 2016).

For boundary conditions, the rim of the cornea was constrained in all degrees of freedom. The friction coefficient was 0.8 between the posterior flap/cap surface and the anterior stromal surface since this value could simulate the clinical situation (Katzengold et al., 2021). Loading was associated with intraocular pressure (IOP). Each model was solved using the IOP: 15 mmHg, 19 mmHg, 23 mmHg, 27 mmHg, and 31 mmHg. The finite element simulations were performed using ABAQUS.

As shown in **Figure 3**, the origin of the coordinate system was set at the center of the cornea. In order to compare different refractive surgeries, four paths were investigated, namely, the paths along the x- and y-axes on the anterior corneal surface, and the paths along the x- and y-axes on the posterior corneal surface.

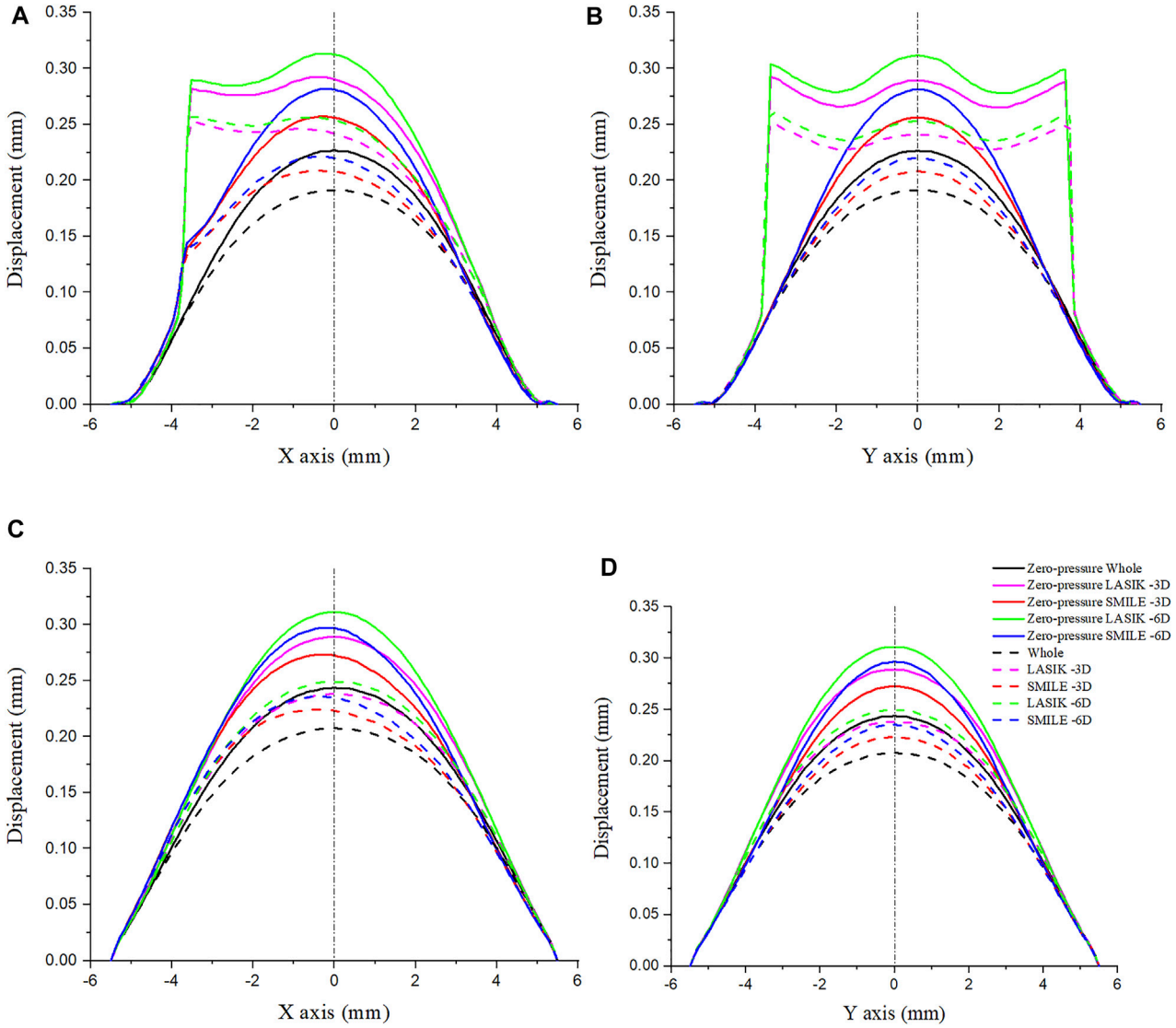

FIGURE 5 | Comparison of displacement on the cornea along the different paths. The IOP was constant at 19 mmHg. **(A)** Displacement on the anterior corneal surface along the *x*-axis. **(B)** Displacement on the anterior corneal surface along the *y*-axis. **(C)** Displacement on the posterior corneal surface along the *x*-axis. **(D)** Displacement on the posterior corneal surface along the *y*-axis. (IOP = intraocular pressure; LASIK = laser *in situ* keratomileusis; SMILE = small-incision lenticule extraction).

Moreover, displacements and Von Mises stresses along different paths were calculated.

RESULTS

Displacement on the Corneal Surface

Figure 5 shows the displacement along four paths for the intact cornea as well as for two different myopic refractive surgeries (LASIK and SMILE), which were obtained using the zero-pressure model and the image-based model. It was obvious that displacement variations along the same path on the anterior corneal surface were different between LASIK and SMILE. However, the trends of displacement along the same path were similar on the posterior corneal surface. In addition, incorporating the zero pressure of the cornea results in a softer corneal response to the IOP (higher displacement along the same path), as shown in **Figure 5**, where the zero-pressure configuration produces a shift in the displacement vs. path curve. For example, the maximum displacement on the anterior corneal surface was 0.221 and 0.188 mm for the zero-pressure and image-based intact corneal model.

To show a more comprehensive mechanical performance between different refractive surgeries, the myopic correction was set to -3D and -6D. Under the same refractive surgery, the more ablation depth is, the greater were displacements induced by the applied IOP. Moreover, the displacement along the *x*- and *y*-axes was obviously increased during the LASIK

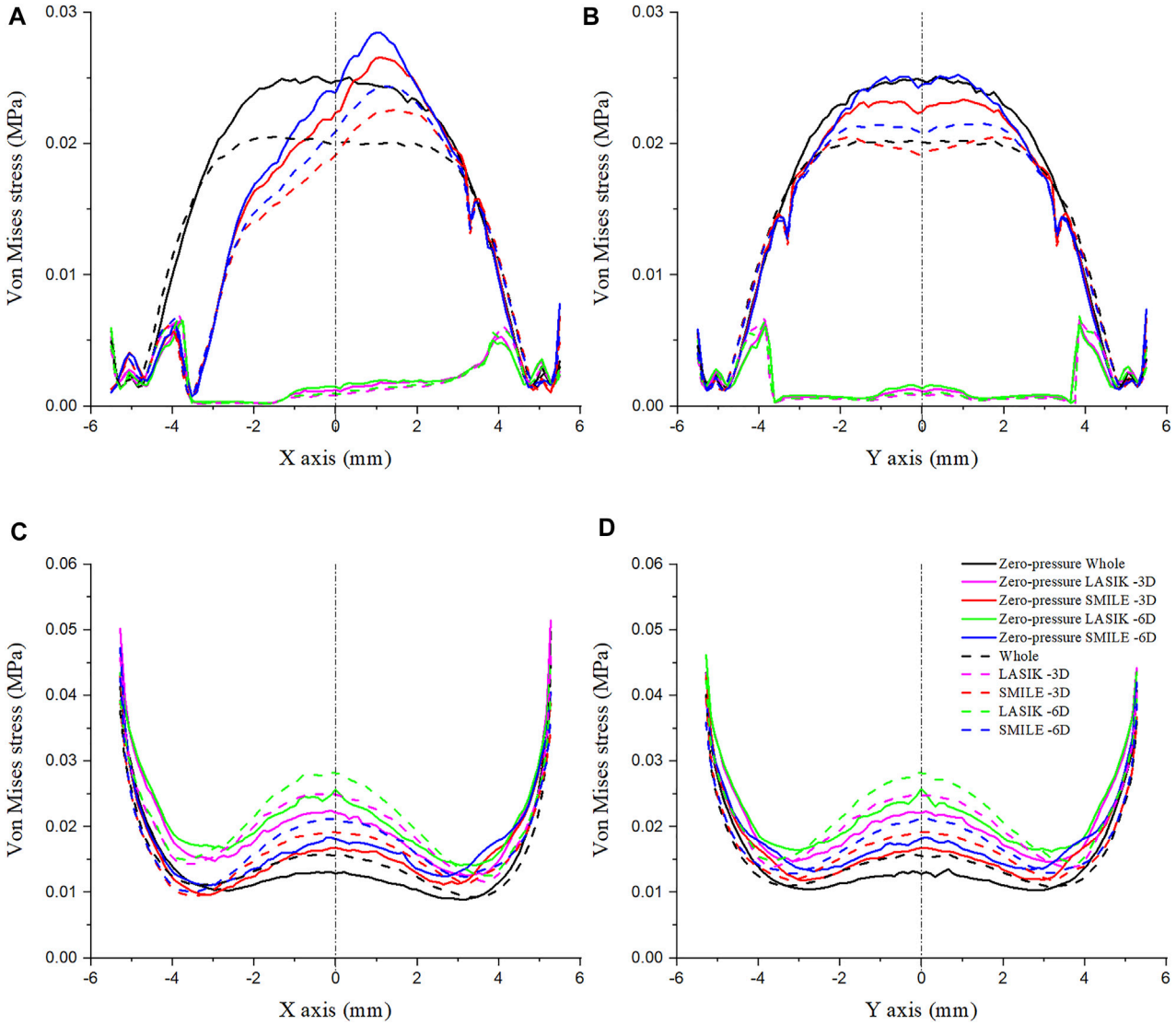

FIGURE 6 | Comparison of Von Mises stress on the cornea along the different paths. The IOP was constant at 19 mmHg. **(A)** Von Mises stress on the anterior corneal surface along the *x*-axis. **(B)** Von Mises stress on the anterior corneal surface along the *y*-axis. **(C)** Von Mises stress on the posterior corneal surface along the *x*-axis. **(D)** Von Mises stress on the posterior corneal surface along the *y*-axis.

surgery, especially in the corneal flap. For the zero-pressure LASIK model with -6D refractive surgery, the corneal vertex displacement on the anterior surface was 0.034 mm larger than that of the SMILE model.

Von Mises Stress on the Corneal Surface

The Von Mises stress along the *x*- and *y*-axes was investigated for LASIK and SMILE (myopic correction with -3D and -6D) in zero- and non-zero-pressure states, as shown in **Figure 6**. IOP was constant at 19 mmHg. The maximum Von Mises stress of LASIK was higher than that of SMILE. In addition, for the same refractive surgery, the vertex stress was higher at the anterior corneal surface in the zero-pressure model compared to the image-based model, while the opposite was observed for the posterior corneal surface.

The Von Mises stress along the *x*- and *y*-axes of the anterior corneal surface showed obvious differences (**Figures 6A**,**B**). The stress along the *y*-axes tended to be bilaterally symmetric, with the maximum stress almost at the center of the cornea; however, the stress along the *x*-axis was not bilaterally symmetric, which may be due to the position of the corneal flap/cap incision. Furthermore, the Von Mises stress along the same path on the posterior corneal surface in the LASIK model was obviously higher than that of the SMILE model (**Figures 6C**,**D**). The results also showed that the stress distribution on the posterior corneal surface was nearly symmetrical. Moreover, a comparison

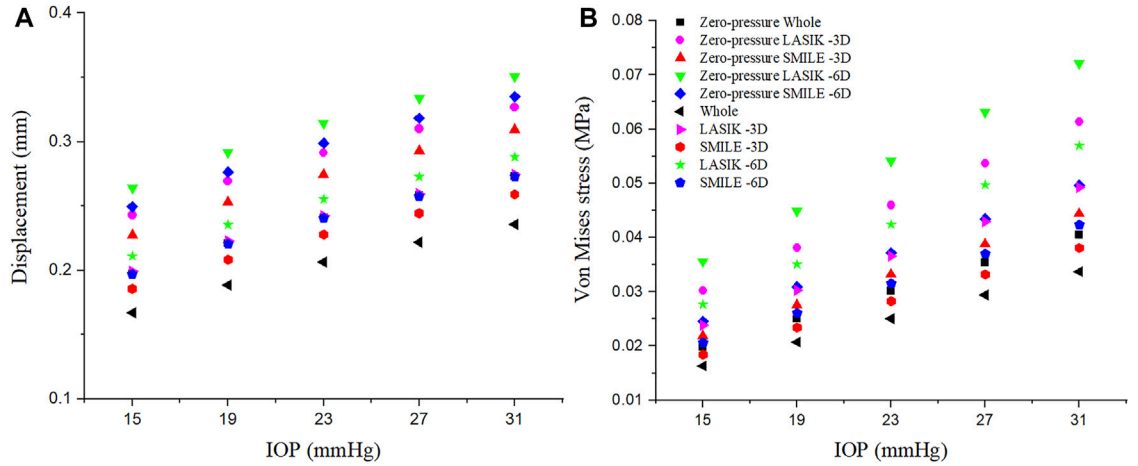

FIGURE 7 | Effects of the IOP on the displacement and Von Mises stress of the corneal residual stromal bed vertex. The IOP was set at 15 mmHg, 19 mmHg, 23 mmHg, 27 mmHg, and 31 mmHg, respectively. **(A)** Displacement. **(B)** Von Mises stress.

of these plots showed that the stress increased with the myopic refractive correction.

Effects of IOP on the Displacement and Von Mises Stress of the Cornea

The relationship between the displacement on the corneal residual stromal bed vertex and IOP is presented in **Figure 7A**. IOP was set to 15 mmHg, 19 mmHg, 23 mmHg, 27 mmHg, and 31 mmHg, respectively. There was an approximately linear relationship between corneal residual stromal bed vertex and IOP. In addition, under the same myopic correction, the displacement was greater in LASIK compared with SMILE (both zero-pressure and image-based model).

Similarly, the linear relationship between the Von Mises stress on the corneal residual stromal bed vertex and IOP could be seen in **Figure 7B**. When the IOP was constant, the Von Mises stress on the corneal residual stromal bed vertex of SMILE was smaller than that of LASIK (both zero-pressure and image-based model). Furthermore, it was obvious that considering the zero-pressure state of the cornea may lead to more deformation and stress.

Displacement Distributions on the Cornea

Displacement distributions through a cross-sectional view of the cornea are presented in **Figure 8**. In all simulations, the greater the myopic correction was, the greater was the displacement induced by the applied IOP. Furthermore, the displacement distributions were the difference between LASIK and SMILE (both zero-pressure and image-based models). In the LASIK model, the displacement was concentrated at the corneal flap. However, the displacement distributions in the SMILE model are nearly symmetrical. The location of the maximum displacement in the SMILE model was at the center of the corneal cap. Overall, for the same myopic correction, the value of displacement in the LASIK model was higher than that of the SMILE model.

DISCUSSION

Laser refractive surgery, through ablation of the stromal tissue and the curvature of the corneal anterior surface, induced changes in the corneal refractive power. LASIK and SMILE have been proven to treat myopia safely and effectively with high satisfaction (Shen et al., 2016). A better understanding of the biomechanical behaviors of the LASIK and SMILE procedure may provide valuable references for the clinician. In this study, the finite element method was used to evaluate the influence of LASIK and SMILE surgery on the corneal displacement and Von Mises stress.

In the present study, the geometrical model of the cornea was reconstructed based on data measurements from the Oculus Pentacam. Then, the LASIK and SMILE refractive surgery were simulated based on a personalized model. However, the finite element corneal model incorporated the initial pre-stress, which is due to physiological IOP. An iterative algorithm was applied to retrieve the zero-pressure configuration of the intact cornea, LASIK and SMILE model. The results showed that the initial corneal pre-stress stiffens the response of the cornea, both in the intact cornea and under refractive surgery. The displacements along the *x*- and *y*-axes were higher obtained with the zero-pressure model than that of the image-based model. Furthermore, results for the zero-pressure SMILE model showed higher Von Mises stress on the corneal cap; however, the maximum stress was still less than that of the image-based SMILE model.

The mechanical properties of the human cornea are closely related to the integrity of the structure. The creation of a corneal flap/cap has an impact on the biomechanical behavior of the cornea. In the LASIK refractive surgery, a corneal flap is created by mechanical microkeratomes or femtosecond laser (Sugar, 2002), only hinge on a small part. However, during the SMILE procedure, a small incision is performed, which is located superiorly or superotemporally. In the present study, the flap

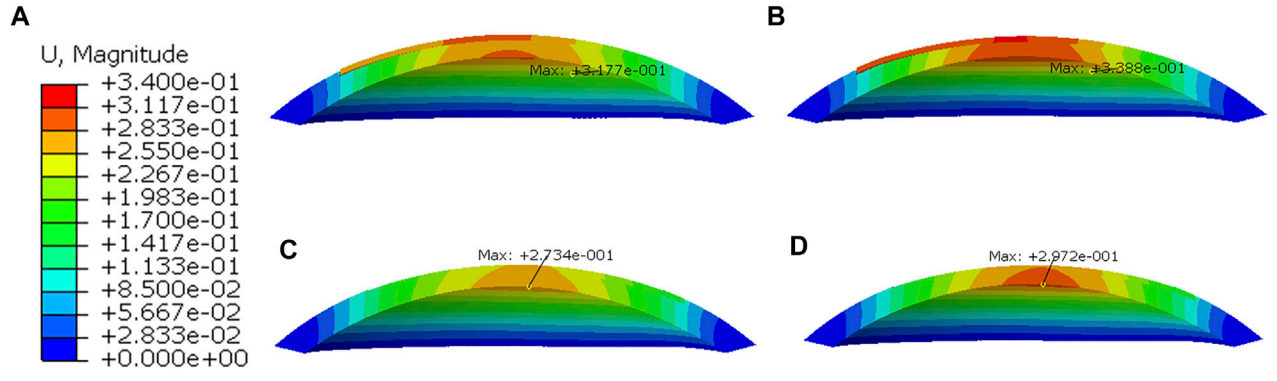

FIGURE 8 | Displacement distributions after applying IOP of 19 mmHg. **(A)** Zero-pressure LASIK with -3D correction, **(B)** Zero-pressure LASIK with -6D correction, **(C)** Zero-pressure SMILE with -3D correction, **(D)** Zero-pressure SMILE with -6D correction.

hinge in the LASIK model and small incision in the SMILE model were also taken into account. The results showed that the displacement of the corneal flap was obviously higher than that of the corneal cap. Randleman et al. also demonstrated that the corneal postoperative strength after SMILE would be greater than that of LASIK due to the intact of the anterior lamellae (Randleman et al., 2008). Lenticule creation and removal in the SMILE procedure were assumed to provide a greater corneal structural stability and ocular surface integrity, and thus the biomechanical strength (Santhiago and Wilson, 2012). SMILE refractive surgery, which is far less invasive than LASIK, with a reduced incidence of postoperative corneal complications (Shah et al., 2011). Moreover, for both LASIK and SMILE, the displacement on the anterior corneal surface was different along the *x*- and *y*-axes, which may be due to the location of the corneal incision. However, the displacement along the *x*- and *y*-axes on the posterior corneal surface was similar. It indicated that the position of the corneal incision has relatively little effect on the posterior corneal surface compared to the anterior corneal surface.

It is generally believed that a certain residual stromal bed thickness is required after ablation to prevent ectasia (Reinstein et al., 2013). Refractive surgery with different ablation depths would influence the thickness of the residual bed under the same flap/cap. Under the same pressure, displacement values measured in LASIK (both zero-pressure and image-based model) with -6D correction were much larger than the ones that were measured in the model with -3D correction. Similar results could be found in the SMILE model. More displacement may increase the risk of corneal ectasia. In addition, the Von Mises stress measured in the LASIK and SMILE model with -3D correction was smaller than those with -6D correction. For example, when the IOP was 19 mmHg, the maximum corneal vertex stress in the zero-pressure SMILE model was 0.031 MPa in a -6D correction, while it was 0.028 MPa in a -3D correction, an increase of 10.71%. The higher Von Mises stress may trigger corneal damage, especially the microstructural tissues of the cornea. Katzengold et al. also demonstrated that the thicker the residual stromal bed was, the lower was the stress occurring as a result of the same IOP (Katzengold et al., 2021).

Furthermore, the creation of a corneal flap/cap affects the stress values on the corneal anterior and posterior surface. In LASIK, the flap is largely decoupled from the anchoring boundary of the corneal stroma, and hence has little effect as a mechanical component of the cornea (Schmack et al., 2005). Consistently, results showed that the stress on the flap was lower than that of the corneal cap. In contrast, LASIK increased the stress on the posterior corneal surface compared with the SMILE model. It should be noted that when comparing the maximum stress value between the corneal cap and residual stromal bed, the value on the cap was lower. This can be attributed to the fact that the corneal cap in the SMILE model was almost intact, which can carry the load together with the residual stromal bed. The increase in myopic correction resulted in greater stress on the cornea in both models.

With the same refractive surgery and myopic correction, the displacement and Von Mises stress of the residual stromal bed vertex increased linearly with the IOP. Fang et al. also presented similar findings (Fang et al., 2020). The results indicated that the IOP had a direct influence on the residual stromal bed. This might be an important reason for the instability postoperative outcomes after the refractive surgery. In this study, the simulation also showed that refractive surgery can affect displacement distributions. In the LASIK model, displacement distributions were not symmetric, while the displacement in the SMILE model was symmetric. It may be beneficial to consider creating a corneal cap in the refractive surgery to provide a more complete structure of the cornea.

There were several limitations in this study. For comparison purposes, the anisotropic, hyperelastic material properties were adopted in this study. However, the properties of the cornea were complex in physiological situations. Anisotropic viscoelastic material properties should be considered in further study. Moreover, although the geometrical model of the cornea was constructed based on the measured data, the perturbation of the collagen fibers was not considered. The corneal model could be improved by adding randomly dispersed collagen fibers. Finally, the finite element results were not compared with real LASIK and SMILE surgical outcomes, and postoperative results related to flap/cap were not measured. In the future, postoperative outcomes related to the LASIK and SMILE surgeries will be investigated, and the biomechanical behavior of the refractive surgery will be further elaborated.

CONCLUSION

The present study evaluated biomechanical behaviors of the cornea after the LASIK and SMILE refractive surgery through a finite element method. The initial pre-stress of the cornea may stiffen the corneal response; therefore, the zero-pressure state of the cornea could not be ignored when considering the mechanical properties of refractive surgery. The corneal flap/cap could obviously change the biomechanical behaviors of the cornea. In this study, displacements of the SMILE model were obviously lower than those of the LASIK model under the same IOP. Moreover, the corneal cap may bear more load compared with the corneal flap. However, the maximum stress in the SMILE model was still smaller than that of the LASIK model. Overall, this study indicates that SMILE refractive surgery has advantages over the LASIK procedure in the aspect of corneal biomechanical stability.

DATA AVAILABILITY STATEMENT

The original contributions presented in the study are included in the article/Supplementary Material. Further inquiries can be directed to the corresponding authors.

ETHICS STATEMENT

The studies involving human participants were reviewed and approved by Ethics Committee of Taiyuan University of Technology. The patients/participants provided their written informed consent to participate in this study.

AUTHOR CONTRIBUTIONS

WC was responsible for performing the finite element analysis and drafting the work. XL, YG, and HG were responsible for revising the work. RH was responsible for designing the finite element analysis. CW was responsible for designing the study, interpreting the result, and revising the work. All authors provided final approval of the version to be published and agreed to be accountable for all aspects of the work.

FUNDING

This work was supported by the National Natural Science Foundation of China (Grant numbers 12072218, 11872262, 3180078, and 11802196) and the Natural Science Foundation of Shanxi Province (20210302123150).

REFERENCES

Agca, A., Ozgurhan, E. B., Demirok, A., Bozkurt, E., Celik, U., Ozkaya, A., et al. (2014). Comparison of Corneal Hysteresis and Corneal Resistance Factor after Small Incision Lenticule Extraction and Femtosecond Laser-Assisted LASIK: A Prospective Fellow Eye Study. *Contact Lens and Anterior Eye* 37, 77–80. doi:10.1016/j.clae.2013.05.003

Ang, M., Mehta, J. S., Rosman, M., Li, L., Koh, J. C. W., Htoon, H. M., et al. (2013). Visual Outcomes Comparison of 2 Femtosecond Laser Platforms for Laser *In Situ* Keratomileusis. *J. Cataract. Refr. Surg.* 39, 1647–1652. doi:10.1016/j.jcrs.2013.04.044

Ariza-Gracia, M. Á., Zurita, J. F., Piñero, D. P., Rodriguez-Matas, J. F., and Calvo, B. (2015). Coupled Biomechanical Response of the Cornea Assessed by Non-contact Tonometry. A Simulation Study. *Plos. One.* 10, e0121486. doi:10.1371/journal.pone.0121486

Ariza-Gracia, M. Á., Zurita, J., Piñero, D. P., Calvo, B., and Rodríguez-Matas, J. F. (2016). Automatized Patient-specific Methodology for Numerical Determination of Biomechanical Corneal Response. *Ann. Biomed. Eng.* 44, 1753–1772. doi:10.1007/s10439-015-1426-0

Bao, F., Wang, J., Cao, S., Liao, N., Shu, B., Zhao, Y., et al. (2018). Development and Clinical Verification of Numerical Simulation for Laser *In Situ* Keratomileusis. *J. Mech. Behav. Biomed. Mater.* 83, 126–134. doi:10.1016/j.jmbbm.2018.04.016

Fang, L., Wang, Y., Yang, R., Deng, S., Deng, J., and Wan, L. (2020). Effects of the LASIK Flap Thickness on Corneal Biomechanical Behavior: a Finite Element Analysis. *BMC. Ophthalmol.* 20, 67. doi:10.1186/s12886-020-01338-8

Farjo, A. A., Sugar, A., Schallhorn, S. C., Majmudar, P. A., Tanzer, D. J., Trattler, W. B., et al. (2013). Femtosecond Lasers for LASIK Flap Creation. *Ophthalmology* 120, e5–e20. doi:10.1016/j.ophtha.2012.08.013

Holden, B. A., Fricke, T. R., Wilson, D. A., Jong, M., Naidoo, K. S., Sankaridurg, P., et al. (2016). Global Prevalence of Myopia and High Myopia and Temporal Trends from 2000 through 2020. *Ophthalmology* 1-7.

Holzapfel, G. A., Gasser, T. C., and Ogden, R. W. (2000). A New Constitutive Framework for Arterial wall Mechanics and a Comparative Study of Material Models. *J. Elasticity.* 61, 1–48. doi:10.1023/a:1010835316564

Ivarsen, A., Asp, S., and Hjortdal, J. (2014). Safety and Complications of More Than 1500 Small-Incision Lenticule Extraction Procedures. *Ophthalmology* 121, 822–828. doi:10.1016/j.ophtha.2013.11.006

Jin, H.-Y., Wan, T., Yu, X.-N., Wu, F., and Yao, K. (2018). Corneal Higher-Order Aberrations of the Anterior Surface, Posterior Surface, and Total Cornea after Small Incision Lenticule Extraction (SMILE): High Myopia versus Mild to Moderate Myopia. *BMC. Ophthalmol.* 18, 295. doi:10.1186/s12886-018-0965-1

Katzengold, R., Gefen, A., Sorkin, N., Smadja, D., and Varssano, D. (2021). Simulation of the Biomechanical Effects Induced by Laser *In Situ* Keratomileusis (LASIK) for Different Levels of Ablation in normal Corneas. *Eye* 35, 996–1001. doi:10.1038/s41433-020-1017-7

Li, T., Wan, T., Yao, X., Qi, H., Chen, X., She, M., et al. (2021). Time Trend of Axial Length and Associated Factors in 4- and 5-Year-Old Children in Shanghai from 2013 to 2019. *Int. Ophthalmol.* 41, 835–843. doi:10.1007/s10792-020-01637-5

Lin, F., Xu, Y., and Yang, Y. (2014). Comparison of the Visual Results after SMILE and Femtosecond Laser-Assisted LASIK for Myopia. *J. Refract. Surg.* 30, 248–254. doi:10.3928/1081597x-20140320-03

Morgan, I. G., French, A. N., Ashby, R. S., Guo, X., Ding, X., He, M., et al. (2018). The Epidemics of Myopia: Aetiology and Prevention. *Prog. Retin. Eye Res.* 62, 134–149. doi:10.1016/j.preteyeres.2017.09.004

Moshirfar, M., McCaughey, M. V., Reinstein, D. Z., Shah, R., Santiago-Caban, L., and Fenzl, C. R. (2015). Small-incision Lenticule Extraction. *J. Cataract. Refr. Surg.* 41, 652–665. doi:10.1016/j.jcrs.2015.02.006

Munnerlyn, C. R., Koons, S. J., and Marshall, J. (1988). Photorefractive Keratectomy: a Technique for Laser Refractive Surgery. *J. Cataract. Refr. Surg.* 14, 46–52. doi:10.1016/s0886-3350(88)80063-4

Nguyen, T. D., and Boyce, B. L. (2011). An Inverse Finite Element Method for Determining the Anisotropic Properties of the Cornea. *Biomech. Model. Mechanobiol* 10, 323–337. doi:10.1007/s10237-010-0237-3

Nordan, L. T., Slade, S. G., Baker, R. N., Suarez, C., Juhasz, T., and Kurtz, R. (2003). Femtosecond Laser Flap Creation for Laser *In Situ* Keratomileusis: Six-Month Follow-Up of Initial U.S. Clinical Series. *J. Refract. Surg.* 19, 8–9. doi:10.3928/1081-597x-20030101-03

Pandolfi, A., and Manganiello, F. (2006). A Model for the Human Cornea: Constitutive Formulation and Numerical Analysis. *Biomech. Model. Mechanobiol* 5, 237–246. doi:10.1007/s10237-005-0014-x

Randleman, J. B., Dawson, D. G., Grossniklaus, H. E., McCarey, B. E., and Edelhauser, H. F. (2008). Depth-dependent Cohesive Tensile Strength in Human Donor Corneas: Implications for Refractive Surgery. *J. Refract. Surg.* 24, S85–S89. doi:10.3928/1081597X-20080101-15

Reinstein, D. Z., Archer, T. J., and Randleman, J. B. (2013). Mathematical Model to Compare the Relative Tensile Strength of the Cornea after PRK, LASIK, and Small Incision Lenticule Extraction. *J. Refract. Surg.* 29, 454–460. doi:10.3928/1081597x-20130617-03

Roberts, C. (2000). The Cornea Is Not a Piece of Plastic. *J. Refract. Surg.* 16, 407–413. doi:10.3928/1081-597x-20000701-03

Roy, A. S., and Dupps, W. J. (2009). Effects of Altered Corneal Stiffness on Native and Postoperative LASIK Corneal Biomechanical Behavior: a Whole-Eye Finite Element Analysis. *J. Refract. Surg.* 25, 875–887. doi:10.3928/1081597x-20090917-09

Roy, A. S., Dupps, W. J., Jr, and Roberts, C. J. (2014). Comparison of Biomechanical Effects of Small-Incision Lenticule Extraction and Laser *In Situ* Keratomileusis: Finite-Element Analysis. *J. Cataract. Refr. Surg.* 40, 971–980. doi:10.1016/j.jcrs.2013.08.065

Santhiago, M. R., and Wilson, S. E. (2012). Cellular Effects after Laser *In Situ* Keratomileusis Flap Formation with Femtosecond Lasers: a Review. *Cornea* 31, 198–205. doi:10.1097/ico.0b013e3182068c42

Schmack, I., Dawson, D. G., McCarey, B. E., Waring, G. O., Grossniklaus, H. E., and Edelhauser, H. F. (2005). Cohesive Tensile Strength of Human LASIK Wounds with Histologic, Ultrastructural, and Clinical Correlations. *J. Refract. Surg.* 21, 433–445. doi:10.3928/1081-597x-20050901-04

Sekundo, W., Kunert, K. S., and Blum, M. (2011). Small Incision Corneal Refractive Surgery Using the Small Incision Lenticule Extraction (SMILE) Procedure for the Correction of Myopia and Myopic Astigmatism: Results of a 6 Month Prospective Study. *Br. J. Ophthalmol.* 95, 335–339. doi:10.1136/bjo.2009.174284

Shah, R., Shah, S., and Sengupta, S. (2011). Results of Small Incision Lenticule Extraction: All-In-One Femtosecond Laser Refractive Surgery. *J. Cataract. Refr. Surg.* 37, 127–137. doi:10.1016/j.jcrs.2010.07.033

Shen, Z., Shi, K., Yu, Y., Yu, X., Lin, Y., and Yao, K. (2016). Small Incision Lenticule Extraction (SMILE) versus Femtosecond Laser-Assisted *In Situ* Keratomileusis (FS-LASIK) for Myopia: a Systematic Review and Meta-Analysis. *Plos. One.* 11, e0158176. doi:10.1371/journal.pone.0158176

Simonini, I., and Pandolfi, A. (2015). Customized Finite Element Modelling of the Human Cornea. *Plos. One.* 10, e0130426. doi:10.1371/journal.pone.0130426

Sugar, A. (2002). Ultrafast (Femtosecond) Laser Refractive Surgery. *Curr. Opin. Ophthalmol.* 13, 246–249. doi:10.1097/00055735-200208000-00011

Vestergaard, A., Ivarsen, A., Asp, S., and Hjortdal, J. Ø. (2013). Femtosecond (FS) Laser Vision Correction Procedure for Moderate to High Myopia: a Prospective Study of ReLExflex and Comparison with a Retrospective Study of FS-Laserin Situkeratomileusis. *Acta Ophthalmol.* 91, 355–362. doi:10.1111/j.1755-3768.2012.02406.x

Wu, W., and Wang, Y. (2016). Corneal Higher-Order Aberrations of the Anterior Surface, Posterior Surface, and Total Cornea after SMILE, FS-LASIK, and FLEx Surgeries. *Eye Contact Lens.* 42, 358–365. doi:10.1097/icl.0000000000000225

Zhang, J., Wang, Y., Wu, W., Xu, L., Li, X., and Dou, R. (2015). Vector Analysis of Low to Moderate Astigmatism with Small Incision Lenticule Extraction (SMILE): Results of a 1-year Follow-Up. *BMC. Ophthalmol.* 15, 8. doi:10.1186/1471-2415-15-8

Conflict of Interest: The authors declare that the research was conducted in the absence of any commercial or financial relationships that could be construed as a potential conflict of interest.

Publisher's Note: All claims expressed in this article are solely those of the authors and do not necessarily represent those of their affiliated organizations, or those of the publisher, the editors, and the reviewers. Any product that may be evaluated in this article, or claim that may be made by its manufacturer, is not guaranteed or endorsed by the publisher.

frontiers | Frontiers in Bioengineering and Biotechnology

ORIGINAL RESEARCH
published: 13 April 2022
doi: 10.3389/fbioe.2022.862947

Determine Corneal Biomechanical Parameters by Finite Element Simulation and Parametric Analysis Based on ORA Measurements

Xiao Qin[1,2†], Lei Tian[3,4†], Hui Zhang[1], Di Zhang[1], Ying Jie[3], Hai-Xia Zhang[1]* and Lin Li[1]**

[1]Beijing Key Laboratory of Fundamental Research on Biomechanics in Clinical Application, School of Biomedical Engineering, Capital Medical University, Beijing, China, [2]Medical Science Research Center, Department of Otolaryngology, Peking Union Medical College Hospital, Shuaifuyuan 1, Dongcheng District, Beijing, China, [3]Beijing Institute of Ophthalmology, Beijing Tongren Eye Center, Beijing Tongren Hospital, Capital Medical University, Beijing Ophthalmology & Visual Sciences Key Laboratory, Beijing, China, [4]Beijing Advanced Innovation Center for Big Data-Based Precision Medicine, Beihang University and Capital Medical University, Beijing Tongren Hospital, Beijing, China*

OPEN ACCESS

Edited by:
Weiyi Chen,
Taiyuan University of Technology, China

Reviewed by:
Fulvio Ratto,
National Research Council (CNR), Italy
Junjie Wang,
Wenzhou Medical University, China

***Correspondence:**
Ying Jie
jie_yingcn@aliyun.com
Hai-Xia Zhang
zhanghx@ccmu.edu.cn
Lin Li
lil@ccmu.edu.cn

†These authors have contributed equally to this work and share first authorship

Specialty section:
This article was submitted to Biomechanics, a section of the journal Frontiers in Bioengineering and Biotechnology

Received: 26 January 2022
Accepted: 23 March 2022
Published: 13 April 2022

Citation:
Qin X, Tian L, Zhang H, Zhang D, Jie Y, Zhang H-X and Li L (2022) Determine Corneal Biomechanical Parameters by Finite Element Simulation and Parametric Analysis Based on ORA Measurements. Front. Bioeng. Biotechnol. 10:862947. doi: 10.3389/fbioe.2022.862947

Purpose: The Ocular Response Analyzer (ORA) is one of the most commonly used devices to measure corneal biomechanics *in vivo*. Until now, the relationship between the output parameters and corneal typical biomechanical parameters was not clear. Hence, we defined the output parameters of ORA as ORA output parameters. This study aims to propose a method to determine corneal biomechanical parameters based on ORA measurements by finite element simulation and parametric analysis.

Methods: Finite element analysis was used to simulate the mechanics process of ORA measurements with different intraocular pressure (IOP), corneal geometrical parameters and corneal biomechanical parameters. A simplified geometrical optics model was built to simulate the optical process of the measurements to extract ORA output parameters. After that, 70% of the simulated data was used to establish the quantitative relationship between corneal biomechanical parameters and ORA output parameters by parametric analysis and 30% of the simulated data was used to validate the established model. Besides, ten normal subjects were included to evaluate the normal range of corneal biomechanical parameters calculated from ORA.

Results: The quantitative relationship between corneal biomechanical parameters and ORA output parameters is established by combining parametric analysis with finite element simulation. The elastic modulus (E) and relaxation limit (G_∞) of the ten normal subjects were 0.65 ± 0.07 MPa and 0.26 ± 0.15, respectively.

Conclusions: A method was proposed to determine corneal biomechanical parameters based on the results of ORA measurements. The magnitude of the corneal biomechanical parameters calculated according to our method was reasonable.

Keywords: ocular response analyzer (ORA), finite element simulation, parametric analysis, corneal biomechanical parameters, ORA output parameters

INTRODUCTION

The cornea is one of the most important refractive media of the eyeball providing 70% ocular refractive power (Hjortdal and Jensen, 1995). The maintenance of corneal refractive function depends on the normal corneal geometry. Abnormal corneal geometry is usually closely related to its biomechanical characteristics (Viswanathan et al., 2015). Therefore, studying corneal biomechanical properties *in vivo* has great significance in diagnosing corneal disease such as keratoconus (Scarcelli et al., 2015; Vellara and Patel, 2015; Elham et al., 2017), individualized surgical design, such as corneal refractive correction (Wang B. et al., 2016; Yildirim et al., 2016; Hwang et al., 2017; Zhang et al., 2017) and corneal cross-linking surgery (Steinberg et al., 2014; Matteoli et al., 2016; Subasinghe et al., 2018).

Ocular Response Analyzer (ORA) and Corneal Visualization Scheimpflug Technology (Corvis ST) are two of the most commonly used devices to evaluate corneal biomechanics in clinic. Both of these two devices assess corneal biomechanical properties based on corneal response under rapid air-puff. Parameters provided by these devices are valuable in diagnosing preliminarily keratoconus (Ayar et al., 2015; Elham et al., 2017; Atalay et al., 2019; Koc et al., 2019). Parameters of these two devices doe not only relate to corneal biomechanics but are also influenced by corneal geometrical parameters and intraocular pressure (IOP) (Wang L.-K. et al., 2016; Vinciguerra et al., 2016; Wu et al., 2016; Nemeth et al., 2017; Herber et al., 2019). The limitation of ORA and Corvis ST in clinical applications make it difficult for researchers to obtain corneal biomechanical parameters to diagnose ocular diseases and evaluate corneal treatment effects. Biomechanically speaking, the morphology of the cornea under the external load depends on its biomechanical properties (Mercatelli et al., 2019), which in turn relies on the inherent properties of corneal tissue. Within the range of the physiological IOP, the cornea is likely a linear elastic and viscoelastic tissue (Zhang et al., 2017; Zhang et al., 2018a; Zhang et al., 2018b), and the corneal biomechanical properties can be determined by the corneal elastic modulus (E) and corneal relaxation parameters. We call these parameters "corneal biomechanical parameters". If the corneal biomechanical parameters can be obtained from these *in vivo* measurements directly, the ORA and Corvis can be used in basic and clinical research more conveniently.

At present, the biomechanical interpretations of ORA output parameters and dynamic corneal response paremeters (DCRs) from Corvis ST have not reached a consensus. Alternatively, appropriate and effective methods to determine corneal biomechanical parameters based on the results of ORA/Corvis ST measurements need to be further explored and verified.

The researchers have explored the mechanical significance of ORA output parameters and DCRs through the following methods: a. analyzing the influencing factors of ORA output parameters and DCRs by *ex vivo* eye globe tests (Bao et al., 2015; Zheng et al., 2016); b. suggesting the correlation between ORA output parameters, DCRs and corneal biomechanical parameters (Glass et al., 2008; Han et al., 2014) based on an ideal simplified model or simulating the process of corneal air-puff test by finite element analysis (Elsheikh et al., 2015); and c. providing new corneal biomechanics-related parameters based on corneal air-puff test (Wang L.-K. et al., 2016; Roberts et al., 2017; Shih et al., 2017; Eliasy et al., 2019). In previous studies, we suggested a method to explore the mechanical interpretation of output parameters of ORA (Qin et al., 2019b) and proposed a method to determine corneal elastic modulus based on Corvis measurements (Qin et al., 2019a). However, an effective method to obtain corneal biomechanical parameters directly from ORA output parameters is still lacking. To this end, the present study proposes a method to determine corneal typical biomechanical parameters from ORA measurements.

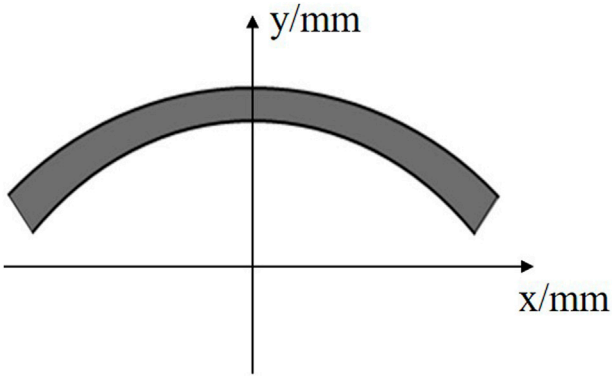

FIGURE 1 | The ideal ellipsoidal axisymmetric corneal geometrical model.

Actually, it is very sophisticated and difficult to establish a theoretical formula. It is expensive and impractical to establish this relationship based on a large number of ORA measurements and biomechanical tests of the cornea *in vitro*. A feasible and economical way is finite element simulation with the advantage of calculating various loading conditions with the same model. Finite element analysis is used increasingly in the field of corneal biomechanics research (Elsheikh et al., 2011; Kling et al., 2014; Elsheikh et al., 2015; Lago et al., 2015; Sinha Roy et al., 2015; Jannesari et al., 2019). In this study, finite element analysis was used to simulate the corneal response with different corneal biomechanical parameters, corneal geometrical parameters and intraocular pressures (IOP). Additionally, parametric analysis was applied to establish the relationship between ORA output parameters and corneal biomechanical parameters based on a geometrical optics model that computes the ORA output parameters from finite element calculation results. Besides, ten normal subjects were included to evaluate the normal range of corneal biomechanical parameters calculated from ORA.

METHODS

Finite Element Simulation of ORA Measurements

A large number of research results show that both the corneal anterior and posterior surfaces can be described with an elliptic

equation (Zhang et al., 2006; Elsheikh, 2010). Therefore, in this study we established an ellipsoidal axisymmetric corneal geometrical model (**Figure 1**) to carry out dynamic finite element analysis of ORA measurements. The corneal anterior and posterior surfaces can be described as **Equation 1** and **2**, respectively.

$$\frac{x^2}{R^2/p} + \frac{y^2}{R^2/p^2} = 1 \quad (1)$$

$$\frac{x^2}{a^2} + \frac{y^2}{(R/p - CCT)^2} = 1 \quad (2)$$

In **Eqs. 1**, **2**, R was the corneal central curvature radius, CCT was the central corneal thickness, p was the ellipse shape factor of the corneal anterior surface. Set x to be R_0 in **Eqn. 1** we can get the coordinates (R_0, y_0) of anterior corneal limbus. Substitute (R_0, y_0-PCT) into **Eqn. 2** we can get a in **Eqn. 2**. R_0 was the X coordinate of corneal limbus, PCT was the thickness of corneal thickness which was set to be 100 μm larger than CCT (Dubbelman, et al., 2009; Elsheikh, et al., 2011; HirjiLarke, 1978).

In the finite element model, the cornea was hypothesized to be linear elastic and viscoelastic material. Corneal elastic modulus (E) and Poisson's ratio (ν = 0.49) were used to characterize the corneal linear elastic properties. Third-order Prony model (**Eqn. 3**) was used to characterize the corneal viscoelastic properties (Qin et al., 2019b). In **Eqn. 3**, a_1, a_2, a_3, τ_1, τ_2, τ_3 are corneal viscoelastic parameters, *G was the normalized stress during stress relaxation experiment*. As corneal topography is measured at a specific intraocular pressure IOP and is distinct from the unloaded shape that would be obtained at an IOP of 0 mm Hg, the undeformed state was solved by a custom finite element model at first. Air-puff force was applied on corneal apex as a 25 ms surface traction with temporal (**Eqn. 4**) and spatial (**Eqn. 5**) normal distribution. **Eqn. 4** was obtained by fitting the force-time curve, and **Eqn. 5** was obtained by fitting the curve provided by Ref (Elsheikh, 2010). x was the distance from the node on the cornea to the corneal symmetry axis. The displacements of limbus are constrained. Cornea was meshed with C3D8R mesh and explicit dynamic analysis was used to simulate the measurements. The finite element analysis was conducted on ABAQUS/Explicit. The variation of corneal anterior surface coordinate along the air-puff force during the measurements was extracted.

$$G(t) = 1 - a_1\left(1 - e^{-t/\tau_1}\right) - a_2\left(1 - e^{-t/\tau_2}\right) - a_3\left(1 - e^{-t/\tau_3}\right) \quad (3)$$

$$f(t) = e^{-\left(\frac{t(s)-0.0121(s)}{0.0057(s)}\right)^2} (\mathrm{mN}) \quad (4)$$

$$f(x) = e^{-\left(\frac{x(mm)}{0.741(mm)}\right)^2} (\mathrm{mN}) + 0.020(\mathrm{mN}) \quad (5)$$

Geometrical Optics Simulation of ORA Measurements

According to the principle of ORA measurement, we constructed the ideal geometrical optics model shown in **Figure 2**.

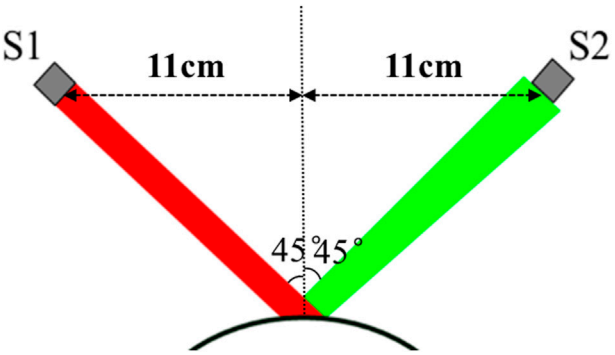

FIGURE 2 | Geometrical optics model of ORA measurement. S1 is a transmitter and S2 is a receiver with a diameter of 3 mm S1 and S2 were on the plane 11 cm away from the corneal apex. The incident angle is 45°. The incident light was reflected by corneal anterior surface and part of the light is received by the receiver S2.

Transmitter S1 and a receiver S2 are on the plane 11 cm away from the corneal apex. The distances between S1 and corneal apex, S2 and corneal apex were both $11\sqrt{2}$ cm. The transmitter emits a parallel incident light (3,000 incident light rays) with a diameter of 3 mm and the incident angle is 45°. The light is reflected by the anterior corneal surface; part of the light is received by the receiver S2 with a diameter of 3 mm. Diffuse reflection from the rough corneal surface and corneal refraction were ignored. Due to the variation of corneal apical position and corneal shape during ORA measurements, the reflected light changes accordingly. According to the ratio of the number of light rays received by the receiver to the total number of incident light rays, we get the normalized light intensity. After that we can obtain the normalized corneal applanation curve which was defined as the variation of the normalized light intensity with time (**Figure 3**). Based on the normalized corneal applanation curve we can extract the two applanation times t_1, t_2 and the two peak widths w_1 and w_2. And the two applanation pressures p_1 and p_2 can be calculated according to **Eqn. 4**. w_1, w_2, p_1 and p_2 were used as ORA output parameters in the subsequent parametric analysis.

Determining Corneal Biomechanical Parameters by Parametric Analysis

Corneal central curvature radius (R), central corneal thickness (CCT) and intraocular pressure (IOP) are important factors affecting ORA measurement results. Therefore, in this study, we set the R, CCT, IOP to be ranged in 6–8 mm, 450–650 μm, 10–30 mmHg, respectively. The corneal biomechanical parameters were mostly reported by biomechanical experiments *in vitro*, such as corneal tensile tests or corneal expansion test. Compared to these *in vitro* experiments, an ORA test was completed within 30 ms, which made there be significant differences between uniaxial tensile test and ORA test in loading mode and magnitude. Corneal non-linear elastic and viscoelastic properties suggest that we adjust the range of corneal biomechanical parameters to make the simulation results

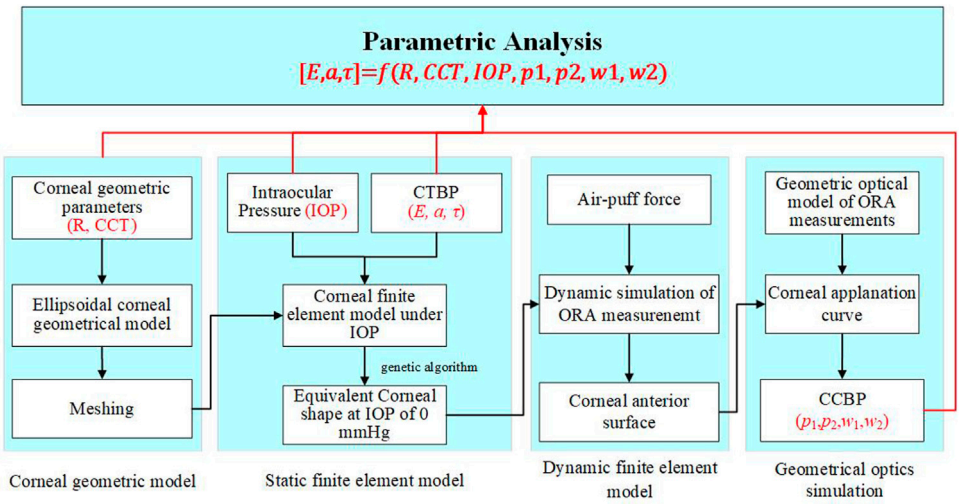

FIGURE 3 | The method to determine corneal biomechanical parameters based on ORA measurement.

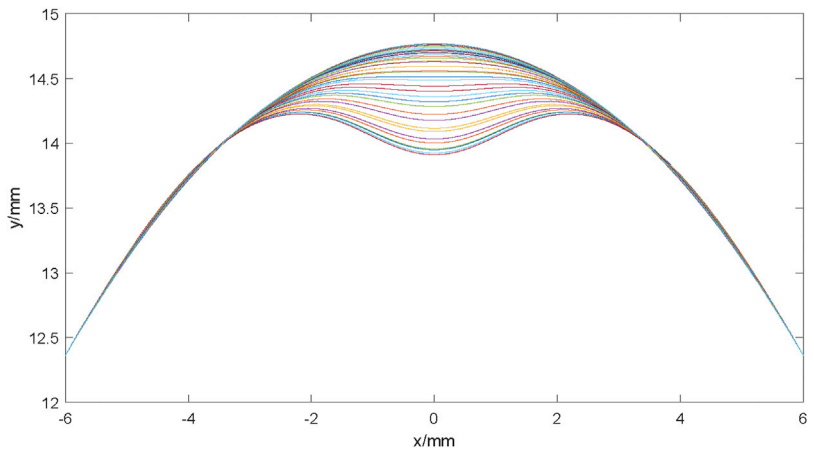

FIGURE 4 | The corneal anterior surface contour at different times during ORA measurements. The cornea gradually deforms from the initial state to the first applanation state, and then to the concave state during the 25 ms measurement. With the air puff pressure removed gradually, the cornea deformed to the initial state gradually.

consistent with the experimental results. Our previous study (Qin et al., 2019b) found that the simulated Corneal Hysteresis (CH) and Corneal Resistance Factor (CRF) have a similar amplitude with the experimental results when we set the corneal elastic (E) to be 1/3 of corneal physiological elastic modulus obtained from the uniaxial tensile test and set the parameters τ_1, τ_2 and τ_3 of third-order Prony series to be 1/10 of the uniaxial tensile test results. According to the reported range of corneal biomechanical parameters, the corneal elastic modulus was varied in the range of 0.2–0.6 MPa (Elsheikh et al., 2008; Shih et al., 2017; Wang et al., 2017; Qin et al., 2019b), a_1 and τ_1 of the third-order Prony series varied in the range of 0.25–0.6 and 0.001–0.1 s, respectively, when we carried out parametric analysis. a_2 and a_3 were set to be 0.1. τ_2, τ_3 were set to be 0.0001 s (Yang et al., 1999).

The flowchart to determine corneal biomechanical parameters based on ORA measurement is shown in **Figure 4**. For any a given set of parameters R, CCT, IOP, E, a_1 and τ_1, the finite element analysis was used to simulate the corneal response to an air-puff. The normalized corneal applanation curve was obtained by geometrical optic simulation. According to our previous studies and the reported results, the first applanation time (t_1), the second applanation time (t_2), the width at the 50% height of the peak of the first peak (w_1) and second peak (w_2) can reflect corneal biomechanical properties. Therefore, in this study, these four parameters were recorded as ORA output parameters for parametrical analysis.

The produce started with a generation of a random matrix of 2000 × 6 with MATLAB, representing 2,000 times input for 6 parameters (R, CCT, IOP, E, a_1 and τ_1) with uniform distribution

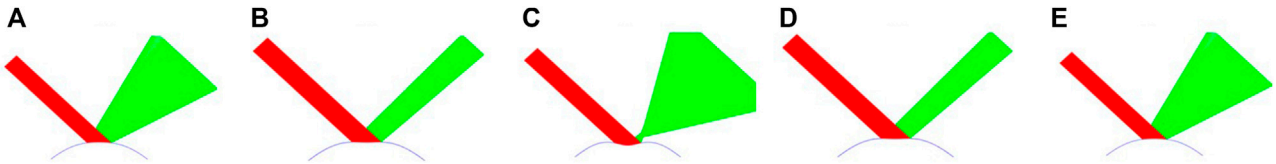

FIGURE 5 | Optical paths at different times during ORA measurements. **(A)** initial state; **(B)** the first applanation state; **(C)** the maximum indentation state; **(D)** the second applanation state; **(E)** the end state.

in the range of each parameter (shown above). After that, the geometric model of the cornea was constructed, followed a start-up of ABAQUS to fulfill the calculation automatically. The relationship model between corneal biomechanical parameters and ORA output parameters, corneal geometric parameters and IOP was established by multiple quadratic regression model. We took 70% of the data randomly to train the model and the other 30% data were used to verify the established model.

Subjects and Measurements

Ten healthy subjects (10 eyes) were included in this study. The age of subjects was between 20 and 25 years old. No subject had any eye diseases, history of corneal or eye surgery and systemic diseases affecting their eye functions. All subjects took off soft contact lenses or hard contact lenses at least 1 month before the examination. For each subject, one eye was selected randomly and included in the study. All subjects were informed the consent and had signed the informed consent form before the examination. The informed consent form was in compliance with the tenets of the Declaration of Helsinki. This study was approved by the institutional review board of the Beijing Tongren Hospital, Beijing Institute of Ophthalmology, Beijing, China.

Since the ORA test did not provide corneal geometrical parameters such as CCT and R, this study conducted three ORA tests and one Corvis test for all subjects. All ORA and Corvis measurements were performed by the same technician. During the ORA test, any measurement result with a waveform score (WS) exceeding 3.5 was included. The Corvis test result was included when the reading of "alignment" was "OK". Otherwise, the measurements were repeated until the reading was "OK". The edge of the first undeformed corneal image obtained by Corvis test is extracted to obtain the CCT and R (Qin et al., 2019a), and the corneal biomechanical corrected IOP (bIOP) was read from the Corvis test results for the subsequent calculating of corneal biomechanical parameters.

RESULTS

From the output database of the finite element simulation model of ORA measurements, we obtained the coordinate files of the anterior corneal surface at different times. The profile of the anterior corneal surface at different times during ORA measurements was drawn by using the file reading and writing function, as well as the drawing function of MATLAB for the subsequent geometrical optical simulation. The results are shown in **Figure 5**.

The results of the geometrical optical simulation are shown in **Figure 6**. Due to the variation of the corneal apical position and the corneal shape during ORA measurements, the reflected light changes accordingly. **Figure 6** (a–f) represents the typical optical path at different times during ORA measurements.

According to the ratio of the number of light rays received by the receiver to the total number of incident light rays during the ORA test (**Figure 6**), the normalized corneal applanation curve was obtained (**Figure 3**). The two applanation times t_1 and t_2 and the two peak widths w_1 and w_2 can be extracted from the normalized corneal applanation curve. The two applanation pressures p_1 and p_2 can be calculated according to **Eqn. 4**.

Figures 7A–D shows the variation of the simulated ORA output parameters with corneal biomechanical parameters, CCT, R and IOP. In **Figure 7**, the vertical axis shows the simulated ORA output parameters while the horizontal axes represent the independent variables. The green solid curves simulate the variation of the average simulated ORA output parameters with one independent variable when other parameters were set to the value in the small boxes below. (i.e., the green curve in the first plot in **Figure 7A** represented the variation of the simulated w1 with E, when the a1, lgτ1, R, CCT, IOP were set to be 0.4, −2.5, 7.0 mm, 550 μm, 20 mm Hg, respectively). The red dotted curves are the ranges of the simulated ORA output parameters. Results shown in **Figure 7** suggest that w_2, p_1 and p_2 are positively correlated with the corneal elastic modulus (E) while w_1, w_2, and p_1 are significantly positively correlated with a_1. Furthermore, w_1, w_2 are likely significantly positively correlated with τ_1. Also, p_2 and a_1, τ_1, IOP have a parabolic relationship, while w_2 are positively and p_1 negatively correlated with IOP. The correlations between other parameters were not significant.

The relationship model based on the 70% of the simulated data was established by multiple quadratic regression model. The results are shown in **Eqs. 6—8**. In the equations, we take the mean value of each parameter (E_0 = 0.4 MPa, τ_{10} = 0.001 s, R_0 = 7 mm, IOP_0 = 15 mmHg, w_{10} = 10, w_{20} = 17, p_{10} = 10 mmHg, p_{20} = 5 mmHg) to make the parameters dimensionless.

$$E = 2.500E_0\left[\begin{array}{c}0.323 - 0.030\,\mathrm{R}/\mathrm{R}_0 - 0.018\,\mathrm{IOP}/\mathrm{IOP}_0 - 0.034w_1/w_{10}\\ -0.078w_2/w_{20} + 0.230p_2/p_{20}\end{array}\right] \tag{6}$$

$$a_1 = 0.298 - 0.055\,\mathrm{R}/\mathrm{R}_0 - 0.104\mathrm{IOP}/\mathrm{IOP}_0 - 0.679w_1/w_{10} + 0.330w_2/w_{20} + 0.536p_1/p_{10} - 0.380p_2/p_{20} + 0.330\left(w_1/w_{10}\right)^2 + 0.075\left(p_2/p_{20}\right)^2 \tag{7}$$

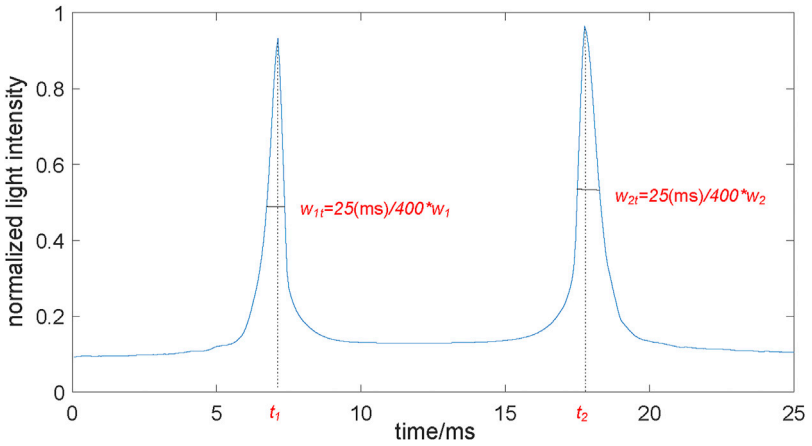

FIGURE 6 | The normalized corneal applanation curve. The normalized lighted intensity was the ratio of the number of light rays received by the receiver to the total number of incident light rays. When the cornea reached the applanation during the load and unload state, the curve reaches at a peak, respectively. t_1, t_2, were the two applanation time. w_{1t}, w_{2t} were the two peak widths, which were proportional to $w1$, $w2$ of the ORA output.

$$\lg(\tau_1/\tau_{10}) = -5.419 + 0.017\,\mathrm{R}/\mathrm{R}_0 - 0.033\,\mathrm{CCT}/\mathrm{CCT}_0 - 0.013 w_1/w_{10} + 0.140 w_2/w_{20} - 0.086 p_1/p_{10} - 0.165 p_2/p_{20} \quad (8)$$

Figure 8 shows the results of the comparison between the predicted value of corneal biomechanical parameters calculated according to **Eqs. 6–8** and the set corneal biomechanical parameters using the remaining 30% data. The results show that there was good consistency for the corneal elastic modulus E, corneal viscoelastic parameter a_1, τ_1 between the predicted value and the true value. This indicates that the multiple regression model might be enough to describe the relationship between corneal biomechanical parameters and ORA output parameters.

For the ten healthy subjects, the CCT, R, and corneal biomechanics corrected intraocular pressure (bIOP) were 526.1 ± 31.1 μm, 7.77 ± 0.47 mm and 18.7 ± 2.4 mmHg, respectively. For each one, t_1, t_2, w_1 and w_2 were extracted from the ORA database. The p_1, p_2 were calculated from t_1, t_2 according to **Eqn. 4**. The average of the three ORA measurement results was used to calculate the corneal biomechanical parameters The ORA test results are shown in **Table 1**, which also provides the results of corneal biomechanical parameters calculated according to **Eqs. 6–8**. We can see that the a_1 of normal subjects were 0.54 ± 0.15, as the a_2 and a_3 were set to 0.1 in the third-order Prony series. The relaxation limit (G_∞ = 1-a_1-a_2-a_3) of the normal subjects were 0.26 ± 0.15. The magnitude of E and G_∞ were basically consistent with the results of corneal uniaxial tensile test (Elsheikh et al., 2008; Wang et al., 2017).

DISCUSSION

In this study, the dynamic finite element simulation and geometric optical simulation of the ORA measurement process with different geometric parameters (CCT and R), intraocular pressure (IOP) and corneal biomechanical parameters (E, a_1 τ_1) were carried out to obtain ORA output parameters. Through a parametric study, we proposed a method to determine the corneal biomechanical parameters based on ORA measurements. The results of these studies are of great significance for the further promotion of ORA in clinical applications.

It is important to determine the range of the parameters in parametric analysis. The range of corneal geometrical parameters and IOP can be get from the reports on corneal Corvis or Pentacam measurements conveniently. The corneal biomechanical parameters were mostly reported by biomechanical experiments *in vitro*, such as corneal tensile tests or corneal expansion test. Compared to these *in vitro* experiments, an ORA test was completed within 30 ms, which made there be significant differences between uniaxial tensile test and ORA test in loading mode and magnitude. Corneal non-linear elastic and viscoelastic properties suggest that we adjust the range of corneal biomechanical parameters to make the simulation results consistent with the experimental results. The results in our previous study showed that when the cornea elastic modulus was set to be 1/3 of the corneal elastic modulus in physiological range obtained by uniaxial tensile test, and τ_1, τ_2 and τ_3 were set to be 1/10 of the corneal stress relaxation results, the amplitudes of ORA output parameters obtained by finite element simulation was basically consistent with the measured values. In this study, we set the E to the range of 0.2–0.6 MPa, a_1 and τ_1 of the third-order Prony series varied in the range of 0.25–0.6 and 0.001–0.01 s, respectively, when we carried out parametric analysis referred to these results (Qin et al., 2019b).

Although CH and CRF are two of the comprehensive ORA output parameters obtained directly from the ORA test, which were derived from the linear combination of the two applanation pressure (p_1 and p_2) (Luce, 2005), there is no consistent report on the relationship between CH, CRF and p_1, p_2. Both ORA test and

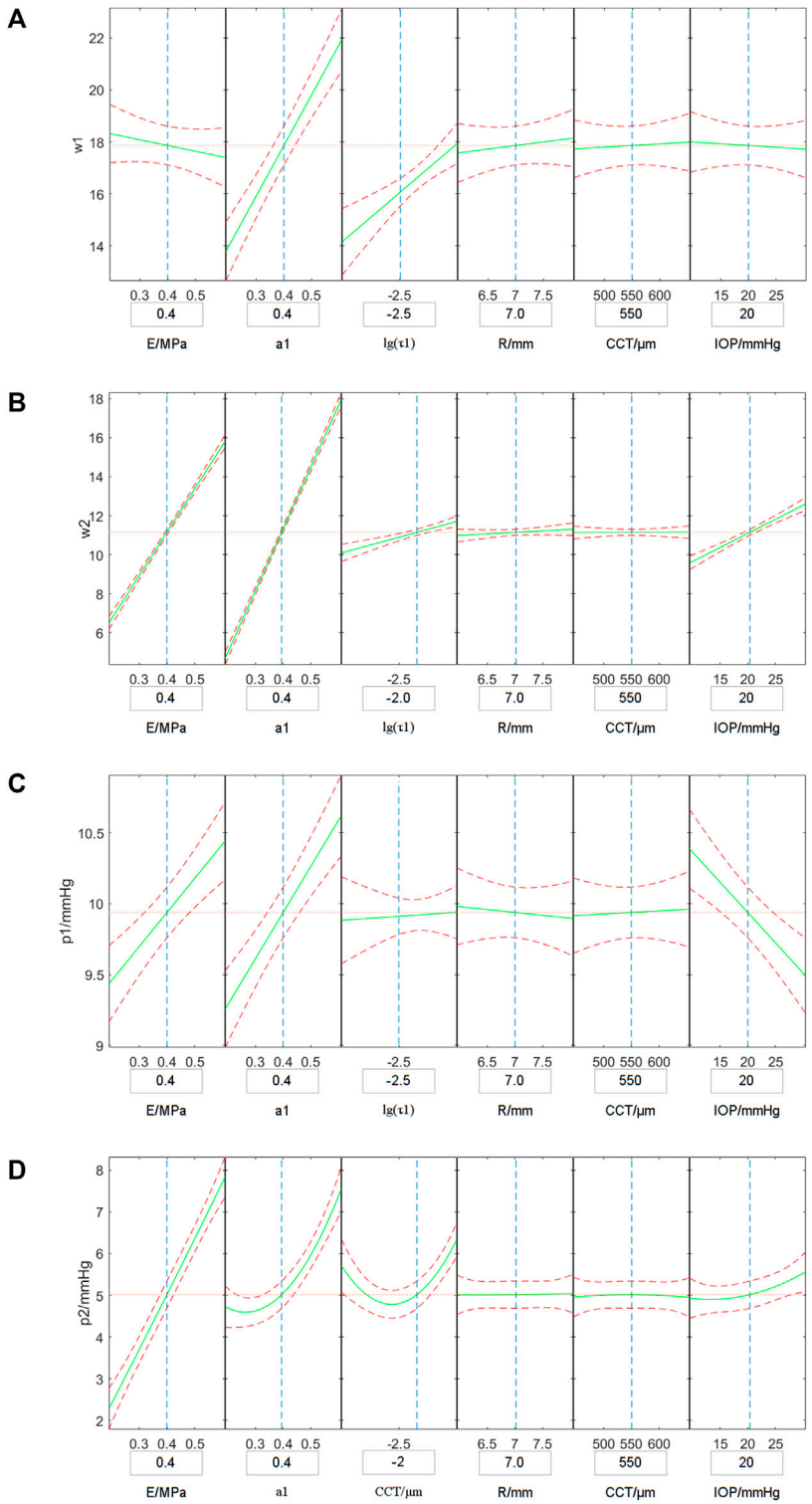

FIGURE 7 | Variations of the simulated w_1 **(A)**, w_2 **(B)**, p_1 **(C)** and p_2 **(D)** with corneal biomechanical parameters, CCT, R and IOP. The vertical axis represents the simulated ORA output parameters and the horizontal axes shows independent variables. The green solid curves simulate the variation of the average simulated ORA output parameters with one independent variable when other parameters set to the value in the boxes under the horizontal axis, and the red dotted curves are the range of the simulated ORA output parameters.

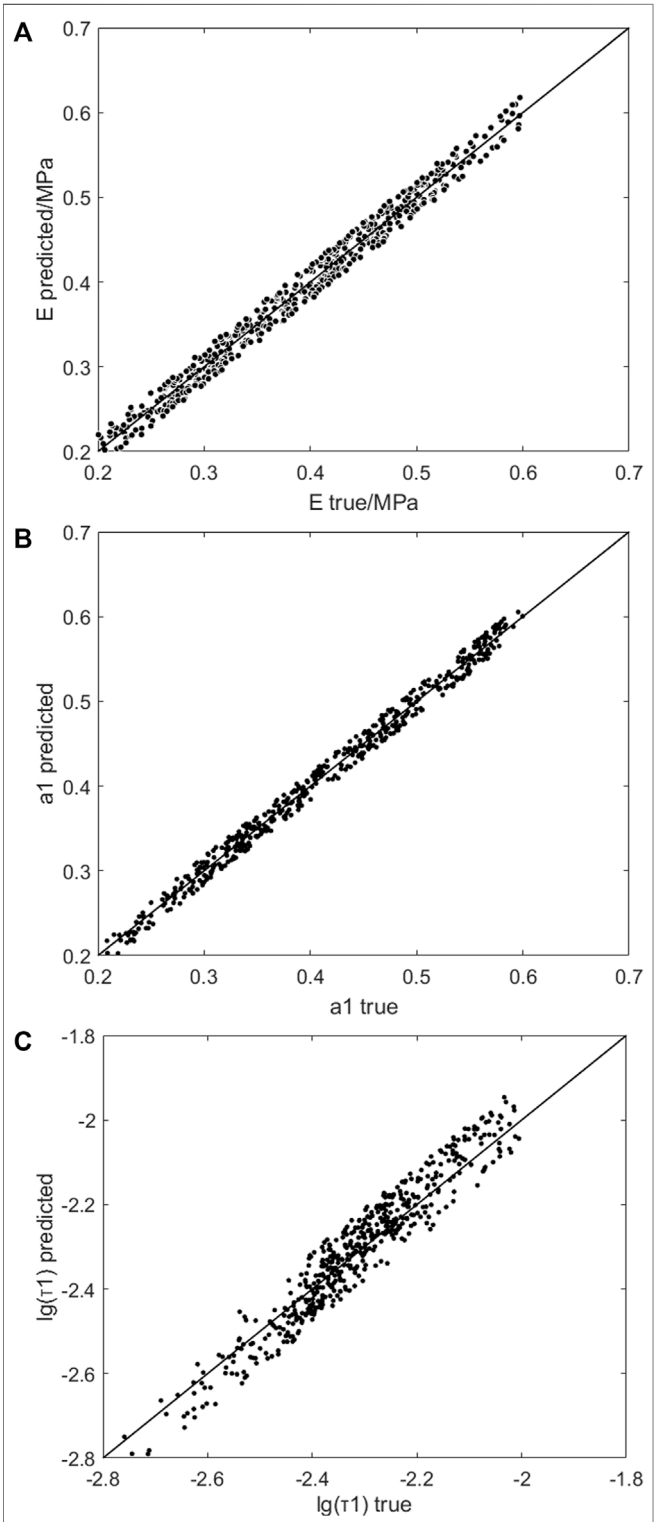

FIGURE 8 | The comparison of the predicted and set E **(A)**, a_1 **(B)** and τ_1 **(C)**. The horizontal axis was the true value in finite element simulation, and the vertical axis was the predicted value of the multiple quadratic regression model.

finite element simulation can easily obtain p_1 and p_2, therefore, this study directly used p_1 and p_2 as ORA output parameters for parametric analysis. In geometric optics simulation of ORA test, corneal surface was regarded as smooth surface. The influence of corneal surface roughness, tear film and other factors were ignored. These factors may affect some of the applanation curve waveform parameters such as the applanation peaks height h_1, h_2, etc. Yet, the influence on the width of peaks (w_1 and w_2) were relatively small (Nakao et al., 2017). Our previous study also found that w_1, w_2 were significantly correlated with corneal biomechanical parameters. Therefore, in this study, w_1 and w_2 were used to determine the corneal biomechanical parameters.

Cornea is a nonlinear elastic and viscoelastic biological soft tissue. As the cornea is still within the physiological range under the action of fast air-puff (Wang et al., 2017; Zhang et al., 2018a; Zhang et al., 2018b), the cornea was regarded as linear elastic and viscoelastic material for the finite element simulation in this study. As can be seen in **Figure 7**, with an increase of corneal elastic modulus (E), the simulated values of p_1 and p_2 also increased. Also, with the increase of the viscoelastic parameter $a1$, the parameters w_1, w_2, p_1 and p_2 showed upward trends. With the increase of the viscoelastic parameter τ_1, the simulated values of w_1 and w_2 increased, and the simulated values of p_2 decreased first and then increased. These results indicate that the four ORA test parameters we selected can reflect the biomechanical properties of the cornea.

In addition to the corneal biomechanical parameters, corneal geometric parameters such as central corneal curvature radius (R), central corneal thickness (CCT) and intraocular pressure (IOP) can also affect the ORA measurement results (Terai et al., 2012; Hwang et al., 2013; Sharifipour et al., 2016; Fujishiro et al., 2020). Therefore, this study further examined the influence of these parameters on the finite element simulation results to obtain more accurate corneal biomechanical parameters. The results showed that with the increase of IOP, the simulated values of w_2 and p_2 increased, while the simulated values of p_1 decreased. With the increase of R, the simulated values of w_1 and w_2 increased.

Based on the finite element simulation results of corneal ORA tests with different corneal geometric parameters, IOP, and corneal biomechanical parameters we established a multiple quadratic regression model to determine corneal biomechanical parameters As shown in **Eqs. 6–8**, E was negatively correlated with w_1 and w_2 while being positively correlated with p_2. This, however, was basically consistent with the negative correlation between E and w_1, w_2 reported in our previous study (Qin et al., 2019a). As high IOP and R will lead to overestimation of corneal elastic modulus, the coefficients of IOP and R in **Eqn. 6** were negative, thus weakening the influence of intraocular pressure and corneal radius of curvature on the calculation results of E. According to **Eqs. 7**, **8**, the viscoelastic parameter a_1 has a postive correlation with w_2, p_1 and a nonlinear relationship with w_1 and p_2. The viscoelastic parameter τ_1 is negatively correlated with w_1, p_1

TABLE 1 | Results of ORA measurements and the calculated corneal biomechanical parameters in healthy subjects.

parameters	p_1/mmHg	p_2/mmHg	w_1	w_2	E/MPa	a_1	τ_1/s
Mean	17.45	10.67	11.10	15.20	0.65	0.54	0.00313
SD	3.09	1.68	1.52	4.10	0.27	0.15	0.00033

and p_2 while being positively correlated with w_2. If one disregarded the differences of IOP and R, the viscoelastic parameter a_1 of subjects with high IOP and R would be overestimated.

The amplitude of air-puff pressure provided by ORA varied among different subjects according to corneal conditions. However, the pattern of air-puff amplitude provided by ORA has not been reported. In this study, the finite element simulation of ORA test ignored the difference of air-puff pressure, and the obtained corneal elastic modulus E ranged from 0.3 to 0.8 MPa, which was basically consistent with the order of magnitude of human corneal elastic modulus reported in literature (Wang et al., 2017). The viscoelastic parameters a_1 and τ_1 ranged from 0.3–0.6 and 0.002–0.005 s, respectively. Since both a_2 and a_3 were set to be 0.1 in the third-order Prony series, the relaxation limit (G_∞) ranged from 0.2 to 0.5, which was basically consistent with the results of corneal uniaxial tensile test (Elsheikh et al., 2008). In addition, it can be seen in **Figure 8** that the CTBP calculated by **Eqs 6–8** are in good consistency with the corneal classical biomechanical parameters input in finite element simulation. Besides, there was a good consistency between the corneal elastic modulus E, a_1, τ_1 between the predicted value and the set value (**Figure 8**). These results reflect the validity of the proposed method for determining corneal biomechanical parameters.

One of the limitations was that when geometric optics simulation, the corneal surface was regarded as a smooth surface, influence of corneal surface roughness, tear film and other factors was ignored. Comparing the applanation curves obtained from ORA test and optical simulation, these factors may affect the peak heights h_1 and h_2 in the waveform parameters, and have relatively little effect on the peak widths w_1 and w_2. Therefore, w_1 and w_2 were extracted for analysis. A more accurate optical model considering the refraction and reflection of the tear film on cornea and the unsmooth corneal surface may be established, which will help us obtain more real waveform parameters and establish a more accurate quantitative relationship between corneal biomechanical parameters and ORA output parameters. Another limitation was that the sample size was limited, future studies should be conducted based on a larger number of clinical data for better clinical application. Besides, the finite element simulation of ORA test ignored the difference of air-puff pressure as the pattern of air-puff amplitude provided by ORA has not been reported. According to our previous study (Qin et al., 2019b), the simulated CH and CRF have same magnitude with the experimental results although we have ignored the variation of air-puff amplitude. This reminded us the influence of ignoring the air-puff pressure difference may be ignored.

In conclusion, this study provides a method to determine linear elastic and viscoelastic material parameters of human cornea based on ORA measurements. The corneal biomechanical parameters identified by the present method need to be verified further with a great number of data. The clinic applications of this method we shall also explore, such as in diagnosis of keratoconus.

DATA AVAILABILITY STATEMENT

The original contributions presented in the study are included in the article/Supplementary Material, further inquiries can be directed to the corresponding authors.

ETHICS STATEMENT

The studies involving human participants were reviewed and approved by institutional review board of the Beijing Tongren Hospital, Beijing Institute of Ophthalmology, Beijing, China. The patients/participants provided their written informed consent to participate in this study.

AUTHOR CONTRIBUTIONS

XQ and LT contributed equally to this work. LL, H-XZ, YJ: Corresponding author, conception and design of the study, revising the manuscript. XQ and LT: acquisition of the data, drafting the article. H-XZ and DZ: analysis and interpretation of the data.

FUNDING

This research was supported by Grants from the National Natural Science Foundation of China (Nos. 32171304, 31370952, 82171101); Beijing Nova Program (Z181100006218099); the Open Research Fund from Beijing Advanced Innovation Center for Big Data-Based Precision Medicine, Beijing Tongren Hospital, Beihang University and Capital Medical University (BHTR-KFJJ-202001).

REFERENCES

Atalay, E., Ozalp, O., Erol, M. A., Bilgin, M., and Yildirim, N. (2019). A Combined Biomechanical and Tomographic Model for Identifying Cases of Subclinical Keratoconus. *Cornea* 39 (4), 461–467. doi:10.1097/ico.0000000000002205

Ayar, O., Ozmen, M. C., Muftuoglu, O., Akdemir, M. O., Koc, M., and Ozulken, K. (2015). *In-vivo* Corneal Biomechanical Analysis of Unilateral Keratoconus. *Int. J. Ophthalmol.* 8, 1141–1145. doi:10.3980/j.issn.2222-3959.2015.06.11

Bao, F., Deng, M., Wang, Q., Huang, J., Yang, J., Whitford, C., et al. (2015). Evaluation of the Relationship of Corneal Biomechanical Metrics with Physical Intraocular Pressure and central Corneal Thickness in *Ex Vivo* Rabbit Eye Globes. *Exp. Eye Res.* 137, 11–17. doi:10.1016/j.exer.2015.05.018

Dubbelman, M., Weeber, H. A., van der Heijde, R. G. L., and Völker-Dieben, H. J. (2009). Radius and Asphericity of the Posterior Corneal Surface Determined by Corrected Scheimpflug Photography. *Acta Ophthalmol. Scand.* 80, 379–383. doi:10.1034/j.1600-0420.2002.800406.x

Elham, R., Jafarzadehpur, E., Hashemi, H., Amanzadeh, K., Shokrollahzadeh, F., Yekta, A., et al. (2017). Keratoconus Diagnosis Using Corvis ST Measured Biomechanical Parameters. *J. Curr. Ophthalmol.* 29, 175–181. doi:10.1016/j.joco.2017.05.002

Eliasy, A., Chen, K. J., Vinciguerra, R., Lopes, B. T., Abass, A., Vinciguerra, P., et al. (2019). Determination of Corneal Biomechanical Behavior *In-Vivo* for Healthy Eyes Using CorVis ST Tonometry: Stress-Strain Index. *Front. Bioeng. Biotechnol.* 7, 105. doi:10.3389/fbioe.2019.00105

Elsheikh, A., Alhasso, D., Gunvant, P., and Garway-Heath, D. (2011). Multiparameter Correction Equation for Goldmann Applanation Tonometry. *Optom. Vis. Sci.* 88, E102–E112. doi:10.1097/opx.0b013e3181fc3453

Elsheikh, A., Alhasso, D., and Rama, P. (2008). Biomechanical Properties of Human and Porcine Corneas. *Exp. Eye Res.* 86, 783–790. doi:10.1016/j.exer.2008.02.006

Elsheikh, A. (2010). Finite Element Modeling of Corneal Biomechanical Behavior. *J. Refract Surg.* 26, 289–300. doi:10.3928/1081597x-20090710-01

Elsheikh, A., Joda, A., Abass, A., and Garway-Heath, D. (2015). Assessment of the Ocular Response Analyzer as an Instrument for Measurement of Intraocular Pressure and Corneal Biomechanics. *Curr. Eye Res.* 40, 1111–1119. doi:10.3109/02713683.2014.978479

Fujishiro, T., Matsuura, M., Fujino, Y., Murata, H., Tokumo, K., Nakakura, S., et al. (2020). The Relationship between Corvis ST Tonometry Parameters and Ocular Response Analyzer Corneal Hysteresis. *J. Glaucoma* 29, 479–484. doi:10.1097/ijg.0000000000001486

Glass, D. H., Roberts, C. J., Litsky, A. S., and Weber, P. A. (2008). A Viscoelastic Biomechanical Model of the Cornea Describing the Effect of Viscosity and Elasticity on Hysteresis. *Invest. Ophthalmol. Vis. Sci.* 49, 3919–3926. doi:10.1167/iovs.07-1321

Han, Z., Tao, C., Zhou, D., Sun, Y., Zhou, C., Ren, Q., et al. (2014). Air Puff Induced Corneal Vibrations: Theoretical Simulations and Clinical Observations. *J. Refract Surg.* 30, 208–213. doi:10.3928/1081597x-20140212-02

Herber, R., Ramm, L., Spoerl, E., Raiskup, F., Pillunat, L. E., and Terai, N. (2019). Assessment of Corneal Biomechanical Parameters in Healthy and Keratoconic Eyes Using Dynamic Bidirectional Applanation Device and Dynamic Scheimpflug Analyzer. *J. Cataract Refract Surg.* 45, 778–788. doi:10.1016/j.jcrs.2018.12.015

HirjiLarke, N. K., and Larke, J. R. (1978). Thickness of Human Cornea Measured by Topographic Pachometry. *Optom. Vis. Sci.* 55, 97–100. doi:10.1097/00006324-197802000-00006

Hjortdal, J. O., and Jensen, P. K. (1995). *In Vitro* measurement of Corneal Strain, Thickness, and Curvature Using Digital Image Processing. *Acta Ophthalmol. Scand.* 73, 5–11. doi:10.1111/j.1600-0420.1995.tb00004.x

Hwang, E. S., Stagg, B. C., Swan, R., Fenzl, C. R., Mcfadden, M., Muthappan, V., et al. (2017). Corneal Biomechanical Properties after Laser-Assisted *In Situ* Keratomileusis and Photorefractive Keratectomy. *Opth* Vol. 11, 1785–1789. doi:10.2147/opth.s142821

Hwang, H. S., Park, S. K., and Kim, M. S. (2013). The Biomechanical Properties of the Cornea and Anterior Segment Parameters. *BMC Ophthalmol.* 13, 49. doi:10.1186/1471-2415-13-49

Jannesari, M., Mosaddegh, P., Kadkhodaei, M., Kasprzak, H., and Jabbarvand Behrouz, M. (2019). Numerical and Clinical Investigation on the Material Model of the Cornea in Corvis Tonometry Tests: Differentiation between Hyperelasticity and Viscoelasticity. *Mech. Time-depend Mater.* 23, 373–384. doi:10.1007/s11043-018-9390-3

Kling, S., Bekesi, N., Dorronsoro, C., Pascual, D., and Marcos, S. (2014). Corneal Viscoelastic Properties from Finite-Element Analysis of *In Vivo* Air-Puff Deformation. *PLoS One* 9, e104904. doi:10.1371/journal.pone.0104904

Koc, M., Aydemir, E., Tekin, K., Inanc, M., Kosekahya, P., and Kiziltoprak, H. (2019). Biomechanical Analysis of Subclinical Keratoconus with Normal Topographic, Topometric, and Tomographic Findings. *J. Refract Surg.* 35, 247–252. doi:10.3928/1081597x-20190226-01

Lago, M. A., Rupérez, M. J., Martínez-Martínez, F., Monserrat, C., Larra, E., Güell, J. L., et al. (2015). A New Methodology for the *In Vivo* Estimation of the Elastic Constants that Characterize the Patient-specific Biomechanical Behavior of the Human Cornea. *J. Biomech.* 48, 38–43. doi:10.1016/j.jbiomech.2014.11.009

Luce, D. A. (2005). Determining *In Vivo* Biomechanical Properties of the Cornea with an Ocular Response Analyzer. *J. Cataract Refract Surg.* 31, 156–162. doi:10.1016/j.jcrs.2004.10.044

Matteoli, S., Virga, A., Paladini, I., Mencucci, R., and Corvi, A. (2016). Investigation into the Elastic Properties of *Ex Vivo* Porcine Corneas Subjected to Inflation Test after Cross-Linking Treatment. *J. Appl. Biomater. Funct. Mater.* 14, E163–E170. doi:10.5301/jabfm.5000262

Mercatelli, R., Mattana, S., Capozzoli, L., Ratto, F., Rossi, F., Pini, R., et al. (2019). Morpho-mechanics of Human Collagen Superstructures Revealed by All-Optical Correlative Micro-spectroscopies. *Commun. Biol.* 2, 117. doi:10.1038/s42003-019-0357-y

Nakao, Y., Kiuchi, Y., and Okimoto, S. (2017). A Comparison of the Corrected Intraocular Pressure Obtained by the Corvis ST and Reichert 7CR Tonometers in Glaucoma Patients. *Plos One* 12, e0170206. doi:10.1371/journal.pone.0170206

Nemeth, G., Szalai, E., Hassan, Z., Lipecz, A., Flasko, Z., and Modis, L. (2017). Corneal Biomechanical Data and Biometric Parameters Measured with Scheimpflug-Based Devices on normal Corneas. *Int. J. Ophthalmol.* 10, 217–222. doi:10.18240/ijo.2017.02.06

Qin, X., Yu, M., Zhang, H., Chen, X., and Li, L. (2019b). The Mechanical Interpretation of Ocular Response Analyzer Parameters. *Biomed. Res. Int.* 2019, 5701236. doi:10.1155/2019/5701236

Qin, X., Tian, L., Zhang, H., Chen, X., and Li, L. (2019a). Evaluation of Corneal Elastic Modulus Based on Corneal Visualization Scheimpflug Technology. *Biomed. Eng. Online* 18, 42. doi:10.1186/s12938-019-0662-1

Roberts, C. J., Mahmoud, A. M., Bons, J. P., Hossain, A., Elsheikh, A., Vinciguerra, R., et al. (2017). Introduction of Two Novel Stiffness Parameters and Interpretation of Air Puff-Induced Biomechanical Deformation Parameters with a Dynamic Scheimpflug Analyzer. *J. Refract Surg.* 33, 266–273. doi:10.3928/1081597x-20161221-03

Scarcelli, G., Besner, S., Pineda, R., Kalout, P., and Yun, S. H. (2015). *In Vivo* biomechanical Mapping of normal and Keratoconus Corneas. *JAMA Ophthalmol.* 133, 480–482. doi:10.1001/jamaophthalmol.2014.5641

Sharifipour, F., Panahi-Bazaz, M., Bidar, R., Idani, A., and Cheraghian, B. (2016). Age-related Variations in Corneal Biomechanical Properties. *J. Curr. Ophthalmol.* 28, 117–122. doi:10.1016/j.joco.2016.05.004

Shih, P. J., Huang, C. J., Huang, T. H., Lin, H. C., Yen, J. Y., Wang, I. J., et al. (2017). Estimation of the Corneal Young's Modulus *In Vivo* Based on a Fluid-Filled Spherical-Shell Model with Scheimpflug Imaging. *J. Ophthalmol.* 2017, 5410143. doi:10.1155/2017/5410143

Sinha Roy, A., Kurian, M., Matalia, H., and Shetty, R. (2015). Air-puff Associated Quantification of Non-linear Biomechanical Properties of the Human Cornea *In Vivo*. *J. Mech. Behav. Biomed. Mater.* 48, 173–182. doi:10.1016/j.jmbbm.2015.04.010

Steinberg, J., Katz, T., Mousli, A., Frings, A., Casagrande, M. K., Druchkiv, V., et al. (2014). Corneal Biomechanical Changes after Crosslinking for Progressive Keratoconus with the Corneal Visualization Scheimpflug Technology. *J. Ophthalmol.* 2014, 579190. doi:10.1155/2014/579190

Subasinghe, S. K., Ogbuehi, K. C., and Dias, G. J. (2018). Current Perspectives on Corneal Collagen Crosslinking (CXL). *Graefes Arch. Clin. Exp. Ophthalmol.* 256, 1363–1384. doi:10.1007/s00417-018-3966-0

Terai, N., Raiskup, F., Haustein, M., Pillunat, L. E., and Spoerl, E. (2012). Identification of Biomechanical Properties of the Cornea: the Ocular Response Analyzer. *Curr. Eye Res.* 37, 553–562. doi:10.3109/02713683.2012.669007

Vellara, H. R., and Patel, D. V. (2015). Biomechanical Properties of the Keratoconic Cornea: a Review. *Clin. Exp. Optom.* 98, 31–38. doi:10.1111/cxo.12211

Vinciguerra, R., Elsheikh, A., Roberts, C. J., Ambrósio, R., Jr., Kang, D. S. Y., Lopes, B. T., et al. (2016). Influence of Pachymetry and Intraocular Pressure on Dynamic Corneal Response Parameters in Healthy Patients. *J. Refract Surg.* 32, 550–561. doi:10.3928/1081597x-20160524-01

Viswanathan, D., Kumar, N. L., Males, J. J., and Graham, S. L. (2015). Relationship of Structural Characteristics to Biomechanical Profile in Normal, Keratoconic, and Crosslinked Eyes. *Cornea* 34, 791–796. doi:10.1097/ico.0000000000000434

Wang, B., Zhang, Z., Naidu, R. K., Chu, R., Dai, J., Qu, X., et al. (2016). Comparison of the Change in Posterior Corneal Elevation and Corneal Biomechanical Parameters after Small Incision Lenticule Extraction and Femtosecond Laser-Assisted LASIK for High Myopia Correction. *Contact Lens and Anterior Eye* 39, 191–196. doi:10.1016/j.clae.2016.01.007

Wang, L.-K., Tian, L., and Zheng, Y.-P. (2016). Determiningin Vivoelasticity and Viscosity with Dynamic Scheimpflug Imaging Analysis in Keratoconic and Healthy Eyes. *J. Biophoton* 9, 454–463. doi:10.1002/jbio.201500245

Wang, X., Li, X., Chen, W., He, R., Gao, Z., and Feng, P. (2017). Effects of Ablation Depth and Repair Time on the Corneal Elastic Modulus after Laser *In Situ* Keratomileusis. *Biomed. Eng. Online* 16, 20. doi:10.1186/s12938-017-0311-5

Wu, Y., Tian, L., and Huang, Y. F. (2016). *In Vivo* Corneal Biomechanical Properties with Corneal Visualization Scheimpflug Technology in Chinese Population. *Biomed. Res. Int.* 2016, 7840284. doi:10.1155/2016/7840284

Yang, J., Zeng, Y., and Li, Z. (1999). Biomechanical Properties of Human Cornea. *Acta Biophys. sinica*.

Yildirim, Y., Olcucu, O., Basci, A., Agca, A., Ozgurhan, E.B., Alagoz, C., et al. (2016). Comparison of Changes in Corneal Biomechanical Properties after Photorefractive Keratectomy and Small Incision Lenticule Extraction. *Turk J. Ophthalmol.* 46, 47–51.

Zhang, H.X., Khan, M.A., Zhang, D., Qin, X., Lin, D., and Li, L. (2018a). Corneal Biomechanical Properties after FS-LASIK with Residual Bed Thickness Less Than 50% of the Original Corneal Thickness. *J. Ophthalmol.* 2018, 2752945. doi:10.1155/2018/2752945

Zhang, H.X., Qian, X.Q., Li, L., and Liu, Z.C. (2017). Understanding the Viscoelastic Properties of Rabbit Cornea Based on Stress Relaxation Tests and Cyclic Uniaxial Tests. *J. Mech. Med. Biol.* 17. doi:10.1142/s0219519417400358

Zhang, H.X., Zhang, D., Qin, X., Wang, H., and Li, L. (2018b). Study of the Transversal Deformation of Corneal Strip under Uniaxial Loading. *J. Mech. Med. Biol.* 18. doi:10.1142/s0219519418400183

Zhang, Y. L., Shao, T. T., and Shi, M. G. (2006). A Study on the Space Form of the Schematic Cornea of the normal Adult Eye-ball. *Zhonghua Yan Ke Za Zhi* 42, 992–997.

Zheng, X., Bao, F., Geraghty, B., Huang, J., Yu, A., and Wang, Q. (2016). High Intercorneal Symmetry in Corneal Biomechanical Metrics. *Eye Vis.* 3, 7. doi:10.1186/s40662-016-0037-7

Conflict of Interest: The authors declare that the research was conducted in the absence of any commercial or financial relationships that could be construed as a potential conflict of interest.

Publisher's Note: All claims expressed in this article are solely those of the authors and do not necessarily represent those of their affiliated organizations, or those of the publisher, the editors and the reviewers. Any product that may be evaluated in this article, or claim that may be made by its manufacturer, is not guaranteed or endorsed by the publisher.

frontiers | Frontiers in Bioengineering and Biotechnology

ORIGINAL RESEARCH
published: 13 April 2022
doi: 10.3389/fbioe.2022.863240

In Vivo Corneal Biomechanical Properties in a Selected Chinese Population, Measured Using the Corneal Visualization Scheimpflug Technology

Yuxin Li[1,2], *Lei Tian*[1,3]*, *Li-Li, Guo*[4], *Yiran Hao*[1] and *Ying Jie*[1]*

[1]Beijing Ophthalmology and Visual Sciences Key Laboratory, Beijing Tongren Eye Center, Beijing Tongren Hospital, Beijing Institute of Ophthalmology, Capital Medical University, Beijing, China, [2]Beijing Chaoyang Hospital, Capital Medical University, Beijing, China, [3]Beijing Advanced Innovation Center for Big Data-Based Precision Medicine, Beihang University, Capital Medical University, Beijing, China, [4]The First People's Hospital of Xuzhou, Xuzhou, China

OPEN ACCESS

Edited by:
FangJun Bao,
Affiliated Eye Hospital of Wenzhou Medical College, China

Reviewed by:
Hong Ouyang,
Sun Yat-sen University, China
Gilbert Yong San Lim,
SingHealth, Singapore

***Correspondence:**
Lei Tian
tianlei0131@163.com
Ying Jie
jie_yingcn@aliyun.com

Specialty section:
This article was submitted to Biomechanics, a section of the journal Frontiers in Bioengineering and Biotechnology

Received: 27 January 2022
Accepted: 14 March 2022
Published: 13 April 2022

Citation:
Li Y, Tian L, Guo L-L, Hao Y and Jie Y (2022) In Vivo Corneal Biomechanical Properties in a Selected Chinese Population, Measured Using the Corneal Visualization Scheimpflug Technology. Front. Bioeng. Biotechnol. 10:863240. doi: 10.3389/fbioe.2022.863240

Purpose: To evaluate the repeatability and reproducibility of recalculated dynamic corneal response (DCR) parameters and the biomechanical-compensated intraocular pressure (bIOP) derived from the Corneal Visualization Scheimpflug Technology (Corvis ST), as well as to study the variations of DCR parameters and their relationship with demographic, and ocular characteristics.

Methods: A total of 544 healthy subjects were recruited in this study and a series of ophthalmological examinations were performed on their right eyes. Three repeated measurements were obtained at 3-min intervals for 291 of the participants to ensure repeatability. A sum of 100 participants was examined twice within 2-h intervals using two different Corvis ST in the reproducibility study. The repeatability and reproducibility of 37 parameters, including 36 DCR parameters and bIOP, were assessed by the coefficient of repeatability (CR), coefficient of variation (CV), intraclass correlation coefficient (ICC), and within-subject standard deviation (sw). Pearson's correlation coefficients and stepwise multivariate linear regression models were performed to investigate whether the DCR parameters were related to demographic and ocular characteristics.

Results: Of all the 37 parameters, 34 showed excellent (ICC ≥0.90) or good (ICC ≥0.75) repeatability while 27 of the 37 parameters showed excellent (ICC ≥0.90) or good (ICC ≥0.75) reproducibility. In particular, a CV of less than 20% was found for all DCR parameters and bIOP. A fraction of 14 out of 36 DCR parameters was selected for correlation analysis, based on measurement reliability and clinical relevance in referring to previous literature. Age was negatively associated with the Highest concavity delta arc length (HCdArcL) and peak distance (PD) but it positively correlated with the Whole Eye Movement Max Length (WEMML). Intraocular pressure (IOP) and central corneal thickness (CCT) were negatively associated with the deformation amplitude ratio (DARM) [1 mm], A1 Velocity (A1V), and PD, while positively related to the stiffness parameter at applanation 1 (SP-A1). The bIOP was negatively associated with A1V but positively associated with A2 Velocity (A2V). The

anterior chamber volume (ACV) was negatively associated with the pachy slope (PS), WEMML, and SP-A1.

Conclusion. The Corvis ST showed good precision for the repeatability and reproducibility of 36 DCR parameters and bIOP parameters in healthy eyes. The IOP, CCT, bIOP, Km, and ACV significantly influenced the DCR parameters of the eyes.

Keywords: CorVis ST, repeatability, reproducibility, intraclass correlation coefficient, correlation

INTRODUCTION

The investigation of corneal biomechanics recently gained space as a hot topic in ophthalmology mainly due to its wide applications (Roberts etal., 2014). Corneal biomechanical properties were known to assist with detecting corneal diseases (Vinciguerra et al., 2017a; Reinprayoon et al., 2021; Ziaei et al., 2021; Henriquez et al., 2022), predicting refractive outcomes before corneal refractive surgery (Chen et al., 2018), judging different protocols of collagen crosslinking treatments (Greenstein et al., 2012), and even selecting intracorneal ring implants (Bao et al., 2016; Shen et al., 2022).

Multifarious methods have been devised to study the biomechanics of cornea *in vivo* (Hollman et al., 2013; Flockerzi et al., 2021). The Ocular Response Analyzer (ORA; Reichert, Buffalo, NY, United States) which provided great knowledge of the corneal biomechanics was one of the methods that were used in the clinic (Luce, 2005) but it cannot exhibit the dynamic corneal response (DCR) parameters. In 2010, a visual display method that was based on corneal dynamic deformation video using an ultra-fast Scheimpflug camera combined with a classic non-contact tonometer was introduced (Eliasy et al., 2018; Krysik et al., 2018; Guo et al., 2021). The non-contact tonometer is called corneal visualization Scheimpflug technology (Corvis ST; Oculus Optikgeräte GmbH, Wetzlar, Germany). The dependence of available parameters on specific disease entities was investigated, together with the changes in their values after performing surgical procedures. Furthermore, in terms of evaluating the impact of biomechanical parameters, the software versions have been changed several times with new parameters. The newer Corvis ST version (1.6r2042) includes the biomechanically corrected IOP (bIOP) (Joda et al., 2015; Salouti et al., 2022) and DCR parameters like max inverse radius (MIR), deformation amplitude ratio (DARM) [1 mm], deformation amplitude ratio (DARM) [2 mm], pachy slope (PS), Ambrosio relational thickness to the horizontal profile (ARTh), integrated radius (IR), stiffness parameter at applanation 1 (SP-A1) (Jędzierowska and Koprowski, 2019), and Corvis Biomechanical Index (CBI) (Vinciguerra et al., 2016a; Vinciguerra et al., 2017a; Vinciguerra et al., 2017b). For diagnosis and follow-up purposes, the reliability of these measurements is important, and its evaluation is carried out by analyzing repeatability and reproducibility factors. Additionally, independent studies should focus on determining "normal" values for different populations so that new technologies can establish wider acceptance and broad utility at clinical levels.

Therefore, this study aimed to evaluate the repeatability and reproducibility of Corvis ST parameters. Moreover, we also demonstrated variations in biomechanical properties that are provided by Corvis ST in healthy Chinese participants, in addition to their relationship with demographic and ocular characteristics.

METHODS

Subject Recruitment

A total of 544 healthy Chinese participants aged between 10 and 75 years were recruited at Beijing TongRen Hospital, which is affiliated to Capital Medical University. The recruitment was done between January 2021 and January 2022. This cross-sectional study was approved by the office of Research Ethics Committee of Beijing TongRen Hospital, in accordance with the principles of the Helsinki Declaration. All the participants provided informed consents before taking part in the study.

Ocular Examinations

All participants underwent a complete ophthalmic examination and a standardized interview procedure. Ophthalmic examination included detailed visual acuity assessment; slit-lamp microscopy and fundus examination; corneal and anterior chamber tomography with Pentacam (Oculus Optikgeräte GmbH, Wetzlar, and Germany); as well as corneal biomechanics and intraocular pressure with Corvis ST. To reduce the effect of diurnal variation, all assessments were performed on a single visit.

The study excluded participants if they had previous corneal or ocular surgery, any ocular pathology or systemic disease that affects the eye, or long-term use of topical ocular medications.

Corvis ST Measurement

IOP and corneal biomechanical parameters were measured by Corvis ST, a noncontact tonometer and imaging device that can provide additional information on the corneal response to specific airflow pulses. An ultrahigh-speed Scheimpflug camera (recorded at 4,330 frames per second) captured corneal deformations in the horizontal range of 8.5 mm. A video clip containing 140 digital frames corresponded to a recording time of 33 msec. The details of measurements on the Corvis ST are described elsewhere (Robert et al., 2019; Zhang et al., 2021a). In the latest release of the software, more DCR parameters [MIR,

TABLE 1 | Abbreviations and explanations of parameters measured by Corvis ST.

Abbreviations of parameter	Full name	Explanation
DAM (mm)	Deformation amplitude Max	Max length at deformation amplitude
A1T (ms)	First applanation time	Time from the initiation of the air puff until the first applanation
A2T (ms)	Second applanation time	Time from the initiation of the air puff until the second applanation
HCT (ms)	Highest concavity time	Time from the start until highest concavity of the cornea is reached
A1V (m/s)	A1 Velocity	Corneal velocity at the first applanation
A2V (m/s)	A2 Velocity	Corneal velocity at the second applanation
PD (mm)	Peak distance	Distance of the two surrounding "knees" at highest concavit
Radius (mm)	Radius	Radius of curvature at the time of highest concavity
A1DA (mm)	A1 Deformation Amplitude	Deformationtion amplitude at the first applanation
HCDA (mm)	Highest concavity Deformation Amplitude	Deformation amplitude at the maximum deformation
A2DA (mm)	A2 Deformation Amplitude	Deformation amplitude at the second applanation
A1DLL (mm)	A1 Deflection Length	Deflection length at the first applanation
A2DLL (mm)	A2 Deflection Length	Deflection length at second applanation
HCDLL (mm)	Highest concavity Deflection Length	Deflection length at maximum deformation
A1DLA (mm)	A1 Deflection Amplitude	Deflection Amplitude deflection amplitude at the first applanation
A2DLA (mm)	A2 Deflection Amplitude	Deflection Amplitude deflection amplitude at the second applanation
HCDLA (mm)	Highest concavity Deflection Amplitude	Deflection Amplitude deflection amplitude at the maximum deformation
DLAML (mm)	Deflection Amplitude Max Length	Max Length at deflection amplitude
DLAMT (ms)	Deflection Amplitude Max Time	Max time at deflection amplitude
WEMML (mm)	Whole Eye Movement Max Length	Max length of whole eye movement
WEMMT (ms)	Whole Eye Movement Max Time	Max time of whole eye movement
A1DLAr (mm)	A1 Deflection Area	Deflection area at the first applanation
A2DLAr (mm)	A2 Deflection Area	Deflection area at the second applanation
HCDLAr (mm)	Highest concavity Deflection Area	Deflection area at the maximum deformation
A1dArcL (mm)	A1 dArc Length	Delta arc length at the first applanation
A2dArcL (mm)	A2 dArc Length	Delta arc length at the second applanation
HCdArcL (mm)	Highest concavity dArc	Length Delta arc length at the maximum deformation
dArcLM (mm)	dArcLengthMax	Max delta arc length
MIR (mm^{-1})	Max Inverse Radius	The maximum value of radius of curvature during concave phase of the deformation
PS (μm)	Pachy Slope	Pachy Slope
IR (mm^{-1})	Integrated Radius	Integrated Radius
DARM [1 mm]	Deformation amplitude ratio [1 mm]	The maximum value of the ratio between deformation amplitude at the apex 1 mm from central cornea
DARM [2 mm]	Deformation amplitude ratio [2 mm]	The maximum value of the ratio between deformation amplitude at the apex 2 mm from central cornea
ARTh	Ambrosio relational thickness to the horizontal profile	Ambrosio relational thickness to the horizontal profile
bIOP (mmHg)	Biomechanical Intra Occular Pressure	Biomechanical Intra Occular Pressure
SP-A1	Stiffness parameter at applanation 1	The adjusted pressure at A1 (adjusted AP1) minus a biomechanically corrected IOP value (bIOP) and then divided by A1 deflection amplitude, stiffness parameter at first applanation
CBI	Corvis biomechanical index	Corvis biomechanical index

DARM (1 mm), DARM (2 mm) PS, ARtH, IR, SP-A1, and CBI) were introduced, together with bIOP. (Hirasawa et al., 2018).

Table 1 shows the abbreviations and interpretations of the 36 DCR parameters and bIOP parameter that were measured by the Corvis ST. The latest version of the Oculus software (version 1.6r2042) was used to recalculate all the Corvis ST measurements and this facilitated more precise parameters and data association. The quality specification section on the output graph was used to check the quality. An "OK" reading was interpreted to reflect an acceptable quality.

A total of 291 participants received three measurements which were repeated until all parameters were obtained with acceptable quality. This was done to determine the intra-observer repeatability. Between measurements, the cornea was allowed to recover from the air puff by resting for 3 minutes. To assess the inter-device reproducibility, a subgroup of 100 patients was randomly selected and analyzed separately. The measurements were performed using two different devices, although they had the same software (version 1.6r2042). The second batch of measurements was taken 2 hours after those of the first batch were taken.

Statistical Analysis

The SPSS version 26.0 (SPSS, Inc., Chicago, IL, United States) was used for statistical analysis. The normality of distribution of the measured variables was estimated using the Kolmogorov-Smirnov test. The recalculated biomechanical parameters were analyzed for repeatability and reproducibility. The statistical significance of the coefficient of repeatability (CR), coefficient of variation (CV), intraclass correlation coefficient (ICC), and within-subject standard deviation (sw) were used to evaluate the parametric repeatability analysis (Herber et al., 2020). The CV values that were less than 20% were considered to reflect high repeatability (Ali et al., 2014). The explanation of the ICC was

TABLE 2 | Demographic and ocular data of participants.

Parameters	All (n = 544)
Age (y)	29.1 ± 12.6 (10–75)
Gender (n)	280 females, 264 males
IOP (mmHg)	14.82 ± 2.92 (8.0–25.5)
bIOP (mmHg)	14.64 ± 2.61 (6.8–23.1)
CCT (μm)	545.9 ± 30.1 (389–638)
Km (D)	43.33 ± 1.38 (36.8–47.1)
Astig (D)	1.20 ± 0.73 (0–3.0)
ACV (mm^3)	183.4 ± 45.3 (53–280)

IOP, intraocular pressure, bIOP, biomechanical-compensated intraoocular pressure, CCT, Central corneal thickness, Astig, astigmia, Km, mean keratometry, ACV, nterior chamber volume.

based on the following stipulations: >0.90 means excellent repeatability, 0.75–0.90 correlates to good repeatability, and <0.75 reflects poor to moderate repeatability of clinical measurement (Ali et al., 2014).

Based on the reliability of the measurements, as well as the clinical relevance with reference to previous literature, 14 of the 36 DCR parameters were selected for correlation analysis (Vinciguerra et al., 2016b; Cui et al., 2019). Pearson's correlation analysis was used to explore the relationship between the DCR parameters and demographic/ocular characteristics, including age, IOP, CCT, bIOP, mean keratometry (Km), and anterior chamber volume (ACV). Stepwise multivariate linear regression analysis was carried out, where all significantly-changed parameters that were retrieved from Pearson's correlation analysis were regarded as the independent variables while the demographic/ocular characteristics were dependent variables. A p-value < 0.05 was interpreted as statistically significant.

RESULTS

Characteristics of Healthy Participants

A total of 544 healthy Chinese participants were recruited in this study. **Table 2** shows the demographic data of all the participants. The mean values of the DCR parameters in the eyes, together with the corresponding SD and range are shown in **Table 3**.

Repeatability and Reproducibility

Table 4 showed the repeatability and reproducibility values of the Corvis ST parameters. Among the 37 parameters, 20 (54.05%) had excellent repeatability (ICC ≥0.90), 14 (37.84%) had good repeatability (ICC ≥0.75), and 3 (8.11%) had poor to moderate repeatability. The CV of all the DCR parameters was less than 20%. Particularly, 12 of 37 parameters (32.43%) were highly reliable (CV < 5%). All the new parameters showed good or excellent repeatability.

Out of the 37 parameters, 9 (24.32%) showed excellent reproducibility (ICC ≥0.90), 18 (48.65%) showed good (ICC ≥0.75), and 10 (27.03%) showed poor to moderate repeatability (ICC d<0.75). A CoV value that was less than 20% was found for each of the DCR parameters. A fraction of 9 out of 37 parameters (24.32%) were highly reliable (CV <5%). All the other new parameters showed good or excellent reproducibility, except for MIR.

Determinants of Dynamic Corneal Response Parameters

Table 5 shows the results of the Pearson's correlation analysis. All the parameters that statistically correlated with age, IOP, CCT, bIOP, Km, Astig, and ACV were selected in a linear regression model using stepwise selection.

Table 6 shows the investigative results of the multivariate linear regression models. Age was negatively associated with HCdArcL and PD, but positively correlated with WEMML. The IOP and CCT were negatively associated with DARM (1 mm), A1V, PD, while being positively related to SP-A1. BIOP was negatively associated with A1V, but the opposite was true when it comes to A2V. ACV was negatively associated with PS, WEMML, and SP-A1.

The coefficients of determination (the adjusted R^2 value) in multiple linear regressions of age, IOP, CCT, bIOP, Km, Astig

TABLE 3 | Dynamic Corneal Response parameters data of participants.

Parameters	Mean	±SD	Range
DAM (mm)	1.03	0.10	0.76–1.45
A1T (ms)	7.44	0.33	6.72–8.75
A1V (ms)	0.13	0.02	0.07–0.18
A2T (ms)	21.76	0.37	20.60–23.21
A2V (ms)	–0.27	0.04	–0.42–0.16
HCT (ms)	16.91	0.47	15.54–18.45
PD (mm)	5.01	0.31	3.93–6.12
R (mm)	7.09	0.76	5.26–10.11
A1DA (mm)	0.13	0.01	0.10–0.17
HCDA (mm)	1.03	0.10	0.76–1.45
A2DA (mm)	0.36	0.07	0.07–0.68
A1DLL (mm)	2.27	0.19	0.40–2.85
HCDLL (mm)	6.54	0.49	4.86–8.23
A2DLL (mm)	2.77	0.57	1.39–5.60
A1DLA (mm)	0.09	0.01	0.04–0.14
HCDLA (mm)	0.89	0.11	0.56–1.32
A2DLA (mm)	0.11	0.08	0.05–1.85
DLAM (mm)	0.90	0.12	0.59–2.03
DLAM (ms)	16.19	0.78	4.00–20.62
WEMML (mm)	0.26	0.07	0.12–0.55
WEMMT (ms)	21.46	0.43	19.75–23.81
A1DLAR (mm^2)	0.17	0.03	0.10–0.26
HCDLAR (mm^2)	3.22	0.56	1.69–5.59
A2DLAR (mm^2)	0.24	0.25	0.03–5.88
A1DARCL (mm)	–0.02	0.01	–0.03–0.06
HCDARCL (mm)	–0.13	0.02	–0.23–0.01
A2DARCL (mm)	–0.02	0.02	–0.45–0.06
DARCLM (mm)	–0.15	0.03	–0.49–0.02
MIR (mm^{-1})	0.17	0.02	0.13–0.26
DARM (2 mm)	4.19	0.33	3.29–5.36
PS (μm)	48.25	9.27	1.62–76.94
DARM [1 mm]	1.58	0.05	1.43–1.80
ARTH	431.16	84.58	273.18–990.06
IR (mm^{-1})	8.09	0.93	5.42–10.71
SP-A1	103.53	17.52	59.49–163.20
CBI	0.11	0.13	0.00–0.44

TABLE 4 | Repeatability and reproducibility of the Corvis ST parameters in healthy eyes.

Parameter	Repeatability				Reproducibility			
	sw	CR	CV (%)	ICC(95%CI)	sw	CR	CV (%)	ICC(95%CI)
DAM (mm)	0.05	0.14	4.75	0.93 (0.91–0.94)	0.06	0.15	5.20	0.88 (0.82–0.92)
A1T (ms)	0.17	0.46	2.32	0.92 (0.91–0.94)	0.18	0.50	2.50	0.88 (0.82–0.92)
A1V (m/s)	0.01	0.02	6.03	0.92 (0.90–0.93)	0.01	0.03	6.80	0.87 (0.80–0.91)
A2T (ms)	0.16	0.45	0.74	0.94 (0.93–0.95)	0.18	0.51	0.84	0.90 (0.86–0.94)
A2V (m/s)	0.02	0.05	-6.12	0.92 (0.90–0.93)	0.02	-12.63	-6.45	0.87 (0.81–0.91)
HCT (ms)	0.37	1.01	2.16	0.65 (0.58–0.72)	0.38	1.06	2.26	0.53 (0.29–0.68)
PD (mm)	0.15	0.41	2.89	0.93 (0.91–0.94)	0.16	0.44	3.10	0.88 (0.82–0.92)
Radius (mm)	0.54	1.49	7.97	0.81 (0.77–0.85)	0.56	1.54	8.32	0.68 (0.53–0.79)
A1DA (mm)	0.01	0.02	5.70	0.84 (0.80–0.87)	0.01	0.02	6.13	0.75 (0.63–0.83)
HCDA (mm)	0.05	0.14	4.55	0.94 (0.92–0.95)	0.05	0.14	4.86	0.88 (0.82–0.92)
A2DA (mm)	0.03	0.08	8.74	0.93 (0.91–0.94)	0.03	0.10	9.71	0.87 (0.80–0.91)
A1DLL (mm)	0.12	0.34	5.55	0.83 (0.80–0.86)	0.13	0.35	5.79	0.76 (0.64–0.84)
HCDLL (mm)	0.22	0.61	3.33	0.92 (0.91–0.94)	0.24	0.66	3.63	0.87 (0.81–0.91)
A2DLL (mm)	0.38	1.04	14.60	0.82 (0.78–0.85)	0.38	1.07	15.04	0.68 (0.53–0.79)
A1DLA (mm)	0.01	0.02	6.54	0.84 (0.81–0.87)	0.01	0.02	7.60	0.69 (0.50–0.79)
HCDLA (mm)	0.04	0.12	4.68	0.96 (0.95–0.96)	0.05	0.14	5.32	0.91 (0.86–0.94)
A2DLA (mm)	0.01	0.03	9.51	0.86 (0.84–0.89)	0.01	0.03	9.95	0.67 (0.50–0.78)
DLAML (mm)	0.04	0.12	4.60	0.95 (0.94–0.96)	0.05	0.13	5.04	0.91 (0.86–0.94)
DLAMT (ms)	0.43	1.19	2.64	0.56 (0.47–0.64)	0.49	1.34	3.00	0.31 (0.03–0.53)
WEMML (mm)	0.03	0.09	12.02	0.92 (0.91–0.94)	0.03	0.09	12.23	0.88 (0.82–0.92)
WEMMT (ms)	0.26	0.71	1.19	0.86 (0.83–0.89)	0.28	0.78	1.31	0.75 (0.63–0.83)
A1DLAr (mm^2)	0.02	0.06	14.22	0.74 (0.74–0.82)	0.03	0.08	14.80	0.65 (0.47–0.76)
HCDLAr (mm^2)	0.22	0.60	6.37	0.96 (0.95–0.96)	0.22	0.62	6.54	0.93 (0.89–0.95)
A2DLAr (mm^2)	0.04	0.10	17.44	0.75 (0.75–0.83)	0.03	0.09	16.51	0.60 (0.41–0.73)
A1dArcL (mm)	0.00	0.01	−14.26	0.85 (0.81–0.88)	0.00	0.01	−15.57	0.79 (0.55–0.79)
HCdArcL (mm)	0.02	0.06	−18.12	0.85 (0.82–0.88)	0.02	0.06	−18.32	0.68 (0.53–0.79)
A2dArcL (mm)	0.00	0.01	−18.17	0.83 (0.79–0.86)	0.00	0.01	−18.33	0.82 (0.73–0.88)
dArcLM (mm)	0.02	0.06	−14.17	0.90 (0.88–0.92)	0.02	0.06	−14.38	0.83 (0.74–0.88)
New parameters								
MIR (mm^{-1})	0.01	0.04	7.37	0.87 (0.84–0.89)	0.01	0.04	7.72	0.74 (0.61–0.82)
DARM [2 mm]	0.36	0.10	7.70	0.89 (0.86–0.91)	0.36	1.00	7.84	0.77 (0.66–0.85)
PS (μm)	5.78	16.00	9.84	0.98 (0.97–0.98)	5.12	14.18	9.07	0.94 (0.91–0.96)
DARM [1 mm]	0.00	0.11	2.36	0.88 (0.85–0.90)	0.04	0.11	2.55	0.75 (0.63–0.83)
ARTh	26.31	72.87	6.62	0.99 (0.98–0.99)	26.77	74.16	6.69	0.98 (0.97–0.99)
bIOP (mmHg)	0.85	2.34	6.35	0.96 (0.95–0.97)	0.95	2.64	6.92	0.95 (0.92–0.96)
IR (mm^{-1})	0.47	1.29	5.27	0.96 (0.96–0.97)	0.52	1.44	5.90	0.91 (0.87–0.94)
SP-A1	6.21	17.20	7.29	0.97 (0.97–0.98)	6.50	18.01	7.66	0.95 (0.92–0.97)
CBI	0.13	0.37	17.69	0.91 (0.89–0.93)	0.13	0.37	18.54	0.82 (0.73–0.88)

CV, coefficient of variation; ICC, interclass correlation coefficient; CI, Confidence interval; RC, repeatability coefficient; Sw, within-subject SD.

TABLE 5 | Correlation of demographics/ocular characteristics and corneal biomechanical parameters.

Variables	Age(y)		IOP(mmHg)		CCT (μm)		bIOP(mmHg)		Km(D)		Astig(D)		ACV	
	rho	P	rho	P	Rho	P	rho	P	rho	P	Rho	P	rho	P
A1V (m/s)	0.106	0.013	−0.806	0.000	−0.177	0.000	−0.74	0.000	0.038	0.376	0.007	0.867	0.078	0.070
A2V (m/s)	0.003	0.948	0.667	0.000	0.064	0.14	0.643	0.000	0.017	0.691	−0.044	0.309	−0.134	0.002
PD (mm)	−0.093	0.030	−0.707	0.000	−0.140	0.001	−0.629	0.000	−0.364	0.000	0.003	0.951	0.319	0.000
Radius (mm)	0.065	0.130	0.255	0.000	0.211	0.000	0.179	0.000	−0.120	0.005	−0.187	0.000	−0.079	0.065
HCDLA (mm)	−0.038	0.377	−0.776	0.000	−0.159	0.000	−0.702	0.000	−0.155	0.000	0.033	0.447	0.279	0.000
WEMML (mm)	0.341	0.000	−0.034	0.432	0.018	0.675	-0.101	0.019	0.182	0.000	−0.148	0.001	−0.418	0.000
HCdArcL (mm)	−0.099	0.022	0.294	0.000	−0.166	0.000	0.357	0.000	−0.054	0.208	0.124	0.004	−0.007	0.876
DARM [1 mm]	−0.081	0.058	−0.524	0.000	−0.468	0.000	−0.357	0.000	0.161	0.000	0.061	0.155	0.217	0.000
DARM [2 mm]	0.001	0.978	−0.564	0.000	−0.464	0.000	−0.407	0.000	0.209	0.000	0.014	0.742	0.216	0.000
PS (μm)	−0.038	0.373	0.141	0.001	0.248	0.000	0.065	0.128	0.166	0.000	0.104	0.015	−0.348	0.000
ARTh	0.022	0.615	−0.049	0.251	0.144	0.001	−0.103	0.017	−0.161	0.000	−0.051	0.237	0.192	0.000
IR (mm^{-1})	0.004	0.936	−0.625	0.000	−0.328	0.000	−0.511	0.000	0.122	0.004	0.132	0.002	0.110	0.010
SP-A1	0.026	0.547	0.782	0.000	0.558	0.000	0.563	0.000	0.075	0.082	0.046	0.283	−0.229	0.000
CBI	−0.011	0.803	−0.208	0.000	−0.377	0.000	−0.082	0.057	0.105	0.014	−0.032	0.451	−0.035	0.412

p < *0.05 considered statistically significant. Rho: Pearson's correlation coefficient.*

TABLE 6 | Results of Stepwise Multiple Regression Analysis between Dynamic Corneal Response Parameters and demographics/ocular characteristics.

Variables	Age(y)*			IOP(mmHg)*			CCT (μm)*			bIOP(mmHg)*			Km(D)*			Astig(D)*			ACV*		
	B	Sta. β	P	β	Sta. β	P	B	Sta. β	P	B	Sta. β	P	β	Sta. β	P	B	Sta. β	P	β	Sta.β	P
A1V (m/s)				−38.532	−0.234	0.000	−582.718	−0.375	0.011	−44.827	−0.306	0.000									
A2V (m/s)										14.961	0.204	0.000									
PD (mm)	−4.179	−0.099	0.028	−2.978	−0.317	0.000	−28.777	−0.299	0.003	−2.608	−0.312	0.000									
Radius (mm)													−0.7.280	−1.521	0.000	−0.209	−0.218	0.000			
HCDLA (mm)													15.556	1.122	0.000						
WEMML (mm)	81.668	0.436	0.000							−8.423	−0.227	0.000				−1.467	−0.141	0.001	−182.982	−0.328	0.002
HCdArcL ([mm]	−76.032	−0.140	0.001																		
DARM [1 mm]				−14.777	−0.264	0.000	−105.792	−0.192	0.032	−9.080	−0.182	0.000									
DARM [2 mm]				1.095	0.124	0.006															
PS (μm)							0.917	0.282	0.005							0.012	0.148	0.000	−2.506	−0.533	0.000
ARTh							0.138	0.301	0.002	−0.004	−0.130	0.000									
IR (mm^{-1})				−0.329	−0.105	0.001															
SP-A1				0.052	0.312	0.000	1.586	0.925	0.000							−0.525	−0.211	0.040	−0.525	−0.211	0.040
CBI																					

Sta.β, Standardized regression coefficient (β); β, regression coefficient (β).

**The coefficients of determination (the adjusted R^2 value) in multiple linear regressions of age, IOP, CCT, bIOP, Km, Astig, and ACV, were 0.235, 0.782, 0.723, 0.675, 0.493, 0.087, and 0.459, respectively.*

and ACV were 0.235, 0.782, 0.723, 0.675, 0.493, 0.087, and 0.459, respectively.

DISCUSSION

In recent years, dynamic corneal response (DCR) parameters helped to optimize the interaction between the eye and several treatment and management procedures. The new DCR parameters that were developed with a software upgrade have shown good results in demonstrating biomechanical features in several eye diseases (Tian et al., 2021). A good example is the biomechanical fragility of the keratoconic cornea (Zhang et al., 2021b; Satitpitakul et al., 2021). To the best of our knowledge, a few studies have evaluated the repeatability and reproducibility of the new Corvis ST DCR parameters and bIOP in healthy participants (Matsuura et al., 2019; Serbecic et al., 2020; Wang et al., 2021; Ye et al., 2021). Moreover, the present study was the largest study of corneal biomechanics that explored the association between DCR parameters (provided by Corvis ST incorporating the latest software) and several demographic and ocular characteristics in a Chinese healthy population.

With the new software version in place, the repeatability and reproducibility of the recalculated biomechanical parameters were quite improved. The present study observed that the repeatability and reproducibility of 37 Corvis ST parameters in healthy eyes were good. Kaili Yang et al. found that 46.15% of all the 37 parameters showed excellent repeatability, 25.64% parameters reflected good repeatability, and 28.21% parameters fell under the poor to moderate repeatability range in Chinese healthy eyes. These results were slightly worse than the ones presented in this study, which are 54.05, 37.84, and 8.11%, respectively (Yang et al., 2019). The present study found that A1T, A1V, A2T, A2V, PD, HCDA, A2DA, A1DLL, HCDLL, HCDLA, DLAML, WEMML, WEMMT, HCDLAr, and A1dArcL showed excellent or good repeatability and reproducibility with CV values that are below 20%. Compared with previous studies, we observed a significant decrease of CV values and an increase of ICC values in most DCR parameters (Ali et al., 2014; Wu and Tian, 2016). The results might be due to software upgrade and different population selection. In our study, the CV, CR, and ICC of reproducibility were comparable as far as repeatability was concerned but showed slightly higher values overall. Reproducibility was determined by the random combination of factors such as subject, device, and interactions between the participants and the device (Herber et al., 2020; Serbecic et al., 2020). The controversial results might be due to usage of different devices, varying software versions, and dissimilar population selection.

The results from this study showed that the new parameters had relatively high ICC and low CV values, which was consistent with previous studies to some extent (Vinciguerra et al., 2016a; Roberts et al., 2017). In this study, the new parameters ARTh, IR, SP-A1, CBI, and PS had excellent repeatability and MIR, DARM [1 mm], DARM [2 mm] had good repeatability. The CVs of these parameters were all below 10%. These results were consistent with what Yang and colleagues (Yang et al., 2019) found in that the

new parameters presented good repeatability in Chinese healthy eyes. The CV values of CBI were higher than those of other parameters. This might have been caused by the fact that the CBI was a combined parameter that was calculated by a logistic regression analysis, which could result in a large deviation among all the measurements. The bIOP results showed very good sw values for repeatability and reproducibility and this was consistent the findings by Lopesand colleagues(Koprowski et al., 2015). who found that IOP and bIOP presented low CV and sw values in Germany, Italy, and Brazil populations.

Stepwise multiple regression analysis results showed that age increased with larger WEMML, as well as smaller HCdArcL and PD. The WEMML contributed the most for age on the basis of the standardized partial regression coefficient. Several studies reported that the age of the participants exhibited a significant correlation with several corneal biomechanical parameters (Elsheikh et al., 2007; Lee et al., 2018). The studies by Lee et al. and Elsheikh et al. experimentally showed that cornea considerably stiffened with age. An older cornea would probably show lower PD and HCdArcL values. The correlation between WEMML and age might be caused by the changes in the retrobulbar fat composition that occur as years go by. The alterations in retrobulbar fat composition may in turn lead to changes that are associated with ocular displacement under the air puff (Regensburg et al., 2011).

In previous studies, the CCT had crucial influence on the DCR parameters that are provided by the Corvis ST (Daxer et al., 1998). In this study, the CCT was negatively associated with several corneal deformation parameters, such as A1V and DARM [1 mm], thereby suggesting greater deformation during applanation in eyes with thin corneas. In particular, the CCT positively correlated with a new parameter called the SP-A1, which serves as a biomarker for corneal stiffness. The SP-A1 value was reported to be lower in thinner cornea than it is in healthy ones (Vinciguerra et al., 2016a; Zhao et al., 2019). Vinciguerra R and colleagues found that there was a statistically significant decrease in stiffness parameters (SP-A1) and a significant increase in DARM [1 mm] after the PRK and PRK procedure combined with the LASIK procedure. It almost aligns with present results (Vinciguerra et al., 2016b).

In terms of measuring DCR parameters, IOP has a significant impact (Vinciguerra et al., 2016b). In the present study, IOP increased with smaller A1V, DARM [1 mm], IR, as well as larger SP-A1. The PD and SP-A1 contributed the most based on standardized partial regression coefficient, reflecting that corneal stiffness substantially contributes to IOP. Another research study demonstrated that there was a positive linear association between Young's modulus and IOP by analyzing the stiffness of 37 corneas from human donors (Elsheikh et al., 2008). Moreover, the above results indicate that the cornea is less likely to deform when IOP is high.

The bIOP correction aims to reduce the influence of the cornea's thickness and age in exhibiting reality IOP values. The bIOP correction has been successfully applied in the estimation of true IOP in *ex vivo* tests that were conducted on human donor eye globes (Eliasy et al., 2018). In the present study, the result of multivariate linear regression models indicated that the PS was more influenced by the CCT but not significantly affected by the bIOP. This finding demonstrated that PS is a good parameter to correctly evaluate *in vivo* corneal biomechanics because of their relative independence from IOP. Furthermore, we found that the bIOP was negatively associated with the A1V, although it was positively associated with A2V. The reason for this may lie in the fact that A2V is not only affected by corneal resistance as it also relates to the viscous damping characteristics of the cornea. The above results might be due to the tissue's viscous damping property or hysteresis [23].

The anterior chamber may also have some effects on DCR parameters. In this study, the results of multivariable linear model showed that ACV increased with smaller SP-A1, WEMML, and PS. In one study, the researchers found that bigger ACV values were associated with lower HCDA values (Cui et al., 2019). Just like the HCDA, HCDLA eliminates the influence of eye movement. Therefore, bigger ACV values might cause limited eye movement. Furthermore, ACV increased with smaller PS and ARTH. This may suggest that the change of corneal thickness in the central region is larger than it is in the peripheral region. This is due to changes in corneal tension as influenced by high ACV. According to your findings, Nemeth et al., (2017) reported conflicting results compared with ours, with regard to the relationship between ACV and DCR parameters. The explanation to this might be that the participants and parameters for both studies were different. Another possible reason was that ACV could be influenced by a number of factors, such as corneal area, anterior chamber volume, and chamber angle whose association with DCR parameters were not proved. Therefore, further studies are required to expound the association between various factors and the DCR parameters and ACV.

Furthermore, we discovered that Km significantly correlated with PD and HCDLA. These results supported the notion that corneal deformation responses are associated with not only biomechanical properties of the cornea, but the corneal geometric factors, such as Km as well (Fontes et al., 2008; Kamiya et al., 2009).

The coefficient of determination (the R^2 value) in multiple linear regressions of Astig was 0.087, which is lower than other parameter values. This implies that the variations in DCR parameters explain about 8.7% of the variance of Astig, which implies that Astig was not significantly associated with the biomechanical properties of the eye.

The advantage of this study lies in the large sample size, homogeneous Chinese population origin, and the use of the latest software with new parameters. However, the present study has some limitations. First, as this study only focused on healthy Chinese population, it is not known whether these results can be generalized to other ethnicities, as well as to individuals with other diseases. Second, this study was an observational cross-sectional study that may limit causal inferences.

In conclusion, we profile DCR and bIOP parameters in corneal biomechanical properties as measured by Corvis ST in a large, healthy Chinese population. IOP, CCT, bIOP, Km, and ACV were significantly associated with the DCR parameters of the eye. These results may be relevant for studying the role of altered

corneal biomechanics in ocular diseases. As the Corvis ST is a relatively new technology, the applicability and feasibility of this technique in characterizing corneal biomechanics need further investigation.

DATA AVAILABILITY STATEMENT

The raw data supporting the conclusion of this article will be made available by the authors, without undue reservation.

ETHICS STATEMENT

The studies involving human participants were reviewed and approved by the office of Research Ethics Committee of Beijing TongRen Hospital affiliated to Capital Medical University. Written informed consent to participate in this study was provided by the participants' legal guardian/next of kin. Written informed consent was obtained from the individual(s), and minor(s)' legal guardian/next of kin, for the publication of any potentially identifiable images or data included in this article.

AUTHOR CONTRIBUTIONS

YJ and LT: Corresponding author, conception, and design of the study; YL: acquisition, analysis, and interpretation of the data, drafting the article. L-LG: acquisition of the data. YH: revise the article. All authors read and approved the final manuscript.

FUNDING

This research was supported by "The Youth Beijing Scholars program", Natural Science Foundation of China (82171101), and the Open Research Fund from Beijing Advanced Innovation Center for Big Data-Based Precision Medicine, Beijing Tongren Hospital, Beihang University & Capital Medical University (BHTR-KFJJ-202001).

REFERENCES

Ali, N. Q., Patel, D. V., and Mcghee, C. N. J. (2014). Biomechanical Responses of Healthy and Keratoconic Corneas Measured Using a Noncontact Scheimpflug-Based Tonometer. *Invest. Ophthalmol. Vis. Sci.* 55, 3651–3659. doi:10.1167/iovs.13-13715

Bao, F., Geraghty, B., Wang, Q., and Elsheikh, A. (2016). Consideration of Corneal Biomechanics in the Diagnosis and Management of Keratoconus: Is it Important? *Eye Vis.* 3, 18. doi:10.1186/s40662-016-0048-4

Chen, K. J., Joda, A., Vinciguerra, R., Eliasy, A., Shervin, M. M. S., Kook, D., et al. (2018). Clinical Evaluation of a New Correction Algorithm for Dynamic Scheimpflug Analyzer Tonometry before and after Laser Insitu Keratomileusis and Small-Incision Lenticule Extraction. *J. Cataract Refractive Surg.* 44(5):581-588. doi:10.1016/j.jcrs.2018.01.023

Cui, X., Yang, Y., Li, Y., Huang, F., Zhao, Y., Chen, H., et al. (2019). Correlation between Anterior Chamber Volume and Corneal Biomechanical Properties in Human Eyes. *Front. Bioeng. Biotechnol.* 7, 379. doi:10.3389/fbioe.2019.00379

Daxer, A., Misof, K., Grabner, B., Ettl, A., and Fratzl, P. (1998). Collagen Fibrils in the Human Corneal Stroma: Structure and Aging. *Invest. Ophthalmol. Vis. Sci.* 39, 644–648.

Eliasy, A., Chen, K.-J., Vinciguerra, R., Maklad, O., Vinciguerra, P., Ambrósio, R., JR., et al. (2018). Ex-vivo Experimental Validation of Biomechanically-Corrected Intraocular Pressure Measurements on Human Eyes Using the CorVis ST. *Exp. Eye Res.* 175, 98–102. doi:10.1016/j.exer.2018.06.013

Elsheikh, A., Alhasso, D., and Rama, P. (2008). Biomechanical Properties of Human and Porcine Corneas. *Exp. Eye Res.* 86, 783–790. doi:10.1016/j.exer.2008.02.006

Elsheikh, A., Wang, D., Brown, M., Rama, P., Campanelli, M., and Pye, D. (2007). Assessment of Corneal Biomechanical Properties and Their Variation with Age. *Curr. Eye Res.* 32, 11–19. doi:10.1080/02713680601077145

Flockerzi, E., Häfner, L., Xanthopoulou, K., Daas, L., Munteanu, C., Langenbucher, A., et al. (2021). Reliability Analysis of Successive Corneal Visualization Scheimpflug Technology Measurements in Different Keratoconus Stages. *Acta ophthalmologica*. 100(1):e83-e90. doi:10.1111/aos.14857

Fontes, B. M., Ambrósio, R., JR., Alonso, R. S., Jardim, D., Velarde, G. C., and Nosé, W. (2008). Corneal Biomechanical Metrics in Eyes with Refraction of -19.00 to +9.00 D in Healthy Brazilian Patients. *J. Refract. Surg.* 24, 941–945. doi:10.3928/1081597X-20081101-14

Greenstein, S. A., Fry, K. L., and Hersh, P. S. (2012). *In Vivo* biomechanical Changes after Corneal Collagen Cross-Linking for Keratoconus and Corneal Ectasia: 1-year Analysis of a Randomized, Controlled, Clinical Trial. *Cornea* 31, 21–25. doi:10.1097/ico.0b013e31821eea66

Guo, L. L., Tian, L., Cao, K., Li, Y. X., Li, N., Yang, W. Q., et al. (2021). Comparison of the Morphological and Biomechanical Characteristics of Keratoconus, Forme Fruste Keratoconus, and normal Corneas. *Semin. Ophthalmol.* 36, 671–678. doi:10.1080/08820538.2021.1896752

Henriquez, M. A., Gomez, I., Camino-Quezada, M., Izquierdo, L., Chauca, J., and Binder, P. S. (2022). Repeatability of Corneal Deformation Response Parameters by Dynamic Ultra High-Speed Scheimpflug Imaging in Normal and Keratoconus Eyes. *Eye & Contact Lens* 48, 14–19. doi:10.1097/icl.0000000000000845

Herber, R., Vinciguerra, R., Lopes, B., Raiskup, F., Pillunat, L. E., Vinciguerra, P., et al. (2020). Repeatability and Reproducibility of Corneal Deformation Response Parameters of Dynamic Ultra-high-speed Scheimpflug Imaging in Keratoconus. *J. Cataract Refract. Surg.* 46, 86–94. doi:10.1016/j.jcrs.2019.08.034

Hirasawa, K., Nakakura, S., Nakao, Y., Fujino, Y., Matsuura, M., Murata, H., et al. (2018). Changes in Corneal Biomechanics and Intraocular Pressure Following Cataract Surgery. *Am. J. Ophthalmol.* 195, 26–35. doi:10.1016/j.ajo.2018.07.025

Hollman, K. W., Shtein, R. M., Tripathy, S., and Kim, K. (2013). Using an Ultrasound Elasticity Microscope to Map Three-Dimensional Strain in a Porcine Cornea. *Ultrasound Med. Biol.* 39, 1451–1459. doi:10.1016/j.ultrasmedbio.2013.02.465

Jędzierowska, M., and Koprowski, R. (2019). Novel Dynamic Corneal Response Parameters in a Practice Use: A Critical Review. *BioMedical Eng. OnLine* 18.

Joda, A. A., Shervin, M. M. S., Kook, D., and Elsheikh, A. (2015). Development and Validation of a Correction Equation for Corvis Tonometry. *Computer Methods Biomech. Biomed. Eng.*, 19(9):943-53. doi:10.1080/10255842.2015.1077515

Kamiya, K., Shimizu, K., and Ohmoto, F. (2009). Effect of Aging on Corneal Biomechanical Parameters Using the Ocular Response Analyzer. *J. Refract. Surg.* 25, 888–893. doi:10.3928/1081597x-20090917-10

Koprowski, R., Ambrósio, R., and Reisdorf, S. (2015). Scheimpflug Camera in the Quantitative Assessment of Reproducibility of High-Speed Corneal Deformation during Intraocular Pressure Measurement. *J. Biophoton.* 8, 968–978. doi:10.1002/jbio.201400137

Krysik, K., Wroblewska-Czajka, E., Lyssek-Boron, A., Wylegala, E. A., and Dobrowolski, D. (2018). Total Penetrating Keratoplasty: Indications, Therapeutic Approach, and Long-Term Follow-Up. *J. Ophthalmol.*, 2018: 9580292.

Lee, H., Kang, D. S. Y., Ha, B. J., Choi, J. Y., Kim, E. K., Seo, K. Y., et al. (2018). Biomechanical Properties of the Cornea Using a Dynamic Scheimpflug Analyzer in Healthy Eyes. *Yonsei Med. J.* 59, 1115–1122. doi:10.3349/ymj.2018.59.9.1115

Luce, D. A. (2005). Determining *In Vivo* Biomechanical Properties of the Cornea with an Ocular Response Analyzer. *J. Cataract Refract. Surg.* 31, 156–162. doi:10.1016/j.jcrs.2004.10.044

Matsuura, M., Murata, H., Fujino, Y., Yanagisawa, M., Nakao, Y., Nakakura, S., et al. (2019). Repeatability of the Novel Intraocular Pressure Measurement from Corvis ST. *Trans. Vis. Sci. Tech.* 8, 48. doi:10.1167/tvst.8.3.48

Nemeth, G., Szalai, E., Hassan, Z., Lipecz, A., Flasko, Z., and Modis, L. (2017). Corneal Biomechanical Data and Biometric Parameters Measured with Scheimpflug-Based Devices on normal Corneas. *Int. J. Ophthalmol.* 10, 217–222. doi:10.18240/ijo.2017.02.06

Regensburg, N. I., Wiersinga, W. M., Van Velthoven, M. E. J., Berendschot, T. T. J. M., Zonneveld, F. W., Baldeschi, L., et al. (2011). Age and Gender-specific Reference Values of Orbital Fat and Muscle Volumes in Caucasians. *Br. J. Ophthalmol.* 95, 1660–1663. doi:10.1136/bjo.2009.161372

Reinprayoon, U., Jermjutitham, M., and Kasetsuwan, N. (2021). Rate of Cornea Endothelial Cell Loss and Biomechanical Properties in Fuchs' Endothelial Corneal Dystrophy. *Front. Med.* 8, 757959. doi:10.3389/fmed.2021.757959

Robert, H., Lisa, R., Eberhard, S., Frederik, R., and Lutz, E. P. (2019). Assessment of Corneal Biomechanical Parameters in Healthy and Keratoconic Eyes Using Dynamic Bidirectional Applanation Device and Dynamic Scheimpflug Analyzer. *J. Cataract Refractive Surg.* 45(6):778-788. doi:10.1016/j.jcrs.2018.12.015

Roberts, C. J., and Dupps, W. J., JR. (2014). Biomechanics of Corneal Ectasia and Biomechanical Treatments. *J. Cataract Refract. Surg.* 40, 991–998. doi:10.1016/j.jcrs.2014.04.013

Roberts, C. J., Mahmoud, A. M., Bons, J. P., Hossain, A., Elsheikh, A., Vinciguerra, R., et al. (2017). Introduction of Two Novel Stiffness Parameters and Interpretation of Air Puff-Induced Biomechanical Deformation Parameters with a Dynamic Scheimpflug Analyzer. *J. Refract. Surg.* 33, 266–273. doi:10.3928/1081597x-20161221-03

Salouti, R., Razeghinejad, R., Eslami, G., Zare, M., Salouti, K., Ghoreyshi, M., et al. (2022). *Agreement of Ocular Response Analyzer Cornea Compensated IOP with Corvis ST Biomechanical IOP Following Femtosecond Laser-Assisted LASIK*. London, England: Eye.

Satitpitakul, V., Taweekitikul, P., Puangsricharern, V., Kasetsuwan, N., Reinprayoon, U., and Kittipibul, T. (2021). Alteration of Corneal Biomechanical Properties in Patients with Dry Eye Disease. *PloS One* 16, e0254442. doi:10.1371/journal.pone.0254442

Serbecic, N., Beutelspacher, S., Markovic, L., Roy, A. S., and Shetty, R. (2020). Repeatability and Reproducibility of Corneal Biomechanical Parameters Derived from Corvis ST. *Eur. J. Ophthalmol.* 30, 1287–1294. doi:10.1177/1120672119864554

Shen, Y., Chen, X., Xian, Y., Wang, X., Wang, X., and Zhou, X. (2022). Safety of Intraocular Pressure Measurement Using Air-Puff Tonometer Following Implantable Collamer Lens Implantation. *J. Cataract Refractive Surg.*. doi:10.1097/j.jcrs.0000000000000886 https://journals.lww.com/jcrs/Abstract/9000/Safety_of_intraocular_pressure_measurement_using.99359.aspx.

Tian, L., Zhang, H., Guo, L.-L., Qin, X., Zhang, D., Li, L., et al. (2021). Distribution of Corneal Geometric Landmarks and Relationship between Their Distances and Biomechanical Parameters in the Development of Keratoconus. *Front. Bioeng. Biotechnol.* 9, 766163. doi:10.3389/fbioe.2021.766163

Vinciguerra, R., Ambrósio, R., JR., Elsheikh, A., Roberts, C. J., Lopes, B., Morenghi, E., et al. (2016a). Detection of Keratoconus with a New Biomechanical Index. *J. Refract. Surg.* 32, 803–810. doi:10.3928/1081597x-20160629-01

Vinciguerra, R., Ambrósio, R., JR., Roberts, C. J., Azzolini, C., and Vinciguerra, P. (2017a). Biomechanical Characterization of Subclinical Keratoconus without Topographic or Tomographic Abnormalities. *J. Refract. Surg.* 33, 399–407. doi:10.3928/1081597x-20170213-01

Vinciguerra, R., Elsheikh, A., Roberts, C. J., Ambrósio, R., JR., Kang, D. S. Y., Lopes, B. T., et al. (2016b). Influence of Pachymetry and Intraocular Pressure on Dynamic Corneal Response Parameters in Healthy Patients. *J. Refract. Surg.* 32, 550–561. doi:10.3928/1081597x-20160524-01

Vinciguerra, R., Romano, V., Arbabi, E. M., Brunner, M., Willoughby, C. E., Batterbury, M., et al. (2017b). *In Vivo* Early Corneal Biomechanical Changes after Corneal Cross-Linking in Patients with Progressive Keratoconus. *J. Refract. Surg.* 33, 840–846. doi:10.3928/1081597x-20170922-02

Wang, X., Mcalinden, C., Zhang, H., Yan, J., Wang, D., Wei, W., et al. (2021). Assessment of Corneal Biomechanics, Tonometry and Pachymetry with the Corvis ST in Myopia. *Sci. Rep.* 11, 3041. doi:10.1038/s41598-020-80915-9

Wu, Y., and Tian, L. (2016). *In Vivo* Corneal Biomechanical Properties with Corneal Visualization Scheimpflug Technology in Chinese Population. *Biomed. Res. Int.* 2016, 7840284.

Yang, K., Xu, L., Fan, Q., Zhao, D., and Ren, S. (2019). Repeatability and Comparison of New Corvis ST Parameters in normal and Keratoconus Eyes. *Sci. Rep.* 9, 15379. doi:10.1038/s41598-019-51502-4

Ye, Y., Li, Y., Zhu, Z., Abu Said, A. Z. M., Nguelemo Mayopa, K., Akiti, S., et al. (2021). Effect of Mydriasis-Caused Intraocular Pressure Changes on Corneal Biomechanical Metrics. *Front. Bioeng. Biotechnol.* 9, 751628. doi:10.3389/fbioe.2021.751628

Zhang, D., Zhang, H., Tian, L., Zheng, Y., Fu, C., Zhai, C., et al. (2021a). Exploring the Biomechanical Properties of the Human Cornea *In Vivo* Based on Corvis ST. *Front. Bioeng. Biotechnol.* 9, 771763. doi:10.3389/fbioe.2021.771763

Zhang, H., Tian, L., Guo, L., Qin, X., and Zhang, H. (2021b). Comprehensive Evaluation of Corneas from normal, Forme Fruste Keratoconus and Clinical Keratoconus Patients Using Morphological and Biomechanical Properties. *Int. Ophthalmol.*, 41(4):1247-1259. doi:10.1007/s10792-020-01679-9

Zhao, Y., Shen, Y., Yan, Z., Tian, M., Zhao, J., and Zhou, X. (2019). Relationship Among Corneal Stiffness, Thickness, and Biomechanical Parameters Measured by Corvis ST, Pentacam and ORA in Keratoconus. *Front. Physiol.* 10, 740. doi:10.3389/fphys.2019.00740

Ziaei, M., Yoon, J. J., Vellara, H. R., Gokul, A., Meyer, J. J., Thakur, S. S., et al. (2021). Prospective One Year Study of Corneal Biomechanical Changes Following High Intensity, Accelerated Cornea Cross-Linking in Patients with Keratoconus Using a Non-contact Tonometer. *Eur. J. Ophthalmol.* 32 (2), 806–814. doi:10.1177/11206721211069740

Conflict of Interest: The authors declare that the research was conducted in the absence of any commercial or financial relationships that could be construed as a potential conflict of interest.

frontiers | Frontiers in Bioengineering and Biotechnology

ORIGINAL RESEARCH
published: 14 April 2022
doi: 10.3389/fbioe.2022.862969

Biomechanical Evaluation of Decellularized and Crosslinked Corneal Implants Manufactured From Porcine Corneas as a Treatment Option for Advanced Keratoconus

Abby Wilson[1,2]*, *John Jones*[3] and *John Marshall*[2]

[1]UCL Mechanical Engineering, London, United Kingdom, [2]Institute of Ophthalmology, UCL, London, United Kingdom, [3]Laser Optical Engineering Ltd., Donington, United Kingdom

Currently corneal transplantation is the main treatment for late-stage keratoconus; however, transplantation procedures are accompanied by significant risk of post-surgical complications; this in addition to supply limitations imposed by a worldwide shortage of human donor corneas, has driven the development of alternative therapies. One such therapy is the use of corneal implants derived from porcine corneas (Xenia®, Gebauer Medizintechnik GmbH, Neuhausen, DE). In contrast to human donor tissue, these implants can be produced on demand and due to the processes used pose no risks for host-immune rejection. Their use has already been demonstrated clinically in patients for preventing the progression of topographic changes in keratoconus whilst improving visual acuity. The implants are derived from natural tissue and not standardised synthetic material, whilst this likely reduces the risk of issues with bio-incompatibility, there is inevitably variability in their intrinsic mechanical properties which requires investigation. Here, speckle interferometry is employed to examine the biomechanical properties, in response to physiologically representative forces, of native porcine corneal tissue prior to processing and after a proprietary 4-stage process involving decellularization, washing, compression and crosslinking. The control lenticules had an average Young's modulus (E) of 11.11 MPa (range 8.39–13.41 MPa), following processing average E of the lenticules increased by 127% over that of the unprocessed tissue to 25.23 MPa (range 18.32–32.9 MPa). The variability in E of the lenticules increased significantly after processing suggesting variability in the propensity of the native tissue to processing. In summary, it is possible to produce thin (<90 µm) lenticules from porcine corneas with enhanced stiffness that are effective for treating late-stage keratoconus. Due to the observed variability in the responses of lenticules to processing, interferometry could be a useful technique for ensuring quality control in commercial production via biomechanical screening.

Keywords: keratoconus, implants, crosslinking, decellularization, interferometry, xenotransplantation, corneal biomechanics

OPEN ACCESS

Edited by:
FangJun Bao, Affiliated Eye Hospital of Wenzhou Medical College, China

Reviewed by:
Tamer Anwar Esmail Ahmed, University of Ottawa, Canada
Manmohan Singh, University of Houston, United States

***Correspondence:**
Abby Wilson
abby.wilson@ucl.ac.uk

Specialty section:
This article was submitted to Biomechanics, a section of the journal Frontiers in Bioengineering and Biotechnology

Received: *26 January 2022*
Accepted: *14 March 2022*
Published: *14 April 2022*

Citation:
Wilson A, Jones J and Marshall J (2022) Biomechanical Evaluation of Decellularized and Crosslinked Corneal Implants Manufactured From Porcine Corneas as a Treatment Option for Advanced Keratoconus. Front. Bioeng. Biotechnol. 10:862969. doi: 10.3389/fbioe.2022.862969

INTRODUCTION

There is a large variability in the reported incidence of keratoconus (Gokhale, 2013) with one publication showing it to be as high as 1 in 375 people worldwide (Godefrooij et al., 2017a). Diagnosis is often made after significant topographic changes have occurred as a result of the progressive biomechanical decompensation that takes place due to the presence of localised abnormalities in the stroma (Roy et al., 2013). The incidence of mild 'sub-clinical' keratoconus may be far in excess of these reported values, but it remains largely undetected due to the sensitivity restrictions of currently available diagnostic tools (Wilson and Marshall, 2020). On diagnosis, patients often have perceivable visual abnormalities which without treatment progressively worsen over time. Treatment options vary from contact lenses, intra-ocular lenses (IOL's), topography-guided keratoplasty, corneal crosslinking (CXL) (Andreanos et al., 2017) and in more advanced-stages of the disease—corneal transplant surgery in the form of penetrating keratoplasty (PK) or the generally preferred—deep anterior lamellar keratoplasty (DALK) (Parker et al., 2015; Andreanos et al., 2017) due to its advantages with regards to maintaining the patient's own endothelium.

Until recently corneal transplant surgery has been the only effective treatment for late-stage keratoconus, however it has several constraints in terms of both procedural challenges and a limited tissue supply bank. Transplantation procedures are often long and difficult, relying upon highly skilled and experienced surgeons. They carry significant risk of post-operative complications including infection, glaucoma, cataracts, and host immune-rejection (Koo et al., 2011) with reported rejection rates ranging from 2% up to 68% (Andreanos et al., 2017). Visual outcomes take several months to stabilise and are generally sub-optimal, with the procedures themselves contributing to astigmatism resulting in patients requiring either complex glasses or contact lenses for refractive correction post-surgery (Andreanos et al., 2017). All these factors contribute to a high economic cost for disease management, alongside a cost to the patient both in monetary terms and with regards to their quality of life. Furthermore, with over 12.7 million people currently waiting for corneal transplant, there is a significant shortage of donor tissue worldwide (Williams and Muir, 2018) with around 185,000 procedures being performed per year, meeting the needs of approximately 1 in every 70 patients (Gain et al., 2016). The United Kingdom falls short by approximately 1,500 corneas every year (Gaum et al., 2012), leading to long waiting times for patients, again impacting their quality of life and ability to work whilst living with severe visual impairment. In the United Kingdom, the economic cost of visual impairment per person may be in excess of £10,000 per annum (Pezzullo et al., 2018), hence, improving current treatment options for late-stage keratoconus and solving the restrictions posed by the current tissue shortage is of high importance.

To address some of these issues, recently, Bowman's layer transplantation (BLT) surgery, where isolated human donor Bowman's layer is inserted into a mid-stromal pocket in keratoconic corneas (Dragnea et al., 2018), has been attempted to address advanced cases of keratoconus, with some success (Van Dijk et al., 2014; van Dijk et al., 2015). It has advantages over traditional corneal transplant surgery as it is a suture-less procedure and the tissue is acellular, reducing recovery times and graft rejection rates (Dragnea et al., 2018). It also makes use of corneas that are otherwise unsuitable for transplantation due to poor endothelium quality, however, still relies on a limited tissue resource, and currently isolation of the Bowman's layer is performed manually and is challenging with reported failure rates of up to 30% (García de Oteyza et al., 2019). Ideal treatment alternatives to corneal transplant surgery for treating both early and later-stage keratoconus are those that do not rely on human tissue supply, and this is where many research efforts are now focussed.

One treatment, aimed at reinforcing biomechanically compromised corneas, which has shown potential for treating late-stage disease (El-Massry et al., 2021) is Xenia® corneal implants (Gebauer Medizintechnik GmbH, Neuhausen, DE). An increasing number of patients are now undergoing this treatment with several now with over 12 months follow-up (El-Massry et al., 2021).

Xenia® corneal implants are created by processing porcine corneal stroma. Due to several structural (Sharifi et al., 2019; Subasinghe et al., 2021) and biomechanical similarities (Zeng et al., 2001; Elsheikh et al., 2008) of porcine and human corneal tissue, the baseline material from which the Xenia® implants are derived, although not identical, more closely resembles the properties and structure of the human cornea in contrast to implants manufactured from synthetic alternatives. Currently available synthetic alternatives have shown poor long-term success rates, which is thought in-part to be due to their bio-incompatibility. Common complications include corneal melt around the prosthetic and the development of glaucoma with long-term adjunct therapies required to try to prevent these conditions (Akpek et al., 2014; Nonpassopon et al., 2020). Hence a drive towards the development of implants centred around natural and structurally similar materials.

To form Xenia® lenticules, tissue obtained from the central anterior portion of porcine corneas, comprising the Bowman's layer (the presence of which has recently been confirmed (Hammond et al., 2020) after some controversy over its existence in pigs) and most anterior portion of stroma, is subjected to a four-stage process. This process involves: de-cellularisation which remove cells, antibodies and antigens negating the risk of rejection by the patient's immune system; washing; compression; and crosslinking to reduce the thickness and increase the stiffness of the lenticule relative to normal corneal tissue, which is important for stabilisation and reshaping of the keratoconic cornea. As with BLT, the Xenia® implant is inserted into the cornea via a pocket in the stroma that is created by a femtosecond laser, once inserted it acts as a splint to increase corneal stiffness and resistance to intraocular pressure, which in turn has been shown to have positive effects on corneal topography (El-Massry et al., 2021). Overall, the Xenia® implant has several significant advantages over conventional corneal transplant surgery; it is a minimally invasive procedure

requiring only topical anaesthetic enabling it to be performed in an out-patient setting, significantly reducing treatment costs and time; it is suture-less meaning faster recovery, lower risk of complications and better visual outcomes. In addition, because Xenia® implants can be used to slightly increase the thickness of the cornea they have the potential to be used to enable other treatments such as corneal crosslinking (CXL) in patients with thinner corneas which may act to further improve stability and visual outcomes (El-Massry et al., 2021).

Further to the aforementioned benefits, with future research these implants may have the potential to be tailored to individual patients to optimise refractive outcomes without the need to remove tissue from the cornea as in traditional laser refractive surgery procedures, which can have negative implications for overall biomechanics (Wolle et al., 2016; Fernández et al., 2018), and increase the risks associated with potential follow-up procedures such as CXL. Hence, they could ultimately prove to be an effective treatment option for both early and late-stage keratoconus.

With biomechanical abnormality being central to the progression of topographic abnormality and visual deterioration in keratoconus, most treatments are centred around preventing the consequences of this. Hence, biomechanical evaluation of the effects of potential treatment options plays a key role in their development and clinical adoption.

A better understanding of the biomechanics of Xenia® implants and their effect on the biomechanics of the host cornea is required to enable optimisation of this treatment in terms of safety, efficacy and the quality of visual outcomes. The biomechanics of the cornea and its resistance to intra-ocular pressure (IOP) is what governs its unique shape and hence refractive properties, as such it is important to understand how the insertion of an implant affects the whole system. Furthermore, as the implants are formed from material derived from biological tissue, a greater understanding of the potential variability of biomechanical properties across implants is required, in addition to a better understanding of the individual biomechanics of the system into which it is inserted. Pilot studies of CXL for both keratoconus (O'Brart et al., 2015) and myopia (Juthani and Chuck, 2021) have shown that there is variability between patients with regards to their response to crosslinking treatments, hence the same is likely to be true of the porcine tissue from which the lenticules are formed. With a better understanding of these factors, it may be possible to accurately control the biomechanical properties of individual implants and in doing so manufacture implants with customised properties for an individual's cornea, or to quantify and standardise the properties of implants used in surgery.

Understanding tissue biomechanics in response to physiologically representative loads is important when dealing with biological tissues, such as the cornea, as they possess viscoelastic properties, resulting in different properties in response to loads of different magnitudes and loading rates (Elsheikh et al., 2007). Since it is of importance to understand how the materials will behave *in vivo*, physiological loads must be replicated. Recently, speckle interferometry has been shown to be a useful method for examining the load-deformation response of corneal tissue in response to pulsatile loads representative of those that occur over a normal cardiac cycle (Wilson et al., 2016; Wilson et al., 2020; Wilson et al., 2021). This empirical data highlighted that speckle interferometry could be a useful tool to assess the load deformation response of Xenia® implants as it has high sensitivity enabling deformation to be quantified with an accuracy of 10s of nanometres, providing high resolution displacement maps in response to pressure changes equivalent to those that occur over a normal cardiac cycle.

The present study investigates the effects of processing (decellularization, washing, compression and crosslinking) on the mechanical strength of porcine cornea lenticules used for Xenia® implants. This is achieved by using displacement speckle pattern interferometry (DSPI) to examine the load-deformation response of samples to pulsatile, physiologically representative, pressure variations.

METHODS AND MATERIALS

Lenticules

Six control lenticules that had not been subjected to any processing and four processed lenticules were prepared for measurement, the lenticules were dissected from porcine corneas obtained from Schlachthof e.G., 71116 Gaertringen, DE. The lenticules were 9 mm in diameter and obtained from the anterior surface of the central porcine corneal stroma, with thicknesses between 190–210 μm prior to processing. Four of the

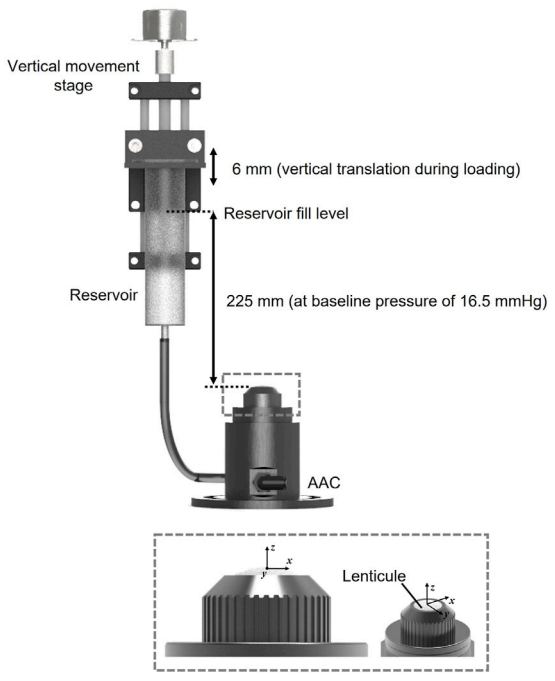

FIGURE 1 | Diagram of loading system configuration and the custom artificial anterior chamber (AAC) with 7 mm aperture into which lenticules were clamped.

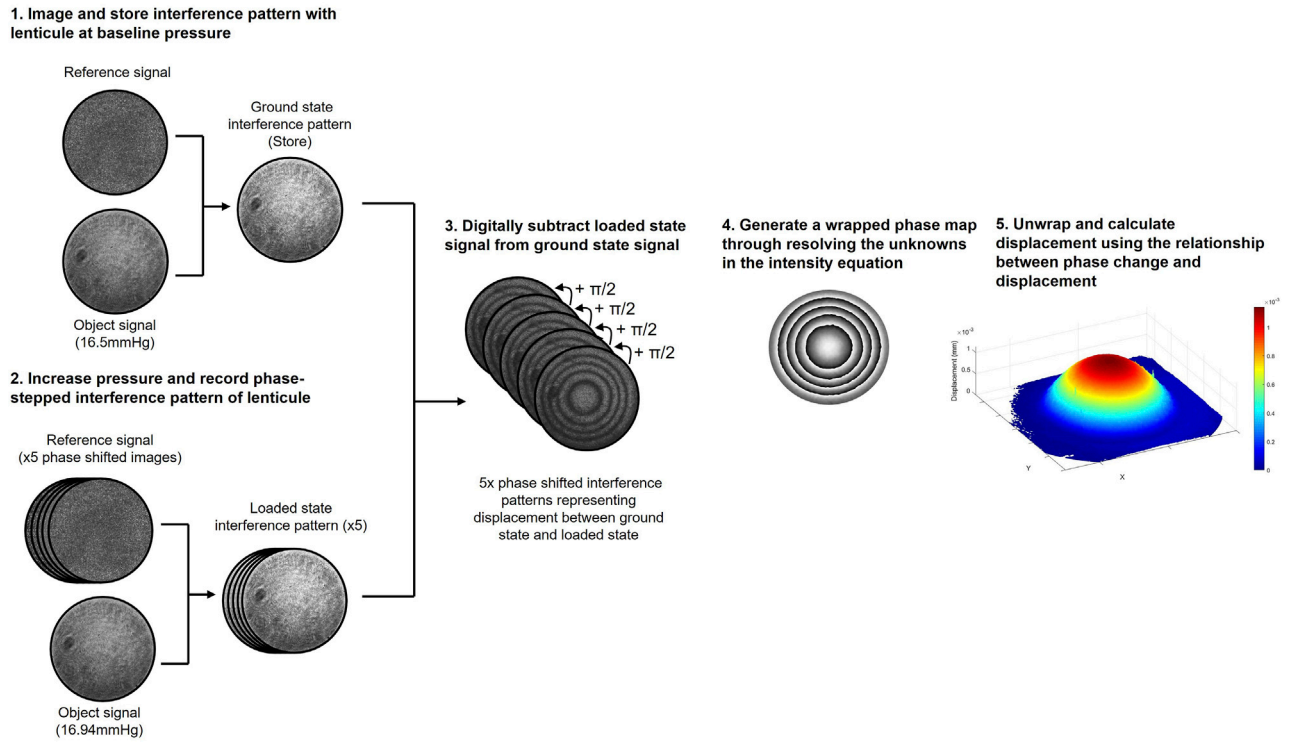

FIGURE 2 | Diagrammatic summary of the DSPI data acquisition and processing procedure used to measure axial displacement.

specimens isolated from porcine corneas underwent a proprietary process (patent pending) at Gebauer Medizintechnik, GmbH, Neuhausen, DE involving 4 stages: decellularization, washing, compression and crosslinking. The process used resulted in a more than 50% reduction in the thickness of the lenticules to 90 μm.

Experimental Set-Up and Measurement Principles

Prior to interferometric measurement lenticules were mounted into a custom-designed artificial anterior chamber as shown in **Figure 1**. The aperture of the chamber was 7 mm in diameter leaving a 1 mm boundary for clamping around the circumference of each of the lenticules. The chamber was attached to a reservoir via the inlet. The reservoir was mounted onto an automated vertical translation stage. Both the chamber and reservoir were filled with phosphate buffered saline (PBS) solution (Sigma-Aldrich, United Kingdom, ρ = 0.995 g/ml at 25°C) The height of the reservoir relative to the top surface of the lenticule was used to control the pressure in the chamber with the baseline pressure set at 16.50 mmHg which is representative of normal IOP in porcine corneas (Ruiz-Ederra et al., 2005). Pressure variations from this baseline pressure were achieved by increasing the height of the reservoir relative to the top surface of the lenticule.

The interferometer used for displacement measurements and the measurement principles (Wilson and Marshall, 2018) were identical to those described in detail in previous recent publications (Wilson et al., 2020; Wilson et al., 2021). **Figure 2** provides a diagrammatic summary of the measurement principles of DSPI. Briefly, monochromatic, coherent light is used to illuminate the surface of a sample, the backscattered light from the surface is interfered with that of a reference beam (in this instance a portion of the illumination beam reflected from a mirror) and imaged through a lens by a camera. The resulting speckle pattern formed from the constructive and destructive interference of light waves from the object and reference portions of the beam is imaged and stored as a reference (ground state). Each speckle in this image can be considered as a unique data point with a specific intensity (I) as described by **Eq. 1** (Petzing and Tyrer, 1998) and related to the phase difference ($\Delta\varphi$) of the object (o) and reference (r) wavefronts, which is proportional to the position of each specific point on the objects surface relative to the reference surface.

$$I = I_r + I_O + 2\sqrt{I_r I_O}\cos\Delta\varphi \quad (1)$$

When the surface of the object moves in response to a stimulus the speckle pattern changes due to a change in the phase difference between the object and reference portions of the beam. Through digitally subtracting the speckle patterns that form as the surface of the object deforms from the reference (ground state) to the final (loaded state) we generate an interferogram composed of interference fringes, which with knowledge of the specific imaging set-up can be deciphered to determine components of surface displacement, the theory of

which is described in greater detail elsewhere (Wilson and Marshall, 2018; Petzing and Tyrer, 1998).

Since, in the set-up described, the illumination and imaging were both configured normal to the surface of the sample (**Supplementary Figure S1**), the interference fringes related to axial surface deformation (Petzing and Tyrer, 1998). Due to the lenticule samples being initially flat, and the nature of the mounting and loading method used, axial deformation was expected to be significantly greater than lateral deformation in response to hydrostatic loading (Wilson et al., 2021) and therefore lateral deformation was not directly measured here. To generate quantitative information from the resulting interferograms, the reference beam was temporally phase-stepped during measurement, facilitating the generation of phase wrapped images. Temporal phase-stepping involves shifting the reference beam by a specific amount over a series of at least 3 images enabling all three unknowns in the intensity equation (**Eq. 1**) to be resolved and quantitative information to be extracted from the interferogram, the mathematics of which is described in greater detail in previous publications (Creath, 1988; Joenathan, 1994; Francis et al., 2010). For the measurements conducted in this study a 5-step phase shifting procedure and complimentary processing algorithm (Francis et al., 2010) was used with a phase step of π/2. A phase-unwrapping algorithm (Herráez et al., 2002) was used to remove the 2π discontinuities from the phase wrapped images (Wilson and Marshall, 2018) and generate smooth phase maps where the phase change ($\Delta\phi_{def}$) was proportional to axial displacement (w), and could be calculated via **Eq. 2** (Wilson and Marshall, 2018), where λ was the wavelength of the illumination source.

$$w = \Delta\phi_{def} \cdot \frac{\lambda}{4\pi} \tag{2}$$

For the set-up used in this study (**Supplementary Figure S1**) illumination was via a diode pumped single-mode solid-state laser (λ = 532 nm) (06-DPL, Cobolt AB, Solna, SE), which was expanded and collimated to a diameter of 25 mm. The illumination beam was passed through a 50:50 beamsplitter with half directed towards the target surface (lenticule surface) and half towards a planar mirror attached to a piezo-electric transducer which was used to accurately phase step the reference beam by π/2 over a series of 5 images. The beams from the object and the reference were interfered, then imaged via a CMOS camera with a resolution of 1,296 by 972 pixels (CMOS Aptina MT9P031, Basler AG, Ahrensburg, DE) through a 12.5–75 mm zoom lens (C31204, Pentax, Tokyo, JP).

Experimental Procedure

All lenticules were shipped to Loughborough, United Kingdom via 24-h delivery from Gebauer Mediziniechnik, 75242 Neuhausen, DE. During transportation and storage the lenticules were fully immersed in sample tubes filled with a trinity solution (50% glycerol, 30% water, 20% ethanol), chosen for the mixtures preservation properties and principal capability to be fully metabolised by cells of the human body. The sample tubes were enclosed in insulated packaging and surrounded by ice packs. On arrival the lenticules were stored at 4°C prior to measurement. Pre-mounting the lenticules were transferred into water and subjected to 30 min of mechanical shaking to facilitate the dilution of the trinity present inside the lenticules from the transportation and storage steps. Following this the lenticules were mounted centrally into the chambers, a light coating of white powder (Sphericel 110P8, Potters Ind. LLC, PA, United States) was applied to the surface of each of the samples. This coating was necessary to generate an adequate signal from the surface. Due to its particulate nature, the coating had no stiffness and moved with the underlying surface, therefore having no effect on the measured deformation of the lenticule when subjected to loading. The lenticules were set under a baseline pressure of 16.50 mmHg where they were rested for 20 min to stabilise under the initial pressure prior to the initiation of measurement. Following this each of the lenticules was subjected to 20 repeated loading cycles where the pressure was increased and then subsequently decreased by 0.44 mmHg in a pulsatile manner. A 3-s pause was programmed between cycles and for each cycle the reference image was captured at the baseline pressure (16.50 mmHg) with the loaded image captured at the highest pressure of 16.94 mmHg. The reason for this specific pressure increase of 0.44 mmHg was to optimise the number of interference fringes generated across samples to maximise the signal to noise ratio in the resulting images. During experimentation, one of the processed lenticules was damaged during the mounting stage and was therefore discounted for analysis.

Data Processing

Post-measurement, the data sets from each lenticule were visually assessed and those with obvious noise or phase-stepping errors (evident from the quality of the fringes in the phase-wrapped images) were removed. All remaining data was imported into Matlab (MathWorks Inc., United States). Phase data from each lenticule was averaged and displacement across the full sample was calculated using the relationship between axial displacement and measured phase change as described in **Eq. 2**.

The deformation of the lenticules indicated relative uniformity in mechanical properties across each of the samples, as the fringes were close to circular with relatively even spacing which is what would be expected from a sample with spatially homogenous bulk material properties. Due to this the mechanical stiffness, in terms of Young's modulus (E) of the samples could be estimated from the central (maximum) displacement (w_{centre}) via **Eq. 3** (Young and Budynas, 2002), where ΔP is the pressure change (0.44 mmHg, 59 Pa), R is the initial sample radius of curvature (7.8 mm, estimated as the average human corneal radius of curvature), t is sample thickness (0.2 mm unprocessed, 0.09 mm processed), and υ is corneal Poisson's ration (0.42).

$$E = \frac{\Delta P \cdot R^2}{2 \cdot w_{centre} \cdot t} (1 - \upsilon) \tag{3}$$

This calculation of stiffness is based on the following assumptions; the boundary conditions impose a pinned edge,

the lenticule acts as a membrane where bending stiffness can be considered negligible and horizontal displacement is zero.

RESULTS

A representative wrapped fringe pattern from one of the control (unprocessed) and one of the processed lenticules is shown in **Figure 3**. The fringes were found to be relatively circular which would indicate x-y homogeneity in mechanical properties, however there were slight deviations from circular fringes evident, and this could be representative of slight variations in the mechanical properties of the superior-inferior and nasal-temporal axis of the corneas from which the samples were derived.

The mechanical stiffness values that were derived from the data obtained during interferometric testing of each of the lenticules is summarised in **Table 1** and in **Figures 4A,B**. One of the processed lenticules was damaged during testing and was therefore discounted in the analysis.

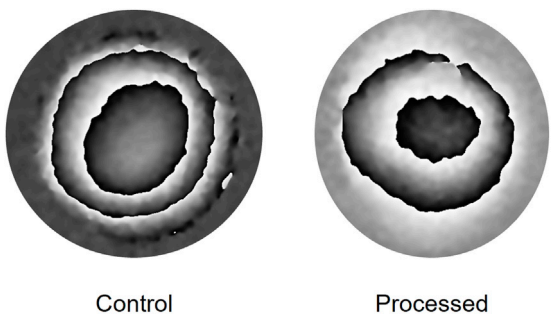

FIGURE 3 | Representative phase wrapped images obtained when imaging the deformation of a lenticule over a pressure increase from 16.50 to 16.94 mmHg.

TABLE 1 | Calculated Young's modulus of unprocessed and processed samples.

Calculated Young's modulus (MPa)	
Control Samples	Processed Samples
9.31±1.31	18.32±1.32
11.68±0.82	24.47±4.34
11.40±0.69	32.9±5.23
8.39±0.66	
12.49±2.15	
13.41±1.25	

The control lenticules had an average Young's modulus (E) of 11.11 MPa (range 8.39–13.41 MPa) compared to the processed lenticules 25.23 MPa (range 18.32–32.9 MPa). Overall processing of the samples resulted in an average increase in estimated Young's modulus of 127% above that of the unprocessed tissue. Variability in the stiffness of the samples was greater between the processed samples with a range of 14.58 vs. 5.02 MPa in the unprocessed lenticules.

DISCUSSION

The purpose of these experiments was to evaluate the mechanical effects of the process used to produce Xenia® corneal implants. Although measurement in this initial investigation was limited to a small number of samples, it was evident that processing of the lenticules resulted in a significant increase in stiffness by on average 127% over the unprocessed tissue that is initially extracted from the central anterior porcine corneal stroma. This increase in relative stiffness when compared to normal corneal tissue is important when considering the potential treatment of keratoconus as it means the implant could act as effective splint to counteract bulging and weakness of the keratoconic cornea into which it is inserted.

Further to the increase in mechanical stiffness, there were several interesting observations from this initial measurement

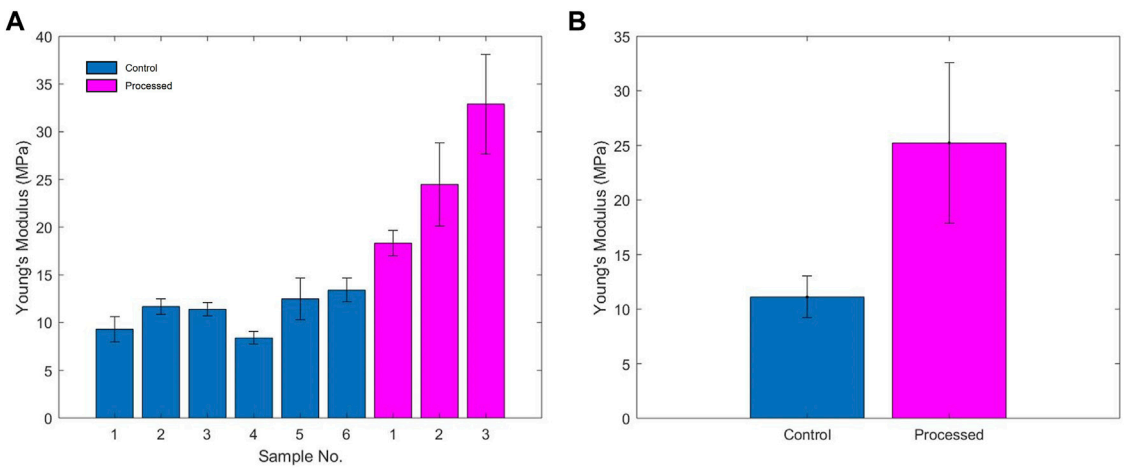

FIGURE 4 | (A) Young's modulus of each of the samples; **(B)** average Young's modulus of unprocessed and processed samples.

data set. Firstly, the slight deviation from circular fringe distribution seen in the interferograms of the control samples indicates slight differences in mechanical properties with respect to different axes of the cornea. The actual axes of the tissue relative to the axes of the cornea from which it had been extracted were not identified in this study. This slight difference in mechanical properties and deviation from circular fringes was predicted from previous studies on the biomechanics of the whole cornea (Boyce et al., 2008; Wilson et al., 2020; Wilson et al., 2021), where it has been shown that mechanical properties are not homogenous across the tissue and particularly with respect to the superior-inferior and nasal-temporal axis. The heterogeneity of the mechanical properties of the native cornea could be an important consideration when manufacturing these implants. To keep properties as consistent as possible it will be important to take the tissue for the implant from the same position in each given cornea. However, as only small deviations were seen from circular fringes in the processed implants, during transplantation it is likely not to be critically important to know the exact orientation of the implant relative to the cornea from which it was removed.

A further interesting observation was that the variability in the calculated stiffness of the processed lenticules was significantly greater than in the control tissue. This may have arisen due to the combined effect of differences in initial tissue mechanical properties between different corneas and differences in their ability to respond to the four processing stages. For example, many crosslinking studies have shown that the response to crosslinking is patient-dependent with some individuals being high-responders and others, low-responders (Godefrooij et al., 2017b). The reasons for this are difficult to identify as there are likely to be several contributing factors and therefore it is difficult to control. It would be expected that the differences in the porcine tissue from which the lenticules are formed may be lesser than in human tissue across the general population as all lenticules were obtained from pigs of the same breed and therefore likely to be genetically more similar to one another (Zhang and Plastow, 2011), and in addition, due to farming procedures are likely to be of a similar age and reared in a similar environment prior to slaughter. However, some variation is likely and may be difficult to control. It is possible however, that the processing of the tissue results in an adequate increase in stiffness in all tissue, whether or not the response to the processes are equal, and a such all implants may be adequately effective for treating keratoconus. However, if the aim was to manipulate the stiffness of the cornea to achieve greater precision in terms of refractive changes in addition to preventing progression of keratoconus this may be a property that requires quantification, and interferometry may be a useful tool to enable this through mechanical pre-screening of the implants.

The findings of this pilot study are clear, however, due to the relatively small sample size, it would be helpful to conduct measurements on a larger number of samples to confirm these current findings. Furthermore, it would be useful to measure samples at different stages in the production process, for example; after removal from porcine cornea; post-decellularisation, post-compression and post-crosslinking to establish individually the effects of each of these processes on material stiffness and across individual corneas to ascertain where variability is likely to be introduced and whether greater repeatability in mechanical properties can be achieved. It would also be useful to use complimentary imaging techniques, such as two-photon microscopy (Steven et al., 2010) on the processed samples to quantify factors such as the degree of crosslinking to establish whether this correlates with the measured increase in stiffness. In addition to mechanical measures, to ensure suitability for implantation and long-term safety and effectiveness, it is important to characterise other properties of the lenticules, including, optical, thermal, and biological properties and to ascertain data on the stability of the properties and performance of the lenticules over their intended lifespan.

Ultimately, it is not only necessary to understand the biomechanics of the lenticule as a standalone material, but it is important to understand the effects that insertion of the implant has on the biomechanics, and subsequently refractive properties, of the cornea and how this changes over time. It is therefore important to investigate the biomechanics of the whole system at different stages of the recovery process and after long term implantation. This is something that is currently difficult to achieve due to a relative absence of measurement systems capable of carrying out a comprehensive analysis of corneal biomechanics. *in vivo*, as has been discussed extensively in the literature (Kling and Hafezi, 2017; Wilson and Marshall, 2020). Whilst DSPI can provide a useful evaluation of the mechanical properties of thin lenticules *ex vivo*, *in vivo* assessment is much more challenging and DSPI has several limitations, including high sensitivity to noise, poor tolerance for unwanted movements, poor signal to noise ratio in the absence of a corneal coating and the ability to obtain information only from the corneal surface. To understand the system as a whole, it is important to examine the 3-D stress and strain distribution through the thickness of the sample, this is especially important when considering the implantation of a lenticule as it is important to understand the biomechanics at the interface between the lenticule and neighbouring corneal tissue and how this changes over time. Several technologies capable of through thickness biomechanical assessment are currently under development for *in vivo* application, including optical coherence elastography (Kling et al., 2020), high frequency ultrasound (Pavlatos et al., 2018) and Brillouin spectroscopy (Shao et al., 2019) based-systems that may have useful application in this regard, however since all are scanning-based technologies comprehensive *in vivo* analysis of the type required here is challenging due to the requirement for long-scanning times to obtain adequate resolution data across the full cornea and the inherent issues this brings with regards to managing the effects of head and eye movement on data collection. A useful intermediate step may be to implant lenticules into corneas *ex vivo* and use DSPI (due to its advantages in obtaining high resolution, high sensitivity, full-surface deformation information in a single image) in combination with one of the aforementioned techniques capable of

through-thickness assessment to understand the deformation patterns of the cornea to pulsatile pressure variations before and after insertion of the lenticule.

Through conducting these types of investigations it may be possible to gain an understanding of how to optimise both the mechanical properties of the lenticule and potentially the surrounding tissue through the use of adjunct and targeted therapies such as collagen crosslinking to increase quality of visual outcomes and long-term stability and biocompatibility.

Lenticule development is an on-going iterative process, therefore these experiments relate to Xenia® implants at the time of experiments. Modifications are continuously being made to the processes used in-order to optimise their properties.

CONCLUSION

The proprietary process used to produce Xenia® corneal implants from porcine corneal tissue results in an average increase of Young's modulus by 127% over unprocessed native porcine tissue when measured using DSPI under physiologically representative pressure fluctuations. There appears to be significant variability in the mechanical properties of both the control tissue and the processed lenticule, with variability across samples being significantly higher after processing. This requires further investigation to determine which part of the process results in this variation to allow more precise control.

Interferometry could potentially provide a means to quantify the mechanical properties of implants which could be useful in terms of developing and standardising their properties prior to clinical use and optimising the properties of lenticules to achieve the best long-term outcomes in terms of stability and bio-compatibility.

DATA AVAILABILITY STATEMENT

The original contributions presented in the study are included in the article/**Supplementary Material**, further inquiries can be directed to the corresponding author.

ETHICS STATEMENT

Ethical review and approval was not required for the animal study because Animal material used in this study was waste material from the meat industry and was not purposefully produced for this research.

AUTHOR CONTRIBUTIONS

AW and JM designed the study. AW and JJ designed and manufactured the interferometric system. AW carried out all the measurements and data analysis and prepared the manuscript. JJ and JM reviewed the manuscript.

FUNDING

At the time of the experiments undertaken in this study AW was supported by an EPSRC Prize Doctoral Fellowship at Loughborough University, United Kingdom. AW is currently supported by an RAEng Fellowship (RF_202021_20_166) and hosted by University College London, United Kingdom.

ACKNOWLEDGMENTS

Steffen Gebauer and Peter Klapotek of Gebauer Medizintechnik GmbH, Neuhausen, DE, were responsible for, and provided all the information regarding the processing of lenticles. Gebauer Medizintechnik GmbH manufactured the artificial anterior chamber for mounting the lenticules and provided and processed all porcine cornea materials.

SUPPLEMENTARY MATERIAL

The Supplementary Material for this article can be found online at: https://www.frontiersin.org/articles/10.3389/fbioe.2022.862969/full#supplementary-material

REFERENCES

Akpek, E. K., Alkharashi, M., Hwang, F. S., Ng, S. M., and Lindsley, K. (2014). Artificial Corneas versus Donor Corneas for Repeat Corneal Transplants. *Cochrane Database Syst. Rev.* 11, CD009561. doi:10.1002/14651858.CD009561.pub2

Andreanos, K. D., Hashemi, K., Petrelli, M., Droutsas, K., Georgalas, I., and Kymionis, G. D. (2017). Keratoconus Treatment Algorithm. *Ophthalmol. Ther.* 6, 245–262. doi:10.1007/s40123-017-0099-1

Boyce, B. L., Grazier, J. M., Jones, R. E., and Nguyen, T. D. (2008). Full-field Deformation of Bovine Cornea under Constrained Inflation Conditions. *Biomaterials* 29, 3896–3904. doi:10.1016/j.biomaterials.2008.06.011

Creath, K. (1988). *Phase-Measurement Interferometry Tech.* 26, 349–393. doi:10.1016/S0079-6638(08)70178-1

Dragnea, D. C., Birbal, R. S., Ham, L., Dapena, I., Oellerich, S., van Dijk, K., et al. (2018). Bowman Layer Transplantation in the Treatment of Keratoconus. *Eye Vis.* 5, 1–6. doi:10.1186/s40662-018-0117-y

El-Massry, A., Ibrahim, O., Abdalla, M., Osman, I., and Mahmoud, S. (2021). Safety and Indicative Effectiveness of Porcine Corneal Lenticular Implants in Patients with Advanced Keratoconus and post Lasik Ectasia: A Retrospective Clinical Study. *Opth* Vol. 15, 3165–3171. doi:10.2147/OPTH.S325666

Elsheikh, A., Alhasso, D., and Rama, P. (2008). Biomechanical Properties of Human and Porcine Corneas. *Exp. Eye Res.* 86, 783–790. doi:10.1016/j.exer.2008.02.006

Elsheikh, A., Wang, D., and Pye, D. (2007). Determination of the Modulus of Elasticity of the Human Cornea. *J. Refract Surg.* 23, 808–818. doi:10.3928/1081-597x-20071001-11

Fernández, J., Rodríguez-Vallejo, M., Martínez, J., Tauste, A., and Piñero, D. P. (2018). Corneal Biomechanics after Laser Refractive Surgery: Unmasking Differences between Techniques. *J. Cataract Refract Surg.* 44, 390–398. doi:10.1016/j.jcrs.2017.10.054

Francis, D., Tatam, R. P., and Groves, R. M. (2010). Shearography Technology and Applications: A Review. *Meas. Sci. Technol.* 21, 1–29. doi:10.1088/0957-0233/21/10/102001

Gain, P., Jullienne, R., He, Z., Aldossary, M., Acquart, S., Cognasse, F., et al. (2016). Global Survey of Corneal Transplantation and Eye Banking. *JAMA Ophthalmol.* 134, 167–173. doi:10.1001/jamaophthalmol.2015.4776

García de Oteyza, G., González Dibildox, L. A., Vázquez-Romo, K. A., Tapia Vázquez, A., Dávila Alquisiras, J. H., Martínez-Báez, B. E., et al. (2019). Bowman Layer Transplantation Using a Femtosecond Laser. *J. Cataract Refract Surg.* 45, 261–266. doi:10.1016/j.jcrs.2018.10.034

Gaum, L., Reynolds, I., Jones, M. N. A., Clarkson, A. J., Gillan, H. L., and Kaye, S. B. (2012). Tissue and Corneal Donation and Transplantation in the UK. *Br. J. Anaesth.* 108, i43–i47. doi:10.1093/bja/aer398

Godefrooij, D. A., Boom, K., Soeters, N., Imhof, S. M., and Wisse, R. P. L. (2017). Predictors for Treatment Outcomes after Corneal Crosslinking for Keratoconus: a Validation Study. *Int. Ophthalmol.* 37, 341–348. doi:10.1007/s10792-016-0262-z

Godefrooij, D. A., de Wit, G. A., Uiterwaal, C. S., Imhof, S. M., and Wisse, R. P. L. (2017). Age-specific Incidence and Prevalence of Keratoconus: A Nationwide Registration Study. *Am. J. Ophthalmol.* 175, 169–172. doi:10.1016/j.ajo.2016.12.015

Gokhale, N. (2013). Epidemiology of Keratoconus. *Indian J. Ophthalmol.* 61, 382–383. doi:10.4103/0301-4738.116054

Hammond, G. M., Young, R. D., Muir, D. D., and Quantock, A. J. (2020). The Microanatomy of Bowman's Layer in the Cornea of the Pig: Changes in Collagen Fibril Architecture at the Corneoscleral Limbus. *Eur. J. Anat.* 24, 399–406.

Herráez, M. A., Burton, D. R., Lalor, M. J., and Gdeisat, M. A. (2002). Fast Two-Dimensional Phase-Unwrapping Algorithm Based on Sorting by Reliability Following a Noncontinuous Path. *Appl. Opt.* 41, 7437–7444. doi:10.1364/AO.41.007437

Joenathan, C. (1994). Phase-measuring Interferometry: New Methods and Error Analysis. *Appl. Opt.* 33, 4147–4155. doi:10.1364/ao.33.004147

Juthani, V. V., and Chuck, R. S. (2021). Corneal Crosslinking in Refractive Corrections. *Trans. Vis. Sci. Tech.* 10, 4–9. doi:10.1167/tvst.10.5.4

Kling, S., and Hafezi, F. (2017). Corneal Biomechanics - a Review. *Ophthalmic Physiol. Opt.* 37, 240–252. doi:10.1111/opo.12345

Kling, S., Khodadadi, H., and Goksel, O. (2020). Optical Coherence Elastography-Based Corneal Strain Imaging during Low-Amplitude Intraocular Pressure Modulation. *Front. Bioeng. Biotechnol.* 7, 7. doi:10.3389/fbioe.2019.00453

Koo, T. S., Finkelstein, E., Tan, D., and Mehta, J. S. (2011). Incremental Cost-Utility Analysis of Deep Anterior Lamellar Keratoplasty Compared with Penetrating Keratoplasty for the Treatment of Keratoconus. *Am. J. Ophthalmol.* 152, 40–47. doi:10.1016/j.ajo.2011.01.017

Wilson, A., and Marshall, J. (2020). A Review of Corneal Biomechanics: Mechanisms for Measurement and the Implications for Refractive Surgery. *Indian J. Ophthalmol.* 68 (12), 2679–2690. doi:10.4103/ijo.IJO_2146_20

Nonpassopon, M., Niparugs, M., and Cortina, M. S. (2020). Boston Type 1 Keratoprosthesis: Updated Perspectives. *Opth* Vol. 14, 1189–1200. doi:10.2147/OPTH.S219270

O'Brart, D. P. S., Patel, P., Lascaratos, G., Wagh, V. K., Tam, C., Lee, J., et al. (2015). Corneal Cross-Linking to Halt the Progression of Keratoconus and Corneal Ectasia: Seven-Year Follow-Up. *Am. J. Ophthalmol.* 160, 1154–1163. doi:10.1016/j.ajo.2015.08.023

Parker, J. S., van Dijk, K., and Melles, G. R. J. (2015). Treatment Options for Advanced Keratoconus: A Review. *Surv. Ophthalmol.* 60, 459–480. doi:10.1016/j.survophthal.2015.02.004

Pavlatos, E., Chen, H., Clayson, K., Pan, X., and Liu, J. (2018). Imaging Corneal Biomechanical Responses to Ocular Pulse Using High-Frequency Ultrasound. *IEEE Trans. Med. Imaging* 37, 663–670. doi:10.1109/TMI.2017.2775146

Petzing, J. N., and Tyrer, J. R. (1998). Recent Developments and Applications in Electronic Speckle Pattern Interferometry. *J. Strain Anal. Eng. Des.* 33, 153–169. doi:10.1243/0309324981512887

Pezzullo, L., Streatfeild, J., Simkiss, P., and Shickle, D. (2018). The Economic Impact of Sight Loss and Blindness in the UK Adult Population. *BMC Health Serv. Res.* 18, 1–13. doi:10.1186/s12913-018-2836-0

Roy, A., Shetty, R., and Kummelil, M. (2013). Keratoconus: A Biomechanical Perspective on Loss of Corneal Stiffness. *Indian J. Ophthalmol.* 61, 392–393. doi:10.4103/0301-4738.116057

Ruiz-Ederra, J., García, M., Hernández, M., Urcola, H., Hernández-Barbáchano, E., Araiz, J., et al. (2005). The Pig Eye as a Novel Model of Glaucoma. *Exp. Eye Res.* 81, 561–569. doi:10.1016/j.exer.2005.03.014

Shao, P., Eltony, A. M., Seiler, T. G., Tavakol, B., Pineda, R., Koller, T., et al. (2019). Spatially-resolved Brillouin Spectroscopy Reveals Biomechanical Abnormalities in Mild to Advanced Keratoconus *In Vivo*. *Sci. Rep.* 9, 1–12. doi:10.1038/s41598-019-43811-5

Sharifi, R., Yang, Y., Adibnia, Y., Dohlman, C. H., Chodosh, J., and Gonzalez-Andrades, M. (2019). Finding an Optimal Corneal Xenograft Using Comparative Analysis of Corneal Matrix Proteins across Species. *Sci. Rep.* 9, 1–10. doi:10.1038/s41598-018-38342-4

Steven, P., Hovakimyan, M., Guthoff, R. F., Hüttmann, G., and Stachs, O. (2010). Imaging Corneal Crosslinking by Autofluorescence 2-photon Microscopy, Second Harmonic Generation, and Fluorescence Lifetime Measurements. *J. Cataract Refract Surg.* 36, 2150–2159. doi:10.1016/j.jcrs.2010.06.068

Subasinghe, S. K., Ogbuehi, K. C., Mitchell, L., and Dias, G. J. (2021). Animal Model with Structural Similarity to Human Corneal Collagen Fibrillar Arrangement. *Anat. Sci. Int.* 96, 286–293. doi:10.1007/s12565-020-00590-8

van Dijk, K., Liarakos, V. S., Parker, J., Ham, L., Lie, J. T., Groeneveld-van Beek, E. A., et al. (2015). Bowman Layer Transplantation to Reduce and Stabilize Progressive, Advanced Keratoconus. *Ophthalmology* 122, 909–917. doi:10.1016/j.ophtha.2014.12.005

Van Dijk, K., Parker, J., Tong, C. M., Ham, L., Lie, J. T., Groeneveld-Van Beek, E. A., et al. (2014). Midstromal Isolated Bowman Layer Graft for Reduction of Advanced Keratoconus. *JAMA Ophthalmol.* 132, 495–501. doi:10.1001/jamaophthalmol.2013.5841

Williams, A., and Muir, K. (2018). Awareness and Attitudes toward Corneal Donation: Challenges and Opportunities. *Opth* Vol. 12, 1049–1059. doi:10.2147/OPTH.S142702

Wilson, A., and Marshall, J. (2018). "Electronic Speckle Pattern Interferometry and Lateral Shearing Interferometry," in *Biomechanics of the Eye*. Editors C. J. Roberts, W. J. Dupps, and J. C. Downs (Kugler publications), 147–157.

Wilson, A., Jones, J., and Marshall, J. (2021). Interferometric *Ex Vivo* Evaluation of the Spatial Changes to Corneal Biomechanics Introduced by Topographic CXL: a Pilot Study. *J. Refract Surg.* 37, 263–273. doi:10.3928/1081597x-20210203-01

Wilson, A., Jones, J., Tyrer, J. R., and Marshall, J. (2020). An Interferometric *Ex Vivo* Study of Corneal Biomechanics under Physiologically Representative Loading, Highlighting the Role of the Limbus in Pressure Compensation. *Eye Vis.* 7, 43. doi:10.1186/s40662-020-00207-1

Wilson, A., Marshall, J., and Tyrer, J. R. (2016). The Role of Light in Measuring Ocular Biomechanics. *Eye* 30, 234–240. doi:10.1038/eye.2015.263

Wolle, M. A., Randleman, J. B., and Woodward, M. A. (2016). Complications of Refractive Surgery. *Int. Ophthalmol. Clin.* 56, 127–139. doi:10.1097/IIO.0000000000000102

Young, W. C., and Budynas, R. G. (2002). *Roark's Formulas for Stress and Strain*. 7th Edition. New York: McGraw-Hill.

Zeng, Y., Yang, J., Huang, K., Lee, Z., and Lee, X. (2001). A Comparison of Biomechanical Properties between Human and Porcine Cornea. *J. Biomech.* 34, 533–537. doi:10.1016/S0021-9290(00)00219-0

Zhang, C., and Plastow, G. (2011). Genomic Diversity in Pig (*Sus scrofa*) and its Comparison with Human and Other Livestock. *Cg* 12, 138–146. doi:10.2174/138920211795564386

Conflict of Interest: JJ was employed by Laser Optical Engineering Ltd.

The remaining authors declare that the research was conducted in the absence of any commercial or financial relationships that could be construed as a potential conflict of interest.

Publisher's Note: All claims expressed in this article are solely those of the authors and do not necessarily represent those of their affiliated organizations, or those of the publisher, the editors and the reviewers. Any product that may be evaluated in this article, or claim that may be made by its manufacturer, is not guaranteed or endorsed by the publisher.

frontiers | Frontiers in Bioengineering and Biotechnology

ORIGINAL RESEARCH
published: 13 May 2022
doi: 10.3389/fbioe.2022.861924

Differences of Corneal Biomechanics Among Thin Normal Cornea, Forme-Fruste Keratoconus, and Cornea After SMILE

Di Zhang[1,2,3†], Lei Tian[4,5†], Haixia Zhang[1,2,3], Yan Zheng[6], Caiyun Fu[6], Changbin Zhai[6], Ying Jie[4*] and Lin Li[1,2,3*]*

[1]School of Biomedical Engineering, Capital Medical University, Beijing, China, [2]Beijing Key Laboratory of Fundamental Research on Biomechanics in Clinical Application, Capital Medical University, Beijing, China, [3]Beijing Advanced Innovation Center for Big Data-based Precision Medicine, Capital Medical University, Beijing, China, [4]Beijing Ophthalmology and Visual Sciences Key Laboratory, Beijing Institute of Ophthalmology, Beijing Tongren Eye Center, Beijing Tongren Hospital, Capital Medical University, Beijing, China, [5]Beijing Advanced Innovation Center for Big Data-Based Precision Medicine, Beijing Tongren Hospital, Beihang University and Capital Medical University, Beijing, China, [6]Beijing Ophthalmology and Visual Sciences Key Laboratory, Beijing Tongren Eye Center, Beijing Tongren Hospital, Capital Medical University, Beijing, China

Background: To compare the corneal biomechanics of thin normal cornea (TNC) with thinnest corneal thickness (TCT) (≤500 μm), forme-fruste keratoconus (FFKC) and cornea after small incision lenticule extraction (Post-SMILE) had their central corneal thickness (CCT) matched by Corneal Visualization Scheimpflug Technology (Corvis ST).

Methods: CCT were matched in 23 eyes with FFKC, 23 eyes by SMILE in 3 months post-operatively, and 23 TNC eyes. The differences in corneal biomechanics by Corvis ST among the three groups were compared.

Results: There was no significant difference in CCT among the three groups, and the biomechanically corrected intraocular pressure (bIOP) did not differ significantly among the three groups (all $p > 0.05$). There were significant differences in most DCR parameters between pre- and post-operatively (all $p < 0.05$). Compared with TNC, the values of corneal deflection amplitude during the first applanation (A1DA), length at the first applanation (A1L), corneal deflection amplitude during the second applanation (A2DA), and maximum deformation amplitude (DA) decreased in 3 months after SMILE (all $p < 0.05$), these values increased in the FFKC (all $p < 0.05$).

Conclusion: The majority of the DCR parameters were different among the three groups. The parameters A1DA, A1L, A2DA, and DA may be different between TNC and Post-SMILE, TNC and FFKC, and Post-SMILE and FFKC.

Keywords: thin normal cornea, FFKC, post-SMILE, corneal biomechanicans, CorVis ST

OPEN ACCESS

Edited by:
FangJun Bao,
Affiliated Eye Hospital of Wenzhou Medical College, China

Reviewed by:
Gilbert Yong San Lim,
SingHealth, Singapore
Manmohan Singh,
University of Houston, United States
Fulvio Ratto,
National Research Council (CNR), Italy

****Correspondence:***
Lin Li
lil@ccmu.edu.cn
Changbin Zhai
17091006117@163.com
Ying Jie
jie_yingcn@aliyun.com

[†]These authors have contributed equally to this work and share first authorship

Specialty section:
This article was submitted to Biomechanics, a section of the journal Frontiers in Bioengineering and Biotechnology

Received: *25 January 2022*
Accepted: *12 April 2022*
Published: *13 May 2022*

Citation:
Zhang D, Tian L, Zhang H, Zheng Y, Fu C, Zhai C, Jie Y and Li L (2022) Differences of Corneal Biomechanics Among Thin Normal Cornea, Forme-Fruste Keratoconus, and Cornea After SMILE. Front. Bioeng. Biotechnol. 10:861924. doi: 10.3389/fbioe.2022.861924

INTRODUCTION

Small incision lenticule extraction (SMILE) has become one of the refractive surgery selected by patients and surgeons because of its good safety, stability, and post-operative effect (Vestergaard et al., 2014; Qin et al., 2018; Sánchez-González and Alonso-Aliste, 2019; Xia et al., 2020). The corneal morphology experiences a series of changes due to the removing part of the corneal tissue. The

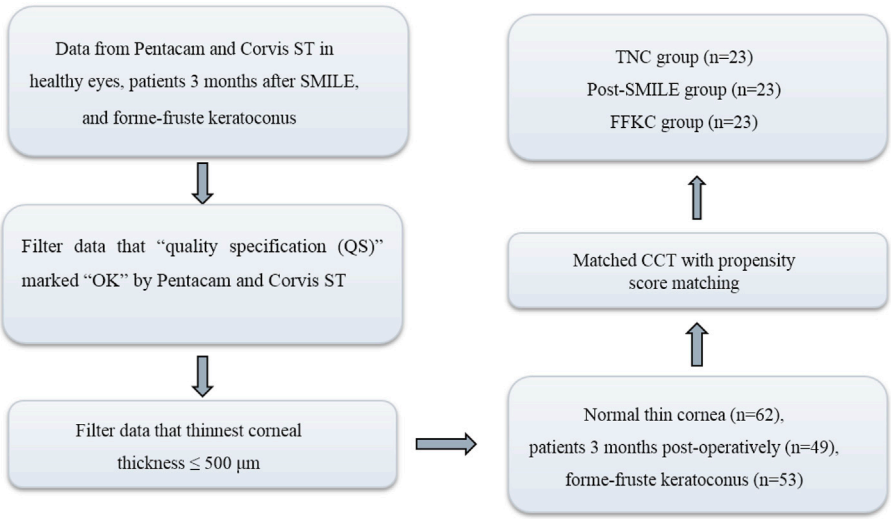

FIGURE 1 | Standard flowchart.

maintenance of post-operative corneal morphology relates to corneal biomechanical properties and intraocular pressure (IOP).

At present, corneal visualization Scheimpflug technology (Corvis ST) has been widely used to understand corneal biomechanical properties through analysis of the recorded dynamic corneal response (DCR) parameters. Several previous studies showed the changes of DCR parameters after SMILE (Cao et al., 2020; Wu et al., 2020). Takeing the effects of thinner central corneal thickness (CCT) (Vinciguerra et al., 2016; Miki et al., 2017) after SMILE on DCR parameters into account there may be misunderstandings about the interpretation of the data recorded after SMILE.

To this end, the study aimed to compare the DCR parameters of the corneas from myopic patients who underwent SMILE (Post-SMILE), forme-fruste keratoconus (FFKC) patients, and thin normal cornea (TNC) subjects with CCT-matched. This will contribute to the understanding of corneal biomechanical properties after SMILE.

METHODS

Subjects

This was a retrospective study that included 23 patients (23 eyes) who underwent SMILE (Post-SMILE group), 23 normal subjects (23 eyes) with thin normal cornea (the TNC group), and 23 FFKC patients (FFKC group). One eye was selected randomly for analysis. Each group included 23 eyes with CCT matched. The flowchart of this study was shown in **Figure 1**. The institutional review board of the Beijing Tongren Hospital (Beijing, China) approved this study. All participants signed an informed consent form in accordance with the tenets of the Declaration of Helsinki.

All patients who underwent SMILE at Beijing Tongren Hospital from September 2020 to January 2021. Healthy subjects and FFKC patients met the following criteria: Thinnest corneal thickness (TCT) range: ≤500 μm (Esporcatte et al., 2020); all participants had no history of corneal or ocular surgery, or trauma or systemic diseases that might affect the eye. Before the examination, if any, they had no soft contact lens utilization within 2 weeks, or had abandoned rigid contact lenses at least 3 months. The diagnostic criteria of FFKC had been described in previous studies (Tian et al., 2021).

Ocular Examination and Collection of the Parameters

A comprehensive ocular examination was performed on the eyes of all subjects, including slit-lamp microscopy, fundus examination, tomographic measurements using the corneal Scheimpflug tomography (Pentacam HR; Oculus; Optikgeräte GmbH, Wetzlar, Germany), and biomechanical examination using the corneal visualization Scheimpflug technology (Corvis ST; Oculus; Optikgeräte GmbH, Wetzlar, Germany, software version: 1.5r1902). The patients in Post-SMILE group were measured pre-operatively, and 3 months after SMILE. Only the "quality specification (QS)" marked "OK" by Pentacam and Corvis ST were considered for further analysis and processing.

During the test of Corvis ST, the cornea will go through the process from the initial position to the first applanation, the first applanation to the highest concavity, the highest concavity to the second applanation and return to the initial position. The parameters evaluated in the analysis are detailed in **Table 1**. The typical states of cornea in Corvis ST test were shown in **Figure 2**. The collected Corvis ST parameters are recorded as DCR.

Surgical Technique

The pre-operative design and surgeries were performed by the same surgeon (CB. Z.) using a repetition rate of 500 kHz VisuMax

TABLE 1 | Corvis ST parameters of eyes by group.

Parameters	Means
A1T	Time from starting until the first applanation
A1V	Velocity of the corneal apex during the first applanation
A1DA	Corneal deflection amplitude during the first applanation
A1L	Length at the first applanation
A2T	Time from starting until the second applanation
A2V	Velocity of the corneal apex during the second applanation
A2DA	Corneal deflection amplitude during the second applanation
A2L	Length at the second applanation
HCT	Time from the measurement beginning to the moment of reaching the highest concavity
HCDA	Corneal deflection amplitude at the moment of the highest corneal concavity
HCDL	Highest concavity deflection length
PD	Peak distance at the highest concavity
HCR	Central concave curvature at highest concavity
DA	Maximum deformation amplitude
ARTh	Ambrósio relational thickness to the horizontal profile
DAR1	Deflection amplitude ratio maximal (1 mm)
DAR2	Deflection amplitude ratio maximal (2 mm)
SPA1	Stiffness parameter at the first applanation
CBI	Corneal biomechanical index
bIOP	Biomechanically corrected IOP

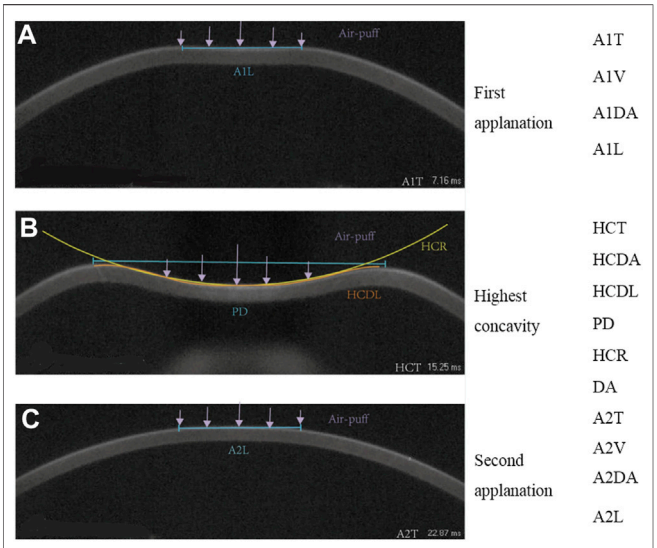

FIGURE 2 | The output parameters of Corvis ST, first applanation **(A)**, highest concavity **(B)**, second applanation **(C)**.

femtosecond laser system (Carl Zeiss Meditec, Jena, Germany). In all cases, the thickness of the cap was 110 or 120 μm, and the cap diameter was 7.5 mm, the lenticule diameter was 6.5 mm. All side-cut angles were 90° at a position of 120°, and incision width was 2 mm. The patients were treated with conventional anti-inflammatory drugs within 1 month post-operatively.

Statistical Analysis

All analyses were performed using SPSS (version 23.0, IBM Corporation, Armonk, NY) and R (version 3.6.3, R Core Team). The data was tested for normality of distribution using Shapiro-Wilk test, and expressed as mean ± SD or median (interquartile range, IQR) (95% confidence interval of difference). Normally distributed data was analyzed using the one-way analysis of variance (one-way ANOVA), and Bonferroni test was used to compare parameters between any two of the three groups. For non-normally distributed data, Kruskal-Wallis test was used to compare parameters, and Bonferroni corrected Mann-Whitney *U* test was used to compare parameters between any two groups. Paired *t* test (normally distributed data) or Wilcoxon signed rank test (non-normally distributed data) was used to compare the parameters between pre- and post-operation. Propensity score matching, a widely used method that can control multiple confounding factors (such as CCT and IOP) at the same time, was used to match the CCT among the three groups. $p < 0.05$ was considered statistically significant.

RESULTS

The information of eyes by group after CCT matched was shown in **Table 2**. Including 69 eyes of 69 individuals, 23 individuals in each group. Among the three groups, no statistical differences (all $p > 0.05$) were detected in the gender (chi-square test), bIOP, TCT (Kruskal-Wallis test for the three groups, and Bonferroni corrected Mann-Whitney *U* test for any two groups.), and CCT (one-way ANOVA for the three groups, and Bonferroni test for any two groups). However, the age in Post-SMILE group was greater than those in group TNC and group FFKC.

Table 3 summarizes the values of the DCR parameters of all individuals. Overall, there were significant differences in the DCR between Pre- and Post-SMILE groups (all $p < 0.05$), except for A2V, A2L, HCT and HCDL. 6/19, 6/19, and 8/19 DCR parameters were significantly different between the TNC and Post-SMILE, between the TNC and FFKC, between the Post-SMILE and FFKC, respectively (all $p < 0.05$). Statistically

TABLE 2 | Baseline information of eyes by group after CCT matched.

Parameters	TNC	Post-SMILE	FFKC	*p*
Gender (Male/Female)	11/12	7/16	10/13	0.458
Age (years)	24 ± 3 (23–26)	31 (9) (28–32)$^{\#}$	21 (9) (21–25)$^{\&}$	<0.001
CCT (μm)	488 ± 10 (484–492)	484 ± 12 (478–489)	491 ± 12 (486–496)	0.116
TCT (μm)	484 (19) (480–488)	482 ± 13 (476–487)	483 (17) (481–490)	0.559
bIOP (mmHg)	14.6 ± 2.1 (13.7–15.5)	13.3 ± 1.7 (12.5–14.0)	13.8 (2.6) (13.6–14.9)	0.086

Data is presented as mean ± SD (95% confidence interval) or median (IQR) (95% confidence interval). The p *value was from the test among the three groups;* $^{\#}$, $^{\&}$ *represent statistically significant difference with TNC and Post-SMILE, and Post-SMILE and FFKC, respectively.*

TABLE 3 | Corvis ST parameters of eyes by group.

Parameters	TNC	Pre-SMILE	Post-SMILE	FFKC	*p*
A1T (ms)	7.282 ± 0.251 (7.173 to 7.390)	7.754 ± 0.208 (7.644 to 7.843)	7.259 (0.362)(7.149 to 7.325)^{§,c}	7.039 (0.294)(6.996 to 7.163)$^{\#,\&}$	0.005^{b}
A1V (m/s)	0.148 (0.018) (0.132 to 0.153)	0.149 ± 0.014 (0.143 to 0.155)	0.159 ± 0.012 (0.153 to 0.164)^{*,§,c}	0.167 ± 0.015 (0.160 to 0.173)$^{\#}$	<0.001^{b}
A2T (ms)	21.787 ± 0.361 (21.631 to 21.943)	22.003 ± 0.293 (21.876 to 22.130)	22.322 ± 0.419 (22.140 to 22.503)^{*,§,d}	22.095 ± 0.315 (21.959 to 22.231)$^{\#}$	<0.001^{a}
A2V (m/s)	−0.288 (0.047)(−0.289 to −0.262)	−0.269 (0.031)(−0.275 to −0.261)	−0.271 ± 0.018 (−0.279 to −0.263)^{d}	−0.299 ± 0.040 (−0.316 to −0.282)$^{\&}$	0.005^{b}
A2L (mm)	2.318 (0.467)(2.075 to 2.557)	2.824 ± 0.534 (2.593 to 3.055)	2.269 (1.523)(2.340 to 3.097)^{c}	2.490 (1.909)(2.405 to 3.188)	0.284^{b}
HCT (ms)	16.792 ± 0.494 (16.578 to 17.006)	17.401 ± 0.396 (17.230 to 17.573)	17.409 ± 0.450 (17.215 to 17.604)^{*,c}	16.724 ± 0.509 (16.504 to 16.944)$^{\&}$	<0.001^{a}
HCDA (mm)	0.942 ± 0.090 (0.903 to 0.981)	0.875 (0.097)(0.855 to 0.913)	0.972 ± 0.080 (0.937 to 1.006)^{§,d}	1.039 ± 0.124 (0.986 to 1.093)$^{\#}$	0.005^{a}
HCDL (mm)	6.409 ± 0.422 (6.227 to 6.592)	6.392 ± 0.272 (6.274 to 6.510)	6.532 ± 0.389 (6.364 to 6.701)^{c}	6.862 ± 0.434 (6.674 to 7.049)$^{\#,\&}$	0.001^{a}
PD (mm)	5.103 ± 0.236 (5.001 to 5.205)	4.914 (0.267)(4.892 to 5.053)	5.287 ± 0.203 (5.199 to 5.375)^{*,§,d}	5.343 ± 0.254 (5.233 to 5.453)$^{\#}$	0.002^{a}
HCR (mm)	6.421 ± 0.585 (6.168 to 6.674)	6.817 (0.595)(6.709 to 7.371)	6.139 ± 0.448 (5.945 to 6.333)^{§,d}	6.738 ± 0.586 (6.485 to 6.992)$^{\&}$	0.002^{a}
ARTh	367.537 (82.236)(337.787 to 415.320)	482.189 ± 75.588 (449.503 to 514.876)	212.309 (43.007)(186.892 to 215.604)^{*,§,c}	445.522 ± 124.505 (391.682 to 499.362)$^{\&}$	<0.001
DAR1	1.643 ± 0.058 (1.618 to 1.668)	1.529 ± 0.032 (1.515 to 1.543)	1.630 ± 0.041 (1.613 to 1.648)^{§,c}	1.617 ± 0.038 (1.600 to 1.633)	0.165^{a}
DAR2	4.859 ± 0.365 (4.701 to 5.017)	4.005 ± 0.225 (3.907 to 4.102)	5.075 ± 0.385 (4.909 to 5.242)^{§,c}	4.971 ± 0.452 (4.776 to 5.167)	0.197^{a}
SPA1	78.532 ± 12.191 (73.260 to 83.803)	114.063 ± 8.818 (110.250 to 117.876)	84.464 ± 13.372 (78.682 to 90.247)^{§,c}	69.935 (9.844)(69.032 to 76.843)$^{\&}$	0.004^{b}
CBI	0.944 (0.085)(0.830 to 0.951)	0.005 (0.016)(0.000 to 0.043)	0.999 (0.003)(0.988 to 1.002)^{*,§,d}	0.699 (0.889)(0.394 to 0.743)$^{\&}$	<0.001^{b}

Data is presented as mean ± SD (95% confidence interval) or median (IQR) (95% confidence interval). The p *value is from the test among the three groups. The statistically significant differences were denoted by* * *between TNC and Post-SMILE, by* $^{\#}$ *between TNC and FFKC, by* $^{\&}$ *between Post-SMILE and FFKC, and by*§ *between Pre- and Post-SMILE;* ^{a}, ^{b}, ^{c}, *and* ^{d} *represent one-way ANOVA, Kruskal-Wallis test, paired* t *test, and Wilcoxon signed rank test, respectively.*

differences were detected in SPA1 between Pre- and Post-SMILE, and between Post-SMILE and FFKC ($p < 0.05$).

Furthermore, there were significant differences in A1DA, A1L, A2DA, and DA among the TNC, Post-SMILE, and FFKC groups. Also these differences were found between the Post-SMILE and FFKC, between the Pre- and Post-SMILE groups, respectively (all $p < 0.05$, **Figure 3**). **Figure 3** shows that the A1DA, A2DA, A1L, and DA values in the Post-SMILE group were lowest, and that the FFKC group had higer A1DA, A2DA, A1L, and DA values compared to TNC group (all $p < 0.05$).

DISCUSSION

The cornea is mainly composed of corneal stroma with regularly arranged collagen fiber bundle lamellae (Mercatelli and Mattana, 2019). Corneal stroma is mainly load-bearing component of cornea. Since part of the corneal tissue is removed after corneal refractive surgery, it needs to explore whether the biomechanical properties of cornea could change when the influence of corneal thickness is discharged. This study compared the biomechanical properties of thin normal corneas, post-operation corneas, and FFKC corneas. The results showed that differences were detected in the majority of DCR parameters among TNC, Post-SMILE, and FFKC, when the CCT matched. The parameters A1DA, A1L, A2DA, and DA were significantly different between the TNC and Post-SMILE, between the TNC and FFKC, between the Post-SMILE and FFKC, and between pre- and post-operation, respectively.

The data showed that there were differences of DCR parameters between pre- and post-operation. Smaller A1L, A1T, and HCR, while larger A2T, PD, DA, and DAR (DAR1/DAR2) post-operatively compared with pre-operation (**Table 3**; **Figure 3**) were consistent with previous studies (Fernández et al., 2017; Cao et al., 2020; Wu et al., 2020). Lager A1DA, A2DA, DA, and A1L in FFKC than TNC (**Figure 3**) were consistent with our previous results (Tian et al., 2021) when the CCT matched. This study shows that the values of 16 and 10 DCR parameters out of the 19 involved parameters, such as A1DA, A2DA, DA, and A1L had significant differences among the three groups, and between any two groups, respectively. The parameters A1DA, DA and A2DA represent the corneal deflection amplitude at the first,

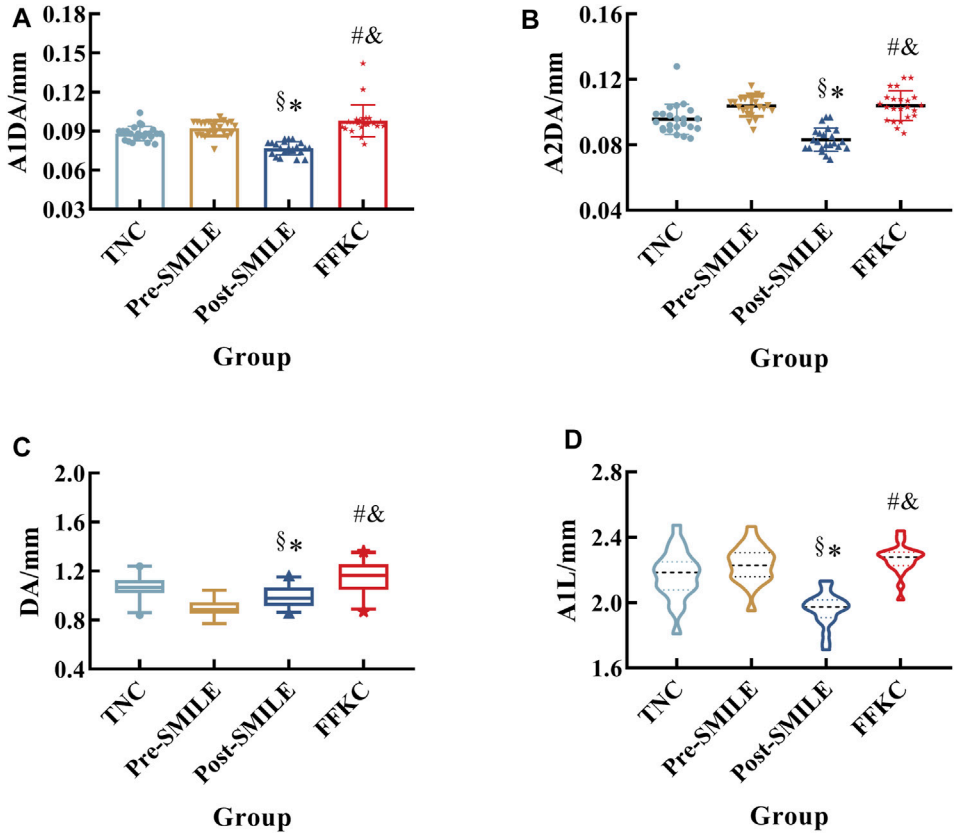

FIGURE 3 | Differences among the three groups with respect to A1DA **(A)**, A2DA **(B)**, DA **(C)**, and A1L **(D)**. (*, #, &, and §represent statistically significant differences between TNC and Post-SMILE, TNC and FFKC, Post-SMILE and FFKC, and Pre- and Post-SMILE, respectively.)

maximum deformation amplitude, highest concavity and second applanation, and A1L is the length at the first applanation. In theory, under the same external loads (air-puff and IOP), the corneas without geometric differences (CCT matched, differences of curvature ignored) should have little differences in deformation. Studies (Huseynova et al., 2014; Wang et al., 2017; Sedaghat et al., 2020) showed that A1L was correlated with CCT and IOP, but not with age and myopia. Our results showed that A1L in Post-SMILE, TNC and FFKC increased in turn (**Figure 2D**), where CCT, TCT, and bIOP were matched with the same baseline level among the three groups (**Table 2**). We tended to attribute the differences of A1L among the three groups to the differences in corneal biomechanical properties. Based on the above analyses, the corneas in the three groups may show some differences on biomechanical properties.

The corneal mechanical properties may have variations after SMILE. The data showed that smaller A1DA, A1L, and A2DA, while larger DA in Post-SMILE group than Pre-SMILE group (**Figure 3**). And after CCT matching, the values of A1DA, A1L, A2DA and DA gave their the largest in the FFKC group, the smallest in the Post-SMILE group, moderate in the TNC group. Since the distribution of the applied air-puff is the same during Corvis ST tests, and the bIOP among the three groups was basically maintained at the same level, these variations of DCR parameters suggest that there may be differences in corneal biomechanics among the TNC group, Post-SMILE, and FFKC.

It can be explained from the micro level why the corneal mechanical properties are different between Post-SMILE and TNC. The corneal stromal cells would be adjusted (Dong et al., 2014), and corneal epithelial will be remolded (Luft et al., 2016; Romito et al., 2020) by observing the microstructure of cornea after SMILE. The cell proliferation reached the peak at 1 week after SMILE, and the transforming growth factor-β1 (TGF-β1), which can promote the proliferation of corneal stromal cells (Ljubimov and Saghizadeh, 2015) and may cause tissue fibrosis (Wang et al., 2011), was still at a high level within 1 month after SMILE by animal experimental observation (Liu et al., 2020). Furthermore, the remodeling of corneal extracellular matrix is affected by the change of mechanical environment (Du et al., 2017), and then affect the migration and metabolism of keratocytes, which may affect the stability of corneal tissue. This may lead to the corneal mechanical properties are different between Post-SMILE and TNC.

However, if we aim to know the characteristics of corneal biomechanical properties of each group, we need to further analysis biomechanical parameters, such as, elastic modulus and nonlinear elasticity, based on the relationship between DCR parameters and corneal biomechanical properties (not

established yet) or the established mechanical models using the data output by Corvis ST (Boszczyk et al., 2017; Jannesari et al., 2019; Qin et al., 2019; Zhang et al., 2021), or direct measuring by optical correlation elastic imaging (Singh et al., 2018; Zhou et al., 2019; De Stefano et al., 2020; Chong and Dupps, 2021; Lan et al., 2021), Brillouin microscopy (Yun and Chernyak, 2018; Shao and Eltony, 2019; Chong and Dupps, 2021). In this study, we did not consider the viscous processes and a plastic deformation of the stroma during the surgical procedure. It is possibly needed to study in the future.

SMILE and FS-LASIK are two of safe and widely applied procedures for corneal refractive surgery. A large number of studies have investigated the biomechanical properties of corneas after FS-LASIK and SMILE *via* Ocular Response Analyzer (ORA) testing or Corvis ST testing, and found no difference in DCR parameters, corneal hysteresis (CH) or corneal resistance factor (CRF) between SMILE and FS-LASIK *in vivo* (Sefat et al., 2016; Xia et al., 2016; Raevdal et al., 2019; Cao et al., 2020). This study explored the changes in corneal biomechanical properties after SMILE, and the biomechanical properties of normal corneas, post-operative corneas, and FFKC corneas were compared when the CCT matched. The method may be used to analyze biomechanical properties of the corneas after FS-LASIK.

There are some limitations in this study. The number of patients included was small, and further clinical studies are needed, including more samples and longer follow up time to confirm these observations. The main purpose of this study is to compare the corneal biomechanicanics of TNC, Post-SMILE, and FFKC when the CCT-matched. There is lack of stratification of data based on low, moderate, and high myopia due to the small sample size.

CONCLUSION

In conclusion, the majority of DCR parameters were different among TNC, Post-SMILE, and FFKC when CCT matched. The parameters A1DA, A1L, A2DA, and DA values may be different between TNC and Post-SMILE, TNC and FFKC, and Post-SMILE and FFKC. Further observations and analyses are needed.

DATA AVAILABILITY STATEMENT

The original contributions presented in the study are included in the article/Supplementary Material, further inquiries can be directed to the corresponding authors.

ETHICS STATEMENT

The studies involving human participants were reviewed and approved by the institutional review board of the Beijing Tongren Hospital (Beijing, China), all participants were informed consent. Written informed consent to participate in this study was provided by the participants' legal guardian/next of kin.

AUTHOR CONTRIBUTIONS

Manuscript writing and review (DZ, LT, HZ, CZ, YJ, and LL); Data collection, analysis and interpretation (DZ, LT, YZ, and CF); designed this study (CZ, YJ, and LL). All authors read and approved the final manuscript.

FUNDING

This study was financially supported by the National Natural Science Foundation of China (Nos 32171304, 31370952, 31470914, 31600758, 82171101); Beijing Nova Program (Z181100006218099); the Open Research Fund from Beijing Advanced Innovation Center for Big Data-Based Precision Medicine, Beijing Tongren Hospital, Beihang University and Capital Medical University (BHTR-KFJJ-202001).

REFERENCES

Boszczyk, A., Kasprzak, H., and Jóźwik, A. (2017). Eye Retraction and Rotation during Corvis ST'air Puff' Intraocular Pressure Measurement and its Quantitative Analysis. *Ophthalmic Physiol. Opt.* 37, 253–262. doi:10.1111/opo.12383

Cao, K., Liu, L., Yu, T., Chen, F., Bai, J., and Liu, T. (2020). Changes in Corneal Biomechanics during Small-Incision Lenticule Extraction (SMILE) and Femtosecond-Assisted Laser *In Situ* Keratomileusis (FS-LASIK). *Lasers Med. Sci.* 35, 599–609. doi:10.1007/s10103-019-02854-w

Chong, J., and Dupps, W. J., Jr. (2021). Corneal Biomechanics: Measurement and Structural Correlations. *Exp. Eye Res.* 205, 108508. doi:10.1016/j.exer.2021.108508

De Stefano, V. S., Ford, M. R., Seven, I., and Dupps, W. J., Jr. (2020). Depth-dependent Corneal Biomechanical Properties in normal and Keratoconic Subjects by Optical Coherence Elastography. *Transl. Vis. Sci. Technol.* 9, 4. doi:10.1167/tvst.9.7.4

Dong, Z., Zhou, X., Wu, J., Zhang, Z., Li, T., Zhou, Z., et al. (2014). Small Incision Lenticule Extraction (SMILE) and Femtosecond Laser LASIK: Comparison of Corneal Wound Healing and Inflammation. *Br. J. Ophthalmol.* 98, 263–269. doi:10.1136/bjophthalmol-2013-303415

Du, G.-L., Chen, W.-Y., Li, X.-N., He, R., and Feng, P.-F. (2017). Induction of MMP-1 and −3 by Cyclical Mechanical Stretch Is Mediated by IL-6 in Cultured Fibroblasts of Keratoconus. *Mol. Med. Rep.* 15, 3885–3892. doi:10.3892/mmr.2017.6433

Esporcatte, L. P. G., Salomão, M. Q., Lopes, B. T., Vinciguerra, P., Vinciguerra, R., Roberts, C., et al. (2020). Biomechanical Diagnostics of the Cornea. *Eye Vis.* 7, 9. doi:10.1186/s40662-020-0174-x

Huseynova, T., Waring, T. O., IV, Roberts, C., Krueger, R. R., and Tomita, M. (2014). Corneal Biomechanics as a Function of Intraocular Pressure and Pachymetry by Dynamic Infrared Signal and Scheimpflug Imaging Analysis in Normal Eyes. *Am. J. Ophthalmol.* 157, 885–893. doi:10.1016/j.ajo.2013.12.024

Fernández, J., Rodríguez-Vallejo, M., Martínez, J., Tauste, A., Salvestrini, P., and Piñero, D. P. (2017). New Parameters for Evaluating Corneal Biomechanics and Intraocular Pressure after Small-Incision Lenticule Extraction by Scheimpflug-Based Dynamic Tonometry. *J. Cataract Refract. Surg.* 43, 803–811. doi:10.1016/j.jcrs.2017.03.035

Jannesari, M., Mosaddegh, P., Kadkhodaei, M., Kasprzak, H., and Jabbarvand Behrouz, M. (2019). Numerical and Clinical Investigation on the Material Model of the Cornea in Corvis Tonometry Tests: Differentiation between

Hyperelasticity and Viscoelasticity. *Mech. Time-Depend. Mater.* 23, 373–384. doi:10.1007/s11043-018-9390-3

Lan, G., Aglyamov, S. R., Larin, K. V., and Twa, M. D. (2021). *In Vivo* human Corneal Shear-Wave Optical Coherence Elastography. *Optom. Vis. Sci.* 98, 58–63. doi:10.1097/OPX.0000000000001633

Liu, L., Cheng, W., Wu, D., Chen, L., Yu, S., Zuo, T., et al. (2020). The Differential Expression of Cytokines and Growth Factors after SMILE Compared with FS-LASIK in Rabbits. *Invest. Ophthalmol. Vis. Sci.* 61, 55. doi:10.1167/iovs.61.5.55

Ljubimov, A. V., and Saghizadeh, M. (2015). Progress in Corneal Wound Healing. *Prog. Retin. Eye Res.* 49, 17–45. doi:10.1016/j.preteyeres.2015.07.002

Luft, N., Ring, M. H., Dirisamer, M., Mursch-Edlmayr, A. S., Kreutzer, T. C., Pretzl, J., et al. (2016). Corneal Epithelial Remodeling Induced by Small Incision Lenticule Extraction (SMILE). *Invest. Ophthalmol. Vis. Sci.* 57, Oct176–183. doi:10.1167/iovs.15-18879

Singh, M., Han, Z., Li, J., Vantipalli, S., Aglyamov, S. R., Twa, M. D., et al. (2018). Quantifying the Effects of Hydration on Corneal Stiffness with Noncontact Optical Coherence Elastography. *J. Cataract Refract. Surg.* 44, 1023–1031. doi:10.1016/j.jcrs.2018.03.036

Mercatelli, R., Mattana, S., Capozzoli, L., Ratto, F., Rossi, F., Pini, R., et al. (2019). Morpho-mechanics of Human Collagen Superstructures Revealed by All-Optical Correlative Micro-spectroscopies. *Commun. Biol.* 2, 117. doi:10.1038/s42003-019-0357-y

Miki, A., Maeda, N., Ikuno, Y., Asai, T., Hara, C., and Nishida, K. (2017). Factors Associated with Corneal Deformation Responses Measured with a Dynamic Scheimpflug Analyzer. *Invest. Ophthalmol. Vis. Sci.* 58, 538–544. doi:10.1167/iovs.16-21045

Qin, B., Li, M., Chen, X., Sekundo, W., and Zhou, X. (2018). Early Visual Outcomes and Optical Quality after Femtosecond Laser Small-Incision Lenticule Extraction for Myopia and Myopic Astigmatism Correction of over −10 Dioptres. *Acta Ophthalmol.* 96, e341–e346. doi:10.1111/aos.13609

Qin, X., Tian, L., Zhang, H., Chen, X., and Li, L. (2019). Evaluation of Corneal Elastic Modulus Based on Corneal Visualization Scheimpflug Technology. *Biomed. Eng. Online* 18, 42. doi:10.1186/s12938-019-0662-1

Raevdal, P., Grauslund, J., and Vestergaard, A. H. (2019). Comparison of Corneal Biomechanical Changes after Refractive Surgery by Noncontact Tonometry: Small-incision Lenticule Extraction versus Flap-based Refractive Surgery - a Systematic Review. *Acta Ophthalmol.* 97, 127–136. doi:10.1111/aos.13906

Romito, N., Trinh, L., Goemaere, I., Borderie, V., Laroche, L., and Bouheraoua, N. (2020). Corneal Remodeling after Myopic SMILE: an Optical Coherence Tomography and *In Vivo* Confocal Microscopy Study. *J. Refract. Surg.* 36, 597–605. doi:10.3928/1081597X-20200713-01

Sánchez-González, J.-M., and Alonso-Aliste, F. (2019). Visual and Refractive Outcomes of 100 Small Incision Lenticule Extractions (SMILE) in Moderate and High Myopia: a 24-month Follow-Up Study. *Graefes Arch. Clin. Exp. Ophthalmol.* 257, 1561–1567. doi:10.1007/s00417-019-04349-4

Sedaghat, M. R., Momeni-Moghaddam, M., Azimi, A., Fakhimi, Z., Ziaei, M., Danesh, Z., et al. (2020). Corneal Biomechanical Properties in Varying Severities of Myopia. *Front. Bioeng. Biotechnol.* 8, 595330. doi:10.3389/fbioe.2020.595330

Sefat, S. M. M., Wiltfang, R., Bechmann, M., Mayer, W. J., Kampik, A., and Kook, D. (2016). Evaluation of Changes in Human Corneas after Femtosecond Laser-Assisted LASIK and Small-Incision Lenticule Extraction (SMILE) Using Non-contact Tonometry and Ultra-high-speed Camera (Corvis ST). *Curr. Eye Res.* 41, 917–922. doi:10.3109/02713683.2015.1082185

Shao, P., Eltony, A. M., Seiler, T. G., Tavakol, B., Pineda, R., Koller, T., et al. (2019). Spatially-resolved Brillouin Spectroscopy Reveals Biomechanical Abnormalities in Mild to Advanced Keratoconus *In Vivo*. *Sci. Rep.* 9, 7467. doi:10.1038/s41598-019-43811-5

Tian, L., Zhang, D., Guo, L., Qin, X., Zhang, H., Zhang, H., et al. (2021). Comparisons of Corneal Biomechanical and Tomographic Parameters Among Thin Normal Cornea, Forme Fruste Keratoconus, and Mild Keratoconus. *Eye Vis.* 8, 44. doi:10.1186/s40662-021-00266-y

Vinciguerra, R., Elsheikh, A., Roberts, C. J., Ambrósio, R., Jr., Kang, D. S., Lopes, B. T., et al. (2016). Influence of Pachymetry and Intraocular Pressure on Dynamic Corneal Response Parameters in Healthy Patients. *J. Refract. Surg.* 32, 550–561. doi:10.3928/1081597X-20160524-01

Vestergaard, A. H., Grauslund, J., Ivarsen, A. R., and Hjortdal, J. ϕ. (2014). Efficacy, Safety, Predictability, Contrast Sensitivity, and Aberrations after Femtosecond Laser Lenticule Extraction. *J. Cataract Refract. Surg.* 40, 403–411. doi:10.1016/j.jcrs.2013.07.053

Wang, L., Ko, C. Y., Meyers, E. E., Pedroja, B. S., Pelaez, N., and Bernstein, A. M. (2011). Concentration-dependent Effects of Transforming Growth Factor β1 on Corneal Wound Healing. *Mol. Vis.* 17, 2835–2846.

Wang, W., He, M., He, H., Zhang, C., Jin, H., and Zhong, X. (2017). Corneal Biomechanical Metrics of Healthy Chinese Adults Using Corvis ST. *Cont. Lens Anterior Eye* 40, 97–103. doi:10.1016/j.clae.2016.12.003

Wu, D., Liu, C., Li, B., Wang, D., and Fang, X. (2020). Influence of Cap Thickness on Corneal Curvature and Corneal Biomechanics after SMILE: a Prospective, Contralateral Eye Study. *J. Refract. Surg.* 36, 82–88. doi:10.3928/1081597X-20191216-01

Xia, L., Zhang, J., Wu, J., and Yu, K. (2016). Comparison of Corneal Biological Healing after Femtosecond LASIK and Small Incision Lenticule Extraction Procedure. *Curr. Eye Res.* 41, 1202–1208. doi:10.3109/02713683.2015.1107590

Xia, F., Qin, B., Shang, J., Chen, Z., Zhou, X., Zhao, J., et al. (2020). Four-year Outcomes of Small Incision Lenticule Extraction for Extreme High Myopia and Myopic Astigmatism. *Front. Med.* 7, 575779. doi:10.3389/fmed.2020.575779

Yun, S. H., and Chernyak, D. (2018). Brillouin Microscopy: Assessing Ocular Tissue Biomechanics. *Curr. Opin. Ophthalmol.* 29, 299–305. doi:10.1097/ICU.0000000000000489

Zhang, D., Zhang, H., Tian, L., Zheng, Y., Fu, C., Zhai, C., et al. (2021). Exploring the Biomechanical Properties of the Human Cornea *In Vivo* Based on Corvis ST. *Front. Bioeng. Biotechnol.* 9, 771763. doi:10.3389/fbioe.2021.771763

Zhou, Y., Wang, Y., Shen, M., Jin, Z., Chen, Y., Zhou, Y., et al. (2019). *In Vivo* evaluation of Corneal Biomechanical Properties by Optical Coherence Elastography at Different Cross-Linking Irradiances. *J. Biomed. Opt.* 24, 1–7. doi:10.1117/1.JBO.24.10.105001

Conflict of Interest: The authors declare that the research was conducted in the absence of any commercial or financial relationships that could be construed as a potential conflict of interest.

Publisher's Note: All claims expressed in this article are solely those of the authors and do not necessarily represent those of their affiliated organizations, or those of the publisher, the editors and the reviewers. Any product that may be evaluated in this article, or claim that may be made by its manufacturer, is not guaranteed or endorsed by the publisher.

frontiers | Frontiers in Bioengineering and Biotechnology

ORIGINAL RESEARCH
published: 20 May 2022
doi: 10.3389/fbioe.2022.882392

Measuring Human Corneal Stromal Biomechanical Properties Using Tensile Testing Combined With Optical Coherence Tomography

Yi Song[1†], Di Wu[2,3†], Min Shen[4], Like Wang[5], Congzheng Wang[4], Yong Cai[1], Chao Xue[2], George P.M. Cheng[6], Yongping Zheng[5,7] and Yan Wang[1,2,8]*

[1]Clinical College of Ophthalmology, Tianjin Medical University, Tianjin, China, [2]Tianjin Eye Hospital, Tianjin Key Lab of Ophthalmology and Visual Science, Tianjin Eye Institute, Tianjin, China, [3]Pacific University College of Optometry, Forest Grove, OR, United States, [4]School of Mechanical Engineering, Tianjin University, Tianjin, China, [5]Department of Biomedical Engineering, The Hong Kong Polytechnic University, Hong Kong, China, [6]School of Optometry, The Hong Kong Polytechnic University, Hong Kong, China, [7]Research Institute for Smart Ageing, The Hong Kong Polytechnic University, Hong Kong, China, [8]Nankai University Eye Institute, Nankai University Affiliated Eye Hospital, Nankai University, Tianjin, China

OPEN ACCESS

Edited by:
Salavat Aglyamov,
University of Houston, United States

Reviewed by:
Joshua Thomas Morgan,
University of California, Riverside, United States
Chiara Giulia Fontanella,
University of Padua, Italy

***Correspondence:**
Yan Wang
wangyan7143@vip.sina.com

[†]These authors have contributed equally to this work and share first authorship.

Specialty section:
This article was submitted to Biomechanics, a section of the journal Frontiers in Bioengineering and Biotechnology

Received: 23 February 2022
Accepted: 02 May 2022
Published: 20 May 2022

Citation:
Song Y, Wu D, Shen M, Wang L, Wang C, Cai Y, Xue C, Cheng GPM, Zheng Y and Wang Y (2022) Measuring Human Corneal Stromal Biomechanical Properties Using Tensile Testing Combined With Optical Coherence Tomography. Front. Bioeng. Biotechnol. 10:882392. doi: 10.3389/fbioe.2022.882392

Purpose: To investigate the *ex vivo* elastic modulus of human corneal stroma using tensile testing with optical coherence tomography (OCT) imaging and its correlation with *in vivo* measurements using corneal visualization Scheimpflug technology.

Methods: Twenty-four corneal specimens extracted from stromal lenticules through small incision lenticule extraction were cut into strips for uniaxial tensile tests. *In vivo* corneal biomechanical responses were evaluated preoperatively using the corneal visualization Scheimpflug technology (CorVis ST). The correlation of the elastic modulus with clinical characteristics and dynamic corneal response parameters were analyzed using *Spearman's* correlation analysis.

Results: The mean low strain tangent modulus (LSTM) of the human corneal stroma was 0.204 ± 0.189 (range 0.010–0.641) MPa, and high strain tangent modulus (HSTM) 5.114 ± 1.958 (range 2.755–9.976) MPa. Both LSTM ($r = 0.447$, $p = 0.029$) and HSTM ($r = 0.557$, $p = 0.005$) were positively correlated with the stress-strain index (SSI). LSTM was also positively correlated with the A1 deflection length ($r = 0.427$, $p = 0.037$) and A1 deflection area ($r = 0.441$, $p = 0.031$). HSTM was positively correlated with spherical equivalent ($r = 0.425$, $p = 0.038$).

Conclusions: The correlation of corneal elastic modulus with A1 deflection parameters and SSI may indicate a relationship between these parameters and tissue elasticity. The HSTM decreased with the degree of myopia. Combining tensile test with OCT may be a promising approach to assess corneal biomechanical properties.

Keywords: cornea, biomechanical properties, tensile testing, optical coherence tomography, dynamic response parameters, myopia

INTRODUCTION

As an important component of the ocular wall, the cornea provides almost 2/3 ocular refractive power and a protection of inner ocular tissues, and helps maintain the physiological shape of the eye. It is also a biological soft tissue with complex biomechanical properties such as nonlinear elasticity, viscoelasticity, anisotropy, and heterogeneity. Corneal biomechanical properties play a vital role in its shape and function, and are generally used to interpret corneal physiological phenomena, diseases and its responses to treatments (e.g., refractive surgeries) (Ruberti et al., 2011; Kling and Hafezi, 2017; Ma et al., 2018; Blackburn et al., 2019). Thus, there is a demand for an accurate and reliable method for assessing the mechanical characteristics of the cornea.

Currently, there are two available devices in clinical practice to characterize *in vivo* corneal biomechanics - the ocular response analyzer (ORA; Reichert Ophthalmic Instruments, Buffalo, United States) and the Corneal visualization Scheimpflug technology (CorVis ST; OCULUS Optikgeräte GmbH; Wetzlar, Germany). The CorVis ST detects the corneal deformation imaging during a Gaussian-distributed air impulse by a high-speed Scheimpflug camera. Various corneal deformation parameters are obtained, as well as material stiffness parameters such as SP A1 and SP HC. More recently, the stress-strain index (SSI) has been developed and validated to estimate corneal biomechanical behavior (Eliasy et al., 2019). Nevertheless, these metrics cannot directly reflect intrinsic mechanical properties, such as the elastic modulus, and most of them relate to intraocular pressure (IOP) and corneal pachymetry (Vinciguerra et al., 2016), which may confuse clinicians.

Laboratory corneal biomechanical evaluations include destructive methods, such as tensile test, inflation test, and atomic force microscopy as well as non-destructive techniques with potential clinical applicability, such as electronic speckle pattern interferometry, ultrasonic elastography, and Brillouin microscopy. Uniaxial tensile testing is a straightforward assessment of corneal mechanical properties *in vitro* by applying a load to a sample and measuring its relative deformation (Elsheikh and Alhasso, 2009). Commonly used samples are corneal strips with specific length and width. In order to calculate the applied stress, the force (load) needs to be divided by the area resisting the force; thus, the measurement of the sample thickness becomes the main challenge (Robinson and Durand-Smet, 2020). Previous studies have used ultrasound pachymetry (Elsheikh et al., 2008; Bell et al., 2018) or surgical parameters (Xue et al., 2018) to obtaining the sample thickness. However, these approaches have some limitations in terms of precision due to tissue swelling during sample preservation, preparation, and the experimental process.

Optical coherence tomography (OCT) is a key ophthalmologic imaging technique can provide rapid, noninvasive, high-resolution *in vivo* imaging of corneal structures, which enables its broad diagnostic and therapeutic applications (Ang et al., 2018; Spaide et al., 2018; Wang et al., 2019). In addition, OCT can assist tissue biomechanical detection when combined with an air-puff (Huang et al., 2011) or shear wave elastography (Wang and Larin, 2015). Among all categories of OCT devices, spectral-domain OCT (SD-OCT) has the advantages of high-speed acquisition and high axial resolution. Recently, Wang et al.(Wang et al., 2018) reported the use of SD-OCT in an inflation testing system for the assessment of corneal mechanical properties.

Given its advantage of real-time and high-resolution imaging, OCT can also be applied to tensile testing to obtain the exact corneal sample thickness. To date, no study has integrated these two testing methods. Hence, the purpose of this study was to investigate the *ex vivo* elastic modulus of the human corneal stroma by uniaxial tensile testing combined with OCT imaging and to determine its correlation with *in vivo* CorVis ST parameters.

TABLE 1 | Demographic and clinical characteristics (n = 24).

Parameters	Mean ± SD (Range)
Age (y)	23.96 ± 5.27 (17–36)
Sphere (D)	−4.96 ± 1.29 (-8.00 to −2.75)
Cylinder (D)	−0.38 ± 0.18 (−0.75to 0)
SE (D)	−5.15 ± 1.28 (−8.125–−2.875)
Km (D)	42.76 ± 1.41 (40.13–45.55)
CCT (μm)	543.96 ± 21.65 (517–595)
IOP (mmHg)	16.19 ± 2.25 (12.3–21.3)

SD, standard deviation; SE, spherical equivalent; Km, mean keratometry; CCT, central corneal thickness; IOP, intraocular pressure.

MATERIALS AND METHODS

Preparation of Specimens

Specimens were human corneal strips obtained from small incision lenticule extraction (SMILE) surgery. The study was approved by the Ethics Committee of Tianjin Eye Hospital and was carried out in accordance with the Declaration of Helsinki. Prior to this study, all participants signed the informed consent to agree with use of clinical data. A comprehensive ophthalmic examination including slit-lamp microscopy, non-contact tonometry and anterior segment tomography was conducted preoperatively to confirm a healthy cornea. The exclusion criteria were as follows: 1) keratoconus or suspected keratoconus, 2) active ocular or systemic diseases, 3) previous ocular trauma or surgeries, and any other condition that could affect the health of the cornea.

Twenty-four corneal specimens from 22 patients (7 men; 15 women) with a mean age of 23.96 ± 5.27 (range 17–36) years were included in the study. The mean preoperative sphere was −4.96 ± 1.29 D, and the mean astigmatism −0.38 ± 0.18 D. All the astigmatism was with the rule and less than −1.00 D to ensure a regular geometric configuration of the corneal strip. Demographic and clinical data are summarized in **Table 1**.

The SMILE procedures were performed by the same experienced physician at Tianjin Eye Hospital using a VisuMax femtosecond laser system (Carl Zeiss Meditec AG, Jena, Germany). A corneal stromal lenticule was created by femtosecond laser, and then dissected and extracted through a

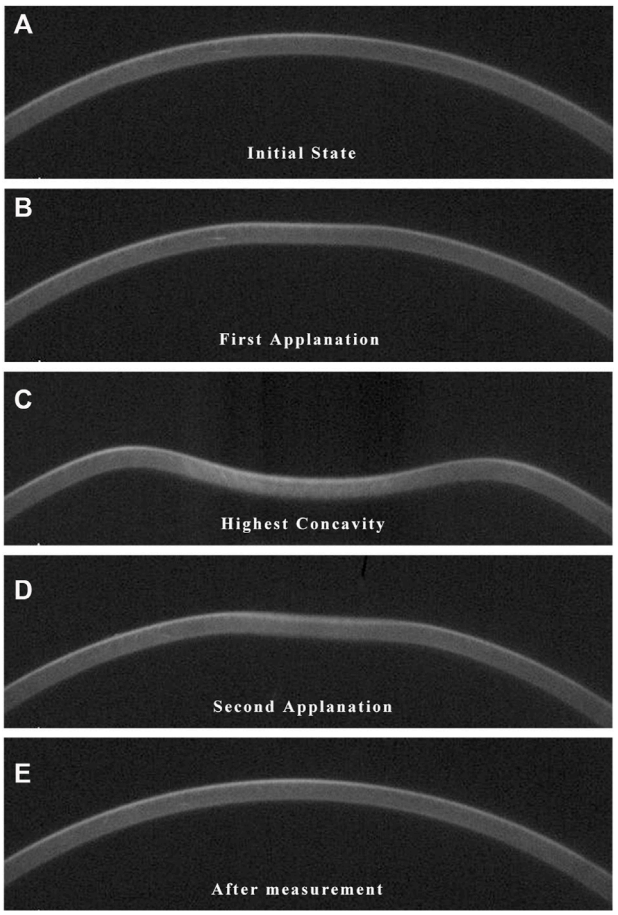

FIGURE1 | Images of corneal deformation during CorVis ST measurement. When applied by an air pulse, the cornea inwards into a concavity state and finally returns to its original shape through the following phases. **(A)** The initial convex state. **(B)** The first applanation. **(C)** The highest concavity. **(D)** The second applanation. **(E)** The final convex state.

small incision by the surgeon. The lenticule was then preserved in corneal storage medium (Eusol-C; Alchima, Padova, Italy) at a temperature of 4°C before preparation for the experiment. All specimens were tested in <2 h to avoid tissue swelling.

Prior to testing, a 1 mm-width strip was cut from the central region of the corneal lenticule with a customized double-blade knife. The strip length varied slightly with the diameter of the lenticule and was approximately 6.6 mm.

CorVis Scheimpflug Technology Measurement

All patients underwent *in vivo* biomechanical examination preoperatively using CorVis ST (*ver. 1.6r2187*). Measurement quality was checked by the reading in the QS window, and the data with an "OK" reading were considered usable.

The details and principles of CorVis ST measurement have been described elsewhere (Roberts, 2014; Wang et al., 2016). Briefly, the CorVis ST captures the corneal dynamic deformation applied by an air-puff force. As illustrated in **Figure 1**, the entire deformation process starts with the ingoing phase, in which the cornea passes from a convex state through the first applanation into a convave state, and finally reaches the point of highest concavity. Then the cornea achieves the oscillation phase, after which it returns to its initial shape through the second applanation. Three important events during the deformation process are the moment of the first applanation, the highest concavity and the second applanation. Corneal dynamic response parameters describing these three events were acquired, including the deformation amplitude, deflection length and deflection amplitude at the first applanation (A1 Deformation Amp., A1 Deflection Length, A1 Deflection Amp.), second applanation (A2 Deformation Amp., A2 Deflection Length, A2 Deflection Amp.) and highest concavity (HC Deformation Amp., HC Deflection Length, HC Deflection Amp.), corneal velocity at the first (A1 velocity) and second applanation (A2 velocity), time from the initiation of air puff until the first applanation (A1 Time), second applanation (A2 Time) and maximum deformation (HC Time), whole eye movement (WEM), peak distance and radius of curvature (Radius), the maximal value of the ratio between deformation amplitude at the apex and that at 2 mm (DA Ratio 2 mm) from the corneal apex, Ambrósio relational thickness to the horizontal profile (ARTh), integrated radius. Corneal stiffness parameters calculated based on the dynamic response parameters were also obtained, including stiffness parameter at first applanation (SPA1) and highest concavity (SP HC), and stress-strain index (SSI).

Uniaxial Tensile Testing With Optical Coherence Tomography Imaging

A custom-built tensile testing system (**Figure 2**) combined with customized SD-OCT was used in this study. The uniaxial tensile testing system includes a load cell capable of 1 N (ELFS-T3E-2L, Entran Devices Inc., Fairfield, NJ, United States) and a platform driven by a stepper motor. The SD-OCT imaging subsystem was similar to that used in previous corneal inflation experiments (Wang et al., 2018). It had a superluminescent diode (Part No. IPSDS804C, Inphenix Inc., Livermore, CA, United States), with a central wavelength of 840 nm, a bandwidth of 45 nm and an output power of 4.5 mW. Corneal cross-section imaging was obtained at an A-scan rate of 24 kHz. The axial and the lateral resolution of the OCT system were 8 and 21 μm, respectively. A CCD camera was incorporated to capture the shape of the sample. The entire system was controlled on a personal computer by a custom-designed program developed by LabVIEW (version 2009, National Instruments, Austin, TX, United States).

The corneal strip was mounted between the two clamps and moistened with phosphate buffered saline solution, after which the OCT probe was adjusted in alignment with the central area of the strip to record its structure during the testing process. The rate of clamp displacement was 0.05 mm/s and the maximal force was 0.25 N. Each specimen underwent two loading/unloading cycles for preconditioning.

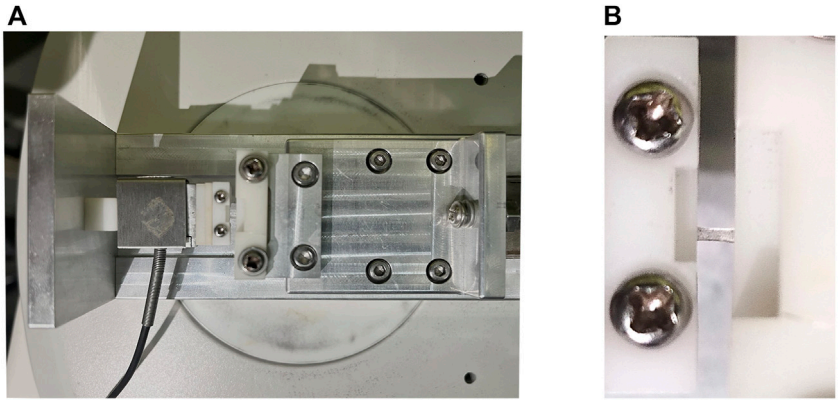

FIGURE 2 | Photographs of the custom-built uniaxial tensile testing system. **(A)** The uniaxial tensile testing platform. **(B)** Corneal strip mounted between the clamps.

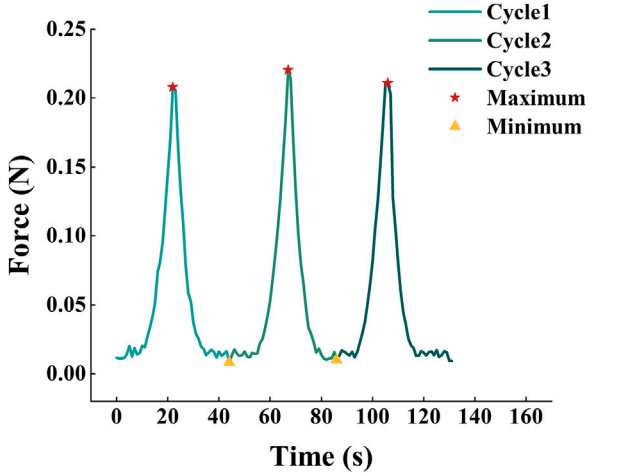

FIGURE 3 | Division of three loading/unloading cycles. The force and the clamp displacement were divided into six segments by the five maximum and minimum force during the loading/unloading process.

The Mathematical Analysis Procedure

The force F and clamp displacement x were divided into six segments by the five maximum and minimum forces during the loading/unloading process as shown in **Figure 3**. Each segment represents one stretching or slacking process. During one loading process, nonload section is located at the beginning of the curve caused by the initial bending of the corneal strips. The zero-load length (l_0) was cut using the formulation (Liu et al., 2020)

$$F(x) = d + \delta(x - l_0)\left[a(x - l_0) + b(x - l_0)^2\right]$$
$$\delta = \begin{cases} 0, & x < l_0 \\ 1, & x \geq l_0 \end{cases} \quad (1)$$

where d is the average force in the zero-load length cause by placing the corneal strips.

The average-stress of the corneal strip can be calculated as:

$$\sigma = \frac{F - d}{b \cdot h} \quad (2)$$

where b and h are the width and thickness of corneal strips measured by OCT images, respectively. The strain of the strip can be calculated as:

$$\varepsilon = \frac{x - l_0}{L_0 + l_0} \quad (3)$$

where L_0 is the original distance between two clamps.

According to the nonlinear property shown in **Figure 4**, the stress and strain curve was nonlinear and could be divided into three segments called toe region, heel region and linear region. The stress-strain relationship of the toe region and the linear region is linear like (Fratzl et al., 1998). Thus, the elastic property of corneal strips can be described by Young's modulus, which is calculated as follows:

$$E = \frac{\sigma}{\varepsilon} \quad (4)$$

The Young's modulus of the toe region and heel region are defined as low-strain tangent modulus (LSTM) and high-strain tangent modulus (HSTM), respectively.

Statistical Analysis

All data were tested for normality using the *Shapiro-Wilk* test. The correlation of the elastic modulus with demographic and CorVis ST parameters were analyzed using *Spearman's* correlation analysis, since the LSTM and HSTM were not distributed normally. All statistical analyses were performed using IBM SPSS software (version 22.0, IBM Corp., Armonk, NY). p value <0.05 was considered statistically significant.

RESULTS

A typical stress-strain curve is shown in **Figure 4**. With the growth of the strain, the stress increases slightly in the OA

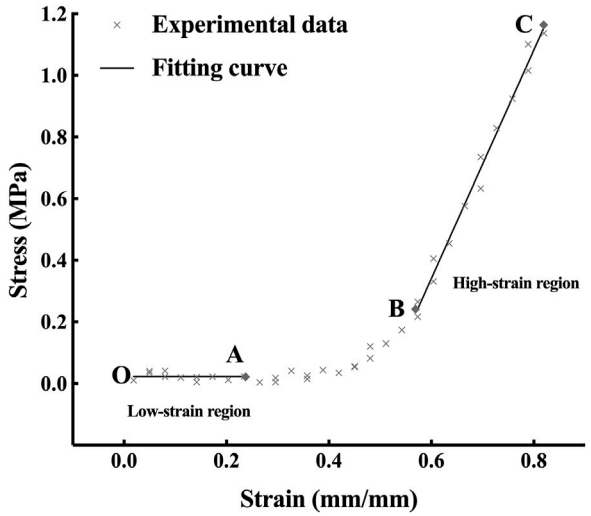

FIGURE 4 | The stress-strain curve of a corneal strip.

TABLE 2 | Correlation between Young's modulus and relevant clinical parameters (n = 24).

	LSTM		HSTM	
	r	*p* value	r	*p* value
Age	0.062	0.773	0.172	0.421
Sphere	0.117	0.587	0.395	0.056
Cylinder	0.175	0.412	0.175	0.412
SE	0.149	0.486	0.425	0.038[a]
Km	–0.262	0.216	–0.086	0.690
CCT	0.268	0.205	0.267	0.208
IOP	0.223	0.294	–0.049	0.819

LSTM, low strain tangent modulus; HSTM, high strain tangent modulus; SE, spherical equivalent; Km, mean keratometry; CCT, central corneal thickness; IOP, intraocular pressure.

[a]p < *0.05.*

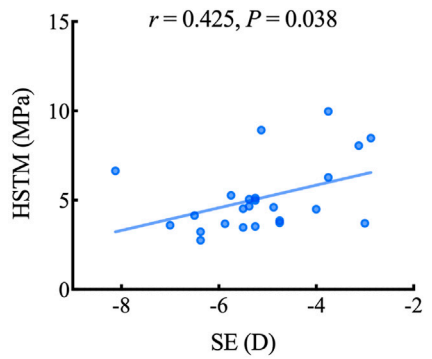

FIGURE 5 | Scatterplot showing the relationship between the HSTM and SE. HSTM, high strain tangent modulus; SE, spherical equivalent.

segment (the toe region), exponentially in the AB segment (the heel region) and linearly in the BC segment (the linear region). The mean LSTM was 0.204 ± 0.189 (range 0.010–0.641) MPa, and the mean HSTM 5.114 ± 1.958 (range 2.755–9.976) MPa.

Table 2 lists the correlation between LSTM, HSTM and the demographic and clinical characteristics. HSTM was positively correlated with spherical equivalent (SE) (r = 0.425, p = 0.038); that is, the higher the degree of myopia, the lower the HSTM, as highlighted in **Figure 5**. In addition, there was no correlation between HSTM and cylindrical diopter. Age, IOP, and central corneal thickness (CCT) were not associated with HSTM. No significant correlation was found between LSTM and demographic characteristics.

Table 3 illustrates the correlation between LSTM, HSTM and corneal dynamic response parameters as well as corneal stiffness parameters obtained by CorVis ST. As shown in **Figure 6**, LSTM was positively correlated with A1 deflection length (r = 0.427, p = 0.037), A1 deflection area (r = 0.441, p = 0.031) and SSI (r = 0.447, p = 0.029). HSTM was significantly correlated with SSI (r = 0.557, p = 0.005).

DISCUSSION

Better characterization of corneal biomechanical properties helps in managing ocular diseases such as glaucoma (Susanna et al., 2019), ectatic corneal disease (Ambrósio et al., 2017) and in predicting surgical outcomes. The elastic modulus is the most frequently used description of corneal stiffness which reflects the capacity to resist an elastic deformation. The human corneal elastic modulus has been reported in several published works, despite some problems in the precise acquisition of sample thickness. This study aimed to propose a new method combining real-time imaging with uniaxial extension testing to obtain the corneal elastic modulus and investigate the correlation between the elastic modulus and *in vivo* biomechanical metrics.

The value of the human corneal elastic modulus obtained in our study was similar in magnitude as the results of Hoeltzel's (Hoeltzel et al., 1992), which was 0.34 MPa. Owing to different experimental conditions including sample preservation, hydration, testing protocols, and calculation methods, the discrepancy of testing results between each study is unavoidable. For example, Xue et al.(Xue et al., 2018) reported that the LSTM of human corneal stroma was 1.17 ± 0.43 MPa in horizontal direction and 1.32 ± 0.50 MPa in vertical direction, and the HSTM was 43.59 ± 7.96 MPa and 51.26 ± 8.23 MPa, respectively. The difference in magnitude may be related to the difference in the testing machine and the experimental conditions. In their study, uniaxial tensile tests were performed using the IBTC-50 *in situ* tension and compression testing system, while in our study, a custom-built uniaxial testing system combined with SD-OCT was used. Furthermore, the OCT imaging subsystem utilized in our study is able to acquire the exact thickness of corneal samples, instead of estimating the sample thickness using surgical parameters. Regarding the experimental conditions, the corneal strip was bathed in normal saline during testing in Xue's study, while in our

TABLE 3 | Correlation between Young's modulus and CorVis ST corneal dynamic response and stiffness parameters (n = 24).

	LSTM (MPa)		HSTM (MPa)	
	***r* (95% CI)**	***p* value**	***r* (95% CI)**	***p* value**
A1 Deformation Amp. (mm)	0.090 (–0.301-0.494)	0.676	–0.320 (–0.648–0.088)	0.128
HC Deformation Amp. (mm)	–0.313 (–0.645-0.071)	0.136	0.005 (–0.411–0.425)	0.982
A2 Deformation Amp. (mm)	–0.230 (-0.599–0.230)	0.279	–0.246 (–0.538–0.165)	0.246
A1 Deflection Length (mm)	0.427 (–0.017–0.734)	0.037[a]	0.001 (–0.445–0.447)	0.997
HC Deflection Length (mm)	–0.170 (–0.609–0.265)	0.426	0.206 (–0.251–0.578)	0.334
A2 Deflection Length (mm)	0.066 (–0.382–0.503)	0.759	–0.277 (–0.622–0.201)	0.189
A1 Deflection Amp. (mm)	0.373 (–0.057–0.697)	0.073	–0.266 (–0.643–0.132)	0.209
HC Deflection Amp. (mm)	–0.298 (0.635–0.109)	0.157	0.103 (–0.314–0.490)	0.632
A2 Deflection Amp. (mm)	0.236 (–0.206–0.576)	0.267	–0.018 (–0.473–0.459)	0.934
Def. Amp. Max (mm)	–0.313 (–0.645–0.071)	0.136	0.005 (–0.411–0.425)	0.982
Deflection Amp. Max (mm)	–0.251 (–0.619–0.149)	0.236	0.136 (–0.296–0.531)	0.526
Deflection Amp. Max (ms)	–0.112 (–0.548–0.397)	0.602	–0.239 (–0.575–0.189)	0.260
A1 Time (ms)	0.220 (–0.162–0.545)	0.302	–0.037 (–0.413–0.381)	0.865
A1 Velocity (m/s)	–0.220 (–0.573–0.174)	0.302	–0.027 (–0.514–0.419)	0.902
A2 Time (ms)	–0.319 (–0.659–0.032)	0.129	0.018 (–0.432–0.481)	0.933
A2 Velocity (m/s)	0.131 (–0.257–0.532)	0.543	–0.006 (–0.439–0.409)	0.977
HC Time (ms)	0.048 (–0.375–0.467)	0.824	0.017 (–0.343–0.346)	0.936
A1 Deflection Area (mm^2)	0.441 (0.020–0.746)	0.031[a]	–0.052 (–0.493–0.373)	0.809
HC Deflection Area (mm^2)	-0.296 (–0.645–0.113)	0.161	0.144 (–0.295–0.530)	0.501
A2 Deflection Area (mm^2)	0.031 (–0.366–0.422)	0.885	0.039 (–0.403–0.504)	0.856
A1 dArc Length (mm)	-0.300 (–0.683–0.121)	0.154	0.197 (–0.276–0.568)	0.355
HC dArc Length (mm)	0.007 (–0.481–0.528)	0.974	–0.243 (–0.648–0.250)	0.253
A2 dArc Length (mm)	–0.010 (–0.428–0.420)	0.963	0.058 (–0.443–0.487)	0.788
dArcLengthMax (mm)	–0.070 (–0.500–0.408)	0.744	–0.087 (–0.510–0.338)	0.686
WEM Max (mm)	–0.194 (–0.536–0.269)	0.364	–0.212 (–0.552–0.213)	0.320
WEM Max (ms)	–0.363 (–0.736–0.085)	0.082	–0.117 (–0.485–0.280)	0.588
Peak Dist. (mm)	–0.163 (–0.566–0.240)	0.448	0.310 (–0.137–0.663)	0.140
Radius (mm)	0.224 (–0.139–0.571)	0.292	0.231 (–0.199–0.666)	0.277
Max Inverse Radius (mm^{-1})	–0.116 (–0.495–0.286)	0.589	–0.210 (–0.606–0.201)	0.324
DA Ratio Max (2 mm)	–0.286 (–0.591–0.131)	0.175	0.066 (-0.403–0.475)	0.759
ARTh	–0.183 (–0.552–0.199)	0.393	–0.227 (–0.601–0.190)	0.286
Integrated Radius (mm^{-1})	–0.337 (–0.676–0.082)	0.108	–0.130 (–0.587–0.323)	0.546
SP A1	0.068 (–0.318–0.458)	0.753	–0.150 (–0.561–0.323)	0.483
SP HC	0.243 (–0.136–0.595)	0.252	–0.135 (–0.515–0.311)	0.530
SSI	0.447 (0.027–0.745)	0.029[a]	0.577 (0.253–0.781)	0.005[b]

LSTM, low strain tangent modulus; HSTM, high strain tangent modulus.
[a]$p < 0.05$.
[b]$p < 0.01$.

study, the corneal strips were moistened with a drop of phosphate buffered saline solution prior to the test. In another relevant study published by Elsheikh and Alhassso (Elsheikh and Alhasso, 2009), 3-mm porcine corneal strips were tested as specimen, and the value of Young's modulus fell between 0.343– 1.264 MPa. In addition, considering the heterogeneity in depth of corneal mechanical properties, our results may also be slightly different from those of other studies, as only corneal stroma was extracted and tested in our study, while other studies involved different layers.

This study introduced the concept of LSTM to describe the elastic modulus of the toe region which corresponds to the physiological level of stress. Relatively, HSTM, the elastic modulus of the linear region, reflects the mechanical behavior under stress that surpasses the physiological intraocular pressure (IOP). We found that subjects with a higher LSTM had a significantly larger A1 deflection length and A1 deflection area. These two parameters represent the length of the applanated segment of the corneal surface and the area of the applanated region at the first applanation, respectively. The applanation length is defined as the length of a line that describes the applanated segment of the corneal surface at the first applanation. Recent research (Roberts et al., 2017) has demonstrated that A1 deflection length/area is strongly affected by corneal stiffness. A stiffer cornea tends to have greater resistance to deformation, which generates a larger flattened length, and therefore area deformed. This observation is consistent with our results.

This study revealed the correlation between the *ex vivo* elastic modulus and SSI parameter provided by the CorVis ST machine, which is a newly introduced *in vivo* stiffness metric based on finite element modeling. Unlike most CorVis ST parameters, SSI is independent of IOP and corneal thickness, and has been validated through comparison with *ex vivo* experimental data of human corneas (Elsheikh et al., 2007; Elsheikh et al., 2010). This consistency could to some extent indicate the reliability of our data.

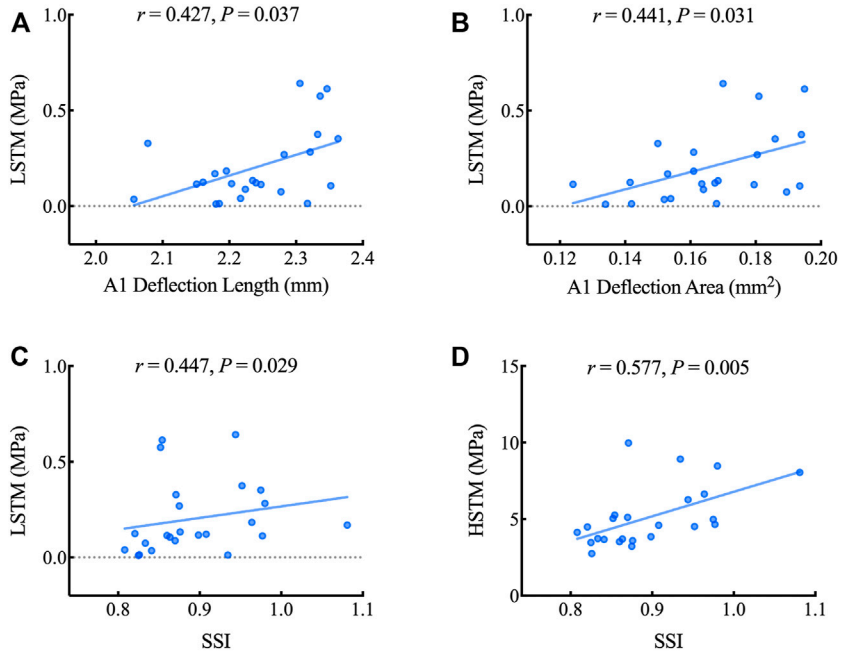

FIGURE 6 | Scatterplots showing the relationship between the LSTM, HSTM and corneal dynamic response and stiffness parameters including A1 deflection length **(A)**, A1 deflection area **(B)** and SSI **(C, D)**. LSTM: low strain tangent modulus; HSTM: high strain tangent modulus; SSI: stress-strain index.

Interestingly, we also found that the HSTM decreased with the degree of myopia. The exact mechanism of the myopia remains unclear. Earlier work has confirmed that eyes with high myopia are biomechanically less stiff than those with low myopia by *in vivo* measurements (Plakitsi et al., 2011; Kang et al., 2018; Han et al., 2020). Our results are in agreement with previous findings, which may suggest the involvement of corneal biomechanics in the progression of myopia. A possible hypothesis might be that, given scleral thinning and localized ectasia of the posterior sclera in high myopia eyes (Rada et al., 2006), the cornea, as another load-bearing structure of the ocular wall, may have a similar alteration in mechanical strength. Further work is required to fully explore this potential mechanism.

Nevertheless, this study had some limitations. First, a relatively small sample size was unavoidable owing to the strict selection of experimental data. Conducting multiple comparison in correlation analysis further increase the possibility of false positive error in the results. Given that, a study with a larger sample size and multiple comparison error control is worthwhile to be conducted in the future. Second, we did not mark the direction of the corneal lenticule, although we chose samples whose astigmatism was <—0.5D to reduce the impact of asymmetrical corneal thickness distribution, and then minimize the effect of corneal anisotropy. Further studies can be followed to investigate whether the stiffness of cornea is directional in astigmatism cases. The elastic modulus measured in this study seemed to be variable, which may be due to the individual difference in mechanical properties and a relatively low sampling frequency in the tensile tests. Additionally, the viscoelastic behavior of cornea tissue was not fully considered when comparing *ex vivo* and *in vivo* measurements, while we focused on investigating the possible correlations, mainly in elastic properties.

In conclusion, we evaluated the elastic modulus of the corneal stroma under low strain and high strain using an advent uniaxial tensile tester incorporating SD-OCT. The LSTM was found to be accompanied by a larger A1 length and A1 deflection area measured by the CorVis ST machine, implying a relationship between these corneal dynamic response parameters and its intrinsic elasticity. The corneal elastic modulus seemed to be lower in highly myopic eyes, which may be a hint of corneal mechanical alteration. The attempt in our study may be a promising approach to better characterize corneal biomechanical properties and to verify the parameters provided by those widely used *in vivo* measurement machines for corneal biomechanics. This can further aid promoting procedures that mechanically interact with the cornea.

DATA AVAILABILITY STATEMENT

The original contributions presented in the study are included in the article/Supplementary Material, further inquiries can be directed to the corresponding author.

ETHICS STATEMENT

The studies involving human participants were reviewed and approved by the Ethics Committee of Tianjin Eye Hospital. Written informed consent to participate in this study was provided by the participants' legal guardian/next of kin.

AUTHOR CONTRIBUTIONS

YS, DW, and YC collected the clinical data, conducted the experiment, and completed the statistical analysis. LW designed the experimental device. YS produced the first draft of the manuscript. MS and CW helped analyse the data and revised the article. CX contributed to revision of the original manuscript. YZ and YW supervised the project and critically revised the article, together with GC, they formed the research idea of this study. All authors contributed to the manuscript revision and agreed to be accountable for the submitted version.

FUNDING

This work was supported by the National Natural Science Foundation of China (Grant No. 81873684).

ACKNOWLEDGMENTS

We thank Hong Kong Polytechnic University for supplying the experimental device.

REFERENCES

Ambrósio, R., Lopes, B. T., Faria-Correia, F., Salomão, M. Q., Bühren, J., Roberts, C. J., et al. (2017). Integration of Scheimpflug-Based Corneal Tomography and Biomechanical Assessments for Enhancing Ectasia Detection. *J. Refract Surg.* 33 (7), 434–443. doi:10.3928/1081597X-20170426-02

Ang, M., Baskaran, M., Werkmeister, R. M., Chua, J., Schmidl, D., Aranha Dos Santos, V., et al. (2018). Anterior Segment Optical Coherence Tomography. *Prog. Retin. eye Res.* 66, 132–156. doi:10.1016/j.preteyeres.2018.04.002

Bell, J. S., Hayes, S., Whitford, C., Sanchez-Weatherby, J., Shebanova, O., Vergari, C., et al. (2018). The Hierarchical Response of Human Corneal Collagen to Load. *Acta Biomater.* 65, 216–225. doi:10.1016/j.actbio.2017.11.015

Blackburn, B. J., Jenkins, M. W., Rollins, A. M., and Dupps, W. J. (2019). A Review of Structural and Biomechanical Changes in the Cornea in Aging, Disease, and Photochemical Crosslinking. *Front. Bioeng. Biotechnol.* 7, 66. doi:10.3389/fbioe.2019.00066

Eliasy, A., Chen, K.-J., Vinciguerra, R., Lopes, B. T., Abass, A., Vinciguerra, P., et al. (2019). Determination of Corneal Biomechanical Behavior *In-Vivo* for Healthy Eyes Using CorVis ST Tonometry: Stress-Strain Index. *Front. Bioeng. Biotechnol.* 7, 105. doi:10.3389/fbioe.2019.00105

Elsheikh, A., and Alhasso, D. (2009). Mechanical Anisotropy of Porcine Cornea and Correlation with Stromal Microstructure. *Exp. Eye Res.* 88 (6), 1084–1091. doi:10.1016/j.exer.2009.01.010

Elsheikh, A., Brown, M., Alhasso, D., Rama, P., Campanelli, M., and Garway-Heath, D. (2008). Experimental Assessment of Corneal Anisotropy. *J. Refract Surg.* 24 (2), 178–187. doi:10.3928/1081597x-20080201-09

Elsheikh, A., Geraghty, B., Rama, P., Campanelli, M., and Meek, K. M. (2010). Characterization of Age-Related Variation in Corneal Biomechanical Properties. *J. R. Soc. Interface.* 7 (51), 1475–1485. doi:10.1098/rsif.2010.0108

Elsheikh, A., Wang, D., Brown, M., Rama, P., Campanelli, M., and Pye, D. (2007). Assessment of Corneal Biomechanical Properties and Their Variation with Age. *Curr. eye Res.* 32 (1), 11–19. doi:10.1080/02713680601077145

Fratzl, P., Misof, K., Zizak, I., Rapp, G., Amenitsch, H., and Bernstorff, S. (1998). Fibrillar Structure and Mechanical Properties of Collagen. *J. Struct. Biol.* 122 (1-2), 119–122. doi:10.1006/jsbi.1998.3966

Han, F., Li, M., Wei, P., Ma, J., Jhanji, V., and Wang, Y. (2020). Effect of Biomechanical Properties on Myopia: a Study of New Corneal Biomechanical Parameters. *BMC Ophthalmol.* 20 (1), 459. doi:10.1186/s12886-020-01729-x

Hoeltzel, D. A., Altman, P., Buzard, K., and Choe, K.-i. (1992). Strip Extensiometry for Comparison of the Mechanical Response of Bovine, Rabbit, and Human Corneas. *J. Biomech. Eng.* 114 (2), 202–215. doi:10.1115/1.2891373

Huang, Y.-P., Wang, S.-Z., Saarakkala, S., and Zheng, Y.-P. (2011). Quantification of Stiffness Change in Degenerated Articular Cartilage Using Optical Coherence Tomography-Based Air-Jet Indentation. *Connect. tissue Res.* 52 (5), 433–443. doi:10.3109/03008207.2011.555824

Kang, B. S., Wang, L.-K., Zheng, Y.-P., Guggenheim, J. A., Stell, W. K., and Kee, C.-S. (2018). High Myopia Induced by Form Deprivation Is Associated with Altered Corneal Biomechanical Properties in Chicks. *PloS one* 13 (11), e0207189. doi:10.1371/journal.pone.0207189

Kling, S., and Hafezi, F. (2017). Corneal Biomechanics - a Review. *Ophthalmic Physiol. Opt.* 37 (3), 240–252. doi:10.1111/opo.12345

Liu, T., Shen, M., Huang, L., Xiang, Y., Li, H., Zhang, Y., et al. (2020). Characterization of Hyperelastic Mechanical Properties for Youth Corneal Anterior Central Stroma Based on Collagen Fibril Crimping Constitutive Model. *J. Mech. Behav. Biomed. Mater.* 103, 103575. doi:10.1016/j.jmbbm.2019.103575

Ma, J., Wang, Y., Wei, P., and Jhanji, V. (2018). Biomechanics and Structure of the Cornea: Implications and Association with Corneal Disorders. *Surv. Ophthalmol.* 63 (6), 851–861. doi:10.1016/j.survophthal.2018.05.004

Plakitsi, A., O'Donnell, C., A Miranda, M., Charman, W. N., and Radhakrishnan, H. (2011). Corneal Biomechanical Properties Measured with the Ocular Response Analyser in a Myopic Population. *Ophthalmic & physiological Opt. J. Br. Coll. Ophthalmic Opt. (Optometrists)* 31 (4), 404–412. doi:10.1111/j.1475-1313.2011.00852.x

Roberts, C. J. (2014). Concepts and Misconceptions in Corneal Biomechanics. *J. cataract Refract. Surg.* 40 (6), 862–869. doi:10.1016/j.jcrs.2014.04.019

Roberts, C. J., Mahmoud, A. M., Bons, J. P., Hossain, A., Elsheikh, A., Vinciguerra, R., et al. (2017). Introduction of Two Novel Stiffness Parameters and Interpretation of Air Puff-Induced Biomechanical Deformation Parameters with a Dynamic Scheimpflug Analyzer. *J. Refract Surg.* 33 (4), 266–273. doi:10.3928/1081597X-20161221-03

Robinson, S., and Durand-smet, P. (2020). Combining Tensile Testing and Microscopy to Address a Diverse Range of Questions. *J. Microsc.* 278 (3), 145–153. doi:10.1111/jmi.12863

Ruberti, J. W., Sinha Roy, A., and Roberts, C. J. (2011). Corneal Biomechanics and Biomaterials. *Annu. Rev. Biomed. Eng.* 13, 269–295. doi:10.1146/annurev-bioeng-070909-105243

Spaide, R. F., Fujimoto, J. G., Waheed, N. K., Sadda, S. R., and Staurenghi, G. (2018). Optical Coherence Tomography Angiography. *Prog. Retin. eye Res.* 64, 1–55. doi:10.1016/j.preteyeres.2017.11.003

Summers Rada, J. A., Shelton, S., and Norton, T. T. (2006). The Sclera and Myopia. *Exp. eye Res.* 82 (2), 185–200. doi:10.1016/j.exer.2005.08.009

Susanna, B. N., Ogata, N. G., Jammal, A. A., Susanna, C. N., Berchuck, S. I., and Medeiros, F. A. (2019). Corneal Biomechanics and Visual Field Progression in Eyes with Seemingly Well-Controlled Intraocular Pressure. *Ophthalmology* 126 (12), 1640–1646. doi:10.1016/j.ophtha.2019.07.023

Vinciguerra, R., Elsheikh, A., Roberts, C. J., Ambrósio, R., Kang, D. S. Y., Lopes, B. T., et al. (2016). Influence of Pachymetry and Intraocular Pressure on Dynamic Corneal Response Parameters in Healthy Patients. *J. Refract Surg.* 32 (8), 550–561. doi:10.3928/1081597X-20160524-01

Wang, L.-K., Tian, L., and Zheng, Y.-P. (2016). Determiningin Vivoelasticity and Viscosity with Dynamic Scheimpflug Imaging Analysis in Keratoconic and Healthy Eyes. *J. Biophot.* 9 (5), 454–463. doi:10.1002/jbio.201500245

Wang, L., Tian, L., Huang, Y., Huang, Y., and Zheng, Y. (2018). Assessment of Corneal Biomechanical Properties with Inflation Test Using Optical Coherence Tomography. *Ann. Biomed. Eng.* 46 (2), 247–256. doi:10.1007/s10439-017-1973-7

Wang, S. B., Cornish, E. E., Grigg, J. R., and McCluskey, P. J. (2019). Anterior Segment Optical Coherence Tomography and its Clinical Applications. *Clin. Exp. Optometry* 102 (3), 195–207. doi:10.1111/cxo.12869

Wang, S., and Larin, K. V. (2015). Optical Coherence Elastography for Tissue Characterization: a Review. *J. Biophot.* 8 (4), 279–302. doi:10.1002/jbio.201400108

Xue, C., Xiang, Y., Shen, M., Wu, D., and Wang, Y. (2018). Preliminary Investigation of the Mechanical Anisotropy of the Normal Human Corneal Stroma. *J. Ophthalmol.* 2018, 1–7. doi:10.1155/2018/5392041

Conflict of Interest: The authors declare that the research was conducted in the absence of any commercial or financial relationships that could be construed as a potential conflict of interest.

Publisher's Note: All claims expressed in this article are solely those of the authors and do not necessarily represent those of their affiliated organizations, or those of the publisher, the editors and the reviewers. Any product that may be evaluated in this article, or claim that may be made by its manufacturer, is not guaranteed or endorsed by the publisher.

frontiers | Frontiers in Bioengineering and Biotechnology

TYPE Original Research
PUBLISHED 15 August 2022
DOI 10.3389/fbioe.2022.939129

OPEN ACCESS

EDITED BY
FangJun Bao,
Affiliated Eye Hospital of Wenzhou Medical College, China

REVIEWED BY
Gilbert Yong San Lim,
SingHealth, Singapore
Qiguo Rong,
Peking University, China
Weiyun Shi,
Shandong Eye Institute, China

*CORRESPONDENCE
Jie Wu,
wjdia5@126.com

†These authors have contributed equally to this work and share first authorship

SPECIALTY SECTION
This article was submitted to Biomechanics, a section of the journal Frontiers in Bioengineering and Biotechnology

RECEIVED 08 May 2022
ACCEPTED 13 July 2022
PUBLISHED 15 August 2022

CITATION
Chu Z, Ren Q, Chen M, Cheng L, Cheng H, Cui W, Bi W and Wu J (2022), The relationship between axial length/corneal radius of curvature ratio and stress–strain index in myopic eyeballs: Using Corvis ST tonometry. *Front. Bioeng. Biotechnol.* 10:939129. doi: 10.3389/fbioe.2022.939129

The relationship between axial length/corneal radius of curvature ratio and stress–strain index in myopic eyeballs: Using Corvis ST tonometry

Zhe Chu[1†], Qi Ren[1†], Meizhen Chen[2], Lu Cheng[2], Hao Cheng[3], Wei Cui[1], Wenjiao Bi[1] and Jie Wu[1*]

[1]Eye Institute of Shandong First Medical University, Qingdao Eye Hospital of Shandong First Medical University, State Key Laboratory Cultivation Base, Shandong Provincial Key Laboratory of Ophthalmology, School of Ophthalmology, Shandong First Medical University, Qingdao, China, [2]State Key Laboratory of Ophthalmology, Zhongshan Ophthalmic Center, Sun Yat-sen University Guangzhou, Guangzhou, China, [3]Department of Ophthalmology, the First Affiliated Hospital of Guangzhou Medical University, Guangzhou, China

Purpose: This study aimed to investigate the correlation of axial length/corneal radius of curvature ratio with stress–strain index (SSI).

Methods: Retrospective analysis was conducted to compare the right eyes of those with high myopia (HM, n = 132; age and 10–48 years) with those without high myopia (NHM, n = 135; age and 7–48 years), where the baseline axial length, corneal radius of curvature ratio, and central corneal thickness were analyzed; the differences in two groups were compared; and the relationship of axial length and axial length/corneal radius of curvature ratio with SSI were explored.

Results: Compared with AL < 26mm, SSI significantly decreased when AL ≥ 26 mm ($p = 0.001$), while there was no correlation with AL in the NHM group ($r = -0.14$, $p = 0.12$) or HM group ($r = -0.09$, $p = 0.32$). AL/CR was significantly associated with SSI in both the NHM ($r = -0.4$, $p < 0.001$) and HM ($r = -0.18$, $p = 0.04$) groups. In the NHM group, AL/CR was significantly associated with SSI (unstandardized beta = -0.514, se = 0.109, $p < 0.001$) with the adjustment of age and gender. Additionally, a significant association of SSI with AL/CR was also found after adjusting for age and gender (unstandardized beta = -0.258, se = 0.096, and $p = 0.0082$) in the HM group.

Conclusion: SSI showed a significant negative correlation with AL/CR in patients without high myopia and in patients with high myopia. However, SSI exhibited no decrease with the worsening of myopia, but it gradually remained stable at a low level. The findings of this study validate, to some extent, the possibility of analyzing the dynamic changes in ocular wall stiffness during the development of myopia by measuring *in vivo* corneal biomechanical parameters.

KEYWORDS
axial length, corneal radius of curvature, AL/CR, stress–strain index, corvis ST, sclera

Introduction

The pathogenesis of myopia has long been viewed as an interesting biological problem, and the development of nearsightedness is inextricably linked to the process of refractive development. Initially, this process was often described in terms of a change in the refractive error; however, it became more sophisticated with the advancement of the equipment used for examination, and we have found that even though the refractive state of the eye is maintained using orthokeratology, the structure of the eye, including the cornea and lens, and parameters such as axial length (AL) change throughout the life Morgan et al., (2014). The AL in newborns is approximately 17 mm. During the period from birth to 2–3 years of age, the corneal refractive power and lens refractive power decline rapidly, while the AL increases; after the relative stabilization of corneal development at 2–3 years of age, the AL increases rapidly, and to match this increase, the lens refractive power declines rapidly. When the rate at which the lens loses its refractive power decreases rapidly at the age of 10–12 years, the refractive state of the eye stabilizes and approaches emmetropia; at this stage, the AL is approximately 23 mm, and this process stabilization is known as emmetropization. However, after the completion of emmetropization, the increase in the AL can continue until at least 30 years of age. This condition, in which the other refractive components no longer change but the AL continues to increase, has been considered an important cause of axial myopia (Tokoro and Suzuki, 1968; Mutti et al., 2012). The increase in the AL is essentially the result of the expansion of the ocular wall. Because the sclera occupies more than 90% of the surface area of the eyeball Olsen et al., (1998), the expansion of the scleral wall is the most central change in patients with axial myopia. The wall of the eyeball is roughly shaped as a flat ellipsoid at birth, and during emmetropization, the scleral wall expands nearly uniformly in all directions, gradually changing from a flat sphere to a round sphere. However, the expansion of the wall of the eyeball is not always uniform in all directions; in normal eyes, the anterior and posterior regions of the sclera reach an adult level at 2 and 13 years of age (Fledelius and Christensen, 1996), respectively. Subsequently, as myopia develops and progresses, the expansion of the sclera is greater along the sagittal axis [0.35 mm/diopter (D)] than along the coronal axis (0.19 mm/D) and horizontal axis (0.10 mm/D), although it can continue to expand in all three axes Atchison et al., (2004). The expansion of the scleral wall on the sagittal axis (i.e., the extension of the AL length) shows the closest relation to the refractive status and prognosis of axial myopia: first, the extension of the AL drives the retina of the posterior pole back, and the degree of distance of the posterior pole retina from the focal plane of the refractive system, such as the cornea and lens, can be regarded as the degree of myopia; consequently, high myopia (HM) is defined by a spherical equivalent of −6 D or less with an AL generally exceeding 26 mm (Wang et al., 2015; Tideman et al., 2016). It should be added here that axial elongation is the primary factor in the development of myopia (Flitcroft et al., 2019; Wolffsohn et al., 2019). Considering that the AL distribution of emmetropia ranges from 21.5 to 25.5 mm Steiger, 1913), AL ≥ 26 mm (or AL ≥ 26.5 mm) is often used as the diagnostic threshold of high myopia in clinical studies. Second, especially in the patients with HM, the prevalence of posterior scleral staphyloma as well as choroidal thinning and vitreoretinal interface traction increases significantly with an increase in the AL, which leads to the impairment of visual function due to pathological myopia (Ohno-Matsui et al., 2021).

It is undeniable that AL is an extremely important parameter that reflects the degree of ocular myopia. Nevertheless, considering the differences in body mass index (BMI) and orbital volume of each individual, we can state that AL alone does not accurately reflect the degree of ocular myopia. Due to the differences in the refractive power of the cornea, lens, and other components of the refractive system between individuals, myopic refraction may vary for the same AL; therefore, the description of the degree of myopia requires the combination of the "refractive power of the refractive system" and the "distance of the photoreceptors from the focal plane of the refractive system of the eye." The spherical equivalent refractive error is the simplest and most direct way to quantify the degree of myopia, which is described by the refractive distance between the focal plane of the refractive system of the eye and the central macular concavity. In addition, because the anterior surface of the cornea carries most of the refractive power of the refractive system of the eye, the ratio of AL and corneal radius of curvature (AL/CR) is likewise a reliable variable for the quantitative description of the degree of ocular myopia. Therefore, the AL/CR shows a better correlation with the refractive error than does AL alone (Grosvenor and Scott, 1994; Scheiman et al., 2016).

With a change in the severity of axial myopia, the biomechanical properties of the ocular wall change, and myopic eyes have been suggested to show lower levels of stiffness than do emmetropic ones (Lam et al., 2002; Berisha et al., 2010). Studies on the isolated scleral tissues have revealed that the scleral collagen fibers in highly myopic eyes show a decrease in diameter, which increases the ocular wall elasticity and viscoelasticity (Rada et al., 2006; Mcbrien et al., 2009), especially in the posterior scleral chylomicron where ultrastructural changes in the scleral tissue make the scleral structure thinner and more susceptible to mechanical stress-induced deformation (Curtin and Teng, 1958; Gentle et al., 2003). Meanwhile, studies on the biomechanical properties of

the *in vivo* cornea in myopic eyes have found that the expansion of the sclera may lead to a decrease in corneal stiffness (Yu et al., 2020). Because the vast majority of the sclera is not exposed to the external environment like the cornea, few studies have focused on the biomechanical properties of the *in vivo* scleral tissue; however, some researchers believe that the above finding is because the corneal stroma is the continuation of the scleral tissue. Some corneal biomechanical parameters are related to the eye axis, and the measurement of corneal biomechanical parameters can reflect the mechanical properties of the sclera to some extent (Yu et al., 2020; Liu et al., 2021).

The CorVis ST tonometry-based stress–strain index (SSI) is a new index of corneal stiffness obtained using a numerical simulation of model eyes and finite element analysis, and it is currently considered to be age-dependent; however, it is not correlated with intraocular pressure (IOP) or central corneal thickness (CCT) (Eliasy et al., 2019). SSI is based on the stress–strain curve of the ocular wall tissue. The stress–strain curve is an important concept in material science, which can be obtained by recording the deformation (strain) of material under different tensile and compressive loading stresses (Luebkeman and Peting). With regard to the ocular wall tissue, while applying a simple stretching factor as a multiplier to all strain values, stress–strain curves that are different and have no intersecting trends could be obtained. For the average experimental behavior observed in the corneal tissue of an individual aged 50 years, SSI was set to 1.0. Higher SSI values would indicate higher tissue stiffness and vice versa (Eliasy et al., 2019). Liu et al. found that SSI, an index of corneal stiffness, was negatively correlated with AL when the latter is <26 mm but not when it is ≥26 mm (Liu et al., 2021). Therefore, it is suggested that due to the non-uniform expansion of the eyeball during myopic development, the eye tends to expand uniformly in all directions in the early stages; the expansion after the development of HM mainly originates in the posterior pole, when the morphological and mechanical properties of the anterior segment of the eye stabilize and are no longer associated with the posterior pole. These studies provide the basis for us to infer changes in the biomechanical characteristics of the myopic ocular wall using SSI.

As noted earlier, the stiffness of the ocular wall increases with age and decreases with the progression of myopia, and the performance of SSI in many studies seems to fit well with this pattern of change in the ocular wall stiffness (Eliasy et al., 2019; Liu et al., 2021). Because the AL/CR shows a better correlation with refractive error than does AL alone and because AL/CR can be used to measure the degree of ocular myopia, we wonder if SSI still fits the pattern of a decrease in wall stiffness with an increase in myopia at AL ≥ 26 mm. In other words, it is unclear whether SSI is still correlated with the expansion of the posterior pole of the eye after the morphologic and mechanical properties of the anterior segment of the eye have developed and stabilized. Therefore, we hypothesized that the biomechanical parameter SSI is not directly related to the "increase in the AL" but rather to the "increase in myopia." To test the abovementioned hypothesis, we analyzed AL/CR and SSI as variables for the evaluation of the degree of ocular myopia and the biomechanical characteristics of the ocular wall, respectively, with the aim to explore the correlation between SSI and the degree of myopia and to investigate whether the dynamic changes in ocular wall stiffness during the development of myopia can be analyzed through the measurement of *in vivo* corneal biomechanical parameters.

Methods

Subjects

A total of 267 patients (534 eyes) admitted to the Qingdao Eye Hospital of Shandong First Medical University, from July 2021 to April 2022, were included in this cross-sectional study. We excluded participants with a history of or those who were suspected of contact lens use, keratoconus, and other corneal lesions and those who had undergone refractive surgery and other ophthalmic surgeries, such as vitreous surgery, and those for uveitis or glaucoma. Depending on the measured AL of the right eye, the subjects were divided into the non-HM (NHM) group (AL < 26 mm) and the HM group (AL ≥ 26 mm). To avoid the mixed influence of both eyes on the results, all the data, except for the baseline data, were obtained from the right eye. All subjects underwent a complete general ophthalmic examination, including slit lamp examination, subjective refraction measurement, fundus examination, and IOP measurement. All research procedures followed the principles of the Helsinki Declaration and were approved by the Ethics Committee of Qingdao Eye Hospital of Shandong First Medical University.

Measurement of ocular structural parameters and biomechanical parameters

An Optical coherence biometrics OA-2000 (Tomey, Japan) was utilized to measure the AL of each subject's eyes. Pentacam (Oculus, Wetzlar, Germany) was utilized to measure the corneal thickness and radius of curvature of the anterior corneal surface. Biomechanical SSI parameters were measured with CorVis ST (Oculus, Wetzlar, Germany). All measurements were performed by certified technicians. Only measurements with "OK" quality specifications were included in this analysis.

Statistical analysis

Sociodemographic and clinical variables of participants were compared between the two groups (NHM vs. HM) using a two-sample *t*-test for continuous variables and Pearson's $\chi 2$ test for categorical variables. We performed Pearson's correlation tests to examine the relationships between continuous variables of interest in the two groups separately. We ran a multivariable linear regression model with SSI as the dependent variable for

TABLE 1 Participants' characteristics of two groups.

Characteristic	Overall, n = 267[a]	NHM, n = 135[a]	HM, n = 132[a]	*p* value[b]
Age, year	22 (8)	20 (8)	24 (7)	<0.001
Gender				0.87
Male	122 (46%)	61 (45%)	61 (46%)	
Female	145 (54%)	74 (55%)	71 (54%)	
SSI (OD)	0.82 (0.15)	0.85 (0.16)	0.79 (0.15)	0.002
SSI (OS)	0.84 (0.15)	0.86 (0.15)	0.82 (0.15)	0.017
CCT (OD), mm	544 (34)	542 (36)	545 (32)	0.5
CCT (OS), mm	544 (34)	543 (35)	545 (33)	0.6
CR (OD), mm	7.78 (0.24)	7.71 (0.24)	7.86 (0.22)	<0.001
CR (OS), mm	7.76 (0.30)	7.68 (0.33)	7.85 (0.24)	<0.001
AL (OD), mm	26.01 (1.48)	24.89 (0.85)	27.16 (1.06)	<0.001
AL (OS), mm	25.88 (1.48)	24.82 (0.88)	26.96 (1.15)	<0.001
AL/CR (OD)	3.34 (0.17)	3.23 (0.13)	3.46 (0.14)	<0.001
AL/CR (OS)	3.34 (0.21)	3.24 (0.17)	3.44 (0.19)	<0.001

Abbreviations: NHM, non-high myopia; HM, high myopia; SSI, stress–strain index; CCT, central corneal thickness; CR, corneal curvature; AL, axial length; AL/CR, axial length/corneal radius of curvature ratio.
[a]Mean (SD); n (%).
[b]Welch two-sample *t*-test; Pearson's Chi-squared test.

each group to investigate the association of AL/CR with SSI. The covariates included age and gender. Cook's distance was used to detect potential influential points that may affect our models. We did not find any influential points. All statistical work was conducted using R statistical software (Version: 4.1.3).

Result

Sample characteristics

As shown in Table 1, the study sample comprised 267 participants, including 135 individuals in the NHM group and 132 individuals in the HM group. There were significant differences in age, SSI, CR, AL, and AL/CR between the two groups (all $p < 0.05$), while the two groups did not differ in the percentage of female gender ($\chi 2 = 0.028$, $p = 0.87$) or CCT ($p > 0.05$).

Correlation between several continuous variables of interest

In order to examine the relationships between several continuous variables of interest, Pearson's correlation tests were performed. As shown in Figure 1, we found that age was positively correlated with AL in the overall sample ($r = 0.36$, $p < 0.001$). Figure 2 demonstrates a positive correlation between AL and CR in both the NHM ($r = 0.31$, $p < 0.001$) and HM ($r = 0.34$, $p < 0.001$) groups. Additionally, age was also found to be associated with AL/CR in both the NHM ($r = 0.42$, $p < 0.001$) and HM ($r = 0.3$, $p < 0.001$) groups (Figure 3).

Nevertheless, we did not find a significant correlation between age and SSI in the NHM ($r = -0.15$, $p = 0.09$) or HM ($r = 0.15$, $p = 0.08$) group (Figure 4). As shown in Figure 5, AL was not associated with SSI in the NHM ($r = -0.14$, $p = 0.1$) or HM group ($r = -0.09$, $p = 0.32$).

To investigate the relationship between AL/CR and SSI in the two groups, Pearson's correlation tests were used. We found that AL/CR was significantly associated with SSI in both the NHM ($r = -0.4$, $p < 0.001$) and HM ($r = -0.18$, $p = 0.04$) groups (Figure 6).

Association of AL/CR with SSI in the NHM and HM groups

To further explore the association between AL/CR and SSI, multivariable linear regression models with the adjustment of age and gender were fitted in the two groups. In the NHM group, AL/CR was significantly associated with SSI (unstandardized beta = -0.514, se = 0.109, $p < 0.001$) with the adjustment of age and gender (Table 2). Additionally, a significant association of SSI with AL/CR was also found after adjusting for age and gender (unstandardized beta = -0.258, se = 0.096, $p = 0.0082$) in the HM group.

Discussion

In this study, we investigated the relationship between SSI and AL/CR, a proxy parameter for the degree of ocular myopia, in the

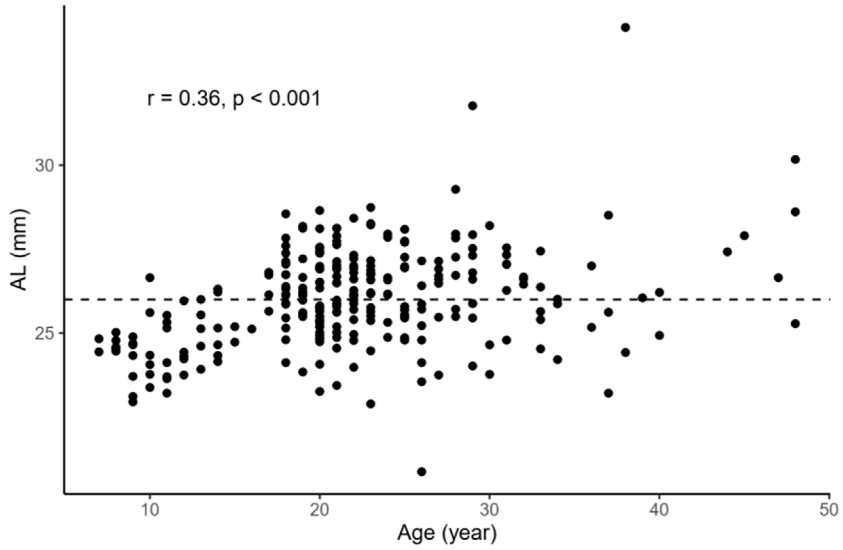

FIGURE 1
Relationship between age and AL in the overall sample. Age was positively correlated with AL in the overall sample (r = 0.36, p < 0.001). The dashed line represents the cutoff point for classifying individuals into the two groups: NHM (AL<26 mm) and HM(AL≥26 mm). Abbreviation: NHM, non-high myopia; HM, high myopia; AL, axial length.

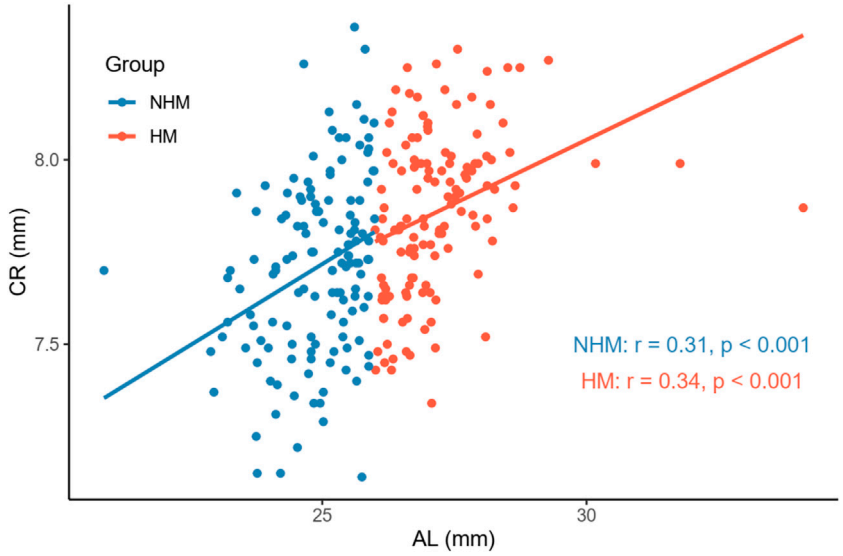

FIGURE 2
Relationship between AL and CR in the two groups. There was a positive correlation between AL and CR in both the NHM (r = 0.31, p < 0.001) and HM (r = 0.34, p < 0.001) groups. Abbreviation: NHM, non-high myopia; HM, high myopia; AL, axial length; CR, corneal curvature.

young and middle-aged populations. Overall, SSI at AL ≥ 26 mm was smaller than that at AL < 26 mm. Both at AL < 26 mm and at AL ≥ 26 mm, AL/CR values were significantly associated with SSI after the adjustment of age and gender; however, the decrease in SSI at AL ≥ 26 mm (HM group) was lower than that at AL < 26 mm (NHM group) for each unit of increase in AL/CR.

The SSI derived using CorVis ST Tonometry is intended to be independent of IOP and corneal geometry and can visually

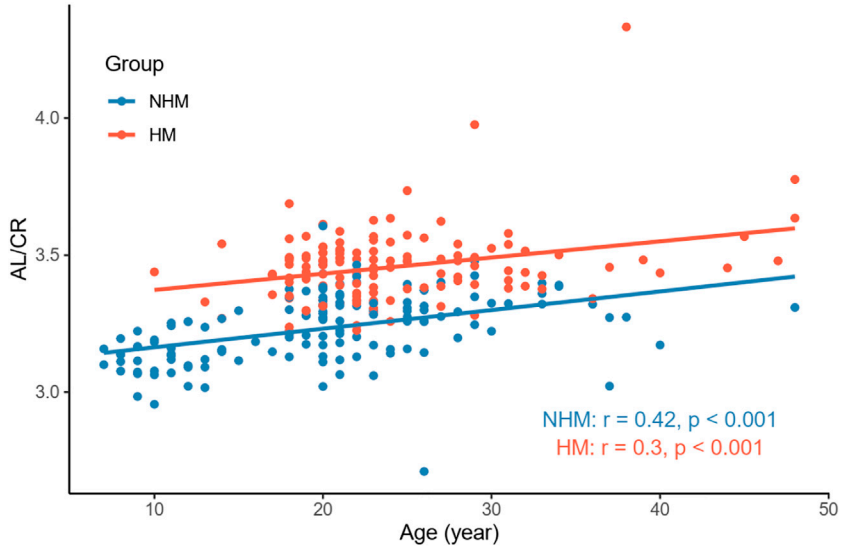

FIGURE 3
Relationship between age and AL/CR in the two groups. Age was associated with AL/CR in both the NHM (r = 0.42, p < 0.001) and HM (r = 0.3, p < 0.001) groups. Abbreviation: NHM, non-high myopia; HM, high myopia; AL/CR: axial length/corneal radius of curvature ratio.

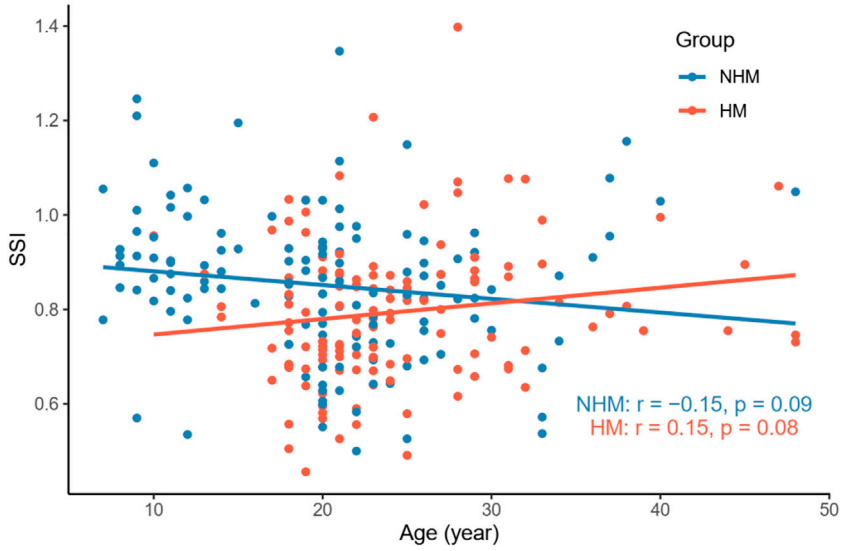

FIGURE 4
Relationship between age and SSI in the two groups. We did not find a significant correlation between age and SSI in the NHM (r = -0.15, p = 0.09) or HM (r = 0.15, p = 0.08) group. Abbreviation: NHM, non-high myopia; HM, high myopia; SSI, stress–strain index.

quantify corneal tissue stiffness: the greater the SSI value, the greater the stiffness of the tissue material and vice versa. In this study, SSI in the HM group was 0.77 ± 0.15 (range, 0.46–1.40), and that in the NHM group was 0.85 ± 0.16 (range, 0.50–1.35); SSI values in both the groups conformed to normal distribution. One study (Liu, 2020) reported that the SSI values in a Chinese Han cohort aged 17–50 years (mean, 27.4 years old) showed a normal distribution with a mean value of 0.895 (range,

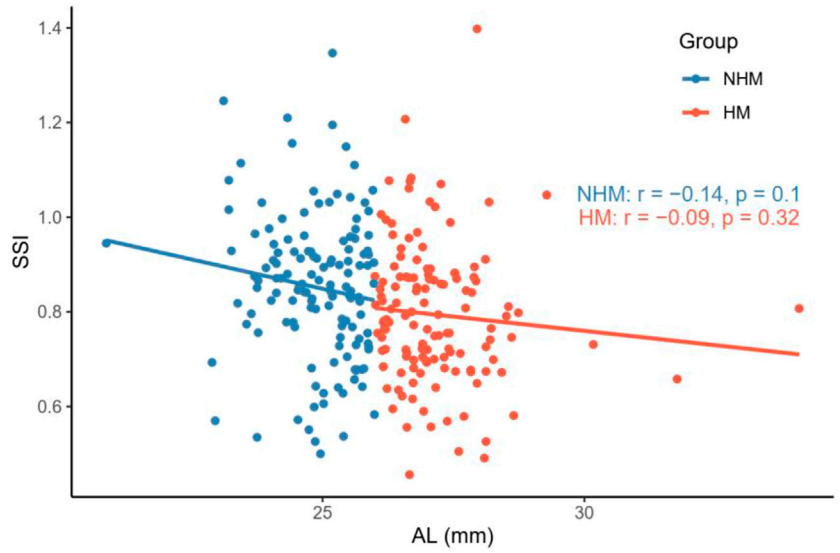

FIGURE 5
Relationship between AL and SSI in the two groups. AL was not associated with SSI in the NHM or HM group. Abbreviation: NHM, non-high myopia; HM, high-myopia; SSI, stress–strain index; AL, axial length.

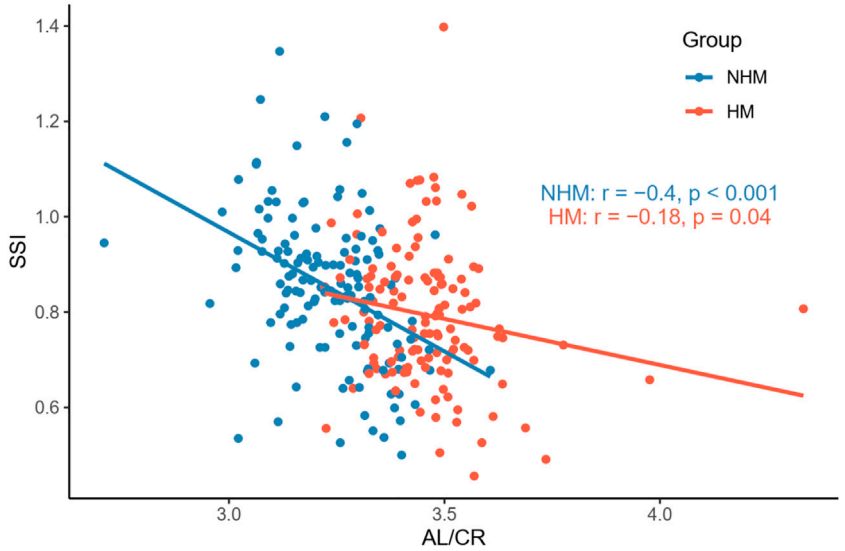

FIGURE 6
Relationship between AL/CR and SSI in the two groups. AL/CR was significantly associated with SSI in both the NHM and HM groups. Abbreviation: NHM, non-high myopia; HM, high myopia; SSI, stress–strain index; AL/CR: axial length/corneal radius of curvature ratio.

1.16–0.57). This finding was consistent with the results of the current study (Table 1).

It has been suggested that as glycation-induced cross-linking increases with age, corneal stiffness increases (Daxer et al., 1998; Elsheikh et al., 2010). Moreover, due to increased non-enzymatic glycosylation and cross-linking of collagen fibers, the stiffness of the sclera increases with age (Schultz et al., 2008; Coudrillier et al., 2012) [stiffnesses of the anterior

TABLE 2 Modeling of the potential association of SSI with AL/CR adjusted for age and gender.

	NHM				HM			
	Beta	**se**	***t* value**	***p* value**	**Beta**	**se**	***t* value**	***p* value**
Age	0.001	0.002	0.394	0.6944	0.005	0.002	2.654	0.009
Female gender	-0.026	0.025	-1.065	0.2888	0.036	0.025	1.463	0.1458
AL/CR	-0.514	0.109	-4.728	<0.001	-0.258	0.096	-2.687	0.0082

AL/CR: axial length/corneal radius of curvature ratio; NHM, non-high myopia; HM, high myopia.
Beta represents unstandardized beta; se represents standard error; R-squared of the regression model for the NHM group is 0.17; R-squared of the regression model for the HM group is 0.09.

and posterior sclerae vary depending on the developmental cycle (Spaide, 2014)]. Thus, the corneal stroma, as a continuation of the sclera, can reflect the biomechanical properties of the sclera to some extent. In a large multicenter clinical trial (Eliasy et al., 2019) (mean age of participants, 40.6 ± 17.1 years; range, 7–87 years), SSI that was measured *in vivo* was demonstrated to increase with age, and this positive correlation between SSI and age was later reported by Liu et al. to be independent of AL (Liu et al., 2021). This relationship between SSI and age was not well reproduced in the current study (Figure 4). One study (Liu et al., 2020) found that SSI was relatively stable before the age of 35 and then increased significantly with age; thus, the relative concentration of participant age in the current study (mean age, 22.1 ± 7.7 years; range, 7–48 years) may explain the contradictory results (Table 1).

A recent study reported a negative correlation between SSI and AL when the latter was <26 mm; this correlation did not exist when AL was ≥26 mm. Liu et al. speculated that this result may be explained by the non-uniform expansion of the eye during the development of myopia: during the early stages of myopia development, the eyeball tends to dilate uniformly in all directions, whereas after the development of HM, the dilatation mainly originates in the posterior pole, and the morphological and mechanical properties of the anterior segment of the eye stabilize and are no longer relevant to the posterior pole, which explains this result (Liu et al., 2021). The current study also showed that SSI was significantly lower in the eyes with AL ≥ 26 mm than in eyes with AL < 26 mm, but the correlation between AL and SSI did not reach a statistically significant level in any of the groups (Figure 5). Therefore, it seems that changes in the biomechanical properties in the ocular wall of the HM group are not directly related to the "increase in the AL." Some studies have shown that the cornea may play an emmetropizing role in preserving emmetropia or low myopia. This emmetropizing capacity could be insufficient when the AL is excessive in the ocular globe; this insufficiency leads to the appearance of myopia (González Blanco et al., 2008). The reason why the negative correlation between SSI and AL is no longer apparent at AL ≥ 26 mm may be related to the stabilization of CR. Moreover, considering the heterogeneity of the ocular wall expansion, perhaps we may obtain a more accurate relationship between SSI and AL by stratifying the eyeball morphology for the same AL after introducing ocular sagittal and coronal diameter variables, which warrants future validation with larger sample sizes.

According to previous studies, AL/CR is more closely related to myopia than AL alone (Fledelius, 1986; Ojaimi et al., 2005; Foo et al., 2016; Scheiman et al., 2016; Jong et al., 2018), and the stronger correlation between AL/CR and refractive error indicates the dynamic balance between AL and the corneal curvature during the development of myopia (Ojaimi et al., 2005). On the basis of this finding, the current study used AL/CR, the variable that is more closely related to the degree of myopia, to investigate the relationship between SSI and HM. First, in the whole sample, age was positively correlated with AL (Figure 1). AL and CR were positively correlated in both the NHM and HM groups (Figure 2). In addition, age was also correlated with AL/CR in the NHM and HM groups (Figure 3). To further explore the relationship between AL/CR and SSI, age- and sex-adjusted multiple linear regression models were fitted for both the groups. First of all, just as myopia is not necessarily more severe at AL ≥ 26 mm than at AL < 26 mm, NHM and HM in this study showed a wide intersection in the interval of approximately 3.2–3.6 on the AL/CR coordinate axis of the function (Figure 6). Meanwhile, as predicted, SSI after adjusting for age and sex showed a significant negative correlation with AL/CR in the NHM group and the HM group (Table 2), but the decrease in SSI was lesser with each unit of increase in AL/CR in the HM group than in the NHM group, indicating that SSI does not keep decreasing with an increase in myopia, but it gradually stabilizes at a lower level. This suggests that the insignificant correlation between SSI and AL at AL ≥ 26 mm may be related to the stabilization of the biomechanical properties of the cornea as well.

This study focuses on the correlation between the corneal biomechanical index SSI and the variable AL/CR, which reflects the degree of myopia, in the population with HM and NHM. We found that if AL/CR is used as the variable to measure the degree of myopia, the SSI still fits the pattern of a decrease with an increase in myopia at AL ≥ 26 mm, which indicates that the SSI is still correlated with the expansion of the posterior pole of the sclera after the morphological and mechanical properties of the anterior segment of the eye have developed and stabilized. However, with regard to the research methods, some limitations need to be acknowledged. First, although we verified the hypothesis that SSI is more strongly related to the degree of myopia than is the increase in the AL, the causal relationship between changes in the biomechanical properties of the ocular wall and changes in the growth of the eye axis cannot be determined because the present study is a cross-sectional study. Second, the results are based on variables associated with axial myopia, and it is not known whether refractive myopia applies to these results due to the lack of "refractive error" in the variables. In addition, it is also difficult to accurately interpret the SSI values measured under the *in vivo* conditions, where the eyeball is suspended in the soft tissue and the posterior sclera. Although the posterior sclera is relatively less rigid, its extension by the support of the retrobulbar tissue itself is limited; the anterior sclera, although more rigid, protrudes mostly outside the orbit and is not supported by the retrobulbar tissue. Therefore, it is difficult to determine the extent to which the anterior and posterior scleral strain contributes to the SSI values (Mcbrien et al., 2009; Girard et al., 2011), although this does not seem to affect the assessment of the overall biomechanical characteristics of the eye *in vivo* using SSI. Further, the findings of this study also validate, to some extent, the possibility of analyzing the dynamic changes in ocular wall stiffness during the development of myopia by measuring *in vivo* corneal biomechanical parameters.

As myopia research continues to advance, our understanding of the mechanisms behind the development of myopia is evolving. However, so far, we do not know the answers to the fundamental questions on the nature of myopia and the reasons for its occurrence and progress. With the development of a series of *in vivo* imaging techniques such as swept-source optical coherence tomography and 3D-MR, our understanding of myopia has evolved from the initial one based on refractive changes and morphological changes in the eye to the present-day *in vivo*, dynamic regulation mechanisms. On this basis, the present study also provides new ideas for us to investigate the effects of myopia on the biomechanical characteristics of the eyeball under *in vivo* conditions.

Conclusion

SSI showed a significant negative correlation with AL/CR in patients without high myopia and in patients with high myopia. However, SSI exhibited no decrease with the worsening of myopia, but it gradually remained stable at a low level. The findings of this study validate, to some extent, the possibility of analyzing the dynamic changes in ocular wall stiffness during the development of myopia by measuring *in vivo* corneal biomechanical parameters.

Data availability statement

The raw data supporting the conclusion of this article will be made available by the authors, without undue reservation.

Author contributions

ZC and QR: Study design, data analysis, and manuscript drafting; MC and LC: Manuscript drafting; HC and JW: Manuscript revision; WC and WB: Data acquisition.

Acknowledgments

We thank Jie Zhang and Wenjun Zhou from Hangzhou Shansier Medical Technologies Ltd. For their statistical advice. We acknowledge TopEdit LLC for the linguistic editing and proofreading during the preparation of this manuscript. The authors thank the associate editor and the reviewers for their useful feedback that helped improve this paper.

Conflict of interest

The authors declare that the research was conducted in the absence of any commercial or financial relationships that could be construed as a potential conflict of interest.

Publisher's note

References

Atchison, D. A., Jones, C. E., Schmid, K. L., Pritchard, N., Pope, J. M., Strugnell, W. E., et al. (2004). Eye shape in emmetropia and myopia. *Invest. Ophthalmol. Vis. Sci.* 45, 3380–3386. doi:10.1167/iovs.04-0292

Berisha, F., Findl, O., Lasta, M., Kiss, B., and Schmetterer, L. (2010). A study comparing ocular pressure pulse and ocular fundus pulse in dependence of axial eye length and ocular volume. *Acta Ophthalmol.* 88, 766–772. doi:10.1111/j.1755-3768.2009.01577.x

Coudrillier, B., Tian, J., Alexander, S., Myers, K. M., Quigley, H. A., and Nguyen, T. D. (2012). Biomechanics of the human posterior sclera: Age- and glaucoma-related changes measured using inflation testing. *Invest. Ophthalmol. Vis. Sci.* 53, 1714–1728. doi:10.1167/iovs.11-8009

Curtin, B. J., and Teng, C. C. (1958). Scleral changes in pathological myopia. *Trans. Am. Acad. Ophthalmol. Otolaryngol.* 62, 777–788.

Daxer, A., Misof, K., Grabner, B., Ettl, A., and Fratzl, P. (1998). Collagen fibrils in the human corneal stroma: Structure and aging. *Invest. Ophthalmol. Vis. Sci.* 39, 644–648.

Eliasy, A., Chen, K. J., Vinciguerra, R., Lopes, B. T., Abass, A., Vinciguerra, P., et al. (2019). Determination of corneal biomechanical behavior *in-vivo* for healthy eyes using CorVis ST Tonometry: Stress-strain index. *Front. Bioeng. Biotechnol.* 7, 105. doi:10.3389/fbioe.2019.00105

Elsheikh, A., Geraghty, B., Rama, P., Campanelli, M., and Meek, K. M. (2010). Characterization of age-related variation in corneal biomechanical properties. *J. R. Soc. Interface* 7, 1475–1485. doi:10.1098/rsif.2010.0108

Fledelius, H. C., and Christensen, A. C. (1996). Reappraisal of the human ocular growth curve in fetal life, infancy, and early childhood. *Br. J. Ophthalmol.* 80, 918–921. doi:10.1136/bjo.80.10.918

Fledelius, H. C. (1986). Myopia and diabetes mellitus with special reference to adult-onset myopia. *Acta Ophthalmol.* 64, 33–38. doi:10.1111/j.1755-3768.1986.tb06868.x

Flitcroft, D. I., He, M., Jonas, J. B., Jong, M., Naidoo, K., Ohno-Matsui, K., et al. (2019). IMI - Defining and classifying myopia: A proposed set of standards for clinical and epidemiologic studies. *Invest. Ophthalmol. Vis. Sci.* 60, M20–M30. doi:10.1167/iovs.18-25957

Foo, V. H., Verkicharla, P. K., Ikram, M. K., Chua, S. Y., Cai, S., Tan, C. S., et al. (2016). On behalf of the gusto study, GAxial length/corneal radius of curvature ratio and myopia in 3-year-old children. *Transl. Vis. Sci. Technol.* 5, 5. doi:10.1167/tvst.5.1.5

Gentle, A., Liu, Y., Martin, J. E., Conti, G. L., and Mcbrien, N. A. (2003). Collagen gene expression and the altered accumulation of scleral collagen during the development of high myopia. *J. Biol. Chem.* 278, 16587–16594. doi:10.1074/jbc.m300970200

Girard, M. J., Suh, J. K., Bottlang, M., Burgoyne, C. F., and Downs, J. C. (2011). Biomechanical changes in the sclera of monkey eyes exposed to chronic IOP elevations. *Invest. Ophthalmol. Vis. Sci.* 52, 5656–5669. doi:10.1167/iovs.10-6927

González Blanco, F., Sanz Ferńandez, J. C., and Muńoz Sanz, M. A. (2008). Axial length, corneal radius, and age of myopia onset. *Optom. Vis. Sci.* 85, 89–96. doi:10.1097/opx.0b013e3181622602

Grosvenor, T., and Scott, R. (1994). Role of the axial length/corneal radius ratio in determining the refractive state of the eye. *Optom. Vis. Sci.* 71, 573–579. doi:10.1097/00006324-199409000-00005

Jong, M., Sankaridurg, P., Naduvilath, T. J., Li, W., and He, M. (2018). The relationship between progression in axial length/corneal radius of curvature ratio and spherical equivalent refractive error in myopia. *Optom. Vis. Sci.* 95, 921–929. doi:10.1097/opx.0000000000001281

Lam, A. K., Wong, S., Lam, C. S., and To, C. H. (2002). The effect of myopic axial elongation and posture on the pulsatile ocular blood flow in young normal subjects. *Optom. Vis. Sci.* 79, 300–305. doi:10.1097/00006324-200205000-00009

Liu, G., Rong, H., Pei, R., Du, B., Jin, N., Wang, D., et al. (2020). Age distribution and associated factors of cornea biomechanical parameter stress-strain index in Chinese healthy population. *BMC Ophthalmol.* 20, 436. doi:10.1186/s12886-020-01704-6

Liu, G., Rong, H., Zhang, P., Xue, Y., Du, B., Wang, B., et al. (2021). The effect of axial length elongation on corneal biomechanical property. *Front. Bioeng. Biotechnol.* 9, 777239. doi:10.3389/fbioe.2021.777239

Liu, L. (2020). "New parameter for evaluating corneal biomechanics: The stress-strain index by CorVis ST in han Chinese with myopia," in 38th Congress of the European Society of Cataract and Refractive Surgeons, 2–4 October 2020, Amsterdam.

Luebkeman, C. H., and Peting, D. *Elasticity and deformation*.

Mcbrien, N. A., Jobling, A. I., and Gentle, A. (2009). Biomechanics of the sclera in myopia: Extracellular and cellular factors. *Optom. Vis. Sci.* 86, E23–E30. doi:10.1097/opx.0b013e3181940669

Morgan, I. G., Rose, K. A., and Ashby, R. S. (2014). "Animal models of experimental myopia: Limitations and synergies with studies on human myopia," in *Pathologic myopia*. Editors R. F. Spaide, K. Ohno-Matsui, and L. A. Yannuzzi (New York, NY: Springer New York), 39–58.

Mutti, D. O., Mitchell, G. L., Sinnott, L. T., Jones-Jordan, L. A., Moeschberger, M. L., Cotter, S. A., et al. (2012). Corneal and crystalline lens dimensions before and after myopia onset. *Optom. Vis. Sci.* 89, 251–262. doi:10.1097/opx.0b013e3182418213

Ohno-Matsui, K., Wu, P. C., Yamashiro, K., Vutipongsatorn, K., Fang, Y., Cheung, C. M. G., et al. (2021). IMI pathologic myopia. *Invest. Ophthalmol. Vis. Sci.* 62, 5. doi:10.1167/iovs.62.5.5

Ojaimi, E., Rose, K. A., Morgan, I. G., Smith, W., Martin, F. J., Kifley, A., et al. (2005). Distribution of ocular biometric parameters and refraction in a population-based study of Australian children. *Invest. Ophthalmol. Vis. Sci.* 46, 2748–2754. doi:10.1167/iovs.04-1324

Olsen, T. W., Aaberg, S. Y., Geroski, D. H., and Edelhauser, H. F. (1998). Human sclera: Thickness and surface area. *Am. J. Ophthalmol.* 125, 237–241. doi:10.1016/s0002-9394(99)80096-8

Rada, J. A., Shelton, S., and Norton, T. T. (2006). The sclera and myopia. *Exp. Eye Res.* 82, 185–200. doi:10.1016/j.exer.2005.08.009

Scheiman, M., Gwiazda, J., Zhang, Q., Deng, L., Fern, K., Manny, R. E., et al. (2016). Longitudinal changes in corneal curvature and its relationship to axial length in the Correction of Myopia Evaluation Trial (COMET) cohort. *J. Optom.* 9, 13–21. doi:10.1016/j.optom.2015.10.003

Schultz, D. S., Lotz, J. C., Lee, S. M., Trinidad, M. L., and Stewart, J. M. (2008). Structural factors that mediate scleral stiffness. *Invest. Ophthalmol. Vis. Sci.* 49, 4232–4236. doi:10.1167/iovs.08-1970

Spaide, R. F. (2014). "The sclera and induced abnormalities in myopia," in *Pathologic myopia*. Editors R. F. Spaide, K. Ohno-Matsui, and L. A. Yannuzzi (New York, NY: Springer New York), 97–112.

Steiger, A. (1913). *Die entstehung der sphärischen refraktionen des menschlichen auges: Übersichtigkeit*. Kurzsichtigkeit: Normalsichtigkeit.

Tokoro, A., and Suzuki, K. (1968). Significance of changes in refractive components for the development of myopia over seven years. *Nippon. Ganka Gakkai Zasshi* 72, 1472–1477.

Tideman, J. W., Snabel, M. C., Tedja, M. S., Van Rijn, G. A., Wong, K. T., Kuijpers, R. W., et al. (2016). Association of axial length with risk of uncorrectable visual impairment for Europeans with myopia. *JAMA Ophthalmol.* 134, 1355–1363. doi:10.1001/jamaophthalmol.2016.4009

Wang, X., Dong, J., and Wu, Q. (2015). Corneal thickness, epithelial thickness and axial length differences in normal and high myopia. *BMC Ophthalmol.* 15, 49. doi:10.1186/s12886-015-0039-6

Wolffsohn, J. S., Kollbaum, P. S., Berntsen, D. A., Atchison, D. A., Benavente, A., Bradley, A., et al. (2019). Imi - clinical myopia control trials and instrumentation report. *Invest. Ophthalmol. Vis. Sci.* 60, M132–M160. doi:10.1167/iovs.18-25955

Yu, A. Y., Shao, H., Pan, A., Wang, Q., Huang, Z., Song, B., et al. (2020). Corneal biomechanical properties in myopic eyes evaluated via Scheimpflug imaging. *BMC Ophthalmol.* 20, 279. doi:10.1186/s12886-020-01530-w

frontiers | Frontiers in Bioengineering and Biotechnology

TYPE Review
PUBLISHED 03 October 2022
DOI 10.3389/fbioe.2022.953590

OPEN ACCESS

EDITED BY
Emilio Isaac Alarcon,
University of Ottawa, Canada

REVIEWED BY
Jiansu Chen,
Aier Eye Institute, China
Joseph van Batenburg-Sherwood,
Imperial College London,
United Kingdom

*CORRESPONDENCE
Youhua Tan,
youhua.tan@polyu.edu.hk
Yan Wang,
wangyan7143@vip.sina.com

†These authors have contributed equally to this work and share first authorship

SPECIALTY SECTION
This article was submitted to Biomechanics, a section of the journal Frontiers in Bioengineering and Biotechnology

RECEIVED 26 May 2022
ACCEPTED 06 September 2022
PUBLISHED 03 October 2022

CITATION
Yang S, Zhang J, Tan Y and Wang Y (2022), Unraveling the mechanobiology of cornea: From bench side to the clinic. *Front. Bioeng. Biotechnol.* 10:953590. doi: 10.3389/fbioe.2022.953590

Unraveling the mechanobiology of cornea: From bench side to the clinic

Shu Yang[1,2,3†], Jing Zhang[1,2,4†], Youhua Tan[5,6*] and Yan Wang[1,2*]

[1]Clinical College of Ophthalmology, Tianjin Medical University, Tianjin, China, [2]Tianjin Eye Institute, Tianjin Key Lab of Ophthalmology and Visual Science, Tianjin Eye Hospital, Tianjin, China, [3]Department of Ophthalmology, The First People's Hospital of Huzhou, Huzhou, Zhejiang, China, [4]School of Optometry, Hong Kong Polytechnic University, Hong Kong SAR, China, [5]Hong Kong Polytechnic University Shenzhen Research Institute, Shenzhen, China, [6]Department of Biomedical Engineering, Hong Kong Polytechnic University, Hong Kong SAR, China

The cornea is a transparent, dome-shaped structure on the front part of the eye that serves as a major optic element and a protector from the external environment. Recent evidence shows aberrant alterations of the corneal mechano-environment in development and progression of various corneal diseases. It is, thus, critical to understand how corneal cells sense and respond to mechanical signals in physiological and pathological conditions. In this review, we summarize the corneal mechano-environment and discuss the impact of these mechanical cues on cellular functions from the bench side (in a laboratory research setting). From a clinical perspective, we comprehensively review the mechanical changes of corneal tissue in several cornea-related diseases, including keratoconus, myopia, and keratectasia, following refractive surgery. The findings from the bench side and clinic underscore the involvement of mechanical cues in corneal disorders, which may open a new avenue for development of novel therapeutic strategies by targeting corneal mechanics.

KEYWORDS

cornea, mechanobiology, mechanotransduction, mechanical cues, corneal diseases

Introduction

The cornea is the outermost transparent connective tissue of an eye and primarily consists of three layers with different cells: an anterior layer with epithelial cells, a middle stromal layer with abundant extracellular matrix (ECM) and keratocytes, and a posterior layer with endothelial cells (Figure 1A). As a load-bearing tissue of the eye, the cornea is constantly subjected to multiple mechanical cues, such as forces from the eyelid (Shaw et al., 2010), tear film (Jones et al., 2008), aqueous humor (Qin et al., 2021), and intraocular pressure (IOP) (Kwok et al., 2021), and even external forces with possible harmful effects, including eye rubbing, contact lens wearing, and surgical intervention.

Corneal cells can sense and respond to mechanical cues such as substrate topography and stiffness (Then et al., 2011), shear stress (Ren and Wilson 1997;

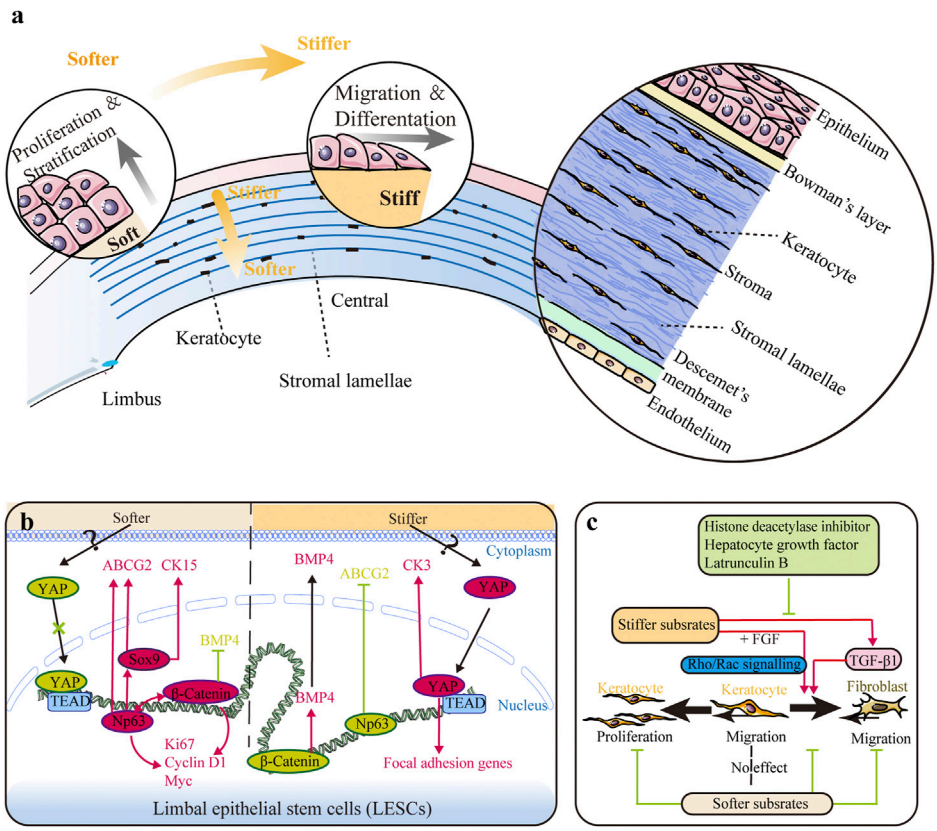

FIGURE 1
Impact of substrate stiffness. **(A)** Schematic representation of the main changes in substrate stiffness and their effects on the corneal epithelium. The central region is stiffer than the peripheral region in both the corneal epithelium and stroma, and the anterior stroma is stiffer than the posterior stroma. Stiffer substrates promote differentiation of limbal epithelial stem cells (LESCs), while softer substrates promote the proliferation process. **(B)** Substrate stiffness affects the behavior of LESCs *via* the YAP-dependent mechanotransduction pathway with involvement of ΔNp63 and β-catenin. **(C)** Substrate stiffness and chemical factors influence the behaviors of keratocytes. Softer substrates inhibit proliferation of keratocytes and migration of fibroblasts. Softer substrates also preserve the phenotype of keratocytes, while stiffer substrate promotes keratocyte–fibroblast–myofibroblast (KFM) transformation induced by transforming growth factor-β1 (TGF-β1). This stiffness-related transformation could be suppressed by histone deacetylase inhibitors, hepatocyte growth factor, and latrunculin B. Furthermore, extracellular matrix (ECM) stiffness also affects the response of fibroblasts to fibroblast growth factor (FGF) by the interplay between Rho and Rac signaling.

Kang et al., 2014; Duan et al., 2021), and tensile and compressive forces (Liu et al., 2014; Feng et al., 2016; Du et al., 2017; Zhang et al., 2021). Different types of cells in the cornea can perceive and transduce mechanical signals in distinct ways, which modulate the expressions of specific genes and influence diverse biological functions. Recent studies have shown that several corneal diseases, including keratoconus (Amit et al., 2020; Dou et al., 2022), keratectasia (Dupps and Wilson 2006), dry eye disease (Yoshioka et al., 2015; Yamaguchi and Shiraishi 2018), myopia (Kang et al., 2018; Xin et al., 2021), and bullous keratopathy after laser iridotomy (Kaji et al., 2005; Yamamoto et al., 2010), are closely related to abnormal responses of corneal cells to mechanical forces.

In this review, we summarize recent progress made in understanding the ways that corneal cells interact with different mechanical microenvironments to achieve several major biological functions (with a focus on the mechanotransduction process). We then discuss abnormal mechanical alterations of the corneal tissue in various diseases and subsequent effects on corneal cells, which enables physicians to understand pathological mechanisms and develop therapeutic strategies for corneal disorders from a mechanobiological perspective.

Corneal structure and functions

The cornea consists of five different layers—the epithelium, Bowman's layer, stroma, Descemet's membrane, and endothelium—from the anterior to the posterior cornea (Figure 1A). As the outermost anterior part of the cornea, the

corneal epithelium is covered by tear fluid and consists of 4–6 layers of nonkeratinized and stratified squamous epithelial cells with various junctional complexes to prevent the passage of external agents into deeper layers of the cornea (Eghrari, 2015). Limbal epithelial stem cells (LESCs) can proliferate in an orderly manner and differentiate to replenish corneal epithelial cells (CEpCs) lost in normal or damaged tissue, thus maintaining the normal layered structure and homeostasis of the corneal epithelium (Secker and Daniels 2008).

Posterior to the epithelial basement membrane is an 8–12 μm acellular, non-regenerating layer called Bowman's layer (Eghrari, 2015). It is characterized by random arrangement of collagen fibrils and proteoglycans and is originally considered an important stabilizer of corneal curvature (Ma et al., 2018). However, recent studies have suggested that the presence of Bowman's layer makes a negligible contribution to the entire corneal biomechanics (Torres-Netto et al., 2021).

The stroma, which constitutes up to 90% of corneal thickness, is the main determinant of corneal biomechanics. It comprises approximately 250 (central cornea) to 500 (peripheral cornea) stacked and interweaving collagen lamellae and a sparse population of keratocytes (Meek and Knupp 2015). The aligned collagen fibrils have diameters less than the wavelength of light, and collagen fiber lamellae are approximately 10–200 μm wide and only 1–2.5 μm thick (Meek and Knupp 2015). The lamellae exhibit a preferred orthogonal collagen alignment in the nasal–temporal and superior–inferior orientations within the central cornea, and the fibers tend to run circumferentially within the peripheral cornea (Meek and Knupp 2015). Moreover, the anterior stroma comprises a denser collagen distribution and highly interwoven of lamellae, inserted into Bowman's layer, which results in relatively stiffer mechanical properties (Meek and Knupp 2015). Type I collagen is the predominant component of collagen fibrils, while type V collagen and small leucine-rich proteoglycans (e.g., lumican and keratocan) potentially modulate collagen-fibril assembly (Massoudi et al., 2016). Biomechanical properties of the stroma are highly dependent on these organizations and interactions among fibrils within different lamellae. Keratocytes are quiescent in the normal cornea and responsible for slow turnover of the stroma. Upon corneal injury, keratocytes adjacent to the injury differentiate into proliferative and metabolically active fibroblasts and subsequently myofibroblasts, which produce greater amounts of collagen, proteases, and cytokines to remodel the arrangement of collagen fibrils in the stroma (Stramer et al., 2003; Chen et al., 2015).

Descemet's membrane is the basement membrane of corneal endothelial cells (CEnCs) and contains types IV and VIII collagen, laminin, and fibronectin (Eghrari, 2015). It forms a hexagonal lattice, gradually increases in thickness from birth (3 μm) to adulthood (8–10 μm), and maintains corneal relative dehydration.

Finally, the corneal endothelium is in direct contact with the aqueous humor and comprises a monolayer of polygonal, predominantly hexagonal CEnCs with tight junctions and adherens junctions. Its ion-transport system associated with Na^+/K^+-ATPase and bicarbonate-dependent Mg^{2+}-ATPase counteracts water imbibition into the stroma (Eghrari, 2015). CEnCs cannot proliferate in humans, and loss of or damage to these interconnected CEnCs results in increased water imbibition. In young adults, the endothelial cell density (ECD) within a healthy cornea is approximately 3,000–4,000 cells/mm^2. However, an abnormal cornea loses its ability to pump sufficient water to maintain its function when ECD decreases below 750–500 cells/mm^2 (Ramirez-Garcia et al., 2018).

Principles of mechanosensing and mechanotransduction

Mechanical signals influence cell behavior during tissue homeostasis and in pathological conditions mainly through mechanotransduction. A cell senses mechanical forces through mechanosensors on the cell surface, such as integrins and cadherin's mechanosensitive ion channels (Ingber 2006). Integrin-mediated adhesion, also known as focal adhesions, can perceive and transfer mechanical cues from the ECM to the cytoskeleton (Sun et al., 2016; Astudillo 2020). This integrin-mediated mechano-transduction relies on several linker proteins (e.g., talin, vinculin), activating downstream signaling molecules, such as focal adhesion kinase, Src, phosphoinositide 3-kinase, YAP/TAZ, myocardin-related transcription factor (MRTF), and serum response factor (SRF) (Sun et al., 2016; Astudillo 2020). Physical stimulus propagation from the ECM to the nucleus might take up to ~1 ms (Martino et al., 2018). Cadherin-mediated adhesion, also known as adherens junctions, mediates force transduction between cells through several critical signaling molecules, such as cadherin, β-catenin, α-catenin, p120-catenin, vinculin, and zyxin (Ravasio et al., 2022). It can mediate force-induced activation of Ca^{2+} influx through mechanosensitive ion channels and associated actin assembly (Ingber 2006; Ravasio et al., 2022).

Mechanosensors perceive mechanical forces and further transmit them from the cytoskeleton and LINC complex (linker of the nucleoskeleton and cytoskeleton) into the nucleus (Sun et al., 2016; Martino et al., 2018; Astudillo 2020), which has been recognized as a mechanosensor recently (Kirby and Jan 2018). The LINC complex connects the cytoplasmic cytoskeleton with the nuclear lamina through nuclear transmembrane protein emerin and the inner nuclear protein SUN. SUN proteins connect to the lamins that form the lamina and nuclear scaffold, which attach to chromatin and DNA, and influence chromatin organization and gene transcription. Therefore, mechanical forces can directly propagate into the nucleus and regulate mRNA transcription

(Tajik et al., 2016). The cytoskeleton provides structural support for cells and bears cellular tension, which is critical in mechanotransduction. Dynamic changes in the components of the cytoskeleton, such as actin fibers (F-actin), microtubules, and intermediate filaments, alter cell mechanical properties. Cytoskeletal tension is closely related to the Rho/ROCK/myosin pathway, which critically regulates actin polymerization and mechanotransduction (Martino et al., 2018). In addition, Yes-associated protein (YAP) and transcriptional coactivator with PDZ-binding motif (TAZ) are potent mechanoresponsive factors, shuttle between the cytoplasm to the nucleus in response to mechanical cues, and regulate transcription of downstream genes (Sun et al., 2016; Astudillo 2020). There are many other mechanosensitive proteins/signaling, such as Wnt, Notch, PI3K/Akt, and MAPK/ERK. In the cornea, only the role of YAP and β-catenin has been identified (Figure 1B).

The impact of mechanical cues from the extracellular matrix

ECM topography and stiffness have a significant impact on corneal cell behavior (Petroll and Miron-Mendoza 2015; Masterton and Ahearne 2018; Xiong et al., 2019).

Substrate topography and stiffness

In vivo, CEpCs and CEnCs grow on basement membranes, while keratocytes grow between collagen lamellae, which provide unique nanotopographic environments around cells (Figure 1A). *In vitro*, substrate topography (e.g., groove, pillar, or pit patterns) represents the geometrically defined, three-dimensional (3D) environments around cells (Petroll and Miron-Mendoza 2015; Xiong et al., 2019). It can mimic the nanotopographic structures appearing around cells *in vivo* by altering the parameters such as height, depth, width, and spacing of the substrate surface.

Mechanical stiffness is the ability of an object to resist deformation in response to an applied force and is usually represented by elastic modulus. The stiffness of the whole cornea is mainly determined by ECM microstructure and composition, namely, the amount and arrangement of collagen fibrils, the content of proteoglycans, and the hydration and dehydration of tissue (Ruberti et al., 2011). As a heterogeneous tissue, the stiffness of different tissue layers in the human cornea differs a lot (Figure 1A), and the details have been discussed comprehensively in our previous review (Ma et al., 2018). Overall, the central region is stiffer than the peripheral region in both the corneal epithelium and stroma (Mikula et al., 2016; Gouveia et al., 2019a), and the anterior stroma is stiffer than the posterior stroma (Mikula et al., 2016). Bowman's layer is nearly three times stiffer than the anterior stroma (Last et al., 2012). However, the stiffness of Descemet's membrane, ranging from kPa to MPa, remains debatable (Ma et al., 2018). Here, substrate stiffness refers to the biomechanical property of the localized ECM that cells experience.

Substrate stiffness determines the fate of limbal epithelial stem cells

LESC differentiation can be promoted by high substrate stiffness (Figures 1A,B). The expressions of mature epithelial markers (cytokeratin 3 and 12) were found to increase as the biomechanics between the limbus and central cornea tissue shifted from soft (6.24 ± 0.09 and 6.40 ± 0.14 GHz Brillouin frequency shifts in the sub-epithelium and the anterior-most stroma, respectively) to stiff (6.66 ± 0.04 and 6.53 ± 0.04 GHz Brillouin frequency shifts in the sub-epithelium and the anterior-most stroma, respectively) (Jones et al., 2012; Gouveia et al., 2019a; Masterton and Ahearne 2019). It is to be noted that the Brillouin spectro-microscope is utilized to measure the bulk modulus, but not Young's modulus of the cornea, and thus requires caution during data interpretation (Wu et al., 2018; Yun and Chernyak 2018). High substrate stiffness triggered maturation of LESCs by activating the YAP-dependent mechanotransduction pathway and suppressing ΔNp63 and Wnt/β-catenin signaling and increased the expression of BMP4 (Figure 1B) (Gouveia et al., 2019a; 2019b). Thus, aberrant stiffening of the limbus promotes excessive differentiation of LESCs, thereafter resulting in stem cell deficiency, corneal opacification, and vision loss (Nowell et al., 2016). Collagenase treatment could rescue these alterations by softening the matrix, leading to inactivation of YAP signaling and inhibition of LESC differentiation (Figure 1B) (Gouveia and Connon 2020). This research highlights the potential of regulating LESC function and corneal epithelial tissue regeneration by controlling tissue biomechanics and mechanotransduction.

Corneal cell growth depends on substrate topography and stiffness

Grooves are the most widely used substrate topography for culturing CEpCs and corneal stromal cells. After culturing on microgrooves or nanogrooves, cells align and elongate along the direction of the groove axis and could be modulated by the depth but not the width of the grooves (Fraser et al., 2008; Xiong et al., 2019). Meanwhile, cytoskeleton fibers and focal adhesions in cells are also aligned along the grooves (Xiong et al., 2019). In contrast, pillar or pit patterns are the most commonly used topographic features in CEnC culture and can mimic the topographical features of hexagonal lattice structures and nanoscale pores on Descemet's membrane (Last et al., 2009). Both micro- (~1 μm)

and nano-sized (~250 nm) pillars were found to facilitate the *in vivo*-like morphology of CEnCs, promote their proliferation with higher cell density and smaller cell size (Muhammad et al., 2015; Rizwan et al., 2017), and enhance the expressions of Na^+/K^+ ATPase and cell–cell tight junction protein Zonula Occludens-1 (ZO-1) (Koo et al., 2014; Muhammad et al., 2015; Palchesko et al., 2015; Rizwan et al., 2017). Recently, a small patterned hydrogel surface with physiologically relevant hexagon densities (~2000 hexagons/mm^2) and a similar elastic modulus to native Descemet's membrane (~50 kPa) was constructed and augmented the formation of monolayers with higher cell density (Erkoc-Biradli et al., 2021). In addition, substrates with hexagonal microtopography can promote differentiation of human mesenchymal stem cells into corneal-endothelial-like cells (Gutermuth et al., 2019).

Substrate stiffness can also impact corneal cell growth. Corneal fibroblasts (CFs) align and compact collagen parallel to the axis of the highest ECM stiffness under constrained (anisotropic) conditions, but there is no preferential orientation in the unconstrained (isotropic) ECM (Karamichos et al., 2007). The biomimetic substrate stiffness of CEpCs (~1.3 KPa) (Molladavoodi et al., 2015), keratocytes (~25 kPa) (Chen et al., 2020), and CEnCs (~50 kPa) (Palchesko et al., 2015) can preserve the cytoskeleton structure (actin fibers) and phenotype of corneal cells. Rac1 has been proven to mediate this process in keratocytes (Chen et al., 2020).

Substrate topography and stiffness facilitate wound healing

Proliferation and migration activities of CEpCs surrounding the wound area facilitate healing of the corneal epithelium (Ljubimov and Saghizadeh 2015). A quiescent keratocyte differentiates into a more proliferative and metabolically active fibroblast, and subsequently a myofibroblast, which is referred to as keratocyte–fibroblast–myofibroblast (KFM) transformation that occurs during the healing of the stroma. This transformation is accompanied by an increased expression of disorganized ECM, collagen-degrading enzymes, and cytokines, resulting in stromal structure remodeling (Hassell and Birk 2010; Ljubimov and Saghizadeh 2015).

Substrates with special patterned topography pitch sizes could prevent the KFM transformation (Pot et al., 2010; Myrna et al., 2012) and limit the migration of CEpCs, fibroblasts, and myofibroblasts only parallel to the grooves (Diehl et al., 2005; Pot et al., 2010). In addition, the proliferation rates of CEpCs and keratocytes on substrates with smaller grooves or groove pitch were inhibited, suggesting that overly narrow grooves may impede cell proliferation (Liliensiek et al., 2006; Xiong et al., 2019). Most importantly, ECM proteins generated by keratocytes cultured on a groove pattern also tended to be parallel to the axis of the grooves, resembling the architecture of a native corneal stroma (Then et al., 2011).

ECM stiffness also affects multiple cellular activities during wound healing. CEpCs displayed a lower migration speed on compliant substrates (Molladavoodi et al., 2015). For stromal cells, ECM stiffness and biochemical cues interact to regulate cell activities (Figure 1C). A compliant microenvironment inhibited proliferation of keratocytes cultured in platelet-derived growth factor BB (PDGF-BB) medium (Iyer et al., 2022). However, reduction of effective ECM stiffness significantly inhibited migration of keratocytes cultured in 10% FBS but had no effect when cultured in PDGF-BB (Kim et al., 2012). Since keratocytes in PDGF maintained a lower level of contractility than those in 10% FBS, substrate stiffness seems to affect migration only under fibroblastic rather than quiescent phenotypes (Kim et al., 2012). Furthermore, low substrate stiffness preserved the phenotype of keratocytes, while high substrate stiffness promoted KFM transformation (Dreier et al., 2013; Chou et al., 2016; Maruri et al., 2020). However, a stiff microenvironment alone is insufficient to induce KFM transformation. The KFM transformation induced by transforming growth factor-β1 (TGF-β1) could be further enhanced on rigid substrates, but this transformation showed no stiffness dependency in the absence of TGF-β1 (Dreier et al., 2013; Maruri et al., 2020). Furthermore, histone deacetylase inhibitors, hepatocyte growth factor, and latrunculin B (an actin cytoskeleton disruptor) could suppress this transformation through their inhibitory effect on α-smooth muscle actin (α-SMA) expression (Koppaka et al., 2015; Miyagi et al., 2018; Thomasy et al., 2018). ECM stiffness also affected the response of CFs to fibroblast growth factor (FGF) and induced stress fiber formation and collagen reorganization, which appeared to be regulated by the interplay between Rho and Rac signaling (Lakshman and Petroll 2012; Petroll and Lakshman 2015). Taken together, these findings demonstrate that substrate topography and stiffness regulate corneal cell behaviors, which may be utilized to maintain the uniform structure of the cornea and impede development of fibrosis and corneal haze in wound healing.

The impact of shear stress

Shear stress is generated when the force is parallel to the cross-section of the material, for instance, when the fluid flows over the material surface. The flow of the tear film and aqueous humor can result in shear stress on the anterior and posterior surfaces of the cornea and mainly affects the epithelium and endothelium (Figure 2).

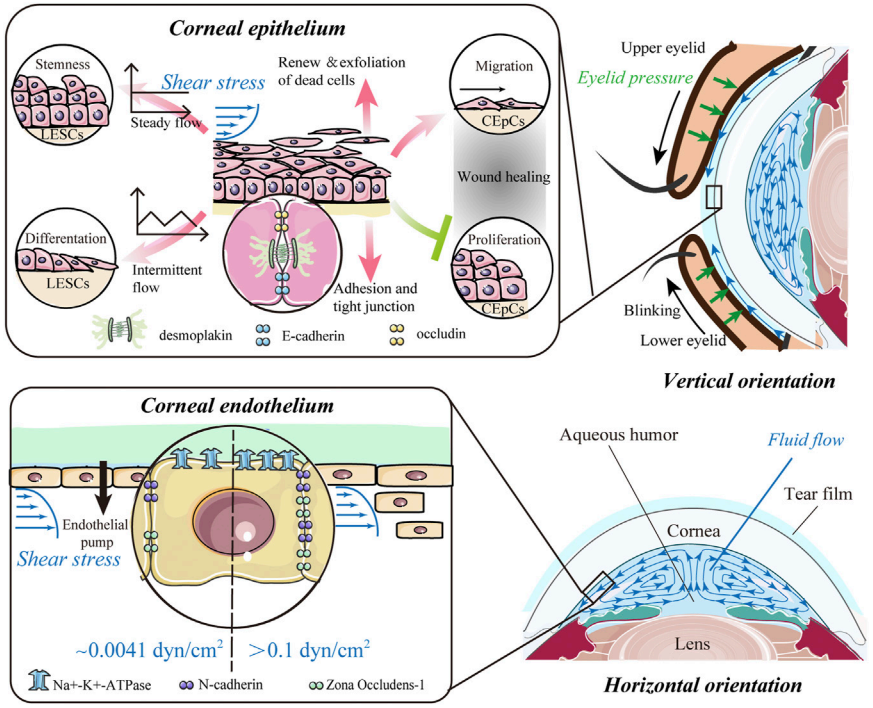

FIGURE 2
Impact of shear stress. The flow of the tear film and aqueous humor potentially results in shear stress on the anterior and posterior surfaces of the cornea and predominantly affects the epithelium and endothelium of the cornea. For corneal epithelial cells (CEpCs), steady flow maintains limbal epithelial stem cell (LESC) stemness, whereas intermittent flow induces their differentiation. Shear stress is crucial for spontaneous renewal and exfoliation of superficial epithelial cells, while it also promotes cell–cell contacts to strengthen barrier function. In the wound healing process, shear stress can mediate migration of CEpCs to facilitate wound healing, while suppressing proliferation of CEpCs to delay wound repair. Corneal endothelial cells (CEnCs) are more likely to be detached from the corneal endothelium with higher shear stress (>0.1 dyn/cm^2). Also, the expressions of the corneal endothelium-related markers, such as ZO-1, N-cadherin, and Na^+-K^+-ATPase, could be upregulated with shear stress in a dose-dependent manner.

The pressure and shear stress generated by eyelid motion

During spontaneous blinking, the eyelids move with respect to the ocular globe and lubricate it with a tear film to maintain a smooth epithelial surface for optical properties of the eye. The motion of the eyelid and the flux of tears also produce different types of mechanical forces over the ocular surface, especially eyelid pressure and fluid shear stress (Figure 2).

It is difficult to directly measure fluid shear stress generated by the motion of the tear film. Eyelid pressure, one of the key factors in determining fluid shear stress, was used as an alternative way to evaluate shear stress on the ocular surface (Yoshioka et al., 2015). The upper eyelid pressure (16.95 ± 6.08 mmHg–31.0 ± 6.8 mmHg) and lower eyelid pressure (16.11 ± 7.27 mmHg–29.9 ± 6.5 mmHg) measured by different approaches are summarized in Table 1 (Miller 1967; Lydon and Tait 1988; Shaw, et al., 2009; Shaw et al., 2010; Sakai et al., 2012; Namiguchi et al., 2018). The measurement using the blepharo-tensiometer showed that eyelid pressure decreased with age for both the upper and lower eyelids in healthy eyes (Sakai et al., 2012). This pressure increased in dry eye and lid-wiper epitheliopathy (Yoshioka et al., 2015; Yamamoto et al., 2016; Yamaguchi and Shiraishi 2018) but decreased in functional nasolacrimal duct obstruction (Kim, Lee, et al., 2018). This eyelid pressure is homogenously dissipated and absorbed by the corneal epithelium and conveyed to the underlying tissue. Any thinning of the epithelium and decrease in layers lead to a decrease in pressure dissipation and an increase in structural stress on each of the cells (van Setten 2020).

The levels of shear stress (and the coefficient of friction) between the cornea and eyelid are also affected by shear distribution within the tear film/mucin system and the extent to which the sliding partners make contact with each other (Pult et al., 2015). Considering these complex

TABLE 1 Instruments to measure eyelid pressure.

Author(s)	Method	Result	Feature
Miller (1967)	Used modified contact lenses to create a chamber that was filled with water and attached to a manometer	During a blink, the average eyelid pressure was 10.3 mmHg	This system was the first method to quantify eyelid pressure *in vivo* The pressure is the average value of the pressure of the eyelid over a large area and the baseline changes markedly. Also, the relatively thick modified contact lenses (more than 2.5 mm) may cause distension of the eyelids and influence the accuracy of the measurements
Lydon and Tait (1988)	Used a contact lens with a silicone elastomer contact lens over the top to create a special contact lens pressure transducer	NA	The quantitative values of the eyelid pressure were not reported
Shaw et al. (2009), Shaw et al. (2010)	Used a rigid contact lens attached with a thin, (0.17 mm) piezoresistive pressure sensor to measure static upper eyelid pressure (without blinking)	The mean central upper eyelid pressure of young adults was 8.0 ± 3.4 mmHg, which was derived using the pressure-sensitive paper imprint widths	The total thickness of the device inserted between the cornea and eyelid was much smaller (less than 0.7 mm) However, the magnitudes of eyelid pressure vary when being measured by different methods
Sakai et al. (2012), Namiguchi et al. (2018)	A thin (0.4 mm) tactile sensor was covered with silicone rubber and placed between a soft contact lens on the cornea and the inner surface of the eyelid, named as blepharo-tensiometer	The mean central eyelid pressure was 16.95 ± 6.08 mmHg to 31.0 ± 6.8 mmHg for the upper lid and 16.11 ± 7.27 mmHg to 29.9 ± 6.5 mmHg for the lower lid	The influence of intraocular pressure cannot be excluded The eyelid pressures under stationary conditions (i.e., eyelids closed) and dynamic conditions (i.e., during blinking) can be directly assessed with good reliability and accuracy

factors, an elastohydrodynamic mathematical model of the human eyelid wiper was developed to predict shear stresses on the ocular surface (Jones et al., 2008). However, the elastic constants or thicknesses of elastic layers, which are essential in this model, remain currently unavailable. Based on the *in vivo* tear flow turnover rate (0.31 ml/min) and a mathematical model, the magnitude of the shear stress was calculated to be 5.0×10^{-3} Pa (0.05 dyn/cm^2) (Kang et al., 2014). More recently, several eye models have been proposed to mimic the interface between the ocular system and external environments (Qin et al., 2018; Phan et al., 2019; Seo et al., 2019). These advance our ability to quantitate blink-induced mechanical forces.

Shear stress generated by aqueous humor flow

Aqueous humor (AH) is secreted by the ciliary process, passes through the pupil into the anterior chamber (AC), and drains from the eye predominantly *via* the trabecular meshwork (TM). Due to natural convection, this water-like fluid continuously circulates in the AC and produces shear stress on the corneal endothelium (lower panel in Figure 2). It is difficult to directly measure the shear stress produced by AH. Thus, several numerical calculations of AH dynamics have been developed to delineate the flow patterns and distributions of shear stress (Kumar et al., 2006; Yamamoto et al., 2010; Qin et al., 2021; Tang et al., 2022). Yamamoto et al. (2010) estimated the physiological shear stress exerted on CEnCs with an anterior chamber depth of 2.8 mm and a temperature difference between the cornea and iris of 1°C. They found that the maximum shear stress at the center of the corneal endothelial surface was 0.0062 dyn/cm^2 (6.2×10^{-4} Pa), and the average shear stress was 0.0041 dyn/cm^2 (4.1×10^{-4} Pa), which had little effect on CEnCs (Yamamoto et al., 2010). Based on a coupled-lattice Boltzmann model, Qin et al. (2021) estimated the average shear stress on CEnCs ranging from 1.22×10^{-5} Pa to 1.85×10^{-3} Pa in a healthy eye. The maximum shear stress was located at the center and midperiphery of the corneal endothelial surface in the standing (vertical orientation in Figure 2) and up-facing orientation (horizontal orientation in Figure 2), respectively. Moreover, shear stress in the standing orientation with a greater temperature difference across

the AC was notably higher, while the inflow velocity, TM permeability, and AH viscosity have no influence on shear stress (Qin et al., 2021).

Shear stress in the barrier function of the corneal epithelium and endothelium

The epithelium is the outer barrier of the cornea and has the highest regenerative capacity. Shear stress can regulate proliferation and differentiation of LESCs, which are crucial for renewal of epithelial cells (Figure 2). Steady flow facilitated the maintenance of LESC stemness, whereas intermittent flow induced their differentiation (Kang et al., 2014). In a model mimicking blink, the force from repetitive eyelid movement also enhanced corneal epithelial cell differentiation (Seo et al., 2019). For differentiated CEpCs, shear stress is crucial for spontaneous exfoliation of superficial epithelial cells (Figure 2). In early 1997, Ren and Wilson showed that shear stress increased the shedding rate of CEpCs and cell apoptosis (Ren and Wilson 1997). Such shear stress from blinking reached a peak at the apex of the corneal surface, which explains the increased exfoliation of dead cells preferentially from the center (Yamamoto et al., 2002). Shear flow stress also promoted cell–cell contacts between the epithelial and stromal layers (Figure 2). CEpCs under flow-induced shear stress conditions became larger, spread more, and showed more cell–cell contacts mediated by desmosomes (Hampel et al., 2018). These CEpCs formed a barrier with high expressions of cell adhesion and tight junction components, including E-cadherin, occludin, and desmoplakin, indicating strengthening of barrier function (Hampel et al., 2018; Abdalkader and Kamei 2020). Fluid shear stress also facilitated the interplay between CEpCs and fibroblasts and increased the epithelial cell layers when cultured *in vitro* (Kawata et al., 2019).

The role of shear stress in wound healing remains unclear (Figure 2). Molladavoodi et al. found that, in comparison with higher shear stress (8 dyn/cm^2), lower shear stress (4 dyn/cm^2) mediated more prominent, organized, and elongated filamentous actin of CEpCs to facilitate wound healing (Molladavoodi et al., 2017). However, Utsunomiya et al. reported that shear stress (1.2 dyn/cm^2 or 12 dyn/cm^2) could delay wound repair and suppress proliferation of CEpCs, which was associated with an increase in TGF-β1 and SMAD2 phosphorylation (Utsunomiya et al., 2016). It is to be noted that the seemingly contradictory effects on wound healing of the corneal epithelium might be due to different levels of shear stress applied in distinct contexts. It is also worth noting that the shear stresses used in these models (Utsunomiya et al., 2016; Molladavoodi et al., 2017) are far beyond the physiological range (0.05 dyn/cm^2) and thus could not mimic the physiological ocular environment. More advanced *in vitro* models are required to better-elucidate the response of CEpCs to shear stress under physiological conditions. Thus, shear stress in the tear film–epithelial interface is essential for homeostasis of the epithelial layer, including maintaining regular turnover and promoting the interaction of CEpCs with their neighbors. However, its role in injured or diseased conditions needs to be assessed by establishing models that closely mimic genuine clinical scenarios.

Shear stress has the potential to regulate ECD and influence the water pump function of CEnCs (Kaji et al., 2005; Yamamoto et al., 2010). The magnitude required to detach CEnCs from the corneal endothelium was 0.1–10 dyn/cm^2 (Kaji et al., 2005), which is considerably higher than the shear stress on normal corneal endothelial surfaces (Figure 2). Furthermore, the loss of CEnCs increased with shear stress in a dose- and time-dependent manner (Kaji et al., 2005). Yamamoto et al. (2010) further confirmed this finding and pointed out that CEnCs were more likely to be detached from the attached substrates under intermittent shear stress of the same magnitude. Recently, the expressions of the corneal endothelium-related markers ZO-1, N-cadherin, and Na^+-K^+-ATPase were found to be upregulated after exposure to shear stress from 0 to 2.0 dyn/cm^2 (Figure 2) (Duan et al., 2021). All these findings show that shear stress is also essential for the corneal endothelium, such as an inner barrier to maintain corneal transparency and protect the stroma from edema.

The impact of tensile and compressive stresses

Tensile or compressive stresses develop when a material is subjected to external stretching or compression, resulting in elongation or shortening of the object. As previously mentioned, the changes in corneal shape and topography are closely related to the altered position or tension of the eyelid, which indicated the existence of compressive stress from eyelid pressure (Collins et al., 2006; Collins, et al., 2006; Shaw, et al., 2009a). However, corneal shape is mainly influenced by the magnitude of intraocular pressure (IOP). As a pressure inside the eye, IOP is the primary cause to generate stretching force on the cornea under physiological conditions. ECM components in the stroma are responsible for maintenance of a normal corneal structure and are closely related to the response to tensile and compressive stresses.

IOP results in the dome-shaped strain of the cornea

IOP is the fluid pressure within an eye and is represented by the pressure difference between the anterior chamber and atmosphere, ranging from 10 to 20 mmHg (1.33–2.66 kPa) in

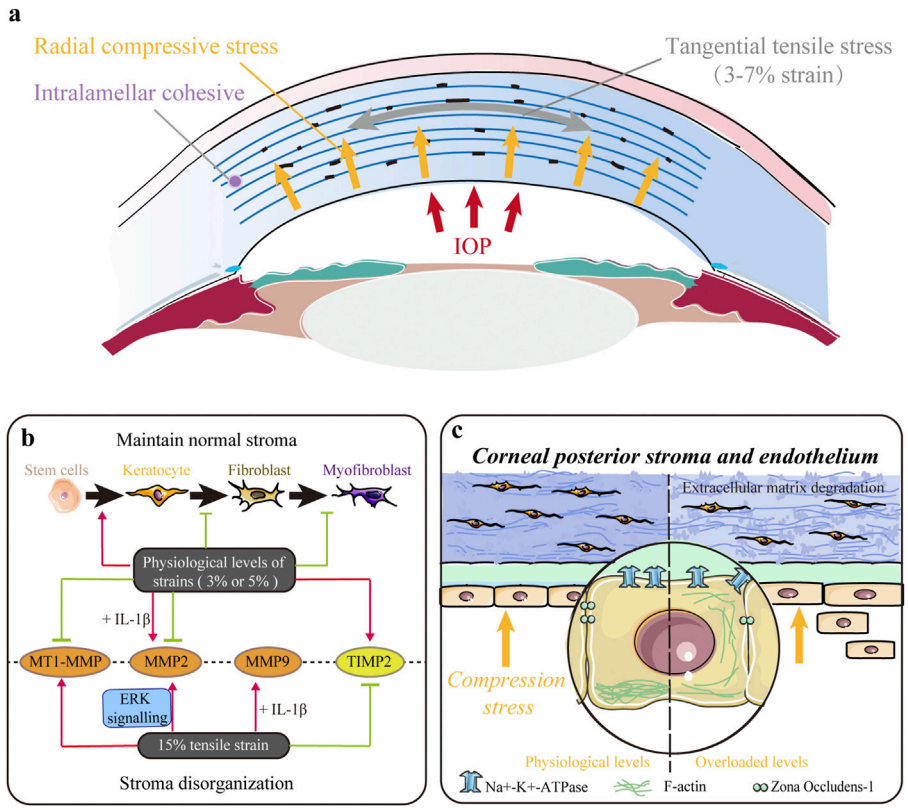

FIGURE 3
Impact of tensile and/or compressive stresses. **(A)** Native cornea is mainly subjected to tangential tensile (parallel to the plane of the cornea) stress and radial compressive stress within the entire corneal thickness. **(B)** Mechanical strains in the physiological range (~3%) maintain a normal keratocyte phenotype, decrease keratocyte–fibroblast–myofibroblast (KFM) transformation, and inhibit the synthesis of proteases to maintain normal stromal structure. However, larger magnitude strains (~15%) upregulate the expression of proteases and contribute to extracellular matrix (ECM) disorganization. **(C)** Mechanical compression stress indirectly controls stromal hydration and thickness by modulating the pump function of the corneal endothelium. Moreover, it also directly influences stromal structure by altering cell morphology, inhibiting proliferation, and promoting apoptosis and extracellular matrix (ECM) degradation in the stroma.

the normal state (Kumar et al., 2006; Liu et al., 2019). IOP induces a tangential tensile (parallel to the plane of the cornea) stress and a radial compressive stress within the entire corneal thickness (Figure 3A). The native cornea is subjected to a dome-shaped strain from IOP *in vivo* (Zhang et al., 2017). With the daily variation in IOP, the deformation of corneal shape fluctuates physiologically. In early 1977, the strains (the percentage of deformation relative to the original shape) on human corneas in the physiologic IOP range (5, 10, 25, and 45 cmH_2O) were measured, varying from small strains (0.28%) up to 1.14% in the apical region (Shin et al., 1997). Later, Zhang et al. (2017) pointed out that the strain was within the range of 0%–3% in the stroma of the cornea.

The biomechanical properties of the cornea and its constituent materials are important in determining the IOP-induced strain. The cornea is a complex anisotropic composite (Dupps and Wilson 2006). Thus, many studies have suggested that the strain distribution varies in different regions of the cornea. In a normal cornea, the tangential stretch in the central region was significantly smaller than that in the paracentral region, and the magnitude of radial strain was significantly larger than that of tangential strain (Kwok et al., 2021). Hennighausen et al. (1998) reported that the maximal strain on the posterior surface was larger than that on the anterior surface and that the strain response to corneal swelling was reduced on the anterior surface but enhanced on the posterior surface. Hollman et al. (2002) showed that the same mechanical loading induced distinct strains in different layers of the cornea owing to differential elastic properties. These findings are consistent with the heterogeneity of the cornea in the central to peripheral, anterior to posterior, and rotational directions. In contrast, the nonlinear elastic and viscoelastic properties of the cornea are determined by the interaction between its structure, such as collagen and a polyanionic ground substance (Dupps and Wilson 2006). As such, any change in its structure in refractive surgery or other disorders can affect its biomechanical properties,

which may alter the distribution of IOP-induced strain on the corneal surface (Dupps and Wilson 2006; Fang et al., 2020). This suggests that mechanical strain may be critical in maintaining the microenvironment of this tissue and the normal behavior of corneal cells.

Tensile and compressive stresses regulate corneal stroma composition

Tensile and compressive stresses influence various behaviors of stromal cells. Acute stretching or compressive stress on the local ECM of corneal fibroblasts (CFs) changed the morphology and cytoskeleton, thus facilitating their adaption to alterations in the mechanical microenvironment through Rho and/or Rac (Petroll et al., 2004). Applying 3% equibiaxial and uniaxial strains downregulated α-SMA expression in rabbit CFs by 35% and 65%, respectively, but no difference was observed under the 15% strain (Figure 3B) (Leonard et al., 2012). Cyclic equibiaxial stretching increased cellular contractility and affected the morphology of CFs (Feng et al., 2016). Keratocytes cultured in the 3D dome-shaped model with 3% mechanical strain showed higher expressions of keratocyte markers (lumican and keratocan) and ECM components (collagen I and collagen V) than those in the flat-shaped model (Zhang et al., 2017). Interestingly, a 3% static dome-shaped mechanical strain promoted the differentiation of periodontal ligament stem cells into keratocytes (Figure 3B) (Chen et al., 2018). Therefore, mechanical strain at the physiological level may be essential in maintaining a normal keratocyte phenotype (Figure 3B).

In addition, the balance between ECM synthesis and degradation, which plays a crucial role in maintaining normal corneal structure, is disrupted by abnormal mechanical strain (Figure 3B). Matrix metalloproteinases (MMPs) are a family of proteinases that contribute to corneal ECM degradation, whereas tissue inhibitors of metalloproteinases (TIMPs) counteract proteolysis by directly binding to MMPs. Previous studies have shown that low-magnitude cyclic equibiaxial stretching (5%) alone decreased the production of MMP2 and membrane type 1 MMP (MT1-MMP) and increased the production of TIMP-2 in rabbit CFs, whereas high-magnitude stretching (15%) increased the expression of MMP2 and MMP9 in an ERK-dependent manner (Liu et al., 2014; Feng et al., 2016). Moreover, IL-1β enhanced the sensitivity of rabbit CFs to mechanical cues and increased MMP2 and MMP9 (Feng et al., 2016). Thus, mechanical strains in the physiological range (approximately 3%) decrease KFM transformation, increase the expression of collagen and proteoglycans, and inhibit the synthesis of ECM-degrading enzymes to maintain normal stromal structure. However, large-magnitude strains (15%) upregulate the expression of proteases and may contribute to ECM disorders.

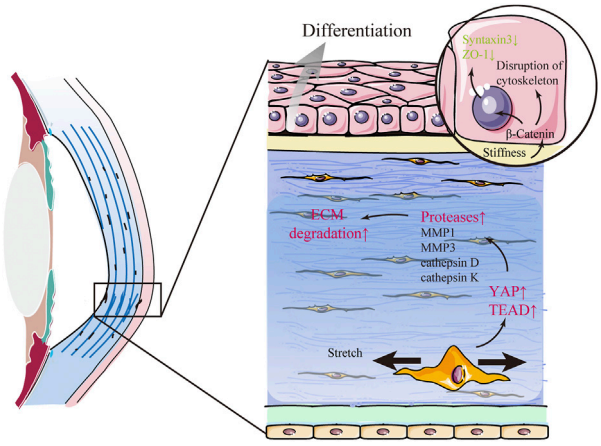

FIGURE 4
Keratoconus (KC) is related to changes in mechanical cues. In KC, β-catenin in corneal epithelial cells acts as a mechano-transducer of substrate stiffness that induces abnormal differentiation and structural changes in the corneal epithelium by delocalizing from the membrane to the cytosol. Furthermore, mechanical stretch promotes the expression of several proteases and aggravates extracellular matrix (ECM) degradation *via* YAP and its cooperator, TEA domain transcription factor (TEAD), in stromal cells.

Furthermore, mechanical compression interferes with the maintenance of normal stromal structures (Figure 3C). Ramirez-Garcia et al. (2018) evaluated the response of corneal endothelial cells to the indentation forces *in vitro* and found that the damage/apoptosis of CEnCs increased and ECD decreased significantly when the contact pressure exceeded 5.7 kPa (42.75 mmHg). When acute ocular hypertension (~82.6 mmHg for 2 h) was induced, the ECD was significantly decreased, and CEnCs became irregular and multiform with disrupted ZO-1 and F-actin (Li et al., 2017). In addition, Na^+-K^+-ATPase was evenly distributed around the cell membrane rather than localized to the basolateral membrane (Li et al., 2017). These results indicate that compression stress indirectly controls stromal hydration and thickness by modulating the pump function of the corneal endothelium. Our latest research found that mechanical compression could also alter cell morphology, inhibit proliferation, induce apoptosis, upregulate genes related to ECM degradation, and downregulate corneal structural genes in human CFs, thus directly demonstrating the critical role of compression stress (Zhang et al., 2021).

The association of corneal diseases with mechanical cues in the clinic

It has been demonstrated in the clinic that mechanical cues change in several primary and secondary corneal

TABLE 2 Case reports on eye rubbing-related keratoconus.

Author(s)	Method	Sample size	Finding
Weed et al. (2008)	Prospective observational study	$n = 200$	Forty-eight percent of subjects reported significant eye rubbing, and there was a statistically significant difference (two samples t-test $p = 0.018$) between keratoconus and control groups
Bawazeer et al. (2000)	Case-control study	$n = 120$	The most significant cause of keratoconus is eye rubbing. Atopy may contribute to keratoconus but most probably *via* eye rubbing associated with the itch of atopy
Bral and Termote, (2017)	Case report	$n = 1$	Unilateral keratoconus described in a patient with the medical history revealed a habit of chronic eye rubbing only in one eye
Yusuf and Salmon (2016)	Case report	$n = 1$	Keratoconus is described in a patient with obsessive–compulsive eye rubbing in the periocular contact dermatitis and allergic eye disease
Panikkar et al. (2016)	Case report	$n = 1$	Keratoconus described in a patient with obsessive–compulsive eye rubbing
Gunes et al. (2015)	Case report	$n = 1$	Keratoconus described in a 4-year-old patient with obsessive–compulsive eye rubbing
Panahi-Bazaz et al. (2014)	Case report	$n = 1$	Keratoconus described in a 7-year-old patient with obsessive–compulsive eye rubbing
Kandarakis et al. (2011)	Case report	$n = 1$	Keratoconus is described in a patient with obsessive–compulsive eye rubbing in the context of Tourette syndrome

disorders, such as keratoconus, complications of contact lens use or surgical treatments, and myopia. Elucidating the influence of these abnormal mechanical cues on the functions of corneal tissue and cells will help us better understand the role of mechanobiology in corneal pathology and bridge the gap between clinical findings and basic research.

Eye rubbing-related keratoconus

Keratoconus (KC) is a progressive corneal ectasia characterized by a cone-shaped cornea with local thinning and weakening in the corneal stroma (Figure 4). Compared with the normal cornea, the KC cornea has marked regional heterogeneity and larger strains in the cone region (Kwok et al., 2021). In the local thinning stroma, the number of lamellae decreases. However, the compaction of collagen fibrils within individual lamellae does not change (Vellara and Patel 2015). It has been proposed that the loss of structural integrity in the KC cornea is caused by redistribution and slippage between the lamellae rather than collagen degradation (Vellara and Patel 2015). The mechanism of structural alterations in space between lamellae is yet to be elucidated. Nonetheless, it is widely considered to be related to changes in mechanical cues. Several factors play a mechanoresponsive role in KC. β-catenin in CEpCs acts as a mechano-transducer of substrate stiffness that induces structural changes, such as the disruption of the cytoskeleton (F-actin), loss of polarity (Syntaxin3), and barrier function (ZO-1), by delocalizing from the membrane to the cytosol in KC (Figure 4) (Amit et al., 2020). YAP and its cooperator, TEA domain transcription factor (TEAD), in stromal cells are the mechanotransducers of stretch that prompt protease production (including MMP1, MMP3, cathepsin D, and cathepsin K) in KC (Figure 4) (Dou et al., 2022). Some case reports have indicated that eye rubbing is closely associated with KC (Table 2) (Bawazeer et al., 2000; Weed et al., 2008; Kandarakis et al., 2011; Panahi-Bazaz et al., 2014; Gunes et al., 2015; Panikkar et al., 2016; Yusuf and Salmon, 2016; Bral and Termote 2017). Eye rubbing is a process that pushes the eyelid against the cornea with horizontal eyelid motion (Masterton and Ahearne 2018). During rubbing, various changes in mechanical cues occur, including large IOP spikes, high hydrostatic tissue pressure, and altered shear stress (McMonnies 2009; Masterton and Ahearne 2018). Vigorous rubbing may increase IOP to more than ten times its normal level (McMonnies 2008), and KC eyes may experience more significant changes in IOP than healthy eyes (Henriquez et al., 2019). Importantly, corneal hysteresis (CH) and corneal resistance factor (CRF), which are used to measure corneal biomechanical properties, were significantly lower after eye rubbing in both keratoconic and healthy eyes (Liu et al., 2011; Henriquez et al., 2019). Nevertheless, many cases of eye-rubbing-related KC remain poorly understood. Standardized clinical analysis to describe the direction, frequency, and magnitude of eye rubbing in individuals is still lacking (Prakasam et al., 2012; Balasubramanian et al., 2013). Previous studies focused on the effect of single-cycle rubbing instead of the long-term effect of multiple rounds of rubbing (Greiner et al., 1985; Greiner et al., 1997). Thus, more rigorous investigations are required in future to demonstrate the causal or other roles of eye rubbing or rubbing forces in KC development.

Homeostasis of the ocular surface

Dry eye disease (DED) is a disease characterized by loss of homeostasis of the tear film (Craig et al., 2017). A sufficient

lubrication film is essential for reducing the shear stress by preventing solid-to-solid contact between the eyelid wiper and ocular surface (Jones et al., 2008). The mean eyelid pressure in DED is approximately 1.25 times greater than that in normal eyes, indicating that higher incidence of DED and ocular surface damage are associated with higher pressure of the lids onto the ocular surface (Yoshioka et al., 2015; Yamaguchi and Shiraishi 2018). In addition, the impairment of lubrication in DED also increases shear stress by decreasing the separation between the eyelid and ocular surface (Van Setten 2020). Hence, DED may affect cell behavior by altering mechanical cues from the tear film and ocular surface.

A contact lens (CL) is an ocular prosthetic device used for vision correction that can also change the mechanical microenvironment of the ocular surface. As eyelids move across the ocular surface during blinking, it creates a mechanical force on the CL, causing it to move laterally (up–down) and transversally (in–out) (Chauhan and Radke 2001; Pult et al., 2015). This force generated on the CL is transferred onto the cornea and causes greater corneal deformation (Ramasubramanian et al., 2022). In general, the force is reduced as CL approaches the inferior cornea and induces less mechanical trauma at the inferior cornea and limbus (Ramasubramanian et al., 2022). On the other hand, CL can directly restrict tear flow over the corneal surface (Mann and Tighe 2013; Muntz et al., 2015), which reduces shear stress where the epithelium is usually subjected and protects epithelial cells from blinking-induced shear force (Yamamoto et al., 2002). However, the movement and deformation of the CL during blinking can also induce tear flow that creates shear stress on the epithelium (Chauhan and Radke 2001; Pult et al., 2015). In addition, the mechanical force imposed on the cornea by a specially designed reverse-geometry gas-permeable rigid CL, the orthokeratology (OK) lens, is expected to be higher than that imposed by a routine CL (Ding et al., 2012). This external force placed against the front surface of the cornea may modify or eliminate the refractive error by reshaping the cornea with thinning of the central part and thickening of the paracentral corneal epithelium (Swarbrick 2004; Li et al., 2016; Chen et al., 2017; Kim WookKyum et al., 2018). In addition, wearing an OK lens reduced CH and CRF (Lam et al., 2019). However, the cellular mechanism for this subtle remodeling of the anterior corneal layers remains limited, and the impact of this external force on the corneal tissue at the microscopic level or cell activities also remains obscure (Swarbrick 2004; Ding et al., 2012).

The progression of myopia

Myopia is one of the most common ocular problems, affecting approximately 22% of the current world population; however, the exact cause of myopia is complicated and remains unclear. Recent studies have focused on the changes in corneal biomechanical properties in myopia. In a meta-analysis of corneal biomechanical properties of 11 related studies using an ocular response analyzer, we found that corneal elasticity decreased significantly in high myopia (Wu et al., 2019). We further showed that corneal stiffness of over 1,000 patients with high myopia provided by Corvis ST also significantly reduced (Han et al., 2020), which is further supported by the findings from other groups (Zhang et al., 2018; Asano et al., 2019; Long et al., 2019; Kenia et al., 2020; Sedaghat et al., 2020; Tubtimthong et al., 2020). With an experimentally induced myopia model in chicks, the reduction of corneal elasticity and weakness of corneal biomechanics were related to development of myopia (Kang et al., 2018). Using an atomic force microscope, we recently observed that the stiffness of single cells harvested from the cornea in chicks with high myopia reduced and then returned to normal after the vision was resumed (Xin et al., 2021). However, to date, it remains unclear whether myopia causes these biomechanical changes in the corneal tissue and cells or vice versa.

Surgical intervention disturbs the balanced mechanical microenvironment

Corneal refractive surgery, such as small-incision lenticular extraction (SMILE), laser-assisted *in situ* keratomileusis (LASIK), and photorefractive keratectomy (PRK), is the most common method for correcting a refractive error by central ablation to remodel the corneal surface structure and curvature. During the surgical procedure and postoperative recovery, different types of mechanical cues change in the corneal microenvironment. IOP fluctuates considerably over time during surgery. The mean IOP measured by an infusion cannula inserted through the limbus was lower in corneal flaps when the surgery was conducted by a femtosecond laser than that by a microkeratome during globe suction (81.78 vs. 122.51 mm Hg) and cutting (62.25 vs. 141.02 mm Hg) (Chaurasia et al., 2010). Our previous study monitored the intraoperative IOP during SMILE surgery and showed that IOP significantly increased after suction initiation (up to 86.55 ± 22.36 mmHg) and was stabilized at the cutting step (up to 75.87 ± 23.17 mmHg) (Cheng et al., 2018). These IOP fluctuations during corneal refractive surgery may contribute to complications in retinal function (Charteris et al., 1997; Qin et al., 2007). However, it remains unclear whether and how corneal cells respond to such a sharp increase in IOP. On the other hand, several forces, including the negative intrastromal fluid pressure generated by the hydrophilia of stromal glycosaminoglycans, cohesive forces between lamellae, centripetal force, and the lamellar tension manifested by the IOP, contribute to the corneal steady state and undergo complex disruptions during corneal refractive surgery (Dupps and Wilson 2006). Thus, corneal cells sense and respond to these mechanical

alterations and remodel such areas to restore mechanical integrity (Dupps and Wilson 2006). Furthermore, understanding of these processes will improve the predictability of refractive surgery and minimize complications such as refractive regression or keratectasia.

Laser iridotomy (LI) is a commonly used treatment for glaucoma. The number of cases of bullous keratopathy after LI has increased over the years (Lim et al., 2006; Ang et al., 2007). The shock wave of the laser, increased temperature of aqueous humor, and changes of cytokines in AH cannot fully explain why bullous keratopathy often develops even years after LI. It has been speculated that hydrodynamic changes in aqueous flow might play a key role in LI-induced bullous keratopathy (Kaji et al., 2005; Yamamoto et al., 2010). Yamamoto et al. (2006) showed in an animal study that during miosis, the AH was ejected into the anterior chamber from the posterior chamber through the LI window to strike the corneal endothelium, while the AH flowed oppositely during mydriasis (Yamamoto et al., 2006). Abnormal aqueous flow might result in excessive tensile and shear stresses on the CEnCs (Yamamoto et al., 2006; Yamamoto et al., 2010). Kaji et al. (2005) postulated a virtual model of LI for analysis and reported a maximum shear stress up to 1 dyn/cm^2, which was hundred-fold higher than the stress under the physiological state and may facilitate development of bullous keratopathy. Yamamoto et al. (2010) used a computational fluid dynamics model to compare shear stress with varied anterior chamber depths and found that the shear stress was 70-fold greater than that under the physiological state when the anterior chamber depth was 1.0 mm (Yamamoto et al., 2010). As a result, patients with insufficient anterior chamber depth after LI may suffer from excessive shear stress caused by the flow of AH through the LI window, leading to a high risk of CEnC damage and loss (Jin and Anderson 1990; He et al., 2007). To understand and avoid these complications involved in excessive mechanical stimuli or structural alterations due to surgical intervention, it is necessary to take into account the mechanical changes of the corneal microenvironment during and after surgery.

Conclusion

Mechanical forces are involved in many aspects of both the physiology and pathology of the cornea and have profound influences on corneal cells. Growing evidence suggests that mechanical factors play an important role in development and progression of various diseases. Moreover, mechanical cues can mediate the differentiation capacity of tissue-specific stem cells. However, the specific effect of mechanical forces at the corneal embryonic stage and the relationship between the changes in mechanical cues and corneal disorders remains unclear. This underscores the urgent need to assess specific mechanotransduction pathways and signals in corneal cells. It is likely that mechanotransduction and biochemical signaling are intertwined, which synergistically influences cellular functions of corneal cells and the mechanical microenvironment. Therefore, elucidating the influence of these mechanical cues on the functions of corneal tissue will help us better understand the mechanisms underlying corneal diseases and facilitate development of novel therapeutic strategies against these diseases from the perspective of biomechanics and mechanobiology.

Author contributions

All authors listed have made a substantial, direct, and intellectual contribution to the work and approved it for publication.

Funding

This work was supported by National Natural Science Foundation of China (No. 81670884 and 81873684, to YW, No. 11972316, to YT) and Shenzhen Science and Technology Innovation Commission (No. JCYJ20200109142001798; SGDX2020110309520303, To YT).

Acknowledgments

The authors sincerely treasured the comments and suggestions from reviewers.

Conflict of interest

The authors declare that the research was conducted in the absence of any commercial or financial relationships that could be construed as a potential conflict of interest.

Publisher's note

References

Abdalkader, Rodi, and Kamei, Ken-Ichiro (2020). Multi-corneal barrier-on-a-chip to recapitulate eye blinking shear stress forces. *Lab. Chip* 20 (8), 1410–1417. doi:10.1039/c9lc01256g

Amit, Chatterjee, Padmanabhan, Prema, and Narayanan, Janakiraman (2020). Deciphering the mechanoresponsive role of β-catenin in keratoconus epithelium. *Sci. Rep.* 10 (1), 21382. doi:10.1038/s41598-020-77138-3

Ang, L. P., Higashihara, H., Sotozono, C., Shanmuganathan, V. A., Dua, H., Tan, D. T., et al. (2007). Argon laser iridotomy-induced bullous keratopathy--a growing problem in Japan. *Br. J. Ophthalmol.* 91 (12), 1613–1615. doi:10.1136/bjo.2007.120261

Asano, Shotaro, Asaoka, Ryo, Yamashita, Takehiro, Aoki, Shuichiro, Matsuura, Masato, Fujino, Yuri, et al. (2019). Correlation between the myopic retinal deformation and corneal biomechanical characteristics measured with the Corvis ST tonometry. *Trans. Vis. Sci. Tech.* 8 (4), 26. doi:10.1167/tvst.8.4.26

Astudillo, Pablo. (2020). Extracellular matrix stiffness and Wnt/β-catenin signaling in physiology and disease. *Biochem. Soc. Trans.* 48 (3), 1187–1198. doi:10.1042/BST20200026

Balasubramanian, S. A., Pye, D. C., and Willcox, M. D. (2013). Effects of eye rubbing on the levels of protease, protease activity and cytokines in tears: Relevance in keratoconus. *Clin. Exp. Optometry* 96 (2), 214–218. doi:10.1111/cxo.12038

Bawazeer, A. M., Hodge, W. G., and Lorimer, B. (2000). Atopy and keratoconus: A multivariate analysis. *Br. J. Ophthalmol.* 84 (8), 834–836. doi:10.1136/bjo.84.8.834

Bral, N., and Termote, K. (2017). Unilateral keratoconus after chronic eye rubbing by the nondominant hand. *Case Rep. Ophthalmol.* 8 (3), 558–561. doi:10.1159/000484712

Charteris, D. G., Cooling, R. J., Lavin, M. J., and McLeod, D. (1997). Retinal detachment following excimer laser. *Br. J. Ophthalmol.* 81 (9), 759–761. doi:10.1136/bjo.81.9.759

Chauhan, A., and Radke, C. J. (2001). Modeling the vertical motion of a soft contact lens. *Curr. eye Res.* 22 (2), 102–108. doi:10.1076/ceyr.22.2.102.5521

Chaurasia, S. S., Gimeno, F., Tan, K., Yu, S., Tan, D. T., Beuerman, R. W., et al. (2010). *In vivo* real-time intraocular pressure variations during LASIK flap creation. *Invest. Ophthalmol. Vis. Sci.* 51 (9), 4641–4645. doi:10.1167/iovs.10-5228

Chen, S., Mienaltowski, M. J., and Birk, D. E. (2015). Regulation of corneal stroma extracellular matrix assembly. *Exp. eye Res.* 133, 69–80. doi:10.1016/j.exer.2014.08.001

Chen, Renai, Mao, Xinjie, Jiang, Jun, Shen, Meixiao, Lian, Yan, Zhang, Bin, et al. (2017). The relationship between corneal biomechanics and anterior segment parameters in the early stage of orthokeratology. *Medicine* 96 (19), e6907. doi:10.1097/MD.0000000000006907

Chen, Jialin, Zhang, Wei, Backman, Ludvig J., Kelk, Peyman, and Danielson, Patrik (2018). Mechanical stress potentiates the differentiation of periodontal ligament stem cells into keratocytes. *Br. J. Ophthalmol.* 102 (4), 562–569. doi:10.1136/bjophthalmol-2017-311150

Chen, Jialin, Backman, Ludvig J., Zhang, Wei, Ling, Ling, and Danielson, Patrik (2020). Regulation of keratocyte phenotype and cell behavior by substrate stiffness. *ACS Biomater. Sci. Eng.* 6 (9), 5162–5171. doi:10.1021/acsbiomaterials.0c00510

Cheng, W., Liu, L., Yu, S., Jing, Y., Zuo, T., Cui, T., et al. (2018). Real-time intraocular pressure measurements in the vitreous chamber of rabbit eyes during small incision lenticule extraction (SMILE). *Curr. eye Res.* 43 (10), 1260–1266. doi:10.1080/02713683.2018.1485949

Chou, S. F., Lai, J. Y., Cho, C. H., and Lee, C. H. (2016). Relationships between surface roughness/stiffness of chitosan coatings and fabrication of corneal keratocyte spheroids: Effect of degree of deacetylation. *Colloids Surfaces B Biointerfaces* 142, 105–113. doi:10.1016/j.colsurfb.2016.02.051

Collins, Michael J., Buehren, Buehren, Trevor, Tasha, Statham, Michael, Hansen, Jacinta, Cavanagh, A., et al. (2006). Factors influencing lid pressure on the cornea. *Eye contact lens* 32 (4), 168–173. doi:10.1097/01.icl.0000189193.28870.81

Craig, Jennifer P., Nichols, Nichols K., Akpek, Esen K., Akpek, Barbara, Dua, Caffery S., Joo, Choun-Ki, et al. (2017). TFOS DEWS II definition and classification report. *ocular Surf.* 15 (3), 276–283. doi:10.1016/j.jtos.2017.05.008

Diehl, K. A., Foley, J. D., Nealey, P. F., and Murphy, C. J. (2005). Nanoscale topography modulates corneal epithelial cell migration. *J. Biomed. Mater. Res. Part A* 75 (3), 603–611. doi:10.1002/jbm.a.30467

Ding, Hui, Pu, Aijun, Hong, He, Xie, Ruo Zhong, Yang, Jun, Liao, Aiping, et al. (2012). Changes in corneal biometry and the associated histology in rhesus monkeys wearing orthokeratology contact lenses. *Cornea* 31 (8), 926–933. doi:10.1097/ICO.0b013e318254688a

Dou, Shengqian, Wang, Qun, Zhang, Bin, Wei, Chao, Wang, Huijin, Liu, Ting, et al. (2022). Single-cell atlas of keratoconus corneas revealed aberrant transcriptional signatures and implicated mechanical stretch as a trigger for keratoconus pathogenesis. *Cell Discov.* 8 (1), 66. doi:10.1038/s41421-022-00397-z

Dreier, B., Thomasy, S. M., Mendonsa, R., Raghunathan, V. K., Russell, P., and Murphy, C. J. (2013). Substratum compliance modulates corneal fibroblast to myofibroblast transformation. *Investigative Ophthalmol. Vis. Sci.* 54 (8), 5901–5907. doi:10.1167/iovs.12-11575

Du, Gen-Lai, Chen, Wei-Yi, Li, Xiao-Na, He, Rui, and Feng, Peng-Fei (2017). Induction of MMP-1 and -3 by cyclical mechanical stretch is mediated by IL-6 in cultured fibroblasts of keratoconus. *Mol. Med. Rep.* 15 (6), 3885–3892. doi:10.3892/mmr.2017.6433

Duan, Sujuan, Li, Yingjie, Zhang, Yanyan, Zhu, Xuan, Mei, Yan, Xu, Dongmei, et al. (2021). The response of corneal endothelial cells to shear stress in an *in vitro* flow model. *J. Ophthalmol.* 2021, 9217866. doi:10.1155/2021/9217866

Dupps, W. J., Jr., and Wilson, S. E. (2006). Biomechanics and wound healing in the cornea. *Exp. eye Res.* 83 (4), 709–720. doi:10.1016/j.exer.2006.03.015

Eghrari, Allen O. S., Riazuddin, Amer, and Gottsch, John D. (2015). Overview of the cornea: Structure, function, and development. *Prog. Mol. Biol. Transl. Sci.* 134, 7–23. doi:10.1016/bs.pmbts.2015.04.001

Erkoc-Biradli, Fatma Zehra, Ozgun, Alp, Öztürk-Öncel, Meftune Özgen, Marcali, Merve, Elbuken, Caglar, Bulut, Osman, et al. (2021). Bioinspired hydrogel surfaces to augment corneal endothelial cell monolayer formation. *J. Tissue Eng. Regen. Med.* 15 (3), 244–255. doi:10.1002/term.3173

Fang, Lihua, Wang, Yan, Yang, Ruizhi, Deng, Sijing, Deng, Jiahao, and Wan, Linsun (2020). Effects of the LASIK flap thickness on corneal biomechanical behavior: A finite element analysis. *BMC Ophthalmol.* 20 (1), 67. doi:10.1186/s12886-020-01338-8

Feng, P., Li, X., Chen, W., Liu, C., Rong, S., Wang, X., et al. (2016). Combined effects of interleukin-1beta and cyclic stretching on metalloproteinase expression in corneal fibroblasts *in vitro*. *Biomed. Eng. Online* 15 (1), 63. doi:10.1186/s12938-016-0198-6

Fraser, Sarah A., Ting, Yuk-Hong, Mallon, Kelly S., Wendt, Amy E., Murphy, Christopher J., and Nealey, Paul F. (2008). Sub-micron and nanoscale feature depth modulates alignment of stromal fibroblasts and corneal epithelial cells in serum-rich and serum-free media. *J. Biomed. Mater. Res. Part A* 86 (3), 725–735. doi:10.1002/jbm.a.31519

Gouveia, Ricardo M., and Connon, Che J. (2020). Biomechanical modulation therapy-A stem cell therapy without stem cells for the treatment of severe ocular burns. *Transl. Vis. Sci. Technol.* 9 (12), 5. doi:10.1167/tvst.9.12.5

Gouveia, R. M., Lepert, G., Gupta, S., Mohan, R. R., Paterson, C., and Connon, C. J. (2019a). Assessment of corneal substrate biomechanics and its effect on epithelial stem cell maintenance and differentiation. *Nat. Commun.* 10 (1), 1496. doi:10.1038/s41467-019-09331-6

Gouveia, R. M., Vajda, F., Wibowo, J. A., Figueiredo, F., and Connon, C. J. (2019b). YAP, ΔNp63, and β-catenin signaling pathways are involved in the modulation of corneal epithelial stem cell phenotype induced by substrate stiffness. *Cells* 8 (4), 347. doi:10.3390/cells8040347

Greiner, J. V., Peace, D. G., Baird, R. S., and Allansmith, M. R. (1985). Effects of eye rubbing on the conjunctiva as a model of ocular inflammation. *Am. J. Ophthalmol.* 100 (1), 45–50. doi:10.1016/s0002-9394(14)74981-5

Greiner, J. V., Leahy, C. D., Welter, D. A., Hearn, S. L., Weidman, T. A., and Korb, D. R. (1997). Histopathology of the ocular surface after eye rubbing. *Cornea* 16 (3), 327–332. doi:10.1097/00003226-199705000-00013

Gunes, A., Tok, L., Tok, O., and Seyrek, L. (2015). The youngest patient with bilateral keratoconus secondary to chronic persistent eye rubbing. *Seminars Ophthalmol.* 30 (5-6), 454–456. doi:10.3109/08820538.2013.874480

Gutermuth, Angela, Maassen, Jessika, Harnisch, Emely, Kuhlen, Daniel, Sauer-Budge, Alexis, Skazik-Voogt, Claudia, et al. (2019). Descemet's membrane biomimetic microtopography differentiates human mesenchymal stem cells into corneal endothelial-like cells. *Cornea* 38 (1), 110–119. doi:10.1097/ICO.0000000000001765

Hampel, U., Garreis, F., Burgemeister, F., Essel, N., and Paulsen, F. (2018). Effect of intermittent shear stress on corneal epithelial cells using an *in vitro* flow culture model. *ocular Surf.* 16 (3), 341–351. doi:10.1016/j.jtos.2018.04.005

Han, Fang, Li, Mengdi, Wei, Pinghui, Ma, Jiaonan, Jhanji, Vishal, and Wang, Yan (2020). Effect of biomechanical properties on myopia: A study of new corneal biomechanical parameters. *BMC Ophthalmol.* 20 (1), 459. doi:10.1186/s12886-020-01729-x

Hassell, John R., and Birk, David E. (2010). The molecular basis of corneal transparency. *Exp. eye Res.* 91 (3), 326–335. doi:10.1016/j.exer.2010.06.021

He, M., Friedman, D. S., Ge, J., Huang, W., Jin, C., Lee, P. S., et al. (2007). Laser peripheral iridotomy in primary angle-closure suspects: Biometric and gonioscopic outcomes: The liwan eye study. *Ophthalmology* 114 (3), 494–500. doi:10.1016/j.ophtha.2006.06.053

Hennighausen, H., Feldman, S. T., Bille, J. F., and McCulloch, A. D. (1998). Anterior-posterior strain variation in normally hydrated and swollen rabbit cornea. *Investigative Ophthalmol. Vis. Sci.* 39 (2), 253–262.

Henriquez, Maria A., Michelle, Cerrate, Hadid, Marta G., Cañola-Ramirez, Laura A., Hafezi, Farhad, and Izquierdo, Luis (2019). Comparison of eye-rubbing effect in keratoconic eyes and healthy eyes using Scheimpflug analysis and a dynamic bidirectional applanation device. *J. cataract Refract. Surg.* 45 (8), 1156–1162. doi:10.1016/j.jcrs.2019.03.017

Hollman, K. W., Emelianov, S. Y., Neiss, J. H., Jotyan, G., Spooner, G. J., Juhasz, T., et al. (2002). Strain imaging of corneal tissue with an ultrasound elasticity microscope. *Cornea* 21 (1), 68–73. doi:10.1097/00003226-200201000-00015

Ingber, D. E. (2006). Cellular mechanotransduction: Putting all the pieces together again. *FASEB J.* 20 (7), 811–827. doi:10.1096/fj.05-5424rev

Iyer, Krithika S., Maruri, Daniel P., Peak, Kara E., Schmidtke, David W., Petroll, W. Matthew, and Varner, Victor D. (2022). ECM stiffness modulates the proliferation but not the motility of primary corneal keratocytes in response to PDGF-BB. *Exp. Eye Res.* 220, 109112. doi:10.1016/j.exer.2022.109112

Jin, J. C., and Anderson, D. R. (1990). The effect of iridotomy on iris contour. *Am. J. Ophthalmol.* 110 (3), 260–263. doi:10.1016/s0002-9394(14)76341-x

Jones, M. B., Fulford, G. R., Please, C. P., McElwain, D. L. S., and Collins, M. J. (2008). Elastohydrodynamics of the eyelid wiper. *Bull. Math. Biol.* 70 (2), 323–343. doi:10.1007/s11538-007-9252-7

Jones, R. R., Hamley, I. W., and Connon, C. J. (2012). *Ex vivo* expansion of limbal stem cells is affected by substrate properties. *Stem Cell Res.* 8 (3), 403–409. doi:10.1016/j.scr.2012.01.001

Kaji, Y., Oshika, T., Usui, T., and Sakakibara, J. (2005). Effect of shear stress on attachment of corneal endothelial cells in association with corneal endothelial cell loss after laser iridotomy. *Cornea* 24 (8), S55–S58. doi:10.1097/01.ico.0000178735.27674.52

Kandarakis, A., Karampelas, M., Soumplis, V., Panos, C., Makris, N., Kandarakis, S., et al. (2011). A case of bilateral self-induced keratoconus in a patient with tourette syndrome associated with compulsive eye rubbing: Case report. *BMC Ophthalmol.* 11, 28. doi:10.1186/1471-2415-11-28

Kang, Y. G., Shin, J. W., Park, S. H., Oh, M. J., Park, H. S., Shin, J. W., et al. (2014). Effects of flow-induced shear stress on limbal epithelial stem cell growth and enrichment. *PLoS One* 9 (3), e93023. doi:10.1371/journal.pone.0093023

Kang, B. S., Wang, L. K., Zheng, Y. P., Guggenheim, J. A., Stell, W. K., and Kee, C. S. (2018). High myopia induced by form deprivation is associated with altered corneal biomechanical properties in chicks. *PLoS One* 13 (11), e0207189. doi:10.1371/journal.pone.0207189

Karamichos, D., Lakshman, N., and Petroll, W. M. (2007). Regulation of corneal fibroblast morphology and collagen reorganization by extracellular matrix mechanical properties. *Investigative Ophthalmol. Vis. Sci.* 48 (11), 5030–5037. doi:10.1167/iovs.07-0443

Kawata, Kosuke, Aoki, Shigehisa, Futamata, Maki, Yamamoto-Rikitake, Mihoko, Nakao, Isao, Enaida, Hiroshi, et al. (2019). Mesenchymal cells and fluid flow stimulation synergistically regulate the kinetics of corneal epithelial cells at the air-liquid interface. *Graefe's archive Clin. Exp. Ophthalmol.* 257 (9), 1915–1924. doi:10.1007/s00417-019-04422-y

Kenia, Vaishal P., Kenia, Raj V., and Pirdankar, Onkar H. (2020). Association between corneal biomechanical parameters and myopic refractive errors in young Indian individuals. *Taiwan J. Ophthalmol.* 10 (1), 45–53. doi:10.4103/tjo.tjo_15_19

Kim, Areum, Zhou, Chengxin, Lakshman, Neema, and Matthew Petroll, W. (2012). Corneal stromal cells use both high- and low-contractility migration mechanisms in 3-D collagen matrices. *Exp. Cell Res.* 318 (6), 741–752. doi:10.1016/j.yexcr.2011.12.018

Kim, Jinsoo, Lee, Sang-Mok, Choi, Youn Joo, and Lee, Min Joung (2018). Estimation of eyelid pressure using a blepharo-tensiometer in patients with functional nasolacrimal duct obstruction. *J. Ophthalmol.* 2018, 8792102. doi:10.1155/2018/8792102

Kim, Wook Kyum, Kim, Bong Jun, Ryu, Ik-Hee, Kim, Jin Kook, and Kim, Sun Woong (2018a). Corneal epithelial and stromal thickness changes in myopic orthokeratology and their relationship with refractive change. *PLoS One* 13 (9), e0203652. doi:10.1371/journal.pone.0203652

Kirby, Tyler J., and Jan, Lammerding. (2018). Emerging views of the nucleus as a cellular mechanosensor. *Nat. Cell Biol.* 20 (4), 373–381. doi:10.1038/s41556-018-0038-y

Koo, Stephanie, Muhammad, Rizwan, Peh, Gary S. L., Mehta, Jodhbir S., and Yim, Evelyn K. F. (2014). Micro- and nanotopography with extracellular matrix coating modulate human corneal endothelial cell behavior. *Acta Biomater.* 10 (5), 1975–1984. doi:10.1016/j.actbio.2014.01.015

Koppaka, Vindhya, Lakshman, Neema, and Petroll, W. Matthew (2015). Effect of HDAC inhibitors on corneal keratocyte mechanical phenotypes in 3-D collagen matrices. *Mol. Vis.* 21, 502–514.

Kumar, S., Acharya, S., Beuerman, R., and Palkama, A. (2006). Numerical solution of ocular fluid dynamics in a rabbit eye: Parametric effects. *Ann. Biomed. Eng.* 34 (3), 530–544. doi:10.1007/s10439-005-9048-6

Kwok, Sunny, Hazen, Nicholas, Clayson, Keyton, Pan, Xueliang, and Liu, Jun (2021). Regional variation of corneal stromal deformation measured by high-frequency ultrasound elastography. *Exp. Biol. Med. (Maywood, N.J.)* 246 (20), 2184–2191. doi:10.1177/15353702211029283

Lakshman, N., and Petroll, W. M. (2012). Growth factor regulation of corneal keratocyte mechanical phenotypes in 3-D collagen matrices. *Invest. Ophthalmol. Vis. Sci.* 53 (3), 1077–1086. doi:10.1167/iovs.11-8609

Lam, Andrew K. C., Hon, Ying, Leung, Stanley Y. Y., Shu-Ho, Lu, Chong, Jones, David, C., et al. (2019). Association between long-term orthokeratology responses and corneal biomechanics. *Sci. Rep.* 9 (1), 12566. doi:10.1038/s41598-019-49041-z

Last, J. A., Liliensiek, S. J., Nealey, P. F., and Murphy, C. J. (2009). Determining the mechanical properties of human corneal basement membranes with atomic force microscopy. *J. Struct. Biol.* 167 (1), 19–24. doi:10.1016/j.jsb.2009.03.012

Last, J. A., Thomasy, S. M., Croasdale, C. R., Russell, P., and Murphy, C. J. (2012). Compliance profile of the human cornea as measured by atomic force microscopy. *Micron* 43 (12), 1293–1298. doi:10.1016/j.micron.2012.02.014

Leonard, E. K., Pai, V. H., Amberg, P., Gardner, J., and Orwin, E. J. (2012). Design and validation of a corneal bioreactor. *Biotechnol. Bioeng.* 109 (12), 3189–3198. doi:10.1002/bit.24587

Li, Fang, Jiang, Zhi-Xin, Peng, Hao, and Li, Xuan (2016). A meta-analysis of central corneal thickness changes with overnight orthokeratology. *Eye contact lens* 42 (2), 141–146. doi:10.1097/ICL.0000000000000132

Li, Xian, Zhang, Zhenhao, Ye, Lijun, Meng, Jufeng, Zhao, Zhongyang, Liu, Zuguo, et al. (2017). Acute ocular hypertension disrupts barrier integrity and pump function in rat corneal endothelial cells. *Sci. Rep.* 7 (1), 6951. doi:10.1038/s41598-017-07534-9

Liliensiek, S. J., Campbell, S., Nealey, P. F., and Murphy, C. J. (2006). The scale of substratum topographic features modulates proliferation of corneal epithelial cells and corneal fibroblasts. *J. Biomed. Mater. Res. Part A* 79 (1), 185–192. doi:10.1002/jbm.a.30744

Lim, L. S., Ho, C. L., Ang, L. P., Aung, T., and Tan, D. T. (2006). Inferior corneal decompensation following laser peripheral iridotomy in the superior iris. *Am. J. Ophthalmol.* 142 (1), 166–168. doi:10.1016/j.ajo.2006.01.070

Liu, Wan-Cherng, Lee, Shui-Mei, Graham, Andrew D., and Lin, Meng C. (2011). Effects of eye rubbing and breath holding on corneal biomechanical properties and intraocular pressure. *Cornea* 30 (8), 855–860. doi:10.1097/ICO.0b013e3182032b21

Liu, C., Feng, P., Li, X., Song, J., and Chen, W. (2014). Expression of MMP-2, MT1-MMP, and TIMP-2 by cultured rabbit corneal fibroblasts under mechanical stretch. *Exp. Biol. Med. (Maywood, N.J.)* 239 (8), 907–912. doi:10.1177/1535370214536650

Liu, Shaobao, Tao, Ru, Wang, Ming, Tian, Jin, Genin, Guy M., Lu, Tian Jian, et al. (2019). Regulation of cell behavior by hydrostatic pressure. *Appl. Mech. Rev.* 71 (4), 0408031–4080313. doi:10.1115/1.4043947

Ljubimov, A. V., and Saghizadeh, M. (2015). Progress in corneal wound healing. *Prog. Retin Eye Res.* 49, 17–45. doi:10.1016/j.preteyeres.2015.07.002

Long, W., Zhao, Y., Hu, Y., Li, Z., Zhang, X., Zhao, W., et al. (2019). Characteristics of corneal biomechanics in Chinese preschool children with different refractive status. *Cornea* 38 (11), 1395–1399. doi:10.1097/ICO.0000000000001971

Lydon, Don, and Tait, Alan (1988). Lid-pressure: Its measurement and probable effects on the shape and form of the cornea rigid contact lens system. *J. Br. Contact Lens Assoc.* 11 (1), 11–22. doi:10.1016/S0141-7037(88)80014-4

Ma, J., Wang, Y., Wei, P., and Jhanji, V. (2018). Biomechanics and structure of the cornea: Implications and association with corneal disorders. *Surv. Ophthalmol.* 63 (6), 851–861. doi:10.1016/j.survophthal.2018.05.004

Mann, A., and Tighe, B. (2013). Contact lens interactions with the tear film. *Exp. eye Res.* 117, 88–98. doi:10.1016/j.exer.2013.07.013

Martino, Fabiana, Perestrelo, Ana R., Vinarský, Vladimír, Pagliari, Stefania, and Forte, Giancarlo (2018). Cellular mechanotransduction: From tension to function. *Front. Physiology* 9, 824. doi:10.3389/fphys.2018.00824

Maruri, Daniel P., Miron-Mendoza, Miguel, Kivanany, Pouriska B., Hack, Joshua M., Schmidtke, David W., Petroll, W. Matthew, et al. (2020). ECM stiffness controls the activation and contractility of corneal keratocytes in response to TGF-β1. *Biophysical J.* 119 (9), 1865–1877. doi:10.1016/j.bpj.2020.08.040

Massoudi, D., Malecaze, F., and Galiacy, S. D. (2016). Collagens and proteoglycans of the cornea: Importance in transparency and visual disorders. *Cell Tissue Res.* 363 (2), 337–349. doi:10.1007/s00441-015-2233-5

Masterton, S., and Ahearne, M. (2018). Mechanobiology of the corneal epithelium. *Exp. eye Res.* 177, 122–129. doi:10.1016/j.exer.2018.08.001

Masterton, Sophia, and Ahearne, Mark (2019). Influence of polydimethylsiloxane substrate stiffness on corneal epithelial cells. *R. Soc. open Sci.* 6 (12), 191796. doi:10.1098/rsos.191796

McMonnies, C. W. (2008). Management of chronic habits of abnormal eye rubbing. *Contact lens anterior eye* 31 (2), 95–102. doi:10.1016/j.clae.2007.07.008

McMonnies, C. W. (2009). Mechanisms of rubbing-related corneal trauma in keratoconus. *Cornea* 28 (6), 607–615. doi:10.1097/ICO.0b013e318198384f

Meek, K. M., and Knupp, C. (2015). Corneal structure and transparency. *Prog. Retin. eye Res.* 49, 1–16. doi:10.1016/j.preteyeres.2015.07.001

Mikula, Eric R., Jester, James V., and Tibor, Juhasz. (2016). Measurement of an elasticity map in the human cornea. *Investigative Ophthalmol. Vis. Sci.* 57 (7), 3282–3286. doi:10.1167/iovs.15-18248

Miller, D. (1967). Pressure of the lid on the eye. *Archives Ophthalmol.* 78 (3), 328–330. doi:10.1001/archopht.1967.00980030330011

Miyagi, Hidetaka, Jalilian, Iman, Murphy, Christopher J., and Thomasy, Sara M. (2018). Modulation of human corneal stromal cell differentiation by hepatocyte growth factor and substratum compliance. *Exp. eye Res.* 176, 235–242. doi:10.1016/j.exer.2018.09.001

Molladavoodi, S., Kwon, H. J., Medley, J., and Gorbet, M. (2015). Human corneal epithelial cell response to substrate stiffness. *Acta Biomater.* 11, 324–332. doi:10.1016/j.actbio.2014.10.005

Molladavoodi, S., Robichaud, M., Wulff, D., and Gorbet, M. (2017). Corneal epithelial cells exposed to shear stress show altered cytoskeleton and migratory behaviour. *PLoS One* 12 (6), e0178981. doi:10.1371/journal.pone.0178981

Muhammad, Rizwan, Peh, Gary S. L., Khadijah, Adnan, Law, Jaslyn B. K., Mehta, Jodhbir S., and Yim, Evelyn K. F. (2015). Micro- and nano-topography to enhance proliferation and sustain functional markers of donor-derived primary human corneal endothelial cells. *Acta biomater.* 19, 138–148. doi:10.1016/j.actbio.2015.03.016

Muntz, A., Subbaraman, L. N., Sorbara, L., and Jones, L. (2015). Tear exchange and contact lenses: A review. *J. optometry* 8 (1), 2–11. doi:10.1016/j.optom.2014.12.001

Myrna, Kathern E., Mendonsa, Rima, Russell, Paul, Pot, Simon A., Liliensiek, Sara J., Jester, James V., et al. (2012). Substratum topography modulates corneal fibroblast to myofibroblast transformation. *Investigative Ophthalmol. Vis. Sci.* 53 (2), 811–816. doi:10.1167/iovs.11-7982

Namiguchi, Koji, Mizoue, Shiro, Ohta, Kiyohiko, and Shiraishi, Atsushi (2018). Effect of botulinum toxin A treatment on eyelid pressure in eyes with blepharospasm. *Curr. eye Res.* 43 (7), 896–901. doi:10.1080/02713683.2018.1464191

Nowell, Craig S., Odermatt, Pascal D., Azzolin, Luca, Hohnel, Sylke, Wagner, Erwin F., Fantner, Georg E., et al. (2016). Chronic inflammation imposes aberrant cell fate in regenerating epithelia through mechanotransduction. *Nat. Cell Biol.* 18 (2), 168–180. doi:10.1038/ncb3290

Palchesko, R. N., Lathrop, K. L., Funderburgh, J. L., and Feinberg, A. W. (2015). *In vitro* expansion of corneal endothelial cells on biomimetic substrates. *Sci. Rep.* 5, 7955. doi:10.1038/srep07955

Panahi-Bazaz, M. R., Sharifipour, F., and Moghaddasi, A. (2014). Bilateral keratoconus and corneal hydrops associated with eye rubbing in a 7-year-old girl. *J. Ophthalmic Vis. Res.* 9 (1), 101–105.

Panikkar, K., Manayath, G., Rajaraman, R., and Saravanan, V. (2016). Progressive keratoconus, retinal detachment, and intracorneal silicone oil with obsessive-compulsive eye rubbing. *Oman J. Ophthalmol.* 9 (3), 170–173. doi:10.4103/0974-620X.192285

Petroll, W. M., and Lakshman, N. (2015). Fibroblastic transformation of corneal keratocytes by rac inhibition is modulated by extracellular matrix structure and stiffness. *J. Funct. biomaterials* 6 (2), 222–240. doi:10.3390/jfb6020222

Petroll, W. Matthew, and Miron-Mendoza, Miguel (2015). Mechanical interactions and crosstalk between corneal keratocytes and the extracellular matrix. *Exp. eye Res.* 133, 49–57. doi:10.1016/j.exer.2014.09.003

Petroll, W. M., Vishwanath, M., and Ma, L. (2004). Corneal fibroblasts respond rapidly to changes in local mechanical stress. *Investigative Ophthalmol. Vis. Sci.* 45 (10), 3466–3474. doi:10.1167/iovs.04-0361

Phan, Chau-Min, Walther, Hendri, Qiao, Ha, Shinde, Ra, and Jones, Lyndo (2019). Development of an eye model with a physiological blink mechanism. *Transl. Vis. Sci. Technol.* 8 (5), 1. doi:10.1167/tvst.8.5.1

Pot, Simon A., Liliensiek, Sara J., Myrna, Kathern E., Bentley, Ellison, Jester, James V., Nealey, Paul F., et al. (2010). Nanoscale topography-induced modulation of fundamental cell behaviors of rabbit corneal keratocytes, fibroblasts, and myofibroblasts. *Investigative Ophthalmol. Vis. Sci.* 51 (3), 1373–1381. doi:10.1167/iovs.09-4074

Prakasam, R. K., Schwiede, M., Hutz, W. W., Guthoff, R. F., and Stachs, O. (2012). Corneal responses to eye rubbing with spectral domain optical coherence tomography. *Curr. eye Res.* 37 (1), 25–32. doi:10.3109/02713683.2011.622850

Pult, Heiko, Tosatti, Samuele G. P., Spencer, Nicholas D., Asfour, Jean-Michel, Ebenhoch, Michael, and Murphy, Paul J. (2015). Spontaneous blinking from a tribological viewpoint. *ocular Surf.* 13 (3), 236–249. doi:10.1016/j.jtos.2014.12.004

Qin, B., Huang, L., Zeng, J., and Hu, J. (2007). Retinal detachment after laser *in situ* keratomileusis in myopic eyes. *Am. J. Ophthalmol.* 144 (6), 921–923. doi:10.1016/j.ajo.2007.07.032

Qin, Guoting, Baidouri, Hasna, Glasser, Adrian, Raghunathan, VijayKrishna, Morris, Carol, Maltseva, Inna, et al. (2018). Development of an *in vitro* model to study the biological effects of blinking. *ocular Surf.* 16 (2), 226–234. doi:10.1016/j.jtos.2017.12.002

Qin, Zhangrong, Meng, Lingjuan, Fan, Yang, Zhang, Chaoying, and Wen, Binghai (2021). Aqueous humor dynamics in human eye: A lattice Boltzmann study. *Math. Biosci. Eng. MBE* 18 (5), 5006–5028. doi:10.3934/mbe.2021255

Ramasubramanian, Vivek Suganthan, Sundaram, S. Meenatchi, Thomas, Rinu, Ramesh, S. Ve, Pai, B. Raghuvir, Hazarika, Manali, et al. (2022). Finite element analysis of cornea and lid wiper during blink, with and without contact lens. *J. Ophthalmol.* 2022, 7930334. doi:10.1155/2022/7930334

Ramirez-Garcia, M. A., Khalifa, Y. M., and Buckley, M. R. (2018). Vulnerability of corneal endothelial cells to mechanical trauma from indentation forces assessed using contact mechanics and fluorescence microscopy. *Exp. eye Res.* 175, 73–82. doi:10.1016/j.exer.2018.06.005

Ravasio, Andrea, Morselli, Eugenia, and Bertocchi, Cristina (2022). Mechanoautophagy: Synergies between autophagy and cell mechanotransduction at adhesive complexes. *Front. Cell Dev. Biol.* 10, 917662. doi:10.3389/fcell.2022.917662

Ren, H., and Wilson, G. (1997). The effect of a shear force on the cell shedding rate of the corneal epithelium. *Acta Ophthalmol. Scand.* 75 (4), 383–387. doi:10.1111/j.1600-0420.1997.tb00394.x

Rizwan, Muhammad, Peh, Gary S. L., Ang, Heng-Pei, Chan Lwin, Nyein, Khadijah, Adnan, Mehta, Jodhbir S., et al. (2017). Sequentially-crosslinked bioactive hydrogels as nano-patterned substrates with customizable stiffness and degradation for corneal tissue engineering applications. *Biomaterials* 120, 139–154. doi:10.1016/j.biomaterials.2016.12.026

Ruberti, J. W., Sinha Roy, A., and Roberts, C. J. (2011). Corneal biomechanics and biomaterials. *Annu. Rev. Biomed. Eng.* 13, 269–295. doi:10.1146/annurev-bioeng-070909-105243

Sakai, Eriko, Shiraishi, Atsushi, Yamaguchi, Masahiko, Ohta, Kiyohiko, and Ohashi, Yuichi (2012). Blepharo-tensiometer: New eyelid pressure measurement system using tactile pressure sensor. *Eye contact lens* 38 (5), 326–330. doi:10.1097/ICL.0b013e318268610a

Secker, G. A., and Daniels, J. T. (2008). *Limbal epithelial stem cells of the cornea*. Cambridge (MA): Harvard Stem Cell Institute.

Sedaghat, Mohammad-Reza, Momeni-Moghaddam, Hamed, Azimi, Abbas, Fakhimi, Zohreh, Ziaei, Mohammed, Danesh, Zeynad, et al. (2020). Corneal biomechanical properties in varying severities of myopia. *Front. Bioeng. Biotechnol.* 8, 595330. doi:10.3389/fbioe.2020.595330

Seo, Jeongyun, Byun, Woo Y., Alisafaei, Farid, Georgescu, Andrei, Yi, Yoon-Suk, Massaro-Giordano, Mina, et al. (2019). Multiscale reverse engineering of the human ocular surface. *Nat. Med.* 25 (8), 1310–1318. doi:10.1038/s41591-019-0531-2

Shaw, Alyra J., Collins, Michael J., Davis, Brett A., and Carney, Leo G. (2009). Eyelid pressure: Inferences from corneal topographic changes. *Cornea* 28 (2), 181–188. doi:10.1097/ICO.0b013e31818a7d61

Shaw, Alyra J., Davis, Brett A., Collins, Michael J., and Carney, Leo G. (2009a). A technique to measure eyelid pressure using piezoresistive sensors. *IEEE Trans. biomedical Eng.* 56 (10), 2512–2517. doi:10.1109/TBME.2009.2022550

Shaw, Alyra J., Collins, Michael J., Davis, Brett A., and Carney, Leo G. (2010). Eyelid pressure and contact with the ocular surface. *Investigative Ophthalmol. Vis. Sci.* 51 (4), 1911–1917. doi:10.1167/iovs.09-4090

Shin, T. J., Vito, R. P., Johnson, L. W., and McCarey, B. E. (1997). The distribution of strain in the human cornea. *J. Biomechanics* 30 (5), 497–503. doi:10.1016/s0021-9290(97)84433-8

Stramer, B. M., Zieske, J. D., Jung, J. C., Austin, J. S., and Fini, M. E. (2003). Molecular mechanisms controlling the fibrotic repair phenotype in cornea: Implications for surgical outcomes. *Invest. Ophthalmol. Vis. Sci.* 44 (10), 4237–4246. doi:10.1167/iovs.02-1188

Sun, Zhiqi, Guo, Shengzhen S., and Fässler, Reinhard (2016). Integrin-mediated mechanotransduction. *J. Cell Biol.* 215 (4), 445–456. doi:10.1083/jcb.201609037

Swarbrick, H. A. (2004). Orthokeratology (corneal refractive therapy): What is it and how does it work? *Eye Contact Lens* 30 (4), 181–185. doi:10.1097/01.icl.0000140221.41806.6e

Tajik, Arash, Zhang, Yuejin, Wei, Fuxiang, Sun, Jian, Jia, Qiong, Zhou, Wenwen, et al. (2016). Transcription upregulation via force-induced direct stretching of chromatin. *Nat. Mater.* 15 (12), 1287–1296. doi:10.1038/nmat4729

Tang, Hao, Qin, Zhangrong, and Wen, Binghai (2022). Geometric model and numerical study of aqueous humor hydrodynamics in the human eye. *Comput. Math. Methods Med.* 2022, 4756728. doi:10.1155/2022/4756728

Then, Kong Y., Yang, Ying, Ahearne, Mark, and El Haj, Alicia J. (2011). Effect of microtopographical cues on human keratocyte orientation and gene expression. *Curr. eye Res.* 36 (2), 88–93. doi:10.3109/02713683.2010.512407

Thomasy, Sara M., Krishna Raghunathan, Vijay, Miyagi, Hidetaka, Evashenk, Alexander T., Sermeno, Jasmyne C., Tripp, Geneva K., et al. (2018). Latrunculin B and substratum stiffness regulate corneal fibroblast to myofibroblast transformation. *Exp. eye Res.* 170, 101–107. doi:10.1016/j.exer.2018.02.003

Torres-Netto, Emilio A., Hafezi, Farhad, Spiru, Bogdan, Gilardoni, Francesca, Hafezi, Nikki L., Gomes, Jose Alvaro P., et al. (2021). Contribution of Bowman layer to corneal biomechanics. *J. Cataract Refract. Surg.* 47 (7), 927–932. doi:10.1097/j.jcrs.0000000000000543

Tubtimthong, Aratchaporn, Chansangpetch, Sunee, Ratprasatporn, Nitee, Manassakorn, Anita, Tantisevi, Visanee, Rojanapongpun, Prin, et al. (2020). Comparison of corneal biomechanical properties among axial myopic, nonaxial myopic, and nonmyopic eyes. *BioMed Res. Int.* 2020, 8618615. doi:10.1155/2020/8618615

Utsunomiya, T., Ishibazawa, A., Nagaoka, T., Hanada, K., Yokota, H., Ishii, N., et al. (2016). Transforming growth factor-beta signaling cascade induced by mechanical stimulation of fluid shear stress in cultured corneal epithelial cells. *Investigative Ophthalmol. Vis. Sci.* 57 (14), 6382–6388. doi:10.1167/iovs.16-20638

van Setten, Gysbert-Botho (2020). Impact of attrition, intercellular shear in dry eye disease: When cells are challenged and neurons are triggered. *Int. J. Mol. Sci.* 21 (12), 4333. doi:10.3390/ijms21124333

Vellara, Hans R., and Patel, Dipika V. (2015). Biomechanical properties of the keratoconic cornea: A review. *Clin. Exp. Optometry* 98 (1), 31–38. doi:10.1111/cxo.12211

Weed, K. H., MacEwen, C. J., Giles, T., Low, J., and McGhee, C. N. (2008). The dundee university scottish keratoconus study: Demographics, corneal signs, associated diseases, and eye rubbing. *Eye (Lond)* 22 (4), 534–541. doi:10.1038/sj.eye.6702692

Wu, Pei-Jung, Kabakova, Irina V., Ruberti, Jeffrey W., Sherwood, Joseph M., Dunlop, Iain E., Paterson, Carl, et al. (2018). Water content, not stiffness, dominates Brillouin spectroscopy measurements in hydrated materials. *Nat. Methods* 15 (8), 561–562. doi:10.1038/s41592-018-0076-1

Wu, W., Dou, R., and Wang, Y. (2019). Comparison of corneal biomechanics between low and high myopic eyes-A meta-analysis. *Am. J. Ophthalmol.* 207, 419–425. doi:10.1016/j.ajo.2019.07.007

Xin, Ying, Kang, Byung Soo, Zheng, Yong-Ping, Shan, Sze Wan, Chea-Su Keeand Tan, Youhua (2021). Biophysical properties of corneal cells reflect high myopia progression. *Biophysical J.* 120 (16), 3498–3507. doi:10.1016/j.bpj.2021.05.010

Xiong, Sijia, Gao, HuiChang, Qin, Lanfeng, Jia, Yong-Guang, and Ren, Li (2019). Engineering topography: Effects on corneal cell behavior and integration into corneal tissue engineering. *Bioact. Mater.* 4, 293–302. doi:10.1016/j.bioactmat.2019.10.001

Yamaguchi, Masahiko, and Shiraishi, Atsushi (2018). Relationship between eyelid pressure and ocular surface disorders in patients with healthy and dry eyes. *Investigative Ophthalmol. Vis. Sci.* 59 (14), DES56–DES63. doi:10.1167/iovs.17-23586

Yamamoto, K., Ladage, P. M., Ren, D. H., Li, L., Petroll, W. M., Jester, J. V., et al. (2002). Effect of eyelid closure and overnight contact lens wear on viability of surface epithelial cells in rabbit cornea. *Cornea* 21 (1), 85–90. doi:10.1097/00003226-200201000-00018

Yamamoto, Y., Uno, T., Shisida, K., Xue, L., Shiraishi, A., Zheng, X., et al. (2006). Demonstration of aqueous streaming through a laser iridotomy window against the corneal endothelium. *Archives Ophthalmol.* 124 (3), 387–393. doi:10.1001/archopht.124.3.387

Yamamoto, Y., Uno, T., Joko, T., Shiraishi, A., and Ohashi, Y. (2010). Effect of anterior chamber depth on shear stress exerted on corneal endothelial cells by altered aqueous flow after laser iridotomy. *Investigative Ophthalmol. Vis. Sci.* 51 (4), 1956–1964. doi:10.1167/iovs.09-4280

Yamamoto, Yasuaki, Shiraishi, Atsushi, Sakane, Yuri, Ohta, Kiyohiko, Yamaguchi, Masahiko, and Ohashi, Yuichi (2016). Involvement of eyelid pressure in lid-wiper epitheliopathy. *Curr. eye Res.* 41 (2), 171–178. doi:10.3109/02713683.2015.1009636

Yoshioka, Eriko, Yamaguchi, Masahiko, Shiraishi, Atsushi, Kono, Tomoko, Ohta, Kiyohiko, and Ohashi, Yuichi (2015). Influence of eyelid pressure on fluorescein staining of ocular surface in dry eyes. *Am. J. Ophthalmol.* 160 (4), 685–692. doi:10.1016/j.ajo.2015.06.028

Yun, Seok Hyun, and Chernyak, Dimitri (2018). Brillouin microscopy: Assessing ocular tissue biomechanics. *Curr. Opin. Ophthalmol.* 29 (4), 299–305. doi:10.1097/ICU.0000000000000489

Yusuf, I. H., and Salmon, J. F. (2016). Iridoschisis and keratoconus in a patient with severe allergic eye disease and compulsive eye rubbing: A case report. *J. Med. Case Rep.* 10 (1), 134. doi:10.1186/s13256-016-0914-7

Zhang, W., Chen, J., Backman, L. J., Malm, A. D., and Danielson, P. (2017). Surface topography and mechanical strain promote keratocyte phenotype and extracellular matrix formation in a biomimetic 3D corneal model. *Adv. Healthc. Mater.* 6 (5), 1601238. doi:10.1002/adhm.201601238

Zhang, Yaohua, Wang, Yan, Li, Liuyang, Dou, Rui, Wu, Wenjing, Wu, Di, et al. (2018). Corneal stiffness and its relationship with other corneal biomechanical and nonbiomechanical parameters in myopic eyes of Chinese patients. *Cornea* 37 (7), 881–885. doi:10.1097/ICO.0000000000001605

Zhang, Jing, Yang, Shu, Tan, Youhua, and Wang, Yan (2021). Effects of mechanical compression on cell morphology and function in human corneal fibroblasts. *Curr. eye Res.* 46 (10), 1467–1473. doi:10.1080/02713683.2021.1904510

frontiers | Frontiers in Bioengineering and Biotechnology

TYPE Original Research
PUBLISHED 04 October 2022
DOI 10.3389/fbioe.2022.981665

OPEN ACCESS

EDITED BY
Yan Wang,
Tianjin Eye Hospital, China

REVIEWED BY
Matthew A. Reilly,
The Ohio State University, United States
Rui B. Ruben,
Polytechnic Institute of Leiria, Portugal

*CORRESPONDENCE
Elena Redaelli,
elena.redaelli@unizar.es

SPECIALTY SECTION
This article was submitted to Biomechanics, a section of the journal Frontiers in Bioengineering and Biotechnology

RECEIVED 29 June 2022
ACCEPTED 13 September 2022
PUBLISHED 04 October 2022

CITATION
Redaelli E, Grasa J, Calvo B, Rodriguez Matas JF and Luraghi G (2022), A detailed methodology to model the Non Contact Tonometry: a Fluid Structure Interaction study. *Front. Bioeng. Biotechnol.* 10:981665. doi: 10.3389/fbioe.2022.981665

A detailed methodology to model the Non Contact Tonometry: a Fluid Structure Interaction study

Elena Redaelli[1]*, Jorge Grasa[1,2], Begoña Calvo[1,2], Jose Felix Rodriguez Matas[3] and Giulia Luraghi[3]

[1]Aragón Institute of Engineering Research (I3A), University of Zaragoza, Zaragoza, Spain, [2]Centro de Investigación Biomecánica en Red en Bioingenieria, Biomateriales y Nanomedicina (CIBER-BBN), Zaragoza, Spain, [3]LaBS, Department of Chemistry, Materials and Chemical Engineering "Giulio Natta", Politecnico di Milano, Milan, Italy

Understanding the corneal mechanical properties has great importance in the study of corneal pathologies and the prediction of refractive surgery outcomes. Non-Contact Tonometry (NCT) is a non-invasive diagnostic tool intended to characterize the corneal tissue response *in vivo* by applying a defined air-pulse. The biomarkers inferred from this test can only be considered as indicators of the global biomechanical behaviour rather than the intrinsic biomechanical properties of the corneal tissue. A possibility to isolate the mechanical response of the corneal tissue is the use of an inverse finite element method, which is based on accurate and reliable modelling. Since a detailed methodology is still missing in the literature, this paper aims to construct a high-fidelity finite-element model of an idealized 3D eye for *in silico* NCT. A fluid-structure interaction (FSI) simulation is developed to virtually apply a defined air-pulse to a 3D idealized eye model comprising cornea, limbus, sclera, lens and humors. Then, a sensitivity analysis is performed to examine the influence of the intraocular pressure (IOP) and the structural material parameters on three biomarkers associated with corneal deformation. The analysis reveals the requirements for the *in silico* study linked to the correct reproduction of three main aspects: the air pressure over the cornea, the biomechanical properties of the tissues, and the IOP. The adoption of an FSI simulation is crucial to capture the correct air pressure profile over the cornea as a consequence of the air-jet. Regarding the parts of the eye, an anisotropic material should be used for the cornea. An important component is the sclera: the stiffer the sclera, the lower the corneal deformation due to the air-puff. Finally, the fluid-like behavior of the humors should be considered in order to account for the correct variation of the IOP during the test which will, otherwise, remain constant. The development of a strong FSI tool amenable to model coupled structures and fluids provides the basis to find the biomechanical properties of the corneal tissue *in vivo*.

KEYWORDS

corneal biomechanics, numerical modeling, fluid-structure interaction (FSI), non-contact tonometry, intraocular pressure (IOP)

1 Introduction

The cornea is the primary refractive surface of the eye, owning 75% of its refractive power (Chong and Dupps Jr, 2021). This optics capability is highly correlated to its mechanical properties (Ávila et al., 2021), therefore understanding the corneal mechanical behaviour is crucial for the study of some ocular pathologies and the prediction of refractive surgery outcomes (Kling and Hafezi, 2017). Non-Contact Tonometry (NCT) is a non-invasive diagnostic tool intended to characterize the corneal response *in vivo* by applying a defined air-puff. During the test, the cornea deforms inward and then recovers to its original shape, hence it goes through three main phases: first applanation point, highest concavity point and second applanation point. In the Corvis ST® (Corvis, Oculus Optikgeräte GmbH, Wetzlar, Germany) (Hong et al., 2013) tonometer, the dynamic deformation of the equatorial plane of the cornea is recorded through a high-speed camera, 140 horizontal 8 mm frames are taken over a period of 33 mas (Esporcatte et al., 2020). Based on the images, biomarkers such as the deflection amplitude and the peak distance are calculated. These parameters can only be considered as indicators of the mechanical behaviour rather than the intrinsic mechanical properties of the corneal tissue. Indeed, the response of the cornea to the air-puff depends on the combination of four factors: the intraocular pressure (IOP), the thickness of the cornea, the external loads, and the mechanical properties of the cornea and the surrounding tissue (Ariza-Gracia et al., 2015). Since only the mechanical properties of the cornea and surrounding tissue are unknown, it is possible to construct an inverse finite element method to isolate the influence of each factor in the corneal response and identify the parameters of the mathematical model used to reproduce the mechanical response of the corneal tissue. The inverse finite element method requires accurate and reliable modelling of the NCT to effectively translate the results of the test into clinical data.

The approaches to model the interaction between the air puff and the structure of the eye can be classified according to the numerical analysis adopted. Initial studies assumed a structural finite element analysis (FEA) technique. In Eliasy et al. (Eliasy et al., 2019) and Rahmati et al. (Rahmati et al., 2021) the eye is the structural part with proper mechanical properties, while the action of the air puff test is simulated by a time-dependent pressure. Montanino et al. (Montanino et al., 2018) (Montanino et al., 2019) employing FEA underlined the need of modelling the filling fluid of the humors, to avoid a wrong estimate of the material properties of the eye tissues. The limitation of FEA modeling is the lack of correlation between the external load and the corneal geometry and mechanical properties. For this reason, other works (Muench et al., 2019) (Nguyen et al., 2019) (Huang et al., 2020) conducted a computational fluid dynamic (CFD) analysis to find the correct pressure profile to be applied to the corneal tissue. The air is modeled as a fluid and the eye as a rigid body. Then, the deformable eye is loaded with the pressure profile obtained from the CFD. In these simulations, the pressure profile depends on the initial geometry of the eye, and is not modulated by the corneal mechanical properties as happens in reality. Hence, the adoption of the fluid-structure interaction (FSI) analysis, where the structural domain is combined with the fluid domain, has become of great interest. Ariza-Gracia et al. (Ariza-Gracia et al., 2018), Maklad et al. (Maklad et al., 2020b) and Issarti et al. (Issarti et al., 2021) demonstrated that the best numerical approach to reproduce the NCT is the FSI simulation. Ariza-Gracia et al. (Ariza-Gracia et al., 2018) considered a 2D model, which limits the study to an isotropic cornea, Maklad et al. (Maklad et al., 2020b) and Issarti et al. (Issarti et al., 2021) used a limited fluid domain. Even though the cornea contains multi-scale structures with distinct patterns of fiber organization (Blackburn et al., 2019), to the best of authors knowledge, current FSI solutions (Ariza-Gracia et al., 2018) (Maklad et al., 2020b) (Issarti et al., 2021) do not account for the anisotropy of the cornea in the simulation. This work presents a high-fidelity fluid-structure finite-element model of an idealized 3D eye to virtually reproduce the NCT.

2 Methods

2.1 Structural model of the eye

2.1.1 Geometry

A 3D model of an eye (Figure 1A) is constructed based on averaged anatomic measures taken from literature (Ariza-Gracia et al., 2018) (Cabeza-Gil et al., 2021). It contains cornea, limbus, sclera, crystalline lens differentiated in cortex and nucleus, aqueous and vitreous humors separated by the vitreous membrane, and ciliary zonule modelled as a thin membrane. Due to the double symmetry only a quarter of a middle eye has been considered and symmetric boundary conditions are imposed, rigid body motions are prevented in the bottom and lateral surfaces. The eye is meshed with hexahedral solid elements (Figure 1C) with full integration except for the vitreous membrane and the ciliary zonule meshed with quadratic shell elements with full integration (further discretization details are in the following section). The mesh is realized through the commercially available software ANSA Pre Processor v22.01 (BETA CAE Systems, Switzerland).

2.1.2 Constitutive material models and zero pressure configuration

The cornea and the limbus are modelled as anisotropic nearly-incompressible hyperelastic materials to account for the

influence of the collagen fibres present in the tissues. In the cornea, two families of mutually perpendicular collagen fibres tangent to the corneal surface (Meek and Knupp, 2015) have been considered: 1) a nasal-temporal direction coincident with the global x-axis, and 2) a superior-inferior direction coincident with the global z-axis, whereas the limbus is composed of one circumferential family of fibres as shown in Figure 1B. The Holzapfel Gasser Ogden strain energy function (Holzapfel et al., 2000) is adopted for the cornea and the limbus

$$\Psi = C_{10}(\bar{I}_1 - 3) + \frac{k_1}{2k_2}\sum_{i=4,6} e^{k_2(\bar{I}_i - 1)^2} + \frac{1}{k}(J-1)^2 \quad (1)$$

where C_{10} is the material constant associated with the extracellular matrix behaviour, k_1 is the material constant associated with the fibres stiffness and k_2 with the fibres non linearity. k is the bulk modulus, in case of nearly incompressibility the parameter can be thought of as a penalty factor enforcing the incompressibility constraint. $\bar{I}_1$ is the first invariant, $\bar{I}_4$, $\bar{I}_6$ are respectively the fourth and sixth pseudo-invariants of the modified right Cauchy Green deformation tensor ($\bar{C}$) and J is the determinant of the deformation gradient (F).

$$C = F^T \cdot F \qquad \bar{C} = J^{-2/3} \cdot C \quad (2)$$

$$\bar{I}_1 = tr(\bar{C}) \qquad \bar{I}_4 = \mathbf{m} \cdot \mathbf{m}^T \qquad \bar{I}_6 = \mathbf{n} \cdot \mathbf{n}^T \quad (3)$$

$\mathbf{m}$ and $\mathbf{n}$ are the vectors defining the direction of the fibres.

In this first study the mechanical parameters of cornea and limbus are estimated fitting experimental stress strain data reported in the literature (Huang et al., 2020). The same mechanical properties have been assumed for all families of fibres. To simplify the subsequent sensitivity analysis, the sclera is modelled as an isotropic hyperelastic material with a Neo Hookean strain energy density function in which the stiffness is only defined by one parameter.

$$\Psi = C_{10}(\bar{I}_1 - 3) + \frac{1}{k}(J-1)^2 \quad (4)$$

C_{10} of the sclera is estimated fitting experimental stress strain data reported in the literature (Eilaghi et al., 2010). Since the deformations of the internal tissues are not large, the crystalline, ciliary zonule and vitreous membrane are modelled as linear elastic materials (Kim et al., 2019) (Wilde et al., 2012) (Krag and Andreassen, 2003). Note that, since the capsule is not included in the model, the Young modulus of the crystalline cortex is arbitrarily selected as the average of the Young modulus of the crystalline cortex reported in (Wilde et al., 2012) and the Young modulus of the capsule reported in (Krag and Andreassen, 2003). All the material constants used in the model are reported in Table 1.

Considerable attention must be paid to the formulation of the humors which are incompressible fluids pressurized at a spatially homogenous intraocular pressure (IOP). The humors are modelled as a cavity in which the relationship between pressure and volume is controlled. Since the initial pressure of the cavities is zero, a positive input flow rate is imposed until the target IOP of 15 mmHg is reached. Then, the volumes are closed, and the humours behave as incompressible fluids.

Since the average dimensions of the eye (Figure 1C) corresponds to the pressurized configuration, in a first step of the simulation, the zero-pressure configuration of the eye is found through the iterative algorithm described in Ariza Gracia et al. (Ariza-Gracia et al., 2016).

In addition, since a dynamic analysis is used for the structural solver, a mass weighted damping has been adopted for all the parts with a damping constant of 0.1 ms^{-1}. The mass weighted damping has the role of damping the oscillations associated with inertial effects.

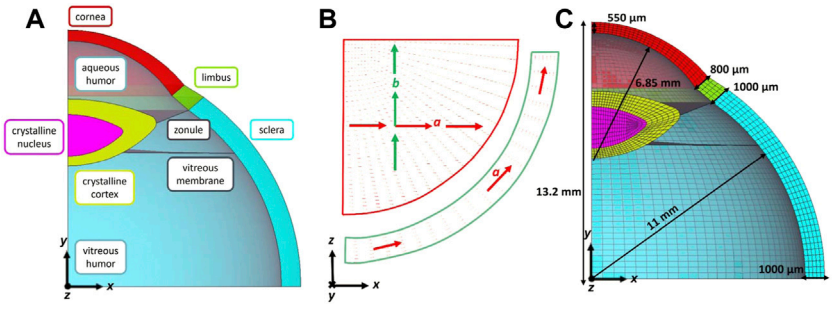

FIGURE 1
(A) Section of the 3D structural parts: cornea, limbus, sclera, crystalline lens nucleus, and cortex, zonule, vitreous membrane, vitreous and aqueous humors; **(B)** local reference systems defined in each element of the cornea and limbus to model two family of collagen fibres **(A,B)** in the corneal plane and one family of fibres **(A)** in the tangential direction of the limbus; **(C)** Hexahedral mesh with five elements in the thickness.

TABLE 1 Material parameters of the different eye tissues incorporated in the finite element model.

Material properties

Part	C_{10} [MPa]	k_1 [MPa]	k_2 [−]	ρ [g/mm^3]	Ref
Cornea	0.05	0.010	100	0.0011	(Huang et al., 2020)
Limbo	0.05	0.010	100	0.0011	(Huang et al., 2020)
Sclera	0.8	–	–	0.0011	(Eilaghi et al., 2010)
Part	**E [MPa]**			**ρ [g/mm^3]**	
Crystalline Lens Nucleus	0.0003			0.0011	(Wilde et al., 2012)
Crystalline Lens Cortex	0.35			0.0011	(Wilde et al., 2012) (Krag and Andreassen, 2003)
Ciliary Zonule	0.35			0.0011	(Kim et al., 2019)
Vitreous Membrane	0.35			0.0011	(Kim et al., 2019)

2.2 Mesh sensitivity analysis

A sensitivity analysis is conducted to determine the optimal mesh density of the structural model. Four different hexahedral grids are constructed by increasing the number of elements in the thickness of the eye, thus decreasing the size of the elements. Mesh data are reported in Table 2. For each mesh, the zero-pressure configuration is computed, then the humors are pressurized at 15 mmHg. Finally, a static pressure is applied to the apex of the eye to study the apical deformation. In each case, the displacement of the apex at the instant of highest concavity is recorded as representative primary variable of the model. The error between two consecutive mesh sizes is calculated as

$$error\,[\%] = \frac{u_{current-configuration} - u_{previous-configuration}}{u_{previous-configuration}} \cdot 100 \quad (5)$$

2.3 Fluid analysis and air puff simulation

The air domain (Figure 2) of the NCT test was set in 50 mm (3 times the radius of the eyeball) as it was observed to minimize boundary effects on the flow over the cornea. It presents two symmetric planes and a nozzle with an inlet Gaussian air-puff velocity (with a maximum of 120 $\frac{m}{s}$ during a period of 20 ms) at 11 mm from the corneal apex, that is the distance between the device and the eye as reported by the manufacturers (OCULUS, 2021). Zero pressure is imposed as an outlet boundary condition. The automatic volume mesher of the ICFD solver fills with 212,678 tetrahedral elements the input meshed surfaces. Five boundary layers are set at the FSI interface. The air domain is solved with an Arbitrary Lagrangian-Eulerian (ALE) kinematic approach. The air is modelled as an incompressible fluid whose density and dynamic viscosity are $\rho = 1.25 \cdot 10^{-6} \frac{g}{mm^3}$, $\mu = 1.8 \cdot 10^{-8}$ MPa·ms respectively. A turbulence model based on a variational multiscale approach is assumed. The fluid parameters are tested comparing the results of the computational fluid dynamic simulation (CFD) with the experimental results presented in Roberts et al. (Roberts et al., 2017). At the interface between the structure and the fluid a no-slip condition is adopted. NCT is simulated by a strongly coupled, 2-way and boundary fitted FSI. The NCT simulation consisted in a single step consisting in the inflation of the eye at a 15 mmHg IOP in the first 30 ms, followed by 10 ms of rest, to then apply the air puff between 40 and 60 ms.

TABLE 2 Mesh data adopted in the mesh sensitivity analysis.

Mesh analysis

Element in the thickness	Total number of elements	Total number of nodes
3	30236	20994
4	31991	22831
5	33746	24668
6	35501	26505

2.4 Material sensitivity analysis

A sensitivity analysis is performed to identify the influence of the IOP and the material constants parameters. Five parameters governing the mechanical response of the eye are analysed: the IOP; the matrix stiffness parameter C_{10-c}, the fibres stiffness parameter k_1 and the fibres non-linearity parameter k_2 of the cornea; and regarding the sclera the matrix stiffness parameter C_{10-s}. A 2^5 full factorial design which takes into account five different variables at two different levels (low

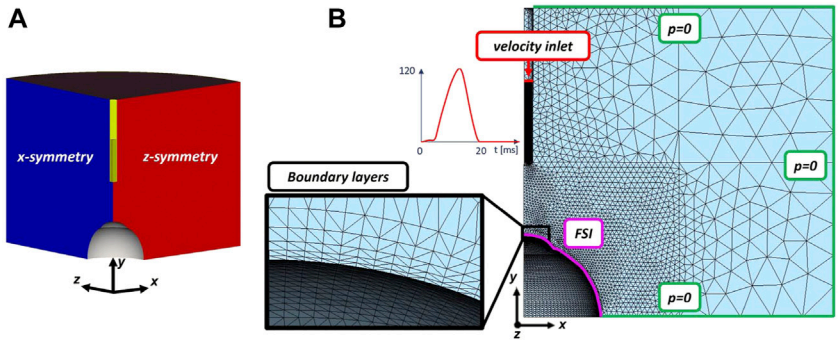

FIGURE 2
(A) 3D air domain with two symmetric planes; **(B)** surface mesh of the fluid domain with a zoom of the mesh on the five boundary layers at the FSI interface. Air velocity inlet in m/s (in red), pressure outlets (in green) and the FSI interface (in purple) are drawn.

TABLE 3 Low and high parameters tested in the material sensitivity analysis.

Material sensitivity analysis

	Cornea		Sclera	Intraocular pressure
Matrix stiffness	Fibres stiffness	Fibres non linearity	Matrix stiffness	
C_{10-c} [MPa]	k_1 [MPa]	k_2 [-]	C_{10-s} [MPa]	IOP [mmHg]
0.25–0.75	0.005–0.015	50–150	0.4–1.2	8–22

and high) for a total of 32 different analysis is used. Data adopted in the analysis are reported in Table 3. The IOP and the material parameters are considered within a 50% of variation relative to the reference value. For each case, the air-puff FSI analysis as described in Section 2.3 is carried out and three biomarkers of the Corvis clinical test are examined:

- The deflection amplitude that is the displacement of the corneal apex at the instant of highest concavity and it gives information about the amplitude of the deformation of the cornea (Lopes et al., 2021) (Figure 6).
- The peak distance i.e., the distance between the two bending peaks on the cornea's anterior surface at the instant of highest concavity. This markers gives information about the shape of the deformed cornea (Lopes et al., 2021) (Figure 6).
- The air pressure at the apex of the cornea at the instant of highest concavity.

To study the main effects and the interaction effects of the input parameters on the responses, an ANOVA analysis is conducted by means of R-studio (RStudio Team, 2020).

2.5 Influence of the internal structures

A FSI analysis of the NCT without the internal structures of the eye (lens, zonule and vitreous membrane) is also conducted to evaluate their influence on three selected biomarkers. The variation of the IOP during the simulation, the deflection amplitude and the peak distance are compared with the same parameters of the simulation including the internal structures.

All the simulations described were performed using an Intel i9-10940X (3.30 GHz) with the finite-element solver LS-Dyna R 13.0 (LSTC, Livermore CA, United States) Dataset, 2021. The structural part is solved through a dynamic implicit structural solver, where as the air is modelled as an incompressible fluid and solved using the implicit ICFD solver ICF (2021).

3 Results

3.1 Mesh sensitivity analysis

The results for the mesh sensitivity analysis are reported in Figure 3. As expected, the simulation time increases with the

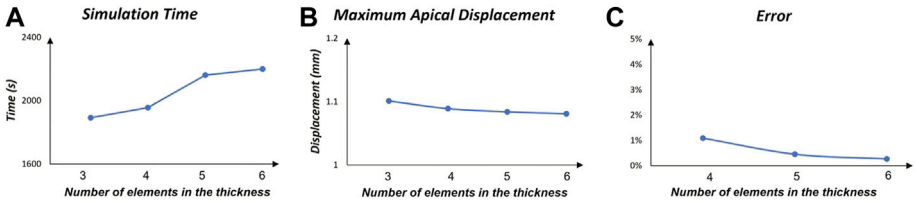

FIGURE 3
Mesh sensitivity analysis. The graphs are functions of the number of elements in the thickness. **(A)** Simulation time; **(B)** Displacement of the apex at the instant of maximum concavity; **(C)** Percentage error between consecutive mesh.

number of degrees of freedom in the model. The maximum apical displacement in the four cases ranges between 1.08 and 1.10 mm with the maximum error of 1.1% between the coarsest mesh and the mesh with four elements in the thickness. Based on the mesh convergence study, the mesh with five elements in the thickness is chosen for all the FSI simulations, which shows an error below 1%.

3.2 Fluid analysis

In order to test the imposed boundary condition of the air-puff, a simulation of the air-puff with the fluid domain defined as described in paragraph 2.3 but without the eye has been carried out, to reproduce the results in Roberts et al. (Roberts et al., 2017). The fluid velocity during the air-puff at different distances from the nozzle along the centerline is recorded and reported in Figure 4. The range of the peak velocity (from 130.55 m/s at 2 mm to 119.9 m/s at 10 mm) from the numerical simulation was within the range reported in the experiments (from 133.57 m/s at 2 mm to 127.43 m/s at 10 mm) indicating that the time velocity profile used as boundary condition was appropriate to describe the air-puff.

3.3 FSI analysis

One of the main objectives of the NCT is the evaluation of the IOP based on the Imbert-Fick principle, which states that in a flattened spherical body with an infinitely thin, dry, and elastic membrane wall, the internal pressure equals the force applied on the body divided by the applanation surface. Knowing the pressure exerted by the air puff and the applanation area derived from the images of Corvis ST Scheimpflug camera, the IOP is derived (Gonzalez Castro et al., 2016). Our simulation shows that the IOP varies during the NCT (Figure 5A). Since the eye is a closed volume filled with incompressible fluids, when the air jet deforms the corneal surface, the IOP increases reaching 22.5 mmHg (+50%).

On the air side, the pressure-time variation at the corneal apex during the air-puff is shown in Figure 5B. The maximum pressure in the apex, 152 mmHg, corresponds with the instant of maximum concavity of the cornea (t = 55 ms). The air pressure exerted over the corneal surface is reported in Figure 5C for A1, A2 and HC as a function of the distance from the apex. As expected, the maximum pressure is located at the apex of the cornea to then decrease. In the three cases, the pressure is zero for a distance from the apex higher than 5.5 mm, meaning that from this position, the eye does not

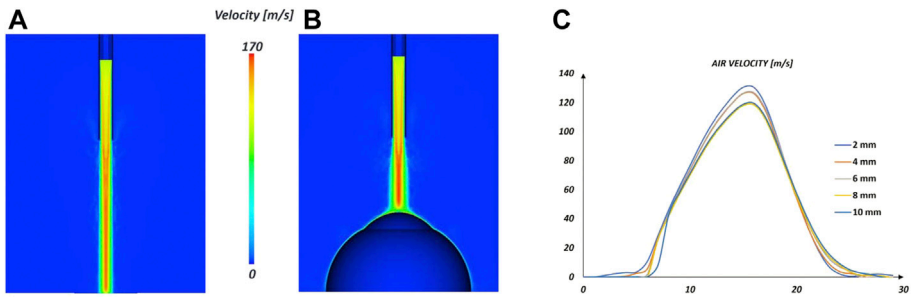

FIGURE 4
Fluid analysis: contour of the air peak velocity in the CFD simulation without the eye shape **(A)** and with the eye shape **(B)**. Centerline velocity distribution as a function of distance from the nozzle used to test the fluid parameters in the case without the eye shape.

perceive directly the air jet, the pressure component is negligible, and the flow follows the eye shape. In the instant of HC, there is a region where the air pressure is negative lending support to previous findings in the literature (Muench et al., 2019) (Ariza-Gracia et al., 2018) (Maklad et al., 2020a). Negative pressure occurs if the fluid reflects from the corneal surface in the opposite direction to the flow, causing the change of concavity of the cornea in the deformed state (Figure 5D, curve HC). The maximum pressure at A1 is higher than the maximum pressure at A2, due to the energy loss caused by the damping of the cornea and the deceleration of the air-jet during this phase of the test.

The deformation profile of the cornea is reported in Figure 5D where it is possible to appreciate the difference between the undeformed shape of the cornea's central section in the zero-pressure configuration, in the pressurized configuration, and in the instant of highest concavity (HC). In the instant of HC, the deflection amplitude of the apex is 1.14 mm found to be within the range of clinical data (1.09 ± 0.10). (Roberts et al., 2017).

The contours of the air velocity in three significant points of the simulation are reported in Figure 6. In the instant of highest concavity the velocity (172 m/s) is higher than the inlet velocity due to an acceleration caused by the turbulent flow and the obstacle that the air meets, the eye structure.

Physiologically, the cornea works in tension because of the IOP. However, during the air-puff, the cornea undergoes bending, therefore its anterior surface changes its state of tension to a compression state, whereas the posterior surface carries on working under tension as shown in the contour of the stress at the instant of HC (Figure 7). This means that the collagen fibres in the anterior surface do not contribute to load bearing during most of the duration of the air-puff, relying in this case on the mechanical properties of the matrix under compression. The evolution of the normal stress and strain values of two points of the apex (anterior and posterior surfaces) is plotted in Figure 7. As anticipated, the plot demonstrates the contribution of the collagen fibres when the cornea is subjected to tension because, after a first response of the matrix, a stiffer behaviour is reported. In compression (blue values), only the matrix contribution is present resulting in a more compliant response.

3.4 Material and IOP sensitivity analysis

The results of the ANOVA analysis for the biomarkers are reported in Table 4 and Table 5. For both the deflection amplitude and the peak distance, the IOP is the most important parameter followed by the matrix stiffness of the cornea, C_{10-c}, with the other material parameters having little effect on the response. However, the effect size of the IOP is more than tenfold the size effect of C_{10-c}. However, this could be associated with the relatively large range of IOP considered in the

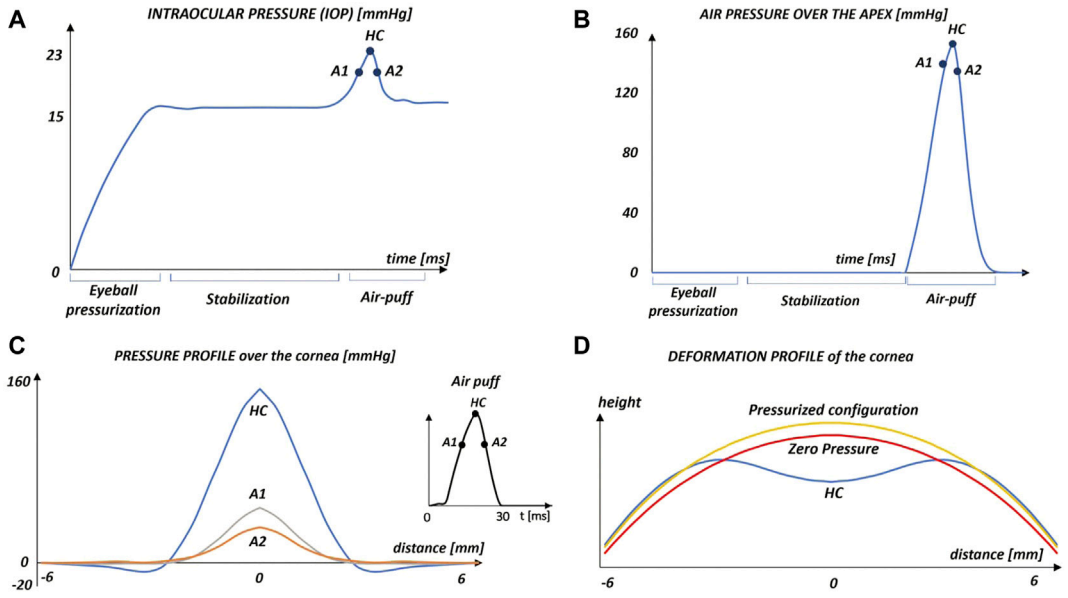

FIGURE 5
Results of the FSI simulation: **(A)** variation of the intraocular pressure (IOP) during the NCT simulation. The first applanation point (A1), highest concavity point (HC) and second applanation point (A2) are highlighted; **(B)** air pressure over the corneal anterior surface during the NCT simulation.**(C)** pressure profile over the cornea in three significant instants of the simulation as a function of the distance from the apex; **(D)** profile of the cornea in the zero pressure configuration, with an intraocular pressure of 15 mmHg and at the instant of highest concavity (HC).

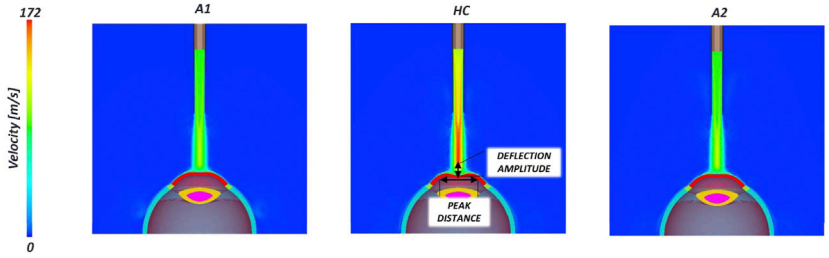

FIGURE 6
Air velocity contour in three-time points (A1, HC and A2) during the air-puff. In the instant of highest concavity two biomarkers (peak distance and deflection amplitude) are highlighted.

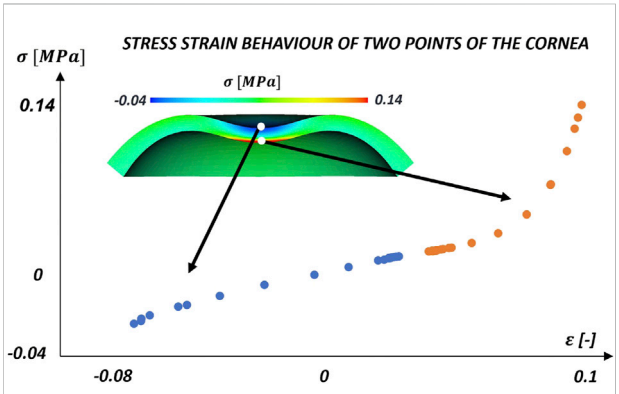

FIGURE 7
Evolution of normal stresses and strains at two locations (anterior and posterior) during the air puff. At the beginning of the air-puff both points are at a tension state due to the IOP. Then, during the air-puff, the anterior surface works in compression (blue) and the posterior in tension (red) with the contribution of the collagen fibres.

TABLE 4 Analysis of variance (ANOVA) results on the deflection amplitude. Degrees of freedom (DF) and Effect size.

ANOVA for the deflection amplitude

Source	DF	Effect
Linear	5	
C_{10-c}	1	0.27
k_1	1	0.03
k_2	1	0.14
C_{10-s}	1	0.14
IOP	1	4.01
2-way interactions	2	
C_{10-c}· IOP	1	0.03
C_{10-s}· IOP	1	0.03

TABLE 5 Analysis of variance (ANOVA) results on the peak distance biomarker. Degrees of freedom (DF) and Effect size.

ANOVA for the peak distance

Source	DF	Effect
Linear	5	
C_{10-c}	1	0.86
k_1	1	0.17
k_2	1	0.37
C_{10-s}	1	0.15
IOP	1	17.05

design of experiments. The results from the ANOVA also indicate a little interaction between the effects, being the C_{10-c}· IOP interaction and the C_{10-s}· IOP the most important, though very low with respect the effect of the singles (see Table 4.

The Pearson correlation matrix in Figure 8 reports the results for the statistical analysis conducted. The dimension of each circle is related to the correlation between the factors of the design of experiment (C_{10-c}, k_1, k_2, C_{10-s}, IOP) and the dependent variables considered (deflection amplitude, peak distance, and air pressure over the apex). The colour of each circle tells whether the linear correlation is direct (blue) or inverse (red). The most important result that emerges from the data is the inverse correlation between the IOP and the deflection amplitude and the peak distance. As the IOP increases, the air pressure encounters a higher mechanical resistance, the deformation of the cornea is lower and, as a consequence, the deflection amplitude and the peak distance are lower. The figure also shows that the maximum air-pressure at the corneal apex is little influenced by the IOP and the material properties of the cornea and sclera.

Given that these findings are based on two IOP levels of 8 and 22 mmHg, (values reached when the intraocular pressure is very

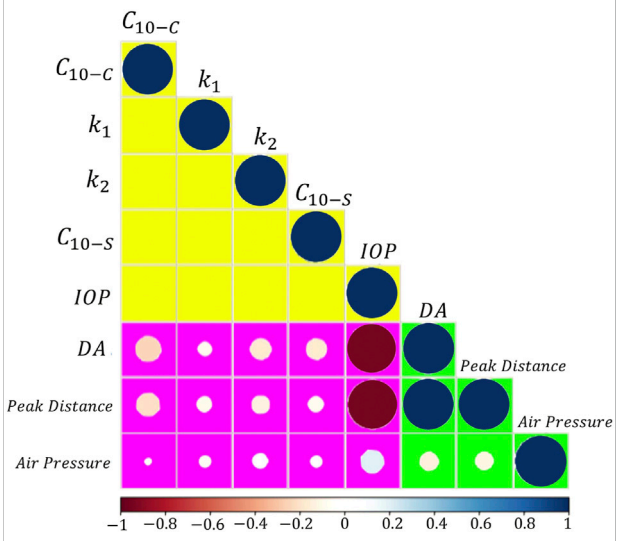

FIGURE 8
Pearson correlation matrix (full-level factorial design, $2^5 = 32$). Factors: matrix stiffness of the cornea (C_{10-C}), fibres stiffness of the cornea (k_1), fibres non linearity of the cornea (k_2), matrix stiffness of the sclera (C_{10-s}), intraocular pressure (IOP). Output parameters: deflection amplitude (DA), peak distance and air pressure over the cornea at the instant of maximum concavity. The colour of each circle depicts whether the linear correlation is direct (positive) or inverse (negative) (blueish palette, direct; reddish palette, inverse). The larger the circle diameter, the higher the correlation.

low and when the patient presents glaucoma), a further analysis is conducted with the IOP ranging between 12 and 15 mmHg (the physiological range) and all the other parameters as described in Section 2.3. The main effect of the parameters on the deformation amplitude and the peak distance is shown in Figure 9. Each line depicts the difference in the mean response between the two levels of a factor, as long as each point represents the mean result for one level of a factor. The horizontal line indicate the average for all runs.

The results obtained for this reduced range of IOP are consistent with those shown in Figure 8, i.e., an inverse relationship with the corneal displacement and peak distance. However, within the physiological range of the IOP, the mechanical properties of the sclera have the same influence as the corneal matrix stiffness, whereas the anisotropic component of the cornea appears to plays a more important role on the corneal deformation against an air-puff.

3.5 Influence of the internal structures

The results for the analysis of the influence of the internal structures of the eye is reported in Table 6. The influence of the crystalline lens, the ciliary zonule and the vitreous membrane on the biomarkers was found to be always below 5%, meaning that they could be removed from the model improving the computational efficiency.

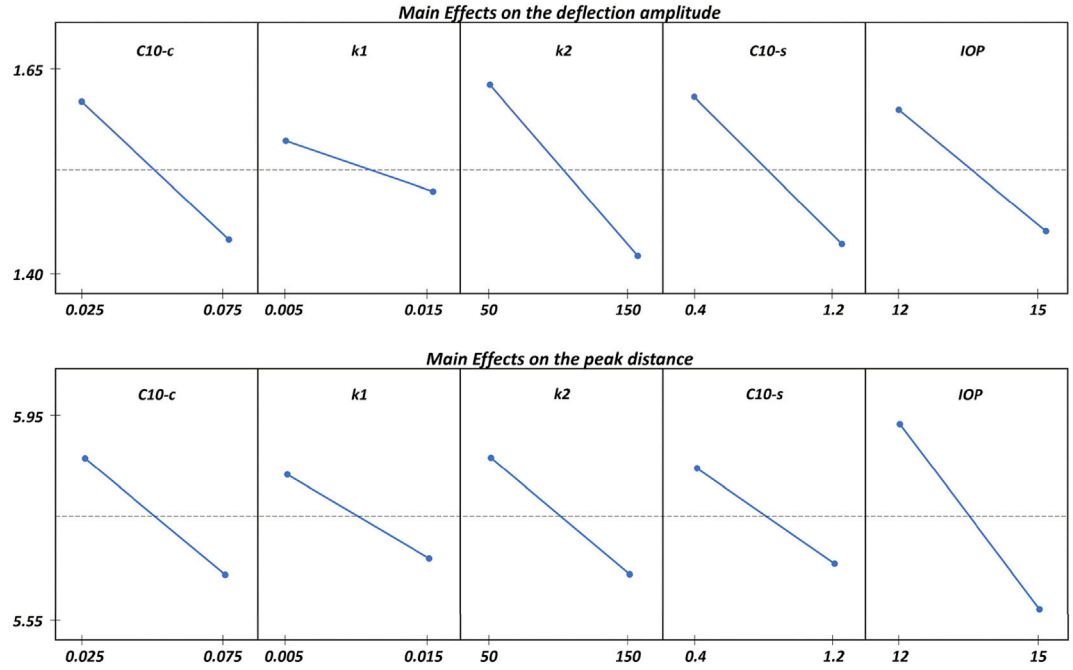

FIGURE 9
Main Effects plot of the analysed factors on the deflection amplitude and on the peak distance. All the parameters show an inverse influence on the results.

TABLE 6 Influence of the internal structure of the eye on the biomarkers.

Influence of the internal structures of the eye

Biomarker	With internal structures	Without internal structures	Error (%)
IOP max	22.40 mmHg	23.25 mmHg	3.7
Deflection amplitude	1.402 mm	1.445 mm	3
Peak distance	5.54 mm	5.60 mm	1.16

4 Discussion

The deformation of the cornea during the NCT stems from the combination of different biomechanical factors; hence, to identify the influence of each factor, an *in silico* study is necessary. To the best of the authors knowledge, this paper is the first to propose a complete methodology capable to model the NCT using FSI considering an anisotropic formulation for the cornea and a complete fluid domain for the air. The results confirm the need of using FSI for the correct simulation of NTC as stated in Ariza Gracia et al. (Ariza-Gracia et al., 2018). The use of FSI, instead of only structural FEA, is key to capture the correct air pressure distribution over the cornea during the air-puff. The simulations show that the interaction of the air-puff with the deformable cornea causes a confinement of the flow in the proximity of the cornea (about 3.5 mm from the corneal apex) that increases the velocity of the jet-stream near the centerline with respect to what is seen in a free-flow condition (without obstacles) shown in Figure 4. This increment in the kinetic energy of the flow causes that the maximum pressure in the cornea reaches values of 152 mmHg, coincident with the moment when the air-puff reaches the maximum speed. Previous works estimated the pressure profile in the cornea as the dynamic pressure associated with the air-puff velocity profile (Ariza-Gracia et al., 2015) (Nguyen et al., 2019). However, doing so, the maximum pressure on the cornea maybe greatly underestimated as demonstrated in this study where the dynamic pressure associated with a velocity of 120 m/s results in 67 mmHg, almost half of the pressure obtained with the FSI analysis. The FSI proposed is 2-way and strongly coupled, thus iteratively the solid mechanics solver transfers the displacements of the eyeball to the fluid solver while the fluid solver transfers the air pressure to the solid mechanics solver. Thanks to this interaction, it is possible to appreciate the negative pressure in correspondence to the corneal peaks at the instant of maximum concavity, thus the dependence of the pressure on the biomechanical behaviour of the eyeball tissues.

The sensitivity analysis demonstrates the important role of the IOP on the corneal biomarkers during NTC. This effect has been found to be comparable to the effect of the material properties of the cornea and the sclera as reported in previous studies based on structural analysis (Ariza-Gracia et al., 2016) (Ariza-Gracia M.Á. et al., 2017). These results demonstrate the interplay between the mechanical properties of the eye and the IOP and the importance of taking into account this interaction when interpreting the results from a NTC test. Regarding the influence of the material properties, the sensitivity analysis confirms the results from (Ariza-Gracia et al., 2016) (Ariza-Gracia M.Á. et al., 2017) about the importance that corneal anisotropy has on the corneal biomarkers extracted during a NCT test, in particular for values of the IOP within the physiological range. This demonstrates the need of accounting for the anisotropic behaviour of the cornea in the models of the eye. At the instant of maximum concavity, the anterior surface of the corneal section works under compression, whereas the posterior surface works under tension. During tension, the collagen fibres are recruited which increases the corneal stiffness, and the load bearing capacity of the tissue. In fact, the material sensitivity analysis shows a contribution of the fibres parameters on the deformation amplitude and on the peak distance comparable to the extracellular matrix of the cornea.

Another remarkable result emerging from the material sensitivity analysis is the importance of the sclera: the stiffer the sclera, the lower the corneal deformation to the air-puff. Nguyen et al. (Nguyen et al., 2019) reported a similar trend in a computational-experimental work with *ex-vivo* human donor eyes. This indicates that an accurate model of the eye-ball to simulate the response to an air-puff should incorporate the sclera since otherwise the corneal displacements will be understimated. On the contrary, the sensitivity analysis shows a negligible effect of the remaining internal structures of the eye i.e., crystalline lens, ciliary zonule and vitreous membrane. This occurs in great part because of the lower stiffness of the components as happens with the zonule and the vitreous membrane which cause the crystalline lens to show a rigid body like motion during the NTC test (see the video in the support material section). Hence, depending on the aim of the simulation, the internal structure could be neglected. Last but not least, the simulation corroborates the findings from Montanino et al. (Montanino et al., 2018) (Montanino et al., 2019) and Ariza et at (Ariza-Gracia et al., 2018). that the humors need to be modelled as a fluid-like material with a specific density when simulating a NCT test. Since the eye-ball is a closed system and the humors behave as an incompressible fluid, the deformation of the cornea during the air-puff causes an increase in the IOP up to a 50% of the nominal value. Most experimental works regarding indentation (Ariza-Gracia M. et al., 2017) (Ortillés et al., 2017) or NTC (Nguyen

et al., 2019) tests, impose a constant pressure in the eye-ball during the test by means of a column of water, which makes the humor to behave as an open system, contrary to what really happens during the actual test. The important influence that IOP has on the deformation of the cornea during the air-puff, makes that considering it as constant in the simulation causes an understimation of the corneal deformation, and therefore to overstimate the corneal stiffenss as a consequence.

The analysis is not absent of limitations. This study is based on an idealized geometry and the carried out sensitivity analysis did not consider the variability in the geometry which may significantly affect corneal deformation as shown in (Ariza-Gracia et al., 2015) (Ariza-Gracia et al., 2016) (Ariza-Gracia M.Á. et al., 2017). Further studies considering patient-specific geometries will be performed in order to quantify the variability in corneal biomarkers associated with the intrinsic geometric variability of the eye-ball. Also, two uniformly distributed families of fibers have been considered in the model (one in the nasal-temporal direction and another in the superior-inferior direction) ignoring the collagen fiber dispersion present in the human cornea (Pandolfi and Holzapfel, 2008; Meek and Boote, 2009). This issue will be accounted for in future developments. Moreover, although the analysis reveals that the removal of the internal structures produces a $<5\%$ change in the data of interest, the influence of the ciliary body in the eye-ball response to an air-puff should be further investigated. Lastly, a future line of the work could be the simulation of the whole eye movement during the air puff incorporating in the model also the posterior half of the eye globe.

5 Conclusion

This paper has highlighted the importance of conducting an FSI simulation to model the NCT. Moreover, it has underlined that the humors should be modeled as a fluid rather than a constant homogeneous pressure. As the results pointed out, the corneal deformation is strongly influenced by the mechanical properties of the cornea and the sclera, therefore a correct formulation for both parts must be included in the simulation. In particular, an anisotropic material is mandatory for the cornea.The simulation proposed can be used as starting point for further analysis regarding the study of eye biomechanics based on clinical data. Future works in modeling the non-contact tonometry should be addressed to patient-specific simulations with the correct corneal geometry and material properties. Last but not least, since for a given geoemetry i.e., a patient specific geometry, the biomarkers derived from the NCT depend mainly on the material parameters of the cornea and sclera, it would be possible to apply the inverse finite element method to find the mechanical properties of these tissues for *in vivo* characterization.

Data availability statement

The original contributions presented in the study are included in the article/Supplementary Material, further inquiries can be directed to the corresponding author.

Author contributions

ER developed the finite-element simulation with the supervision of GL and the help of JFRM; BC helped supervise the research project; JG was in charge of overall direction and planning. All authors gave final approval for publication and agree to be held accountable for the work performed therein.

Funding

This project has received funding from the European Union's Horizon 2020 research and innovation program under the Marie Skłodowska-Curie grant agreement No 956720, grant PID 2020-113822RB-C21 funded by MCIN/AEI/10.13039/501100011033 and the Department of Industry and Innovation (Government of Aragon) through the research group Grant T24-20R (cofinanced with Feder 2014-2020: Construyendo Europa desde Aragon). Part of the work was performed by the ICTS "NANBIOSIS" specifically by the High Performance Computing Unit (U27), of the CIBER in Bioengineering, Biomaterials & Nanomedicne (CIBER-BBN at the University of Zaragoza).

Conflict of interest

The authors declare that the research was conducted in the absence of any commercial or financial relationships that could be construed as a potential conflict of interest.

Publisher's note

Supplementary material

The Supplementary Material for this article can be found online at: https://www.frontiersin.org/articles/10.3389/fbioe.2022.981665/full#supplementary-material

References

Ariza-Gracia, M. Á., Redondo, S., Llorens, D. P., Calvo, B., and Matas, J. F. R. (2017b). A predictive tool for determining patient-specific mechanical properties of human corneal tissue. *Comput. methods Appl. Mech. Eng.* 317, 226–247. doi:10.1016/j.cma.2016.12.013

Ariza-Gracia, M. Á., Wu, W., Calvo, B., Malvè, M., Büchler, P., and Matas, J. F. R. (2018). Fluid–structure simulation of a general non-contact tonometry. a required complexity? *Comput. methods Appl. Mech. Eng.* 340, 202–215. doi:10.1016/j.cma.2018.05.031

Ariza-Gracia, M. Á., Zurita, J. F., Piñero, D. P., Rodriguez-Matas, J. F., and Calvo, B. (2015). Coupled biomechanical response of the cornea assessed by non-contact tonometry. a simulation study. *PloS one* 10, e0121486. doi:10.1371/journal.pone.0121486

Ariza-Gracia, M. Á., Zurita, J., Piñero, D. P., Calvo, B., and Rodríguez-Matas, J. F. (2016). Automatized patient-specific methodology for numerical determination of biomechanical corneal response. *Ann. Biomed. Eng.* 44, 1753–1772. doi:10.1007/s10439-015-1426-0

Ariza-Gracia, M., Ortillés, Á., Cristóbal, J., Matas, J. R., and Calvo, B. (2017a). A numerical-experimental protocol to characterize corneal tissue with an application to predict astigmatic keratotomy surgery. *J. Mech. Behav. Biomed. Mater.* 74, 304–314. doi:10.1016/j.jmbbm.2017.06.017

Ávila, F. J., Marcellán, M. C., and Remón, L. (2021). On the relationship between corneal biomechanics, macrostructure, and optical properties. *J. Imaging* 7, 280. doi:10.3390/jimaging7120280

Blackburn, B. J., Jenkins, M. W., Rollins, A. M., and Dupps, W. J. (2019). A review of structural and biomechanical changes in the cornea in aging, disease, and photochemical crosslinking. *Front. Bioeng. Biotechnol.* 7, 66. doi:10.3389/fbioe.2019.00066

Cabeza-Gil, I., Grasa, J., and Calvo, B. (2021). A validated finite element model to reproduce helmholtz's theory of accommodation: A powerful tool to investigate presbyopia. *Ophthalmic Physiol. Opt.* 41, 1241–1253. doi:10.1111/opo.12876

Chong, J., and Dupps, W. J., Jr (2021). Corneal biomechanics: Measurement and structural correlations. *Exp. Eye Res.* 205, 108508. doi:10.1016/j.exer.2021.108508

[Dataset] (2021). *Ls-dyna*. Computer Software.

[Dataset] Oculus (2021). *Corvis® ST - tonometer - highlights - oculus optikgeräte gmbh*.

Eilaghi, A., Flanagan, J. G., Tertinegg, I., Simmons, C. A., Brodland, G. W., and Ethier, C. R. (2010). Biaxial mechanical testing of human sclera. *J. biomechanics* 43, 1696–1701. doi:10.1016/j.jbiomech.2010.02.031

Eliasy, A., Chen, K.-J., Vinciguerra, R., Lopes, B. T., Abass, A., Vinciguerra, P., et al. (2019). Determination of corneal biomechanical behavior *in-vivo* for healthy eyes using corvis st tonometry: Stress-strain index. *Front. Bioeng. Biotechnol.* 7, 105. doi:10.3389/fbioe.2019.00105

Esporcatte, L. P. G., Salomão, M. Q., Lopes, B. T., Vinciguerra, P., Vinciguerra, R., Roberts, C., et al. (2020). Biomechanical diagnostics of the cornea. *Eye Vis. (Lond).* 7, 9–12. doi:10.1186/s40662-020-0174-x

Gonzalez Castro, G., Fitt, A. D., and Sweeney, J. (2016). On the validity of the imbert-fick law: Mathematical modelling of eye pressure measurement. *World J. Mech.* 6, 35–51. doi:10.4236/wjm.2016.63005

Holzapfel, G. A., Gasser, T. C., and Ogden, R. W. (2000). A new constitutive framework for arterial wall mechanics and a comparative study of material models. *J. Elast.* 61, 1–48. doi:10.1023/a:1010835316564

Hong, J., Xu, J., Wei, A., Deng, S. X., Cui, X., Yu, X., et al. (2013). A new tonometer—the corvis st tonometer: Clinical comparison with noncontact and goldmann applanation tonometers. *Invest. Ophthalmol. Vis. Sci.* 54, 659–665. doi:10.1167/iovs.12-10984

Huang, L., Shen, M., Liu, T., Zhang, Y., and Wang, Y. (2020). Inverse solution of corneal material parameters based on non-contact tonometry: A comparative study of different constitutive models. *J. Biomechanics* 112, 110055. doi:10.1016/j.jbiomech.2020.110055

ICFD Theory Manual - Incompressible fluid solver in LS-DYNA (2021). n.d.

Issarti, I., Koppen, C., and Rozema, J. J. (2021). Influence of the eye globe design on biomechanical analysis. *Comput. Biol. Med.* 135, 104612. doi:10.1016/j.compbiomed.2021.104612

Kim, Y., Roy, S., Jung, G.-Y., Oh, J.-S., and Kim, G.-W. (2019). Dual optical signal-based intraocular pressure-sensing principle using pressure-sensitive mechanoluminescent Zns: Cu/pdms soft composite. *Sci. Rep.* 9 (01), 1–10. doi:10.1038/s41598-019-51771-z

Kling, S., and Hafezi, F. (2017). Corneal biomechanics–a review. *Ophthalmic Physiol. Opt.* 37, 240–252. doi:10.1111/opo.12345

Krag, S., and Andreassen, T. T. (2003). Mechanical properties of the human lens capsule. *Prog. Retin. eye Res.* 22, 749–767. doi:10.1016/s1350-9462(03)00063-6

Lopes, B. T., Bao, F., Wang, J., Liu, X., Wang, L., Abass, A., et al. (2021). Review of *in-vivo* characterisation of corneal biomechanics. *Med. Nov. Technol. Devices* 11, 100073. doi:10.1016/j.medntd.2021.100073

Maklad, O., Eliasy, A., Chen, K.-J., Theofilis, V., and Elsheikh, A. (2020a). Simulation of air puff tonometry test using arbitrary Lagrangian–eulerian (ale) deforming mesh for corneal material characterisation. *Int. J. Environ. Res. Public Health* 17, 54. doi:10.3390/ijerph17010054

Maklad, O., Eliasy, A., Chen, K.-J., Wang, J., Abass, A., Lopes, B. T., et al. (2020b). Fluid-structure interaction based algorithms for iop and corneal material behavior. *Front. Bioeng. Biotechnol.* 8, 970. doi:10.3389/fbioe.2020.00970

Meek, K. M., and Boote, C. (2009). The use of x-ray scattering techniques to quantify the orientation and distribution of collagen in the corneal stroma. *Prog. Retin. eye Res.* 28, 369–392. doi:10.1016/j.preteyeres.2009.06.005

Meek, K. M., and Knupp, C. (2015). Corneal structure and transparency. *Prog. Retin. eye Res.* 49, 1–16. doi:10.1016/j.preteyeres.2015.07.001

Montanino, A., Angelillo, M., and Pandolfi, A. (2019). A 3d fluid-solid interaction model of the air puff test in the human cornea. *J. Mech. Behav. Biomed. Mater.* 94, 22–31. doi:10.1016/j.jmbbm.2019.02.030

Montanino, A., Angelillo, M., and Pandolfi, A. (2018). Modelling with a meshfree approach the cornea-aqueous humor interaction during the air puff test. *J. Mech. Behav. Biomed. Mater.* 77, 205–216. doi:10.1016/j.jmbbm.2017.05.042

Muench, S., Roellig, M., Spoerl, E., and Balzani, D. (2019). Numerical and experimental study of the spatial stress distribution on the cornea surface during a non-contact tonometry examination. *Exp. Mech.* 59, 1285–1297. doi:10.1007/s11340-018-00449-0

Nguyen, B. A., Roberts, C. J., and Reilly, M. A. (2019). Biomechanical impact of the sclera on corneal deformation response to an air-puff: A finite-element study. *Front. Bioeng. Biotechnol.* 6, 210. doi:10.3389/fbioe.2018.00210

Ortillés, Á., Rodríguez-Matas, J. F., Ariza-Gracia, M. Á., Pascual, G., and Calvo, B. (2017). Why non-contact tonometry tests cannot evaluate the effects of corneal collagen cross-linking. *J. Refract. Surg.* 33, 184–192. doi:10.3928/1081597x-20161206-02

Pandolfi, A., and Holzapfel, G. A. (2008). Three-dimensional modeling and computational analysis of the human cornea considering distributed collagen fibril orientations. *J. Biomech. Eng.* 130, 061006. doi:10.1115/1.2982251

Rahmati, S. M., Razaghi, R., and Karimi, A. (2021). Biomechanics of the keratoconic cornea: Theory, segmentation, pressure distribution, and coupled fe-optimization algorithm. *J. Mech. Behav. Biomed. Mater.* 113, 104155. doi:10.1016/j.jmbbm.2020.104155

Roberts, C. J., Mahmoud, A. M., Bons, J. P., Hossain, A., Elsheikh, A., Vinciguerra, R., et al. (2017). Introduction of two novel stiffness parameters and interpretation of air puff–induced biomechanical deformation parameters with a dynamic scheimpflug analyzer. *J. Refract. Surg.* 33, 266–273. doi:10.3928/1081597x-20161221-03

RStudio Team (2020). *RStudio*. Boston, MA: Integrated Development Environment for R. RStudio, PBC.

Wilde, G., Burd, H., and Judge, S. (2012). Shear modulus data for the human lens determined from a spinning lens test. *Exp. eye Res.* 97, 36–48. doi:10.1016/j.exer.2012.01.011

Frontiers in
Bioengineering and Biotechnology

Accelerates the development of therapies, devices, and technologies to improve our lives

A multidisciplinary journal that accelerates the development of biological therapies, devices, processes and technologies to improve our lives by bridging the gap between discoveries and their application.

Discover the latest Research Topics

See more →

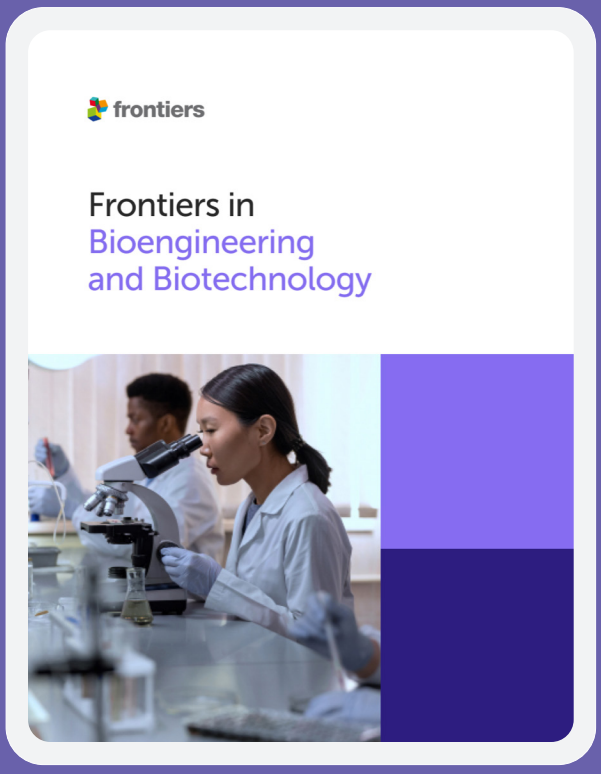

Frontiers

Avenue du Tribunal-Fédéral 34
1005 Lausanne, Switzerland
frontiersin.org

Contact us

+41 (0)21 510 17 00
frontiersin.org/about/contact